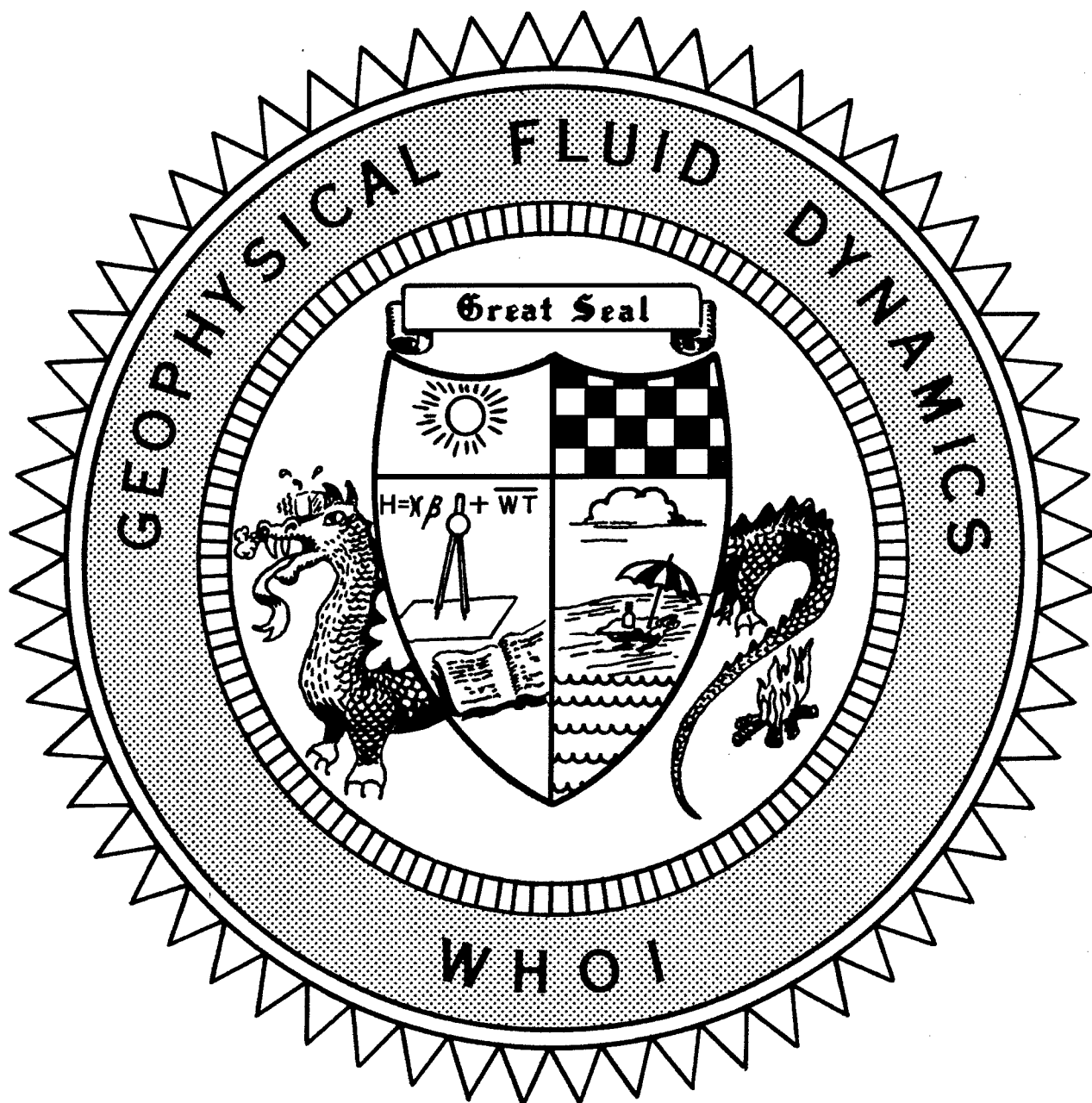


***2005 Program of Study: Fast Times and Fine Scales***



20060731024

**Course Lectures  
Fellows Project Reports**

WHOI-2006-12

**2005 Program of Studies: Fast Times and Fine Scales**

by

Oliver Buhler and Charles Doering, Co-Directors;  
Joseph Keller, George C. Papanicolaou and Eric Vanden Eijnden, Principal Lecturers

July 2006

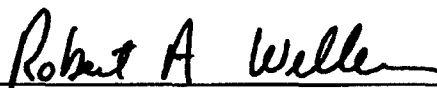
**Technical Report**

Funding was provided by the National Science Foundation under Contract No. OCE 03-25296.

Reproduction in whole or in part is permitted for any purpose of the United States Government. This report should be cited as Woods Hole Oceanog. Inst. Tech. Rept., WHOI-2006-12.

Approved for public release; distribution unlimited.

**Approved for Distribution:**

A handwritten signature in black ink, reading "Robert A. Weller", is written over a horizontal line.

**Robert A. Weller, Chair**

Department of Physical Oceanography

This page intentionally left blank.

## Abstract

The 2005 GFD program was entitled "Fast Times and Fine Scales" with a focus on asymptotic and stochastic modeling methods that exploit a physical scale separation of some kind. An extremely strong application pool resulted in the appointment of the unusually large class of eleven GFD Fellows for the summer. The first week consisted of principal lectures from Joe Keller on waves in fluids, ray methods, and a variety of applications. The second week was divided between Eric Vanden-Eijnden's lectures on Brownian motion and stochastic differential equations, and George Papanicolaou's lectures on variational principles and asymptotic methods in homogenization theory. The principal lectures were particularly well-attended but the lecture room at Walsh Cottage proved up to the task of accommodating the full audience.

Research lectures by staff and visitors were delivered daily throughout the program addressing topics ranging from applications of multiscale modeling methods in ocean and atmosphere dynamics, to applications of stochastic methods in populations dynamics and chemical kinetics, to applications of homogenization theory in materials science and engineering. The program also included a popular public lecture on the timely subject of tsunamis. As usual this summer ended with the Fellows' reports including two experimental projects and theoretical work on a variety of problems inspired by the summer's research theme.

Oliver Bühler and Charlie Doering acted as co-Directors for the summer. Janet Fields, Jeanne Fleming and Penny Foster provided the administrative backbone for the program. Keith Bradley supplied technical support, and Matt Finn ran the computer network and graciously helped with the production of the summer's proceedings volume. As always we are grateful to Woods Hole Oceanographic Institution for the use of Walsh Cottage, the perfect setting for the GFD program.



## TABLE OF CONTENTS

I	ABSTRACT.....	i
	TABLE OF CONTENTS .....	ii
II	PARTICIPANTS.....	v
III	LECTURE SCHEDULE .....	ix
IV	PRINCIPAL LECTURES	
	Presented by Joseph Keller, Stanford University, Eric Vanden Eijnden, Courant Institute, New York University, George C. Papanicolaou, Stanford University	
	Lecture 1: <b><i>Fluid Equations</i></b> Joseph Keller .....	1
	Lecture 2: <b><i>Gravity Waves and the Method of Stationary Phase</i></b> Joseph Keller .....	8
	Lecture 3: <b><i>Asymptotic Methods for the Reduced Wave Equation</i></b> Joseph Keller .....	14
	Lecture 4: <b><i>Geometrical Theory of Diffraction (continued) and the Shallow Water Theory</i></b> Joseph Keller .....	22
	Lecture 5: <b><i>Amplitude Dynamics, Boundary Layers and Harbor Resonance</i></b> Joseph Keller .....	33
	Lecture 6: <b><i>Wiener Process</i></b> Eric Vanden-Eijnden .....	50
	Lecture 7: <b><i>Stochastic Integrals and Stochastic Differential Equations</i></b> Eric Vanden-Eijnden .....	57
	Lecture 8: <b><i>Asymptotic Techniques for SDEs</i></b> Eric Vanden-Eijnden .....	65

Lecture 9:	
<b><i>The Use of Variational Methods for High-Contrast Conductivity Problems</i></b>	
George C. Papanicolaou .....	73
Lecture 10:	
<b><i>Convection-Diffusion Problems</i></b>	
George C. Papanicolaou .....	81
Lecture 11:	
<b><i>Analysis of the Childress Cell Problem and Stability of Cellular Flows</i></b>	
George C. Papanicolaou .....	87

## V FELLOW'S REPORTS

Report One:	
<b><i>Shallow Water through a Contraction</i></b>	
Benjamin Akers, University of Wisconsin, Madison .....	97
Report Two:	
<b><i>Bounds on Multiscale Mixing Efficiencies</i></b>	
Tiffany Shaw, University of Toronto, Canada .....	118
Report Three:	
<b><i>Transport in Cellular Flows from the Viewpoint of Stochastic Differential Equations</i></b>	
Walter Pauls, University of Nice, France .....	144
Report Four:	
<b><i>Scattering Past a Cylinder with Weak Circulation</i></b>	
John Rudge, University of Cambridge, U.K. ....	157
Report Five:	
<b><i>Fluctuations in Chemical Reactions in a Large Volume</i></b>	
Khachik Sargsyan, University of Michigan .....	180
Report Six:	
<b><i>Simple Models with Cascade of Energy and Anomalous Dissipation</i></b>	
Ravi Srinivasan, Brown University .....	192
Report Seven:	
<b><i>Vibrating Pendulum and Stratified Fluids</i></b>	
Inga Koszalka, Politecnico di Torino, Italy .....	205
Report Eight:	
<b><i>A Search for Baroclinic Structures</i></b>	
Alexander Hasha, New York University .....	225

Report Nine:	
<b><i>Intermittency in Some Simple Models for Turbulent Transport</i></b>	
Arghir Dani Zarnescu, University of Chicago .....	248
Report Ten:	
<b><i>Internal Wave Breaking and Mixing in the Deep Ocean</i></b>	
Marcus Roper, DEAS, Harvard University .....	260
Report Eleven:	
<b><i>Laboratory Experiments on Mesoscale Vortices Colliding with Multiple Islands</i></b>	
Aya Tanabe, Imperial College of London .....	277

## 2005 GFD FELLOWS, STAFF AND VISITORS

### Fellows

Benjamin Akers	University of Wisconsin, Madison
Alexander Hasha	New York University
Inga Koszalka	Politecnico di Torino, Italy
Walter Pauls	University of Nice, France
Marcus Roper	DEAS, Harvard University
John Rudge	University of Cambridge, U.K.
Khachik Sargsyan	University of Michigan
Tiffany Shaw	University of Toronto, Canada
Ravi Srinivasan	Brown University
Aya Tanabe	Imperial College of London
Arghir Dani Zarnescu	University of Chicago

### Staff and Visitors

Alexandros Alexakis	NCAR
Neil J. Balmforth	Penn State
Andrew Belmonte	Penn State University
Manuel Berlingiero	Columbia University
Joseph Biello	Rensselaer Polytech Institute
Onno Bokhove	University of Twente
Gregory Buck	Saint Anselm College
Oliver Buhler	New York University
Mattias Cape	University of California, San Diego
Claudia Cenedese	WHOI
Paola Cessi	University of California, San Diego
Gregory Chini	University of New Hampshire
Charles Doering	University of Michigan
Predrag Cvitanovic	Georgia Institute of Technology
Paul Dellar	Imperial College
William Dewar	Florida State University
Jinqiao Duan	Illinois Institute of Technology
Alexey Fedorov	Yale University
Matt Finn	Imperial College
Sandip Ghosal	Northwestern University
John Gibbon	Imperial College
Graf von Hardenberg	ISAC-CNR
Louis Howard	Massachusetts Institute of Technology
Hans Johnston	University of Massachusetts
Panayotis Kevrekidis	University of Massachusetts, Amherst
Rachel Kuske	University of British Columbia
Joseph B. Keller	Stanford University
Norman R. Lebovitz	University of Chicago
Philip Li-Fan	Cornell University
Lu Lu	University of Michigan

Willem V.R. Malkus  
 Paul Milewski  
 Joel Miller  
 Philip J. Morrison  
 Marcel Oliver  
 George C. Papanicolaou  
 Arakel Petrosyan  
 Stephen Plasting  
 Michael Proctor  
 Antonello Provenzale  
 Joel Rogers  
 Anshuman Roy  
 Claes G. Rooth  
 Richard Salmon  
 Jennifer Siggers  
 Leslie Smith  
 Edward Spiegel  
 Esteban Tabak  
 Jean-Luc Thiffeault  
 Andrew Thompson  
 Edris Titi  
 Tadashi Tokieda  
 Salvatore Torquato  
 Eric Vanden-Eijnden  
 Jacques Vanneste  
 David Vener  
 George Veronis  
 Marshall Ward  
 Matthew Wells  
 William Young  
 Yuan-Nan

Massachusetts Institute of Technology  
 University of Wisconsin  
 DAMTP  
 University of Texas at Austin  
 International University, Bremen  
 Stanford University  
 Russian Academy of Sciences  
 University of California, San Diego  
 University of Cambridge  
 Istituto di Scienze Dell'Atmosfera  
 Brooklyn Polytechnic Institute  
 University of Michigan  
 University of Miami  
 University of California, San Diego  
 University of Nottingham  
 University of Wisconsin  
 Columbia University  
 New York University  
 Imperial College  
 Scripps Institution of Oceanography  
 University of California, Irvine  
 University of Cambridge  
 Princeton University  
 New York University  
 University of Edinburgh  
 Massachusetts Institute of Technology  
 Yale University  
 Florida State University  
 Yale University  
 Scripps Institution of Oceanography  
 New Jersey Institute of Technology

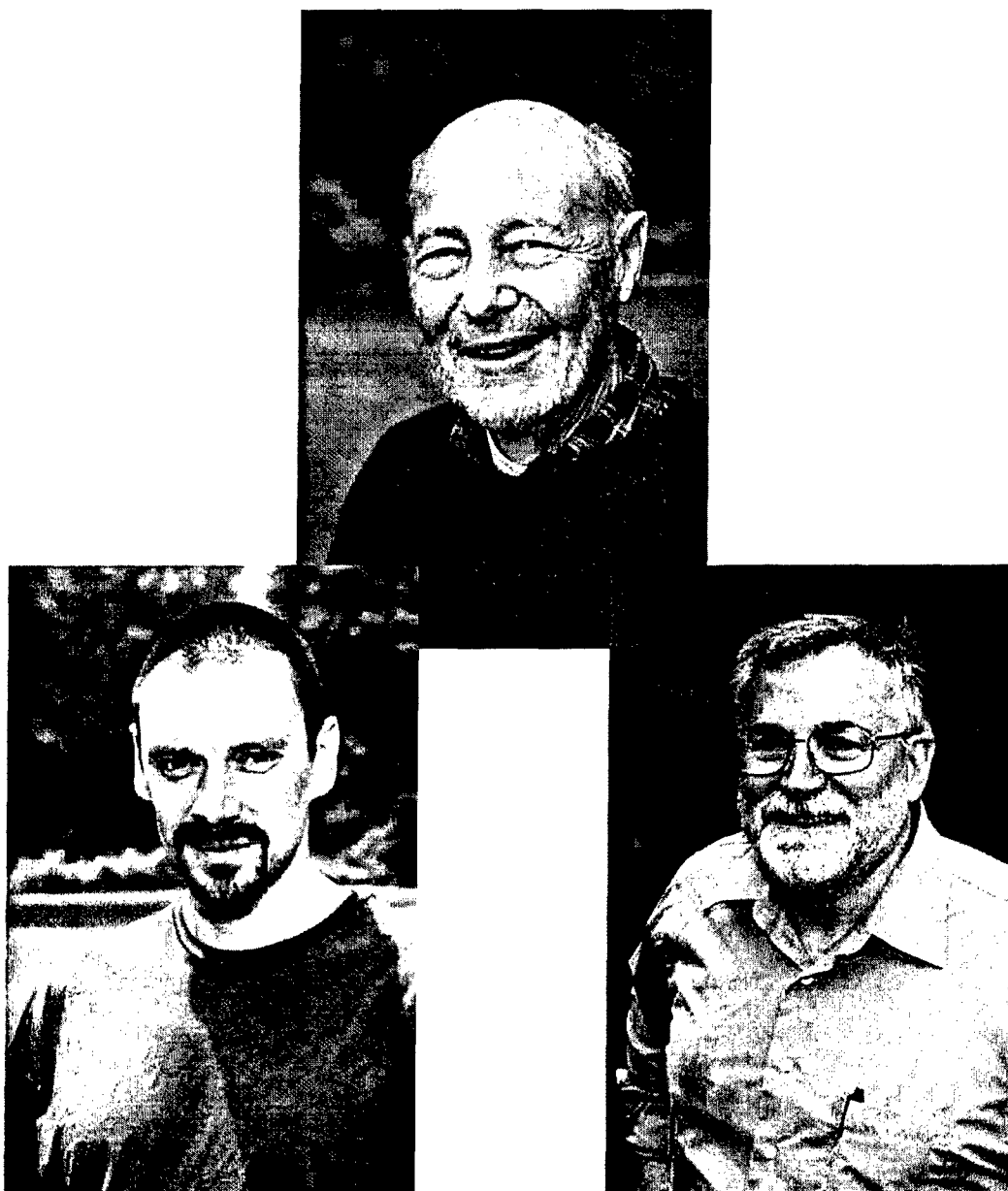


### 2005 Participants

**Front row:** Ed Spiegel (standing), Charlie Doering, Joseph Keller, Alexander Hasha, Inga Kozalska, Tiffany Shaw, Benjamin Akers, John Rudge, George Veronis, Ravi Srinivasan, Walter Pauls, Aghir Dani Zarnescu, Khachik Sargysan, Marcus Roper, Aya Tanabe, Phil Morrison, and Oliver Buhler (standing).

**Back Row:** Greg Chini, George Papanicolaou, Matt Finn, Manuel Berlingiero, Claudia Cenedese, Jacques Vanneste, Jack Whitehead, Yuan-Nan Young, Edriss Titi, Stefan Llewellyn-Smith, Joe LaCasce, Jennifer Siggers, Eric Vanden Eijnden, Alexandros Alexakis, Norman Lebovitz, James Anderson, Onno Bokhove, and Neil Balmforth.

## 2005 Principal Lecturers



**Clockwise from top:** Joseph Keller, George Papanicolaou, and Eric Vanden Eijnden.

## **GFD 2005 Lecture Schedule**

*(All talks held in Walsh cottage unless otherwise noted.)*

### **June 20 – July 1, 2005 - Principal Lectures Schedule**

**Monday, June 20 - Friday, June 24, 10:00 AM**

**Joseph B. Keller, Stanford University**

- Review of ideal fluid dynamics; derivation of surface and gravity wave equations.
- Linear perturbation theory, short wave asymptotics and ray methods.
- Applications: shoaling, scattering, and waves in channels of variable depth.
- Heat conduction in inhomogeneous media, effective conductivities and multiscale analysis.
- Longwave dynamics; example: harbor with a small opening and energy exchange with the outside.

**Monday, June 27 - Wednesday, June 29, 10:00 AM**

**Eric Vanden-Eijnden, Courant Institute, New York University**

- Brownian motion, stochastic integrals, stochastic differential equations.
- Kolmogorov backward and forward equations, Feynman-Kac formula, Girsanov theorem.
- Averaging theorems for Markov chains and stochastic differential equations.

**Thursday, June 30, 10 AM and Friday, July 1, 10:00 AM and 2:30 PM**

**George C. Papanicolaou, Stanford University**

- Introduction to the use of variational methods for high-contrast diffusivity problems.
- Variational principles for convection-diffusion and their use for the analysis of high Peclet number behavior.
- The notion of eddy viscosity for 2D cellular flows and its behavior at large Rayleigh numbers.



**Week of June 20 - 24, 2005 - Regular Seminar Schedule**

**Thursday, June 23**

**2:30 pm**

Edriss Titi, Weizmann Institute and Univ. of California, San Diego  
*Global Regularity for the 3-D Primitive Equations of Large  
Scale Ocean and Atmospheric Dynamics*

**Week of June 27 - July 1, 2005**

**Monday, June 27**

**2:30 pm**

Stefan Llwelllyn-Smith, University of California, San Diego  
*Impact of a Cylinder*

**Tuesday, June 28**

**3:00 pm**

Physical Oceanography Department Seminar, Quissett Campus  
Olaf Dahl, Goteborg University  
*Development of Perturbations on a Buoyant Coastal Current*

**Week of July 4 - 8, 2005**

**Monday, July 4**

**HOLIDAY**

**Tuesday, July 5**

**10:00 AM**

Salvatore Torquato, Princeton University  
*Random Heterogeneous Materials for Fun and Profit*

**Wednesday, July 6**

**10:00 AM**

Jacques Vanneste, University of Edinburgh  
*Passive-scalar Decay in Smooth Random Flows*

**Thursday, July 7**

**10:00 AM**

Charles Doering, University of Michigan and  
Bill Young, University of California, San Diego  
*Stirring up Trouble: Estimates of Mixing Efficiency  
for Incompressible Flows*

**Friday, July 8**

**10:00 AM**

Jean-Luc Thiffeault, Imperial College  
*Mixing with Ghost Rods*

**Week of July 11-15, 2005**

**Monday, July 11**

**10:00 AM**

Rachel Kuske, University of British Columbia

*Multiscale and Noise Sensitivity*

**Tuesday, July 12**

**10:00 AM**

Oliver Buhler, Courant Institute

*Wave Capture, Wave-Vortex Duality, and the  
Gait of the Waterstrider*

**Wednesday, July 13**

**10:00 AM**

Onno Bokhove, University of Twente

*Reservoir Formation in Shallow Granular Flows  
through a Contraction*

**Thursday, July 14**

**10:00 AM**

Matt Finn, Imperial College

*Topological Chaos in Spatially Periodic Mixers*

**Friday, July 15**

**10:00 AM**

Rachel Zammett, Oxford University

*Spiral Troughs and Katabatic Winds on Mars*

Geoff Evatt, Oxford University

*Dansgaard-Oeschger Events and Subglacial Formation*

Andrew Fowler, Oxford University

*The Day after Tomorrow*

**Week of July 18 – 22, 2005**

**Monday, July 18**

**10:00 AM**

Andrew Majda, Courant Institute

*A New Multi-scale Model for the Madden-Julian Oscillation*

**Tuesday, July 19**

**10:00 AM**

Marcel Oliver, International University, Bremen

*Averaging by Degenerate Asymptotics*

**Wednesday, July 20**

**10:00 AM**

Herbert Keller, Caltech

*Kolmogorov Flows via Continuation, Bifurcation and RPM*

**Thursday, July 21**

**10:00 AM**

Norman Lebovitz, University of Chicago and Joseph Biello, Courant  
Institute/UC Davis

*Hamiltonian Reduction and Dirac Brackets*

**Friday, July 22**

**10:00 AM**

Andrew Belmonte, Penn State University

*Fast Times and Fine Pasta: Stress Waves, Buckling, and  
Breaking*

**Week of July 25-29, 2005**

**Monday, July 25**

**10:30 am**

Jack Whitehead, P.O. Department, WHOI

*Temperature-salinity Laboratory Climate Experiments*

**Tuesday, July 26**

**10:30 am**

William Young, Scripps Institution of Oceanography

*Bugery and Fockery*

**Wednesday, July 27**

**10:30 am**

Alexey Federov, Yale University

*ENSO Dynamics in a Quasi-fast-wave Approximation and Energy  
Dissipation Rates in the Tropical Ocean*

**Thursday, July 28**

**10:30 am**

Joel Rogers, NRL and Brooklyn Polytechnic Institute

*Nonclassical Hydrodynamics*

**Friday, July 29**

**10:30 am**

Neil Balmforth, Univ. of British Columbia and David Vener, M.I.T.

*Snail Balls and More*

**Week of August 1– 5, 2005**

**Monday, August 1**

**10:30 am**

John D. Gibbon, Imperial College, London

*Cluster Formation on Complex Multi-Scale Systems*

**Tuesday, August 2**

**10:30 am**

Eric Vanden-Eijnden, Courant Institute

*Large Deviations (A pseudo-pedagogical lecture!)*

**Wednesday, August 3**

**10:30 am**

Leslie Smith, University of Wisconsin

*A Mechanism for the Formation of Jets and Vortices  
in Rotating Flows*

**Thursday, August 4**

**10:30 am**

Fabian Waleffe, University of Wisconsin

*Structures of Shear Turbulence*

**Friday, August 5**

**10:30 am**

Predrag Cvitanovic, Georgia Tech

*Unstable Recurrent Patterns in Kuramoto-Sivashinsky Dynamics*

**Week of August 8-12, 2005**

**Monday, August 8**

**10:30 am**

George Veronis, Yale University

*Experiments and Theory on the Dynamics and Energetics of  
Double Diffusive Systems*

**Tuesday, August 9**

**10:30 am**

Paul Milewski, University of Wisconsin

*Breaking Waves and Mixing in Shallow Water*

**Wednesday, August 10**

**10:30 am**

Christopher Wolfe, Oregon State University

*Special Seminar - Disturbance Growth in a Time Periodic  
Baroclinic System*

**Thursday, August 11**

**10:30 am**

Ed Spiegel, Columbia University

*Phenomenological Photofluidynamics in Hot Stars*

**Friday, August 12**

**10:30 am**

Jost von Hardenberg, ISAC-CNR, Torino

*Vegetation Patterns in Drylands*

**August 22-25, 2005**

**FELLOWS' PRESENTATIONS**

**Monday, August 22**

**10:00 - 11:00 AM**

Benjamin Akers, University of Wisconsin-Madison

*Shallow Water Flows through a Contraction*

**11:00 AM - 12:00**

Tiffany Shaw, University of Toronto

*Bounds on Multiscale Mixing Efficiency*

**2:00 - 3:00 PM**

Walter Pauls, University of Nice

*Diffusion Processes in Cellular Flow*

**Tuesday, August 23**

**10:00 - 11:00 AM**

John Rudge, University of Cambridge

*Scattering Past a Cylinder with Weak circulation*

**11:00 AM - 12:00**

Khachik Sargsyan, University of Michigan

*Fluctuations in Chemical Systems in the Large Volume  
Regime*

**2:00 - 3:00 PM**

Ravi Srinivasan, Brown University

*Simple Models with Cascade of Energy and Anomalous Dissipation*

**Wednesday, August 24**

**10:00 - 11:00 AM**

Inga Koszalka, Politecnico di Torino

*The Vibrating Pendulum and Stratified Fluids*

**11:00 AM - 12:00**

Alexander Hasha, New York University

*A Search for Baroclinic Structures*

**2:00 - 3:00 PM**

Arghir Dani Zarnescu, University of Chicago

*Intermittency in Simple Models for Turbulent Transport*

**Thursday, August 25**

**10:00 - 11:00 AM**

Marcus Roper, DEAS, Harvard University

*Internal Wave Breaking and Mixing in the Deep Ocean*

**11:00 AM - 12:00**

Aya Tanabe, Imperial College of London

*Laboratory Experiments on Mesoscale Vortices Colliding with Multiple Islands*

# Lecture 1: Fluid Equations

Joseph B. Keller

## 1 Euler Equations of Fluid Dynamics

We begin with some notation;  $x$  is position,  $t$  is time,  $g$  is the acceleration of gravity vector,  $u(x,t)$  is velocity,  $\rho(x,t)$  is density,  $p(x,t)$  is pressure. The Euler equations of fluid dynamics are:

$$\rho_t + \nabla \cdot (\rho u) = 0 \quad \text{Mass conservation} \quad (1)$$

$$\rho[u_t + (u \cdot \nabla)u] = -\nabla p - \rho g \quad \text{Momentum equation} \quad (2)$$

$$\rho = \rho(p, S, T) \quad \text{Equation of state.} \quad (3)$$

Here  $T$  = temperature and  $S$  = salinity in the ocean or humidity in the atmosphere. (1)-(3) represent five equations for five unknown functions  $(\rho, u, p)$ . We assume  $T, S$  are given.

Note

- (a) (1)-(3) hold in air with the ideal gas law
- (b) (1)-(3) hold in water with the equation of state for water
- (c) instead of (1)-(3), the equations of solid mechanics (elasticity, plasticity) hold in the interior of the Earth
- (d) certain conditions must hold at the interfaces between air and water, water and solid, where the solutions are discontinuous

### 1.1 Boundary conditions

To study the motion of the water and its upper surface we assume that:

- (a) the location of the bottom surface is known:

$$z = -h(x, y, t)$$

- (b) the pressure in the air at the top surface is known:

$$p^{air}(x, y, t) = p^{air}[x, y, \eta(x, y, t), t].$$

At the top surface  $z = \eta(x, y, t)$ ;  $\eta$  is to be determined.

- Kinematic condition

At each free surface, the normal velocity  $u \cdot \nu$  of the fluid in the direction of the unit normal  $\nu$  is equal to  $V$ , the normal velocity of the surface.

$$\text{Bottom:} \quad \nu = \frac{(h_x, h_y, 1)}{\sqrt{h_x^2 + h_y^2 + 1}}, \quad V = \frac{-h_t}{\sqrt{h_x^2 + h_y^2 + 1}}$$

$$uh_x + vh_y + w = -h_t \quad \text{at } z = -h(x, y, t) \quad (4)$$

$$-u\eta_x - v\eta_y + w = \eta_t \quad \text{at } z = \eta(x, y, t) \quad (5)$$

• Dynamic condition

At  $z = \eta(x, y, t)$ , the pressure in the water equals the pressure in the air (ignoring surface tension):

$$p[x, y, \eta(x, y, t), t] = p^{air}(x, y, t) \quad \text{at } z = \eta(x, y, t) \quad (6)$$

Note

(a) one condition at the bottom where  $h(x, y, t)$  is known.

(b) two conditions at top where  $\eta(x, y, t)$  is unknown.

## 1.2 Initial conditions

$$\rho(x, 0) = R(x) \quad (7)$$

$$u(x, 0) = U(x) \quad (8)$$

$$\eta(x, y, 0) = N(x, y) \quad (9)$$

To solve the initial boundary value problem for motion of the water we must find  $\rho(x, t)$ ,  $u(x, t)$ ,  $p(x, t)$ ,  $\eta(x, y, t)$  satisfying (1)-(9) given  $g$ , an equation of state,  $T(x, t)$ ,  $S(x, t)$ ,  $h(x, y, t)$ ,  $p^{air}(x, y, t)$ ,  $R(x)$ ,  $U(x)$ ,  $N(x, y)$ .

## 1.3 Hydrostatic equilibrium in a horizontally stratified ocean

Suppose

$$p^{air} = \text{constant} = p_0, \quad h = h(x, y), \quad T = T(z), \quad S = S(z). \quad (10)$$

Then a solution to the Euler equations is:

$$u = 0, \quad \eta = 0, \quad \rho = \rho(z), \quad p = p(z). \quad (11)$$

Equation (1) is satisfied as are the boundary conditions (4), (5) and the  $x, y$  components of (2). The  $z$  component of (2) becomes:

$$\frac{dp}{dz} = -g\rho[p(z), T(z), S(z)], \quad z \leq 0 \quad (12)$$

with boundary condition

$$p(0) = p_0. \quad (13)$$

The solution of (12) and (13) is called the hydrostatic pressure.

To solve for  $p(z)$  we need an equation of state. An approximate equation of state for seawater is:

$$\rho = \rho_0 - \alpha T + \beta S, \quad \rho_0, \alpha, \beta = \text{constants} > 0. \quad (14)$$

The solution of (12) and (13) is:

$$p(z) = p_0 - g \left[ \rho_0 z + \alpha \int_0^z T(z') dz' - \beta \int_0^z S(z') dz' \right], \quad z \leq 0. \quad (15)$$

The solution (11) solves the initial boundary value problem when the initial values (7)-(9) are also given by (11). How do we find solutions for different initial and boundary data?

#### 1.4 Perturbation method for solving problems

Consider an equation depending on a parameter  $\epsilon$

$$F(u, \epsilon) = 0. \quad (16)$$

The unknown  $u$  may be a function of  $x, t$  or a collection of functions like  $\rho, u, p, \eta$ , and  $F$  may be a set of equations like (1)-(6) with initial conditions (7)-(9). The solution of (16),  $u(\epsilon)$ , will depend upon  $\epsilon$ . If it is a smooth regular function of  $\epsilon$ , we can expand it in a Taylor series:

$$u(\epsilon) = u(0) + \epsilon \dot{u}(0) + \mathcal{O}(\epsilon^2) \quad (17)$$

$$\dot{u} = \left. \frac{du(\epsilon)}{d\epsilon} \right|_{\epsilon=0}.$$

Suppose that we can solve (16) when  $\epsilon = 0$ , i.e. we know  $u(0)$ . Then we can differentiate (16) with respect to  $\epsilon$  and set  $\epsilon = 0$ :

$$F_u[u(0), 0] \dot{u}(0) + F_\epsilon[u(0), 0] = 0. \quad (18)$$

If we solve (18) for  $\dot{u}(0)$  then (17) will give  $u(\epsilon)$  with an error  $\mathcal{O}(\epsilon^2)$ . A better approximation can be obtained by keeping the term  $\frac{\epsilon^2}{2} \ddot{u}(0)$  and differentiating (16) twice to get an equation for  $\ddot{u}(0)$  etc.

This is the regular perturbation method, and  $\epsilon$  is the perturbation parameter. Equation (18) is called the variational equation of (16). It is linear in the unknown  $\dot{u}(0)$ , so it is called the linearized equation (linearized about  $u(0)$ ). It can also be derived by substituting (17) into (16) and expanding in powers of  $\epsilon$ .

Note that  $\epsilon$  can be any parameter, or set of parameters, which occurs in one or more



of the differential equations or in the boundary or initial conditions. The linear operator  $F_u[u(0), 0]$  in (18) is always the same. Only the inhomogeneous term  $F_\epsilon[u(0), 0]$  depends on what the parameter is.

Here are some examples of how we can perturb hydrostatic equilibrium.

Let  $p_0, h_0(x, y), \rho_0$  be the equilibrium solution, and then set

$$p^{air} = p_0 + \epsilon p_1(x, y, t) \quad \text{atmospheric disturbance} \quad (19)$$

$$h = h_0(x, y) + \epsilon h_1(x, y, t) \quad \text{bottom motion (earthquake, landslide)} \quad (20)$$

$$\eta(x, t) = 0 + \epsilon \eta_1(x, y) \quad \text{initial elevation or depression} \quad (21)$$

$$u(x, \eta, 0) = 0 + \epsilon u_1(x, y) \quad \text{initial motion} \quad (22)$$

$$\rho(x, \eta, t) = \rho_0(z) + \epsilon \rho_1(x, y, z) \quad \text{initial density anomaly.} \quad (23)$$

To get the linearized equations, we linearize about the equilibrium solution. We start with (1):

$$\rho_t + \nabla(\rho u) = 0.$$

We differentiate with respect to  $\epsilon$

$$\dot{\rho}_t + \nabla \cdot (\dot{\rho} u + \rho \dot{u}) = 0.$$

We set  $\epsilon = 0$  and then  $u = 0, \rho = \rho_0$ . Hence

$$\dot{\rho}_t + \nabla \cdot (\rho_0(z) \dot{u}) = 0. \quad (i)$$

Similarly, linearizing (2)-(9) we get

$$\rho_0 \dot{u}_t = -\nabla \dot{p} - \dot{\rho} g \quad (2)$$

$$\dot{\rho} = \rho_p(\rho_0, T, S) \dot{p} + \rho_T \dot{T} + \rho_S \dot{S} \quad (3)$$

$$\dot{u} h_{0x} + \dot{v} h_{0y} + \dot{w} = -\dot{h}_t \quad \text{at } z = -h_0(x, y) \quad \text{BC at bottom} \quad (4)$$

$$\dot{w} = \dot{\eta}_t \quad \text{at } z = 0 \quad \text{BC at top} \quad (5)$$

$$\dot{p} + p_z \dot{\eta} = p_1 \quad \text{at } z = 0 \quad \text{BC at top} \quad (6)$$

$$\dot{\rho}(x, 0) = \rho_1 \quad \text{at } t = 0 \quad (7)$$

$$\dot{u}(x, 0) = u_1 \quad \text{at } t = 0 \quad (8)$$

$$\dot{\eta}(x, 0) = \eta_1 \quad \text{at } t = 0. \quad (9)$$

Equations (1) - (9) are the linear equations for  $\dot{\rho}, \dot{u}, \dot{p}, \dot{\eta}$  and constitute an initial boundary value problem.

## 2 Fluids of Constant Density

Now let's suppose that  $\rho$  is a constant. Then we can cancel  $\rho$  from the continuity equation to get

$$\nabla \cdot u = 0.$$

This condition states that  $u$  is divergence free. The momentum equation becomes

$$u_t + (u \cdot \nabla)u = -\frac{1}{\rho}p - g.$$

Recall we also had an equation of state, relating the density to temperature and salinity. Here this equation is simply  $\rho = \rho_0$ , a constant.

Since the density is constant, (15) becomes

$$p(z) = p_0 - g\rho_0 z.$$

Linearizing the equations around a rest state yields the linear system

$$\begin{aligned}\nabla \cdot \dot{u} &= 0 \\ \dot{u}_t &= -\frac{1}{\rho} \nabla \dot{p}.\end{aligned}$$

At the beginning of this section we assumed the fluid was of constant density, and showed that this implies a divergence free velocity field. If we assume instead that when we follow a fluid element the density does not change (rather than assume that the whole fluid has constant density), we get

$$\frac{D\rho}{Dt} = \rho_t + u \cdot \nabla \rho = 0.$$

The conservation of mass equation is then  $\rho(\nabla \cdot u) = 0$ . Thus if the fluid is incompressible, this also implies a divergence free velocity field.

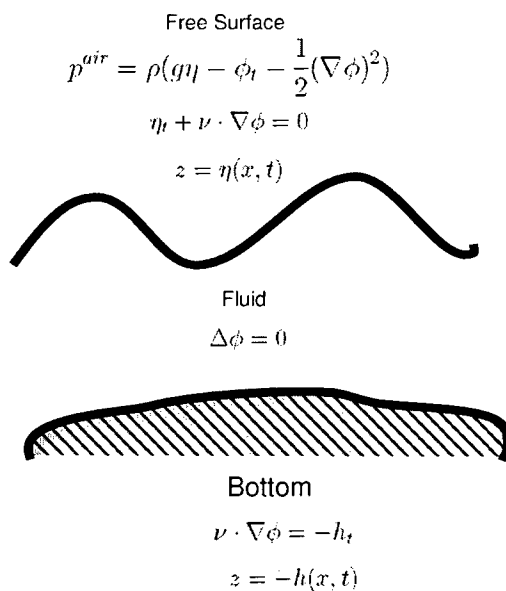


Figure 1: Irrotational flow of an incompressible ideal fluid

### 3 Irrotational Motion

Now let's introduce the quantity  $\omega = \nabla \times u$ , the vorticity of the fluid. If we assume that (or begin with) a fluid where this quantity is zero, then we say the motion is irrotational. When  $u(x, t)$  is a curl-free vector field, then we can introduce a potential function

$$\phi(x, t) = \int_{x_0}^x u(s, t) ds.$$

Here this integral is evaluated along any curve  $C$  from  $x_0$  to  $x$ . It is a calculus exercise to show that this potential is well defined only when we have an irrotational vector field (hint: use Stokes' Theorem). Notice now that  $u = \nabla\phi$  so if an incompressible fluid is in irrotational motion, then conservation of mass gives

$$\nabla \cdot u = \nabla \cdot \nabla\phi = \Delta\phi = 0.$$

Thus  $\phi$  solves Laplace's equation, or in other words,  $\phi$  harmonic. Now consider the momentum equation

$$u_t + (u \cdot \nabla)u + \frac{1}{\rho}\nabla p = \nabla V.$$

Here  $V$  is a potential function for the force,  $f$ , acting on the fluid. Now we can plug in  $u = \nabla\phi$ , to get:

$$\nabla\phi_t + 1/2\nabla(\nabla\phi)^2 + \frac{1}{\rho}\nabla p - \nabla V = 0.$$

If  $\rho$  is a constant, we can integrate this equation, to get:

$$\phi_t + 1/2(\nabla\phi)^2 + \frac{1}{\rho}p - V = B(t).$$

This is called Bernoulli's Equation. Here  $B(t)$  is an integration constant, which we can set to zero. If  $B$  was not zero then we could consider a new system where  $\phi$  is redefined to be  $\psi = \phi + \int_0^t B(s)ds$ , and see that  $\psi$  solves Bernoulli's equation with zero right hand side. Since the gradient of  $\psi$  and  $\phi$  agree, and it is this gradient we are interested in, we can safely set  $B$  to zero. Now we can solve for the velocity and pressure by solving for  $\phi$  using Laplace's Equation, and then solving for  $p$  using Bernoulli's equation. The boundary value problem for  $\phi$  and  $\eta$  is shown in Figure 1.

In Figure 1, we have a linear pde for  $\phi$  with a linear boundary condition at the bottom boundary. On the surface, we have two nonlinear boundary conditions imposed at a location which depends upon the solution. In linearizing this system about a rest state, all the equations stay the same except those on the free surface. There we get

$$\begin{aligned} \dot{\eta}_t + \dot{\nu} \cdot \nabla\phi + \nu \cdot \nabla\dot{\phi} + (\nu \cdot \nabla\phi_z)\dot{\eta} &= 0 & z = 0 \\ \dot{p}^{air} &= \rho g \dot{\eta} - \dot{\phi}_t - \phi_{tz}\dot{\eta} + \frac{1}{2}(\nabla\dot{\phi})^2 & z = 0. \end{aligned}$$

Since the rest state is  $\phi = 0$  and  $\eta = 0$ , these linearized surface equations become

$$\begin{aligned} \dot{\eta}_t - \dot{\phi}_z &= 0 & z = 0 \\ \dot{\phi}_t + g\dot{\eta} &= -\frac{1}{\rho}\dot{p}^{air} & z = 0. \end{aligned}$$

Now we can differentiate the second equation and plug it into the first to get a single linear free surface condition

$$\dot{\phi}_{tt} + g\dot{\phi}_z = -\frac{1}{\rho}\dot{p}_t^{air}.$$

When  $p$  and  $\phi$  are time harmonic with time dependence  $\exp(-i\omega t)$  this becomes

$$-\frac{\omega^2}{g}\dot{\phi} - \frac{i\omega}{\rho g}\dot{p}^{air} - \dot{\phi}_z = 0 \quad z = 0.$$

The equations for the fluid below the surface are

$$\begin{aligned} \dot{\phi}_n &= -\dot{h}_t & z &= -h \\ \Delta\dot{\phi} &= 0 & -h &\leq z \leq 0. \end{aligned}$$

These last three equations govern time harmonic small amplitude irrotational motion of an inviscid fluid of constant density.

*Notes by Benjamin Akers and Tiffany Shaw.*

# Lecture 2: Gravity waves and the method of stationary phase

Joseph B. Keller

## 1 Gravity waves on a layer of uniform depth

In addition to the boundary conditions on the upper and lower interfaces,  $\phi$  must satisfy both the initial conditions and boundary conditions on lateral surfaces or at infinity. We consider free vibrations, in which neither the bottom elevation nor the pressure at the free surface are perturbed. Moreover, we specialize to the case of uniform depth  $h^{(0)}$ . We now summarize the governing equations derived in the last lecture:

$$\nabla^2 \tilde{\phi} = 0, \quad -h^{(0)} \leq z \leq 0, \quad (1)$$

subject to the boundary conditions

$$\frac{\partial \tilde{\phi}}{\partial z} = 0 \quad \text{on} \quad z = -h^{(0)}, \quad \frac{\partial \tilde{\phi}}{\partial z} = \beta \tilde{\phi} \quad \text{at} \quad z = 0. \quad (2)$$

Recall that  $\tilde{\phi}$  represents the spatial variation of the velocity potential, and we have defined a wavenumber  $\beta \equiv \omega^2/g$ . We seek to solve this system of equations using separation of variables:  $\tilde{\phi}(x, y, z) = U(x, y)f(z)$ . After this substitution, (1) yields

$$\frac{U_{xx} + U_{yy}}{U} = -\frac{f''}{f} = -k^2. \quad (3)$$

The boundary conditions (2) become

$$f'(-h^{(0)}) = 0, \quad \text{and} \quad f'(0) = \beta f(0). \quad (4)$$

In equation (3) since the left hand side is a function of only  $x$  and  $y$  and the right hand side is a function of  $z$  only, both must be constant, equal to some  $-k^2$ .  $f$  and  $U$  then must satisfy

$$U_{xx} + U_{yy} + k^2 U = 0, \quad (5)$$

$$f'' = k^2 f. \quad (6)$$

(5) is called the Helmholtz or *reduced wave* equation. Solving for  $f$  and applying the first of the boundary conditions (4), we obtain

$$f(z) = A \cosh[k(z + h)] , \quad (7)$$

where  $A$  is an arbitrary constant, and we have suppressed the superscript upon  $h$ . In order to satisfy the free surface boundary condition, we need that  $k \sinh(kh) = \beta \cosh(kh)$ , or equivalently

$$\omega^2 = gk \tanh(kh) . \quad (8)$$

This is the *dispersion relation*,  $k$  is the *wavenumber*, and  $\omega$  is the *angular frequency*. It may seem surprising that (8) only has one positive and one negative real solution. There are infinitely many pure imaginary roots  $k = i\kappa$  to this equation, but these represent evanescent modes.

There are two physically interesting special limits

- Deep water:

$$kh \rightarrow \infty \quad \omega^2 \sim gk. \quad (9)$$

- Shallow water

$$kh \rightarrow 0 \quad \omega^2 \sim ghk^2. \quad (10)$$

Another useful concept is the *phase velocity* defined by

$$c \equiv \frac{\omega}{k} \sim \begin{cases} \sqrt{g/k} & \text{as } kh \rightarrow \infty \\ \sqrt{gh} & \text{as } kh \rightarrow 0 \end{cases} \quad (11)$$

Notice that to leading order the phase velocity is independent of the wavenumber in the shallow water limit. Media with this property are said to be *non-dispersive*.

We can now solve for the  $x$  and  $y$  variations of the velocity field. Plane wave solutions of the Helmholtz equation have the form

$$U(x, y) = e^{i\mathbf{k} \cdot \mathbf{x}}, \quad \text{where } |\mathbf{k}| = k . \quad (12)$$

Therefore

$$\phi(x, y, z, t, k) = Ae^{i(\mathbf{k} \cdot \mathbf{x} - \omega t)} \cosh[k(z + h)], \quad (13)$$

$$\eta(x, y, t, k) = -\frac{1}{g} \phi_t \Big|_{z=0} = \frac{i\omega}{g} Ae^{i(\mathbf{k} \cdot \mathbf{x} - \omega t)} \cosh(kh). \quad (14)$$

Finding the wavenumber for a prescribed frequency  $\omega$  requires solving a transcendental equation (8). It is easier to give  $k$  and then determine  $\omega$  directly from (8).

## 2 Trajectories of fluid particles

By further integration we can obtain expressions for the motion of the water particles. We choose axes so that  $\mathbf{k}$  points in the  $x$ -direction, and consider the small excursions of a fluid particle  $(x + \delta x(t), z + \delta z(t))$ , where  $\delta x$  and  $\delta z$  evolve according to the linearized equations:

$$\frac{d\delta x}{dt} = ikAe^{i(kx - \omega t)} \cosh[k(z + h)] \quad (15)$$

$$\frac{d\delta z}{dt} = kAe^{i(kx - \omega t)} \sinh[k(z + h)] . \quad (16)$$

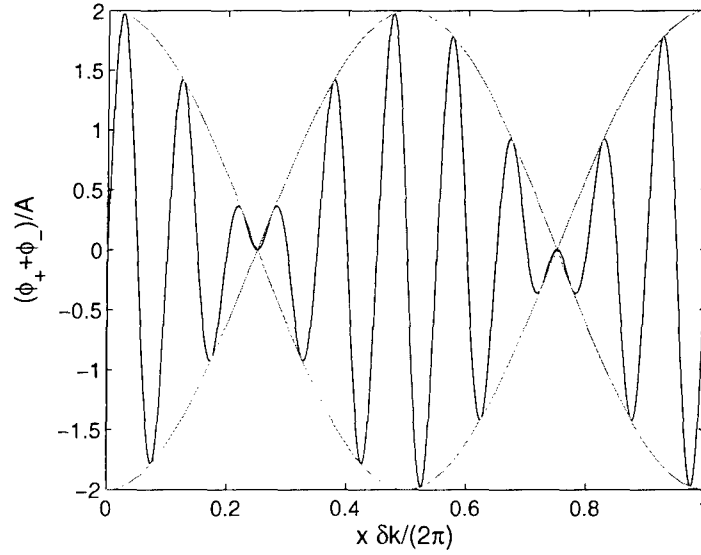


Figure 1: (Blue curve) Superposition of two waves of narrowly separated wavenumber and frequency. (Green curve) The predicted curve envelope. Here  $\delta k = k/10$ .

On integrating up, and explicitly writing out the real part (assuming that  $A$  is real for convenience) we arrive at:

$$\delta x(t) = -\frac{Ak}{\omega} \cos(kx - \omega t) \cosh[k(z + h)] \quad (17)$$

$$\delta z(t) = -\frac{Ak}{\omega} \sin(kx - \omega t) \sinh[k(z + h)] . \quad (18)$$

The particles therefore trace out an ellipse in the  $(x, z)$  plane, with horizontal axis  $(Ak/\omega) \cosh[k(z + h)]$  and vertical axis  $(Ak/\omega) \sinh[k(z + h)]$ .

### 3 Group velocity

First consider the superposition of disturbances having slightly different wavenumbers, and identical amplitudes:

$$\phi_{\pm} = A \sin[(k \pm \delta k)x - (\omega \pm \delta \omega)t] . \quad (19)$$

The sum of the two velocity potentials may be simply written:

$$\phi_+ + \phi_- = 2A \cos(\delta kx - \delta \omega t) \sin(kx - \omega t) . \quad (20)$$

The sin and cos factors describe respectively the wave, traveling at the phase velocity  $c = \omega/k$ , and the much slower oscillations in the amplitude envelope, which propagates at the *group velocity*  $c_g \equiv d\omega/dk \approx \delta\omega/\delta k$ . This ‘beat’ structure persists for wave packets with any small spread of wavenumbers. The wave packet travels at the group velocity, while

individual wave components move through the wave packet at their phase velocities. For gravity waves on a uniform fluid layer we have:

$$c_g = \frac{c}{2} \left( 1 + \frac{2kh}{\sinh(2kh)} \right). \quad (21)$$

Again we consider two limits for (21):

$$c_g \rightarrow \begin{cases} \frac{1}{2}c & \text{as } kh \rightarrow \infty \\ c & \text{as } kh \rightarrow 0 \end{cases}. \quad (22)$$

Now we calculate the period-integrated energy flux  $F$  through a surface  $x=\text{const}$ , with unit width in the  $y$ -direction. This is equal to the rate of working of the pressure force across the surface, or since in the linear approximation  $p = -\rho \partial \phi / \partial t$ , to:

$$F = -\rho \int_t^{t+T} \left[ \int_S \frac{\partial \phi}{\partial t} \frac{\partial \phi}{\partial n} dS \right] dt, \quad (23)$$

where  $T = \frac{2\pi}{\omega}$ . Note that it is only necessary to evaluate the  $z$  integral over the interval  $-h < z < 0$ ; the contribution from the sliver  $0 < z < \eta$  is of lower order. After some calculations, we discover

$$F_{av} = \frac{F}{T} = \frac{A^2 \rho \omega^2}{2g} \cosh^2(kh) c_g. \quad (24)$$

Next let us calculate the total energy (associated with the flow) in a box  $R$ :  $\{x_0 < x < x_0 + \lambda, y_0 < y < y_0 + 1, -h < z < \eta\}$ .

$$E = \rho \int \int \int_R \left[ \frac{1}{2} (\nabla \phi)^2 + gz \right] dV + \frac{1}{2} \lambda g h^2. \quad (25)$$

The integral represents the total (kinetic plus potential) energy of the fluid contained within the box, and the additional summand is simply the hydrostatic potential energy which must be subtracted off. With a little algebra, we find that

$$E_{av} = \frac{E}{\lambda} = \frac{A^2 \rho \omega^2}{2g} \cosh^2(kh). \quad (26)$$

From (21), (24) and (26) we get

$$F_{av} = E_{av} c_g, \quad (27)$$

so that the energy of the wave propagates with the group velocity  $c_g$ .

## 4 Superposition of plane waves

A general solution of the wave equation can be written as a linear combination of plane wave solutions of the type considered:

$$\eta(x, y, t) = \int d^2 \mathbf{k} \frac{i\omega(\mathbf{k})}{g} \left( A(\mathbf{k}) \cosh kh e^{i(\mathbf{k} \cdot \mathbf{x} - \omega t)} - B(\mathbf{k}) \cosh kh e^{i(\mathbf{k} \cdot \mathbf{x} + \omega t)} \right) \quad (28)$$



The amplitude functions  $A(\mathbf{k})$  and  $B(\mathbf{k})$  can be determined to make  $\eta$  and  $\eta_t$  satisfy initial conditions. The fluid elevation at time  $t = 0$  is

$$\eta(x, y, 0) = \int d^2\mathbf{k} \frac{i\omega(\mathbf{k})}{g} \cosh kh (A(\mathbf{k}) - B(\mathbf{k})) e^{i\mathbf{k}\cdot\mathbf{x}} . \quad (29)$$

Thus the Fourier transform  $\tilde{\eta}$  of the initial fluid height is related to  $A$  and  $B$  by

$$\tilde{\eta}(\mathbf{k}, 0) = \frac{i\omega(\mathbf{k})}{g} \cosh kh (A(\mathbf{k}) - B(\mathbf{k})) . \quad (30)$$

Similarly for the Fourier transform of the initial velocity of the free surface,

$$\tilde{\eta}_t(\mathbf{k}, 0) = \frac{\omega(\mathbf{k})^2}{g} \cosh kh (A(\mathbf{k}) + B(\mathbf{k})) . \quad (31)$$

Thus from (30) and (31) the amplitude functions are determined by:

$$\tilde{\eta}_t - i\omega\tilde{\eta}|_{t=0} = \frac{2\omega^2}{g} \cosh kh A(\mathbf{k}) , \quad (32)$$

$$\tilde{\eta}_t + i\omega\tilde{\eta}|_{t=0} = \frac{2\omega^2}{g} \cosh kh B(\mathbf{k}) . \quad (33)$$

However convoluted the initial conditions upon the surface elevation, we can obtain the complete evolution of the fluid surface height if only we can evaluate these integrals. In the days when computation was expensive, this was a knotty problem, since the range of integration in wave number space extends out to infinity, and the amplitude functions may decay only weakly as the wavenumber is made vanishingly small. In the next section, we describe a powerful asymptotic method for evaluation of the integral far from any disturbance sources.

## 5 Asymptotic evaluation of integrals

We consider the simplest case of a one-dimensional disturbance, and seek to evaluate the following integral:

$$\eta(x, t) = \int_{-\infty}^{\infty} A(k) e^{i(kx - \omega(k)t)} dk . \quad (34)$$

When  $x$  and  $t$  are large, the integrand of (34) oscillates very rapidly and everything is canceled out. So the dominant contribution to  $\eta(x, t)$  comes from the neighborhood of  $k = k_s$ , a stationary point at which the derivative of the phase function  $S(k, x, t) \equiv kx - \omega(k)t$  with respect to  $k$  vanishes. We approximate  $S$  about  $k = k_s$  by a Taylor series expansion:

$$S(k) \approx S(k_s) + S_k(k_s)(k - k_s) + \frac{1}{2}S_{kk}(k_s)(k - k_s)^2 + \dots . \quad (35)$$

Noting that  $S_k(k_s) = 0$ , we find that (34) can be approximated by the Gaussian integral

$$\begin{aligned} \eta(x, t) &\sim A(k_s) e^{iS(k_s)} \int_{-\infty}^{\infty} e^{\frac{i}{2}S_{kk}(k_s)(k - k_s)^2} dk \\ &\sim A(k_s) e^{iS(k_s)} \frac{\sqrt{2\pi} e^{\pm i\frac{\pi}{4}}}{\sqrt{|S_{kk}(k_s)|}} , \end{aligned} \quad (36)$$

where  $\pm = \text{sgn}(S_{kk}(k_s))$ . Therefore, for  $x, t \gg 1$ ,

$$\eta(x, t) \sim \sum_{\pm k_s(\frac{x}{t})} A\left(k_s\left(\frac{x}{t}\right)\right) e^{i(k_s x - \omega(k_s)t)} \frac{\sqrt{2\pi} e^{\pm i\frac{\pi}{4}}}{\sqrt{|\omega''(k_s)|t}}, \quad (37)$$

since  $S_{kk} = -\omega''(k)t$ . We must sum over the contributions from each of the wavenumbers  $k_s$  giving group velocities  $c_g(k_s) = x/t$ . For the given dispersion relation (8), there is precisely one such wavenumber. This method is called the *method of stationary phase*.

There is a singularity in (37) if  $\omega''(k_s) = 0$ , i.e. at the maximum attainable group velocity. From the form of the dispersion relation (8) it may be determined that this occurs iff  $k = 0$  (the 'if' statement is an obvious corollary of  $c_g$  being an even function of  $k$ , but the converse statement requires a little more work). Much of the energy introduced into the medium at the source piles up in the fastest-traveling part of the wave packet. It follows that the formula is not valid in the neighborhood of values  $x, t$  where  $x/t = c_g(0) = \sqrt{gh}$ . To correct it, it is necessary to extend the Taylor series for  $x/t$  close to  $\sqrt{gh}$ :

$$\begin{aligned} \eta(x, t) &\sim A(k_s) e^{iS(k_s)} \int_{-\infty}^{\infty} dk e^{i(k-k_s)^3 S_{kkk}(k_s)/6} \\ &\sim A(k_s) e^{i(k_s x - \omega t)} \int_{-\infty}^{\infty} d\sigma \frac{e^{\pm i\sigma^3/6}}{|S_{kkk}(k_s)|^{1/3}} = \left( \frac{16\pi^3}{|S_{kkk}(k_s)|} \right)^{1/3} e^{ik_s x - i\omega t} Ai(0) \end{aligned} \quad (38)$$

Since  $S_{kkk}(k_s)$  is proportional to  $t$  at  $k_s = 0$ ,  $\eta$  decays as  $t^{-1/3}$ . This decay is significantly weaker than the  $t^{-1/2}$  decay at points behind the front. In order to obtain a uniform approximation which combines (37) for  $x/t \neq \sqrt{gh}$  and (38) for  $x/t \approx \sqrt{gh}$ , we can retain both the cubic and quadratic terms in the expansion of  $S(k)$ . The resulting integral can be written as an Airy function for  $\eta$ . This integral was first used by George Airy in his analysis of light-scattering by spherical raindrops, the first quantitative model for the distribution of colors in a rainbow.

This transitional expression is valid near the front  $x/t = \sqrt{gh}$  but it becomes inaccurate far from the front. A result valid over the whole range of  $x$  and  $t$  can be obtained by writing  $S(k)$  as a cubic polynomial in a new variable in a suitable way. This method, developed by Chester, Friedman and Ursell, yields an Airy function of a more complicated argument. It was applied recently to tsunami waves by Berry.

*Notes by Marcus Roper and Aya Tanabe.*

# Lecture 3: Asymptotic Methods for the Reduced Wave Equation

Joseph B. Keller

## 1 The Reduced Wave Equation

Let  $v(t, \mathbf{x})$  satisfy the wave equation

$$\Delta v - \frac{1}{c^2(\mathbf{X})} \frac{\partial^2 v}{\partial t^2} = 0, \quad (1)$$

where  $c(\mathbf{X})$  is the *propagation speed* at the point  $\mathbf{X}$ . Separate variables, letting  $v(t, \mathbf{X}) = g(t)u(\mathbf{X})$ . Then

$$c^2(\mathbf{X}) \frac{\Delta u(\mathbf{X})}{u(\mathbf{X})} = \frac{g''(t)}{g(t)} = -\omega^2. \quad (2)$$

So

$$g''(t) + \omega^2 g(t) = 0 \quad (3)$$

and

$$\Delta u + \frac{\omega^2}{c^2(\mathbf{X})} u = 0. \quad (4)$$

Here the constant  $\omega$  is the *angular frequency*. Equation 4 is known as the *reduced wave equation* or the *Helmholtz equation*. Introduce a constant reference speed  $c_0$ , and define the *index of refraction*  $n(\mathbf{X}) = c_0/c(\mathbf{X})$  and the *propagation constant* (or *wave number*)  $k = \omega/c_0$ . Then the reduced wave equation (4) becomes

$$\Delta u + k^2 n^2(\mathbf{X}) u = 0. \quad (5)$$

## 2 Leading order asymptotics

When  $n(\mathbf{X})$  is constant, the reduced wave equation has the plane wave solution

$$u(\mathbf{X}, \mathbf{K}) = z(\mathbf{K}) e^{in\mathbf{K}\cdot\mathbf{X}}. \quad (6)$$

Here the *propagation vector*  $\mathbf{K}$  is any constant vector such that  $|\mathbf{K}| = k$ , and the amplitude  $z(\mathbf{K})$  is a constant. In the case of  $n(\mathbf{X})$  not constant, the plane wave solution motivates looking for solutions to (5) of the form

$$u(\mathbf{X}) = z(\mathbf{X}, k) e^{iks(\mathbf{X})}. \quad (7)$$

Here  $z(\mathbf{X}, k)$  is the amplitude and  $s(\mathbf{X})$  the phase. Substituting this form into the reduced wave equation (5) yields

$$-k^2 \left[ (\nabla s)^2 - n^2 \right] z + 2ik \nabla s \cdot \nabla z + ikz \Delta s + \Delta z = 0. \quad (8)$$

We are interested in looking at the asymptotic behavior of solutions to the reduced wave equation (5) as  $k \rightarrow \infty$ . To explore this, we suppose  $z(\mathbf{X}, k)$  has an *asymptotic expansion* of the form

$$z(\mathbf{X}, k) \sim \sum_{m=0}^{\infty} z_m(\mathbf{X}) (ik)^{-m} = \sum_{m=-\infty}^{\infty} z_m(\mathbf{X}) (ik)^{-m}, \quad z_m = 0 \text{ for } m = -1, -2, \dots \quad (9)$$

Here  $\sim$  denotes *asymptotic equality*. The asymptotic expansion above means that for each  $n \geq 0$

$$z(\mathbf{X}, k) = \sum_{m=0}^n z_m(\mathbf{X}) (ik)^{-m} + o(k^{-n}), \quad (10)$$

where the notation  $o(k^{-n})$  denotes a term for which  $\lim_{k \rightarrow \infty} k^n |o(k^{-n})| = 0$ . Note that an asymptotic expansion may not converge! However, by truncation of the series we get an approximation with an error which tends to zero as  $k \rightarrow \infty$ . Substituting the asymptotic expansion (9) for  $z(\mathbf{X}, k)$  into (8) yields

$$\sum_m (ik)^{1-m} \left\{ \left[ (\nabla s)^2 - n^2 \right] z_{m+1} + [2\nabla s \cdot \nabla z_m + z_m \Delta s] + \Delta z_{m-1} \right\} \sim 0. \quad (11)$$

The coefficient of each power of  $k$  must be zero. For  $m = -1$  this gives

$$\left[ (\nabla s)^2 - n^2 \right] z_0 = 0, \quad (12)$$

since  $z_m = 0$  for  $m = -1, -2, \dots$ . Assuming  $z_0 \neq 0$ , this implies the *eikonal equation* for the phase  $s$ ,

$$(\nabla s)^2 = n^2(\mathbf{X}). \quad (13)$$

$m = 0$  yields the *transport equation* for the leading order amplitude  $z_0$ ,

$$2\nabla s \cdot \nabla z_0 + z_0 \Delta s = 0. \quad (14)$$

$m = 1, 2, \dots$  yield further transport equations for determining the other  $z_m$ . We shall concentrate on the leading order amplitude  $z_0$  in what follows. The leading order solution  $z_0(\mathbf{X}) e^{iks(\mathbf{X})}$  is known as the *geometrical optics field*.

### 3 Phase, Wavefronts, and Rays

Surfaces of constant phase, defined by  $s(\mathbf{X}) = \text{constant}$ , are called *wavefronts*. Curves orthogonal to the wavefronts are called *rays* (or more generally, *characteristics*), and are used to solve for  $s(\mathbf{X})$ . We write the equation of a ray in terms of a parameter  $\sigma$  in the form

$$\mathbf{X} = (x_1, x_2, x_3) = \mathbf{X}(\sigma) \quad (15)$$

Orthogonality of the ray and the wavefronts implies

$$\frac{dx_j}{d\sigma} = \lambda \frac{\partial s}{\partial x_j}, \quad (16)$$

where  $\lambda(\mathbf{X})$  is an arbitrary proportionality factor, and  $j = 1, 2, 3$ . Now, dividing the above expression by  $\lambda$ , differentiating with respect to  $\sigma$ , and using the summation convention we have that

$$\frac{d}{d\sigma} \left( \frac{1}{\lambda} \frac{dx_j}{d\sigma} \right) = \frac{d}{d\sigma} \left( \frac{\partial s}{\partial x_j} \right) = \frac{dx_i}{d\sigma} \frac{\partial^2 s}{\partial x_i \partial x_j} = \lambda \frac{\partial s}{\partial x_i} \frac{\partial^2 s}{\partial x_i \partial x_j} = \frac{\lambda}{2} \frac{\partial}{\partial x_j} \left( \frac{\partial s}{\partial x_i} \frac{\partial s}{\partial x_i} \right). \quad (17)$$

Then, using the eikonal equation (13) on the right hand side we have that

$$\frac{1}{\lambda} \frac{d}{d\sigma} \left( \frac{1}{\lambda} \frac{dx_j}{d\sigma} \right) = \frac{\partial}{\partial x_j} \left( \frac{n^2}{2} \right). \quad (18)$$

Furthermore, substituting the orthogonality equation (16) into the eikonal equation (13) yields

$$\frac{dx_j}{d\sigma} \frac{dx_j}{d\sigma} = \lambda^2 n^2. \quad (19)$$

The four equations given by (18) and (19) are known as the *ray equations*. The three equations given by (18) are second order ordinary differential equations for the rays  $\mathbf{X}(\sigma)$ , and (19) gives the variation of  $\sigma$  along the ray. The rays are determined solely by  $n(\mathbf{X})$  once the initial values for (18) are specified and the arbitrary proportionality factor  $\lambda(\mathbf{X})$  chosen.

Since  $\lambda$  is arbitrary, we may choose it as we please. When  $\lambda = n^{-1}$  the ray equations become

$$n \frac{d}{d\sigma} \left( n \frac{dx_j}{d\sigma} \right) = \frac{\partial}{\partial x_j} \left( \frac{n^2}{2} \right), \quad (20)$$

$$\frac{dx_j}{d\sigma} \frac{dx_j}{d\sigma} = 1. \quad (21)$$

(21) implies that  $\sigma$  is simply the arc length along the ray. When  $\lambda = 1$  with  $\sigma$  replaced by  $\tau$ , the ray equations become

$$\frac{d^2 x_j}{d\tau^2} = \frac{\partial}{\partial x_j} \left( \frac{n^2}{2} \right), \quad (22)$$

$$\frac{dx_j}{d\tau} \frac{dx_j}{d\tau} = n^2. \quad (23)$$

(22) has a natural interpretation in terms of classical mechanics, with the left hand side being an acceleration and the right hand side being the gradient of a potential. Also, from (21) and (23) we can see  $\sigma$  is related to  $\tau$  by

$$d\sigma = \sqrt{dx_j dx_j} = n d\tau. \quad (24)$$

$c_0 \tau$  is known as the *optical length* along a ray.

## 4 Ray solution

The eikonal equation (13) can be solved for the phase  $s$ . Using the orthogonality (16) we have for the derivative of  $s$  along a ray

$$\frac{d}{d\sigma} s[\mathbf{X}(\sigma)] = \frac{\partial s}{\partial x_j} \frac{dx_j}{d\sigma} = \lambda \frac{\partial s}{\partial x_j} \frac{\partial s}{\partial x_j} = \lambda n^2. \quad (25)$$

This can be integrated to give the solution for  $s$

$$s[\mathbf{X}(\sigma)] = s[\mathbf{X}(\sigma_0)] + \int_{\sigma_0}^{\sigma} \lambda [\mathbf{X}(\sigma')] n^2 [\mathbf{X}(\sigma')] d\sigma'. \quad (26)$$

The transport equation (14) can be solved for the leading order amplitude  $z_0$ . Again using orthogonality, we find that

$$\nabla s \cdot \nabla z_0 = \frac{\partial s}{\partial x_j} \frac{dz_0}{dx_j} = \frac{1}{\lambda} \frac{dx_j}{d\sigma} \frac{dz_0}{dx_j} = \frac{1}{\lambda} \frac{d}{d\sigma} z_0 [\mathbf{X}(\sigma)]. \quad (27)$$

Thus the transport equation (14) becomes a first order ordinary differential equation along the ray

$$\frac{2}{\lambda} \frac{dz_0}{d\sigma} + z_0 \Delta s = 0. \quad (28)$$

Given initial conditions (28) can also be integrated to solve for  $z_0$ . However, there is a more direct way to solve for  $z_0$ . Note that (14) implies

$$\nabla \cdot (z_0^2 \nabla s) = z_0 (2 \nabla z_0 \cdot \nabla s + z_0 \Delta s) = 0. \quad (29)$$

Introduce a region  $R$  bounded by a tube of rays containing the given ray, and by two wavefronts  $W(\sigma_0)$  and  $W(\sigma)$  at the points  $\sigma_0$  and  $\sigma$  of the given ray (Figure 1). Then the gradient of the phase,  $\nabla s$ , is parallel to the sides of the tube and normal to its ends. Integrating (29) over  $R$  and using the divergence theorem yields

$$0 = \int_R \nabla \cdot (z_0^2 \nabla s) dV = \int_{W(\sigma)} z_0^2 \nabla s \cdot \mathbf{N} da - \int_{W(\sigma_0)} z_0^2 \nabla s \cdot \mathbf{N} da. \quad (30)$$

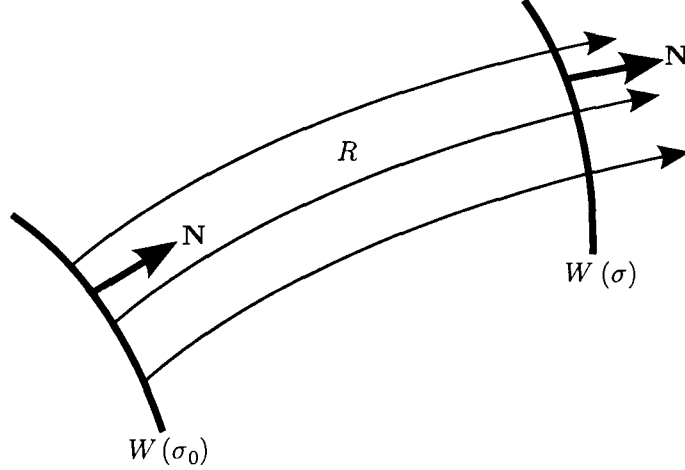
Here  $\mathbf{N}$  is a unit vector orthogonal to the wavefront and  $da$  is an element of area on the wavefront. From the eikonal equation (13) we have that  $\nabla s \cdot \mathbf{N} = n$ . Then, by shrinking the tube of rays to the given ray we obtain the solution for  $z_0$  from (30)

$$z_0^2(\sigma) n(\sigma) da(\sigma) = z_0^2(\sigma_0) n(\sigma_0) da(\sigma_0). \quad (31)$$

This can be written more conveniently in terms of the *expansion ratio*  $\xi(\sigma)$  with respect to a reference point  $\sigma_1$  on the ray, defined by

$$\xi(\sigma) = \frac{da(\sigma)}{da(\sigma_1)}. \quad (32)$$

Figure 1: Ray tube and wavefronts defining region  $R$ .



The expansion ratio measures the expansion of the cross-section of a tube of rays, and is simply the Jacobian of the mapping by rays of  $W(\sigma_1)$  on  $W(\sigma)$ . (31) then becomes

$$z_0(\sigma) = z_0(\sigma_0) \left[ \frac{\xi(\sigma_0) n(\sigma_0)}{\xi(\sigma) n(\sigma)} \right]^{1/2}. \quad (33)$$

Importantly we note that the amplitude  $z_0(\sigma)$  varies inversely as the square root of  $n\xi$  along a ray. Thus for  $n$  constant, as rays converge the amplitude  $z_0$  increases, and as rays diverge  $z_0$  decreases.

## 5 Case of Homogeneous Media

A homogeneous medium is defined as one where the propagation speed  $c(\mathbf{X})$ , and thus  $n(\mathbf{X}) = c_0/c(\mathbf{X})$ , are constants. If  $\lambda = n^{-1}$ , the ray equations (22) become

$$\frac{d^2 x_j}{d\tau^2} = \frac{\partial}{\partial x_j} \left( \frac{n^2}{2} \right) = 0. \quad (34)$$

(34) gives that the rays are straight lines. The equation (26) for the phase  $s$  becomes

$$s(\sigma) = s(\sigma_0) + n(\sigma - \sigma_0). \quad (35)$$

To determine the amplitude  $z_0(\sigma)$  using (33), we need to determine the expansion ratio  $\xi(\sigma)$ . To calculate the expansion ratio, look at two intersecting rays which form an infinitesimal angle  $d\theta_1$ , as in Figure 2. Now take any two wavefronts  $W(0)$  and  $W(\sigma)$  intersecting these two rays. Denote the distance between them as  $\sigma$ , and the distance to the intersection point to be  $\rho_1$ , the radius of curvature of  $W(0)$ . Then we can calculate the infinitesimal area ratio to be

$$\xi(\sigma) = \frac{da(\sigma)}{da(0)} = \frac{(\rho_1 + \sigma)d\theta_1}{\rho_1 d\theta_1} = \frac{\rho_1 + \sigma}{\rho_1}, \quad (36)$$

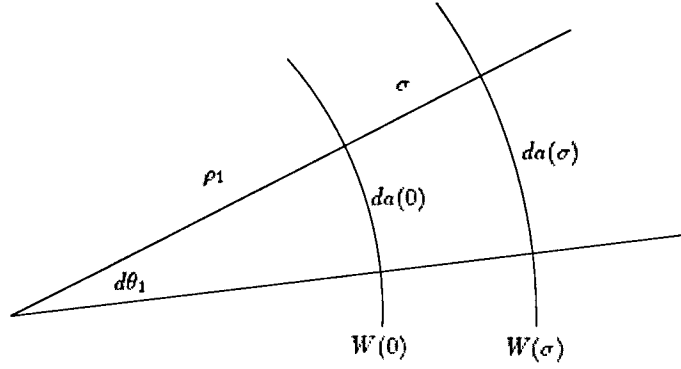


Figure 2: Calculating the expansion ratio.

$\rho_1 + \sigma$  is the radius of curvature of  $W(\sigma)$ . (36) states that the expansion ratio is just the ratio of the radii of curvature of the two wavefronts. (33) then becomes

$$z_0(\sigma) = z_0(\sigma_0) \left[ \frac{\rho_1 + \sigma_0}{\rho_1 + \sigma} \right]^{1/2}. \quad (37)$$

To use this analysis works in three dimensions, we must take two cross sections which slice the wavefront into its curves of maximal and minimal curvature. In 3-D this analysis gives the expansion ratio

$$\xi(\sigma) = \frac{(\rho_1 + \sigma)(\rho_2 + \sigma)}{\rho_1 \rho_2}. \quad (38)$$

The 3-D analogue of (37) is

$$z_0(\sigma) = z_0(\sigma_0) \left[ \frac{(\rho_1 + \sigma_0)(\rho_2 + \sigma_0)}{(\rho_1 + \sigma)(\rho_2 + \sigma)} \right]^{1/2}. \quad (39)$$

## 6 An Initial Value Problem for the Eikonal Equation

Here we consider the solution of the eikonal equation with initial data  $s(x)$  given at  $x$  on a manifold  $M$ , ie a point, line or surface. The eikonal equation is

$$(\nabla s)^2 = n^2. \quad (40)$$

To make  $s(x)$  unique, we impose the condition that the solution is outgoing. Mathematically, this condition can be expressed as

$$\nabla s \cdot \mathbf{N} > 0, \quad \text{with } \mathbf{N} = \text{The unit outward normal from } M. \quad (41)$$

Here  $M$  is the initial surface from which the solution is outgoing.

We will solve this problem using the method of characteristics. When the initial data is given at a point  $p$ , we can define the solution, using the previous theory, on each ray emanating from  $p$ .



When the initial data is given on a curve  $C$  we must determine the angle at which rays emanate. This can be done by parameterizing the curve by arc length,  $\eta$ . Now the initial condition  $s|_C = s_0(\eta)$  with a parameterization  $\mathbf{X}_0(\eta)$  of the curve  $C$ , yields the equation  $s_0(\eta) = s(\mathbf{X}_0(\eta))$ . Differentiation yields

$$\nabla s \cdot \frac{d\mathbf{X}_0}{d\eta} = \frac{ds_0}{d\eta}. \quad (42)$$

Now we use the vector identity  $\mathbf{a} \cdot \mathbf{b} = |\mathbf{a}||\mathbf{b}| \cos \beta$ , where  $\mathbf{a}$  and  $\mathbf{b}$  are vectors and  $\beta$  is the angle between them. Then (42) gives that the angle  $\beta(\eta)$  between the tangent vector  $\frac{d\mathbf{X}_0}{d\eta}$  to the curve  $C$  and the direction  $\nabla s$  of the ray is given by

$$\cos(\beta(\eta)) = \frac{1}{|\nabla s|} \frac{ds_0}{d\eta} = \frac{1}{n[\mathbf{X}_0(\eta)]} \frac{ds_0}{d\eta}. \quad (43)$$

We have now shown how to solve the initial value problem with initial data at a point  $p$  or on a curve  $C$  in an infinite domain. Similar analysis works when initial data is given on a surface. Next we will consider what happens when the domain has boundaries.

## 7 Reflection From a Boundary

In order to consider reflection from a boundary  $B$ , we must first prescribe a boundary condition. We will take the general impedance boundary condition, with impedance  $Z$ :

$$\frac{\partial u}{\partial \nu} + ikZ(\mathbf{X})u = 0, \quad \mathbf{X} \text{ on } B, \nu = \nabla B. \quad (44)$$

Notice that the limits  $Z \rightarrow 0$  and  $Z \rightarrow \infty$  yield the simpler Neumann and Dirichlet boundary conditions. To satisfy the boundary condition (44), we must introduce a reflected wave,  $u^r$  in addition to the incident wave,  $u^i$ . Here we will try the same type of expansion for  $u^r$  that we have been using for  $u^i$

$$u^r \sim e^{iks^r} \sum_{m=0}^{\infty} z_m^r (ik)^{-m}. \quad (45)$$

Now plugging  $u = u^r + u^i$  into the boundary condition, we see immediately that the phases must match on the boundary for these waves to add to zero

$$s^r(\mathbf{X}) = s^i(\mathbf{X}), \quad \mathbf{X} \text{ on } B. \quad (46)$$

Now collecting powers of  $(ik)$  we get the following equation for the leading order amplitudes

$$z_0^i \left( \frac{\partial s^i}{\partial \nu} + Z \right) + z_0^r \left( \frac{\partial s^r}{\partial \nu} + Z \right) = 0. \quad (47)$$

Thus

$$z_0^r = - \left( \frac{\frac{\partial s^i}{\partial \nu} + Z}{\frac{\partial s^r}{\partial \nu} + Z} \right) z_0^i. \quad (48)$$

We have found the phase and amplitude of the reflected wave on the boundary. Then we can use the previous method to construct the reflected wave.

## 8 Reflection From a Parabolic Cylinder

To illustrate how this method works we will consider the example of waves reflected by a parabolic cylinder. Physically we could envision this to be the example of waves hitting a vertical cliff with a parabolic profile when viewed from above. Here we will consider the

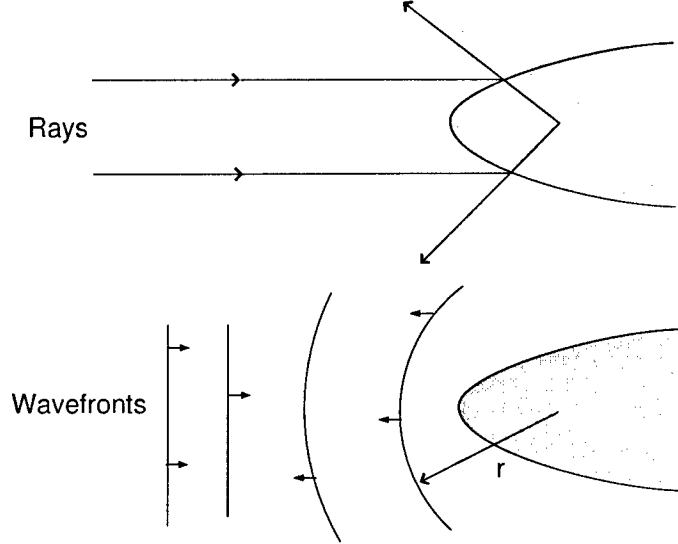


Figure 3: Reflection from a parabolic cylinder.

simple problem of an incoming plane wave  $e^{ikx}$ , with the  $x$  axis the axis of symmetry of the parabola. We will also take a uniform bottom, so that  $n \equiv 1$ , and the cliff face to be rigid,  $\frac{\partial u}{\partial \nu} = 0$  for  $\mathbf{x} \in B$ . Now using the fact that parabolas focus all rays to a point, we see that the rays reflected from the boundary of the cliff will all emanate from the focus of the parabola. Thus the wavefronts will be circles centered at the focus of the parabola (Figure 3). If we define our coordinate system with origin at the focus of the parabola, we get the phase of the reflected wave to be

$$s(r) = s_0 + r. \quad (49)$$

Here  $r$  is the distance from the origin, as in polar coordinates. We can also determine the reflected amplitude. Here matching the incident and reflected amplitude on the boundary and using equation (37) give

$$z_0(r) = \sqrt{\frac{r_0(\theta)}{r}}. \quad (50)$$

Here  $r = r_0(\theta)$  is the equation of the parabola. Thus we get the leading order solution to be

$$u = u^i + u^r \sim e^{ikx} + \sqrt{\frac{r_0(\theta)}{r}} e^{ik(s_0+r)}. \quad (51)$$

Similar analysis enables us to determine the higher order terms in  $u^r$ .

*Notes by Ben Akers and John Rudge.*

# Lecture 4: Geometrical Theory of Diffraction (continued) and the Shallow Water Theory

Joseph B. Keller

## 1 Introduction

In this lecture we will finish discussing the reflection from a boundary (Section 2). Next, in Section 3 we will switch to the geometric theory of diffraction without formal details (see [3]). Further, in Section 4, we will generalize the surface water wave theory to a case of non-uniform depth (see [2]). This theory predicts infinite amplitude at the shoreline, hence, in Section 5, the shallow water theory is introduced to fix that problem.

## 2 Reflection from a boundary

In the previous lectures we developed a method for solving the *Helmholtz equation*

$$\Delta U + k^2 n^2(X)U = 0. \quad (1)$$

It yields an asymptotic approximation like geometrical optics. It was applied to reflection by a parabolic cylinder. Now let us analyze reflection of waves, in water of constant depth  $h = \text{const}$ , by an arbitrary smooth boundary  $B$ , e.g. a vertical river bank. In this case the velocity potential is given by an incident contribution  $\phi^i$  and a reflected part  $\phi^r$ . Since the normal velocity on the boundary vanishes,  $\partial_\nu \phi|_B = 0$ . The zero-order asymptotic solution is given by

$$\phi = \phi^i + \phi^r \sim z_0^i(x)e^{ikS^i} + z_0^r(x)e^{ikS^r}. \quad (2)$$

The condition of vanishing normal derivative yields

$$\left(ik \frac{\partial}{\partial n} S^i\right) e^{ikS^i} z_0^i(x) + e^{ikS^i} \frac{\partial}{\partial n} z_0^i(x) + \left(ik \frac{\partial}{\partial n} S^r\right) e^{ikS^r} z_0^r(x) + e^{ikS^r} \frac{\partial}{\partial n} z_0^r(x) \sim 0. \quad (3)$$

Upon equating the exponents in (3), we get

$$S^i = S^r \text{ on } B. \quad (4)$$

Then upon equating to zero the coefficient of  $k$  in (3), we get

$$z_0^i \frac{\partial}{\partial n} S^i + z_0^r \frac{\partial}{\partial n} S^r = 0. \quad (5)$$

From (4), the tangential derivative  $\frac{\partial s^i}{\partial \tau}$  equals  $\frac{\partial s^r}{\partial \tau}$ . Then from the eiconal equation, the normal derivatives are related by

$$\left(\frac{\partial S^i}{\partial n}\right)^2 = n^2 - \left(\frac{\partial S^i}{\partial \tau}\right)^2 = n^2 - \left(\frac{\partial S^r}{\partial \tau}\right)^2 = \left(\frac{\partial S^i}{\partial n}\right)^2. \quad (6)$$

Thus  $\partial S^r / \partial n = \pm \partial S^i / \partial n$ . The “+” sign would yield  $S^r(x) \equiv S^i(x)$ , so we must choose the “-” sign

$$\frac{\partial S^r}{\partial n} = -\frac{\partial S^i}{\partial n}. \quad (7)$$

Then (5) yields

$$z_0^r = z_0^i \text{ on } B. \quad (8)$$

From  $\partial S^r / \partial \tau = \partial S^i / \partial \tau$  and (7) we get *law of reflection*, familiar from geometrical optics.

Instead of a rigid boundary, we can also consider the *impedance boundary condition*

$$\frac{\partial}{\partial n} \phi + ikZ\phi = 0. \quad (9)$$

This condition is frequently used in electrodynamics, and in acoustics for compliant boundaries. In this case it follows that

$$s^r(X) = s^i(X), \quad X \text{ on } B, \quad (10)$$

$$z_0^i \left( \frac{\partial s^i}{\partial \nu} + Z \right) + z_0^r \left( \frac{\partial s^r}{\partial \nu} + Z \right) = 0, \quad X \text{ on } B, \quad (11)$$

$$z_m^i \left( \frac{\partial s^i}{\partial \nu} + Z \right) + z_m^r \left( \frac{\partial s^r}{\partial \nu} + Z \right) + \frac{\partial z_{m-1}^i}{\partial \nu} + \frac{\partial z_{m-1}^r}{\partial \nu} = 0, \quad m \geq 1, \quad X \text{ on } B. \quad (12)$$

In terms of the incidence angle  $\alpha$  and the impedance  $Z$ , (11) gives the reflection coefficient

$$\frac{z_0^r}{z_0^i} = \frac{n \cos \alpha - Z}{n \cos \alpha + Z}, \quad (13)$$

again for  $X$  on  $B$ .

Fermat's principle of geometrical optics follows from the eiconal equation. It states that a ray travelling between two points takes the path with the shortest optical distance. For media with  $n(x) = \text{const}$ , we can find this path by imagining a string tightly spanned between these two points. Then the ray path will lie along this string.

To calculate the wave field numerically one often uses the finite element method. Due to the oscillatory nature of the wave field, this procedure requires very small elements. But we know that the leading order approximation has the form  $z_0^i(x)e^{ikS^i} + z_0^r(x)e^{ikS^r}$ . We can use this ansatz, calculating the phase by means of rays. After that the amplitudes  $z_0^i(x)$  and  $z_0^r(x)$  can be calculated by the finite element method. This allows us to use much larger elements.

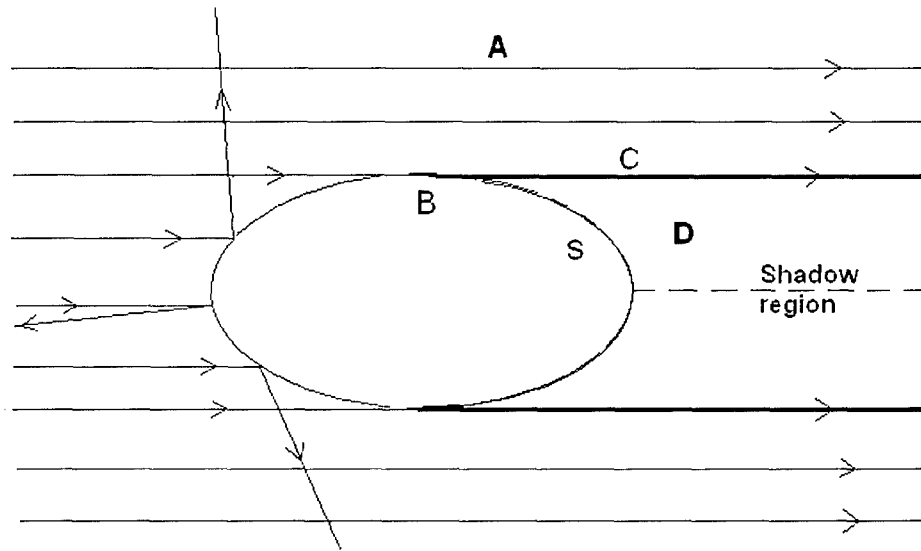


Figure 1: Scattering by a smooth object. Regions for asymptotic expansion:  $A$  - region of ordinary geometrical optics,  $B$  - point at which incident rays are tangent to the boundary,  $S$  - the object boundary,  $C$  - shadow boundary,  $D$  - shadow region.

### 3 Geometrical theory of diffraction

The asymptotic expansion method presented in the previous lectures is incomplete because of phenomena which are usually not taken into account by ordinary geometrical optics. Let us for example consider water waves being scattered by an island which we assume to be an oval-shaped object with smooth boundary. From ordinary geometrical optics follows that there exists a *shadow region*  $D$  (see Figure 1) in which the intensity of waves is zero. This region is separated from the region  $A$ , reached by incident and reflected rays, by a surface called the *shadow boundary*. Obviously, along this boundary the solution obtained by the ordinary geometrical optics method is discontinuous. However, this is in sharp contradiction with the fact that solutions of the Helmholtz equation (1) are smooth away from the boundary. Agreement of asymptotic solutions with actual solutions can be achieved by introducing boundary layer solution in the neighborhood of shadow boundaries. They can be found by using asymptotic expansions of certain exactly solvable problems, or constructed by boundary layer techniques. The construction of asymptotic solutions requires different expansions in different regions.

We first will consider asymptotic solutions in the shadow region  $D$ . The only rays which reach this region are rays diffracted by the boundary  $S$ . They are called *surface diffracted rays*. To construct them we introduce *surface rays* (or *creeping rays*) which propagate along the boundary  $S$ . The point  $B$  (see Figure 2) on the boundary between the shadow region  $D$  and the illuminated region  $A$  acts as a source for these rays. Note that at this

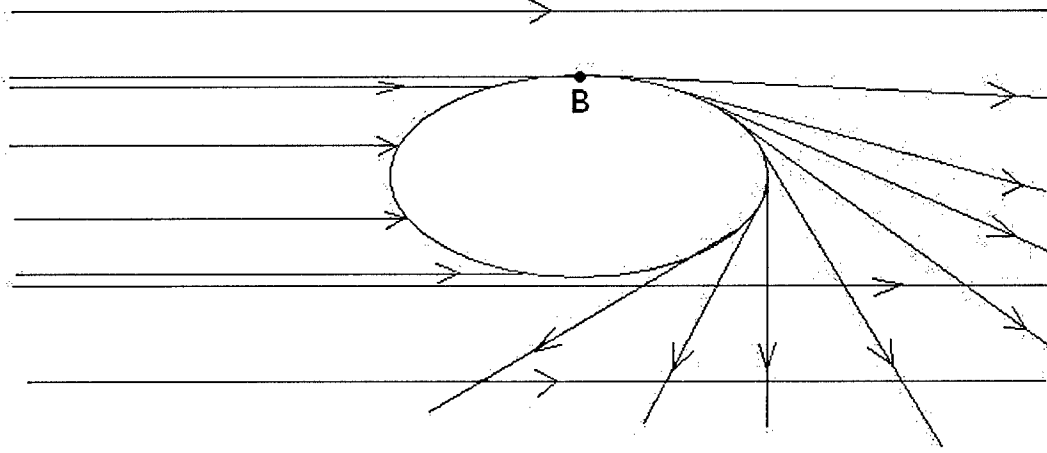


Figure 2: Surface diffracted rays omitted by the propagating surface ray starting at the point  $B$ .

point the incident ray is tangent to the boundary. Therefore, the incident ray splits into two branches. One branch goes along the shadow boundary  $C$  while the other is the ray travelling along the boundary  $S$ . The latter radiates surface diffracted rays into the shadow region, and therefore the boundary  $S$  acts as a secondary source. Because of this radiation, the intensity on the surface decays exponentially with distance along the ray. The surface ray travels infinitely many times around the boundary. Thus it sends an infinite number of surface rays to each point in the shadow, and also to each point in the illuminated region. Thus the complete wave field in the shadow region is an infinite sum of diffracted fields on surface diffracted rays.

The wave field on and near the shadow boundary can be obtained by using boundary layer theory. It yields Fresnel integrals which were used in the method of stationary phase. In the neighborhood of the separation point  $B$  there is yet another kind of asymptotic solution, given by the Fock function.

The asymptotics of the wave field in the neighborhood of the boundary  $S$  can be obtained from the exact solution of the Helmholtz equation for diffraction by a circular cylinder of radius  $a$ . In cylindrical coordinates a mode of the two dimensional wave field can be written as

$$u = e^{i\nu\theta} H_\nu^{(1)}(kr). \quad (14)$$

Here  $H_\nu^{(1)}$ , the Hankel function of first kind [1], is outgoing. Suppose the boundary condition is  $u(r)|_{r=a} = 0$ . This leads to the equation

$$H_\nu^{(1)}(ka) = 0. \quad (15)$$

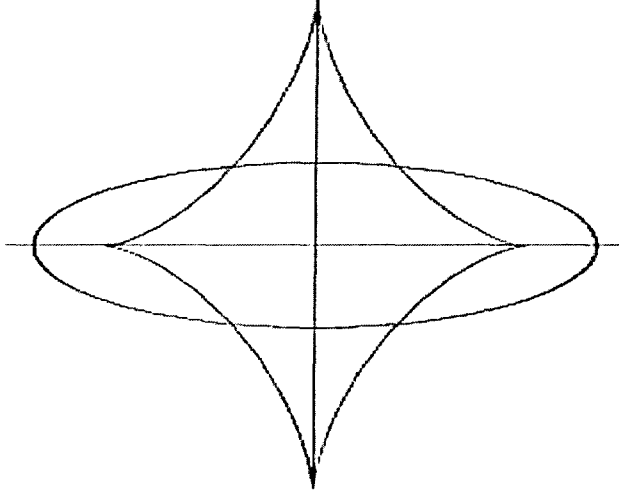


Figure 3: The Lamé curve.

This equation (15) has infinitely many complex roots  $\nu_m$ . The asymptotic behaviour of  $\nu_m$  for  $ka \gg 1$  is given by

$$\nu_m \sim ka + (ka)^{1/3} \tau_m e^{i\pi/3}. \quad (16)$$

When (16) is used for  $\nu$  in (14),  $u$  becomes

$$u_m = e^{i\nu_m \theta} H_{\nu_m}^{(1)}(kr) \sim e^{ika\theta + ie^{i\pi/3} \tau_m (ka)^{1/3} \theta} H_{\nu_m}^{(1)}(kr). \quad (17)$$

The result (17) shows that a single mode  $u_m(r, \theta)$  decays exponentially with  $\theta$  at a rate proportional to  $(ka)^{1/3}$ . For a noncircular boundary, the local decay rate can be obtained by replacing  $a$  by the local radius of curvature  $a(s)$  and setting  $d\theta = a^{-1}(s)ds$ . Then the exponent for the  $n$ -th mode becomes

$$iks + ie^{i\pi/3} \tau_m k^{1/3} \int_0^s (a(s'))^{-2/3} ds'. \quad (18)$$

The amplitude of each mode also involves diffraction coefficients at the point  $B$ , where the surface ray begins, and at the point  $B'$  where it leaves the surface. Then the total field in the shadow is a sum of all the modes.

When a wave is diffracted by an axially symmetric object in three dimensions, the diffracted waves have a caustic along the axis. This yields a bright spot in the cross-section of the shadow. The wave field on and near this caustic can be expressed in terms of Bessel functions.

Now let us consider diffraction of a normally incident plane wave by a planar screen of arbitrary shape, with a smooth boundary  $S$ . Instead of a bright spot, there is a bright curved line in each normal cross-section of the shadow. The form of the bright line is given by the *evolute* of the curve  $S$ , and it is a caustic of the edge diffracted rays. For a planar curve, the evolute is the locus of centers of curvature of the normals to the curve. For example, for an ellipse the bright line is given by the Lamé curve, see Figure 3. To summarize: an asymptotic solution will usually consist of a sum of waves. Every wave

is constructed by means of rays. They are obtained by solving the ray equations. Then the phase  $S$  and the amplitude  $z_0$  are found along each ray by the formulae given above. The other  $z_m$  can be found as solutions of the appropriate transport equations. This same approach is used in the next sections.

## 4 Surface waves on water of nonuniform depth

Previously we suggested that in water of nonuniform depth, we could determine the wave motion by using the reduced wave equation. That suggestion yields the correct phase, but not the correct amplitude. Therefore we shall now present an analysis which determines correctly both the phase and the amplitude<sup>1</sup>.

As before, we assume that the water is inviscid, incompressible and in irrotational motion. It is bounded above by an unknown free surface  $Z = \Re[e^{i\omega t}\eta(x, y)]$  ( $\eta$  is the complex amplitude of the surface wave motion of angular frequency  $\omega$ ) and bounded below by a rigid, non-uniform surface  $Z = -H(x, y)$ . The exact linear theory of surface waves yields for the free surface height

$$\eta(x, y) = \frac{i\omega}{g}\Phi(x, y, 0),$$

where  $\Phi(x, y, Z)$  is the *velocity potential* and  $g$  is the gravitational acceleration<sup>2</sup>.

The velocity potential satisfies (see Stoker [5])

$$\Delta\Phi = 0 \quad \text{in} \quad 0 \geq Z \geq -H(x, y), \quad (19)$$

$$\Phi_Z = \beta\Phi \quad \text{on} \quad Z = 0 \quad (\beta = \omega^2/g), \quad (20)$$

$$\Phi_Z + H_x\Phi_x + H_y\Phi_y = 0 \quad \text{on} \quad Z = -H(x, y). \quad (21)$$

In the constant-depth case, the solution decays exponentially with depth, so short waves do not “feel” the bottom. To keep the influence of the depth variability, we rescale the vertical axis by introducing

$$z = \beta Z, \quad h = \beta H, \quad \phi(x, y, z) = \Phi(x, y, Z). \quad (22)$$

Then the problem (19)-(21) becomes that of finding solutions  $\phi$  of the set of rescaled equations

$$\beta^2\phi_{zz} + \phi_{xx} + \phi_{yy} = 0 \quad \text{in} \quad 0 \geq z \geq -h(x, y), \quad (23)$$

$$\phi_z = \phi \quad \text{on} \quad z = 0, \quad (24)$$

$$\beta^2\phi_z + h_x\phi_x + h_y\phi_y = 0 \quad \text{on} \quad z = -h(x, y). \quad (25)$$

<sup>1</sup>It fails at the shoreline, where there is a boundary layer, see Section 5.

<sup>2</sup>The reason for using upper-case letters is to save the lower-case ones for the rescaled variables.



We seek solutions of (23)-(25) for large values of  $\beta$ .

Motivated by the constant-depth solution, we express  $\phi$  in the form

$$\phi = A \cosh [k(z + h)] e^{i\beta S}. \quad (26)$$

Here  $k = k(x, y)$ ,  $S = S(x, y)$  and  $A(x, y, z, \beta)$  are functions to be determined.

Plugging (26) into the system of equations (23)-(25) leads to

$$\begin{aligned} & \beta^2 ((k^2 - (\nabla S)^2) A \cosh \alpha + A_{zz} \cosh \alpha + 2k A_z \sinh \alpha) + \\ & + i\beta ((\nabla^2 S) A \cosh \alpha + 2\nabla S \cdot \nabla (A \cosh \alpha)) + \nabla^2 (A \cosh \alpha) = 0, \end{aligned} \quad (27)$$

$$A_z \cosh kh + k A \sinh kh = A \cosh kh \quad z = 0, \quad (28)$$

$$\beta^2 A_z + i\beta A \nabla h \cdot \nabla S + \nabla h \cdot \nabla A = 0 \quad z = -h. \quad (29)$$

Here  $\alpha = k(z + h)$  and  $\nabla = (\partial/\partial x, \partial/\partial y)$ .

Next we assume that  $A$  admits the following asymptotic expansion for large  $\beta$ :

$$A(x, y, z, \beta) \sim A_0(x, y) + \sum_{n=1}^{\infty} A_n(x, y, z)/(i\beta)^n. \quad (30)$$

Again, motivated by the constant-depth case, we have assumed that the first term  $A_0$  does not depend on the vertical coordinate. We also assume that termwise differentiation in (30) is allowed.

Inserting the asymptotic expansion (30) into (27)-(29), and equating coefficients of the corresponding powers of  $\beta$ , we obtain the following three systems of equations:

$$\left\{ \begin{array}{l} (\nabla S)^2 = k^2 \\ (A_1)_{zz} \cosh \alpha + 2k(A_1)_z \sinh \alpha = 2\nabla S \cdot \nabla (A_0 \cosh \alpha) + A_0 \cosh \alpha \nabla^2 S \\ (A_n)_{zz} \cosh \alpha + 2k(A_n)_z \sinh \alpha = 2\nabla S \cdot \nabla (A_{n-1} \cosh \alpha) + A_{n-1} \cosh \alpha \nabla^2 S + \\ \quad + \nabla^2 (A_{n-2} \cosh \alpha) \quad (n \geq 2), \end{array} \right. \quad (31)$$

$$\left\{ \begin{array}{l} k \tanh kh = 1 \\ (A_n)_z = 0 \quad \text{at} \quad z = 0 \quad (n \geq 1), \end{array} \right. \quad (32)$$

and, finally,

$$\left\{ \begin{array}{l} (A_1)_z = A_0 \nabla h \cdot \nabla S \quad \text{at} \quad z = -h \\ (A_n)_z = A_{n-1} \nabla h \cdot \nabla S + \nabla h \cdot \nabla A_{n-2} \quad \text{at} \quad z = -h \quad (n \geq 2). \end{array} \right. \quad (33)$$

The first equation in (32) determines  $k(x, y)$  as a function of the known depth  $h(x, y)$ . Then the eiconal equation  $(\nabla S)^2 = k^2$  can be solved for  $S(x, y)$  by the ray method discussed in the previous lectures.

In order to find the amplitude  $A_0$ , we use the identity

$$(A_n)_{zz} \cosh \alpha + 2k(A_n)_z \sinh \alpha = \frac{((A_n)_z \cosh^2 \alpha)_z}{\cosh \alpha}. \quad (34)$$

Inserting (34) into (31.2) we obtain

$$((A_1)_z \cosh^2 \alpha)_z = (2\nabla S \cdot \nabla A_0 + A_0 \nabla^2 S) \cosh^2 \alpha + A_0 \nabla S \cdot \nabla \cosh^2 \alpha. \quad (35)$$

Now we integrate (35) from 0 to  $z$ , using the boundary conditions (32.2)

$$(A_1)_z \cosh^2 \alpha = \frac{1}{2} (2\nabla S \cdot \nabla A_0 + A_0 \nabla^2 S + A_0 \nabla S \cdot \nabla) (k^{-1} [\sinh \alpha \cosh \alpha - \sinh kh \cosh kh] + y). \quad (36)$$

Solving (36) will give  $A_1$  up to an additive function of  $(x, y)$ , if  $A_0$  is known.

Next we set  $z = -h$  in (36) and eliminate  $(A_1)_z$ , using the boundary condition (33.1). This leads to an equation for  $A_0$

$$2A_0 \nabla h \cdot \nabla S = -(2\nabla S \cdot \nabla A_0 + A_0 \nabla^2 S)(\sinh^2 kh + h) + A_0 \nabla S \cdot (\nabla h - \nabla \sinh^2 kh). \quad (37)$$

Equivalently, (37) can be written

$$\nabla S \cdot \nabla (A_0^2 (\sinh^2 kh + h)) + (A_0^2 (\sinh^2 kh + h)) \nabla^2 S = 0. \quad (38)$$

We note that  $\nabla S \cdot \nabla = k(d/d\tau)$ , where  $\tau$  measures arc-length along a ray. Then the solution of (38) can be written in the form

$$A_0^2 (\sinh^2 kh + h) = [A_0^2 (\sinh^2 kh + h)]_{\tau_0} \exp \left( - \int_{\tau_0}^{\tau} k^{-1} \nabla^2 S d\tau \right). \quad (39)$$

In [4], Luneberg has shown that the exponential above is given by

$$\exp \left( - \int_{\tau_0}^{\tau} k^{-1} \nabla^2 S d\tau \right) = \frac{k(\tau_0) da(\tau_0)}{k(\tau) da(\tau)}. \quad (40)$$

Here  $da(\tau)$  is the width of an infinitesimally narrow strip of rays at  $\tau$ . Plugging (40) into (39), we finally get the following equation for  $A_0$  along a ray:

$$A_0^2 (\sinh^2 kh + h) k da = \text{const.} \quad (41)$$

Equation (41) simply expresses the fact that the energy flux is constant along a tube of rays. By using (41) for  $A_0(x, y)$  in (26), we get the leading term in the asymptotic expansion of  $\phi$  in water of variable depth.

The amplitude  $A_0$  is infinite at the shoreline, where  $h = 0$ . This means that there is a boundary layer at the shore. To analyze the solution in this layer, we use the shallow water theory, which is introduced in the next section.

## 5 Shallow water theory

The main reference for this section is Stoker's famous monograph [5]. For simplicity, we consider the 2-dimensional case with horizontal  $x$ -axis and vertical  $z$ -axis. The free surface is given by  $z = \eta(x, t)$ , while the bottom is  $z = -h(x)$ . The equation of continuity for the components  $u(x, z, t)$  and  $v(x, z, t)$  of the water velocity is

$$u_x + v_z = 0. \quad (42)$$

At the free surface we have both the kinematic condition

$$(\eta_t + u\eta_x - v)|_{z=\eta} = 0 \quad (43)$$

and the dynamic condition

$$p|_{z=\eta} = 0. \quad (44)$$

The bottom boundary condition is

$$(uh_x + v)|_{z=-h} = 0. \quad (45)$$

Integrating (42) gives

$$\int_{-h}^{\eta} u_x dz + v|_{-h}^{\eta} = 0. \quad (46)$$

Using the top and bottom boundary conditions in (46) leads to

$$\int_{-h}^{\eta} u_x dz + \eta_t + u|_{\eta} \cdot \eta_x + u|_{-h} \cdot h_x = 0. \quad (47)$$

We can rewrite (47) as

$$\frac{\partial}{\partial x} \int_{-h}^{\eta} u dz = -\eta_t. \quad (48)$$

Notice that up to this point no approximation has been introduced. The sole approximation of the shallow water theory is to ignore the vertical acceleration. This is assumed because the water is shallow. Hence the pressure is given as in hydrostatics, namely

$$p = g\rho(\eta - z). \quad (49)$$

Here  $\rho$  is the water density and  $g$  is the acceleration of gravity. Differentiating (49) with respect to  $x$  gives

$$p_x = g\rho\eta_x. \quad (50)$$

Note that since  $\eta_x$  is independent of  $y$ , so is  $p_x$ .

Next, we assume that  $u$  is independent of  $z$  at  $t = 0$  (This is true if the water is initially at rest). This will imply that  $u$  is independent of  $z$  at all times, since its horizontal acceleration  $\rho^{-1}p_x$  does not depend on  $z$  either, as (50) shows. Then (48) becomes

$$[u(\eta + h)]_x = -\eta_t. \quad (51)$$

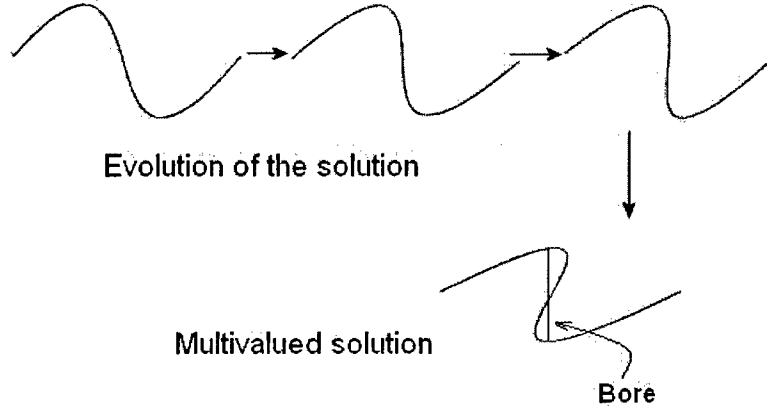


Figure 4: The "bore" formation.

The Eulerian equation of motion for  $u(x, t)$  is

$$u_t + uu_x = -g\eta_x. \quad (52)$$

Eqs. (51) and (52) constitute the (*nonlinear*) *shallow water theory* for determining  $u$  and  $\eta$ .

When  $u$  and  $\eta$  and their derivatives are small enough, we can linearize (51) and (52). This yields the *linear shallow water theory*, in which  $u$  and  $\eta$  satisfy

$$\begin{cases} u_t = -g\eta_x, \\ (uh)_x = -\eta_t. \end{cases} \quad (53)$$

Eliminating  $\eta$  from (53) yields

$$(hu)_{xx} - \frac{1}{gh}(hu)_{tt} = 0. \quad (54)$$

We have multiplied and divided by  $h(x)$  to get the linear wave equation for the quantity  $(hu)$ . The propagation speed is  $\sqrt{gh}$ . If  $h = \text{const}$ , (54) is a linear wave equation just for  $u$ . The linear shallow water theory is used for the tides, where large wavelengths are involved.

The equations of the nonlinear shallow water theory admit an interesting analogy with the differential equations of gas dynamics. Let us define  $\bar{\rho}$ , the mass per unit area, by

$$\bar{\rho} = \rho(\eta + h). \quad (55)$$

From (55)

$$\bar{\rho}_t = \rho\eta_t. \quad (56)$$

Then the force per unit width  $\bar{p} = \int_{-h}^{\eta} p \, dz$  is given by

$$\bar{p} = \frac{g\rho}{2}(\eta + h)^2 = \frac{g}{2\rho}\bar{\rho}^2. \quad (57)$$

Now we multiply (52) by  $\rho(\eta + h)$  to get

$$\rho(\eta + h)(u_t + uu_x) = -g\rho(\eta + h)\eta_x. \quad (58)$$

Then using (55) and (57), we can write (58) as

$$\bar{\rho}(u_t + uu_x) = -\bar{p}_x + g\bar{\rho}h_x. \quad (59)$$

In terms of  $\bar{\rho}$ , we can write (51) as

$$(\bar{\rho}u)_x = -\bar{\rho}_t. \quad (60)$$

The equations (57), (59) and (60) are exactly the equations for the one dimensional flow of a compressible gas with adiabatic exponent  $\gamma = 2$  and an external force  $g\bar{\rho}h_x$ . This force vanishes when the depth is uniform. The sound speed is

$$c = \sqrt{\frac{g\bar{\rho}}{\rho}} = \sqrt{g(\eta + h)}. \quad (61)$$

This is the speed of a small disturbance.

As in gas dynamics, the solutions of the nonlinear shallow water equation cease to be single valued at a finite time for certain initial conditions. They can be made single valued by introducing a discontinuity, called a “shock” in gas dynamics, and a “bore” in water waves. See Fig. 4. Such discontinuities can be observed in some rivers, and in kitchen sinks.

*Notes by Khachik Sargsyan and Walter Pauls.*

## References

- [1] M. ABRAMOWITZ AND I. STEGUN, *Handbook of mathematical functions*, Dover Publications, New York, 1965.
- [2] J. B. KELLER, *Surface waves on water of non-uniform depth*, J. Fluid Mech., 4 (1958).
- [3] J. B. KELLER AND R. M. LEWIS, *Asymptotic methods for PDEs*, Plenum Publishing, New York, 1995.
- [4] R. K. LUNEBERG, *Mathematical theory of optics*, Brown University Lecture Notes, 1944.
- [5] J. STOKER, *Water waves*, Wiley Interscience, 1957.

# Lecture 5: Amplitude Dynamics, Boundary Layers, and Harbor Resonance

Jospeh B. Keller

## 1 Amplitude Amplification at the Shore

We will now consider the consequences of ray theory for the amplification of wave amplitudes near a shoreline. In the deep ocean, tsunami waves have small amplitude and long wavelength, on the order of tens of kilometers. But when they reach the shore, as mentioned in the last lecture, they can grow to towering heights. We can gain insight into the nature of this amplitude growth using the linear methods of the previous lecture.

We will consider the evolution of a wave train incident on a sloping beach. Let the depth be a linear function of distance from the shore

$$h = x \tan \alpha \sim \alpha x, \quad \alpha \ll 1 \quad (1)$$

Following the method of the previous lectures, factor the velocity potential into a horizontal oscillation and a vertical mode shape

$$\phi(x, y, z) = A \cosh(k(z + h)) e^{i\beta S(x, y)}. \quad (2)$$

Consequently,

$$(\nabla S)^2 = k^2 \quad (3)$$

$$k \tanh kh = 1. \quad (4)$$

We now specialize to the case of one dimensional long waves. These are waves with long wavelength compared to the depth and wavefronts parallel to the shore. Mathematically, these assumptions imply

$$kh \ll 1 \quad (5)$$

$$S = S(x). \quad (6)$$

In this limit, Equation (4) becomes

$$k^2 h = 1, \quad (7)$$

which implies

$$k = \frac{1}{\sqrt{h}}. \quad (8)$$

Therefore, as the waves approach shore and  $h \rightarrow 0$ ,  $k \rightarrow \infty$  and the wavelength decreases to zero. The parameter  $kh$ , however, remains small throughout:

$$kh = \frac{1}{k} \rightarrow 0$$

Incidentally, the one dimensional wave approaching parallel to the shore is the most physically relevant case. Recall from Lecture 3 the equation for the path of characteristic curves

$$\frac{d}{d\sigma} \nabla S = \frac{\lambda}{2} \nabla n^2(\mathbf{x}). \quad (9)$$

Using  $n^2(\mathbf{x}) = h_0/h(\mathbf{x})$ , we have

$$\frac{d}{d\sigma} \nabla S = -\frac{h_0}{h^2(\mathbf{x})} \nabla h. \quad (10)$$

Since  $\nabla S$  is parallel to rays, and  $-\nabla h$  points in the direction of the shore, this equation shows that rays curve in the direction of the shore. Figure 1 illustrates the intuition behind this result. As a wave approaches a beach at an angle, the section of the wavefront further from the beach is over deeper water, and therefore has a relatively faster wave speed. Accordingly, the wavefront will swing towards the shore until it is parallel with the beach, and all points on the wavefront have the same wave speed. For this reason, the one dimensional formulation is adequate to investigate the late stages of a wave's approach to the shore.

The reduction to one dimension also makes it easy to compute the phase. We have

$$\begin{aligned} \frac{\partial S}{\partial x} &= \pm k \\ &= \pm \frac{1}{\sqrt{h}} \\ &= \pm \frac{1}{\sqrt{x \tan \alpha}}. \end{aligned} \quad (11)$$

Though the derivative is singular at  $x = 0$ , it is integrable and we can compute the phase

$$\begin{aligned} S(x) &= \pm \int_{x_0}^x \frac{1}{\sqrt{h(x')}} dx' \\ &= \pm \int_{x_0}^x \frac{1}{\sqrt{x' \tan \alpha}} dx' \\ &= \pm \frac{2x^{1/2}}{\sqrt{\tan \alpha}} + C \end{aligned} \quad (12)$$

We choose the minus sign to be consistent with waves moving toward the shore.

We are now prepared to compute the amplitude evolution. Because the rays are straight lines in one dimension, the ray tube area  $d\sigma = \text{constant}$ . We showed in Lecture 4 that

$$A_0^2 (\sinh^2 kh + h) k d\sigma = \text{constant}.$$

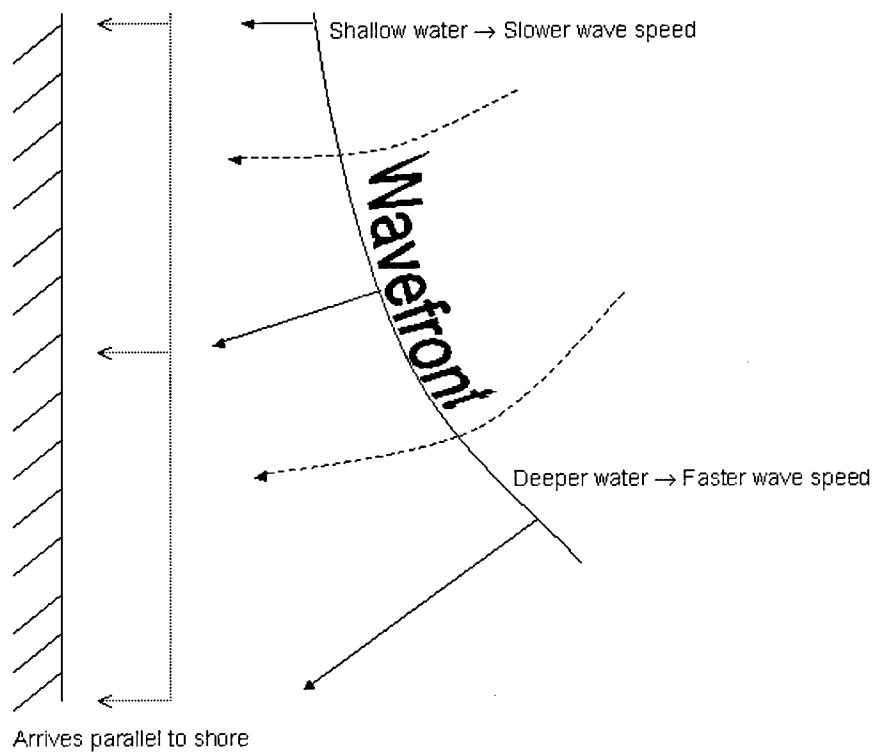


Figure 1: Waves on a sloping beach are refracted so as to approach with wavefronts parallel to the shoreline



Therefore,

$$\begin{aligned} A_0^2 &\sim \frac{1}{k(h + \sinh^2 kh)} \\ &\sim \frac{1}{k(k^2 h^2 + h)}. \end{aligned} \tag{13}$$

Using equation (8), we have

$$A_0 = \frac{C'}{h^{1/4}} = \frac{C}{x^{1/4}}. \tag{14}$$

Thus, the theory predicts wave amplitudes going to infinity at the shoreline. That's why tsunamis do so much damage.

This result seems natural considering that we have held the example of a tsunami in mind as we derived it. But one might ask what, in this theory, differentiates tsunamis from any other wave? The ocean is full of waves satisfying  $kh \ll 1$  that reach shore without catastrophic consequences. Clearly, something is wrong with the theory very close to the shore.

A typical trouble with asymptotic theories is the presence of certain regions where the solutions become singular. In these regions, the asymptotic expansions fail. We need a different theory that applies in this singular region, which we call a boundary layer. If all goes well, we will be able to find a solution that applies in the boundary layer and that blends continuously into exterior solution we have just derived.

## 2 Boundary layer and shallow water equations

### 2.1 The concept of the wave boundary layer

The asymptotic analysis based on the linear wave theory discussed above, which was asymptotic in the sense that the depth and wavelength were small compared to the characteristic horizontal scale, proved to be successful for deep water waves (see the previous lecture and [3]). However, the theory fails in the proximity of the shore, yielding an infinite amplitude there. Wave propagation near the shore can be analyzed by means of the shallow water theory and the boundary layer concept.

The idea is to use the shallow water equations in the vicinity of the shore, where the depth is small, and the wavelength is large compared to the depth. It is worth noting, however, that shallow water theory is applicable over large regions of ocean basins, if we study phenomena on the synoptic scale, large ( $L \approx 100$  km) compared to the mean depth of the basin ( $H \approx 500 - 1000$  m), see e.g. [4].

First of all, we will ruminate for a while on the derivation of the shallow water equations, formulated for an incompressible fluid in an inertial frame - Coriolis acceleration will not be included.

Naturally, at this point anyone merely conversant with physical oceanography<sup>1</sup> would ask about the relevance of linear shallow water theory to the reality which occurs on the noninertial frame of the rotating Earth, where the Coriolis acceleration should be taken

---

<sup>1</sup>and we assume that some of our readers belong to this group

into account. In fact, this effect is crucial in studies of tidal phenomena as well as for the more general model of Poincare waves (the latter problem being formulated in the shallow water approximation in the synoptic-scale ocean gives dispersive waves). However, neglecting the coriolis force may be justified in two classes of wave problems:

- waves propagating in lakes and small, shelf seas (i.e the Baltic sea) where the long (with respect to the basin depth) waves are locally generated by a strong wind yet they are short enough not to be effected by the Coriolis acceleration,
- Shoaling waves approaching normal to a shoreline. Then the waves, irrespective of whether they were nondispersive or dispersive far from the shore due to the Coriolis effect, undergo shoaling on scales on which the Coriolis effect does not contribute.

### 3 The structure of the boundary layer

While toying with the idea of the **horizontal wave boundary layer**  $\mathfrak{D}$  for the problem of waves approaching the shore and affected by its presence, we could attempt to find an analogy with the **vertical** terrestrial and oceanic boundary layer (table 1). By this analogy, we may expect that the solution obtained for the wave boundary layers may be matched at the borderline between the boundary layer and the outer one, just like in the case of vertical boundary layers.

#### 3.1 Shallow water equations

We consider long waves propagating in relatively shallow water in an inertial frame of reference. We assume two-dimensional motion in the  $(x, y)$  plane. The equation of continuity for an incompressible fluid is:

$$u_x + w_z = 0, \quad (15)$$

The kinematic condition and the dynamic conditions at the free surface are:

$$(\eta_t + u\eta_x - w)|_{z=\eta} = 0, \quad p|_{z=\eta} = 0 \quad (16)$$

The kinematic condition at the bottom is:

$$(uh_x + w)|_{z=-h} = 0, \quad p|_{z=-h} = 0 \quad (17)$$

It is convenient to formulate the problem in terms of the depth integrated horizontal velocity, namely:

$$\frac{\partial}{\partial x} \int_{-h}^{\eta} u dz, \quad (18)$$

using the boundary conditions and the Leibniz rule of integration:

$$\frac{\partial}{\partial x} \int_{-h}^{\eta} u dz = -\eta_t \quad (19)$$

In the shallow water theory the hydrostatic pressure approximation is used. That is, vertical acceleration is ignored. Then, the pressure at a point is determined entirely by the weight of the water column above it:

$$p = g\rho(\eta - z) \quad (20)$$

vertical (terrestrial/ocean)	horizontal (wave)
ground/free water surface/ice	shoreline
Prandtl layer	shore wave boundary layer $\delta$ where the shallow water theory applies; for the sake of use of asymptotic methods, $\delta$ can be further divided into inner shore wave boundary layer $\delta_i$ in the immediate proximity of the shoreline and the outer shore wave boundary layer $\delta_o$
Ekman layer	the outer layer where the shallow water might also apply but the Coriolis term should be taken into account causing waves to be dispersive
free flow (geostrophic layer)	the outermost layer where gravity deep water wave theory applies

Table 1: Boundary layer structure and the analogy between vertical and horizontal boundary layers.

The horizontal pressure gradient is then  $p_x = g\rho\eta_x$ . From the equation of motion in the  $x$  direction,  $u_t + uu_x = -g\eta_x$ , the horizontal acceleration is independent of depth. Therefore so is  $u$ , provided that it was initially independent of  $z$ . The depth integrated  $u$  is now  $\int_{-h}^{\eta} u dz = u(\eta + h)$ . Using this, we obtain **the nonlinear shallow water equations**:

$$u_t + uu_x = -g\eta_x \quad (21)$$

$$(u(h + \eta))_x = -\eta_t, \quad (22)$$

Where  $\eta = \eta(x, t)$ ,  $u = u(x, t)$ ,  $h = h(x)$ . If we assume that  $u$ ,  $\eta$  and their derivatives are small, their products can be neglected compared with linear terms. Then (21) and (22) yield **the linear shallow water equations** :

$$u_t = -g\eta_x \quad (23)$$

$$(uh)_x = -\eta_t \quad (24)$$

Eliminating  $\eta$  from (23) and (24) gives

$$(uh)_{xx} - \frac{1}{g}u_{tt} = 0. \quad (25)$$

### 3.2 Linear SWE and the variable depth - asymptotic approach

Since  $h = h(x)$  is independent of  $t$ , we can rewrite (25) as

$$(uh)_{xx} - \frac{1}{gh}(uh)_{tt} = 0. \quad (26)$$

This is the wave equation for a variable  $U^* = uh$  with propagation velocity  $c = \sqrt{gh(x)}$ . For time harmonic waves  $U^*(x, t) = U(x) \exp(-i\omega t)$ , (26) becomes the Helmholtz equation:

$$U_{xx} + \frac{\omega^2}{gh(x)}U = 0. \quad (27)$$

We now define  $k = \omega/\sqrt{gh_0}$ ,  $n(x)^2 = gh_0/gh(x)$ , in terms of a typical depth  $h_0$ . Then we can rewrite (26) as

$$U_{xx} + k^2 n^2(x)U = 0. \quad (28)$$

Away from the shoreline  $h(x) = 0$ , the asymptotic form of  $U(x, k)$  for  $kh_0 \gg 1$  is

$$U(x) \approx Z^{in}(x) \exp(ik S^{in}(x)) + Z^r(x) \exp(ik S^r(x)). \quad (29)$$

Here  $Z^{in}(x)$ ,  $S^{in}(x)$  and  $Z^r(x)$ ,  $S^r(x)$  are the amplitudes and phases of the incident and reflected waves, respectively. We call (29) **the outer asymptotic expansion** of  $U$ . It is not valid where  $h(x) = 0$  because  $Z^{in}(x)$ ,  $Z^r(x)$  become infinite there. To determine  $U(x)$  near the shore, we define  $x' = kx$  and  $V(x', k) = U(x, k)$ . Then  $h(x) = h(\frac{x'}{k}) = h(0) + h_x(0)(\frac{x'}{k}) + \mathcal{O}(k^{-2})$ . Then at the shoreline  $x = 0$  we get  $h(0) = 0$  and we define  $\alpha$ , the slope of the bottom, by  $\tan \alpha = h_x(0)$ . Then  $n(x)^2 = h_0/h(x) = (kh_0)/(x' \tan \alpha) + \mathcal{O}(1)$  and (28) becomes:

$$V_{x'x'} + \left( \frac{h_0}{\tan \alpha} \frac{k}{x'} + \mathcal{O}(1) \right) V = 0. \quad (30)$$

When we neglect the  $\mathcal{O}(1)$  term, (30) becomes a form of the Bessel equation. Although the coefficient of  $V$  is singular at  $x' = 0$ , the equation has a solution which is regular there. It is

$$V(x', k) = A\sqrt{x'} J_1\left(2\sqrt{\frac{kh_0}{\tan \alpha}} x'\right). \quad (31)$$

Here,  $A$  is an arbitrary constant. Then the solution of (31) vanishes at  $x' = 0$ . There is also a solution which is infinite at  $x' = 0$ . The asymptotic solution of (31) for  $x'$  large is:

$$V(x', k) \sim A(\sqrt{x'}) e^{i\left(2\sqrt{\frac{kh_0}{\tan \alpha}} x'\right)} + B(\sqrt{x'}) e^{-i\left(2\sqrt{\frac{kh_0}{\tan \alpha}} x'\right)}, \quad (32)$$

This can be matched with the outer expansion (29). The system of linear, variable depth shallow water equations is satisfactory for small amplitude waves. It does not capture effects like breaking, for which the nonlinear theory is needed.

## 4 Nonlinear Wave Propagation Along Rays

In these lectures, we have discussed the linear theory of waves in some detail. It would be a shame not to discuss nonlinearity a little further. For decades, models of water waves have been an interesting source of nonlinear equations. One of the most famous of these equations is that of Kordeveg and de Vries, which was derived to model the cumulative effect of nonlinearity in water waves travelling over long distances.

In this section, we will derive KdV in the context of a ray tracing theory for nonlinear long waves on a layer with spatially varying depth. In linear theories, the amplitude typically takes the form of a nearly sinusoidal wave train with amplitude and wavenumber slowly varying along a ray. Instead, we will find that the amplitude is governed by an equation of KdV form. Specifically, we will consider the equations for a disturbance on the surface of an incompressible flow of constant density without rotation. This computation is a simplified presentation of a more general analysis presented in [5], in which the effects of bottom topography, incompressibility, rotation, stratification, and a polytropic equation of state are taken into account. By including only one dimensional bottom topography, we will be examining the simplest case in which nontrivial amplitude dynamics occurs.

### 4.1 Scaling the Equations of Motion

We begin by introducing a carefully chosen scaling of the equations of fluid motion. The key method of asymptotic analysis is to rescale equations to introduce small parameters, thus allowing complex problems to be considered as a sequence of simpler problems. The art of this method is to tailor one's scaling to access a physically interesting limit. In this case, the scaling will pertain to waves with wavelength long compared to the depth of the layer, propagating over long distances.

Let us consider a layer of incompressible fluid in two dimensions bounded above by the free surface  $z^* = \eta^*(x^*, t^*)$  and below by the rigid surface  $z^* = -h^*(x^*)$ . Before writing the

equations of motion, we introduce stretched dimensionless variables  $x, z, t$ , etc., as follows:

$$\begin{aligned} \epsilon &= \left(\frac{H}{L}\right)^{2/3}, & (x^*, z^*) &= H (\epsilon^{-3/2} x, z), \\ h^* &= H h, & \eta^* &= H \eta, \\ p^* &= g H \rho_0 p, & t^* &= \epsilon^{-3/2} t \left(\frac{H}{g}\right)^{1/2} \\ (u^*, w^*) &= \sqrt{g H} (u, \epsilon^{1/2} w). \end{aligned} \quad (33)$$

and  $\mathbf{v} = (u, w)$ . Here,  $L$  is a typical horizontal scale of variation, so  $\epsilon$  is determined by the characteristic aspect ratio of the motion.

In these stretched variables, the equations of motion take the following form:

$$\frac{\partial w}{\partial z} + \epsilon \frac{\partial u}{\partial x} = 0, \quad (34)$$

$$\epsilon \left( \frac{\partial u}{\partial t} + u \frac{\partial u}{\partial x} + \frac{\partial p}{\partial x} \right) + w \frac{\partial u}{\partial z} = 0, \quad (35)$$

$$\epsilon^2 \left( \frac{\partial w}{\partial t} + u \frac{\partial w}{\partial x} \right) + \epsilon w \frac{\partial w}{\partial z} + \frac{\partial p}{\partial z} + 1 = 0. \quad (36)$$

The kinematic condition and the normal force balance at the free surface are, respectively,

$$\frac{\partial \eta}{\partial t} + u \frac{\partial \eta}{\partial x} = w, \quad (37)$$

$$p = C, \quad (38)$$

evaluated at  $z = \eta(x)$ . The kinematic condition at the lower boundary is

$$w = -\epsilon u \frac{\partial h}{\partial x} \quad (39)$$

evaluated at  $z = -h(x)$ .

When  $\epsilon = 0$ , equations (34) - (39) have, as a solution, the state of rest given by

$$\mathbf{v}_0 = 0, \quad (40)$$

$$p_0 = C - z \quad (41)$$

$$\eta_0 = 0. \quad (42)$$

To find approximate solutions for  $\epsilon \neq 0$ , we introduce a phase function  $S(x, t)$  and the "fast" variable  $\xi = \epsilon^{-1} S$ . We then express  $\mathbf{v}$ ,  $p$ , and  $\eta$ , as functions of  $\xi$  as well as of  $x, z, t$ , and  $\epsilon$ . We also assume that these functions possess asymptotic expansions in  $\epsilon$  of the form

$$\mathbf{v}(\xi, t, x, z, \epsilon) \sim \mathbf{v}_0(t, x, z) + \epsilon \mathbf{v}_1(\xi, t, x, z) + \epsilon^2 \mathbf{v}_2 + \dots, \quad (43)$$

where the variables with subscript 0 are the rest state solutions given above. Under this change of variables, the derivatives transform as

$$\frac{\partial}{\partial x} \rightarrow \frac{\partial}{\partial x} + \epsilon^{-1} S_x \frac{\partial}{\partial \xi}, \quad (44)$$

$$\frac{\partial}{\partial t} \rightarrow \frac{\partial}{\partial t} + \epsilon^{-1} S_t \frac{\partial}{\partial \xi}. \quad (45)$$

Since,  $\frac{\partial h}{\partial \xi} = 0$ , the equations of motion become

$$\epsilon \frac{\partial u}{\partial x} + S_x \frac{\partial u}{\partial \xi} + \frac{\partial w}{\partial z} = 0, \quad (46)$$

$$\epsilon \left( \frac{\partial u}{\partial t} + u \frac{\partial u}{\partial x} + \frac{\partial p}{\partial x} \right) + (S_t + u S_x) \frac{\partial u}{\partial \xi} + S_x \frac{\partial p}{\partial \xi} + w \frac{\partial u}{\partial z} = 0, \quad (47)$$

$$\epsilon^2 \left( \frac{\partial w}{\partial t} + u \frac{\partial w}{\partial x} \right) + \epsilon \left( w \frac{\partial w}{\partial z} + (S_t + u S_x) \frac{\partial w}{\partial \xi} \right) + \frac{\partial p}{\partial x} + 1 = 0. \quad (48)$$

The boundary conditions become

$$\epsilon \left( \frac{\partial \eta}{\partial t} + u \frac{\partial \eta}{\partial x} \right) + (S_t + u S_x) \frac{\partial \eta}{\partial \xi} - w = 0, \quad z = \eta, \quad (49)$$

$$w + \epsilon u \frac{\partial h}{\partial x} = 0, \quad z = -h. \quad (50)$$

We will now substitute the asymptotic series forms into these equations and equate coefficients of successive powers of  $\epsilon$ . Additionally, we transform the boundary conditions at  $z = \eta$  into boundary conditions at  $z = 0$  by writing the boundary terms as a Taylor expansion around  $z = 0$ . In this way we obtain sets of equations for the successive determination of  $S$  and of the various coefficients in the asymptotic expansion of the solution.

Equating the coefficients of order  $\epsilon$  yields

$$S_x \frac{\partial u_1}{\partial \xi} + \frac{\partial w_1}{\partial z} = 0, \quad (51)$$

$$S_t \frac{\partial u_1}{\partial \xi} + S_x \frac{\partial p_1}{\partial \xi} = 0, \quad (52)$$

$$\frac{\partial p_1}{\partial z} = 0, \quad (53)$$

$$S_t \frac{\partial \eta_1}{\partial \xi} - w_1 = 0, \quad z = 0, \quad (54)$$

$$p_1 = \eta_1, \quad z = 0, \quad (55)$$

$$w_1 = 0, \quad z = -h. \quad (56)$$

## 4.2 Modes Structure and the Eiconal equation

We can solve equations (51)-(56) for the structure of wave solutions at leading order. A PDE governing the phase function  $S$  will emerge as a solvability condition for these equations, and will be seen to be equivalent to the eiconal equation of shallow water theory.

First, we eliminate  $\eta_1$  and  $u_1$  using equations (51) and (55) to write

$$\frac{\partial \eta_1}{\partial \xi} = \frac{\partial p_1}{\partial \xi}, \quad (57)$$

$$\frac{\partial u_1}{\partial \xi} = -\frac{1}{S_x} \frac{\partial w_1}{\partial z}. \quad (58)$$

Equality in equation ( 57) holds for all  $z$  by equation ( 53). The system simplifies to

$$-\frac{S_t}{S_x} \frac{\partial w_1}{\partial z} + S_x \frac{\partial p_1}{\partial \xi} = 0, \quad (59)$$

$$\frac{\partial p_1}{\partial z} = 0, \quad (60)$$

$$\frac{\partial p_1}{\partial \xi} - \frac{w_1}{S_t} = 0, \quad z = 0, \quad (61)$$

$$w_1 = 0, \quad z = -h. \quad (62)$$

In order to solve these equations, we seek a product solution of the form

$$p_1 = A(\xi, t)\psi(x, z), \quad (63)$$

$$w_1 = -S_t \frac{\partial A}{\partial \xi} \phi(x, z). \quad (64)$$

These forms are analogous to that used in Lecture 3, the well known WKB ansatz. In those cases the solution consists of a rapid sinusoidal oscillation with a slowly varying amplitude. In the present case, we also imagine the solution will take the form of a rapidly oscillating waveform, represented by  $A(\xi, t)$ , with a slow modulation and vertical structure represented by  $\phi$  and  $\psi$ . However, because of nonlinearity, the fast waves do not take the form of sinusoids. Rather, the appropriate wave shape will emerge from the analysis.

Substituting these solution forms into equations ( 59)-( 62) and simplifying yields

$$\psi = -\theta^2(x, t) \frac{\partial \phi}{\partial z}, \quad (65)$$

$$\frac{\partial \psi}{\partial z} = 0, \quad (66)$$

$$\psi = -\phi, \quad z = 0, \quad (67)$$

$$\phi = 0, \quad z = -h. \quad (68)$$

where

$$\theta^2(x, t) = \frac{S_t^2}{S_x^2}. \quad (69)$$

This is a first order system of ordinary differential equations in  $z$  in which  $x$  and  $t$  appear only as parameters. For the system to have a solution, we must have

$$\frac{S_t^2}{S_x^2} = h. \quad (70)$$

A particular solution of the system is then

$$w_1 = S_t \frac{\partial A}{\partial \xi} \psi(x) \left( \frac{z}{h} + 1 \right), \quad (71)$$

$$u_1 = -\frac{S_t}{S_x} \frac{\psi(x)}{h} A, \quad (72)$$

$$p_1 = A\psi(x), \quad (73)$$

$$\eta_1 = A\psi(x). \quad (74)$$



Note that, in principle,  $\psi$  may have an arbitrary  $x$  dependence, and  $u_1$ . This freedom corresponds physically to the fact that an arbitrary slowly varying order  $\epsilon$  height field could be added to  $\eta_1$ , and an arbitrary order  $\epsilon$  velocity field  $U(x, z, t)$  could be added to  $u_1$ , that would have to be balanced only at higher order due to the form of equations (34)-(39). Since we are not interested in the interaction of waves with higher order mean flows, we will assume  $U = 0$  and  $\frac{\partial \psi}{\partial x} = 0$ .

Equation (70) is the same as the eiconal equation computed when we derived shallow water theory. To solve this equation we can use the method of characteristics, as in the previous lectures. It is interesting to note that the modes and rays we have computed are the same as those determined by the linear theory of wave propagation. It is only in the determination of the amplitude  $A(\xi, t)$  that nonlinearity plays a role, and to that we now turn.

### 4.3 Amplitudes

To determine the equations governing the amplitude function  $A(\xi, t)$ , we must analyze the set of equations obtained by equating the coefficients of order  $\epsilon^2$  in equations (34)-(39). Doing so, we obtain

$$S_x \frac{\partial u_2}{\partial \xi} + \frac{\partial w_2}{\partial z} = -\frac{\partial u_1}{\partial x}, \quad (75)$$

$$S_t \frac{\partial u_2}{\partial \xi} + S_x \frac{\partial p_2}{\partial \xi} = -\frac{\partial u_1}{\partial t} - S_x u_1 \frac{\partial u_1}{\partial \xi} - w_1 \frac{\partial u_1}{\partial z} - \frac{\partial p_1}{\partial x}, \quad (76)$$

$$\frac{\partial p_2}{\partial z} = -S_t \frac{\partial w_1}{\partial \xi}, \quad (77)$$

$$S_t \frac{\partial \eta_2}{\partial \xi} - w_2 = -\frac{\partial \eta_1}{\partial t} - u_1 S_x \frac{\partial \eta_1}{\partial \xi} + \eta_1 \frac{\partial w_1}{\partial z}, \quad z = 0, \quad (78)$$

$$p_2 = \eta_2 - \eta_1 \frac{\partial p_1}{\partial z} = \eta_2, \quad z = 0, \quad (79)$$

$$w_2 = u_1 \frac{\partial h}{\partial x}, \quad z = -h. \quad (80)$$

$$(81)$$

This system is an inhomogeneous form of equations (51)-(56), with forcing given by the solutions computed at lower order. Substituting in the solutions found in equations (71)-(74) yields

$$-\frac{S_t}{S_x} \frac{\partial w_2}{\partial z} + S_x \frac{\partial p_2}{\partial \xi} = G_1(\xi, x, z, t), \quad (82)$$

$$\frac{\partial p_2}{\partial z} = G_2(\xi, x, z, t), \quad (83)$$

$$S_t \frac{\partial p_2}{\partial \xi} - w_2 = G_3(\xi, x, t), \quad z = 0, \quad (84)$$

$$w_2 = u_1 \frac{\partial h}{\partial x}, \quad z = -h. \quad (85)$$

where

$$G_1 = \frac{S_t \psi}{S_x h} \frac{\partial A}{\partial t} - S_x \frac{\psi^2}{h} A \frac{\partial A}{\partial \xi}, \quad (86)$$

$$G_2 = -S_t^2 \frac{\partial^2 A}{\partial \xi^2} \psi \left( \frac{z}{h} + 1 \right), \quad (87)$$

$$G_3 = -\frac{\partial A}{\partial t} + 2S_t \frac{\psi^2}{h} A \frac{\partial A}{\partial \xi}. \quad (88)$$

As before, we seek a solvability condition for this system. This time, the condition will impose a constraint on  $A$  that will allow us to solve for the amplitude along rays.

Begin by solving (83) for  $p_2$ ,

$$p_2 = \int_{-h}^z G_2 dz' + P(\xi, x, t). \quad (89)$$

Inserting this solution into equation (82) and integrating over  $z$  gives

$$w_2 = -\frac{S_x}{S_t} \int_{-h}^z G_1 dz' + \frac{S_x^2}{S_t} \int_{-h}^z \int_{-h}^{z'} \frac{\partial G_2}{\partial \xi} dz'' dz' - \frac{S_x^2}{S_t} \frac{\partial P}{\partial \xi} z + D(\xi, x, t). \quad (90)$$

Applying the boundary condition at  $z = -h$  gives

$$S_t \frac{\partial P}{\partial \xi} = D + \frac{S_t}{h S_x} \frac{\partial h}{\partial x} \psi A. \quad (91)$$

Finally, applying the boundary condition at  $z = 0$  gives the constraint

$$-\frac{S_x}{S_t} \int_{-h}^0 G_1 dz' + \frac{S_x^2}{S_t} \int_{-h}^0 \int_{-h}^{z'} \frac{\partial G_2}{\partial \xi} dz'' dz' = -G_3 - S_t \int_{-h}^0 \frac{\partial G_2}{\partial \xi} dz' + \frac{S_t}{h S_x} \frac{\partial h}{\partial x} \psi A. \quad (92)$$

By substituting for  $G_1$ ,  $G_2$ , and  $G_3$  into (92), and making extensive use of equation (70), we find an equation for  $A$ :

$$\frac{\partial A}{\partial t} - \left[ \frac{3\psi}{2h} S_t \right] A \frac{\partial A}{\partial \xi} + \left[ \frac{1}{6} h S_t^3 \right] \frac{\partial^3 A}{\partial \xi^3} = \mp \frac{1}{2\sqrt{h}} A. \quad (93)$$

The sign of the right hand side is determined by the branch of the solution to the eiconal equation that is selected. It is negative for rightward travelling waves, and positive for leftward travelling waves.

Equation (93) is of KDV form, with a linear growth term reflecting the expansion and compression of ray tubes in space-time. Note that

$$\frac{1}{2\sqrt{h}} \frac{dh}{dx} = \frac{d}{dx} \sqrt{h}$$

is the gradient of the ray speed, and thus reflects expansion and contraction of ray tubes. For a rightward travelling wave travelling into deeper water,  $\frac{dc}{dx} > 0$ , ray tubes expand, and equation (93) predicts the decay of  $A$  along a ray.

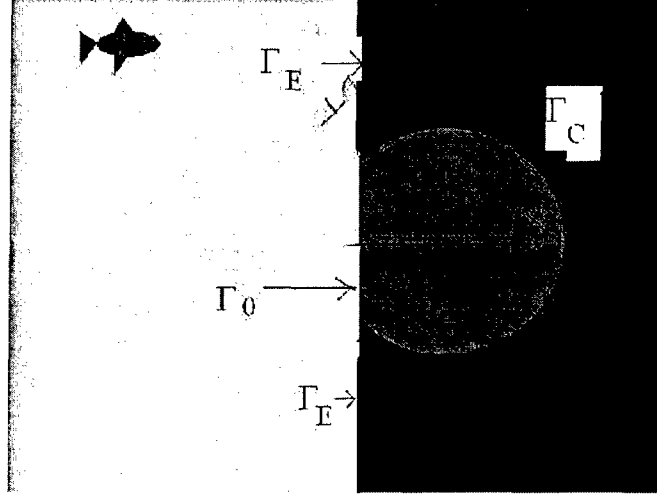


Figure 2: The configuration of the cavity resonator.

Let us now examine the case of constant depth, in which equation ( 93) reduces to the form

$$\frac{\partial A}{\partial t} - \lambda_1 A \frac{\partial A}{\partial \xi} + \lambda_2 \frac{\partial^3 A}{\partial \xi^3} = 0 \quad (94)$$

where  $\lambda_1$  and  $\lambda_2$  are constants. If we seek travelling wave solutions of the form  $A(\nu)$ , where  $\nu = \xi - ct$ , we find the ODE

$$-cA' + \lambda_1 AA' + \lambda_2 A''' = 0.$$

One periodic solution to this equation is the Jacobi function,

$$A = \sigma cn(\lambda^{-1}(\xi - ct)).$$

These are “cnoidal” waves. They resemble cosines, but with flatter troughs and sharper peaks. Furthermore, the wavespeed  $c$  is a function of the amplitude  $\sigma$ .

It is helpful to be quite clear about the physical picture of wave propagation that has emerged from this analysis. Due to the eiconal equation ( 70), surfaces of constant  $\xi$  propagate with the shallow water wave speed  $\sqrt{h}$ . The amplitude equation has solutions that propagate *relative* to surfaces of constant  $\xi$ . Thus, for example, the full propagation velocity of the cnoidal wave solutions above is  $v = \sqrt{h} + c(\sigma)$ . It is possible for these nonlinear disturbances to travel at supercritical speeds.

## 5 Closed and semiclosed basins

Asymptotic methods will now be applied to determine waves in semiclosed basins linked to the ocean by a small opening, such as harbors and marinas, subjected to the wave field incoming from the open ocean. The configuration considered here is a semicircular cavity, with the origin at the centre, as shown in figure 2. The boundary  $\Gamma$  consists of a circular arc with  $r = a$  and two straight lines. The opening, of half-width  $s$ , is small compared to the

radius of the cavity. The system is a two-dimensional version of an acoustic **Helmholtz resonator**, and will lead to harbour resonance. The problem may be stated as follows: given a prescribed potential at infinity  $\phi_\infty$ , corresponding to a plane wave incident at an angle  $\alpha$ , that is  $\phi_\infty = e^{ik(x \cos \alpha + y \sin \alpha)}$ , find the potential  $\phi(x, y)$  satisfying:

$$\begin{aligned} \nabla^2 \phi + k^2 \phi &= 0 \\ \frac{\partial \phi}{\partial n} &\text{ on } \Gamma \\ \phi &\rightarrow \phi_\infty(x, y) + \phi_s \quad \text{as } r \rightarrow \infty \end{aligned} \quad (95)$$

Here  $\phi_s$  is an outgoing wave potential. The problem can be solved numerically, but to get an analytic insight into the behavior of the solution, we shall adopt the asymptotic approach presented in [2]. For a small opening  $ks \ll 1$ , the disturbance due to the cavity as seen from afar is that of a point source of some strength  $m$ . Therefore, we can write:

$$\phi = \phi_\infty - (1/4)imH_0^{(1)}(kr). \quad (96)$$

Expanding the Hankel function in (96) for  $kr \rightarrow 0$ :

$$\phi = \phi_\infty(0, 0) - (1/4)im[1 + (2i/\pi) \log((1/2)\tilde{\gamma}kr)] + \mathcal{O}(mk^2r^2 \log(kr)), \quad (97)$$

where  $\log \tilde{\gamma} = 0.577..$  is Euler constant. Note that  $\phi_\infty(0, 0) = 1$  and define  $\phi^0 = 1 - (1/4)im + (m/2\pi) \log((1/2)\tilde{\gamma}ks)$ . Three asymptotic expansions are needed.

1. The outer expansion  $\phi_{out}$ , valid in the infinite region away from the opening. The opening appears as a source and the solution is:

$$\phi_{out} \rightarrow \phi^0 + (m/2\pi) \log(r/s), \quad r/s \ll 1, \quad (98)$$

2. The potential in the cavity:

$$\phi_{in}(x, y) = -m \phi_C(x, y). \quad (99)$$

Here  $\phi_C$  is a mode of the closed basin. As  $r \rightarrow 0$ :

$$\phi_C \rightarrow (2\pi)^{-1} \log r + \text{const.} \quad (100)$$

From the first two equations in (95), the solution  $\phi_C$  is given by:

$$4\phi_C = Y_0(kr) - \frac{Y_0'(ka)}{J_0'(ka)} J_0(kr). \quad (101)$$

3. A potential  $\phi_G$  in the neighborhood of the opening, obtained by conformal mapping (see [2]).

Matching  $\phi_G$  to the expansion in the cavity, and to that outside of it, gives the source strength  $m$  in terms of the conductivity  $C$ . The source strength  $m$  corresponds to the flux through the opening, given by  $m = C(\phi_{in} - \phi_{out})$ , where  $C$  is the conductivity of the opening.

With the value of  $m$  determined, the value of the potential on the cavity wall is:

$$\phi_C = \frac{m}{2ka\pi J'(ka)} = \frac{2}{\pi ka} \left( \frac{1}{Y'(ka) + J'(ka) \left[ i - \frac{2}{\pi} \left( 1 + \log\left(\frac{1}{2}\tilde{\gamma}ks\right) \right) \right]} \right) \quad (102)$$

An example of the potential response, given by (102) and (99) for a large cavity for three different opening widths (characterized by the values of  $s$ ) is presented in figure (3a). The peaks of the response occur when the term in the denominator in (102) is small. Due to the oscillatory behavior of the Bessel functions, this coincides with zeros of either  $J_1(ka) = -J'_0(ka)$  or  $Y_1(ka) = -Y'_0(ka)$  [1] see also figure (3b). In case when  $ka$  is small, the  $Y'_0$  term dominates, and this corresponds with the highest peak in figure (3a), which defines the Helmholtz mode. For the larger values of  $ka$  the  $J'_0$  term takes over and condition  $J'_0 = 0$  determines the position of the natural eigenmodes of the closed cavity. For the cavity with small opening, the response is modified by the effect of the  $-\log(\tilde{\gamma}ks)$  term, large when  $ks$  is small. We can also observe the influence of the opening size  $s$ : reduction in the size  $s$  moves the Helmholtz peak to smaller frequency and increases the amplitude of the response.

These results, obtained by asymptotic methods were tested in [2] against numerical solutions. They provide a theoretical explanation of harbor resonance, a phenomenon of practical importance in ocean engineering.

*Notes by Alex Hasha and Inga Koszalka.*

## References

- [1] M. ABRAMOWITZ AND I. A. STEGUN, *Handbook of Mathematical Functions with Formulas, Graphs, and Mathematical Tables*, National Bureau of Standards, Applied Math. Series # 55, Dover Publications, New York, 1972.
- [2] G. R. BIGG AND E. O. TUCK, *Two-dimensional resonators with small openings*, Austral. Math. Soc. (Series B), 24 (1982), pp. 2–27.
- [3] J. B. KELLER, *Surface waves on water of non-uniform depth*, J. Fluid Mech., 4 (1958), pp. 607–614.
- [4] R. SALMON, *Lectures On Geophysical Fluid Dynamics*, Oxford University Press, New York, 1998.
- [5] M. SHEN AND J. KELLER, *A ray method for nonlinear wave propagation in a rotating fluid of variable depth*, Phys. Fluids, 16 (1973), pp. 1565–1572.

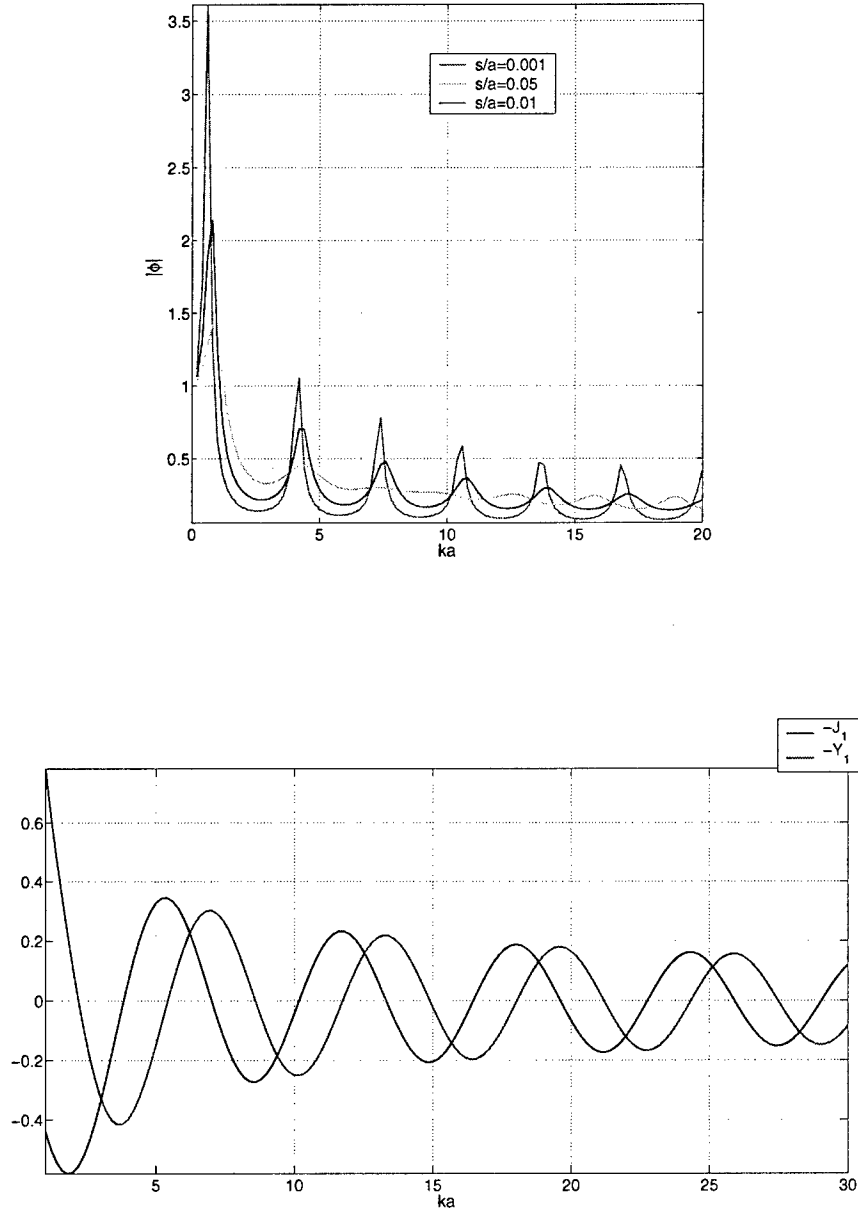


Figure 3: (a) Response, given by (102) and (99) for a large sector cavity, with unit source strength  $m = 1$ , for three different values of the opening width  $s$ . (b) The shape of the Bessel functions  $-J_1(ka) = J'_0(ka)$  and  $-Y_1(ka) = Y'_0(ka)$  for different values of  $ka$ .

# Lecture 6: Wiener Process

Eric Vanden-Eijnden

Chapters 6, 7 and 8 offer a (very) brief introduction to stochastic analysis. These lectures are based in part on a book project with Weinan E. A standard reference for the material presented hereafter is the book by R. Durrett, “Stochastic Calculus: A Practical Introduction” (CRC 1998). For a discussion of the Wiener measure and its link with path integrals see e.g. the book by M. Kac, “Probability and Related Topics in Physical Sciences” (AMS, 1991).

## 1 The Wiener process as a scaled random walk

Consider a simple random walk  $\{X_n\}_{n \in \mathbb{N}}$  on the lattice of integers  $\mathbb{Z}$ :

$$X_n = \sum_{k=1}^n \xi_k, \quad (1)$$

where  $\{\xi_k\}_{k \in \mathbb{N}}$  is a collection of independent, identically distributed (i.i.d) random variables with  $\mathbb{P}(\xi_k = \pm 1) = \frac{1}{2}$ . The Central Limit Theorem (see the Addendum at the end of this chapter) asserts that

$$\frac{X_N}{\sqrt{N}} \rightarrow N(0, 1) \quad (\equiv \text{Gaussian variable with mean 0 and variance 1})$$

in distribution as  $N \rightarrow \infty$ . This suggests to define the piecewise constant random function  $W_t^N$  on  $t \in [0, \infty)$  by letting

$$W_t^N = \frac{X_{\lfloor Nt \rfloor}}{\sqrt{N}}, \quad (2)$$

where  $\lfloor Nt \rfloor$  denotes the largest integer less than  $Nt$  and in accordance with standard notations for stochastic processes, we have written  $t$  as a subscript, i.e.  $W_t^N = W^N(t)$ .

It can be shown that as  $N \rightarrow \infty$ ,  $W_t^N$  converges in distribution to a stochastic process  $W_t$ , termed the *Wiener process* or *Brownian motion*<sup>1</sup>, with the following properties:

- (a) *Independence*.  $W_t - W_s$  is independent of  $\{W_\tau\}_{\tau \leq s}$  for any  $0 \leq s \leq t$ .

---

<sup>1</sup>The Brownian motion is termed after the biologist Robert Brown who observed in 1827 the irregular motion of pollen particles floating in water. It should be noted, however, that a similar observation had been made earlier in 1765 by the physiologist Jan Ingenhousz about carbon dust in alcohol. Somehow Brown's name became associated to the phenomenon, probably because Ingenhouszian motion does not sound very good. Some of us with complicated names are moved by this story.

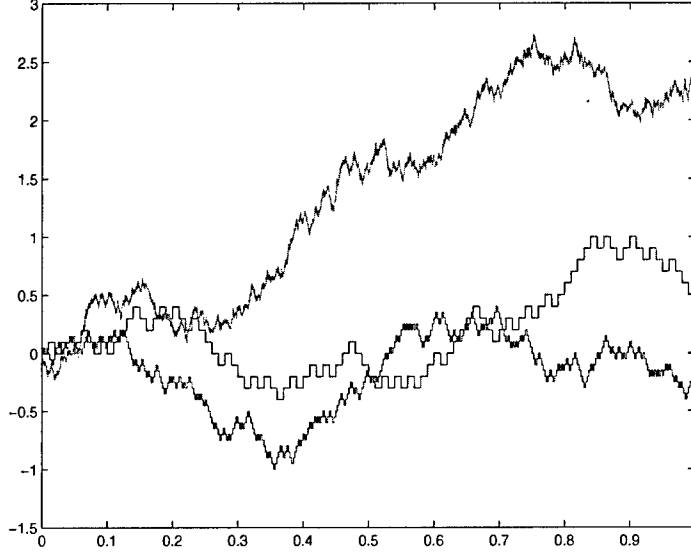


Figure 1: Realizations of  $W_t^N$  for  $N = 100$  (blue),  $N = 400$  (red), and  $N = 10000$  (green).

(b) *Stationarity*. The statistical distribution of  $W_{t+s} - W_s$  is independent of  $s$  (and so identical in distribution to  $W_t$ ).

(c) *Gaussianity*.  $W_t$  is a Gaussian process with mean and covariance

$$\mathbb{E}W_t = 0, \quad \mathbb{E}W_t W_s = \min(t, s).$$

(d) *Continuity*. With probability 1,  $W_t$  viewed as a function of  $t$  is continuous.

To show independence and stationarity, notice that for  $1 \leq m \leq n$

$$X_n - X_m = \sum_{k=m+1}^n \xi_k$$

is independent of  $X_m$  and is distributed identically as  $X_{n-m}$ . It follows that for any  $0 \leq s \leq t$ ,  $W_t - W_s$  is independent of  $W_s$  and satisfies

$$W_t - W_s \stackrel{d}{=} W_{t-s}, \quad (3)$$

where  $\stackrel{d}{=}$  means that the random processes on both sides of the equality have the same distribution. To show Gaussianity, observe that at fixed time  $t \geq 0$ ,  $W_t^N$  converges as  $N \rightarrow \infty$  to Gaussian variable with mean zero and variance  $t$  since

$$W_t^N = \frac{X_{[Nt]}}{\sqrt{N}} = \frac{X_{[Nt]}}{\sqrt{[Nt]}} \frac{\sqrt{[Nt]}}{\sqrt{N}} \rightarrow N(0, 1)\sqrt{t} \stackrel{d}{=} N(0, t).$$

In other words,

$$\mathbb{P}(W_t \in [x_1, x_2]) = \int_{x_1}^{x_2} \rho(x, t) dx \quad (4)$$



where

$$\rho(x, t) = \frac{e^{-x^2/2t}}{\sqrt{2\pi t}}. \quad (5)$$

In fact, given any partition  $0 \leq t_1 \leq t_2 \leq \dots \leq t_n$ , the vector  $(W_{t_1}^N, \dots, W_{t_n}^N)$  converges in distribution to a  $n$ -dimensional Gaussian random variable. Indeed, using (3) recursively together with (4), (5) and the independence property (a), it is easy to see that the probability density that  $(W_{t_1}, \dots, W_{t_n}) = (x_1, \dots, x_n)$  is simply given by

$$\rho(x_n - x_{n-1}, t_n - t_{n-1}) \cdots \rho(x_2 - x_1, t_2 - t_1) \rho(x_1, t_1) \quad (6)$$

A simple calculation using

$$\mathbb{E}W_t = \int_{\mathbb{R}} x \rho(x, t) dx, \quad \mathbb{E}W_t W_s = \int_{\mathbb{R}^2} xy \rho(y - x, t - s) \rho(x, s) dx dy.$$

for  $t \geq s$  and similarly for  $t < s$  gives the mean and covariance specified in (b). Notice that the covariance can also be specified via

$$\mathbb{E}(W_t - W_s)^2 = |t - s|,$$

and this equation suggests that  $W_t$  is not a smooth function of  $t$ . In fact, it can be showed that even though  $W_t$  is continuous almost everywhere (in fact Hölder continuous with exponent  $\gamma < 1/2$ ), it is differentiable almost nowhere. This is consistent with the following property of self-similarity: for  $\lambda > 0$

$$W_t \stackrel{d}{=} \lambda^{-1/2} W_{\lambda t},$$

which is easily established upon verifying that both  $W_t$  and  $\lambda^{-1/2} W_{\lambda t}$  are Gaussian processes with the same (zero) mean and covariance.

More about the lack of regularity of the Wiener process can be understood from *first passage times*. For given  $a > 0$  define the first passage time by  $T_a \equiv \inf\{t : W_t = a\}$ . Now, observe that

$$\mathbb{P}(W_t > a) = \mathbb{P}(T_a < t \text{ \& } W_t > a) = \frac{1}{2} \mathbb{P}(T_a < t). \quad (7)$$

The first equality is obvious by continuity, the second follows from the symmetry of the Wiener process; once the system has crossed  $a$  it is equally likely to step upwards as downwards. Introducing the random variable  $M_t = \sup_{0 \leq s \leq t} W_s$ , we can write this identity as:

$$\mathbb{P}(M_t > a) = \mathbb{P}(T_a < t) = 2\mathbb{P}(W_t > a) = 2 \int_a^\infty \frac{e^{-z^2/2t}}{\sqrt{2\pi t}} dz, \quad (8)$$

where we have invoked the known form of the probability density function for  $W_t$  in the last equality. Similarly, if  $m_t = \inf_{0 \leq s \leq t} W_s$ ,

$$\mathbb{P}(m_t < -a) = \mathbb{P}(M_t > a). \quad (9)$$

But this shows that the event “ $W_t$  crosses  $a$ ” is not so tidy as it may at first appear since it follows from (8) and (9) that for all  $\varepsilon > 0$ :

$$\mathbb{P}(M_\varepsilon > 0) > 0 \quad \text{and} \quad \mathbb{P}(m_\varepsilon < 0) > 0. \quad (10)$$

In particular,  $t = 0$  is an accumulation point of zeros: with probability 1 the first return time to 0 (and thus, in fact, to any point, once attained) is arbitrarily small.

## 2 Two alternative constructions of the Wiener process

Since  $W_t$  is a Gaussian process, it is completely specified by its mean and covariance,

$$\mathbb{E}W_t = 0 \quad \mathbb{E}W_t W_s = \min(t, s). \quad (11)$$

in the sense that any process with the same statistics is also a Wiener process. This observation can be used to make other constructions of the Wiener process. In this section, we recall two of them.

The first construction is useful in simulations. Define a set of independent Gaussian random variables  $\{\eta_k\}_{k \in \mathbb{N}}$ , each with mean zero and variance unity, and let  $\{\phi_k(t)\}_{k \in \mathbb{N}}$  be any orthonormal basis for  $L^2[0, 1]$  (that is, the space of square integral functions on the unit interval). Thus any function  $f(t)$  in this set can be decomposed as  $f(t) = \sum_{k \in \mathbb{N}} \alpha_k \phi_k(t)$  where (assuming that the  $\phi_k$ 's are real)  $\alpha_k = \int_0^1 f(t) \phi_k(t) dt$ . Then, the stochastic process defined by:

$$W_t = \sum_{k \in \mathbb{N}} \eta_k \int_0^t \phi_k(t') dt', \quad (12)$$

is a Wiener process in the interval  $[0, 1]$ . To show this, it suffices to check that it has the correct pairwise covariance – since  $W_t$  is a linear combination of zero mean Gaussian random variables, it must itself be a Gaussian random variable with zero mean. Now,

$$\begin{aligned} \mathbb{E}W_t W_s &= \sum_{k, l \in \mathbb{N}} \mathbb{E}\eta_k \eta_l \int_0^t \phi_k(t') dt' \int_0^s \phi_l(s') ds' \\ &= \sum_{k \in \mathbb{N}} \int_0^t \phi_k(t') dt' \int_0^s \phi_k(s') ds', \end{aligned} \quad (13)$$

where we have invoked the independence of the random variables  $\{\eta_k\}$ . To interpret the summands, start by defining an indicator function of the interval  $[0, \tau]$  and argument  $t$

$$\chi_\tau(t) = \begin{cases} 1 & \text{if } t \in [0, \tau] \\ 0 & \text{otherwise.} \end{cases}$$

If  $\tau \in [0, 1]$ , then this function further admits the series expansion

$$\chi_\tau(t) = \sum_k \phi_k(t) \int_0^\tau \phi_k(t') dt'. \quad (14)$$

Using the orthogonality properties of the  $\{\phi_k(t)\}$ , the equation (13) may be recast as:

$$\begin{aligned} \mathbb{E}W_t W_s &= \sum_{k, l \in \mathbb{N}} \int_0^1 \left( \int_0^t \phi_k(t') dt' \phi_k(u) \right) \left( \int_0^s \phi_l(s') ds' \phi_l(u) \right) du \\ &= \int_0^1 \chi_t(u) \chi_s(u) du \\ &= \int_0^1 \chi_{\min(t, s)}(u) du = \min(t, s) \end{aligned} \quad (15)$$

as required.

One standard choice for the set of functions  $\{\phi_k(t)\}$  is the *Haar basis*. The first function in this basis is equal to 1 on the half interval  $0 < t < 1/2$  and to -1 on  $1/2 < t < 1$ , the second function is equal to 2 on  $0 < t < 1/4$  and to -2 on  $1/4 < t < 1/2$  and so on. The utility of these functions is that it is very easy to construct a *Brownian bridge*: that is a Wiener process on  $[0, 1]$  for which the initial and final values are specified:  $W_0 = W_1 = 0$ . This may be defined by:

$$\hat{W}_t = W_t - tW_1, \quad (16)$$

if using the above construction then it suffices to omit the function  $\phi_1(t)$  from the basis.

The second construction of the Wiener process (or, rather, of the Brownian bridge), is empirical. It comes under the name of *Kolmogorov-Smirnov statistics*. Given a random variable  $X$  uniformly distributed in the unit interval (i.e.  $\mathbb{P}(0 \leq X < x) = x$ ), and data  $\{X_1, X_2, \dots, X_n\}$ , define a sample-estimate for the probability distribution of  $X$ :

$$F_n(x) \equiv \frac{1}{n}(\text{number of } X_k < x, k = 1, \dots, n) = \frac{1}{n} \sum_{k=1}^n \chi_{(-\infty, x)}(X_k), \quad (17)$$

equal to the relative number of data points that lie in the interval  $x_k < x$ . For fixed  $x$   $F_n(x) \rightarrow x$  as  $n \rightarrow \infty$  by the Law of Large Numbers tells us that, whereas

$$\sqrt{n}(\hat{F}_n(x) - x) \xrightarrow{d} N(0, x(1-x)). \quad (18)$$

by the Central Limit Theorem. This result can be generalized to the function  $\hat{F}_n : [0, 1] \rightarrow [0, 1]$  (i.e. when  $x$  is not fixed): as  $n \rightarrow \infty$

$$\sqrt{n}(F_n(x) - x) \xrightarrow{d} W_x - xW_1 = \hat{W}_x. \quad (19)$$

### 3 The Feynman-Kac formula

Given a function  $f(x)$ , define

$$u(x, t) = \mathbb{E}f(x + W_t) \quad (20)$$

This is the *Feynman-Kac formula* for the solution of the diffusion equation:

$$\frac{\partial u}{\partial t} = \frac{1}{2} \frac{\partial^2 u}{\partial x^2} \quad u(x, 0) = f(x). \quad (21)$$

To show this note first that:

$$\begin{aligned} u(x, t+s) &= \mathbb{E}f(x + W_{t+s}) = \mathbb{E}f(x + (W_{t+s} - W_t) + W_t) \\ &= \mathbb{E}u(x + W_{t+s} - W_t, t) \equiv \mathbb{E}u(x + W_s, t) \end{aligned}$$

where we have used the independence of  $W_{t+s} - W_t$  and  $W_t$ . Now, observe that

$$\begin{aligned} \frac{\partial u}{\partial t}(x, t) &= \lim_{s \rightarrow 0+} \frac{1}{s} (u(x, t+s) - u(x, t)) \\ &= \lim_{s \rightarrow 0+} \frac{1}{s} \mathbb{E}(u(x + W_s, t) - u(x, t)) \\ &= \lim_{s \rightarrow 0+} \frac{1}{s} \left( \frac{\partial u}{\partial x}(x, t) \mathbb{E}W_s + \frac{1}{2} \frac{\partial^2 u}{\partial x^2}(x, t) \mathbb{E}W_s^2 + o(s) \right), \end{aligned}$$

where we have Taylor-series expanded to obtain the final equality. The result follows by noting that  $\mathbb{E}W_s = 0$  and  $\mathbb{E}W_s^2 = s$ .

The formula admits many generalizations. For instance: If

$$v(x, t) = \mathbb{E}f(x + W_t) + \mathbb{E} \int_0^t g(x + W_s) ds, \quad (22)$$

then the function  $v(x, t)$  satisfies the diffusion equation with source-term the arbitrary function  $g(x)$ :

$$\frac{\partial v}{\partial t} = \frac{1}{2} \frac{\partial^2 v}{\partial x^2} + g(x) \quad v(x, 0) = f(x). \quad (23)$$

Or: If

$$w(x, t) = \mathbb{E} \left( f(x + W_t) \exp \left( \int_0^t c(x + W_s) ds \right) \right) \quad (24)$$

then  $w(x, t)$  satisfies diffusive equation with an exponential growth term:

$$\frac{\partial w}{\partial t} = \frac{1}{2} \frac{\partial^2 w}{\partial x^2} + c(x)w \quad w(x, 0) = f(x). \quad (25)$$

## Addendum: The Law of Large Numbers and the Central Limit Theorem

Let  $\{X_j\}_{j \in \mathbb{N}}$  be a sequence of i.i.d. (independent, identically distributed) random variables, let  $\eta = \mathbb{E}X_1$   $\sigma^2 = \text{var}(X_1) = \mathbb{E}(Z_1 - \eta)^2$  and define

$$S_n = \sum_{j=1}^n X_j$$

The (weak) *Law of Large Numbers* states that if  $\mathbb{E}|X_j| < \infty$ , then

$$\frac{S_n}{n} \rightarrow \eta \quad \text{in probability.}$$

The *Central Limit Theorem* states that if  $\mathbb{E}X_j^2 < \infty$  then

$$\frac{S_n - n\eta}{\sqrt{n\sigma^2}} \rightarrow N(0, 1) \quad \text{in distribution.}$$

We first give a proof of the Law of Large Numbers under the stronger assumption that  $\mathbb{E}|X_j|^2 < \infty$ . Without loss of generality we can assume that  $\eta = 0$ . The proof is based the *Chebychev inequality*: Suppose  $X$  is a random variable with distribution function  $F(x) = \mathbb{P}(X < x)$ . Then, for any  $\lambda > 0$ ,

$$\mathbb{P}(|X| \geq \lambda) \leq \frac{1}{\lambda^p} \mathbb{E}|X|^p, \quad (26)$$

provided only that  $\mathbb{E}|X|^p < \infty$ . Indeed:

$$\lambda^p \mathbb{P}(|X| \geq \lambda) = \lambda^p \int_{|x| \geq \lambda} dF(x) \leq \int_{|x| \geq \lambda} |x|^p dF(x) \leq \int_{\mathbb{R}} |x|^p dF(x) = \mathbb{E}|X|^p.$$

Using Chebychev's inequality, we have

$$\mathbb{P} \left\{ \left| \frac{S_n}{n} \right| > \varepsilon \right\} \leq \frac{1}{\varepsilon^2} \mathbb{E} \left| \frac{S_n}{n} \right|^2$$

for any  $\varepsilon > 0$ . Using the i.i.d. property, this gives

$$\mathbb{E}|S_n|^2 = \mathbb{E}|X_1 + X_2 + \dots + X_n|^2 = n\mathbb{E}|X_1|^2.$$

Hence

$$\mathbb{P} \left\{ \left| \frac{S_n}{n} \right| > \varepsilon \right\} \leq \frac{1}{n\varepsilon^2} \mathbb{E}|X_1|^2 \rightarrow 0,$$

as  $n \rightarrow \infty$ , and this proves the law of large numbers.

Next we prove the Central Limit Theorem. Let  $f$  be the *characteristic function* of  $X_1$ , i.e.

$$f(k) \equiv \mathbb{E}e^{ikX_1}, \quad k \in \mathbb{R}. \quad (27)$$

and similarly let  $g_n$  be the characteristic function of  $S_n/\sqrt{n\sigma^2}$ . Then

$$\begin{aligned} g_n(\xi) &= \mathbb{E}e^{i\xi S_n/\sqrt{n\sigma^2}} = \prod_{j=1}^n \mathbb{E}e^{i\xi X_j/\sqrt{n\sigma^2}} = \left( \mathbb{E}e^{i\xi X_1/\sqrt{n\sigma^2}} \right)^n \\ &= \left( 1 + \frac{ik}{\sqrt{n}\sigma} \mathbb{E}X_1 - \frac{k^2}{2n\sigma^2} \mathbb{E}X_1^2 + o(N^{-1}) \right)^n \\ &= \left( 1 - \frac{k^2}{2n} + o(N^{-1}) \right)^n \\ &\rightarrow e^{-k^2/2} \quad \text{as } n \rightarrow \infty. \end{aligned}$$

This shows that the characteristic function of  $S_n/\sqrt{n\sigma^2}$  converges to the the characteristic function of  $N(0, 1)$  as  $n \rightarrow \infty$  and terminates the proof.

It is instructive to note that the only property of  $X_1$  that we have required in the central limit theorem is that  $\mathbb{E}X_1^2 < \infty$ . In particular, the theorem holds even if the higher moments of  $X_1$  are infinite! For one illustration of this, consider a random variable having probability density function

$$\rho(x) = \frac{2}{\pi(1+x^2)^2}, \quad (28)$$

for which all moments of order higher than 2 are infinite. Nevertheless, we have:

$$\begin{aligned} f(k) &\equiv \int_{\mathbb{R}} e^{ikx} \rho(x) dx = (1 + |k|) e^{-|k|} \\ &= 1 - \frac{1}{2}k^2 + o(k^2), \end{aligned}$$

and hence the Central Limit Theorem applies. Intuitively, the reason is that the fat tails of the density  $\rho(x)$  disappear in the limit owing to the rescaling of the partial sum by  $1/\sqrt{nt}$ .

*Notes by Marcus Roper and Ravi Srinivasan.*

# Lecture 7: Stochastic integrals and stochastic differential equations

Eric Vanden-Eijnden

Combining equations (1) and (2) from Lecture 6, one sees that  $W_t^N$  satisfies the recurrence relation

$$W_{t_n}^N = W_{t_n}^N + \xi_{n+1}\sqrt{\Delta t}, \quad W_0^N = 0. \quad (1)$$

where  $t_n = n/N$ ,  $\Delta t = 1/N$  and  $\{\xi_n\}_{n \in \mathbb{N}}$  are i.i.d. random variables taking values  $\pm 1$  with probability  $\frac{1}{2}$  as before. A natural generalization of this relation is

$$X_{t_{n+1}}^N = X_{t_n}^N + b(X_{t_n}^N, t_n)\Delta t + \sigma(X_{t_n}^N, t_n)\xi_{n+1}\sqrt{\Delta t}, \quad X_0 = x \quad (2)$$

If the last term were absent, this would be the forward Euler scheme for the ordinary differential equation (ODE)  $\dot{X}_t = b(X_t, t)$ . If  $b(x, t)$  and  $\sigma(x, t)$  meet appropriate regularity requirements, it can be shown that  $X_t^N$  converges to a stochastic process  $X_t$  as  $N \rightarrow \infty$  (i.e. as  $\Delta t \rightarrow 0$  with  $n\Delta t \rightarrow t$ ). The limiting equation for  $X_t$  is denoted as the *stochastic differential equation* (SDE)

$$dX_t = b(X_t, t)dt + \sigma(X_t, t)dW_t, \quad X_0 = x, \quad (3)$$

as a remainder that the last term in (2) divided by  $\Delta t$  does not have a standard function as limit. The notation  $dW_t$  comes from (1) since this equation can be written as  $W_{t_{n+1}}^N - W_{t_n}^N = \xi_{n+1}\sqrt{\Delta t}$ . We note that the convergence of  $X_t^N$  to  $X_t$  holds provided only that the  $\xi_n$ 's are i.i.d. random variables with mean zero,  $\mathbb{E}\xi_n = 0$ , and variance one,  $\mathbb{E}\xi_n^2 = 1$ . The standard choice in numerical schemes is to take  $\xi_n = N(0, 1)$ , in which case

$$\sqrt{\Delta t}\xi_{n+1} \stackrel{d}{=} W_{t_{n+1}} - W_{t_n}.$$

In the discussion below, however, we will stick to the choice where  $\{\xi_n\}_{n \in \mathbb{N}}$  are i.i.d. random variables taking values  $\pm 1$  with probability  $\frac{1}{2}$  since it facilitates the calculations.

Next, we study the properties of  $X_t$  solution of (3) and introduce some nonstandard calculus due to Itô to manipulate this solution.

## 1 Itô isometry and Itô formula

Consider the recurrence relation

$$X_{t_{n+1}}^N = X_{t_n}^N + f(W_{t_n}^N)\xi_{n+1}\sqrt{\Delta t}, \quad X_0^N = 0.$$

Let us investigate the properties of the limit of  $X_{n\Delta t}^N$  as  $N \rightarrow \infty$ , assuming that this limit exists. The limiting form of the recurrence relation above is traditionally denoted as

$$dX_t = f(W_t, t)dW_t, \quad X_0 = 0,$$

which can also be expressed as the *stochastic integral*

$$X_t = \int_0^t f(W_s, s)dW_s.$$

Stochastic integral have special properties called the *Itô isometry*

$$\begin{aligned} \mathbb{E} \int_0^t f(W_s, s)dW_s &= 0, \\ \mathbb{E} \left( \int_0^t f(W_s, s)dW_s \right)^2 &= \int_0^t \mathbb{E} f^2(W_s, s)ds. \end{aligned}$$

The first of these identity is often written and used in differential form

$$\mathbb{E} f(W_s, s)dW_s = 0.$$

The Itô isometry is easy to demonstrate. The first identity is implied by

$$\begin{aligned} \mathbb{E} X_{t_n}^N &= \mathbb{E} \sum_{m=0}^{n-1} f(W_{t_m}^N, t_m) \xi_{m+1} \sqrt{\Delta t} \\ &= \sum_{m=0}^{n-1} \mathbb{E} f(W_{t_m}^N, t_m) \mathbb{E} \xi_{m+1} \sqrt{\Delta t} = 0, \end{aligned}$$

where we used the independence of the  $\xi_m$ 's and  $\mathbb{E} \xi_m = 0$ . The second identity is implied by

$$\begin{aligned} \mathbb{E} (X_{t_n}^N)^2 &= \mathbb{E} \sum_{m,p=0}^n f(W_{t_m}^N, t_m) f(W_{t_p}^N, t_p) \xi_{m+1} \xi_{p+1} \Delta t \\ &= \sum_{m=0}^n \mathbb{E} f^2(W_{t_m}^N, t_m) \Delta t, \end{aligned}$$

where we use the fact that  $\xi_m$  and  $\xi_p$  are independent unless  $m = p$ , and  $\xi_m^2 = 1$  by definition.

Going back to (3), a very important formula to manipulate the solution of this equation is *Itô formula* which states the following. Assume that  $X_t$  is the solution of (3) and let  $f$  be a smooth function. Then  $g(X_t)$  satisfies the SDE

$$\begin{aligned} dg(X_t) &= g'(X_t)dX_t + \frac{1}{2}g''(X_t)\sigma^2(X_t, t)dt \\ &= (g'(X_t)b(X_t, t) + \frac{1}{2}g''(X_t)\sigma^2(X_t, t))dt + g'(X_t)\sigma(X_t, t)dW_t. \end{aligned}$$

If  $g$  depends explicitly on  $t$ , then an additional term  $\partial g / \partial t dt$  is present at the right hand-side. Itô formula is the analog of the chain rule in ordinary differential calculus. However ordinary chain rule would give

$$dg(X_t) = g'(X_t)dX_t.$$

Here because of the non-differentiability of  $X_t$ , we have the additional term that depends on  $g''(x)$ .

The proof of Itô formula can be outlined as follows. We Taylor expand  $g(X_{t_{n+1}}^N) - g(X_{t_n}^N)$  using the recurrence relation (2) for  $X_{t_n}^N$  and keep terms up to  $O(\Delta t)$ :

$$\begin{aligned}
g(X_{t_{n+1}}^N) - g(X_{t_n}^N) &= g'(X_{t_n}^N)(X_{t_{n+1}}^N - X_{t_n}^N) + \frac{1}{2}g''(X_{t_n}^N)(X_{t_{n+1}}^N - X_{t_n}^N)^2 + \dots \\
&= g'(X_{t_n}^N)(X_{t_{n+1}}^N - X_{t_n}^N) \\
&\quad + \frac{1}{2}g''(X_{t_n}^N)\left(b(X_{t_n}^N, t_n)\Delta t + \sigma(X_{t_n}^N, t_n)\xi_{n+1}\sqrt{\Delta t}\right)^2 + O(\Delta t^{3/2}) \\
&= g'(X_{t_n}^N)(X_{t_{n+1}}^N - X_{t_n}^N) + \frac{1}{2}g''(X_{t_n}^N)\sigma^2(X_{t_n}^N, t_n)\xi_{n+1}^2\Delta t + O(\Delta t^{3/2}) \\
&= g'(X_{t_n}^N)(X_{t_{n+1}}^N - X_{t_n}^N) + \frac{1}{2}g''(X_{t_n}^N)\sigma^2(X_{t_n}^N, t_n)\Delta t + O(\Delta t^{3/2}),
\end{aligned}$$

where in the last equality we used  $\xi_{n+1}^2 = 1$ . The Itô formula follows in the limit as  $\Delta t \rightarrow 0$ .

## 2 Examples

The Itô isometry and the Itô formula are the backbone of the *Itô calculus* which we now use to compute some stochastic integrals and solve some SDEs. As an example of stochastic integral, consider

$$\int_0^t W_s dW_s.$$

Taking  $f(x) = x^2$  in Itô formula gives

$$\frac{1}{2}dW_t^2 = W_t dW_t + \frac{1}{2}dt.$$

Therefore

$$\int_0^t W_s dW_s = \frac{1}{2}W_t^2 - \frac{1}{2}t.$$

Notice that the second term at the right hand-side would be absent by the rules of standard calculus. Yet, this term must be present for consistency, since the expectation of the left hand-side is

$$\mathbb{E} \int_0^t W_s dW_s = 0,$$

using the first Itô isometry, and the expectation of the right hand-side is zero only with the term  $\frac{1}{2}t$  included since  $\frac{1}{2}\mathbb{E}W_t^2 = \frac{1}{2}t$ .

As a first example of SDE, consider

$$dX_t = -\gamma X_t dt + \sigma dW_t, \quad X_0 = x$$

This is the *Ornstein-Uhlenbeck process*. Using Itô formula with  $f(x, t) = e^{\gamma t}x$ , we get (this is Duhammel principle)

$$d(e^{\gamma t}X_t) = \gamma e^{\gamma t}X_t dt + e^{\gamma t}dX_t = \sigma e^{\gamma t}dW_t.$$



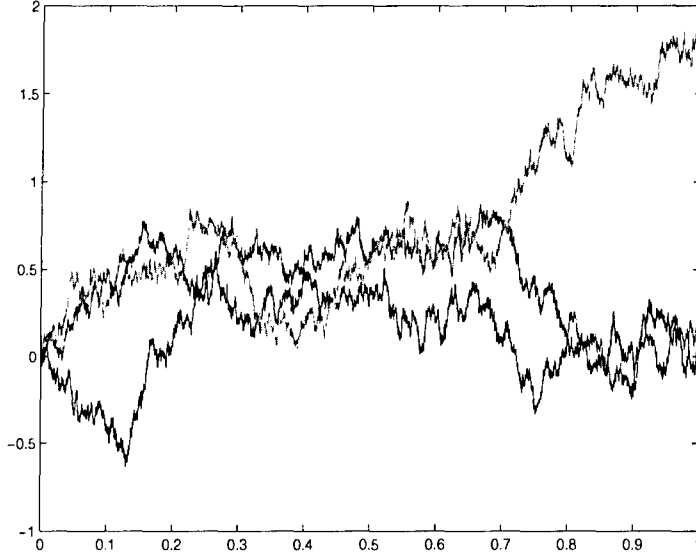


Figure 1: Three realizations of the Ornstein-Uhlenbeck process with  $X_0 = 0$  and  $\gamma = \sigma = 1$ .

Integrating gives

$$X_t = e^{-\gamma t}x + \sigma \int_0^t e^{-\gamma(t-s)} dW_s.$$

This process is Gaussian being a linear combination of the Gaussian process  $W_t$ . Its mean and variance are (using the Itô isometry)

$$\begin{aligned} \mathbb{E}X_t &= e^{-\gamma t}x \\ \mathbb{E}(X_t - \mathbb{E}X_t)^2 &= \sigma^2 \int_0^t (e^{-\gamma(t-s)})^2 ds = \frac{\sigma^2}{2\gamma}(1 - e^{-2\gamma t}). \end{aligned}$$

Thus when  $\gamma > 0$

$$X_t \xrightarrow{d} N\left(0, \frac{\sigma^2}{2\gamma}\right),$$

as  $t \rightarrow \infty$ .

As a second example of SDE, consider the so-called *geometric Brownian motion*

$$dY_t = Y_t dt + \alpha Y_t dW_t, \quad Y_0 = y.$$

This process has some application in mathematical finance. Itô's formula with  $f(x) = \log x$  gives

$$d \log Y_t = \frac{1}{Y_t}(Y_t dt + \alpha Y_t dW_t) - \frac{1}{2Y_t^2} \alpha^2 Y_t^2 dt.$$

Integrating we get

$$Y_t = y e^{t - \frac{1}{2}\alpha^2 t + \alpha W_t}.$$

Note that by the rules of standard calculus, we would have obtained the wrong answer

$$Y_t = y e^{t + \alpha W_t} \quad (\text{wrong!})$$

Indeed the term  $-\frac{1}{2}\alpha^2 t$  in the exponential is important for consistency since taking the expectation of the SDE for  $Y_t$  using the first Itô isometry gives

$$d\mathbb{E}Y_t = \mathbb{E}Y_t dt,$$

and hence

$$\mathbb{E}Y_t = ye^t.$$

The solution above is consistent with this since

$$\mathbb{E}e^{\alpha W_t} = e^{\frac{1}{2}\alpha^2 t}.$$

### 3 Generalization in multi-dimension

The definition of Itô integrals and SDE's can be extended to multi-dimension in a straightforward fashion. The SDE

$$dX_t^j = b_j(X_t, t)dt + \sum_{k=1}^K \sigma_{jk}(X_t, t)dW_t^k, \quad j = 1, \dots, J$$

where  $\{W_t^k\}_{k=1}^K$  are independent Wiener processes, defines a vector-valued stochastic process  $X_t = (X_t^1, \dots, X_t^J)$ . The only point worth noting is the Itô formula, which in multi-dimension reads:

$$df(X_t) = \sum_{j=1}^J \frac{\partial f(X_t)}{\partial x_j} dX_t^j + \frac{1}{2} \sum_{j,j'=1}^J \frac{\partial^2 f(X_t)}{\partial x_j \partial x_{j'}} \left( \sum_{k=1}^K \sigma_{jk}(X_t, t) \sigma_{kj'}(X_t, t) \right) dt$$

### 4 Forward and backward Kolmogorov equations

Consider the stochastic ODE

$$dX_t = b(X_t)dt + \sigma(X_t)dW_t, \quad X_0 = y.$$

Define the transition probability density  $\rho(x, t|y)$  via

$$\int_{x_1}^{x_2} \rho(x, t|y) dx = \mathbb{P}\{X_{t+s} \in [x_1, x_2] | X_s = y\}.$$

( $\rho(x, t|y)$  does not depend on  $s$  because  $b(x)$  and  $\sigma(x)$  are time-independent.) The transition probability density is an essential object because the process  $X_t$  is *Markov*, in other words: for any  $t, s \geq 0$

$$\mathbb{P}(X_{t+s} \in B[x_1, x_2] | \{X_{s'}\}_{0 \leq s' \leq s}) = \mathbb{P}(X_{t+s} \in B[x_1, x_2] | \{X_s\}),$$

i.e. the future behavior of  $X_t$  given what has happened up to time  $s$  depends only on what  $X_s$  was. We will derive equation for  $\rho$ . Let  $f$  be an arbitrary smooth function. Using Itô formula, we have

$$f(X_t) - f(y) = \int_0^t f'(X_s) dX_s + \frac{1}{2} \int_0^t f''(X_s) a(X_s) ds,$$

where  $a(x) = \sigma^2(x)$ . Taking expectation on both sides, we get

$$\mathbb{E}f(X_t) - f(y) = \mathbb{E} \int_0^t f'(X_s)b(X_s)ds + \frac{1}{2}\mathbb{E} \int_0^t f''(X_s)a(X_s)ds.$$

or equivalently using  $\rho$

$$\begin{aligned} & \int_{\mathbb{R}} f(x)\rho(x, t|y)dx - f(y) \\ &= \int_0^t \int_{\mathbb{R}} f'(x)b(x)\rho(x, s|y)dxds + \frac{1}{2} \int_0^t \int_{\mathbb{R}} f''(x)a(x)\rho(x, s|y)dxds. \end{aligned}$$

Since this holds for all smooth  $f$ , we obtain

$$\frac{\partial \rho}{\partial t} = -\frac{\partial}{\partial x}(b(x)\rho) + \frac{1}{2}\frac{\partial^2}{\partial x^2}(a(x)\rho) \quad (4)$$

with the initial condition  $\lim_{t \rightarrow 0} \rho(x, t|y) = \delta(x - y)$ . This is the *forward Kolmogorov equation* for  $\rho$  in terms of the variables  $(x, t)$ . It is also called the *Fokker-Planck equation*.

Equivalently, an equation for  $\rho$  in terms of the variables  $(y, t)$  can be derived. The Markov property implies that

$$\rho(x, t + s|y) = \int_{\mathbb{R}} \rho(x, t|z)\rho(z, s|y)dz.$$

Hence

$$\begin{aligned} \rho(x, t + \Delta t|y) - \rho(x, t|y) &= \int_{\mathbb{R}} \rho(x, t|z)\rho(z, \Delta t|y)dz - \rho(x, t|y) \\ &= \int_{\mathbb{R}} \rho(x, t|z)(\rho(z, \Delta t|y) - \delta(z - y))dz. \end{aligned}$$

Dividing both side by  $\Delta t$  and taking the limit as  $\Delta t \rightarrow 0$  using the forward Kolmogorov equation one obtains

$$\frac{\partial \rho}{\partial t} = \int_{\mathbb{R}} \rho(x, t|z) \left( -\frac{\partial}{\partial z}(b(z)\delta(z - y)) + \frac{1}{2}\frac{\partial^2}{\partial z^2}(a(z)\delta(z - y)) \right) dz,$$

which by integration by parts gives

$$\frac{\partial \rho}{\partial t} = b(y)\frac{\partial \rho}{\partial y} + \frac{1}{2}a(y)\frac{\partial^2 \rho}{\partial y^2}. \quad (5)$$

This is the *backward Kolmogorov equation* for  $\rho$  in terms of the variables  $(y, t)$ . The operator

$$L = b(y)\frac{\partial}{\partial y} + \frac{1}{2}a(y)\frac{\partial^2}{\partial y^2},$$

is called the *infinitesimal generator* of the process. The coefficient  $b$  and  $a$  can be expressed as

$$b(y) = \lim_{t \rightarrow 0} \frac{1}{t}(\mathbb{E}_y X_t - y), \quad a(y) = \lim_{t \rightarrow 0} \frac{1}{t}\mathbb{E}_y (X_t - y)^2,$$

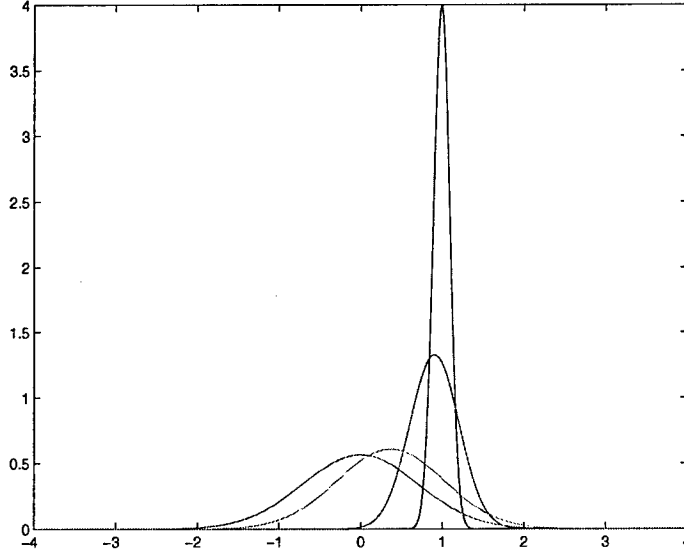


Figure 2: Snapshots of the density of the Ornstein-Uhlenbeck process at time  $t = 0.01$  (blue),  $t = 0.1$  (red),  $t = 1$  (green), and  $t = 10$  (magenta). Here  $X_0 = y = 1$  and  $\gamma = \sigma = 1$ . The last snapshot at  $t = 10$  is very close to the equilibrium density.

where  $\mathbb{E}_y$  denotes expectation conditional on  $X_0 = y$ ,

Both the forward and the backward equations can be considered with different initial conditions. In particular, given a smooth function  $f$ , if we define

$$u(y, t) = \mathbb{E}_y f(X_t),$$

then  $u(y, t) = \int_{\mathbb{R}} f(x) \rho(x, t|y)$  and hence it satisfies

$$\frac{\partial u}{\partial t} = b(y) \frac{\partial u}{\partial y} + \frac{1}{2} a(y) \frac{\partial^2 u}{\partial y^2},$$

with the initial condition  $u(y, 0) = f(y)$ . In this sense, the SDE for  $X_t$  is the characteristic equation that is associated with this parabolic PDE, much in the same way as the ODE  $\dot{X}_t = b(X_t)$  is the characteristic equation associated with the first order PDE  $\partial u / \partial t = b(y) \partial u / \partial y$ . This can be generalized in many ways. For instance, the solution of

$$\frac{\partial v}{\partial t} = c(y) v(y) + b(y) \frac{\partial v}{\partial y} + \frac{1}{2} a(y) \frac{\partial^2 v}{\partial y^2}.$$

with the initial condition  $v(y, 0) = f(y)$ , can be expressed as

$$v(y, t) = \mathbb{E}_y f(X_t) e^{\int_0^t c(X_s) ds}.$$

This is the celebrated *Feynman-Kac formula* in the context of SDEs.

Let us consider an example. The forward differential equation associated with the Ornstein-Uhlenbeck process introduced in the last section is

$$\frac{\partial \rho}{\partial t} = \gamma \frac{\partial}{\partial x} (x \rho) + \frac{\sigma^2}{2} \frac{\partial^2 \rho}{\partial x^2}$$

The solution of this equation is

$$\rho(x, t|y) = \frac{1}{\sqrt{\pi\sigma^2(1 - e^{-2\gamma t})/\gamma}} \exp\left(-\frac{\gamma(x - ye^{-\gamma t})^2}{\sigma^2(1 - e^{-2\gamma t})}\right).$$

This shows that the Ornstein-Uhlenbeck process is a Gaussian process with mean  $ye^{-\gamma t}$  and variance  $\sigma^2(1 - e^{-2\gamma t})/2\gamma$ . It also confirms that this process tends to  $N(0, \sigma^2/2\gamma)$  as  $t \rightarrow \infty$  since

$$\rho(x) = \lim_{t \rightarrow \infty} \rho(x, t|y) = \frac{e^{-\gamma x^2/\sigma^2}}{\sqrt{\pi\sigma^2/\gamma}}.$$

Generally, the limit of  $\rho(x, t|y)$  as  $t \rightarrow \infty$ , when it exists, gives the equilibrium density  $\rho$  of the process. It satisfies

$$0 = -\frac{\partial}{\partial x}(b(x)\rho) + \frac{1}{2}\frac{\partial^2}{\partial x^2}(a(x)\rho).$$

Forward and backward Kolmogorov equations can also be derived for multi-dimensional processes. They read respectively

$$\frac{\partial \rho}{\partial t} = -\sum_{j=1}^J \frac{\partial}{\partial x_j}(b_j(x)\rho) + \frac{1}{2} \sum_{j,j'=1}^J \frac{\partial^2}{\partial x_i \partial x_j}(a_{jj'}(x)\rho)$$

and

$$\frac{\partial \rho}{\partial t} = \sum_{j=1}^J b_j(x) \frac{\partial \rho}{\partial x_j} + \frac{1}{2} \sum_{j,j'=1}^J a_{jj'}(x) \frac{\partial^2 \rho}{\partial x_i \partial x_j},$$

where  $a_{jj'}(x) = \sum_{k=1}^K \sigma_{jk}(x)\sigma_{j'k}(x)$ .

*Notes by Walter Pauls and Arghir Dani Zarnescu.*

# Lecture 8: Asymptotic techniques for SDEs

Eric Vanden-Eijnden

Here we discuss techniques by which one can study SDEs evolving on very different time-scales and derive closed equations for the slow variables.

## 1 The case of stiff ordinary differential equations

We start with an ODE example. Consider

$$\begin{cases} \dot{X}_t = -Y_t^3 + \sin(\pi t) + \cos(\sqrt{2}\pi t) & X_0 = x \\ \dot{Y}_t = -\frac{1}{\varepsilon}(Y_t - X_t) & Y_0 = y. \end{cases} \quad (1)$$

If  $\varepsilon$  is very small,  $Y_t$  is very fast and one expects that it will adjust rapidly to the current value of  $X_t$ , i.e.  $Y_t = X_t + O(\varepsilon)$  at all times. Then the equation for  $X_t$  reduces to

$$\dot{X}_t = -X_t^3 + \sin(\pi t) + \cos(\sqrt{2}\pi t). \quad (2)$$

The solutions of (1) and (2) are compared in figure 1.

Here is a formal derivation of the limiting equation (2) which uses the backward Kolmogorov equation. For simplicity we drop the term  $\sin(\pi t) + \cos(\sqrt{2}\pi t)$ . Generalizing the derivation below with this term included is easy but requires a slightly different backward equation because (2) is non-autonomous. Let  $f$  be a smooth function and consider

$$u(x, y, t) = f(X_t).$$

(This function depends on both  $x$  and  $y$  since  $X_t$  depends on both these variable because  $X_t$  and  $Y_t$  are coupled in (1), and there is no expectation since (1) is deterministic.) The backward equation is

$$\frac{\partial u}{\partial t} = L_x u + \frac{1}{\varepsilon} L_y u,$$

where

$$L_x = -y \frac{\partial}{\partial x}, \quad L_y = -(y - x) \frac{\partial}{\partial y}.$$

Look for a solution of the form  $u = u_0 + \varepsilon u_1 + O(\varepsilon^2)$ , so that  $u \rightarrow u_0$  as  $\varepsilon \rightarrow 0$ . Inserting this expansion into the backward equation, and grouping terms of same order in  $\varepsilon$ , one obtains

$$\begin{aligned} L_y u_0 &= 0, \\ L_y u_1 &= \frac{\partial u_0}{\partial t} - L_x u_0, \end{aligned} \quad (3)$$

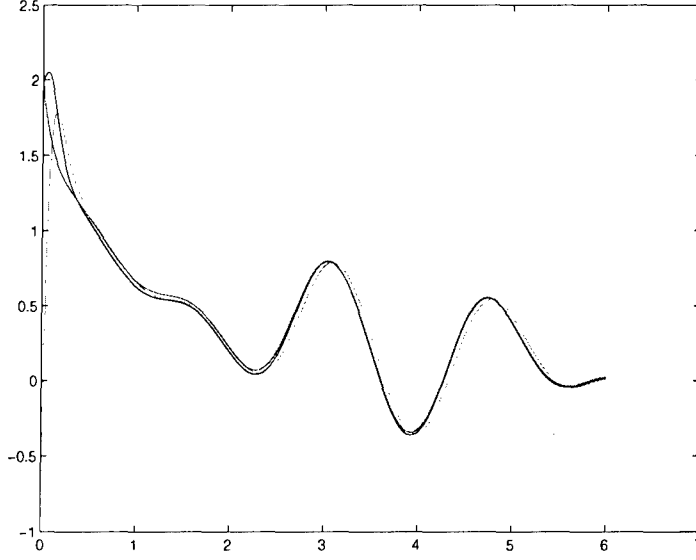


Figure 1: The solution of (1) when  $\varepsilon = 0.05$  and we took  $X_0 = 2$ ,  $Y_0 = -1$ .  $X_t$  is shown in blue, and  $Y_t$  in green. Also shown in red is the solution of the limiting equation (2).

and so on. The first equation tells that  $u_0$  belong to the null-space of  $L_y$ , i.e.  $u_0 = u_0(x, t)$ . The second equation requires as a solvability condition that the right hand-side belongs to the range of  $L_y$ . To see what this condition actually is, multiply the second equation in (3) by a test function  $\rho(y)$ , and integrate both sides over  $\mathbb{R}$ . After integration by part at the left hand-side, this gives

$$\int_{\mathbb{R}} L_y^* \rho(y) u_1 dy = \int_{\mathbb{R}} \rho(y) \left( \frac{\partial u_0}{\partial t} - L_x u_0 \right) dy.$$

where  $L_y^*$  is the adjoint of  $L_y$  viewed as an operator in  $y$  at fixed  $x$ , i.e.

$$L_y^* \rho(y) = \frac{\partial}{\partial y} ((y - x) \rho(y)).$$

Choosing  $\rho(y)$  such that

$$0 = L_y^* \rho(y), \tag{4}$$

one concludes that the solvability of (3) requires that

$$0 = \int_{\mathbb{R}} \rho(y) \left( \frac{\partial u_0}{\partial t} - L_x u_0 \right) dy. \tag{5}$$

It can be shown that this equation is also sufficient for the solvability of (3) – the calculation above actually tells the range of  $L_y$  is the space perpendicular to the null-space of the adjoint of  $L_y$ . Now, (4) is simply the forward Kolmogorov equation for the equilibrium density of the process  $Y_t$  at fixed  $X_t = x$ . Here the equilibrium density is a generalized function

$$\rho(y|x) = \delta(y - x).$$

Using this  $\rho(y|x)$ , the solvability condition (5) becomes

$$0 = \frac{\partial u_0}{\partial t} + x \frac{\partial u_0}{\partial x},$$

which is the backward equation for

$$\dot{X}_t = -X_t^3, \quad X_0 = x.$$

A similar argument with the term  $\sin(\pi t) + \cos(\sqrt{2}\pi t)$  included gives the backward equation for (2).

## 2 Generalization to stochastic differential equation

The derivation that lead to (2) can be generalized to SDEs. Consider

$$\begin{cases} dX_t = f(X_t, Y_t)dt, & X_0 = x \\ dY_t = \frac{1}{\varepsilon}b(X_t, Y_t)dt + \frac{1}{\sqrt{\varepsilon}}\sigma(X_t, Y_t)dW_t, & Y_0 = y, \end{cases} \quad (6)$$

and assume that the equation for  $Y_t$  at  $X_t = x$  fixed has an equilibrium density  $\rho(y|x)$  for every  $x$ . Then going through a derivation as above with

$$u(x, y, t) = \mathbb{E}f(X_t),$$

one concludes that the backward equation associated with this SDE also reduces to (5) as  $\varepsilon \rightarrow 0$ , i.e.

$$\frac{\partial u_0}{\partial t} = F(x) \frac{\partial u_0}{\partial x},$$

where

$$F(x) = \int_{\mathbb{R}} f(x, y) \rho(y|x) dy.$$

Thus the limiting equation for  $X_t$  is

$$\dot{X}_t = F(X_t), \quad X_0 = 0.$$

The main difference with the deterministic example treated before is that the fast process  $Y_t$  does not rapidly settle to an equilibrium point depending on the current value of  $X_t$  – only its density does.

Here is an example generalizing (1). Consider

$$\begin{cases} dX_t = -Y_t^3 dt + \sin(\pi t) + \cos(\sqrt{2}\pi t), & X_0 = x \\ dY_t = -\frac{1}{\varepsilon}(Y_t - X_t)dt + \frac{\alpha}{\sqrt{\varepsilon}}dW_t, & Y_0 = y. \end{cases} \quad (7)$$

The equation for  $Y_t$  at fixed  $X_t = x$  defines an Ornstein-Uhlenbeck process whose equilibrium density is

$$\rho(y|x) = \frac{e^{-(y-x)^2/\alpha^2}}{\sqrt{\pi}\alpha}.$$



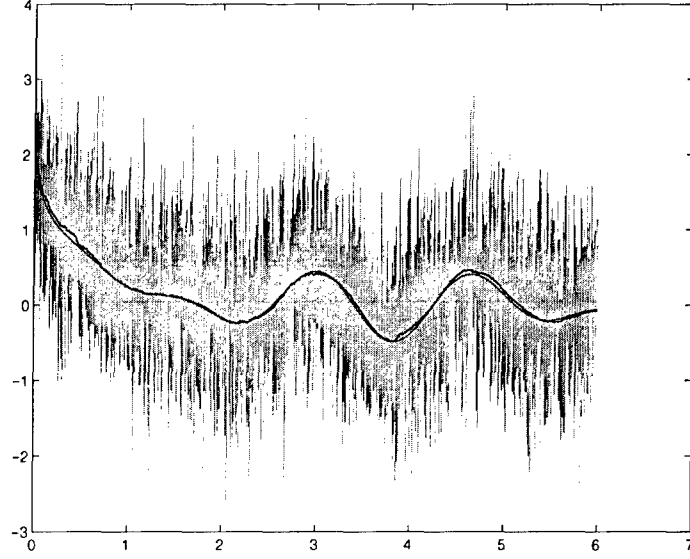


Figure 2: The solution of (7) with  $X_0 = 2$ ,  $Y_0 = -1$  when  $\varepsilon = 10^{-3}$  and  $\alpha = 1$ .  $X_t$  is shown in blue, and  $Y_t$  in green. Also shown in red is the solution of the limiting equation (8). Notice how noisy  $Y_t$  is.

Therefore

$$F(x) = - \int_{\mathbb{R}} y^3 \frac{e^{-(y-x)^2/\alpha^2}}{\sqrt{\pi}\alpha} dy = -x^3 - \frac{3}{2}\alpha^2 x,$$

and the limiting equation is

$$\dot{X}_t = -X_t^3 - \frac{3}{2}\alpha^2 X_t + \sin(\pi t) + \cos(\sqrt{2}\pi t), \quad X_0 = x. \quad (8)$$

Note the new term  $-\frac{3}{2}\alpha^2 X_t$ , due to the noise in (7). The solution of (7) and (8) are shown in figure 2.

### 3 Strong convergence and the property of self-averaging

The derivation in section 2 only give weak convergence, or convergence in distribution. But stronger results can be obtained. Consider a system of the form

$$\dot{X}_t^\varepsilon = f(X_t^\varepsilon, Y_{t/\varepsilon}), \quad (9)$$

where  $Y_t$  is a given stochastic process. Assume that  $Y_t$  is ergodic, in the sense that for any fixed  $x$ ,

$$\lim_{T \rightarrow \infty} \frac{1}{T} \int_0^T f(x, Y_s) ds = \bar{f}(x). \quad (10)$$

Then we can show that, as  $\varepsilon \rightarrow 0$ ,  $X_t^\varepsilon$  converges strongly to the solution of

$$\dot{\bar{X}}_t = \bar{f}(\bar{X}_t) \quad (11)$$

To see this, consider the integral form of (9):

$$X_{t+\Delta t}^\varepsilon - X_t^\varepsilon = \int_t^{t+\Delta t} f(X_s, Y_{s/\varepsilon}) ds. \quad (12)$$

We rewrite this equation in a way that allows us to exploit the self-averaging property (10).

$$X_{t+\Delta t}^\varepsilon - X_t^\varepsilon = \int_t^{t+\Delta t} f(X_t, Y_{s/\varepsilon}) ds + \int_t^{t+\Delta t} (f(X_s, Y_{s/\varepsilon}) - f(X_t, Y_{s/\varepsilon})) ds. \quad (13)$$

We will consider the behavior of these two integrals as  $\varepsilon \rightarrow 0$  separately.

Using (10), the first integral

$$\int_t^{t+\Delta t} f(X_t, Y_{s/\varepsilon}) ds = \varepsilon \int_{t/\varepsilon}^{(t+\Delta t)/\varepsilon} f(X_t, Y_s) ds \rightarrow \Delta t \bar{f}(X_t), \quad (14)$$

as  $\varepsilon \rightarrow 0$ . To investigate the contribution of the second integral, let

$$A(t, \Delta t, \varepsilon) = \int_t^{t+\Delta t} (f(X_s, Y_{s/\varepsilon}) - f(X_t, Y_{s/\varepsilon})) ds. \quad (15)$$

We then have

$$|A(t, \Delta t, \varepsilon)| \leq \int_t^{t+\Delta t} |f(X_s, Y_{s/\varepsilon}) - f(X_t, Y_{s/\varepsilon})| ds. \quad (16)$$

Assuming  $f$  is uniformly Lipschitz in  $Y_t$  with constant  $K$ , we then write

$$\begin{aligned} |A(t, \Delta t, \varepsilon)| &\leq \int_t^{t+\Delta t} K |X_s - X_t| ds \\ &\leq \int_t^{t+\Delta t} K \left| X_s - X_t - \int_t^s f(X_t, Y_{s'/\varepsilon}) ds' \right| \\ &\quad + \int_t^{t+\Delta t} K \left| \int_t^s f(X_t, Y_{s'/\varepsilon}) ds' \right| ds \end{aligned}$$

It is straightforward to show using (14) that, for sufficiently small  $\varepsilon$ ,

$$\int_t^{t+\Delta t} K \left| \int_t^s f(X_t, Y_{s'/\varepsilon}) ds' \right| ds < C \Delta t^2 \quad (17)$$

for some constant  $C < \infty$ . Gronwall's lemma then implies that

$$\begin{aligned} \left| X_{t+\Delta t}^\varepsilon - X_t^\varepsilon - \int_t^{t+\Delta t} f(X_t, Y_{s/\varepsilon}) ds \right| &= |A(t, \Delta t, \varepsilon)| \\ &\leq C \Delta t^2 \exp K \Delta t = o(\Delta t). \end{aligned} \quad (18)$$

This shown that

$$\lim_{\varepsilon \rightarrow 0} (X_{t+\Delta t}^\varepsilon - X_t^\varepsilon) = \Delta t \bar{f}(X_t) + o(\Delta t). \quad (19)$$

which is sufficient to demonstrate that  $X_t^\varepsilon$  converges strongly to  $\bar{X}_t$ .

## 4 Diffusive time-scale

An interesting generalization of the situation presented in section 2 arises when

$$\int_{\mathbb{R}} f(x, y) \rho(y|x) dy = 0. \quad (20)$$

In this case the limiting equation reduces to the trivial ODE,  $\dot{X}_t = 0$ , i.e. no evolution at all. In fact, the interesting evolution then occurs on a longer time-scale of order  $\varepsilon^{-1}$ , and the right scaling to study (6) is

$$\begin{cases} dX_t = \frac{1}{\varepsilon} f(X_t, Y_t) dt, & X_0 = x \\ dY_t = \frac{1}{\varepsilon^2} b(X_t, Y_t) dt + \frac{1}{\varepsilon} \sigma(X_t, Y_t) dt, & Y_0 = y, \end{cases} \quad (21)$$

To obtain the limiting equation for  $X_t$  as  $\varepsilon \rightarrow 0$ , we proceed as above and consider the backward equation for  $u(x, y, t) = \mathbb{E}f(X_t)$ , which is now rescaled as

$$\frac{\partial u}{\partial t} = \frac{1}{\varepsilon} L_x u + \frac{1}{\varepsilon^2} L_y u.$$

Inserting the expansion  $u = u_0 + \varepsilon u_1 + \varepsilon^2 u_2 + O(\varepsilon^2)$  (we will have to go one order in  $\varepsilon$  higher than before) in this equation now gives

$$\begin{aligned} L_y u_0 &= 0, \\ L_y u_1 &= -L_x u_0, \\ L_y u_2 &= \frac{\partial u_0}{\partial t} - L_x u_1, \end{aligned} \quad (22)$$

and so on. The first equation tells that  $u_0(x, y, t) = u_0(x, t)$ . The solvability condition for the second equation is satisfied by assumption because of (20) and therefore this equation can be formally solved as

$$u_1 = -L_y^{-1} L_x u_0.$$

Inserting this expression in the third equation in (22) and considering the solvability condition for this equation, we obtain the limiting equation for  $u_0$ :

$$\frac{\partial u_0}{\partial t} = \bar{L}_x u_0,$$

where

$$\bar{L}_x = \int_{\mathbb{R}} dy \rho(y|x) L_x L_y^{-1} L_x.$$

To see what this equation is explicitly, notice that  $-L_y^{-1} g(y)$  is the steady state solution of

$$\frac{\partial v}{\partial t} = L_y v + g(y).$$

The solution of this equation with the initial condition  $v(y, 0) = 0$  can be represented by Feynman-Kac formula as

$$v(y, t) = \mathbb{E} \int_0^t g(Y_s^x) ds,$$

where  $Y_t^x$  denotes the solution of the second SDE in (21) at  $X_t = x$  fixed and  $\varepsilon = 1$ , i.e.

$$dY_t^x = b(x, Y_t^x)dt + \sigma(x, Y_t^x)dW_t, \quad Y_0^x = y.$$

Therefore

$$-L_y^{-1}g(y) = \mathbb{E} \int_0^\infty g(Y_t^x)dt,$$

and the limiting backward equation above can be written as

$$\frac{\partial u_0}{\partial t} = \mathbb{E} \int_0^\infty dt \int_{\mathbb{R}} dy \rho(y|x) f(x, y) \frac{\partial}{\partial x} \left( f(x, Y_t^x) \frac{\partial u_0}{\partial x} \right),$$

This is the backward equation of the SDE

$$dX_t = \bar{b}(X_t)dt + \bar{\sigma}(X_t)dW_t, \quad X_0 = x,$$

where

$$\begin{aligned} \bar{b}(x) &= \mathbb{E} \int_0^\infty \int_{\mathbb{R}} \rho(y|x) f(x, y) \frac{\partial}{\partial x} f(x, Y_t^x) dy dt, \\ \bar{\sigma}^2(x) &= 2\mathbb{E} \int_0^\infty \int_{\mathbb{R}} \rho(y|x) f(x, y) f(x, Y_t^x) dy dt. \end{aligned}$$

The interesting new phenomena is that the limiting equation for  $X_t$  has become an SDE. This means that fluctuations are important on the long-time scale and give rise to stochastic effects in the evolution of  $X_t$  that were absent on the shorter time-scale.

The calculation above is easy to generalize if there is a slow term in the original equation for  $X_t$ , i.e. if instead of (21) one considers

$$\begin{cases} dX_t = g(X_t, Y_t)dt + \frac{1}{\varepsilon} f(X_t, Y_t)dt, & X_0 = x \\ dY_t = \frac{1}{\varepsilon^2} b(X_t, Y_t)dt + \frac{1}{\varepsilon} \sigma(X_t, Y_t)dt, & Y_0 = y, \end{cases}$$

The limiting equation for  $X_t$  is then

$$dX_t = G(X_t)dt + \bar{b}(X_t)dt + \bar{\sigma}(X_t)dW_t, \quad X_0 = x,$$

with  $\bar{b}(x)$  and  $\bar{\sigma}(x)$  as above, and

$$G(x) = \int_{\mathbb{R}} \rho(y|x) g(x, y) dy.$$

It is also straightforward to generalize to higher dimensions.

Here is an example.

$$\begin{cases} dX_t = \frac{2\alpha}{\varepsilon} Y_t Z_t dt - (X_t + X_t^3)dt, \\ dY_t = \frac{3\alpha}{\varepsilon} Z_t X_t dt - \frac{1}{\varepsilon^2} Y_t dt + \frac{1}{\varepsilon} dW_t^y, \\ dZ_t = -\frac{\alpha}{\varepsilon} b_3 Y_t X_t dt - \frac{1}{\varepsilon^2} Z_t dt + \frac{1}{\varepsilon} dW_t^z. \end{cases}$$

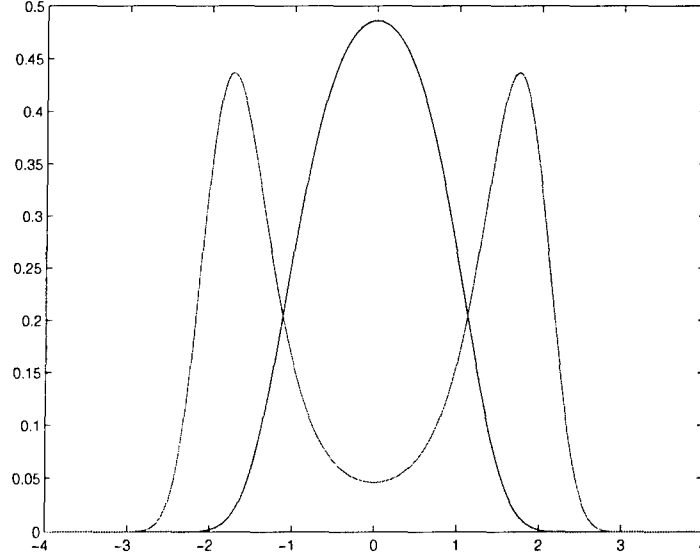


Figure 3: The equilibrium density  $\rho(x) = Z^{-1}e^{\frac{1}{2}(\alpha^2-1)x^2 - \frac{1}{4}x^4}$  for  $\alpha = \frac{1}{2}$  (blue) and  $\alpha = 2$  (red).

where  $W_t^y, W_t^z$  are independent Wiener processes and  $\alpha$  is a parameter. There are two fast variables,  $Y_t$  and  $Z_t$ , in this example. There is also a slow term,  $-(X_t + X_t^3)dt$ , in the equation for  $X_t$  which, in the absence of coupling with  $Y_t$  and  $Z_t$ , would drive  $X_t$  to the position  $x = 0$ . We ask to what extent this equilibrium of the uncoupled dynamics is relevant with coupling with  $Y_t$  and  $Z_t$ .

The limiting equation for  $X_t$  is

$$dX_t = ((\alpha^2 - 1)X_t - X_t^3)dt + \alpha dW_t.$$

The equilibrium density for this equation is

$$\rho(x) = Z^{-1}e^{\frac{1}{2}(\alpha^2-1)x^2 - \frac{1}{4}x^4}.$$

This density is shown in figure 3. For  $|\alpha| \leq 1$ ,  $\rho(x)$  is mono-modal and centered around  $x = 0$ , the stable equilibrium of the uncoupled dynamics. However, for  $|\alpha| > 1$ ,  $\rho(x)$  becomes bi-modal, with two maxima at  $x = \pm\sqrt{\alpha^2 - 1}$  and a minimum at  $x = 0$ . Thus coupling with the fast modes may destroy the structures apparent in the uncoupled dynamics and induce bifurcations.

*Notes by Inga Koszalka and Alex Hasha.*

# Lecture 9: The use of variational methods for high-contrast conductivity problems

George C. Papanicolaou

## 1 Introduction

In this lecture we will consider the conductivity in a high-contrast medium. Besides its physical importance, the model under consideration will serve as an illustration of the use of variational principles. This will provide a good introduction to variational principles before using them in a more difficult form in the next lecture, where convection-diffusion problems at high Péclet numbers (strong convection versus weak diffusion) are considered.

## 2 General formulation

Consider a smooth region  $\Omega \subset \mathbb{R}^2$  with outward unit normal  $\mathbf{n}(\mathbf{x})$  and with given non-negative *conductivity*  $\sigma(\mathbf{x})$ <sup>1</sup>. The governing equation for the *potential*  $\Phi$  is

$$\nabla \cdot [\sigma(\mathbf{x}) \nabla \Phi] = 0, \quad \mathbf{x} \in \Omega, \quad (1)$$

with Neumann boundary condition<sup>2</sup>

$$\sigma(\mathbf{x}) \frac{\partial \Phi}{\partial n} = I(\mathbf{x}), \quad \mathbf{x} \in \partial\Omega. \quad (2)$$

The *outgoing current*  $I(\mathbf{x})$  is assumed to be equilibrated, hence

$$\int_{\partial\Omega} I dS = 0. \quad (3)$$

Next, let us introduce  $s(\mathbf{x})$  by assuming that the conductivity has the form

$$\sigma(\mathbf{x}) = \sigma_0 e^{-s(\mathbf{x})/\epsilon}, \quad (4)$$

where we are interested in the *high-contrast* limit characterised by  $\epsilon \downarrow 0$ .

Plugging (4) into (1) leads to

$$\epsilon \Delta \Phi - \nabla s \cdot \nabla \Phi = 0. \quad (5)$$

---

<sup>1</sup>The analysis will not be affected qualitatively in 3 dimensions, but for simplicity we will consider  $\mathbb{R}^2$ .

<sup>2</sup>Dirichlet boundary condition  $\Phi|_{\partial\Omega} = \Psi$  can be analysed as well, without qualitative changes.

Notice that the operator on  $\Phi$  in (5) is self-adjoint, as opposed to the similar equation for a divergence-free fluid, which will be discussed in more detail in the next lecture. In fact, (5) is difficult to solve in general, hence in the following section the classical variational principles will be introduced to help us estimate the solution without solving the equation itself.

### 3 Variational principles

To introduce the classical variational principles, we first need to define *Dirichlet-to-Neumann* (DtN) and *Neumann-to-Dirichlet* (NtD) maps.

The DtN map  $\Lambda$  takes Dirichlet boundary data  $\Phi|_{\partial\Omega} = \Psi$  to the outgoing current  $I = \sigma \frac{\partial\Phi}{\partial n}$ , hence  $\Lambda\Psi = I$ . Furthermore, given (3) the NtD map can be defined as the inverse of the DtN map, namely,  $\Psi = \Lambda^{-1}I$ . Without going into details, let us note that after determining these two maps, one has almost all the information about the problem that can be observed at the boundary.

$\Lambda$  is a self-adjoint, positive semidefinite map with respect to the standard inner product. Indeed,

$$\begin{aligned} (\Lambda\Psi, \Psi) &= \int_{\partial\Omega} \Lambda\Psi(\mathbf{x})\Psi(\mathbf{x}) dS = \int_{\partial\Omega} I(\mathbf{x})\Psi(\mathbf{x}) dS = (\text{using the boundary conditions}) \\ &= \int_{\partial\Omega} \sigma(\mathbf{x}) \frac{\partial\Phi(\mathbf{x})}{\partial n} \Phi(\mathbf{x}) dS = \int_{\partial\Omega} \Phi(\mathbf{x}) \sigma(\mathbf{x}) \nabla\Phi \cdot \mathbf{n} dS = (\text{by the divergence theorem}) \\ &= \int_{\Omega} \nabla \cdot (\Phi(\mathbf{x}) \sigma(\mathbf{x}) \nabla\Phi) dV = \int_{\Omega} \sigma(\mathbf{x}) \nabla\Phi \cdot \nabla\Phi dV \geq 0. \end{aligned} \quad (6)$$

which demonstrates that  $\Lambda$  is positive semidefinite. In the last step we integrated by parts and used (1). Now let  $\Psi_1$  and  $\Psi_2$  be two different sets of Dirichlet boundary data. Using (6) we see that

$$\begin{aligned} (\Lambda\Psi_1, \Psi_2) &= \int_{\partial\Omega} \Lambda\Psi_1(\mathbf{x})\Psi_2(\mathbf{x}) dS = \int_{\Omega} \sigma(\mathbf{x}) \nabla\Phi_1 \cdot \nabla\Phi_2 dV = (\text{by symmetry}) \\ &= \int_{\partial\Omega} \Lambda\Psi_2(\mathbf{x})\Psi_1(\mathbf{x}) dS = (\Psi_1, \Lambda\Psi_2) \end{aligned} \quad (7)$$

and thus the map  $\Lambda$  is self adjoint.

Now we are ready to introduce the *Dirichlet variational principle* (DVP):

$$(\Lambda\Psi, \Psi) = \min_{\tilde{\Phi}} \left\{ \int_{\Omega} \sigma \nabla\tilde{\Phi} \cdot \nabla\tilde{\Phi} dV \mid \nabla\tilde{\Phi} \text{ is square-integrable and } \tilde{\Phi}|_{\partial\Omega} = \Psi \right\}. \quad (8)$$

To prove the DVP (8), we consider the Euler-Lagrange equations for the variational problem on the right hand side. If an integral  $K$  is of the form

$$K = \int_{\Omega} f(\tilde{\Phi}, \tilde{\Phi}_{x_i}) dV, \quad \text{where } \tilde{\Phi}_{x_i} = \frac{\partial\tilde{\Phi}}{\partial x_i}, \quad (9)$$

then the corresponding Euler-Lagrange equations for solving  $\delta K = 0$  by varying  $\Phi$  are, using the summation convention,

$$\frac{\partial f}{\partial \tilde{\Phi}} - \frac{\partial}{\partial x_i} \left( \frac{\partial f}{\partial \tilde{\Phi}_{x_i}} \right) = 0. \quad (10)$$

For equation (8)  $f(\tilde{\Phi}, \tilde{\Phi}_{x_i}) = \sigma \tilde{\Phi}_{x_i} \tilde{\Phi}_{x_i}$  and thus the Euler-Lagrange equations become

$$\frac{\partial}{\partial x_i} (\sigma \tilde{\Phi}_{x_i}) = 0. \quad (11)$$

This is simply our original conductivity equation (1), and thus the integral in the DVP (8) is minimised when  $\tilde{\Phi} = \Phi$  where  $\Phi$  solves (1). The integral in the DVP is called the *Dirichlet integral* and measures the rate of energy dissipation.

The DVP can be written in another form, namely,

$$(\Lambda \Psi, \Psi) = \min_{\tilde{\mathbf{E}}} \left\{ \int_{\Omega} \sigma \tilde{\mathbf{E}} \cdot \tilde{\mathbf{E}} dV \mid \tilde{\mathbf{E}} = \nabla \tilde{\Phi} \text{ is a curl-free field and } \tilde{\Phi}|_{\partial\Omega} = \Psi \right\}. \quad (12)$$

This form of the DVP helps to illustrate better the *duality* of DVP with the *Kelvin variational principle (KVP)*:

$$(I, \Lambda^{-1} I) = \min_{\tilde{\mathbf{j}}} \left\{ \int_{\Omega} \sigma^{-1} \tilde{\mathbf{j}} \cdot \tilde{\mathbf{j}} dV \mid \nabla \cdot \tilde{\mathbf{j}} = 0 \text{ and } \tilde{\mathbf{j}} \cdot \mathbf{n}|_{\partial\Omega} = I \right\}, \quad (13)$$

where  $\tilde{\mathbf{j}} = \sigma \nabla \tilde{\Phi}$  is the divergence-free current. A similar calculation shows that the minimum is realized by  $\mathbf{j} = \sigma \nabla \Phi$ , where  $\Phi$  is again the solution of (1).

Notice that while we cannot solve the conductivity equation (1) in general, we know *beforehand* that the solution must be the minimiser of the functionals appearing in both the DVP and KVP. This important feature allows us to bound both  $\Lambda$  and  $\Lambda^{-1}$  from above by taking appropriately well-constructed test functions  $\tilde{\Phi}$  and  $\tilde{\mathbf{j}}$ . It can be shown that this is equivalent to finding both upper and lower bounds for the map  $\Lambda$ . In some problems these bounds coincide, giving rise to the *exact* solution. This method is particularly well-suited for problems in the high-contrast limit, where we try to find an asymptotic form for the solution or at least bound it from both above and below.

## 4 The high-contrast conductivity problem

In this part of the lecture, we consider a particular problem which will serve as a benchmark to illustrate the application of the variational principles in the conductivity-related problems.

Consider the conductivity equation (1) with  $\Phi(x, y) = \chi(x, y) + x$ ,

$$\nabla \cdot [\sigma(\nabla \chi + \mathbf{e}_1)] = 0, \quad (14)$$



where for simplicity we have dropped the arguments  $(x, y)$ . Here  $\mathbf{e}_1$  is the unit vector along the  $x$ -axis. Let the domain be the square region  $D = [-1/2, 1/2] \times [-1/2, 1/2]$ . Consider solutions with periodic potential  $\chi(x, y)$ , which must be unique up to an additive constant. We will be interested in the quantity

$$\sigma^*(\mathbf{e}_1) = \langle \sigma(\nabla\chi + \mathbf{e}_1) \cdot \mathbf{e}_1 \rangle, \quad (15)$$

where the average  $\langle \cdot \rangle$  is taken over  $D$ .  $\sigma^*(\mathbf{e}_1)$  can be interpreted as the *average flux* per unit average gradient in the direction  $\mathbf{e}_1$ .

Suppose  $\sigma(x, y)$  satisfies  $\sigma(x, y) = \sigma_0 e^{-s(x, y)/\epsilon}$  with the high-contrast assumption  $0 < \epsilon \ll 1$ . Then we can write  $\sigma^*(\mathbf{e}_1)$  in the following form (justified by an integration by parts and (15)):

$$\sigma^*(\mathbf{e}_1) = \langle \sigma(\nabla\chi + \mathbf{e}_1) \cdot (\nabla\chi + \mathbf{e}_1) \rangle = \int_D \sigma(\nabla\chi + \mathbf{e}_1) \cdot (\nabla\chi + \mathbf{e}_1) dx dy. \quad (16)$$

Furthermore, using the Dirichlet variational principle,

$$\sigma^*(\mathbf{e}_1) = \min_{\tilde{\chi}} \int_D \sigma_0 e^{-s/\epsilon} (\nabla\tilde{\chi} + \mathbf{e}_1) \cdot (\nabla\tilde{\chi} + \mathbf{e}_1) dx dy. \quad (17)$$

We will now consider the case where there is a single saddle point in our domain (Figure 1). The integral in (17) cannot be tackled by Laplace's method, since  $\chi$  itself depends on the infinitesimal parameter  $\epsilon$ . In fact, the major contribution in the integral comes from the neighbourhood of the saddle point, which, without loss of generality, can be assumed to be at the origin with principal axes aligned with the coordinate axes. Since the gradient of the function at a saddle point vanishes, we have the following Taylor expansion of  $s(x, y)$  up to second order:

$$s(x, y) \approx s_0 - \frac{k_1}{2} x^2 + \frac{k_2}{2} y^2, \quad (18)$$

where  $k_1$  and  $k_2$  are the principal curvatures of the level curves of  $s$  intersecting at the saddle point.

Next, we pass into an approximate inequality by shrinking the integration region to  $\Delta = [-\delta, \delta] \times [-\delta, \delta]$  and plugging the truncated expansion (18) into (17), as well as by minimising only among the functions  $\chi(x, y) = \chi(x)$ :

$$\begin{aligned} \sigma^*(\mathbf{e}_1) &\lesssim \min_{\tilde{\chi}(x)} \int_{\Delta} \sigma_0 \exp \left( -\frac{1}{\epsilon} \left[ s_0 - \frac{k_1}{2} x^2 + \frac{k_2}{2} y^2 \right] \right) (\tilde{\chi}_x + 1)^2 dx dy \\ &\approx \sigma_0 e^{-s_0/\epsilon} \sqrt{\frac{2\pi\epsilon}{k_2}} \min_{\tilde{\chi}(x)} \int_{-\delta}^{\delta} e^{\frac{k_1}{2\epsilon} x^2} (\tilde{\chi}_x + 1)^2 dx. \end{aligned} \quad (19)$$

By DVP, the solution of (14) is the minimiser of the functional above, hence we will look for  $\chi(x)$  satisfying the equation

$$(e^{\frac{k_1}{2\epsilon} x^2} (\tilde{\chi}_x + 1))_x = 0, \quad (20)$$

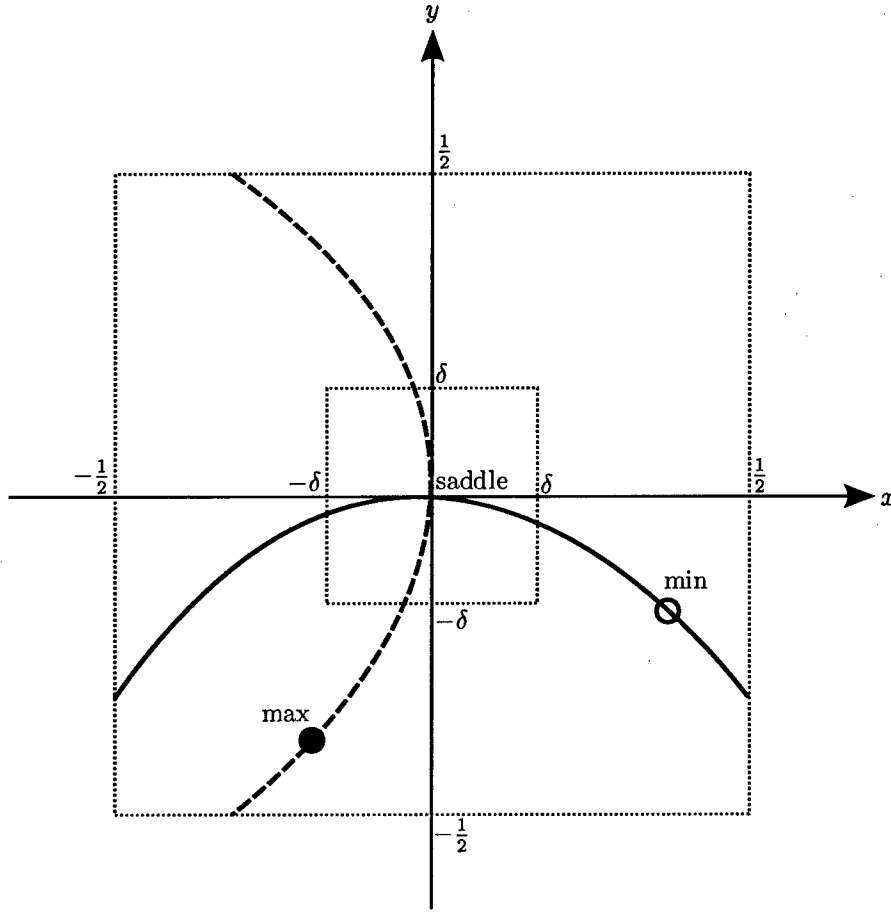


Figure 1: Topography of  $s(x, y)$  in the square region  $D$ . At the origin there is a saddle point. The filled line through the origin is a valley, the dashed line a ridge. The local maximum is a filled circle, the local minima a hollow circle. The analysis focuses on a small region  $\Delta$  near the saddle point.

as well as the periodicity condition for  $\chi$ , which implies

$$\langle \tilde{\chi}_x \rangle = 0. \quad (21)$$

Since  $\epsilon$  is very small, the average in (21) can be taken over the neighbourhood of the saddle point  $[-\delta, \delta]$  as well as over the whole interval  $[-1/2, 1/2]$  without changing the leading order asymptotic term.

Solving (20), one finds

$$\tilde{\chi}_x + 1 = C e^{-\frac{k_1}{2\epsilon} x^2}, \quad (22)$$

while the constant  $C$  can be found from (21):

$$1 = \langle \tilde{\chi}_x + 1 \rangle = \langle C e^{-\frac{k_1}{2\epsilon} x^2} \rangle \sim C \sqrt{2\pi \frac{\epsilon}{k_1}}, \quad (23)$$

Hence the optimising function satisfies the approximate equation, which is asymptotic to the solution of (14) as  $\epsilon \rightarrow 0$

$$\tilde{\chi}_x + 1 \sim \frac{1}{\sqrt{2\pi \frac{\epsilon}{k_1}}} e^{-\frac{k_1}{2\epsilon} x^2}. \quad (24)$$

Plugging into the integral (19) leads to

$$\sigma^*(\mathbf{e}_1) \lesssim \sigma_0 e^{-s_0/\epsilon} \sqrt{2\pi \frac{\epsilon}{k_2}} \int_{-\delta}^{\delta} \frac{e^{-\frac{k_1}{2\epsilon} x^2}}{2\pi \frac{\epsilon}{k_1}} \sim \sigma_0 e^{-s_0/\epsilon} \sqrt{\frac{k_1}{k_2}}, \quad (25)$$

which is the conductivity at the saddle point  $\sigma_0 e^{-s_0/\epsilon}$ , multiplied by the factor  $\sqrt{\frac{k_1}{k_2}}$  determined by the curvatures of the level sets passing through that saddle point. For instance, small  $k_2$  corresponds to a narrow saddle point, where the conductivity is large.

Using KVP for the backward NtD map, one can find a lower asymptotic bound for  $\sigma^*(\mathbf{e}_1)$  which turns out to be exactly the same as in (25)! This leads to the *exact* asymptotic expression for the average resulting flux in the  $x$ -direction

$$\sigma^*(\mathbf{e}_1) \sim \sigma_0 e^{-s_0/\epsilon} \sqrt{\frac{k_1}{k_2}}, \quad \text{as } \epsilon \rightarrow 0. \quad (26)$$

The corresponding resistance  $\rho^* = 1/\sigma^*$  is given by

$$\rho^*(\mathbf{e}_1) \sim \frac{1}{\sigma_0} e^{s_0/\epsilon} \sqrt{\frac{k_2}{k_1}}, \quad \text{as } \epsilon \rightarrow 0. \quad (27)$$

## 5 Complicated topography

We now consider the situation where we have multiple saddle points in our domain. Figure 2 gives an example of such a situation.

To understand how current flows through the domain in Figure 2 it is useful to make an analogy with the flow of water. Consider the case where current flows into the domain over  $a$ . It will flow directly to the nearest point of maximum conductivity, node 1. There current will “pool” before escaping through the “channels” (saddle points) to the adjacent nodes. From these nodes current will then flow either to other nodes via the channels, or out of the boundary. Hence intuitively the domain can be thought of as behaving as a network of channels.

More formally, we have that the dominant contribution to the DtN map  $\Lambda$  as  $\epsilon \downarrow 0$  is determined by the saddle points of  $s(x, y)$ . At each saddle point we can calculate the resistance of the saddle using the result for a single saddle (27). Denote the resistance of the saddle point between node  $i$  and node  $j$  as  $R_{ij}$ . Note that  $R_{ij}$  is symmetric:  $R_{ij} = R_{ji}$ . Since each saddle can be considered as a single resistor, we can reduce the problem to a simple resistor network (Figure 3).

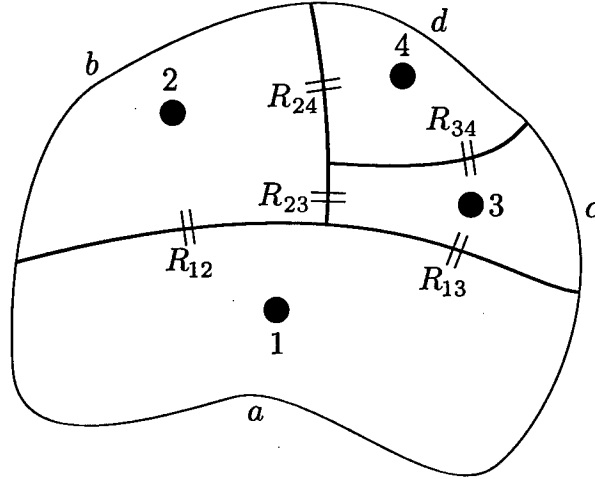


Figure 2: An example domain with multiple saddle points. The topography of  $s(x, y)$  is shown. The filled circles are local maxima of conductivity, and are numbered 1, 2, 3, 4 (we will refer to these as the *nodes*). The lines dividing the domain are the valleys. The corresponding divided parts of the boundary are labelled  $a$ ,  $b$ ,  $c$ ,  $d$ . The saddle points are shown as two short parallel lines, resembling channels. The resistance  $R_{ij}$  has been labelled by each saddle (see later discussion).

The DtN map  $\Lambda$  of the full problem is asymptotic as  $\epsilon \downarrow 0$  to the DtN map of the resistor network. Consider the Dirichlet problem where the potential  $\Phi$  is specified on the boundary,  $\Phi|_{\partial\Omega} = \Psi$ . Then equation (8) becomes

$$(\Lambda\Psi, \Psi) = \min_{\tilde{\Phi}, \tilde{\Phi}|_{\partial\Omega} = \Psi} \int_{\Omega} \sigma \nabla \tilde{\Phi} \cdot \nabla \tilde{\Phi} dV \lesssim \min_{\tilde{\Phi}_k, \tilde{\Phi}_k|_{\partial\Omega} = \Psi_k} \sum_{j \in \text{nodes}} \sum_{k \in \nu_j} \frac{1}{R_{jk}} (\tilde{\Phi}_j - \tilde{\Phi}_k)^2. \quad (28)$$

The above expression specifies an asymptotic upper bound for the DtN map  $\Lambda$ . Here the set  $\nu_j$  is the set of nodes adjacent to the node  $j$ , and  $\tilde{\Phi}_j$  is the potential at node  $j$ .  $\Psi_k$  are the integrated potentials specified on the sections of boundaries  $k$ . The boundary condition is now that the potentials  $\tilde{\Phi}_k$  of nodes adjacent to the boundary are equal to the potentials  $\Psi_k$  on the boundaries. For the example domain, the boundary condition becomes  $\tilde{\Phi}_1 = \Psi_a$ ,  $\tilde{\Phi}_2 = \Psi_b$ ,  $\tilde{\Phi}_3 = \Psi_c$ , and  $\tilde{\Phi}_4 = \Psi_d$ . In this simple case it means that all  $\tilde{\Phi}_k$  have been determined, but in more complicated cases there can be  $\tilde{\Phi}_k$  in the interior of the domain which are not directly specified by the boundary condition. Even in these more complicated cases, the minimisation is now just an easy to solve matrix problem.

Similarly we can solve the dual problem (13) where the current  $\mathbf{j}$  is specified on the boundary rather than the potential  $\Phi$ . The dual problem yields a corresponding asymptotic upper bound for the inverse map  $\Lambda^{-1}$ , and thus an asymptotic lower bound for  $\Lambda$ . As in the single saddle case it turns out that the asymptotic lower bound for  $\Lambda$  is the same as the asymptotic upper bound, and thus we get an asymptotic equality.

*Notes by Khachik Sargsyan and John Rudge.*

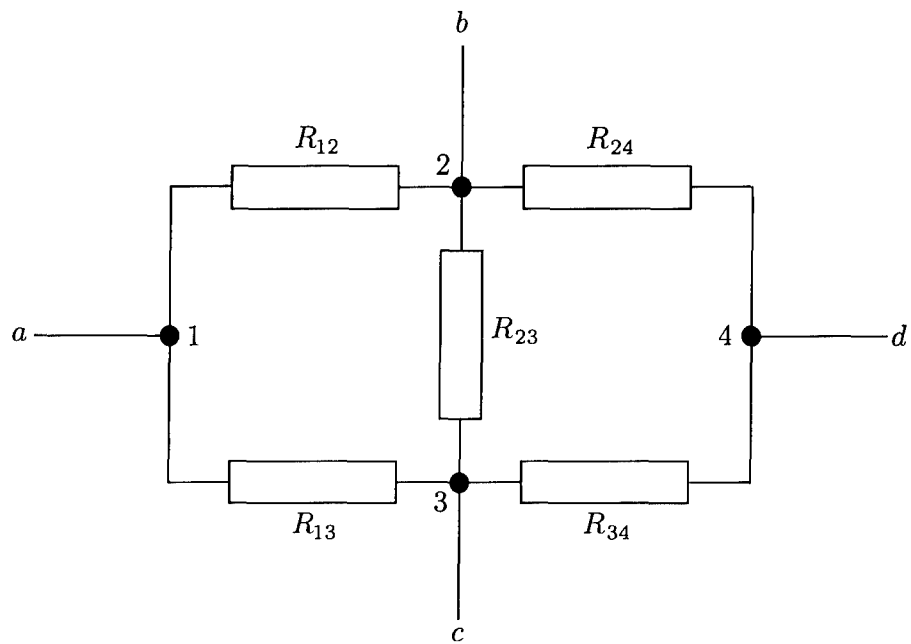


Figure 3: Resistor network corresponding to the domain in Figure 2. Current flows into or out of the network over the boundaries  $a$ ,  $b$ ,  $c$ ,  $d$ .

# Lecture 10: Convection Diffusion Problems

George C. Papanicolaou

## 1 2-D Convection-Diffusion

Consider a 2-D divergence-free, periodic, steady flow field  $u(t, x)$  in a domain without any boundaries. Let  $\tilde{\rho}(t, x)$  be the concentration of a passive scalar, say temperature. Then the non-dimensional governing equations for the non-dimensional variables  $\tilde{\rho}$  and  $u$  are:

$$\tilde{\rho}_t + u \cdot \nabla \tilde{\rho} = \epsilon \Delta \tilde{\rho} , \quad (1)$$

$$\nabla \cdot u = 0 , \quad (2)$$

together with the initial condition  $\tilde{\rho}(0, x) = \tilde{\rho}^0(x)$ . Note that  $\epsilon$  is dimensionless parameter since  $\epsilon^{-1} \sim UL/\nu = Pe$ , where  $Pe$  is the *Peclet number* and  $L$  is the size of the periodic cell. By integrating (1) over  $\mathfrak{R}^2$  and using (2), we see that if  $\int_{\mathfrak{R}^2} \tilde{\rho}^0(x) dx = 1$ , then  $\int_{\mathfrak{R}^2} \tilde{\rho}(t, x) dx = 1$ . Also if  $\tilde{\rho}^0(x) \geq 0$ , then  $\tilde{\rho}(t, x) \geq 0$ . Since  $\nabla \cdot u = 0$  and the flow is 2-D, it is possible to introduce a stream function  $\psi(x)$ :

$$u = (-\psi_y, \psi_x) . \quad (3)$$

If  $\psi(x, y) = \sin x \sin y + \delta \cos x \cos y$ , then we have a cellular flow if  $\delta = 0$ , and a shear flow if  $\delta = 1$ . Since  $x(t)$  is the position of a diffusing particle, the evolution equation for  $x(t)$  can be written as the following SDE:

$$dx(t) = u(x(t))dt + \sqrt{2\epsilon} dW(t). \quad (4)$$

If there is no diffusion (i.e. there is no  $\sqrt{2\epsilon} dW(t)$  term in (4)), a particle starting on a particular streamline remains on the streamline. If we have diffusion, there is a possibility for a particle which starts in the region (a) to move to the region (b) (See Figure 1). In that case,  $\tilde{\rho}$  can be interpreted as the probability density of  $x(t)$ .

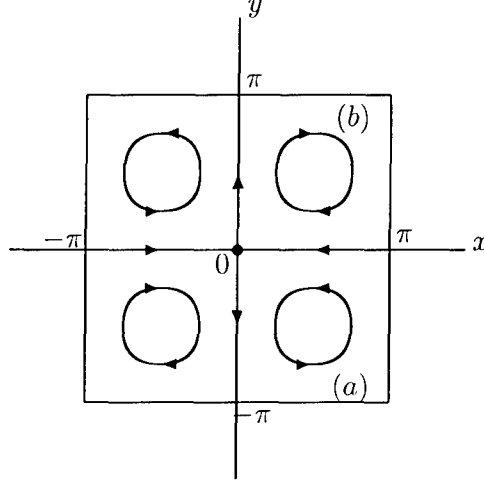


Figure 1: Rough sketch of the periodic cell

## 2 Effective diffusivities

Consider a diffusing particle,  $\lim_{t \rightarrow \infty} \frac{1}{t} \mathbb{E} [\{(x(t) - x(0)) \cdot e\}^2]$  always exists for  $u(x)$  which is periodic and satisfies  $\nabla \cdot u = 0$  and  $\langle u(x) \rangle = 0$ , where  $\langle \cdot \rangle$  represents the periodic cell average. We denote this limit as  $\sigma_e^*(e)$ , so called the *effective diffusivity*. It is a quadratic form of  $e$ .

We now take the large time, long distance limit of the PDE (1) by changing the variables  $t \rightarrow n^2 t$ ,  $x \rightarrow nx$  and letting  $n \rightarrow \infty$ . (This process is called the *homogenization*.)  $\rho_n(t, x) = \rho(n^2 t, nx)$  converges to  $\rho(t, x)$  in an appropriate sense as  $n \rightarrow \infty$ , where  $\rho(t, x)$  is the solution of the homogenized equation

$$\rho_t = \nabla \cdot (\sigma_e^* \nabla \rho) , \quad (5)$$

with  $\rho(0, x) = \rho^0(x)$ .  $\sigma_e^*(e)$  is a constant matrix, or more precisely

$$\sigma_e^*(e) = \langle (\epsilon I + \Psi)(\nabla \chi + e) \cdot e \rangle , \quad (6)$$

where  $I$  is the identity matrix,  $\chi(x)$  is a periodic function in  $\mathfrak{R}^2$ , and

$$\Psi(x) = \begin{pmatrix} 0 & -\psi(x, y) \\ \psi(x, y) & 0 \end{pmatrix} . \quad (7)$$

It is found that  $\sigma_e^*(e)$  satisfies the polarization relation

$$(\sigma_e^*)_{ij} = \frac{1}{4} [\sigma_e^*(e_i + e_j) - \sigma_e^*(e_i - e_j)] , \quad i, j = 1, 2, \quad (8)$$

where  $e_1 = (1, 0)$ ,  $e_2 = (0, 1)$ . Apart from the homogenized equation (5), the homogenization process also yields the cell problem, that is

$$\nabla \cdot [(\epsilon I + \Psi(x))(\nabla \chi + e)] = 0 . \quad (9)$$

$\sigma_e^*$  can be calculated by solving (9) for  $\chi$  and plugging it into (6). The full derivation of (5), (6) and (9) will be shown in the next section. The physical interpretation of  $\sigma_e^*(e)$  is the average flux in the direction  $e$  when there is a unit average gradient in the direction  $e$ .

### 3 Asymptotics for $\rho_n(t, x)$

Recall the passive scalar advection equation in the fast variables

$$\frac{\partial \rho_n}{\partial t} = \nabla \cdot ([I + \Psi_n(x)] \nabla \rho_n) \quad (10)$$

with initial condition

$$\rho_n(0, x) = \rho^0(x)$$

where  $I$  is the identity matrix,  $\Psi_n$  was defined previously, and we have set  $\epsilon = 1$ . First we must check that (10) solves (1)

$$\begin{aligned} \frac{\partial \rho_n}{\partial t} &= \left( \frac{\partial \rho_n}{\partial x} + \psi_n \frac{\partial \rho_n}{\partial y} \right)_x + \left( \frac{\partial \rho_n}{\partial y} - \psi_n \frac{\partial \rho_n}{\partial x} \right)_y \\ &= (\rho_n)_{xx} + (\rho_n)_{yy} - (\psi_n)_x (\psi_n)_y + (\psi_n)_y (\psi_n)_x - \psi_n (\rho_n)_{xy} + \psi_n (\rho_n)_{yx} \\ &= \Delta \rho_n - u \cdot \nabla \rho_n. \end{aligned}$$

Next we expand  $\rho_n$  in an asymptotic series

$$\rho_n(t, x) = \rho(t, x) + \frac{1}{n} \rho^{(1)}(t, x, nx) + \frac{1}{n^2} \rho^{(2)}(t, x, nx) + \dots$$

It is clear that for this problem we have a clean separation of scales. The fast time scale does not appear because the coefficients are time homogeneous.

Let  $nx = \xi$  so that  $\nabla \rightarrow \nabla_x + n \nabla_\xi$ . Plugging  $\rho_n$  into (10) we get

$$\begin{aligned} \frac{\partial}{\partial t} \left( \rho + \frac{1}{n} \rho^{(1)} + \frac{1}{n^2} \rho^{(2)} + \dots \right) &= \\ (\nabla_x + n \nabla_\xi) \cdot \left[ (I + \Psi_n(\xi)) \cdot (\nabla_x + n \nabla_\xi) \left( \rho + \frac{1}{n} \rho^{(1)} + \frac{1}{n^2} \rho^{(2)} + \dots \right) \right]. \end{aligned}$$

As is standard procedure, we equate the coefficients for powers of  $n$ . At  $O(n^2)$ :

$$\nabla_\xi \cdot [(I + \Psi_n(\xi)) \nabla_\xi \rho] = 0. \quad (11)$$

Note (11) is automatically satisfied since  $\rho$  is not a function of  $\xi$ . At  $O(n)$ :

$$\nabla_\xi \cdot [(I + \Psi_n(\xi)) \nabla_x \rho] + \nabla_x \cdot [(I + \Psi_n(\xi)) \nabla_\xi \rho] + \nabla_\xi \cdot [(I + \Psi_n(\xi)) \nabla_\xi \rho^{(1)}] = 0. \quad (12)$$



The second term in (12) is zero via (11). Upon rewriting (12) we get

$$\nabla_\xi \cdot \left[ (I + \Psi_n(\xi)) \left( \nabla_\xi \rho^{(1)} + \nabla_x \rho \right) \right] = 0 \quad (13)$$

which resembles the cell problem (9). Equation (13) is a PDE for  $\rho^{(1)}(\xi)$  (periodic in  $\xi$ ).

We can cast (13) into the cell problem by letting

$$\rho^{(1)}(t, x, \xi) = \sum_{j=1}^d \chi_{e_j}(\xi) \frac{\partial \rho}{\partial x_j}(t, x)$$

which separates the  $\xi$  dependence from the  $t, x$  dependence. The function  $\chi_e(\xi)$  satisfies

$$\nabla_\xi \cdot [(I + \Psi_n(\xi)) (\nabla_\xi \chi_e(\xi) + e)] = 0. \quad (14)$$

At  $O(1)$ :

$$\begin{aligned} \frac{\partial \rho}{\partial t} = & \nabla_\xi \cdot \left[ (I + \Psi_n(\xi)) \nabla_x \rho^{(2)} \right] + \nabla_\xi \cdot \left[ (I + \Psi_n(\xi)) \nabla_x \rho^{(1)} \right] + \\ & \nabla_x \cdot \left[ (I + \Psi_n(\xi)) \nabla_\xi \rho^{(1)} \right] + \nabla_x \cdot [(I + \Psi_n(\xi)) \nabla_x \rho] \end{aligned}$$

which is a PDE for  $\rho^{(2)}(\xi)$  (periodic in  $\xi$ ) with  $t, x$  as parameters. This can be re-written as

$$\nabla_\xi \cdot \left[ (I + \Psi_n(\xi)) \nabla_\xi \rho^{(2)} \right] + S = 0 \quad (15)$$

where

$$S = \nabla_\xi \cdot \left[ (I + \Psi_n(\xi)) \nabla_x \rho^{(1)} \right] + \nabla_x \cdot \left[ (I + \Psi_n(\xi)) \nabla_\xi \rho^{(1)} \right] + \nabla_x \cdot [(I + \Psi_n(\xi)) \nabla_x \rho] - \frac{\partial \rho}{\partial t}.$$

Upon taking the cell average of (15), we obtain

$$\left\langle \nabla_x \cdot \left[ (I + \Psi_n(\xi)) \nabla_\xi \rho^{(2)} \right] \right\rangle + \langle S \rangle = 0 \quad (16)$$

and since  $\nabla_\xi \rho^{(2)}$  is a gradient of a periodic function,  $\langle S \rangle = 0$  which yields

$$\begin{aligned} \frac{\partial \rho}{\partial t} = & \left\langle \nabla_\xi \cdot \left[ (I + \Psi_n(\xi)) \nabla_x \rho^{(1)} \right] \right\rangle + \left\langle \nabla_x \cdot \left[ (I + \Psi_n(\xi)) \nabla_\xi \rho^{(1)} \right] \right\rangle + \\ & \langle \nabla_x \cdot [(I + \Psi_n(\xi)) \nabla_x \rho] \rangle \\ = & \nabla_x \cdot \left[ \left\langle (I + \Psi_n(\xi)) \left( \nabla_\xi \rho^{(1)} + \nabla_x \rho \right) \right\rangle \right] \end{aligned}$$

since  $\nabla_x \rho^{(1)}$  is the gradient of a periodic function. In component form

$$\begin{aligned}
\frac{\partial \rho}{\partial t} &= \sum_{i,j} \frac{\partial}{\partial x_i} \left\langle A_{ij}(\xi) \left( \frac{\partial \rho^{(1)}}{\partial \xi_j} + \frac{\partial \rho}{\partial x_j} \right) \right\rangle \\
&= \sum_{i,j} \frac{\partial}{\partial x_i} \left\langle A_{ij}(\xi) \left( \frac{\partial}{\partial \xi_j} \left( \sum_k \chi_{e_k}(\xi) \frac{\partial \rho(t,x)}{\partial x_k} \right) + \frac{\partial \rho}{\partial x_j} \right) \right\rangle \\
&= \sum_{i,j} \sum_k \left\langle A_{ij} \left( \frac{\partial \chi_{e_k}}{\partial \xi_j} \frac{\partial^2 \rho}{\partial x_i \partial x_k} + \delta_{jk} \frac{\partial^2 \rho}{\partial x_i \partial x_k} \right) \right\rangle \\
&= \sum_{i,k} \left( \sum_j \left\langle A_{ij} \left( \frac{\partial \chi_{e_k}}{\partial \xi_j} + \delta_{jk} \right) \right\rangle \right) \frac{\partial^2 \rho}{\partial x_i \partial x_k}
\end{aligned}$$

where  $A_{ij} = I_{ij} + \Psi_{ij}(\xi)$ . Thus, we obtain the homogenized equation

$$\frac{\partial \rho}{\partial t} = \sum_{i,k} \sigma_{ik}^* \frac{\partial^2 \rho}{\partial x_i \partial x_k} \quad (17)$$

with

$$\sigma_{ik}^* = \sum_j \left\langle A_{ij} \left( \frac{\partial \chi_{e_k}}{\partial \xi_j} + \delta_{jk} \right) \right\rangle$$

or

$$\frac{\partial \rho}{\partial t} = \nabla \cdot (\sigma_\epsilon^* \nabla \rho). \quad (18)$$

In summary, the key ideas for homogenization are:

1) Perform a multiscale expansion

$$\begin{aligned}
t, x &\sim \text{macroscopic scales} && (\text{slow}) \\
n^2 t, nx &\sim \text{microscopic scales} && (\text{fast})
\end{aligned}$$

the resulting PDE will involve both fast and slow variables. In our case  $\psi \rightarrow \psi(nx)$ . In general  $\psi \rightarrow \psi(n^2 t, nx, t, x)$ .

2) Seek an expansion in which the principle term is slowly varying  $(t, x)$ .

3) The coefficients of the slowly varying equation come from a cell problem. In this case the term of interest was  $\rho$  and we had to go to  $O(1)$  to get the cell problem.

The effective diffusivity matrix,  $\sigma_\epsilon^*$  is given by

$$\begin{aligned}\sigma_\epsilon^* &= \langle (\epsilon I + \Psi) (\nabla \chi) \cdot e \rangle \\ &= \langle (\epsilon I + \Psi) (\nabla \chi + e) \cdot (\nabla \chi + e) \rangle\end{aligned}$$

where we added  $\nabla \chi$  to  $e$  because  $\nabla \cdot [(\epsilon I + \Psi) (\nabla \chi + e)] = 0$  (9). Also since  $(\nabla \chi + e) \cdot (\nabla \chi + e)$  is a quadratic form and  $\Psi$  is skew symmetric, we obtain

$$\begin{aligned}\sigma_\epsilon^*(e) &= \epsilon \langle |\nabla \chi + e|^2 \rangle \\ &= \epsilon + \epsilon \langle |\nabla \chi|^2 \rangle.\end{aligned}$$

From this it is clear that convection always enhances diffusion since  $\sigma_\epsilon^*(e) \geq \epsilon$ .

Finally we check convergence of the asymptotic expansion

1)

$$\max_{0 \leq t \leq T, x \in \mathbb{R}^2} |\rho_n(t, x) - \rho(x, t)| \leq \max_{0 \leq t \leq T, x \in \mathbb{R}^2} \left| \frac{1}{n} \rho^{(1)} + O\left(\frac{1}{n}\right) \right| \leq C_T \frac{1}{n}$$

provided  $\rho_0$  decays rapidly at infinity and is smooth.

2)

$$\int_0^\infty \int_{\mathbb{R}^2} (\nabla \rho_n - \nabla \rho) \theta(t, x) dx dt \rightarrow 0$$

where  $\theta$  is a test function. This says that on average the gradient converges. Calculating  $\nabla \rho_n$  we obtain

$$\nabla \rho_n = \nabla \rho + \nabla_\xi \rho^{(1)}(t, x, nx) + \dots$$

3)

$$\sup_{0 \leq t \leq T} \int_{\mathbb{R}^2} \left| \nabla \rho_n - \left( \nabla \rho + \nabla_\xi \rho^{(1)} \right) \right|^2 dx \leq C_T \frac{1}{n}$$

thus  $\rho^{(1)}$  closes the problem and allows us to determine  $\nabla \rho_n$ . Note that 3) implies 2).

*Notes by Tiffany A. Shaw and Aya Tanabe.*

# Lecture 11: Analysis of the Childress cell problem and stability of cellular flows

George C. Papanicolaou

## 1 Introduction

In the first part of this lecture we will discuss the Childress analysis of the cell flow problem and apply to it variational methods. Furthermore the general case of coupled Childress cells will be briefly analyzed. In the second part of the lecture we will discuss the stability of 2D cell flows for the forced Navier–Stokes equation.

## 2 Childress analysis of the advection-diffusion problem for a simple cell flow

In the previous lecture we have seen that the multiscale analysis gives us the following large scale equation

$$\nabla [(\epsilon \mathbf{I} + \Psi)(\nabla \chi + \mathbf{e})] = 0, \quad (1)$$

where  $\mathbf{I}$  is the unit matrix and  $\Psi$  is the matrix given by

$$\Psi(x, y) = \begin{pmatrix} 0 & -\psi(x, y) \\ \psi(x, y) & 0 \end{pmatrix} \quad (2)$$

The effective diffusivity is equal to

$$\sigma_\epsilon^*(\mathbf{e}) = \langle (\epsilon \mathbf{I} + \Psi)(\nabla \chi + \mathbf{e}) \cdot \mathbf{e} \rangle = \sigma_\epsilon^*(\mathbf{e}) = \langle (\epsilon \mathbf{I} + \Psi)(\nabla \chi + \mathbf{e}) \cdot (\nabla \chi + \mathbf{e}) \rangle = \epsilon + \epsilon \langle \nabla \chi \cdot \nabla \chi \rangle. \quad (3)$$

The background flow is assumed to be given by a very simple velocity field  $\mathbf{u} = (-\partial_y \psi, \partial_x \psi)$  with stream function

$$\psi(x, y) = \sin x \sin y, \quad (4)$$

which is represented on Figure 1. Note that due to the symmetries of the flow (4) it is sufficient to consider a quarter of the original cell  $[0, 2\pi] \times [0, 2\pi]$ . Indeed, a fluid particle which is initially contained in the cell  $[0, \pi] \times [0, \pi]$  will stay in this cell for all times, see Figure 1.

Equation (1) can be also written as

$$\epsilon \Delta \chi + \mathbf{u} \cdot \nabla \chi + \mathbf{e} \cdot \mathbf{u} = 0. \quad (5)$$

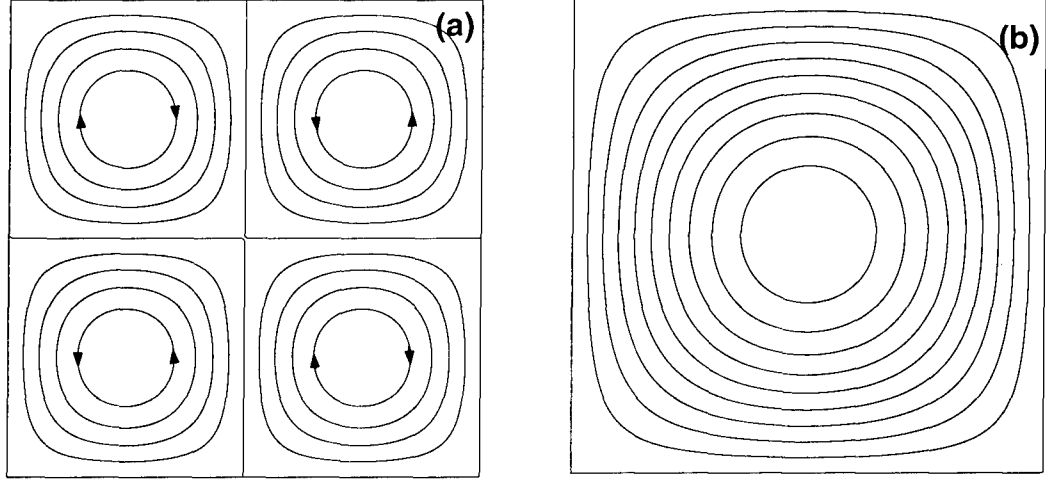


Figure 1: Simple cellular flow with stream function  $\psi(x, y) = \sin x \sin y$  within the cell  $[0, 2\pi] \times [0, 2\pi]$  (a) and the quarter cell  $[0, \pi] \times [0, \pi]$  (b).

Chose  $\mathbf{e} = (1, 0)$  and let  $\rho = \chi + x$ . Then we obtain the equation

$$\epsilon \Delta \rho + \mathbf{u} \cdot \nabla \rho = 0. \quad (6)$$

The boundary conditions are specified as follows

$$\rho(0, y) = 0 \quad \rho(\pi, y) = 0; \quad (7)$$

$$\frac{\partial}{\partial y} \rho(x, 0) = 0 \quad \frac{\partial}{\partial y} \rho(x, \pi) = 0. \quad (8)$$

The effective diffusivity can be calculated as follows

$$\sigma_\epsilon^* = \frac{\epsilon}{\pi^2} \int_0^\pi \int_0^\pi (\nabla \rho)^2 dx dy, \quad (9)$$

where  $\sigma_\epsilon^*(\mathbf{e}_1) = \sigma_\epsilon^*$ . To calculate the effective diffusivity (9) boundary layer theory can be applied [1]. On dimensional grounds the thickness of the boundary layer is expected to be of order  $\sqrt{\epsilon}$ . Indeed, the boundary layer can be estimated by equating the convection time scale  $t_{\text{conv}} \sim L/U_0$  and the diffusion time scale  $t_{\text{diff}} \sim l^2/\nu$  ( $U_0$  is the characteristic velocity and  $\nu$  is the viscosity). The quantity  $l/L$  is the width of the boundary layer. Equating  $t_{\text{conv}}$  and  $t_{\text{diff}}$  we obtain  $\frac{L}{U_0} \sim \frac{l^2}{\nu}$  and  $\frac{L\nu}{U_0 L^2} \sim \left(\frac{l}{L}\right)^2$ . Since  $\epsilon = \frac{1}{Pe} \sim \left(\frac{l}{L}\right)^2$  it follows that the width of the boundary layer is given by  $\frac{l}{L} \sim \sqrt{\epsilon}$ . The same arguments apply to the case of more general periodic flows (discussed in [2]) such as the one given by the stream function

$$\psi(x, y) = \sin x \sin y + \delta \cos x \cos y, \quad (10)$$

see Figure 2.

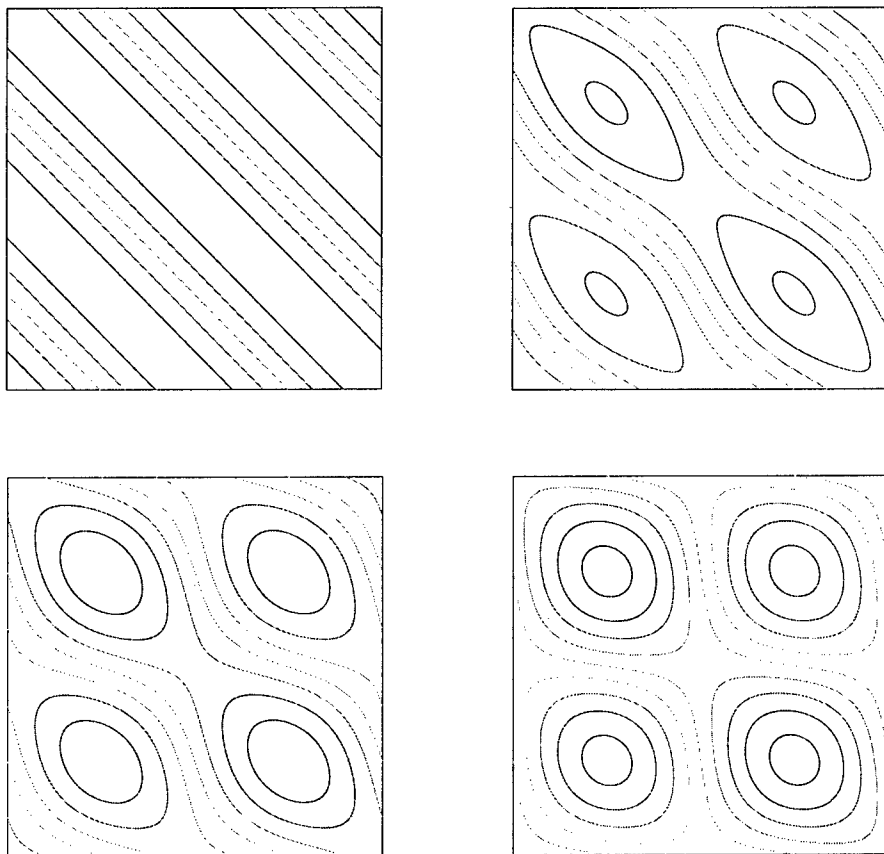


Figure 2: Cellular flows with stream function  $\psi(x, y) = \sin x \sin y + \delta \cos x \cos y$  for different  $\delta$ 's.

Cellular flows connected with each other by slight random deformations of saddle points have been considered by Isichenko in [3]. The deformation is assumed to be of the form

$$\psi(x, y) = \sin x \sin y + \delta \tilde{\psi}(x, y), \quad (11)$$

where the parameter  $\delta$  is assumed to be small and the function  $\tilde{\psi}$  is random with certain properties [4].

In the periodic case the effective diffusivity can be estimated by using the fact that  $\rho$  changes significantly only in the boundary layer. Therefore  $\nabla \rho$  is of the order of  $1/\sqrt{\epsilon}$  and  $\sigma_\epsilon^* \sim \epsilon \left(\frac{1}{\sqrt{\epsilon}}\right)^2 \sqrt{\epsilon} \sim \sqrt{\epsilon}$ .

More precise results can be obtained by using the boundary layer method. We introduce boundary coordinates

$$(x, y) \longrightarrow (\psi, \theta), \quad 0 \leq \psi \leq 1, \quad -4 \leq \theta \leq 4. \quad (12)$$

Note that  $\psi$  is just the value of the stream function which is equal to zero on the boundary.

Furthermore , the level lines of  $\psi$  and  $\theta$  are orthogonal

$$\nabla\psi \cdot \nabla\theta = 0, \quad |\nabla\psi| = |\nabla\theta| \text{ on } \psi = 0. \quad (13)$$

It is suitable to rescale the coordinate  $\psi$  in the neighborhood of the boundary. We define

$$(h, \theta) = \left( \frac{\psi}{\sqrt{\epsilon}}, \theta \right). \quad (14)$$

The standard chain rule yields

$$\frac{\partial \rho}{\partial x} = \frac{\partial h}{\partial x} \frac{\partial \rho}{\partial h} + \frac{\partial \theta}{\partial x} \frac{\partial \rho}{\partial \theta}$$

and

$$\rho_{xx} = h_{xx}\rho_x + h_x^2\rho_{hh} + 2h_x\theta_x\rho_{h,\theta} + \theta_{xx}\rho_\theta + \theta_x^2\rho_{\theta\theta}.$$

For  $\epsilon \ll 1$  the left hand side of (6) can be written as

$$\epsilon(\rho_x x + \rho_y y) \rightarrow \frac{\epsilon}{\sqrt{\epsilon}} \Delta\psi \rho_h + |\nabla\psi|^2 \rho_{hh} + \epsilon \Delta\theta \rho_\theta + \epsilon (\nabla\theta)^2 \rho_{\theta\theta}.$$

Form the condition (13) follows

$$-\psi_y \rho_x + \psi_x \rho_y = -\nabla^\perp \psi \cdot \nabla \theta \rho_\theta = |\nabla\psi|^2 \rho_\theta + \text{h.o.t.}$$

The boundary layer equation has the form

$$\rho_{hh} + \rho_\theta = 0, \quad h > 0, \quad -4 \leq \theta \leq 4 \quad (15)$$

with boundary conditions

$$\rho(0, \theta) = 0, \quad \text{for } 0 \leq \theta \leq 2 \quad (16)$$

$$\rho(0, \theta) = \pi, \quad \text{for } -4 \leq \theta \leq -2 \quad (17)$$

$$\frac{\partial \rho}{\partial n} = 0, \quad \text{for } -2 \leq \theta \leq 0 \text{ and } 2 \leq \theta \leq 4. \quad (18)$$

Finally, we obtain the Childress equation

$$\frac{1}{\sqrt{\epsilon}} \sigma_\epsilon^* \rightarrow \frac{1}{\pi^2} \int_0^\infty \int_{-4}^4 \rho_n^2 dh d\theta. \quad (19)$$

This problem has been treated by A. Soward in [5].

Finally, let us remark that boundary layer coordinates can be used to give an estimation of the scaling of  $\sigma_\epsilon^*$  in the case of random flows. As before we suppose that the boundary is given by the level set  $\psi = 0$ . However, due to the randomness of the flow this boundary has a complicated fractal structure. For small  $\psi$  let the characteristic velocity at  $\psi$  be denoted as  $U(\psi)$  and the width of the boundary layer by  $l(\psi)$ . Just as in the case of periodic flows we equate the diffusion time scale to the convection time scale  $U^2(\psi)/\epsilon \sim l(\psi)/U_0$ . Percolation methods can be applied to calculate the width of the boundary layer in dependence on  $\psi$

[4]. This gives  $l(\psi) \sim \psi^{-7/4}$ . Since the velocity is assumed to be smooth it follows that  $U(\psi) \sim \psi$  and  $U_0 = O(1)$ . Therefore

$$\psi \sim \epsilon^{4/15}. \quad (20)$$

Supposing that the gradient of  $\rho$  is of order  $\frac{1}{\psi}$  we obtain from (9)

$$\sigma_\epsilon^* \sim \epsilon \left( \frac{1}{\psi} \right)^2 l(\psi) U(\psi) \sim \epsilon^{3/13}, \quad (21)$$

where  $l(\psi)U(\psi)$  is the area of the boundary layer. Therefore, for random flows the effective diffusivity scales like  $\epsilon^{\frac{3}{13}}$ .

### 3 Variational analysis

The discussion of variational method results in this section is largely based on [2]. Denoting  $E_{e_1}^+ = \nabla \chi + e_1$  equation (1) becomes

$$\nabla \cdot (\mathbf{I} + \Psi) E_{e_1}^+ = 0 \quad (22)$$

and  $E_{e_1}^+$  satisfies conditions  $\nabla \times E_{e_1}^+ = 0$  and  $\langle E_{e_1}^+ \rangle = 0$ . We also consider the adjoint problem

$$\nabla \cdot (\mathbf{I} - \Psi) E_{e_2}^- = 0, \quad (23)$$

with  $\nabla \times E_{e_2}^- = 0$  and  $\langle E_{e_2}^- \rangle = 0$ . For convenience of notation define

$$D_{e_1}^+ = (\mathbf{I} + \Psi) E_{e_1}^+, \quad E_{e_2}^- = (\mathbf{I} - \Psi) E_{e_2}^-. \quad (24)$$

Then the effective diffusivity becomes

$$\sigma^*(e_1, e_2) = \langle D_{e_1}^+ \cdot e_2 \rangle. \quad (25)$$

Define now

$$E'_{12} = \frac{1}{2}(E_{e_1}^+ - E_{e_2}^-) \quad D'_{12} = \frac{1}{2}(D_{e_1}^+ - D_{e_2}^-), \quad (26)$$

$$E_{12} = \frac{1}{2}(E_{e_1}^+ + E_{e_2}^-) \quad D_{12} = \frac{1}{2}(D_{e_1}^+ + D_{e_2}^-), \quad (27)$$

$$(28)$$

It follows that

$$D'_{12} = E'_{12} + \Psi E_{12}, \quad \nabla \cdot D'_{12} = 0, \quad \nabla \times E'_{12} = 0 \quad (29)$$

$$D_{12} = E_{12} + \Psi E'_{12}, \quad \nabla \cdot D_{12} = 0, \quad \nabla \times E_{12} = 0. \quad (30)$$

The effective diffusivity can be written as

$$\sigma^* = \langle D_{e_1}^+ \cdot e_2 \rangle = \left\langle \frac{1}{2} \langle D_{e_1}^+ \cdot e_2 \rangle + \frac{1}{2} \langle D_{e_2}^- \cdot e_1 \rangle \right\rangle = \frac{1}{2} \langle D_{e_1}^+ \cdot E_{e_2}^- \rangle + \frac{1}{2} \langle D_{e_2}^- \cdot E_{e_1}^+ \rangle =$$



$$\frac{1}{4}\langle(D_{\mathbf{e}_1}^+ + D_{\mathbf{e}_2}^-)(E_{\mathbf{e}_1}^+ + E_{\mathbf{e}_2}^-)\rangle - \frac{1}{4}\langle(D_{\mathbf{e}_1}^+ - D_{\mathbf{e}_2}^-)(E_{\mathbf{e}_1}^+ - E_{\mathbf{e}_2}^-)\rangle = \langle D_{12} \cdot E_{12} \rangle - \langle D'_{12} \cdot E'_{12} \rangle.$$

Then we obtain the following matrix equation

$$\sigma^* = \left\langle \begin{pmatrix} -\mathbf{I} & \Psi \\ \Psi & \mathbf{I} \end{pmatrix} \begin{pmatrix} E'_{12} \\ E_{12} \end{pmatrix} \cdot \begin{pmatrix} E'_{12} \\ E_{12} \end{pmatrix} \right\rangle. \quad (31)$$

Note that the matrix  $\begin{pmatrix} -\mathbf{I} & \Psi \\ \Psi & \mathbf{I} \end{pmatrix}$  is symmetric but indefinite.

Effective diffusivity can be computed as solution of the following variational problem

$$\sigma^{ast}(\mathbf{e}_1, \mathbf{e}_2) = \inf_{\langle F \rangle = \frac{\mathbf{e}_1 + \mathbf{e}_2}{2}, \nabla \times F = 0} \sup_{\langle F' \rangle = \frac{\mathbf{e}_1 - \mathbf{e}_2}{2}, \nabla \times F' = 0} \{\mathcal{A}(F, F')\} \quad (32)$$

where the matrix  $\mathcal{A}(F, F')$  is given by

$$\mathcal{A}(F, F') = \left\langle \begin{pmatrix} -\mathbf{I} & \Psi \\ \Psi & \mathbf{I} \end{pmatrix} \begin{pmatrix} F' \\ F \end{pmatrix} \cdot \begin{pmatrix} F' \\ F \end{pmatrix} \right\rangle.$$

The algebraic technique which underlies this calculation is that of a partial Legendre transform.

We will now give upper and lower bounds. First analyze the supremum. Consider the equation

$$\nabla F' + \nabla \cdot (\Psi F) = 0 \quad (33)$$

with

$$F' = \frac{\mathbf{e}_1 - \mathbf{e}_2}{2} - \Gamma \Psi F, \quad (34)$$

where  $\Gamma \nabla \Delta^{-1} \nabla$  is the projection operator on the space of divergence-free vector fields. It is easily verified that (34) gives (33). Now we plug  $F'$  into the expression (32) setting  $\mathbf{e}_1 = \mathbf{e}_2$ . Then we obtain the following upper bound for the effective diffusivity

$$\sigma_\epsilon^*(\mathbf{e}) = \inf_{\nabla \times F = 0, \langle F \rangle = \mathbf{e}} \left\{ \epsilon \langle F \cdot F \rangle + \frac{1}{\epsilon} \langle \Gamma \Psi F \cdot \Gamma \Psi F \rangle \right\}. \quad (35)$$

Choose  $F = \nabla f$  with  $f = f(h, \theta)$ . Then the first term  $\langle F \cdot F \rangle$  in (35) gives

$$|\nabla f|^2 = |\nabla h|^2 \left( \frac{\partial f}{\partial h} \right)^2 + |\nabla \theta|^2 \left( \frac{\partial f}{\partial \theta} \right)^2, \quad (36)$$

where we have used (13). Since the second term in (36) is of order  $\epsilon$  in comparison to the first term we obtain

$$\epsilon \langle F \cdot F \rangle \sim \frac{\epsilon}{\pi^2} \int_0^\infty \int_{-4}^4 |\nabla h|^2 \frac{1}{J(h, \theta)} \left( \frac{\partial f}{\partial h} \right)^2 dh d\theta \sim \frac{\sqrt{\epsilon}}{\pi^2} \int_0^\infty \int_{-4}^4 \left( \frac{\partial f}{\partial h} \right)^2 dh d\theta. \quad (37)$$

Here we have used the fact that near the boundary  $J(h, \theta) \sim \sqrt{\epsilon} |\nabla h|^2$ .

To calculate the second term in (35) suppose that  $\frac{1}{\epsilon} \Gamma \Psi \nabla f = \nabla f'$  so that  $f'$  is the solution of the Poisson equation

$$\epsilon \Delta f' = (-\psi_y, \psi_x) \cdot \nabla f. \quad (38)$$

The second term of (35) becomes now

$$\frac{1}{\epsilon} \langle \Gamma \Psi \nabla f \cdot \Gamma \Psi \nabla f \rangle = \epsilon \langle \nabla f' \cdot \nabla f' \rangle. \quad (39)$$

To obtain  $f'$  up to the leading order in  $\epsilon$  it suffices to replace equation (38) by

$$\frac{\partial^2 f'}{\partial h^2} \sim \frac{\partial f'}{\partial \theta}, \quad (40)$$

where we have again used the fact that  $J(h, \theta) \sim \sqrt{\epsilon} |\nabla h|^2$  near the boundary. Solving (40) by direct integration we can calculate the left hand side in (39) in the same way as we have done for  $\epsilon \langle \nabla f \cdot \nabla f \rangle$ . This gives

$$\frac{1}{\epsilon} \langle \Gamma \Psi \nabla f \cdot \Gamma \Psi \nabla f \rangle \sim \frac{\sqrt{\epsilon}}{\pi^2} \int_0^\infty \int_{-4}^4 \left( \int_\infty^h \frac{\partial f}{\partial h'} dh' \right)^2 dh d\theta. \quad (41)$$

Finally we obtain the following inequality

$$\lim_{\epsilon \rightarrow 0} \frac{1}{\sqrt{\epsilon}} \sigma_\epsilon^*(e) \lesssim \frac{1}{\pi^2} \inf_f \int_0^\infty \int \left[ \left( \frac{\partial f}{\partial h} \right)^2 + \left( \int_\infty^h \left( \frac{\partial f}{\partial \theta} \right) dh' \right)^2 \right] dh d\theta. \quad (42)$$

In a similar a lower bound can be given. Note that Childress problem appears in both lower and upper bounds and represents therefore an asymptotic relation [2].

## 4 Coupled Childress problems

In each cell we have different functions  $f_i(h_i, \theta)$  and the following system of Childress equations

$$\frac{\partial^2 f_i}{\partial h^2} + \frac{\partial f_i}{\partial \theta} = 0, \quad h > 0, \quad \theta \in [0, l_i]. \quad (43)$$

We have to impose the following boundary conditions:  $f_i|_{\text{edges}} = f_{ik}(\theta)$ , where  $k$  is one of the edges.

For common interior edges we have the conditions

$$\frac{\partial f_i}{\partial h} + \frac{\partial f_j}{\partial h} \Big|_{h=0} = 0. \quad (44)$$

This allows us to construct a network approximation for convection-diffusion problems with many cells, see Figure 3.

## 5 The Stability of Cellular Flows

Let us consider the two dimensional Navier-Stokes equations driven by a spatially periodic force  $F(y)$ :

$$\begin{cases} \mathbf{U}_\tau + (\mathbf{U} \cdot \nabla) \mathbf{U} = -\nabla \tilde{p} + \frac{1}{Re} \Delta \mathbf{U} + F \\ \nabla \cdot \mathbf{U} = 0 \end{cases}$$

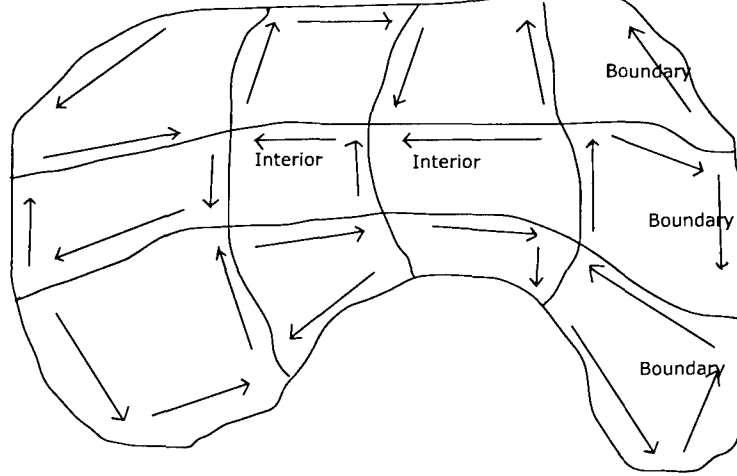


Figure 3: Network approximation for problem of many coupled cells.

where the Reynolds number  $Re = \frac{UL}{\nu}$  is based on a length scale  $L$  which is proportional to the period of the forcing, taken to be equal to  $2\pi$ .

As we are in two dimensions, the incompressibility condition  $\nabla \cdot \mathbf{U} = 0$  implies that there exists a stream function  $\Phi$  so that  $\mathbf{U} = \begin{pmatrix} -\Phi_2 \\ \Phi_1 \end{pmatrix}$ .

Writing the Navier-Stokes equations above in terms of the stream function  $\Phi$  we have:

$$\frac{\partial}{\partial t} \Delta \Phi + J_{yy}(\Phi, \Delta \Phi) = \frac{1}{Re} \Delta^2 \Phi + f \quad (45)$$

where  $J_{yy}(u, v) = -u_2 v_1 + u_1 v_2$ . Here  $f = -F_{1,2} + F_{2,1}$  is  $2\pi$  periodic in  $R^2$ . It is chosen so that it gives rise to a stream function  $\phi$  which is a time independent, mean-zero, periodic solution of the Navier-Stokes equations:

$$J_{yy}(\phi(y), \Delta \phi(y)) = \frac{1}{Re} \Delta^2 \phi(y) + f(y) \quad (46)$$

Let  $\Phi(\tau, y) = \phi(y) + \tilde{\Phi}(\tau, y)$  be a perturbation of the stationary solution  $\phi(y)$ . If the stream function of the basic flow is an *eddy* of size  $k^{-\frac{1}{2}}$ , that is if  $\phi(y)$  is an eigenfunction of the Laplacian

$$\Delta \phi = -k\phi, \quad (47)$$

then the driving force  $f(y)$  is

$$f(y) = -\frac{k^2}{Re} \phi(y)$$

and  $\tilde{\Phi}(\tau, y)$  satisfies:

$$\partial_\tau \Delta \tilde{\Phi}(\tau, y) + J_{yy}(\phi(y), (k + \Delta) \tilde{\Phi}(\tau, y)) + J_{yy}(\tilde{\Phi}(\tau, y), \Delta \tilde{\Phi}(\tau, y)) = \frac{1}{Re} \Delta^2 \tilde{\Phi}(\tau, y) \quad (48)$$

What concerns us here is the stability of eddy flows like (46) and (47) subject to an initial *modulational* perturbation, a perturbation on a scale much larger than that of the eddy (see Dubrulle and Frisch ([8] for references about previous works in this direction). For this purpose, we introduce a small parameter  $\epsilon$  and define the large-scale time and space variable

$$t = \epsilon^2 \tau, x = \epsilon y \quad (49)$$

respectively and analyse a special class of asymptotic solutions of (48), where  $\tilde{\Phi}(\tau, y) = \Psi^\epsilon(t, x)$  is expressed in the large-scale or slow variables as:

$$\Psi^\epsilon(t, x) = \Psi(t, x) + \epsilon \Psi^1(t, x, x/\epsilon) + \epsilon^2 \Psi^2(t, x, x/\epsilon) + \dots \quad (50)$$

One can derive (see [6] for details) from (48) the large scale modulational equation for  $\Psi(t, x)$  in the vorticity form:

$$\partial_t \nabla^2 \Psi(t, x) + \alpha_{jkl}^{nonlin} \nabla_{ji} (\nabla_k \Psi(t, x) \nabla_l \Psi(t, x)) = \nu_{jkl} \nabla_j \nabla_i \nabla_k \nabla_l \Psi(t, x) \quad (51)$$

(where we used the convention  $\nabla_i = \frac{\partial}{\partial x_i}$ ).

The coefficients  $\nu_{jkl}$  are the tensor of eddy viscosity and  $\alpha_{jkl}^{nonlin}$  are the effective coefficients of another tensor which we call the nonlinear  $\alpha$ -tensor (see [6] for details). Both tensors are derived as necessary solvability conditions of auxiliary cell problems that guarantee the validity of the separation of scales for some finite time.

We will consider a family of cellular flows with a stream function

$$\phi = \sin(y_1) \sin(y_2) + \delta \cos(y_1) \cos(y_2), 0 \leq \delta \leq 1$$

All coefficients of the eddy viscosity tensor  $\nu_{jkl}$  but one, called  $\nu'$  can be computed analytically. The large-scale modulation equation corresponding to  $\nu'$  is:

$$\begin{aligned} & \frac{\partial}{\partial t} \nabla^2 \Psi + \frac{Re^2}{8} (\nabla_2^2 - \nabla_1^2) [\delta ((\nabla_1 \Psi)^2 + (\nabla_2 \Psi)^2) + (1 + \delta^2) \nabla_1 \Psi \nabla_2 \Psi] + J_{xx}(\Psi, \nabla^2 \Psi) \\ &= \frac{1}{Re} \nabla^4 \Psi - \frac{Re}{8} [(\nabla_1 + \delta \nabla_2)^2 + (\delta \nabla_1 + \nabla_2)^2] \nabla^2 \Psi + \left( \frac{Re}{2} (1 + \delta^2) + \nu' \right) (\nabla_2^2 - \nabla_1^2) \Psi \end{aligned} \quad (52)$$

The  $\nu'$  can be computed numerically for  $Re \leq 32$ , and for closed cellular flows  $\phi = \sin(y_1) \sin(y_2)$  it can be shown that  $\nu' = O(Re^{2.5})$  for large  $Re$ . This is done using an extension of the variational principles discussed earlier in this lecture (for details see [6]). Previously, Sivashinsky and Yakhot ([7]) and also Dubrulle and Frisch ([8]) have done a small Reynolds number linear stability analysis (see [7]), but in our case we are concerned with large Reynolds number flow.

The modulational perturbations of closed cellular flows ( $\delta = 0$  in (5)) are much more stable than the shear cellular flows ( $\delta = 1$  in (5)) for large Reynolds numbers. More specifically, exponential solutions  $\Psi(t, x) = \exp(\sigma t) \exp(k_1 x_1 + k_2 x_2)$  are asymptotically unstable

as  $Re \rightarrow \infty$  only if  $k_1 \approx \pm k_2$  for closed cellular flows. This result is to be contrasted with a similar stability result for shear flows, where exponential solutions are asymptotically unstable as  $Re \rightarrow \infty$  if  $C_1 \leq |k_1|/|k_2| \leq C_2$  where  $C_1 = 1/C_2 \approx 0.45 \neq 1$ . It can also be shown that because of the presence of  $\nu' = O(Re^{2.5})$  for closed cellular flows, the stability at high Reynolds numbers is significantly better for flows with closed streamlines. Cell-like mesoscale ocean flows (which are at high Reynolds numbers in the range of  $10 - 10^3$ ) are close to closed cellular flows, and so the previous analysis may explain their persistence.

*Notes by Ravi Srinivasan, Dani Zarnescu and Walter Pauls.*

## References

- [1] S. Childress, Alpha-effect in flux ropes and sheets, *Phys. Earth Planet Inter.* **20**, pp. 172–180, 1979.
- [2] A. Fannjiang and G. Papanicolaou, Convection enhanced diffusion for periodic flows, *SIAM J. Appl. Math.* **54:2**, pp. 333–408, 1994.
- [3] M. B. Isichenko and J. Kalda, Statistical topography II. 2-D transport of a passive scalar, *J. Nonlinear Sci.* **1**, pp. 375–396, 1991.
- [4] A. Fannjiang and G. Papanicolaou, Convection enhanced diffusion for random flows, *J. Stat. Phys.* **88**, pp. 1033–1076, 1997.
- [5] A. M. Soward, Fast dynamo action in steady flow, *J. Fluid Mech.* **180**, pp. 267–295.
- [6] A. Novikov and G. Papanicolaou, Eddy viscosity of cellular flows, *J. Fluid Mech.* **446**, 173–198, 2001.
- [7] G. Sivashinsky and V. Yakhot, Negative viscosity effect in large-scale flows, *Physics of Fluids* **28**, pp. 1040–1042, 1985.
- [8] B. Dubrulle and U. Frisch, Eddy viscosity of parity-invariant flow, *Phys. Rev. A* **43** (3), no. 10, pp. 5355–5364, 1991.

# Shallow Water Flow through a Contraction

Benjamin Akers

Department of Mathematics, University of Wisconsin, U.S.A.

July 18, 2006

## 1 Introduction

Shallow water flows in channels are of interest in a variety of physical problems. These include river flow through a canyon, river deltas, and canals. Under certain conditions we can get large hydraulic jumps, or their moving counterparts bores, in the channel. There are a number of places where these bores are generated in rivers around the world, including the River Severn in England, and the Amazon in Brazil [6].



Figure 1: A surfer riding a tidal bore on the Amazon.

In this work, we will be concerned with the effect that geometry and flow rate have on the formation and stability of hydraulic jumps. The general setup is inspired by Al-Tarazi et al. [2] and Baines and Whitehead [4]. The motivations are to use the present study to investigate shallow water flow and also as a tool for comparison with the granular media flows studied in [2]. The idea being that this will lay a foundation for the study of mixed media flows.

The body of this report is divided into five sections. First we will present the one dimensional inviscid hydraulic theory. Then we will compare the inviscid theory with the experimental results. Next we will discuss some two dimensional and frictional effects. Finally, we will discuss some areas for future research and make some concluding remarks.

## 2 Experimental setup

We conducted a series of experiments in a linear flume with a flat bottom and piecewise linear cross section. Water flows through a sluice gate at the beginning of our channel, pours out of the end into a large reservoir, and is recirculated using pumps. The setup is shown in Figure 2.

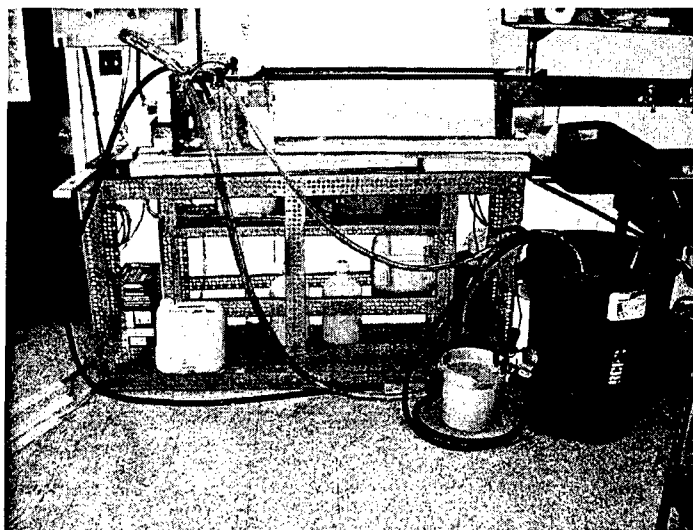


Figure 2: The experiments were done in a linear plexiglass flume, where water was recirculated using pumps in a large trash can, seen on the right, downstream of the contraction.

The flume had a 20 cm cross section, and was approximately 1.5 m in length. When all three of the pumps were in operation, we could generate a volume flux up to 4 liters/sec. For each experiment two plexiglass paddles, 30.5 cm long, are fixed at a given angle at the end of the channel. The flow rate is set by turning on the desired number of pumps and restricting the flow until the various flow states are observed. The flow rate is then measured using a bucket and a stopwatch at the end of the channel. In order to increase the accuracy of our flow measurement, the discharge was measured a minimum of five times and the mean of these measurements was taken as the flow rate. In each experiment the height of the fluid is measured by placing a thin ruler in the fluid parallel to the flow velocity and visually estimating the depth. Data was taken at a variety of nozzle widths and flow speeds. A schematic of the experimental setup is shown in Figure 3.

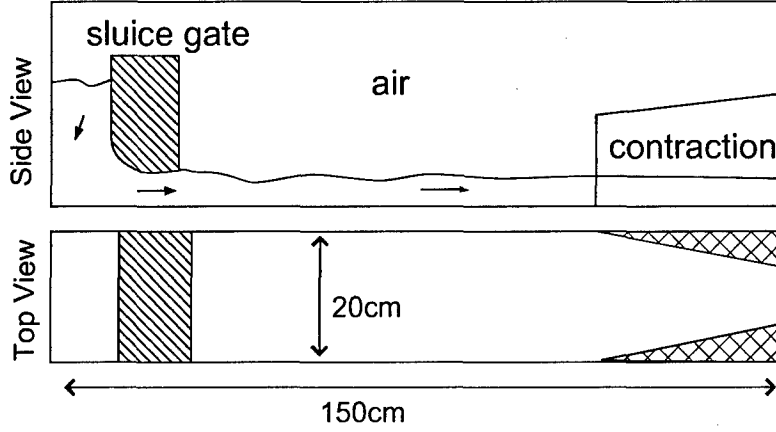


Figure 3: A sketch of the tank is given. The tank is piecewise linear, with paddles at the end to regulate the nozzle width.

### 3 One Dimensional Inviscid Flows

Here we will present the mathematical formulation of the problem of flow through a channel with a contraction. We will derive the governing equations from conservations laws and use these to give predictions for steady one dimensional (1-D) flows. Next, we will determine the necessary flow conditions for moving shocks, as well as for stationary shocks. Finally, we will derive a stability condition for steady shocks in a contraction.

#### 3.1 Conservation Laws

Conservation of mass of a constant density fluid in a shallow channel can be written as

$$\frac{d}{dt} \int_{x_0}^{x_1} \int_0^{b(x)} \int_0^{h(x,y,t)} \rho dz dy dx = \int_0^{b(x)} \int_0^{h(x,y,t)} \rho (u(x_0, y, t) - u(x_1, y, t)) dz dy, \quad (1)$$

where the  $x$ -axis is measured down the centerline of the channel,  $x_0$  and  $x_1$  are arbitrary points on this axis, and  $t$  is time. If we use the divergence theorem on the integral on the right hand side, and take  $h$  and  $u$  to be independent of  $y$  this becomes

$$\int_{x_0}^{x_1} [\rho b(x) h(x, t)]_t + [\rho b(x) h(x, t) u(x, t)]_x dx = 0. \quad (2)$$

Since  $x_0$  and  $x_1$  are arbitrary we get that the argument of our integral must be equal zero pointwise

$$(bh)_t + (bhu)_x = 0. \quad (3)$$

Here  $u$  is the velocity,  $h$  the height of the free surface,  $b$  the width of the channel, and  $\rho$  the density of the fluid. Partial derivatives are written in two ways as  $\partial_t(\cdot) = (\cdot)_t$  and so forth.



For water,  $\rho$ , is taken constant, and we therefore have dropped the  $\rho$  dependence from (3). We can also get a momentum equation using Newton's second law of motion

$$\frac{d}{dt} \int_{CV} \rho u(x, y, t) dV = \int_{CS} \rho u(x, y, t)^2 \cdot \mathbf{n} dA + \int_{CV} F dV + \int_{CS} \mathbf{S} \cdot \mathbf{n} dA, \quad (4)$$

where  $dA$  and  $dV$  are infinitesimal area and volume elements. To make the notation simpler we have omitted the bounds of our integrals, instead writing  $CV$  for an arbitrary control volume, and  $CS$  for the surface of that volume. If we make the assumption that the pressure forces are hydrostatic, then the acceleration in the vertical direction is negligible, and the body forces must balance the surface stress to give hydrostatic pressure  $p - p_0 = \rho g(h - y)$  (see, e.g., [9]), where  $g$  is the acceleration due to gravity. We can use Stokes' theorem to turn (4) into a volume integral, and after assuming again  $h = h(x, t)$ ,  $u = u(x, t)$  we obtain

$$(bhu)_t + (bhu^2)_x + \frac{1}{2}gb(h^2)_x = 0. \quad (5)$$

### 3.2 Smooth Hydraulic Flow

In this section, we are looking at flows which have reached a steady state. This allows us to simplify (3) and (5) into

$$(bhu)_x = 0 \quad (6a)$$

$$(bhu^2)_x + \frac{1}{2}gb(h^2)_x = 0. \quad (6b)$$

When the solutions are smooth we can expand the derivatives in (6b) to get

$$\left(\frac{1}{2}u^2 + gh\right)_x = 0. \quad (7)$$

Next, introduce the local Froude number,  $F = u/\sqrt{gh}$ . Eliminating  $u_x$  from (6) yields

$$-\frac{u^2}{gh}(bh)_x + bh_x = 0 \quad (8)$$

or

$$(1 - F^2)bh_x = F^2hb_x. \quad (9)$$

Thus we see that if  $F = 1$  then  $b$  must be stationary, or in our case at a minimum. Note that the converse is not true, when  $b_x = 0$  we have that  $F = 1$  or  $h_x = 0$  but not necessarily both. We will define the flow to be subcritical when  $F < 1$  and supercritical when  $F > 1$ . Equation (9) tells us that for smoothly contracting  $b(x)$ , the subcritical fluid flow must have a minimum in  $h$  at the nozzle. Similarly, supercritical flow must have a maximum at the nozzle, see Figure 4.

Next we will examine for what range of far field Froude numbers  $F_0 = u_0/\sqrt{gh_0}$  and contraction ratios  $B = b_c/b_0$ , we can have smooth solutions. Since the flow is smooth we can follow the two constants of the flow

$$Q = b_0h_0u_0 = b_ch_cu_c \quad (10a)$$

$$E = u_0^2/2 + gh_0 = u_c^2/2 + gh_c. \quad (10b)$$

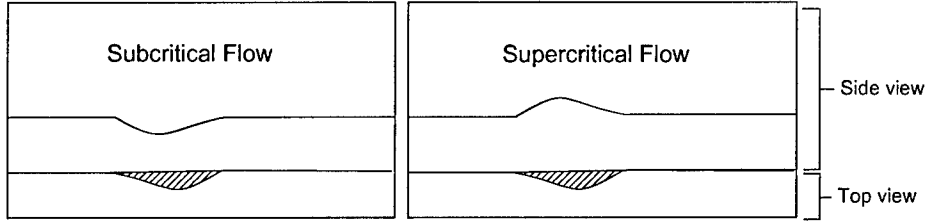


Figure 4: The shape of the free surface of supercritical and subcritical smooth flow through a nozzle. Both the top view and a profile are shown in this figure.

If we non-dimensionalize,  $H = h_c/h_0$  and  $B = b_c/b_0$ , then (10) is equivalent to the cubic polynomial,  $p(H) = 0$ , with parameters  $B$  and  $F_0$ , where

$$P(H) = H^3 B^2 - \left(\frac{1}{2}F_0^2 + 1\right)B^2 H^2 + \frac{1}{2}F_0^2 = 0. \quad (11)$$

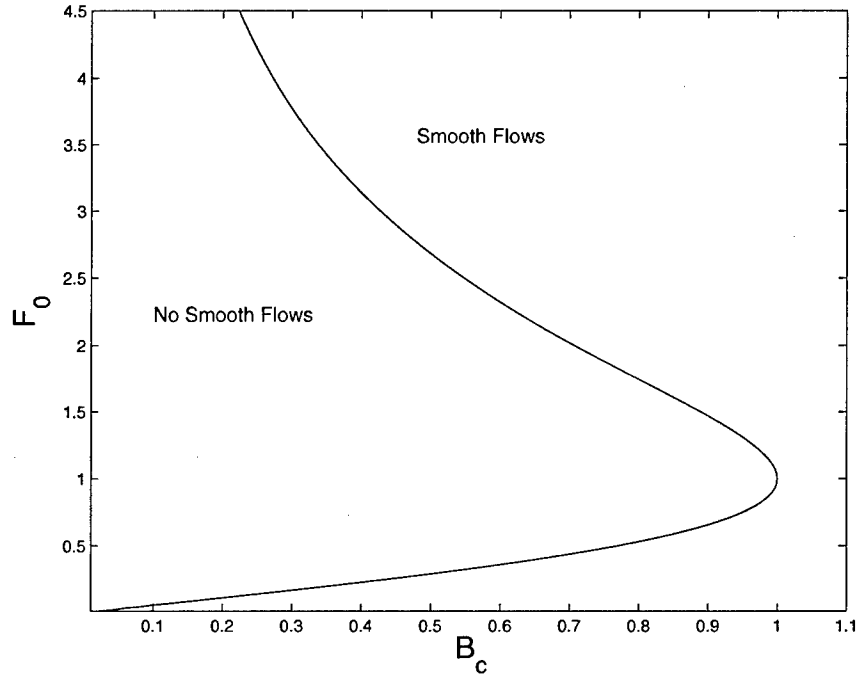


Figure 5: The smooth solution boundary is plotted in the  $B_c F_0$ -plane, where  $B_c$  is the nondimensional contraction width, and  $F_0$  is the ratio of the flow speed to the characteristic flow rate of the fluid. We note that  $B_c = 1$  corresponds to a blocked flow and  $B_c = 1$  corresponds to a straight channel.

The stationary points of this cubic are at  $H = 0$  and  $H^* = \frac{2}{3}(\frac{1}{2}F_0^2 + 1)$ . Now since physically meaningful roots exist only for  $H > 0$ , we can determine when there are positive roots by evaluating  $P(H)$  at  $H = H^*$ . When  $p(H^*) \leq 0$  there are positive roots, and when  $p(H^*) > 0$  there are no positive roots. Thus the point  $p(H^*) = 0$  determines the

boundary between smooth and nonsmooth solutions in the  $B_c F_0$ -plane. This is a standard technique in hydraulic theory [7]. We obtain

$$\frac{3}{2} \left( \frac{F_0}{B_c} \right)^{2/3} - \left( 1 + \frac{1}{2} F_0^2 \right) = 0. \quad (12)$$

Figure 5 illustrates how for a given geometry  $B_c$  and incoming depth  $h_0$  there is a maximum speed at which a subcritical smooth flow can pass. It is also interesting to note that for channels with expanding width  $B > 1$  we can find a smooth flow regardless of the speed. In the next section we will look at non-smooth flows.

### 3.3 Upstream Moving Bores

Here we will look for solutions with a discontinuity, or jump, at one point. We will allow this jump to move upstream at speed  $s$ , where  $s$  is positive when moving to the left, as in Figure 6.

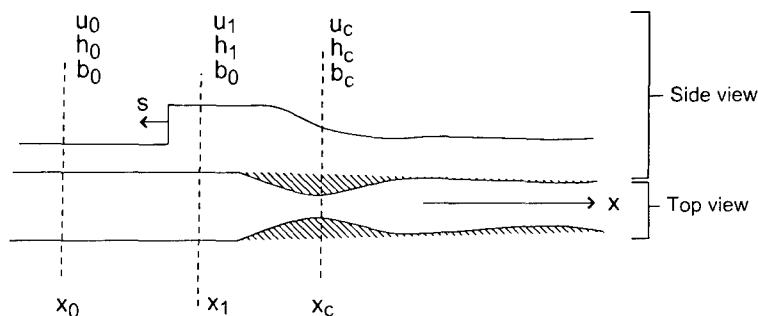


Figure 6: Both the free surface profile and the planar view are shown. Here we have a shock moving upstream with speed  $s$ . Conservation laws will be used to couple the fluid motion between points  $x_0$ ,  $x_1$ , and  $x_c$ .

As in Figure 6, we will pick a point upstream,  $x_0$ , one between the jump and the nozzle,  $x_1$ , and the point of minimum width at the nozzle,  $x_c$ . We will label the width, height, and velocity at these points with subscripts that match the respective points. The goal is to find in which regions of the  $B_c F_0$ -plane there exist shock solutions. We can couple the flow at points  $x_1$  and  $x_c$  using Bernoulli's equation (13c) and conservation of mass (13b) as before. The flow at points  $x_0$  and  $x_1$  can be coupled by conservation of mass in the frame of the jump (13a) and a jump condition (13d) which we can derive from the conservative form of the momentum equation. Consequently, we have four equations for five unknowns,

so we impose the restriction that flow is critical (13e) at the nozzle, and obtain the system

$$(u_0 + s)h_0b_0 = (u_1 + s)h_1b_1 \quad (13a)$$

$$u_1h_1b_1 = u_ch_cb_c \quad (13b)$$

$$\frac{1}{2}u_1^2 + gh_1 = \frac{1}{2}u_c^2 + gh_c \quad (13c)$$

$$(u_0 + s)^2 = \frac{gh_1}{2} \left(1 + \frac{h_1}{h_0}\right) \quad (13d)$$

$$u_c^2 = gh_c. \quad (13e)$$

Taking a critical condition at the nozzle is a common assumption in hydraulics. It is equivalent to imposing the restriction that there are no waves at infinity [5]. Now, we have a system of five equations for five unknowns  $u_1, u_c, h_c, h_1, s$ , with parameters  $h_0, u_0, b_1 = b_0, b_c$ . Nondimensionalizing  $B = b_c/b_0, F_0 = u_0/\sqrt{gh_0}, H_1 = h_1/h_0, S = s/\sqrt{gh_0}$ , system (13) simplifies to

$$\frac{1}{2}(F_0 + (1 - H_1)S)^2 = \frac{3}{2}H_1^2 \left( \frac{F_0 + (1 - H_1)S}{B_c} \right)^{2/3} - H_1^3 \quad (14a)$$

$$(F_0 + S)^2 = \frac{1}{2}H_1(1 + H_1). \quad (14b)$$

Figure 7 shows the region of the  $B_cF_0$ -plane where (14) has physically meaningful solutions. This region was obtained by first fixing  $H_1$  and then finding the solution curves for  $S$  and then fixing  $S$  and finding the solution curves for  $H_1$ . The boundaries correspond to smooth flow  $H_1 = 1$  and steady shocks  $S = 0$ .

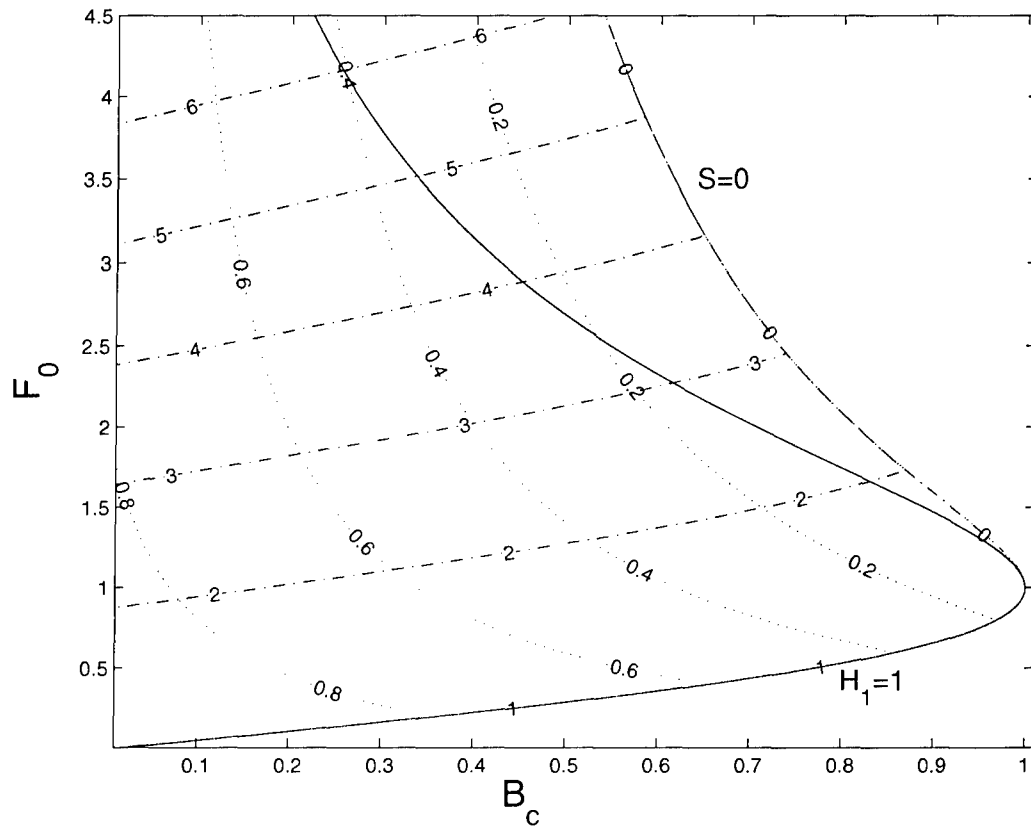


Figure 7: The level sets of the shock speed (dotted lines) and height ratio (dashed lines) are plotted. The solid line is the smooth solution boundary. Notice there is a wedge where there are both smooth and moving shock solutions.

### 3.4 Hydraulic Jumps in the Contraction

Here we examine for which flow rates  $F_0$  and contraction widths  $B_c$  there can be steady shocks. Steady shocks in a contraction are solutions to

$$u_0 h_0 b_0 = u_1 h_1 b_1 = u_2 h_2 b_1 = u_c h_c b_c \quad (15a)$$

$$\frac{1}{2}u_0^2 + gh_0 = \frac{1}{2}u_1^2 + gh_1 \quad (15b)$$

$$\frac{1}{2}u_2^2 + gh_2 = \frac{1}{2}u_c^2 + gh_c \quad (15c)$$

$$u_1^2 = \frac{gh_2}{2} \left(1 + \frac{h_2}{h_1}\right) \quad (15d)$$

$$u_c^2 = gh_c. \quad (15e)$$

These seven equations are mass and momentum balance between four locations plus the critical condition. The four locations are the far upstream,  $h_0, u_0, b_0$ , the upstream limit of the shock  $u_1, h_1, b_1$ , the downstream limit  $h_2, u_2, b_1$ , and the nozzle  $u_c, h_c, b_c$ . If we nondimensionalize as follows,  $H_1 = h_1/h_0$ ,  $H_2 = h_2/h_0$ ,  $B_c = b_c/b_0$ , then we can reduce (15) to

$$\frac{1}{4}H_2^2 - \left(\frac{1}{2}F_0^2 + 1\right)H_1 + \frac{1}{4}H_1H_2 + H_1^2 = 0 \quad (16a)$$

$$H_2^2 - \frac{3}{2}\left(\frac{F_0}{B_c}\right)^{2/3}H_2 + \frac{1}{4}H_1H_2 + \frac{1}{4}H_1^2 = 0. \quad (16b)$$

We will use (16) to find where in the  $F_0 B$ -plane we have steady shocks. A simple way to do this is to consider what the boundaries of this region should be. If we have a shock we know from the energy condition that  $H_1 \leq H_2$  [3]. Now if we look at where this upper bound on  $H_1$  is satisfied with equality  $H_1 = H_2$ , we can then reduce (16) to

$$\frac{1}{2}F_0^2 + 1 - \frac{3}{2}\left(\frac{F_0}{B_c}\right)^{2/3} = 0, \quad (17)$$

which is the boundary (12) of smooth solutions we already determined. This boundary came from considering an upper bound on  $H_1$ . The other boundary should then come from a lower bound. Since we are working here with supercritical flow in a contracting region, we expect  $H_1$  to grow the farther we move into the contraction. Thus the other boundary should be when the shock is at the mouth of the contraction, or when  $H_1 = 1$ . Substituting this into equations (16a) and (16b) yields

$$5 + 16F_0^2 + 6\left(\frac{F_0}{B_c}\right)^{2/3} - 3\sqrt{1 + 8F_0^2} - 6\left(\frac{F_0}{B_c}\right)^{2/3}\sqrt{1 + 8F_0^2} = 0. \quad (18)$$

This is the limiting curve we found for moving shocks when the speed goes to zero. Thus we have steady shocks in the contraction only in the wedge of Figure 7 where we had both smooth solutions and upstream moving shocks.

Next we examine the stability of steady shocks. Consider a system with a steady shock in the contraction region, with  $u_1$  and  $h_1$  the upstream limit of the velocity and height at

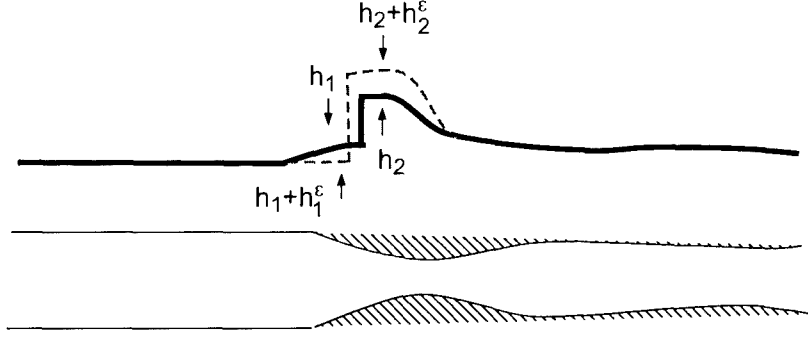


Figure 8: Sketch of the unperturbed solution (solid curve) juxtaposed over the perturbed shock (dashed curve).

the shock and  $u_2, h_2$  the downstream limit. Now we will assume a small perturbation which generates a shock moving at a small speed  $s$ , see Figure 3.4.

Let us present equations which govern the perturbed flow. The perturbations are denoted with a superscript  $\epsilon$ . The perturbed flow balances mass and momentum over the shock

$$(u_1 + u_1^\epsilon + s)(h_1 + h_1^\epsilon) = (u_2 + u_2^\epsilon + s)(h_2 + h_2^\epsilon) \quad (19)$$

$$(u_1 + u_1^\epsilon + s)^2(h_1 + h_1^\epsilon) + \frac{g}{2}(h_1 + h_1^\epsilon)^2 = (u_2 + u_2^\epsilon + s)^2(h_2 + h_2^\epsilon) + \frac{g}{2}(h_2 + h_2^\epsilon)^2. \quad (20)$$

Mass will be conserved upstream of the jump

$$(u_1 + u_1^\epsilon)(b + b^\epsilon)(h_1 + h_1^\epsilon) = Q. \quad (21)$$

We will assume that the perturbation does not affect the far field momentum upstream  $E_1$  or downstream  $E_2$ , so the Bernoulli constants are unchanged

$$\frac{1}{2}(u_1 + u_1^\epsilon)^2 + g(h_1 + h_1^\epsilon) = E_1 = \frac{1}{2}u_1^2 + gh_1 \quad (22)$$

$$\frac{1}{2}(u_2 + u_2^\epsilon)^2 + g(h_2 + h_2^\epsilon) = E_2 = \frac{1}{2}u_2^2 + gh_2. \quad (23)$$

Now we assume that we have a small perturbation and small resulting shock speed. Linearizing all these equations gives a linear system of six unknowns and five equations

$$u_1^\epsilon h_1 b + u_1 h_1 b^\epsilon + u_1 b h_1^\epsilon = 0 \quad (24a)$$

$$u_1^\epsilon h_1 + s h_1 + u_1 h_1^\epsilon - u_2^\epsilon h_2 - s h_2 - u_2 h_2^\epsilon = 0 \quad (24b)$$

$$2h_1 u_1(u_1^\epsilon + s) + h_1^\epsilon u_1^2 + g h_1 h_1^\epsilon - 2h_2 u_2(u_2^\epsilon + s) - h_2^\epsilon u_2^2 - g h_2 h_2^\epsilon = 0 \quad (24c)$$

$$u_1 u_1^\epsilon + g h_1^\epsilon = 0 \quad (24d)$$

$$u_2 u_2^\epsilon + g h_2^\epsilon = 0. \quad (24e)$$

The goal is to reduce this to a single equation for the perturbed shock speed  $s$  in terms of the change in channel width  $b^\epsilon$ . If  $b^\epsilon$  and  $s$  have opposite signs and we are in a contraction, then the solution is stable, because the shock speed will force the shock back to its previous

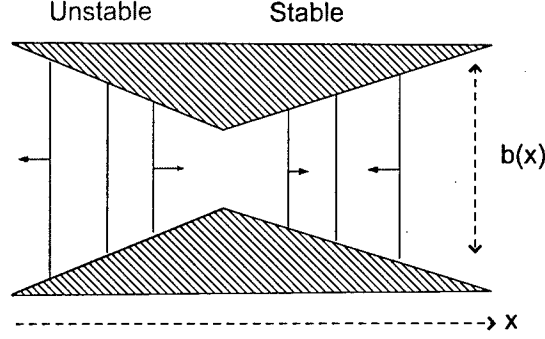


Figure 9: A sketch of the contraction region as viewed from above. The solid vertical lines denote shocks. In a contracting region steady shocks are unstable, while in a dilation they are stable.

position. If instead they have the same sign, then it is unstable, because the shock will propagate away from its previous location, as shown in Figure 9.

After some algebra we obtain the relationship

$$S = \frac{F_1(1 - \frac{u_1}{u_2})}{(1 - \frac{h_2}{h_1})} B^\epsilon. \quad (25)$$

Here  $S = s/\sqrt{gh_1}$  and  $B^\epsilon = b^\epsilon/b_0$ . We know that across a physical shock,  $h_2 > h_1$  and also that  $u_2 < u_1$ , so this gives that  $\text{sign}(S) = \text{sign}(B^\epsilon)$ . Details of the above calculation are found in an appendix to this work [1].

## 4 Results

Experiments were conducted over a variety of flow speeds and channel geometries. In each experiment, the contraction width  $B_c$  was set and then the flow rate  $Q$  was varied. The inflow height was kept fixed for all experiments at  $h_0 = 1.3\text{cm}$ . The upstream channel width was also a constant  $b_0 = 20\text{cm}$ . For each flow rate we recorded the category of the flow, either smooth flow, moving shock, steady shock, or oblique shock. These flow state are depicted in Figure 10. For moving shocks the speed and height ratios across the shock were measured. There is an experimental difficulty, in that we cannot measure the speed of fast moving shocks. When measuring a flow, there is a time delay between when we initiate the flow and when it reaches a steady state. In this experiment the time delay is on the order of five seconds. Thus for flows with shock speeds larger than 15 cm/sec, the shock will move to the end of our channel before we can properly measure the speed. The data for the moving shocks where we could measure both the speed and the height are found in Table 1.

In addition to measuring the speed of moving shocks, we also took measurements when we had oblique shocks in the flow. Oblique shocks are a stationary phenomena in our flow,



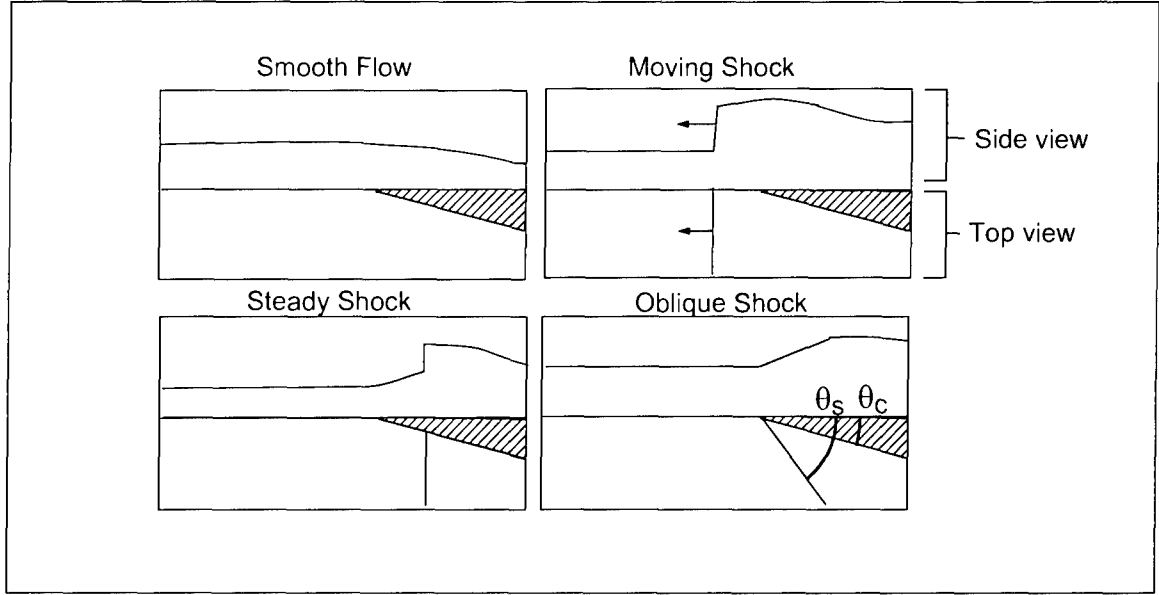


Figure 10: Shown are sketches of the four types of flow behavior. Each sketch shows a profile of the flow and a planar view.

$B_c = b_c/b_0$	$F_0 = u_0/\sqrt{gh_0}$	$H_1 = h_1/h_0$	$S = s/\sqrt{gh_0}$
0.6	3.19	3.54	0.15
0.6	3.55	3.77	0.08
0.7	2.31	2.54	0.11
0.7	2.40	2.85	0.19
0.7	2.49	2.69	0.05
0.7	2.80	3.08	0.08
0.7	2.98	3.23	0.02
0.8	2.10	2.31	0.08
0.81	2.20	2.62	0.09
0.875	2.07	2.23	0.06

Table 1: The experimental data for moving shocks are presented here.  $B_c$  is the nondimensional contraction ratio;  $F_0$  the upstream Froude number;  $H_1$  the nondimensional height ratio across the shock; and  $S$  the nondimensional shock speed.

so we do not have the difficulty of measuring speed as in the moving case. There is a new difficulty. When oblique shocks are very weak, surface tension effects will become important, and rather than a shock, we see capillary waves in our contraction region. A picture of this phenomena is shown in Figure 11.



Figure 11: Weak shocks can be distorted by capillary waves.

Since we only want to measure oblique shocks, we need a criterion to determine when we have an oblique shock and when we have capillary waves. The criteria used here is that when there is a measurable height difference between the fluid upstream and downstream of the front, we call it an oblique shock. When the mean fluid height is the same on both side of the front we call it a capillary wave. The data from the oblique shocks we measured are presented in Table 2.

$H_1 = h_1/h_0$	$F_0 = u_0/\sqrt{gh_0}$	$\theta_c$	$\theta_s$
1.9	2.79	9.5	26.7
1.5	2.94	3.8	26.7
1.7	3.13	9.5	27.1
1.5	3.32	3.8	21.6
1.5	3.37	5.7	22.1
1.9	3.47	7.6	25.4
1.7	3.56	9.5	20.1
1.8	3.65	7.6	25.2

Table 2: The experimentally measured flow variables for the oblique shocks are presented here.  $H_1$  is the nondimensionalized height ratio across the shock,  $F_0$  is the upstream Froude number,  $\theta_c$  is the angle of the contraction,  $\theta_s$  is the angle of the shock, see also Figure 10.

We measured the flow rate and geometry for every experiment. The different flow types are plotted in the  $B_c F_0$ -plane in Figure 12.

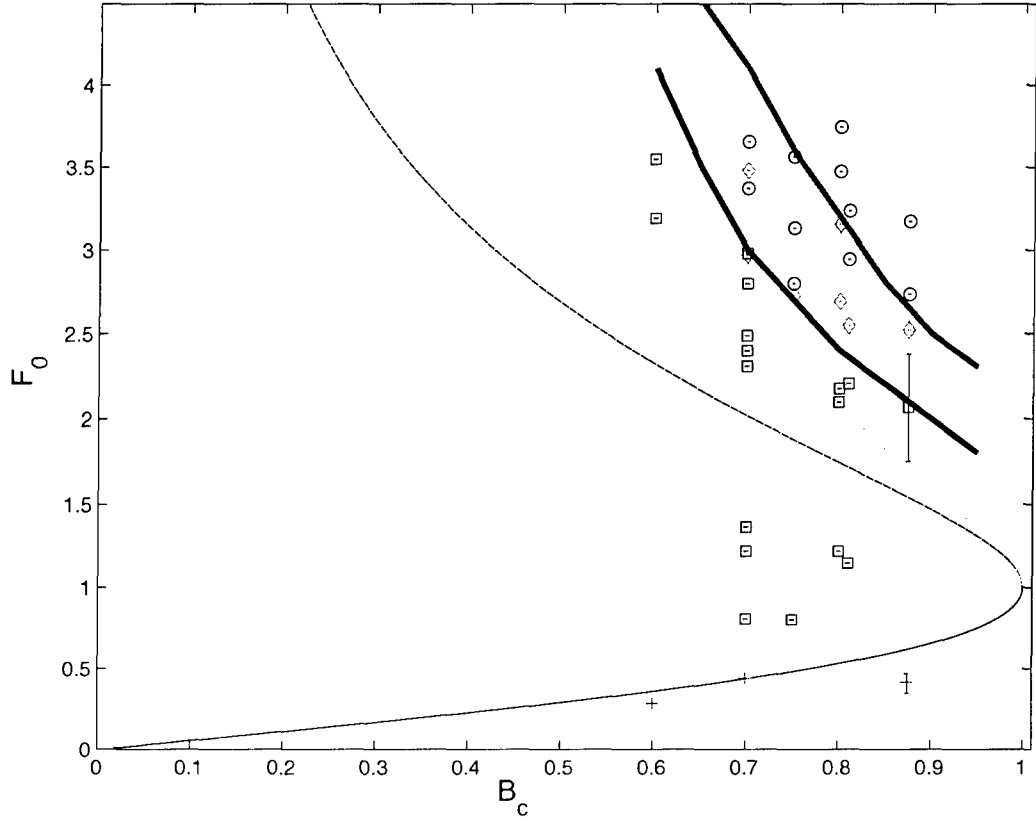


Figure 12: Experiments plotted in the predicted inviscid state space. Here circles are oblique shocks, diamonds are steady shocks, squares are moving shocks, pluses are smooth flows. Representative error bars are plotted on a smooth flow and a moving flow at  $B_c = 0.875$ . The thick lines are the numerically computed boundaries for the regions where an upstream moving shock can be stopped via friction.

## 5 Discussion

In this section we will compare the experimental results to mathematical theory. The models used in this report assume no effects of surface tension or viscosity. The importance of these effects are commonly measured using nondimensional numbers, Weber  $We$  for surface tension and Reynolds  $Re$  for viscosity. Table 3 shows the range for these parameters in the experiments considered.

Parameter	Min	Max
Reynolds ( $Re = UL/\nu$ )	1,300	20,100
Weber ( $We = \rho U^2 L/\sigma$ )	1.85	433
Froude ( $F_0 = U_0/\sqrt{gh_0}$ )	0.28	4.34
Contraction ( $B_c = b_c/b_0$ )	0.6	0.875

Table 3: The nondimensional parameters are estimated for the main body of our flow. Here  $We \approx 14F_0^2$  and  $Re \approx 3300F_0$ . If we look at some local phenomena, for instance near weak oblique shocks, we can have smaller Weber and Reynolds numbers.

If we look at Equation (14) we see that for a given upstream Froude number  $F_0$  and nondimensional shock speed  $S$ , we can predict the height ratio across the shock. We can then compare this prediction to the measured height ratios across the jump. This comparison is shown in Figure 13.

### 5.1 Oblique Shocks

All the analysis at the beginning of this report considered only 1-D phenomena. Oblique shocks are a two-dimensional (2-D) phenomena, so our model does not take them into account. Following [2] and [8], we can derive a system of equations for the oblique shock angle  $\theta_s$  and shock height  $h_1$ . These equations will allow us to predict  $\theta_s$  and  $h_1$  given the upstream conditions  $h_0, F_0$  and the angle of the contraction  $\theta_c$ , as follows

$$\frac{h_1}{h_0} = \frac{\tan \theta_s}{\tan(\theta_s - \theta_c)} \quad (26a)$$

$$\sin \theta_s = \sqrt{\frac{1}{2F_0^2} \frac{h_1}{h_0} \left(1 + \frac{h_1}{h_0}\right)}. \quad (26b)$$

Using (26) we can plot our predicted oblique shock angles against the experimental ones. This plot is shown in Figure 14.

In our experiments we saw oblique shocks that exit our channel before interacting with another shock, and oblique shocks that intersect in the channel, see Figure 15. A similar calculation was also done which can be used to predict the angles of intersecting oblique shocks.

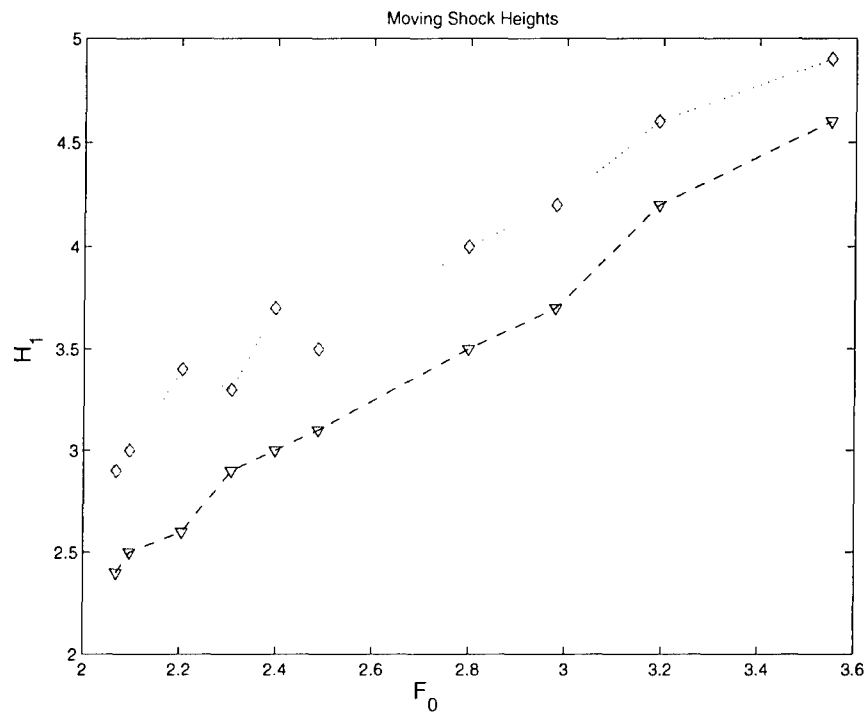


Figure 13: The experimental height ratios are plotted against the inviscid predictions. The dotted curve (diamonds) corresponds to the experimental measurements; the dashed curve (triangles) to the inviscid predictions. The experimental measurements are systematically lower than the predicted curve due to the effect of friction.

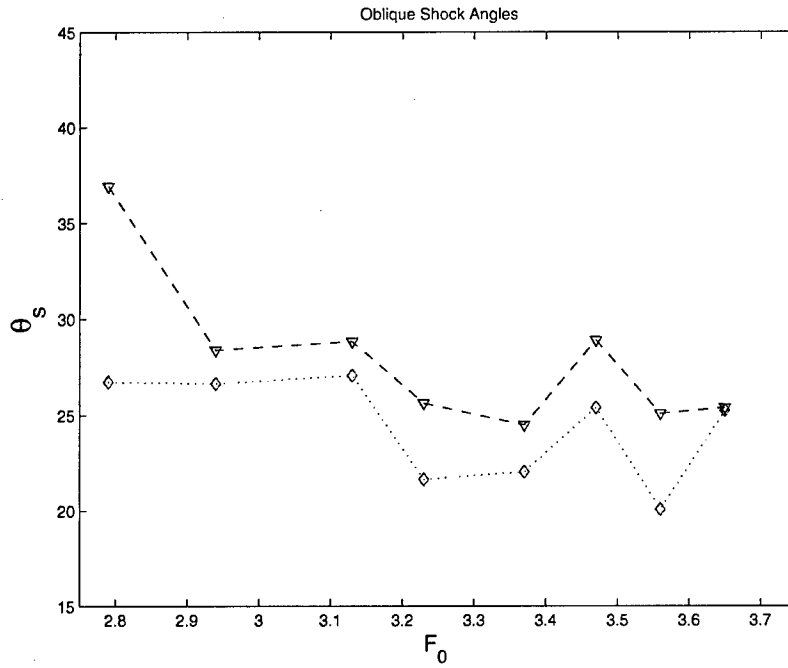


Figure 14: The observed oblique shock angles (diamonds, dotted curve) are plotted against the calculated angles (triangles, dashed curve).

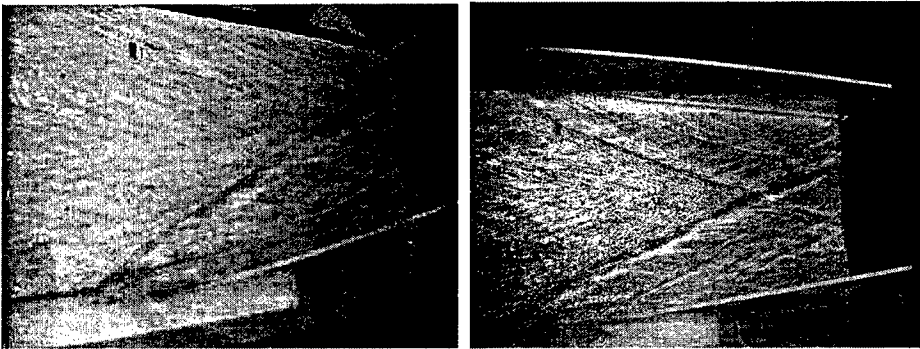


Figure 15: The left image is a single oblique shock in an asymmetric contraction,  $F_0 = 3.56$ ,  $B_c = 0.75$ . The right image shows the intersection of two oblique shocks in a symmetric contraction,  $F_0 = 3.65$ ,  $B_c = 0.7$ .

## 5.2 Turbulent Drag

If we examine Figure 12 we see that there are steady shocks outside of the region predicted by the inviscid theory. To explain this, we must reexamine the assumptions of the original model. The real fluid does have some viscosity, so we should take this into account. In the hydraulic equations, viscous effects are usually added with a drag term. The most physical drag term comes from a quadratic drag law [3]. Adding such a term changes the hydraulic equations (6) to the system

$$uu_x + gh_x = -C_d u^2/h \quad (27a)$$

$$(buh)_x = 0. \quad (27b)$$

This system of ordinary differential equations (ODE's) can now be solved using standard numerical techniques. When we do not have smooth solutions we can find steady shocks by using the inflow conditions at the sluice gate and critical condition at the nozzle as boundary conditions to march the solutions together until they match with a shock.

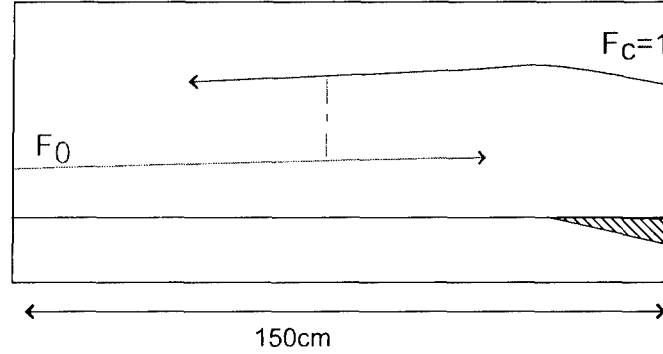


Figure 16: A cartoon of the numerical method for finding steady shocks. We use an ODE solver to find the smooth flow with a prescribed upstream Froude number  $F_0$  and the smooth flow that meets the critical condition  $F_c = 1$ . These two smooth flows are then matched using the shock condition.

Depending on the Froude number  $F_0$  and geometry  $B_c$ , we may or may not be able to have a steady shock of this type. If we solve this system throughout our state space we get numerically computed boundaries for when we can have steady shocks with friction. These boundaries are plotted in Figure 12. For our computations we have used  $C_d = 0.004$  [4].

## 5.3 Multiple States

In our inviscid calculations, we predicted a region in the  $B_c F_0$ -plane where we can have three different steady states: steady shocks, moving shocks, and supercritical smooth flows. We have shown that the steady shocks in the contraction region are unstable, so we don't expect to see these. We also have observed that friction can stop slowly moving shocks, and that supercritical smooth flows correspond to oblique shocks. Thus this region of multiple states really corresponds to flow speeds where we can have upstream steady shocks, stopped

via friction, and oblique shocks in the contraction region. These phenomena were observed in the lab. Figure 12 shows both oblique shocks and steady shocks in the same region of state space. We also observed that large perturbations of these flows can cause the flow to change from one steady state to another. If we have a steady upstream shock, we can physically push most of the water that is behind the shock out of the channel, and see a steady oblique shock. If we have an oblique shock, we can block the flow for a small time period, and the resulting flow will evolve into a steady upstream shock. Figure 17 shows snapshots of the transition from oblique shocks to an upstream steady shock.

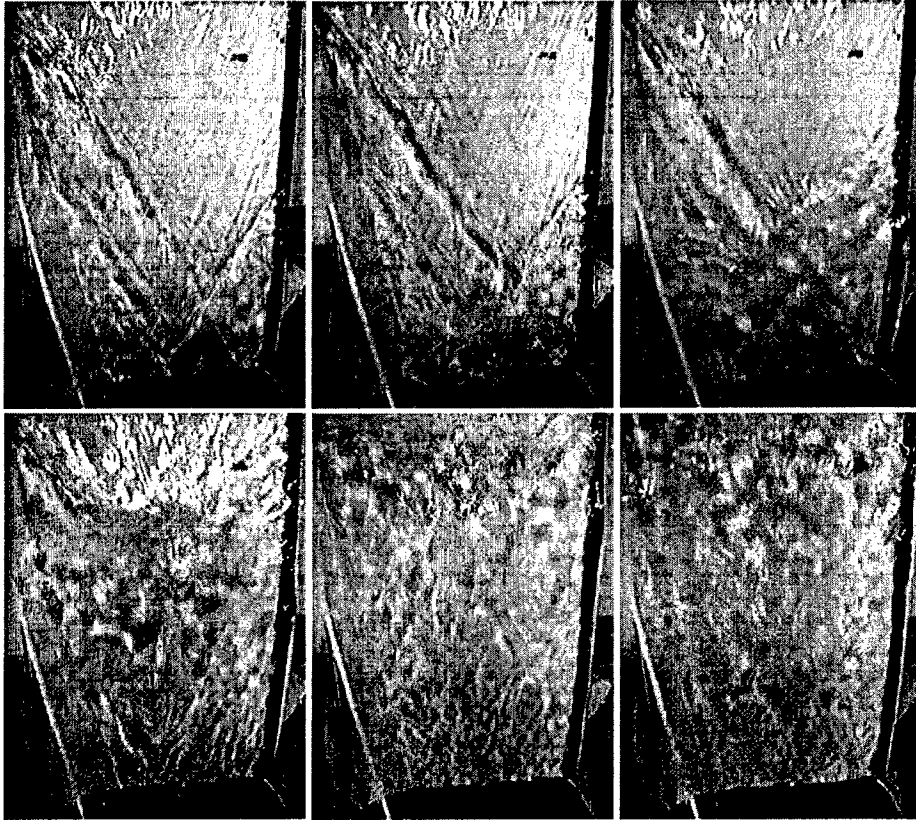


Figure 17: Shown are snapshots of the flow transition from oblique shocks to a steady upstream shock. The time interval between each frame is 1 second. Here we have the Froude number  $F_0 = 2.8$  and the contraction ratio  $B_c = 0.7$ . A ruler is used to restrict the flow for a small time period to induce this state change.

## 6 Conclusion and future work

We presented a mathematical and experimental investigation into shallow water flow through a contraction. We began by making predictions using a simple 1-D inviscid theory. We saw that for slow speeds this 1-D analysis performs well. For higher speeds boundary drag becomes important and we saw a departure from the 1-D inviscid predictions. The addition of drag forces improved the performance of the 1-D theory. To predict oblique shocks, a



fundamentally 2-D feature, we had to use the 2-D shallow water equations.

We also set out to investigate the existence and stability of steady shocks. We presented a perturbation method for finding when steady shocks in the contraction are stable. Experimentally we observed that shocks which are stopped via friction are stable. If we look at how the shock speed depends on flow rate, see Figure 7, we see that there is a heuristic stability result which agrees with our predictions and observations. When the flow rate is increased, shocks move slower, and when the flow rate is decreased shocks move faster. If we apply this knowledge to a steady shock, we see that in accelerating flows, steady shocks will be unstable. If we displace a steady shock upstream in an accelerating flow it will have a faster speed, and will move upstream. Also downstream displacements will generate slower speeds, and the shocks will move downstream. A similar argument shows that in decelerating flows steady shocks are stable. This argument is incomplete however, in that it does not deal with flows where the velocity is not monotone. This is precisely the case of a steady shock in a contraction, so here we used the perturbation method of [4].

There are a variety of avenues for future research illuminated by the experiments and analysis presented here. First, we have observed that supercritical flows that are 1-D smooth have additional 2-D shock structure which is not accounted for with 1-D theory. In the appendices of this report [1] we have predictions for some of these 2-D structures. We also observed a structure like a Mach stem near the intersection of two oblique shocks. This structure has not been accounted for in the work presented in this report. Another avenue for future research is to use this work in conjunction with [2] as a base for investigating shallow flow of composite media, i.e. water carrying sediment. Also this report does not include analysis of the time dependent problem. Here we could investigate the relationship between initial data and steady state in the region of multiple steady states. Future work is currently being done to compare 2-D simulations with experimental results. A few experiments have been done on Mach stems and adding polystyrene beads to simulate granular media. For updates on the current state of the work, see <http://www.math.wisc.edu/~akers/contraction>.

## 7 Acknowledgements

This work was funded via a summer fellowship from the Geophysical Fluid Dynamics Program at the Woods Hole Oceanographic Institution. Thanks are due to Larry Pratt and Jack Whitehead for valuable discussions. Keith Bradley was instrumental in the construction and design of the tank where the experiment was conducted. Also a special thank you to Onno Bokhove for the inspiration and guidance of this project.

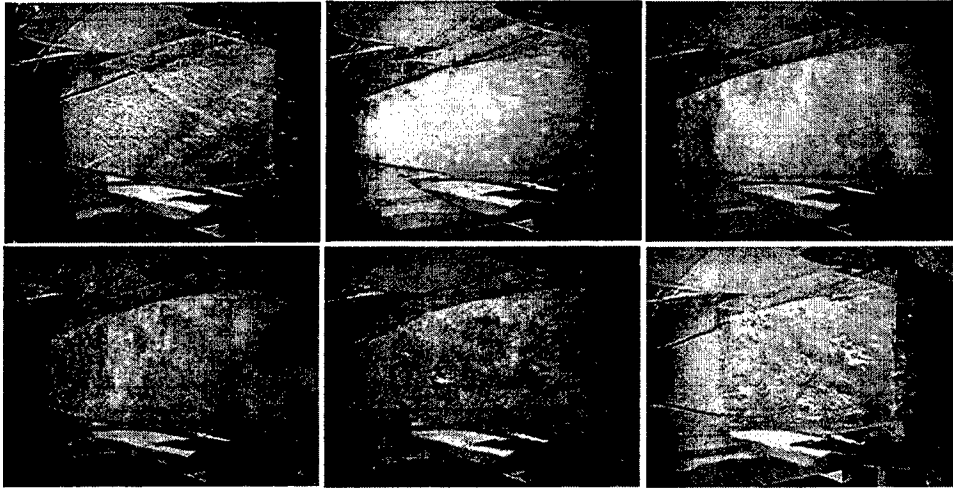


Figure 18: Here are snapshots of an experiment where polystyrene beads are impulsively dumped into a flow that exhibits three states: upstream shocks, Mach stems, and oblique shocks. The flow begins in the state of oblique shocks, with  $F_0 = 3.08$ ,  $B_c = 0.7$ . Beads are dumped into the flow, and the resulting flow is an upstream shock.

## References

- [1] B. AKERS, *Oblique and steady shock calculations*, 2005. Appendix, available upon request.
- [2] M. AL-TARAZI, O. BOKHOVE, J. KUIPERS, M. VAN SINT ANNALAND, AND A. W. VREMAN, *Reservoir formation in shallow granular flows through a contraction*, Physical Review Letters, (Under Revision).
- [3] P. BAINES, *Topographical effects in stratified flows*, Cambridge University Press, 1995.
- [4] P. BAINES AND J. WHITEHEAD, *On multiple states in single layer flows*, Physics of fluids, (2003).
- [5] J. KELLER, *Personal communication*, 2005.
- [6] K. MULLER, *Tsunami-like river tides are surfing's new frontier*, National Geographic, (2005).
- [7] L. PRATT, C. HILLS, AND J. PARSONS, *Review of hydraulics for non-rotating 1-d single layer flows*, tech. rep., Woods Hole Oceanographic Institution: Geophysical Fluid Dynamics Program, 1997.
- [8] A. SHAPIRO, *The Dynamics and Thermodynamics of Compressible Fluid Flow*, The Ronald Press Company, 1954.
- [9] G. B. WHITHAM, *Linear and Nonlinear Waves*, Wiley-Interscience, 1999.

# Bounds on Multiscale Mixing Efficiencies

Tiffany A. Shaw

July 18, 2006

## 1 Introduction

We are motivated by the following problem: given the heat sources and sinks on the Earth and a stirring field with certain statistical properties what are the maximum and minimum possible degrees of temperature variance that must be present? The flow in the Earth's atmosphere is an example of a stirring field which acts to redistribute heat. Here we are interested in the optimal solution to this redistribution problem. We expect any stirring would suppress fluctuations in the temperature field and lead to a more uniform distribution, but what kind of stirring minimizes the variance? Can we, given some bulk statistical properties of the stirring field, derive bounds on the variance? What are the characteristics of a good stirring field and how do they depend on the source distribution? Can we define and estimate the eddy diffusivity and mixing efficiency of a stirrer on different length scales? Here we work toward answering these questions by computing rigorous bounds on multiscale mixing efficiencies.

Bounds on mixing have important implications in both physics and engineering. Thiffeault, Doering, and Gibbon [5], hereafter TDG, have shown how techniques used to bound bulk dissipation quantities in the Navier-Stokes equation [2] can be applied to the advection-diffusion of a passive scalar maintained by a steady source. They derived rigorous bounds on the scalar variance and defined an *equivalent diffusivity*, the diffusivity required to produce the same amount of mixing in the absence of stirring. Plasting and Young [4], hereafter PY, enhanced that analysis by including the variance dissipation as a constraint.

Here we construct bounds on the multiscale mixing efficiency of a stirring field for a passive scalar maintained by a time independent but spatially inhomogeneous source. We focus on the mixing efficiency of a stirring field on different scales by considering the fluctuations of the variance, gradient variance, and inverse gradient variance. Comparing the three measures (the variance, gradient variance, and inverse gradient variance) gives a range of information about the stirring properties of a flow. It has been recognized that  $L^p$  norms of the passive scalar fail to quantify the *stirring efficiency* of a mixing process because they are insensitive to small scale structures [1]. We gauge the effectiveness of a stirring field based on its ability to suppress variance relative to the variance in the absence of stirring. On all scales, a smaller variance implies the velocity field is a better stirrer. Thus, a velocity field that gives a larger mixing efficiency than another will be considered more efficient with respect to a particular measure.

Our approach for bounding the multiscale mixing efficiencies follows that of TDG. The bounds are derived in section 3. In section 4 we show that the bounds for a monochromatic source on the torus can be saturated. In an effort to distinguish the three measures more convincingly, in section 5 we investigate the efficiency of a steady shearing flow for a monochromatic source

using boundary layer asymptotics. Finally, in section 6, we find bounds on the multiscale mixing efficiencies for a decaying passive scalar maintained by a spatially inhomogeneous source.

## 2 Advection-diffusion in a space of $d$ -dimensions

The advection-diffusion equation of a passive scalar with a body source  $s(\mathbf{x})$  in a  $d$ -dimensional domain ( $d = 2, 3, \dots$ ) is:

$$\frac{\partial \theta}{\partial t} + \mathbf{u} \cdot \nabla \theta = \kappa \Delta \theta + s(\mathbf{x}) \quad (2.1)$$

where  $s(\mathbf{x})$  is a source with spatial mean zero without loss of generality and  $\kappa$  is the molecular diffusivity. Since the body source has spatial mean zero the passive scalar will also have zero spatial mean. The velocity field here is a given steady or time-dependent  $L^2$  divergence-free vector field. The velocity field could be a solution of the Navier-Stokes equation or a specified stochastic process. We will focus on a particular class of stirring fields that are steady, statistically homogeneous, and isotropic with single point statistical properties characteristic of Homogeneous Isotropic Turbulence (HIT):

$$\overline{u_i(\mathbf{x}, \cdot)} = 0, \quad \overline{u_i(\mathbf{x}, \cdot) u_j(\mathbf{x}, \cdot)} = \frac{U^2}{d} \delta_{ij} \quad (2.2)$$

and

$$\overline{u_i(\mathbf{x}, \cdot) \frac{\partial u_j(\mathbf{x}, \cdot)}{\partial x_k}} = 0, \quad \overline{\frac{\partial u_i(\mathbf{x}, \cdot)}{\partial x_k} \frac{\partial u_j(\mathbf{x}, \cdot)}{\partial x_k}} = \frac{\Gamma^2}{d} \delta_{ij} \quad (2.3)$$

where where  $U^2 := \langle |\mathbf{u}|^2 \rangle$  is the kinetic energy density,  $\lambda = U/\Gamma$  is the so-called Taylor microscale for HIT, and the overbar denotes the steady average defined below. Let us define the advection-diffusion operator and its formal adjoint:

$$\mathcal{L} := \partial_t + \mathbf{u} \cdot \nabla - \kappa \Delta, \quad \mathcal{L}^\dagger := -\partial_t - \mathbf{u} \cdot \nabla - \kappa \Delta. \quad (2.4)$$

We also define the steady average (assuming it exists),

$$\overline{F}(\mathbf{x}) := \lim_{t \rightarrow \infty} \frac{1}{t} \int_0^t F(\mathbf{x}, t') dt', \quad (2.5)$$

and the space time average,

$$\langle F \rangle := \frac{1}{V} \int \overline{F}(\mathbf{x}) d^d \mathbf{x}. \quad (2.6)$$

From here on our domain will be a periodic box of size  $L$ , i.e.  $x \in \mathbb{T}^d$ , the  $d$ -dimensional torus. The Fourier decomposition of the spatially dependent variables are written conventionally as

$$F(\mathbf{x}, t) = \sum_{\mathbf{k}} e^{i\mathbf{k} \cdot \mathbf{x}} \hat{F}(\mathbf{k}) \quad \text{where} \quad \hat{F}(\mathbf{k}) = \frac{1}{L^d} \int_{\mathbb{T}^d} e^{-i\mathbf{k} \cdot \mathbf{x}} F(\mathbf{x}, t) d^d \mathbf{x} \quad (2.7)$$

and  $\mathbf{k} = (2\pi/L)\mathbf{n}$  for  $\mathbf{n} = (n_1, \dots, n_d)$ . The  $L^2$  norms of derivatives of the passive scalar will be denoted, for example,

$$\langle |\nabla^p \theta|^2 \rangle = \sum_{\mathbf{k}} k^{2p} |\hat{\theta}(\mathbf{k})|^2. \quad (2.8)$$

The conventional non-dimensional number measuring the relative importance of advection to diffusion is the Péclet number

$$Pe := \frac{UL}{\kappa}. \quad (2.9)$$

A standard measure of the well-mixedness of a scalar field is its variance (presuming spatial mean zero) [1]. Weighting the variances at different length scales introduces a family of variances that are sensitive to mixing on different scales. The variances  $\langle |\nabla^p \theta|^2 \rangle$  for  $p = 1, 0, -1$  measure mixing on small, intermediate, and large scales respectively. To gauge the effect of stirring, the variances are compared with variances in the absence of stirring  $\langle |\nabla^p \theta_0|^2 \rangle = \kappa^{-2} \langle |\nabla^p \Delta^{-1} s|^2 \rangle$  for  $p = 1, 0, -1$ .

We define a non-dimensional *mixing efficiency* for each scale  $p$

$$M_p := \frac{\langle |\nabla^p \theta_0|^2 \rangle}{\langle |\nabla^p \theta|^2 \rangle} \quad \text{for } p = 1, 0, -1 \quad (2.10)$$

which increases as stirring increases. The mixing efficiency has the advantage of depending only on the structure of the stirring and source and not on their scales.

The *equivalent diffusivity* is the equivalent amount of diffusivity required to achieve the same degree of mixing in the absence of stirring (i.e. a corresponding diffusivity for the diffusion equation) and is defined as

$$\kappa_{\text{eq},p} := \kappa \frac{\langle |\nabla^p \theta_0|^2 \rangle^{1/2}}{\langle |\nabla^p \theta|^2 \rangle^{1/2}}. \quad (2.11)$$

Equivalent diffusivity should not be confused with effective diffusivity defined in homogenization theory. The effective diffusivity is defined in terms of large-scale transport, i.e. in the presence of large scale gradients of the concentration (G. Papanicolaou lectures) [6]. The equivalent diffusivity is specific to the source and stirring. Lower bounds on the variances provide upper bounds on the mixing efficiencies. These bounds depend on details of the source and stirring as shown in the next section.

### 3 Bounds on the multiscale mixing efficiencies

Following the method developed by TDG we derive bounds on the multiscale mixing efficiencies.

#### 3.1 Bounds on variance

Multiplying (1) by a smooth, time independent, spatially periodic projector function  $\varphi(\mathbf{x})$ , taking the space-time average and integrating by parts we obtain

$$\langle \theta(\mathbf{u} \cdot \nabla + \kappa \Delta) \varphi \rangle = -\langle \varphi s \rangle. \quad (3.1)$$

A lower bound on the variance is achieved via the variational principle

$$\langle \theta^2 \rangle \geq \max_{\varphi} \min_{\tilde{\theta}} \{ \langle \tilde{\theta}^2 \rangle \mid \langle \tilde{\theta}(\mathbf{u} \cdot \nabla \varphi + \kappa \Delta \varphi) \rangle = -\langle \varphi s \rangle \}. \quad (3.2)$$

We note that TDG derived bounds on the mixing efficiency without optimizing over  $\varphi$ . The optimization over  $\tilde{\theta}$  is equivalent to applying the Cauchy-Schwarz inequality

$$\langle \theta^2 \rangle \geq \max_{\varphi} \frac{\langle \varphi s \rangle^2}{\langle (\mathbf{u} \cdot \nabla \varphi + \kappa \Delta \varphi)^2 \rangle} = \frac{\langle \varphi s \rangle^2}{\langle \varphi \mathcal{L} \mathcal{L}^\dagger \varphi \rangle}. \quad (3.3)$$

Maximizing over  $\varphi$  is equivalent to minimizing the denominator over  $\varphi$ . We constrain  $\varphi$  to have a unit projection onto the source. The corresponding variational problem is:

$$\frac{1}{\langle \theta^2 \rangle} \leq \min_{\varphi} \{ \langle \varphi \overline{\mathcal{L}\mathcal{L}^\dagger} \varphi \rangle \mid \langle \varphi s \rangle = 1 \}. \quad (3.4)$$

Thus we must minimize the functional  $\mathcal{F} := \left\langle \frac{1}{2} \varphi \overline{\mathcal{L}\mathcal{L}^\dagger} \varphi - \mu(\varphi s - 1) \right\rangle$ , whose Euler-Lagrange equation is

$$\frac{\delta \mathcal{F}}{\delta \varphi} = \overline{\mathcal{L}\mathcal{L}^\dagger} \varphi - \mu s = 0 \quad (3.5)$$

where  $\mu$  is a Lagrange multiplier to enforce the constraint. The minimizer is (after some algebra)

$$\varphi = \frac{\mathcal{M}_0 s}{\langle s \mathcal{M}_0 s \rangle} \quad (3.6)$$

where  $\mathcal{M}_0 := (\overline{\mathcal{L}\mathcal{L}^\dagger})^{-1}$  and

$$\langle s \mathcal{M}_0 s \rangle = \langle s \{ \kappa^2 \Delta^2 - \nabla \cdot (\overline{\mathbf{u}\mathbf{u}}) + \kappa(2\nabla \overline{\mathbf{u}} : \nabla \nabla + \Delta \overline{\mathbf{u}} \cdot \nabla) \}^{-1} s \rangle. \quad (3.7)$$

Thus we obtain the lower bound

$$\langle \theta^2 \rangle \geq \langle s \mathcal{M}_0 s \rangle \quad (3.8)$$

which depends only on the mean and quadratic correlations of the stirring field. For flows satisfying HIT this simplifies to the quadratic form

$$\langle s \mathcal{M}_0 s \rangle = \langle s \{ \kappa^2 \Delta^2 - (U^2/d) \Delta \}^{-1} s \rangle. \quad (3.9)$$

This lower bound on the variance depends on the source function and on the stirring. In Fourier space it is expressed as

$$\langle \theta^2 \rangle \geq \sum_{\mathbf{k}} \frac{|\hat{s}(\mathbf{k})|^2}{\kappa k^4 + U^2 k^2/d}. \quad (3.10)$$

An upper bound on the variance may be obtained from simple application of the Cauchy-Schwarz and Poincaré inequalities to the bulk variance dissipation constraint:

$$\langle \theta^2 \rangle \leq \frac{L^2}{4\pi^2} \frac{\langle |\nabla^{-1} s|^2 \rangle}{\kappa^2}. \quad (3.11)$$

The variance in the absence of stirring is

$$\langle \theta_0^2 \rangle = \frac{1}{\kappa^2} \langle (\Delta^{-1} s)^2 \rangle \quad (3.12)$$

and thus we obtain bounds on the mixing efficiency from bounds on the variance

$$\frac{4\pi^2}{L^2} \frac{\langle |\Delta^{-1} s|^2 \rangle}{\langle |\nabla^{-1} s|^2 \rangle} \leq M_0^2 \leq \left( \sum_{\mathbf{k}} \frac{|\hat{s}(\mathbf{k})|^2}{k^4} \right) \left( \sum_{\mathbf{k}} \frac{|\hat{s}(\mathbf{k})|^2}{k^4 + Pe^2 k^2/d} \right)^{-1}. \quad (3.13)$$

One might expect the variance efficiency to have a lower bound of 1, implying that stirring *always* decreases the variance. We can search for a sharper lower bound by actually optimizing the variance subject to the variance dissipation constraint

$$\langle \theta^2 \rangle \geq \min_{\hat{\theta}} \{ \langle \tilde{\theta}^2 \rangle \mid \kappa \langle |\nabla \tilde{\theta}|^2 \rangle = \langle s \tilde{\theta} \rangle \}. \quad (3.14)$$

That is, we can seek the minimum possible variance subject only to the entropy production balance. The solution of the optimization problem in Fourier space is

$$\hat{\theta}(\mathbf{k}) = \frac{1}{2} \frac{\hat{s}(\mathbf{k})}{\kappa k^2 + \lambda} \quad (3.15)$$

where  $\lambda = -1/2\mu$  and  $\mu$  is the Lagrange multiplier. Enforcing the constraint,

$$\kappa \sum_{\mathbf{k}} k^2 |\hat{\theta}(\mathbf{k})|^2 = \sum_{\mathbf{k}} \hat{\theta}(\mathbf{k}) \hat{s}^*(\mathbf{k}) \Rightarrow \kappa \sum_{\mathbf{k}} \frac{k^2 |\hat{s}(\mathbf{k})|^2}{(\kappa k^2 + \lambda)^2} = 2 \sum_{\mathbf{k}} \frac{|\hat{s}(\mathbf{k})|^2}{\kappa k^2 + \lambda}. \quad (3.16)$$

where  $*$  denotes the complex conjugate.

In the case of a monochromatic source this simplifies to

$$\kappa \frac{k^2}{(\kappa k^2 + \lambda)^2} = 2 \frac{1}{\kappa k^2 + \lambda} \Rightarrow \kappa k^2 = 2(\kappa k^2 + \lambda) \Rightarrow \lambda = -\frac{\kappa k^2}{2} \quad (3.17)$$

and hence

$$\hat{\theta}(\mathbf{k}) = \frac{\hat{s}}{\kappa k^2} = \hat{\theta}_0(\mathbf{k}) \quad (3.18)$$

which implies  $M_0 \geq 1$ .

In the case of a dichromatic source ( $k_1$  with amplitude  $s_1$ ,  $k_2$  with amplitude  $s_2$ ), the constraint requires one to solve a cubic equation for  $\xi = \lambda/k_1$

$$(1 + \alpha)\xi^3 + \frac{1}{2}(1 + \alpha\beta + 4\beta + 4\alpha)\xi^2 + (\beta + \alpha\beta + \beta^2 + \alpha)\xi + \frac{1}{2}(\beta^2 + \alpha\beta) = 0 \quad (3.19)$$

where  $\alpha = c_1/c_2$ ,  $\beta = \mu_1/\mu_2$ ,  $c_1 = s_1^2$ ,  $c_2 = s_2^2$ ,  $\mu_1 = \kappa k_1^2$ , and  $\mu_2 = \kappa k_2^2$ . Then the mixing efficiency is

$$\frac{|\hat{\theta}_0(\mathbf{k})|^2}{|\hat{\theta}(\mathbf{k})|^2} = \frac{4(1 + \frac{\alpha}{\beta^2})}{\frac{1}{(1+\xi)^2} + \frac{\alpha}{(\beta+\xi)^2}}. \quad (3.20)$$

The efficiency goes to 1 in the monochromatic limit  $\alpha \rightarrow 0$  ( $\xi \rightarrow -1/2$ ) as expected. But the minimum value the efficiency bound is less than 1 for  $\forall \xi$  implying that the variance dissipation constraint is not sufficient to guarantee that there are no stirring flows that could possibly increase the scalar variance. So this analysis does not rule out the existence of *ineffective* stirring fields.

### 3.1.1 Delta function source

Here we consider a  $\delta$ -function point source (measure valued) with Fourier coefficients  $|\hat{s}(\mathbf{k})| = 1$  as  $|\mathbf{k}| \rightarrow \infty$ . We note this includes white noise sources. As we are interested in the high- $Pe$

limit we approximate the sums in (3.16) by integrals. The asymptotic form of the upper bound is

$$M_0^2 \lesssim \left( \int_{2\pi/L}^{\infty} \frac{k^{d-1} dk}{k^4} \right) \left( \int_{2\pi/L}^{\infty} \frac{k^{d-1} dk}{k^4 + \frac{U^2}{d\kappa^2} k^2} \right)^{-1}. \quad (3.21)$$

Letting  $\xi = kL : 2\pi \rightarrow \infty$  we obtain

$$M_0^2 \lesssim \left( \int_{2\pi}^{\infty} \xi^{d-5} d\xi \right) \left( \int_{2\pi}^{\infty} \frac{\xi^{d-1} d\xi}{\xi^4 + Pe^2 \xi^2/d} \right)^{-1}. \quad (3.22)$$

For  $d = 2$  the integrals become

$$\int_{2\pi}^{\infty} \xi^{-3} d\xi = \frac{1}{8\pi^2}, \quad \int_{2\pi}^{\infty} \frac{\xi d\xi}{\xi^4 + Pe^2 \xi^2/2} \sim \frac{\log Pe}{Pe^2} \quad (3.23)$$

resulting in the asymptotic bound

$$M_0 \lesssim \frac{Pe}{\sqrt{\log Pe}}. \quad (3.24)$$

In  $d=3$

$$\int_{2\pi}^{\infty} \xi^{-2} d\xi = \frac{1}{2\pi}, \quad \int_{2\pi}^{\infty} \frac{d\xi}{\xi^4 + Pe^2 \xi^2/2} \sim \frac{1}{Pe} \quad (3.25)$$

resulting in the asymptotic bound

$$M_0 \lesssim \sqrt{Pe}. \quad (3.26)$$

An efficiency scaling of  $Pe$  leads to an eddy diffusivity proportional to  $UL$  from (3.2). For  $d = 3$  there is a dramatic modification to the scaling that implies the eddy diffusivity is proportional to  $\sqrt{\kappa}$ .

### 3.2 Bounds on the gradient variance

Beginning with the first step in the TDG procedure

$$\langle \theta(\mathbf{u} \cdot \nabla + \kappa \Delta) \varphi \rangle = -\langle \varphi s \rangle \quad (3.27)$$

we integrate by parts and apply the Cauchy-Schwarz inequality to obtain

$$\langle \varphi s \rangle^2 = \langle (\mathbf{u} \varphi + \kappa \nabla \varphi) \cdot \nabla \theta \rangle^2 \leq \langle |\mathbf{u} \varphi + \kappa \nabla \varphi|^2 \rangle \langle |\nabla \theta|^2 \rangle. \quad (3.28)$$

The sharpness of this bound is discussed at the end of this section. Continuing as usual, we construct a variational principle to obtain a lower bound on the gradient variance

$$\langle |\nabla \theta|^2 \rangle \geq \max_{\varphi} \frac{\langle \varphi s \rangle^2}{\langle |\mathbf{u} \varphi + \kappa \nabla \varphi|^2 \rangle}. \quad (3.29)$$

Thus we minimize the denominator subject to the constraint of  $\varphi$  having a unit projection on the source. Under the homogeneity and isotropy assumptions of HIT the variational problem becomes one of evaluating

$$\min_{\varphi} \{ \langle \kappa |\nabla \varphi|^2 + U^2 \varphi^2 \rangle \mid \langle \varphi s \rangle = 1 \}. \quad (3.30)$$



We want to minimize the functional  $\mathcal{F} := \langle \frac{1}{2}(\kappa|\nabla\varphi|^2 + U^2\varphi^2) - \mu(s\varphi - 1) \rangle$ . The solution of the optimization problem is (after some algebra)

$$\langle |\nabla\theta|^2 \rangle \geq \langle s\mathcal{M}_1 s \rangle \quad (3.31)$$

where  $\mathcal{M}_1 = (-\kappa^2\Delta + U^2)^{-1}$ .

A sharp lower bound on the gradient variance is easily proven. Upon taking the inner product of  $\theta$  with the advection-diffusion equation we obtain the variance dissipation constraint

$$\kappa\langle |\nabla\theta|^2 \rangle = \langle s\theta \rangle. \quad (3.32)$$

Inserting  $\nabla^{-1}\nabla = 1$  on the right hand side, integrating by parts and applying the Cauchy-Schwarz inequality, we deduce

$$\kappa^2\langle |\nabla\theta|^2 \rangle \leq \langle |\nabla^{-1}s|^2 \rangle = \kappa^2\langle |\nabla\theta_0|^2 \rangle \Rightarrow M_1 \geq 1. \quad (3.33)$$

Hence stirring *always* reduces the gradient variance which was *not* proven for the variance (previous section).

Given the upper and lower bounds on the gradient variance we can bound the small scale mixing efficiency according to

$$1 \leq M_1^2 \leq \frac{1}{\kappa^2} \frac{\langle |\nabla^{-1}s|^2 \rangle}{\langle s\mathcal{M}_1 s \rangle}. \quad (3.34)$$

In Fourier space this is

$$1 \leq M_1^2 \leq \left( \sum_{\mathbf{k}} \frac{|\hat{s}(\mathbf{k})|^2}{k^2} \right) \left( \sum_{\mathbf{k}} \frac{|\hat{s}(\mathbf{k})|^2}{k^2 + \frac{U^2}{\kappa^2}} \right)^{-1}. \quad (3.35)$$

These bounds only make sense when the sums on the right hand side converge.

Note that if  $\kappa \rightarrow 0$  and if  $s(\mathbf{x}) \in L^2$  then

$$M_1^2 \rightarrow \frac{U^2}{\kappa^2} \left( \sum_{\mathbf{k}} \frac{|\hat{s}(\mathbf{k})|^2}{k^2} \right) \left( \sum_{\mathbf{k}} |\hat{s}(\mathbf{k})|^2 \right)^{-1} = \frac{\langle |\nabla^{-1}s|^2 \rangle U^2}{\langle s^2 \rangle \kappa^2} = \frac{U^2 \ell_s^2}{\kappa^2}. \quad (3.36)$$

where  $\ell_s = \langle |\nabla^{-1}s|^2 \rangle^{1/2} / \langle s^2 \rangle^{1/2}$ . So if  $s \in L^2$  then  $M_1 \leq Pe_s$ , but if  $s \notin L^2$  then  $M_1 = 1$  i.e. there is only suppression of gradient variance if  $U\langle |\nabla^{-1}s|^2 \rangle^{1/2} / \kappa\langle s^2 \rangle^{1/2} \gg 1$ .

Here we re-examine our application of the Cauchy-Schwarz inequality which was the first step when deriving an upper bound on the gradient variance. In fact the analysis can be improved a bit. We expect the bound to involve only the curl-free part of the field  $\mathbf{u}\varphi + \kappa\nabla\varphi$ . This can be seen by first evaluating

$$\min_{\tilde{\theta}} \{ \langle |\nabla\tilde{\theta}|^2 \rangle \mid \langle \varphi s \rangle = \langle (\mathbf{u}\varphi + \kappa\nabla\varphi) \cdot \nabla\tilde{\theta} \rangle \} \quad (3.37)$$

with functional  $\mathcal{F} := \langle \frac{1}{2}|\nabla\tilde{\theta}|^2 + \lambda(\mathbf{v} \cdot \nabla\tilde{\theta} - \varphi s) \rangle$  where  $\mathbf{v} = \mathbf{u}\varphi + \kappa\nabla\varphi$ . The solution to the variational problem is (after some algebra):

$$\langle |\nabla\theta|^2 \rangle = \frac{\langle \varphi s \rangle^2}{\langle (\nabla \cdot \mathbf{v})(-\Delta^{-1})\nabla \cdot \mathbf{v} \rangle} \geq \frac{\langle \varphi s \rangle^2}{\langle |\mathbf{v}|^2 \rangle}. \quad (3.38)$$

The inequality follows immediately from examining the Fourier representation of the denominator. Note that we can decompose  $\mathbf{v}$  as follows

$$\mathbf{v} = \underbrace{\mathbf{v} - \nabla \Delta^{-1} \nabla \cdot \mathbf{v}}_{\text{divergence-free}} + \underbrace{\nabla \Delta^{-1} \nabla \cdot \mathbf{v}}_{\text{curl-free}}. \quad (3.39)$$

The denominator above is

$$\begin{aligned} \langle (\nabla \cdot \mathbf{v})(-\Delta^{-1})(\nabla \cdot \mathbf{v}) \rangle &= \langle [\Delta \Delta^{-1}(\nabla \cdot \mathbf{v})](-\Delta^{-1})(\nabla \cdot \mathbf{v}) \rangle \\ &= \langle \nabla(\Delta^{-1}(\nabla \cdot \mathbf{v})) \cdot \nabla(\Delta^{-1}(\nabla \cdot \mathbf{v})) \rangle \\ &= \langle |\nabla \Delta^{-1} \nabla \cdot \mathbf{v}|^2 \rangle. \end{aligned} \quad (3.40)$$

From this it is clear that the explicit optimization over  $\tilde{\theta}$  yields a sharper bound by picking out the component of  $\mathbf{v}$  which is curl-free.

Interestingly, this new bound depends on the two point correlation and involves a non-local integral operator i.e. for  $d = 2$

$$\langle (\nabla \cdot \mathbf{v})(-\Delta^{-1})\nabla \cdot \mathbf{v} \rangle = \frac{1}{L^d} \int d\mathbf{x} \int d\mathbf{y} \nabla_x \cdot \mathbf{v}(\mathbf{x}) G(\mathbf{x} - \mathbf{y}) \nabla_y \cdot \mathbf{v}(\mathbf{y}) \quad (3.41)$$

where  $G(\mathbf{x} - \mathbf{y})$  is the Green's function of  $-\Delta$ . After integrating by parts

$$\langle (\nabla \cdot \mathbf{v})(-\Delta^{-1})\nabla \cdot \mathbf{v} \rangle = \frac{1}{L^d} \int d\mathbf{x} \int d\mathbf{y} (-\nabla \nabla G) : \overline{\mathbf{v} \mathbf{v}} \quad (3.42)$$

where under the homogeneity assumption,

$$\overline{\mathbf{v} \mathbf{v}} = \varphi(\mathbf{x})\varphi(\mathbf{y})\overline{\mathbf{u}(\mathbf{x})\mathbf{u}(\mathbf{y})} + \kappa^2 \nabla \varphi(\mathbf{x}) \nabla \varphi(\mathbf{y}). \quad (3.43)$$

It is the first term that prevents the expression from collapsing to  $|\mathbf{v}|^2$  (the second term becomes  $\kappa^2(\Delta \varphi)^2$  after integrating by parts). The first term depends on the two-point correlation of the velocity field. Under the assumptions of HIT, the velocity field has single-point statistical properties and hence the first term collapses to  $U^2 \varphi^2/d$  which implies that for HIT a strict application of Cauchy-Schwarz (without minimizing over  $\tilde{\theta}$ ) yields a sharp bound. In turbulence theory, the two-point correlation for Homogeneous Isotropic Turbulence is written as

$$\overline{u_i(\mathbf{x}, \cdot) u_j(\mathbf{y}, \cdot)} = \delta_{ij} g(|\mathbf{x} - \mathbf{y}|) + \frac{(x_i - y_i)(x_j - y_j)}{|\mathbf{x} - \mathbf{y}|^2} (f - g). \quad (3.44)$$

Incompressibility implies that  $g(r) = f(r) + r f'(r)/(d-1)$ . This new bound introduces dependence on the two-point correlation property of the velocity field. The implication of such two-point statistical properties on the scaling of the bound will be the subject of future investigation. We note that the Cauchy-Schwarz bound cannot be improved for both the variance, because it is a scalar field, and the inverse gradient variance (next section) because it manifestly involves a curl-free field. We will revisit the implications of the two-point statistical properties when we examine the bounds including scalar decay (section 6).

### 3.2.1 Delta function source

It is clear that a  $\delta$ -function or white noise source ( $|\hat{s}(\mathbf{k})| \sim 1$ ) will cause the sums in (3.37) to diverge in both  $d = 2$  and 3. Thus, in the case of  $\delta$ -like sources or sinks the mixing efficiency bound is sharp and equal to 1.

### 3.3 Bounds on the inverse gradient variance

Beginning again with the first step of the TDG procedure

$$\begin{aligned}\langle \varphi s \rangle &= -\langle (\mathbf{u} \cdot \nabla \varphi + \kappa \Delta \varphi) \theta \rangle \\ &= \langle \nabla (\mathbf{u} \cdot \nabla \varphi + \kappa \Delta \varphi) \cdot \nabla \Delta^{-1} \theta \rangle \\ &\leq \langle |\nabla (\mathbf{u} \cdot \nabla \varphi + \kappa \Delta \varphi)|^2 \rangle^{\frac{1}{2}} \langle |\nabla^{-1} \theta|^2 \rangle^{\frac{1}{2}}.\end{aligned}\quad (3.45)$$

Continuing as usual, we construct a variational principle to obtain a lower bound on the inverse gradient variance

$$\langle |\nabla^{-1} \theta|^2 \rangle \geq \max_{\varphi} \frac{\langle \varphi s \rangle^2}{\langle |\nabla (\mathbf{u} \cdot \nabla \varphi + \kappa \Delta \varphi)|^2 \rangle} \quad (3.46)$$

Thus we minimize the denominator subject to the constraint of  $\varphi$  having a unit projection on the source, i.e. we evaluate

$$\min_{\varphi} \{ \langle |(\nabla \mathbf{u}) \cdot \nabla \varphi + \mathbf{u} \cdot \nabla \nabla \varphi + \kappa \nabla \Delta \varphi|^2 \rangle \mid \langle \varphi s \rangle = 1 \}. \quad (3.47)$$

The assumptions of HIT simplify the problem:

$$\begin{aligned} |(\nabla \mathbf{u}) \cdot \nabla \varphi + \mathbf{u} \cdot \nabla \nabla \varphi + \kappa \nabla \Delta \varphi|^2 &= (\nabla \varphi, i) \cdot \overline{\mathbf{u} \mathbf{u}} \cdot (\nabla \varphi, i) + \nabla \varphi \cdot [(\overline{\nabla \mathbf{u}})^{\text{tr}} (\overline{\nabla \mathbf{u}})] \cdot \nabla \varphi + \kappa^2 |\Delta \nabla \varphi|^2 \\ &= \kappa^2 |\Delta \nabla \varphi|^2 + (\Gamma^2/d) |\nabla \varphi|^2 + (U^2/d) (\Delta \varphi)^2.\end{aligned}\quad (3.48)$$

Thus the variational problem reduces to evaluating

$$\min_{\varphi} \{ \langle \kappa^2 |\Delta \nabla \varphi|^2 + (\Gamma^2/d) |\nabla \varphi|^2 + (U^2/d) (\Delta \varphi)^2 \rangle \mid \langle \varphi s \rangle = 1 \}. \quad (3.49)$$

The solution of the variational problem is (after some algebra)

$$\langle |\nabla^{-1} \theta|^2 \rangle = \langle s \mathcal{M}_{-1} s \rangle \quad (3.50)$$

$\mathcal{M}_{-1} := (\kappa^2 \Delta^3 - (\Gamma^2/d) \Delta + (U^2/d) \Delta^2)^{-1}$ . A lower bound on the inverse gradient variance is obtained from simple application of the Cauchy-Schwarz and Poincaré inequalities to the bulk variance dissipation constraint:

$$\langle |\nabla^{-1} \theta|^2 \rangle \leq \frac{L^8}{256\pi^8 \kappa^2} \langle |\nabla s|^2 \rangle. \quad (3.51)$$

Because it uses the Poincaré inequality the lower bound is only sharp if the source is monochromatic at the lowest wavenumber,  $2\pi/L$ .

Given the upper and lower bound on the inverse gradient variance and the value in the absence of stirring,  $\langle |\nabla^{-1} \Delta^{-1} s|^2 \rangle$ , we obtain bounds on the mixing efficiency on large scales

$$\frac{256\pi^8}{L^8} \frac{\langle \nabla^{-1} \Delta^{-1} s|^2 \rangle}{\langle |\nabla s|^2 \rangle} \leq M_{-1} \leq \frac{\langle |\nabla^{-1} \Delta^{-1} s|^2 \rangle}{\langle s \mathcal{M}_{-1} s \rangle}. \quad (3.52)$$

In Fourier space,

$$\frac{256\pi^8}{L^8} \left( \sum_{\mathbf{k}} \frac{|\hat{s}(\mathbf{k})|^2}{k^6} \right) \left( \sum_{\mathbf{k}} k^2 |\hat{s}(\mathbf{k})|^2 \right)^{-1} \leq M_{-1}^2 \leq \left( \sum_{\mathbf{k}} \frac{|\hat{s}(\mathbf{k})|^2}{k^6} \right) \left( \sum_{\mathbf{k}} \frac{|\hat{s}(\mathbf{k})|^2}{k^6 + \frac{U^2}{d\kappa^2} k^4 + \frac{\Gamma^2}{d\kappa^2} k^2} \right)^{-1} \quad (3.53)$$

For a monochromatic source the upper bound is

$$M_{-1}^2 \leq 1 + \frac{U^2}{d\kappa^2 k^2} + \frac{\Gamma^2}{d\kappa^2 k^4} = 1 + \frac{U^2}{d\kappa^2 k^2} \left(1 + \frac{\Gamma^2}{U^2 k^2}\right) = 1 + \frac{Pe^2}{d} \left(1 + \frac{1}{\lambda^2 k^2}\right) \quad (3.54)$$

where we define  $Pe = U/\kappa k$ . Note that the efficiency depends on the shear in the flow directly through  $\Gamma$ . Interestingly,  $\Gamma$  allows for an increase in the mixing efficiency on large scales via stirring on small scales (coupling the different scales). We investigate this potential effect for a steady shearing wind in section 5.

### 3.3.1 Delta function source

Consider a  $\delta$ -function source (measure valued). Suppose  $\kappa \rightarrow 0$  while  $U^2$  and  $\Gamma^2$  are fixed then the asymptotic form of the upper bound is

$$M_{-1}^2 \lesssim \left( \int_{2\pi/L}^{\infty} \frac{k^{d-1} dk}{k^6} \right) \left( \int_{2\pi/L}^{\infty} \frac{k^{d-1} dk}{k^6 + \frac{U^2}{d\kappa^2} k^4 + \frac{\Gamma^2}{d\kappa^2} k^2} \right)^{-1}. \quad (3.55)$$

Letting  $\xi = kL/2\pi : 1 \rightarrow \infty$  we obtain

$$M_{-1} \lesssim \left( \int_1^{\infty} \xi^{d-7} d\xi \right) \left( \int_1^{\infty} \frac{\xi^{d-3} d\xi}{\xi^4 + \frac{U^2 L^2}{4\pi^2 d\kappa^2} \xi^2 + \frac{\Gamma^2 L^4}{16\pi^4 d\kappa^2}} \right)^{-1} \quad (3.56)$$

In  $d=2$ , letting  $\eta = \xi^2$

$$\int_1^{\infty} \xi^{-5} d\xi = \frac{1}{4}, \quad \int_1^{\infty} \frac{\xi^{-1} d\xi}{\xi^4 + \frac{Pe^2}{d} \xi^2 + \frac{L^2 Pe^2}{\lambda^2 d}} = \frac{1}{2} \int_1^{\infty} \frac{d\eta}{\eta(\eta^2 + \alpha\eta + \beta)}, \quad (3.57)$$

where  $\alpha = Pe^2/d$  and  $\beta = L^2 Pe^2/\lambda^2 d$ . In the limit  $Pe \rightarrow \infty$

$$\int_1^{\infty} \frac{\xi^{-1} d\xi}{\xi^4 + \frac{Pe^2}{d} \xi^2 + \frac{L^2 Pe^2}{\lambda^2 d}} = \frac{1}{2} \int_1^{\infty} \frac{d\eta}{\eta(\alpha\eta + \beta)}. \quad (3.58)$$

After some algebra we find

$$\int_1^{\infty} \frac{\xi^{-1} d\xi}{\xi^4 + \frac{Pe^2}{d} \xi^2 + \frac{L^2 Pe^2}{\lambda^2 d}} \cong \frac{1}{2\beta} \ln \left( 1 + \frac{\beta}{\alpha} \right) \quad (3.59)$$

note that  $\beta/\alpha = L^2/\lambda^2$ . The efficiency bound becomes (as  $Pe \rightarrow \infty$ )

$$M_{-1}^2 \lesssim \frac{\beta}{2} \frac{1}{\ln \left( 1 + \frac{\beta}{\alpha} \right)} = Pe^2 \frac{L^2}{\lambda^2} \frac{1}{\ln \left( 1 + \frac{L^2}{\lambda^2} \right)} \quad (3.60)$$

Interestingly, the prefactor can be larger for smaller scale flow.

In  $d=3$

$$\int_1^{\infty} \xi^{-4} d\xi = \frac{1}{4}, \quad \int_1^{\infty} \frac{d\xi}{\xi^4 + \frac{Pe^2}{d} \xi^2 + \left(\frac{pL}{2\pi}\right)^2 \frac{Pe^2}{d}} \rightarrow \int_1^{\infty} \frac{d\xi}{Pe(\xi^2 + \frac{L^2}{\lambda^2})} \quad (3.61)$$

after a change of variables  $\eta = \frac{\lambda}{L} \xi : \frac{\lambda}{L} \rightarrow \infty$

$$\int_1^{\infty} \frac{d\xi}{\xi^4 + \frac{Pe^2}{d} \xi^2 + \left(\frac{pL}{2\pi}\right)^2 \frac{Pe^2}{d}} \cong \frac{1}{Pe} \frac{\lambda}{L} \int_{\frac{\lambda}{L}}^{\infty} \frac{d\eta}{\eta^2 + 1} = \frac{1}{Pe} \frac{\lambda}{L} \left( \frac{\pi}{2} - \arctan \frac{\lambda}{L} \right) \quad (3.62)$$

hence

$$M_{-1}^2 \lesssim \frac{L}{\lambda} Pe^2 \frac{1}{\left( \frac{\pi}{2} - \arctan \frac{\lambda}{L} \right)}. \quad (3.63)$$

## 4 Saturating the multiscale mixing efficiency bounds

The HIT bounds on the multiscale mixing efficiencies derived in the previous section simplify in the case of a monochromatic source

$$M_1 \leq \sqrt{1 + Pe^2/k_s^2}, \quad (4.1a)$$

$$M_0 \leq \sqrt{1 + Pe^2/k_s^2 d}, \quad (4.1b)$$

$$M_{-1} \leq \sqrt{1 + Pe^2/k_s^2 d + L^2 Pe^2/\lambda^2 k_s^4 d} \quad (4.1c)$$

where we have rescaled  $[0, L]^d$  to  $[0, 1]^d$  so that  $k_s$  is a multiple of  $2\pi$ . We note that each efficiency scales as  $Pe$  which corresponds to replacing the molecular diffusivity by an eddy diffusivity proportional to  $UL$ . An anomalous scaling results if the efficiencies are not linear in  $Pe$ . Figure 2 from TDG showed the mixing efficiency  $M_0$  versus Péclet number from direct numerical simulations (DNS) of the advection-diffusion equation for a monochromatic source  $\sin k_s x$  and the Zeldovich sine flow [3]. TDG discussed the possibility of saturating the upper bound for the  $\sin k_s x$  source; however it was clear from the DNS calculations that the sine flow was not the optimal stirrer and no other stirring field was put forth.

Here we show that the TDG upper bound on the variance for  $s(\mathbf{x}) = \sin k_s x_1$  and  $\mathbf{x} \in \mathbb{T}^d$  i.e.,  $\mathbf{x} \in [0, L]^d$ , is saturated by the sweeping flow suggested by W. R. Young. Consider the steady advection-diffusion equation with source  $s(\mathbf{x}) = \sqrt{2}S \sin k_s x_1$  and uniform stirring field  $\mathbf{u}(\mathbf{x}) = (U/\sqrt{d}) \sum_{n=1}^d \hat{\mathbf{i}}_n$ :

$$\frac{U}{\sqrt{d}} \sum_{n=1}^d \frac{\partial \theta}{\partial x_n} = \kappa \sum_{n=1}^d \frac{\partial^2 \theta}{\partial x_n^2} + \sqrt{2}S \sin(k_s x_1). \quad (4.2)$$

We sweep on an angle for a long time (to kill the transients) and then switch the sweeping by an appropriate angle (repeating appropriately) as to satisfy the HIT assumptions.

Letting  $\theta(\mathbf{x}) = \sum_{n=1}^d F_n(x_n)$ , we end up with a system of constant coefficient ODEs

$$\frac{d^2 F_1}{dx_1^2} - \frac{U}{\sqrt{d}\kappa} \frac{dF_1}{dx_1} + \frac{\sqrt{2}S}{\kappa} \sin(k_s x_1) = 0 \quad (4.3a)$$

$$\frac{d^2 F_n}{dx_n^2} - \frac{U}{\sqrt{d}\kappa} \frac{dF_n}{dx_n} = 0 \quad \text{for } 2 \leq n \leq d \quad (4.3b)$$

with periodic boundary conditions  $F_n(0) = F_n(L)$  whose solution is

$$F_1 = \frac{\sqrt{2}SL^2}{(4\pi^2\kappa^2 + \frac{U^2}{d}L^2)} \left[ \kappa \sin(k_s x_1) - \frac{UL}{2\sqrt{d}\pi} \cos(k_s x_1) \right] \quad (4.4a)$$

$$F_n = 0 \quad \text{for } 2 \leq n \leq d. \quad (4.4b)$$

The variance is

$$\langle \theta^2 \rangle = \frac{S^2 L^4}{(4\pi^2\kappa^2 + \frac{U^2}{d}L^2)^2} \left[ \kappa^2 + \frac{U^2 L^2}{4\pi^2 d} \right] \quad (4.5)$$

and since  $\langle \theta_0^2 \rangle = S^2 L^4 / 16\pi^4 \kappa^2$  the mixing efficiency is

$$M_0 = \sqrt{1 + \frac{U^2 L^2}{4\pi^2 d \kappa^2}} = \sqrt{1 + \frac{Pe^2}{4\pi^2 d}} \quad (4.6)$$

which is the bound derived by TDG. Given the steady solution we can compute the other two mixing efficiencies. After some straight-forward algebra we find

$$M_1 = M_{-1} = \sqrt{1 + \frac{Pe^2}{4\pi^2 d}} = M_0. \quad (4.7)$$

Interestingly,  $M_0$  and  $M_{-1}$  are precisely saturated but  $M_1$  is off by a  $d$  factor. Since the uniform flow lacks shear the large scale mixing efficiency,  $M_{-1}$ , is identical to the others.

The result is fairly intuitive: to reduce the variance (on any length scale) one should simply blow the source onto the sink and vice versa — if one can do this simply. We note that this type of sweeping flow is somewhat pathological in the sense that it simply transports the source onto the sink which can be done simply on the torus. There is no dependence on diffusion. However, such sweeping flows are not allowed on the sphere or in bounded domains. Furthermore, the sweeping flow is not optimal for non-1D sources. This makes it clear that the optimal stirrer is a function of both the source shape and the domain. Formulating the optimization problem for the optimal stirring field is a subject of current and future investigation. It is a nasty non-linear problem.

To emphasize the relationship between the source and the stirring field which saturates the bound we perform an analogous calculation to the previous one (for  $d = 2, 3$ ) however we impose a  $\delta$ -function source distribution. Taking the Fourier transform of the steady advection-diffusion equation with  $s = \delta(\mathbf{x})$  we obtain

$$\sum_{\mathbf{k}} \hat{\theta}(\mathbf{k}) = \sum_{\mathbf{k}} \frac{\hat{s}(\mathbf{k})}{\kappa k^2 + iUk_d} \quad (4.8)$$

where  $k_d$  is the  $d$ th component of the horizontal wavenumber. Approximating the integrals by sums (we are only interested in the asymptotic behaviour)

$$d = 2 : \quad \langle |\nabla^p \theta|^2 \rangle = \int_0^{2\pi} d\phi \int_{2\pi/L}^\infty \frac{k^{2p+1} dk}{\kappa^2 k^4 + U^2 k^2 \cos^2 \theta} \quad (4.9a)$$

$$d = 3 : \quad \langle |\nabla^p \theta|^2 \rangle = \int_0^{2\pi} d\phi \int_0^\pi \sin \theta d\theta \int_{2\pi/L}^\infty \frac{k^{2(p+1)} dk}{\kappa^2 k^4 + U^2 k^2 \cos^2 \theta}. \quad (4.9b)$$

The variances in the absence of stirring are found by calculating the above integrals with  $U = 0$ . Straight-forward evaluation of the integrals yields

$$d = 2 : \quad M_1 = 1, \quad M_0 \sim \frac{\sqrt{Pe}}{4\pi}, \quad M_{-1} \sim \frac{3\sqrt{Pe}}{8\pi} \quad (4.10)$$

$$d = 3 : \quad M_1 = 1, \quad M_0 \sim \frac{\sqrt{Pe}}{\sqrt{2\pi}} \frac{1}{\sqrt{\log(Pe/2)}}, \quad M_{-1} \sim \frac{2\sqrt{Pe}}{\sqrt{3\pi}}. \quad (4.11)$$

The anomalous scaling in  $Pe$  suggests that the uniform flow is far from the optimal allowed by the bound for the  $\delta$ -function source in both  $d = 2$  and  $3$ . This emphasizes the source-dependent nature of the optimal stirrer.

Given that the the optimal HIT stirrer for  $s = \sin k_s x$  was at an angle, the calculations from TDG were repeated for a tilted source and the Zeldovich sine flow to see if we could get closer to the bound. Tilting the source is equivalent to tilting the stirring. Figure 1 shows the results of the DNS calculation for  $p = 1, 0, -1$ . The plot of  $M_0$  includes the PY bound. What is clear from this figure is that for a non-optimal flow the three bounds scale differently in  $Pe$ . In the next section we investigate the bounds for a simple steady shear flow in an effort to understand the scaling in  $Pe$  as well as to explore the dependence of  $M_{-1}$  on the Taylor microscale.

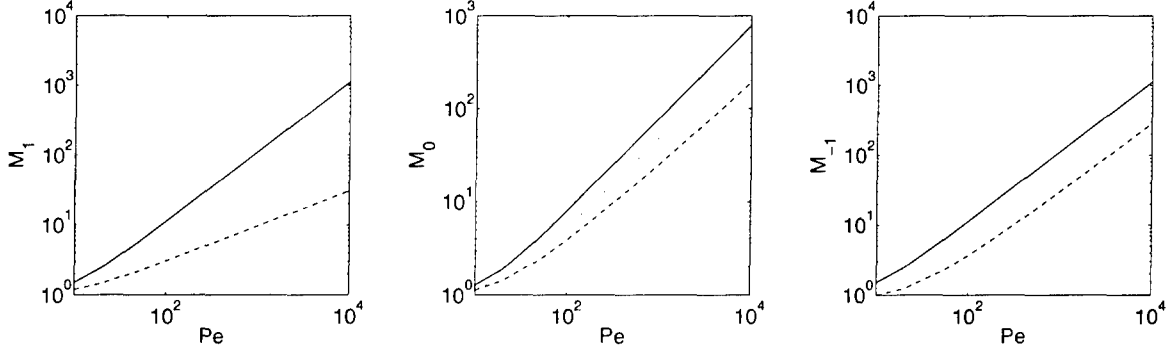


Figure 1: From left to right, mixing efficiencies  $M_p$   $p = 1, 0, -1$  for the Zeldovich sine flow with source  $\sin k(x + y)$ . The solid lines are the respective upper bounds from section 3. The dotted line is the PY variance bound and the dashed lines are the result of direct numerical simulations with  $U$  fixed.

## 5 Steady Shear Flows

From the previous section it is clear that the most efficient stirring for monochromatic sources on the torus is the sweeping flow. Here we investigate the effect of shear on the mixing efficiency on different scales to understand the scaling behaviour at large  $Pe$  (i.e. the scaling when we do not saturate the bound). The results would directly apply to HIT stirring analogous to blowing for a very long time (the sine flow having a long period). From the analysis of section 3 we would expect to see a large difference between the three norms for such sheared stirring. We treat the simplest problem by considering the long time behaviour of a passive tracer governed by the advection-diffusion equation

$$\mathbf{u} \cdot \nabla \theta = \kappa \Delta \theta + s(\mathbf{x}) \quad (5.1)$$

with a stirring field  $\mathbf{u} = \sqrt{2}U \sin k_u y \hat{\mathbf{i}}$  and source  $s(\mathbf{x}) = \sqrt{2}S \sin k_s x$  ( $\sqrt{2}$  for normalization). Here the domain is the 2-dimensional torus  $x \in \mathbb{T}^2$ . The non-dimensional number governing the amount of shear is  $r = k_u/k_s$ . We are particularly interested in the limits  $Pe \gg 1$  with  $r$  fixed and  $r \gg 1$  with  $Pe$  fixed. The solution takes the form

$$\theta(\mathbf{x}) = f(y) \sin(k_s x) + g(y) \cos(k_s x) \quad (5.2)$$

which results in a system of ODEs:

$$-\sqrt{2}U k_s \sin(k_u y) g(y) = \kappa \left[ -k_s^2 + \frac{d^2}{dy^2} \right] f(y) + \sqrt{2}S \quad (5.3a)$$

$$\sqrt{2}U k_s \sin(k_u y) f(y) = \kappa \left[ -k_s^2 + \frac{d^2}{dy^2} \right] g(y). \quad (5.3b)$$

The stirring field is an odd function of  $y$  and hence from (5.4a) we deduce that  $g(y)$  is also odd in  $y$  and hence that  $f(y)$  is even in  $y$ . This can also be seen by integrating (5.4a) over a period. Since the functions  $f(y)$  and  $g(y)$  are periodic we consider the domain  $y \in [0, l/2]$  where  $l = 2\pi/p$ . We infer boundary conditions given the even-oddness of the functions  $f$  and  $g$ :

$$g(0) = g(l/2) = 0, \quad f'(0) = f'(l/2) = 0. \quad (5.4)$$

Upon setting  $\tilde{y} = k_s y$ ,  $\hat{f} = f U k_s / S$ ,  $\hat{g} = g U k_s / S$ ,  $r = k_u / k_s$ , and  $Pe = \sqrt{2} U / \kappa k_s$  we obtain the non-dimensional ODEs

$$\frac{1}{Pe} \left[ -1 + \frac{d^2}{d\tilde{y}^2} \right] \hat{f}(\tilde{y}) + 1 = -\sin(r\tilde{y})\hat{g}(\tilde{y}) \quad (5.5a)$$

$$\frac{1}{Pe} \left[ -1 + \frac{d^2}{d\tilde{y}^2} \right] \hat{g}(\tilde{y}) = \sin(r\tilde{y})\hat{f}(\tilde{y}). \quad (5.5b)$$

The next sections outline the boundary layer analysis (since the solution is slowly varying except in isolated boundary layers) and regular perturbation theory which were used to investigate the limits mentioned above.

## 5.1 Boundary layer solution

This is the limit  $Pe \gg 1$  and  $r$  fixed. Proceeding as usual, we construct an inner and outer solution. The outer solution is obtained by expanding in powers of  $Pe^{-1}$ :

$$\hat{f}_{out} = \sum_{n=0}^{\infty} Pe^{-n} \hat{f}_n, \quad \hat{g}_{out} = \sum_{n=0}^{\infty} Pe^{-n} \hat{g}_n. \quad (5.6)$$

Thus, in the outer region the solution is approximated to leading order by

$$\hat{f}_{out} = 0, \quad \hat{g}_{out} = -\frac{1}{\sin(k_u y)}. \quad (5.7)$$

The boundary layer scaling was determined from a dominant balance argument. The left hand side of (5.6a) is  $\mathcal{O}(1)$ ,  $\forall \epsilon$  thus we choose  $\epsilon = Pe^{-1/3}$  and rescale  $y$ :  $\eta = \tilde{y}/\epsilon$  to achieve a self-consistent scaling of the leading order terms. Expanding in  $\epsilon$  according to

$$\hat{f}_{in} = \sum_{n=-1}^{\infty} \epsilon^n \hat{f}_n, \quad \hat{g}_{in} = \sum_{n=-1}^{\infty} \epsilon^n \hat{g}_n \quad (5.8)$$

(note that the leading term is  $\mathcal{O}(1/\epsilon)$ ) yields at order  $\mathcal{O}(1/\epsilon)$ :

$$\frac{d^2 \hat{f}_{-1}}{d\eta^2} + r\eta \hat{g}_{-1} + 1 = 0, \quad \frac{d^2 \hat{g}_{-1}}{d\eta^2} - r\eta \hat{g}_{-1} = 0. \quad (5.9)$$

Letting  $\xi = r^{1/3} \eta$ ,  $F = r^{2/3} \hat{f}_{-1}$ , and  $G = r^{2/3} \hat{g}_{-1}$  this simplifies the system of ODEs to

$$F'' + \xi G + 1 = 0, \quad G'' - \xi F = 0. \quad (5.10)$$

with boundary conditions

$$F'(0) = 0, \quad G(0) = 0. \quad (5.11)$$

The other boundary conditions come from the requirement of matching to the outer solution:  $F(\xi) \rightarrow 0$  and  $G(\xi) \rightarrow -1/\xi$  as  $\xi \rightarrow \infty$ .

We note that this system of ODEs can be cast into the Airy equation with a complex argument  $\phi(z) = F + iG$  but we resorted instead to shooting to get the solution numerically. The solution was obtained by shooting backward (which was the more stable direction) from the  $\xi \rightarrow \infty$  solution whose asymptotic behavior may be deduced from (5.10)

$$F \approx -\frac{2}{\xi^4} + \frac{\beta}{\xi^{10}}, \quad G \approx -\frac{1}{\xi} + \frac{\alpha}{\xi^7} \quad (5.12)$$



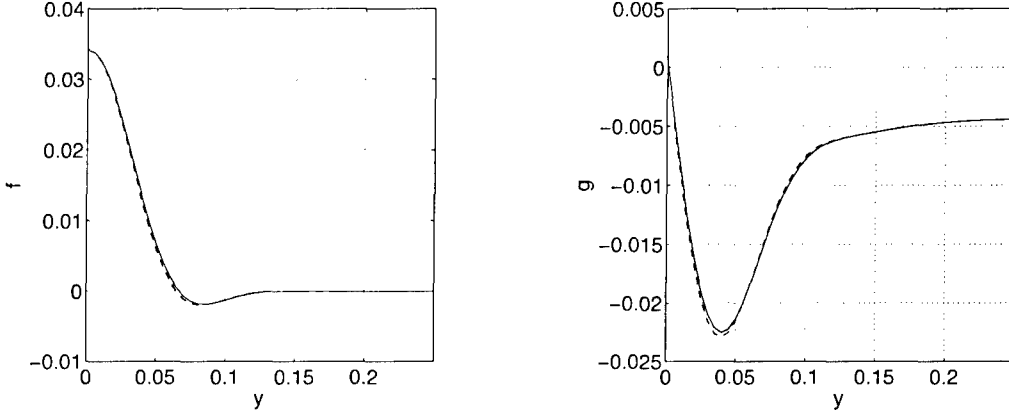


Figure 2: Comparison of the direct numerical solution (solid) and the boundary layer solution (dashed) for  $Pe = 1000$ .

where  $\alpha$  and  $\beta$  were adjusted numerically to obtain a solution which satisfied the boundary conditions at  $\xi = 0$ . Before calculating higher order terms, we compared the boundary layer solution against the solution from a direct numerical simulation of the advection-diffusion equation. Figure 2 shows a plot of the two solutions for  $Pe = 1000$ . The agreement suggests that leading terms do indeed capture the asymptotic behaviour. The inner solution is thus well described by

$$\hat{f}_{in} = \frac{r^{-2/3}}{\epsilon} F(\xi), \quad \hat{g}_{in} = \frac{r^{-2/3}}{\epsilon} G(\xi). \quad (5.13)$$

The final approximate solution to the coupled ODEs to leading order is the composite of the inner and outer solutions (recovering all the scalings and letting  $\delta = \epsilon/r^{1/3}k_s$ )

$$f(y) = \frac{S}{Uk_s} \hat{f}_{in} = \frac{S}{Uk_s} \frac{r^{-2/3}}{\epsilon} F\left(\frac{r^{1/3}k_s}{\epsilon} y\right) = \frac{S}{Uk_s} \frac{1}{k_u \delta} F\left(\frac{y}{\delta}\right) \quad (5.14a)$$

$$\begin{aligned} g(y) &= \frac{S}{Uk_s} k_u y \hat{g}_{in} \hat{g}_{out} = \frac{S}{Uk_s} \frac{r^{-2/3}}{\epsilon} G\left(\frac{r^{1/3}k_s}{\epsilon} y\right) \frac{k_u y}{\sin(k_u y)} \\ &= \frac{S}{Uk_s} \frac{1}{k_u \delta} G\left(\frac{y}{\delta}\right) \frac{k_u y}{\sin(k_u y)}. \end{aligned} \quad (5.14b)$$

Armed with this we can compute the multiscale mixing measures  $\langle |\nabla^p \theta|^2 \rangle$  for  $p = 0, 1, -1$ .

### 5.1.1 Variance

The variance is (N.B. only computing over 1/4 period)

$$\langle \theta^2 \rangle = \frac{1}{2} (\langle f^2 \rangle + \langle g^2 \rangle) = \frac{1}{2} \frac{4}{l} \left( \int_0^{l/4} f^2(y) dy + \int_0^{l/4} g^2(y) dy \right) \quad (5.15)$$

letting  $\eta = y/\delta : 0 \rightarrow \pi/2k_u\delta$

$$\langle \theta^2 \rangle = \frac{1}{\pi} \frac{S^2}{U^2 k_s^2} \frac{1}{k_u \delta} \left( \int_0^{\pi/2k_u\delta} F^2(\eta) d\eta + \int_0^{\pi/2k_u\delta} G^2(\eta) \frac{k_u^2 \eta^2 \delta^2}{\sin^2(k_u \eta \delta)} d\eta \right). \quad (5.16)$$

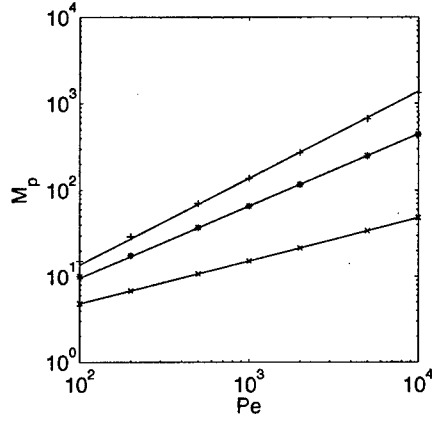


Figure 3: Mixing efficiencies for  $p = 1$  denoted by  $x$ ,  $p = 0$  denoted by  $*$ , and  $p = -1$  denoted by  $+$  for the steady shearing flow with  $r = 1$  from direct numerical simulations with  $U$  fixed. The solid lines are the asymptotic scalings.

Here we are interested in the scaling as  $\delta \rightarrow 0$ . In that case we are justified in replacing the upper limit of the integral of  $F^2(\eta)$  by infinity since the outer solution is zero. More care must be taken with the integral involving  $G^2(\eta)$ . We note that  $k_u^2 \eta^2 \delta^2 / \sin^2(k_u \eta \delta)$  is bounded by 0 and  $\pi/2$  and hence we can apply Lebesgue's dominated convergence theorem to obtain

$$\langle \theta^2 \rangle \approx \frac{1}{\pi} \frac{S^2}{U^2 k_s^2} \frac{1}{k_u \delta} \left( \int_0^\infty F^2(\eta) d\eta + \int_0^\infty G^2(\eta) d\eta \right). \quad (5.17)$$

Recall from section 2 that  $\langle \theta_0^2 \rangle = S^2 / \kappa^2 k_s^4$  and hence the mixing efficiency is

$$M_0 \sim C r^{1/3} \mathcal{P}e^{5/6}, \quad C = \sqrt{\frac{\pi}{2}} \frac{1}{\sqrt{\int_0^\infty F^2(\eta) d\eta + \int_0^\infty G^2(\eta) d\eta}}. \quad (5.18)$$

Figure 3 shows  $M_0$  as a function of  $Pe$  from direct numerical simulations. The scaling fits  $Pe^{5/6}$ . There is only a 5% difference between the prefactor calculated from the boundary layer solution and that calculated from the direct numerical simulation for  $Pe = 1000$  (after rescaling  $Pe$  to  $\mathcal{P}e$ ). Remarkably, the  $Pe^{5/6}$  scaling is also observed for the HIT stirring (figure 1). The scaling in  $r$  was also confirmed. The  $Pe^{5/6}$  scaling would hold for different values of  $r$  with a corresponding change in the value of the prefactor.

### 5.1.2 Gradient variance

The gradient is

$$\langle |\nabla \theta|^2 \rangle = \frac{k^2}{2} [\langle f^2 \rangle + \langle g^2 \rangle] + \frac{1}{2} [\langle (f')^2 \rangle + \langle (g')^2 \rangle] \quad (5.19)$$

noting that the first term was computed in the previous section we focus attention on the second term. Computing the gradient we obtain

$$\begin{aligned} \frac{1}{2} [\langle (f')^2 \rangle + \langle (g')^2 \rangle] &= \left\langle \left( \frac{S}{U k_s} \frac{1}{k_u \delta^2} F'(y/\delta) \right)^2 \right\rangle + \\ &\left\langle \left( \frac{S}{U k_s} \frac{1}{k_u \delta^2} G'(y/\delta) \frac{k_u y}{\sin(p y)} + \frac{S}{U k_s} \frac{1}{k_u \delta} G(y/\delta) \left[ \frac{k_u y}{\sin(k_u y)} \right]' \right)^2 \right\rangle. \end{aligned} \quad (5.20)$$

The leading order contribution to the integral is the square of the first term ( $1/\delta^2$  versus  $1/\delta$ ). Hence

$$\frac{1}{2} [\langle (f')^2 \rangle + \langle (g')^2 \rangle] \approx \frac{1}{\pi} \frac{S^2}{U^2 k_s^2} \frac{1}{k_u \delta^3} \left[ \int_0^{\frac{\pi}{2k_u \delta}} (F')^2(\eta) d\eta + \int_0^{\frac{\pi}{2k_u \delta}} (G')^2(\eta) \frac{k_u^2 \eta^2 \delta^2}{\sin^2(k_u \eta \delta)} d\eta \right] \quad (5.21)$$

and by the same arguments as the previous section (DCT etc.) we obtain

$$\langle |\nabla \theta|^2 \rangle \approx \frac{1}{\pi} \left( \int_0^\infty (F')^2(\eta) d\eta + \int_0^\infty (G')^2(\eta) d\eta \right) \frac{S^2}{U^2 k_s^2} \frac{1}{p \delta^3}. \quad (5.22)$$

Recall from section 2 that  $\langle |\nabla \theta_0|^2 \rangle = S^2 / \kappa^2 k_s^2$  and hence the mixing efficiency is

$$M_1 \approx C Pe^{1/2}, \quad C = \sqrt{\frac{\pi}{2}} \frac{1}{\sqrt{\int_0^\infty (F')^2(\eta) d\eta + \int_0^\infty (G')^2(\eta) d\eta}}. \quad (5.23)$$

The boundary layer and direct numerical solution prefactors differ by approximately 1% for  $Pe = 1000$ . Figure 3 shows the scaling of  $M_1$  from the direct numerical solution that confirms the  $Pe^{1/2}$  scaling. The scaling in  $r$  was also confirmed. Interestingly, stirring at small scales does not enhance the mixing efficiency on small scales. This is because the decrease in gradient variance due to stirring on small scales is compensated by the increase in gradient variance in the boundary layer.

### 5.1.3 Inverse gradient variance

The inverse gradient variance is

$$\langle |\nabla^{-1} \theta|^2 \rangle = \langle |\nabla^{-1} (f(y) \sin(k_s x) + g(y) \cos(k_s x))|^2 \rangle \quad (5.24)$$

This is the trickiest of the three multiscale mixing measures. We can simplify the integral by noting that the leading Fourier component of  $g(y)$  is zero. Expanding  $f(y)$  in a Fourier series

$$f(y) = \sum_{n=0}^{\infty} f_n \cos(n k_u y) \quad (5.25)$$

we obtain

$$\begin{aligned} \nabla^{-1} (f(y) \sin(k_s x)) &= \sum_{n=0}^{\infty} \frac{k_s}{k_s^2 + n^2 k_u^2} f_n \sin(n k_u y) \sin(k_s x) \hat{\mathbf{i}} + \\ &\quad \frac{n k_u}{k_s^2 + n^2 k_u^2} f_n \sin(n k_u y) \cos(k_s x) \hat{\mathbf{j}} \end{aligned} \quad (5.26)$$

and

$$\begin{aligned} \langle |\nabla^{-1} (f(y) \sin(k_s x))|^2 \rangle &= \sum_{n=0}^{\infty} \frac{|f_n|^2}{k_s^2 + n^2 k_u^2} = \frac{1}{k_s^2} |f_0|^2 + \frac{1}{k_u^2} \sum_{n=1}^{\infty} \frac{|f_n|^2}{n^2 + r^2} \\ &\leq \frac{1}{k_s^2} |f_0|^2 + \frac{1}{k_u^2} \sum_{n=1}^{\infty} \frac{|f_n|^2}{n^2} \leq \frac{1}{k_s^2} |f_0|^2 + \frac{1}{k_u^2} \frac{\pi}{6} \sup_n |f_n|^2. \end{aligned} \quad (5.27)$$

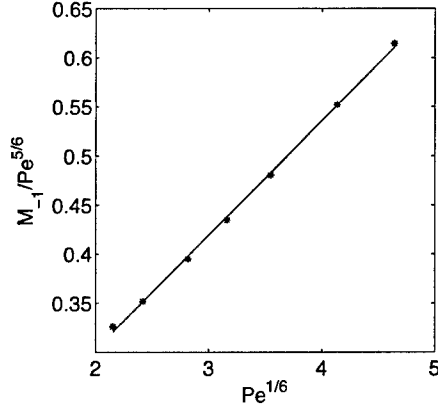


Figure 4:  $M_{-1}/Pe^{5/6}$  versus  $Pe^{1/6}$  from direct numerical simulations (\*). The solid line is the asymptotic scaling.

Computing the first Fourier coefficient

$$|f_0| = \frac{1}{\pi} \int_0^{l/4} f(y) dy = \frac{1}{\pi} \frac{S}{U k_s} \int_0^\infty F(\eta) d\eta \quad (5.28)$$

and recalling from section 2 that  $\langle |\nabla^{-1} \theta_0|^2 \rangle = S^2 / \kappa^2 k_s^6$  we obtain the large scale mixing efficiency scaling

$$M_{-1} \sim C Pe \quad (5.29)$$

where  $C$  is a prefactor depending on the integral of  $F$  (square of the mean versus the mean of the square). Figure 3 of the direct numerical solution confirms the  $Pe$  scaling. The boundary layer and direct numerical solution prefactors differ by 15%.

We note two interesting things; first to leading order there is no dependence on  $r$  even though we might have expected that increased shear would increase mixing on large scales (see section 3). Second we expect that the next order term would be proportional to  $M_0$  i.e. that

$$M_{-1} \sim Pe + r^{1/3} Pe^{5/6}. \quad (5.30)$$

Figure 4 shows a plot of  $M_{-1}/Pe^{5/6}$  versus  $Pe^{1/6}$  from direct numerical simulations. A very non-rigorous check of the scaling involves comparing the slope of the line in figure 4 to the prefactor above. The slopes differ by 20%. Note in that plot the current limit of large Péclet and fixed  $r$  requires  $r < 0.1\sqrt{Pe}$  i.e.  $r < 3$  ( $\delta < 1$ ).

There are still some things we do not understand. Are there universal scalings in  $Pe$ ? Namely for the steady flow and the Zeldovich sine flow we get the same scalings. Do these scalings appear for other flows with this source?

## 5.2 Regular perturbation expansion

We now seek the behaviour of the multiscale mixing efficiencies for  $r \gg 1$ ,  $Pe$  fixed. Going back to our system of ODEs and setting  $\tilde{y} = k_u y$  we obtain

$$\frac{Pe}{r^2} \sin(\tilde{y}) f = \left[ -\frac{1}{r^2} + \frac{d^2}{d\tilde{y}^2} \right] g \quad (5.31a)$$

$$-\frac{Pe}{r^2} \sin(\tilde{y}) g = \left[ -\frac{1}{r^2} + \frac{d^2}{d\tilde{y}^2} \right] f + \frac{\sqrt{2}S}{\kappa k_s^2} \frac{1}{r^2}. \quad (5.31b)$$

Now we perform a regular perturbation expansion in powers of  $r^{-2}$ :

$$f = \sum_{n=0}^{\infty} f_n r^{-2n}, \quad g = \sum_{n=0}^{\infty} g_n r^{-2n} \quad (5.32)$$

At  $\mathcal{O}(1)$  we obtain

$$f_0'' = 0 \rightarrow f_0 = \text{const}, \quad g_0'' = 0 \rightarrow g_0 = \text{const} \quad (5.33)$$

continuing as usual we obtain at  $\mathcal{O}(r^{-2})$

$$\mathcal{P}e \sin(\tilde{y}) f_0 = -g_0 + g_1'', \quad -\mathcal{P}e \sin(\tilde{y}) g_0 = -f_0 + f_1'' + \frac{\sqrt{2}S}{\kappa k_s^2}. \quad (5.34)$$

The average over a period of the first and second equations implies  $g_0 = 0$  and  $f_0 = \sqrt{2}S/\kappa k_s^2$ . Thus,  $f_1 = \text{const}$ , and  $g_1 = -(\sqrt{2}S/\kappa k_s^2)\mathcal{P}e \sin(\tilde{y}) + \text{const}$ . Continuing, we obtain at  $\mathcal{O}(r^{-4})$ :

$$\mathcal{P}e \sin(\tilde{y}) f_1 = -g_1 + g_2'', \quad -\mathcal{P}e \sin(\tilde{y}) g_1 = -f_1 + f_2''. \quad (5.35)$$

The average over a period of the first and second equations imply

$$f_1 = -\frac{\sqrt{2}}{2\pi} \frac{S}{\kappa k_s^2} \mathcal{P}e^2, \quad g_1 = -\frac{\sqrt{2}S}{\kappa k_s^2} \mathcal{P}e \sin(\tilde{y}). \quad (5.36)$$

Hence to leading order the solution is

$$\theta \approx \frac{\sqrt{2}S}{\kappa k_s^2} \left[ \left( 1 - \frac{\mathcal{P}e^2}{2\pi r^2} \right) \sin(k_s x) - \frac{\mathcal{P}e}{r^2} \sin(\tilde{y}) \cos(k_s x) \right]. \quad (5.37)$$

Given the asymptotic solution for  $r \gg 1$  at fixed  $\mathcal{P}e$  we compute the variance as (keeping only the leading order term and the  $\mathcal{O}(r^{-2})$  term)

$$\langle \theta^2 \rangle \approx \frac{S^2}{\kappa^2 k_s^4} \left( 1 - \frac{1}{\pi} \frac{\mathcal{P}e^2}{r^2} \right) \quad (5.38)$$

which implies

$$M_0 \sim 1 + \frac{1}{\pi} \frac{\mathcal{P}e^2}{r^2}. \quad (5.39)$$

It is clear from this result that stirring on ever small scales (increased shear) ceases to suppress the variance. This is because in the limit  $r \gg 1$  the flow is diffusion dominated hence the mixing efficiency goes to one.

The gradient to leading order is

$$\begin{aligned} \nabla \theta \approx \frac{\sqrt{2}S}{\kappa k_s^2} \left[ \left( 1 - \frac{1}{\pi} \frac{\mathcal{P}e^2}{r^2} \right) k_s \cos(k_s x) + \frac{\mathcal{P}e}{r^2} \sin(\tilde{y}) k \sin(k_s x) \right] \hat{\mathbf{i}} + \\ \left[ -\frac{\mathcal{P}e}{r^2} \cos(\tilde{y}) \cos(k_s x) \right] \hat{\mathbf{j}} \end{aligned} \quad (5.40)$$

and so the gradient variance is

$$\langle |\nabla \theta|^2 \rangle \approx \frac{S}{\kappa k_s^2} \left( 1 - \frac{1}{\pi} \frac{\mathcal{P}e^2}{r^2} \right) \quad (5.41)$$

which implies the mixing efficiency is identical on small and intermediate scales  $M_1 = M_0$ .

The inverse gradient to leading order is

$$\begin{aligned} \nabla^{-1}\theta \approx \frac{\sqrt{2}S}{\kappa k_s^2} \left[ 1 - \frac{1}{\pi} \frac{\mathcal{P}e^2}{r^2} \frac{k}{k_s^2} \sin(k_s x) + \frac{\mathcal{P}e}{r^2} \sin(\tilde{y}) \frac{k_s}{k_s^2 + p^2} \cos(k_s x) \right] \hat{\mathbf{i}} + \\ \left[ -\frac{\mathcal{P}e}{r^2} \cos(\tilde{y}) \frac{p}{k_s^2 + p^2} \cos(k_s x) \right] \hat{\mathbf{j}} \end{aligned} \quad (5.42)$$

and hence the inverse gradient variance is

$$\langle |\nabla^{-1}\theta|^2 \rangle \approx \frac{S}{\kappa k_s^6} \left( 1 - \frac{1}{\pi} \frac{\mathcal{P}e^2}{r^2} \right) \quad (5.43)$$

and hence  $M_{-1} = M_0$  (as suspected). Thus in the limit  $r \gg 1$  and  $\mathcal{P}e$  fixed all of the efficiencies are the same.

Summarizing the different limits, we find that the norms scale differently in  $\mathcal{P}e$  for fixed  $r$  and the scalings were confirmed with the direct numerical solution. However, the norms behave similarly for fixed  $\mathcal{P}e$  and  $r \gg 1$  where the flow is diffusion dominated.

## 6 Bounds on the multiscale mixing efficiencies with scalar decay

Now consider the advection-diffusion equation for the concentration of a passive scalar  $\theta(\mathbf{x}, t)$  which has a slow decay rate  $\alpha$  maintained by a body source  $s(\mathbf{x})$  with spatial mean zero:

$$\frac{\partial \theta}{\partial t} + \mathbf{u} \cdot \nabla \theta = \kappa \Delta \theta + s(\mathbf{x}) - \alpha \theta \quad (6.1)$$

where  $\kappa$  is the molecular diffusivity. The decay rate may have various interpretations such as the decay rate due to chemical kinetics, or radiative relaxation in meteorology (relevant for the sphere). We follow the procedure of TDG which was used to derive upper bounds on mixing efficiency for  $\alpha = 0$  to derive upper bounds on  $\langle |\nabla^p \theta|^2 \rangle$  for  $p = 0, 1, -1$  when  $\alpha \neq 0$ . We re-define the advection-diffusion operator and its formal adjoint to include the slow decay:  $\mathcal{L}_\alpha := \partial_t + \mathbf{u} \cdot \nabla - \kappa \Delta - \alpha$  and  $\mathcal{L}_\alpha^\dagger := -\partial_t - \mathbf{u} \cdot \nabla + \kappa \Delta - \alpha$ . Now we proceed with computing bounds on the multiscale mixing efficiencies.

### 6.1 Bounds on the variance

Following the TDG procedure, we perform the following optimization:

$$\langle \theta^2 \rangle \geq \max_{\varphi} \min_{\tilde{\theta}} \{ \langle \tilde{\theta}^2 \rangle \mid \langle \tilde{\theta}(\mathbf{u} \cdot \nabla \varphi + \kappa \Delta \varphi - \alpha \varphi) \rangle = -\langle \varphi s \rangle \} \quad (6.2)$$

upon applying the Cauchy-Schwarz inequality and maximizing over  $\varphi$  we obtain

$$\langle \theta^2 \rangle \geq \langle s \mathcal{M}_0^\alpha s \rangle \quad (6.3)$$

where  $\mathcal{M}_0^\alpha := (\mathcal{L}_\alpha \mathcal{L}_\alpha^\dagger)^{-1}$ . Substituting the definition of  $\mathcal{L}_\alpha$  and restricting to HIT

$$\begin{aligned} \langle s \mathcal{M}_0^\alpha s \rangle &= \langle s \{ \kappa^2 \Delta^2 - \overline{\mathbf{u}\mathbf{u}} : \nabla \nabla + \kappa (2 \nabla \overline{\mathbf{u}} \cdot \nabla \nabla + \nabla \overline{\mathbf{u}} \cdot \nabla) - \alpha \overline{\mathbf{u}} \cdot \nabla - 2 \alpha \kappa \Delta + \alpha^2 \}^{-1} s \rangle \\ &= \langle s \{ \kappa^2 \Delta^2 - (U^2/d) \Delta - 2 \kappa \alpha \Delta + \alpha^2 \}^{-1} s \rangle. \end{aligned} \quad (6.4)$$

The variance in the absence of stirring is

$$\langle \theta_0^2 \rangle = \langle s \{ \kappa^2 \Delta^2 - 2\kappa\alpha\Delta + \alpha^2 \}^{-1} s \rangle \quad (6.5)$$

and hence an upper bound on the mixing efficiency is

$$(M_0^\alpha)^2 \leq \frac{\langle s \{ \kappa^2 \Delta^2 - 2\kappa\alpha\Delta + \alpha^2 \}^{-1} s \rangle}{\langle s \{ \kappa^2 \Delta^2 - (U^2/d)\Delta - 2\kappa\alpha\Delta + \alpha^2 \}^{-1} s \rangle}. \quad (6.6)$$

In Fourier space this is

$$(M_0^\alpha)^2 \leq \left( \sum_{\mathbf{k}} \frac{|\hat{s}(\mathbf{k})|^2}{\kappa^2 k^4 + 2\kappa\alpha k^2 + \alpha^2} \right) \left( \sum_{\mathbf{k}} \frac{|\hat{s}(\mathbf{k})|^2}{\kappa^2 k^4 + (U^2/d + \kappa\alpha)k^2 + \alpha^2} \right)^{-1}. \quad (6.7)$$

Clearly, the upper bound depends on the Fourier transform of the source function  $s$ . In the next section we investigate the high- $Pe$  behaviour of  $M_0^\alpha$  for a measure valued source. To determine the high- $Pe$  behaviour we approximate the sums by integrals and take the limit of infinite volume noting that the  $\alpha$  term allows the integrals to converge:

$$(M_0^\alpha)^2 \lesssim \left( \int_0^\infty \frac{|\hat{s}(\mathbf{k})|^2 k^{d-1} d^d k}{k^4 + 2\kappa\alpha k^2 + \alpha^2} \right) \left( \int_0^\infty \frac{|\hat{s}(\mathbf{k})|^2 k^{d-1} d^d k}{\kappa^2 k^4 + (\frac{U^2}{d} + 2\kappa\alpha)k^2 + \alpha^2} \right)^{-1}. \quad (6.8)$$

Letting  $\xi = \mathbf{k}\sqrt{\frac{\kappa}{\alpha}}$  in  $d$ -D we obtain:

$$(M_0^\alpha)^2 \lesssim \left( \int_0^\infty \frac{|\hat{s}(\xi\sqrt{\frac{\alpha}{\kappa}})|^2 \xi^{d-1} d\xi}{\xi^4 + 2\xi^2 + 1} \right) \left( \int_0^\infty \frac{|\hat{s}(\xi\sqrt{\frac{\alpha}{\kappa}})|^2 \xi^{d-1} d\xi}{\xi^4 + (\tilde{Pe}^2 + 2)\xi^2 + 1} \right)^{-1}. \quad (6.9)$$

where  $\tilde{Pe} := U\ell/\kappa = U/\sqrt{\kappa\alpha}$  where  $\ell = \sqrt{\kappa/\alpha}$  is the diffusive length scale i.e. the distance travelled by diffusion before decay.

### 6.1.1 Delta function source

Consider a delta function point source so that there is a separation of scales between the source and the stirring field. In  $d = 2$  we obtain

$$\int_0^\infty \frac{\xi d\xi}{\xi^4 + 2\xi^2 + 1} = \frac{1}{2}, \quad \int_0^\infty \frac{\xi d\xi}{\xi^4 + (\tilde{Pe}^2 + 2)\xi^2 + 1} = \frac{1}{2} \frac{\ln \frac{\xi_1}{\xi_2}}{\xi_1 - \xi_2} \quad (6.10)$$

where  $\xi_1$  and  $\xi_2$  are the solutions of the quartic equation:

$$\xi_{1,2} = \frac{(\tilde{Pe}^2 + 2) \mp \tilde{Pe}^2 \sqrt{1 + 4\tilde{Pe}^{-2}}}{2} = \frac{(\tilde{Pe}^2 + 2) \mp \tilde{Pe}^2 (1 + 2\tilde{Pe}^{-2} - 2\tilde{Pe}^{-4} + \dots)}{2}.$$

In the large  $\tilde{Pe}$  limit the mixing efficiency is

$$M_0^\alpha \lesssim \frac{\tilde{Pe}}{2 \ln \tilde{Pe}}. \quad (6.11)$$

Note this is a distinct scaling as regards  $\kappa$  compared to the problem with  $\alpha = 0$ . An efficiency scaling of  $\sim \tilde{\mathcal{P}}e$  implies the eddy diffusivity would scale as  $\sqrt{\kappa}$ . For  $d = 3$  we have

$$\int_0^\infty \frac{\xi^2 d\xi}{\xi^4 + 2\xi^2 + 1} = \frac{\pi}{4}, \quad \int_0^\infty \frac{\xi^2 d\xi}{\xi^4 + (\tilde{\mathcal{P}}e^2 + 2)\xi^2 + 1} = \frac{\pi}{2} \frac{\sqrt{\xi_1} - \sqrt{\xi_2}}{\xi_1 - \xi_2}. \quad (6.12)$$

In this limit the mixing efficiency is

$$M_0^\alpha \lesssim \frac{1}{2} \sqrt{\tilde{\mathcal{P}}e}. \quad (6.13)$$

Thus for  $d = 3$  we also have an anomalous scaling in  $\tilde{\mathcal{P}}e$  with an equivalent diffusivity proportional to  $\kappa^{1/4}$ .

## 6.2 Bounds on the gradient variance

For the gradient variance the optimization problem is

$$\langle |\nabla\theta|^2 \rangle \geq \max_{\varphi} \min_{\tilde{\theta}} \{ \langle |\nabla\tilde{\theta}|^2 \rangle \mid \langle \nabla\tilde{\theta} \cdot (\mathbf{u}\varphi + \kappa\nabla\varphi - \alpha(\nabla(\Delta^{-1}\varphi))) \rangle = -\langle \varphi s \rangle \} \quad (6.14)$$

upon applying the Cauchy-Schwarz inequality (we will revisit this approach at the end of this section) we obtain

$$\langle |\nabla\theta|^2 \rangle \geq \max_{\varphi} \leq \frac{\langle s\varphi \rangle^2}{\langle |\kappa\nabla\varphi + \varphi\mathbf{u} - \alpha(\nabla(\Delta^{-1}\varphi))|^2 \rangle}. \quad (6.15)$$

Under the assumptions of HIT

$$\langle |\kappa\nabla\varphi + \mathbf{u}\varphi - \alpha(\nabla(\Delta^{-1}\varphi))|^2 \rangle = \langle \kappa^2 |\nabla\varphi|^2 + |\bar{\mathbf{u}}|^2 \varphi^2 + \alpha^2 |\nabla(\Delta^{-1}\varphi)|^2 - 2\kappa\alpha \nabla(\Delta^{-1}\varphi) \cdot \nabla\varphi \rangle \quad (6.16)$$

The solution to the optimization problem is (after some algebra)

$$\langle |\nabla\theta|^2 \rangle \geq \langle s\mathcal{M}_1^\alpha s \rangle \quad (6.17)$$

where  $\mathcal{M}_1^\alpha := (-\kappa^2\Delta + \frac{U^2}{d} + 2\kappa\alpha + \alpha^2\Delta^{-1})^{-1}$ . Given the gradient variance in the absence of stirring we obtain a bound on the small scale mixing efficiency

$$(M_1^\alpha)^2 \leq \frac{\langle s\{-\kappa^2\Delta + 2\kappa\alpha + \alpha^2\Delta^{-1}\}^{-1}s \rangle}{\langle s\{-\kappa^2\Delta + \frac{U^2}{d} + 2\kappa\alpha + \alpha^2\Delta^{-1}\}^{-1}s \rangle}. \quad (6.18)$$

In Fourier space the bound is expressed as

$$(M_1^\alpha)^2 \leq \left( \sum_{\mathbf{k}} \frac{|\hat{s}(\mathbf{k})|^2}{k^2(\kappa + \frac{\alpha}{k^2})^2} \right) \left( \sum_{\mathbf{k}} \frac{|\hat{s}(\mathbf{k})|^2}{k^2(\kappa + \frac{\alpha}{k^2})^2 + \frac{U^2}{d}} \right)^{-1}. \quad (6.19)$$

Once again since we are interested in the high- $\tilde{\mathcal{P}}e$  behaviour we approximate the sums by integrals

$$(M_1^\alpha)^2 \lesssim \left( \int_0^\infty \frac{k^2 |\hat{s}(\mathbf{k})|^2 k^{d-1} d^d k}{\kappa^2 k^4 + 2\kappa\alpha k^2 + \alpha^2} \right) \left( \int_0^\infty \frac{k^2 |\hat{s}(\mathbf{k})|^2 k^{d-1} d^d k}{\kappa^2 k^4 + (\frac{U^2}{d} + 2\kappa\alpha) k^2 + \alpha^2} \right)^{-1}. \quad (6.20)$$



Letting  $\xi = \mathbf{k}\sqrt{\frac{\kappa}{\alpha}}$  in  $d$ -D we obtain:

$$(M_1^\alpha)^2 \lesssim \left( \int_0^\infty \frac{\xi^2 |\hat{s}(\xi\sqrt{\frac{\alpha}{\kappa}})|^2 \xi^{d-1} d\xi}{\xi^4 + 2\xi^2 + 1} \right) \left( \int_0^\infty \frac{\xi^2 |\hat{s}(\xi\sqrt{\frac{\alpha}{\kappa}})|^2 \xi^{d-1} d\xi}{\xi^4 + (\frac{U^2}{\kappa\alpha} + 2)\xi^2 + 1} \right)^{-1}. \quad (6.21)$$

Clearly the convergence of these integrals depends on the property of the source. We must have for  $\alpha \neq 0$ ,  $s \in H^{-1}$ .

Here we re-examine the application of the Cauchy-Schwarz inequality. The analysis can be improved by evaluating

$$\min_{\tilde{\theta}} \{ \langle |\nabla \tilde{\theta}|^2 \rangle \mid \langle \nabla \tilde{\theta} \cdot (\mathbf{u}\varphi + \kappa \nabla \varphi - \alpha(\nabla(\Delta^{-1}\varphi))) \rangle = \langle \varphi s \rangle \} \quad (6.22)$$

with functional  $\mathcal{F} := \langle \frac{1}{2} |\nabla \tilde{\theta}|^2 + \lambda(\mathbf{v} \cdot \nabla \tilde{\theta} - \varphi s) \rangle$  where  $\mathbf{v} = \mathbf{u}\varphi + \kappa \nabla \varphi - \alpha(\nabla(\Delta^{-1}\varphi))$ . As in section 3 the solution to the optimization problem depends on the two-point correlation statistics of the velocity field

$$\langle |\nabla \theta|^2 \rangle = \frac{\langle \varphi s \rangle^2}{\langle (\nabla \cdot \mathbf{v})(-\Delta^{-1}) \nabla \cdot \mathbf{v} \rangle} \geq \frac{\langle \varphi s \rangle^2}{\langle |\mathbf{v}|^2 \rangle}. \quad (6.23)$$

In the case of HIT a strict application of the Cauchy-Schwarz inequality yields the optimal bound. Again this analysis does not apply to either the variance or inverse gradient variance.

### 6.2.1 Delta function source

As for the case of  $\alpha = 0$ , a  $\delta$ -function or white noise source will cause the integrals in (6.21) to diverge and thus  $M_1^\alpha = 1$  for  $\delta$ -function sources.

### 6.3 Bounds on the inverse gradient variance

For the inverse gradient variance the variational problem is

$$\langle |\nabla^{-1} \theta|^2 \rangle \geq \max_{\varphi} \min_{\tilde{\theta}} \{ \langle |\nabla^{-1} \tilde{\theta}|^2 \rangle \mid \langle \nabla \Delta^{-1} \tilde{\theta} \cdot \nabla(\mathbf{u} \cdot \nabla \varphi + \kappa \Delta \varphi - \alpha \varphi) \rangle = \langle \varphi s \rangle \} \quad (6.24)$$

upon applying the Cauchy-Schwarz inequality

$$\langle |\nabla^{-1} \theta|^2 \rangle \geq \max_{\varphi} \frac{\langle \varphi s \rangle^2}{\langle |\nabla(\mathbf{u} \cdot \nabla \varphi + \kappa \Delta \varphi - \alpha \varphi)|^2 \rangle}. \quad (6.25)$$

Under the HIT assumptions

$$\langle |\nabla(\mathbf{u} \cdot \nabla \varphi + \kappa \Delta \varphi - \alpha \varphi)|^2 \rangle = \langle \kappa |\Delta \nabla \varphi|^2 + \frac{\Gamma^2}{d} |\nabla \varphi|^2 + \frac{U^2}{d} (\Delta \varphi)^2 + \alpha^2 |\nabla \varphi|^2 - 2\alpha \kappa \nabla \varphi \cdot \Delta \nabla \varphi \rangle.$$

The solution to the optimization problem is (after some algebra)

$$\langle |\nabla^{-1} \theta|^2 \rangle \geq \langle s \mathcal{M}_{-1}^\alpha s \rangle \quad (6.26)$$

where  $\mathcal{M}_{-1}^\alpha := (\kappa^2 \Delta^3 - (\Gamma^2/d)\Delta + (U^2/d)\Delta^2 + 2\kappa\alpha\Delta^2 - \alpha^2\Delta)^{-1}$ . Given the inverse gradient variance in the absence of stirring we obtain a bound on the large scale mixing efficiency

$$(M_1^\alpha)^2 \leq \frac{\langle s \{ \kappa^2 \Delta^3 + 2\kappa\alpha\Delta^2 - \alpha^2\Delta \}^{-1} s \rangle}{\langle s \{ \kappa^2 \Delta^3 - \frac{\Gamma^2}{d}\Delta + \frac{U^2}{d}\Delta^2 + 2\kappa\alpha\Delta^2 - \alpha^2\Delta \}^{-1} s \rangle}. \quad (6.27)$$

In Fourier space the bound is expressed as

$$(M_{-1}^\alpha)^2 \leq \left( \sum_{\mathbf{k}} \frac{|\hat{s}(\mathbf{k})|^2}{\kappa^2 k^6 + 2\kappa\alpha k^4 + \alpha^2 k^2} \right) \left( \sum_{\mathbf{k}} \frac{|\hat{s}(\mathbf{k})|^2}{\kappa^2 k^6 + (\frac{U^2}{d} + 2\kappa\alpha)k^4 + (\alpha^2 + \Gamma^2)k^2} \right)^{-1}. \quad (6.28)$$

Once again since we are interested in the high  $\tilde{P}e$  behaviour we approximate the sums by integrals

$$(M_{-1}^\alpha)^2 \lesssim \left( \int_0^\infty \frac{|\hat{s}(k)|^2 k^{d-1} d^d k}{k^2(\kappa^2 k^4 + 2\kappa\alpha k^2 + \alpha^2)} \right) \left( \int_0^\infty \frac{k^2 |\hat{s}(k)|^2 k^{d-1} d^d k}{k^2(\kappa^2 k^4 + (\frac{U^2}{d} + 2\kappa\alpha)k^2 + \alpha^2 + \Gamma^2)} \right)^{-1} \quad (6.29)$$

Letting  $\xi = \mathbf{k}\sqrt{\frac{\kappa}{\alpha}}$  in  $d=D$  we obtain:

$$(M_{-1}^\alpha)^2 \lesssim \left( \int_0^\infty \frac{|\hat{s}(\xi\sqrt{\frac{\alpha}{\kappa}})|^2 \xi^{d-1} d^d \xi}{\xi^2(\xi^4 + 2\xi^2 + 1)} \right) \left( \int_0^\infty \frac{|\hat{s}(\xi\sqrt{\frac{\alpha}{\kappa}})|^2 \xi^{d-1} d^d \xi}{\xi^2(\xi^4 + (\tilde{P}e^2 + 2)\xi^2 + 1 + \frac{\Gamma^2}{\alpha^2})} \right)^{-1}. \quad (6.30)$$

In  $d=2$  there may be an infra-red divergence problem. The integrals converge if  $|\hat{s}(\mathbf{k})|^2 = f(k)$  if  $f(k) \approx k^\beta$  where  $\beta > 0$  (we require mean zero sources as to prevent blow up at 0). This is our only restriction on the source. How the Fourier transform decays as  $\mathbf{k} \rightarrow 0$  indicates the large scale structure of the source. Exploration of the bound's behavior remains a task for the future.

### 6.3.1 Delta function sources

In  $d=3$

$$\int_0^\infty \frac{d\xi}{\xi^4 + 2\xi^2 + 1} = \frac{\pi}{4}, \quad \int_0^\infty \frac{d\xi}{\xi^4 + (\tilde{P}e^2 + 2)\xi^2 + 1 + \frac{\Gamma^2}{\alpha^2}} = \frac{\pi}{2} \frac{\sqrt{\xi_1} - \sqrt{\xi_2}}{(\xi_2 - \xi_1)\sqrt{\xi_1\xi_2}} \quad (6.31)$$

where  $\xi_1$  and  $\xi_2$  are roots of the quadratic equation:

$$\xi_{1,2} = (\tilde{P}e^2 + 2) \pm \sqrt{\tilde{P}e^4 + 4\tilde{P}e^2 - \frac{4\Gamma^2}{\alpha^2}}. \quad (6.32)$$

In the limit of  $\tilde{P}e \gg 1$  we get to leading order in  $\tilde{P}e$ :

$$\xi_1 = \tilde{P}e^2 - \tilde{P}e^2 \sqrt{1 - 4\frac{\Gamma^2\kappa^2}{U^4}} \approx \frac{1}{2} \frac{\tilde{P}e^2}{Pe_\lambda^2}, \quad \xi_2 \approx 2\tilde{P}e, \quad \xi_1 - \xi_2 \approx \tilde{P}e^2 \sqrt{1 - 4\frac{\Gamma^2\kappa^2}{U^4}} \quad (6.33)$$

hence

$$\int_0^\infty \frac{d\xi}{\xi^4 + (\frac{U^2}{\kappa\alpha} + 2)\xi^2 + 1 + \frac{\Gamma^2}{\alpha^2}} = \frac{\pi}{2} \frac{\sqrt{2\tilde{P}e}}{2\tilde{P}e \sqrt{\frac{\tilde{P}e^3}{Pe_\lambda^2}}} \quad (6.34)$$

where  $Pe_\lambda = U\lambda/\kappa$  where  $\lambda$  (a Péclet number using a length scale of the velocity field). Hence

$$(M_{-1}^\alpha)^2 \leq \frac{Pe^2}{Pe_\lambda} \quad (6.35)$$

note that the efficiency may be larger when there is stronger shear  $\Gamma \gg 1$  as was found in the case of  $\alpha = 0$ . Table 2 summarizes the high- $Pe$  scaling for HIT in the case of  $\alpha = 0$  and  $\alpha \neq 0$  for a  $\delta$ -function source.

$\alpha = 0$	$d=2$	$d=3$	$\alpha \neq 0$	$d=2$	$d=3$
$M_1$	1	1	$M_1^\alpha$	1	1
$M_0$	$\frac{Pe}{\sqrt{\log Pe}}$	$\sqrt{Pe}$	$M_0^\alpha$	$\frac{\tilde{Pe}}{\sqrt{\log \tilde{Pe}}}$	$\sqrt{\tilde{Pe}}$
$M_{-1}$	$\frac{PeL}{\lambda\sqrt{\log(1+L^2/\lambda^2)}}$	$Pe\sqrt{\frac{L}{\lambda}}$	$M_{-1}^\alpha$	*	$\frac{\tilde{Pe}}{\sqrt{Pe_\lambda}}$

Table 2. High- $Pe$  scalings of the multiscale mixing efficiencies for a  $\delta$ -function source. The  $\star$  indicates that the scaling depends on  $|\hat{s}(\mathbf{k})|$  as  $k \rightarrow 0$  and  $\tilde{Pe} := U\ell/\kappa = U/\sqrt{\kappa\alpha}$  where  $\ell = \sqrt{\kappa/\alpha}$ .

## 7 Conclusions and future work

Multiscale mixing efficiencies are susceptible to rigorous analysis. Upper (lower) bounds on multiscale mixing efficiencies were obtained from lower (upper) bounds on appropriately weighted variances. Bounds on large-scale mixing are sensitive to small-scale stirring. The bounds can be sharp (sweeping flows on the torus). Furthermore, the efficiency of some complex random flows can be understood via simple steady state scalings. Finally, the inclusion of a decay term in the advection-diffusion equation introduces new features namely new high- $Pe$  dependences of the equivalent diffusivity on the molecular diffusivity.

The current analysis has only answered some of the questions posed in the introduction hence, there are exciting problems that are the subject of current and future investigation. For example, extending the current analysis to bounded domains (sphere etc.) and formulating an appropriately constrained variational problem for the optimal (source specific) stirring field.

## 8 Acknowledgements

Special thanks to both Charlie Doering and Jean-Luc Thiffeault for their guidance and insight. Specifically to Charlie for many early morning discussions and to J-L for many Coffee O. discussions. I could not have asked for better advisors. Thanks also to Matt "Digger" Finn and his unending computer wizardry, to Bill Young for a number of insightful discussions, and to Paola Cessi for helpful boundary layer advice. I would also like to thank MEM for helpful discussions and comments on the report. Finally I would like to thank my fellow fellows: Alex, Aya, Ben, Dani, Inga, John, Khachik, Marcus, Ravi, and Walter for all of those magic moments. I cannot imagine a better way to spend the summer.

## References

- [1] P. V. DANCKWERTS, The definition and measurement of some characteristics of mixtures, *Appl. Sci. Res.*, 3 (1952), pp. 279–296.
- [2] C. R. DOERING AND C. FOIAS, Energy dissipation in body-forced turbulence, *J. Fluid Mech.*, 467 (2002), pp. 289–306.
- [3] R. T. PIERREHUMBERT, On tracer microstructure in the large-eddy dominated regime, *Chaos Solitons and Fractals*, 4 (1994), pp. 1091–1110.
- [4] S. PLASTING AND W. R. YOUNG, Bounds on scalar variance. *J. Fluid Mech.* preprint, 2005.

- [5] J.-L. THIFFEAULT, C. R. DOERING, AND J. D. GIBBON, A bound on mixing efficiency for the advection-diffusion equation, *J. Fluid Mech.*, 521 (2004), pp. 105–114.
- [6] W. R. YOUNG, Stirring and Mixing. *Proc. 1999 Summer Program in Geophysical Fluid Dynamics* (ed. J.-L. Thiffeault and C. Pasquero). Woods Hole Oceanographic Institution, Woods Hole, MA, USA. <http://gfd.whoi.edu/proceedings/1999/PDFvol11999.html>, 1999.

# Transport in cellular flows from the viewpoint of stochastic differential equations

W. Pauls

July 18, 2006

## 1 Introduction

The behaviour of passive scalar tracers moving in a prescribed velocity field can be described using two equivalent formulations: (i) the passive scalar equation which in two dimensions can be written as

$$\partial_t \theta + \nabla^\perp H \cdot \nabla \theta = \varepsilon \Delta \theta, \quad (1)$$

(ii) probabilistic description in terms of stochastic differential equations

$$dX_t = -\partial_y H(X_t, Y_t) + \sqrt{2\varepsilon} dW_t^{(x)}; \quad (2a)$$

$$dY_t = \partial_x H(X_t, Y_t) + \sqrt{2\varepsilon} dW_t^{(y)}. \quad (2b)$$

Here  $H(x, y)$  is a periodic stream function defined in such a way that the velocity field is given by  $\mathbf{u} = (-\partial_y H, \partial_x H)$ . In what follows the velocity field will always be deterministic and time-independent.

The subject of study in this report is the asymptotic behaviour of the process (2) in the limit  $\varepsilon \rightarrow 0$ . In fact, this question can be analyzed using the passive scalar equation (1). Here the homogenization technique from the theory of partial differential equations is applied which gives a description of the behaviour of solutions of (1) on large scales, see [1]. Separating slow and fast variables and performing a multiscale analysis one obtains the effective diffusion equation for the evolution of  $\theta$  on large scales

$$\partial_t \theta = \nabla \cdot D_\varepsilon^* \nabla \theta. \quad (3)$$

The effective diffusivity  $D_\varepsilon^*$  is a constant matrix given by the following expression

$$D_\varepsilon^*(\mathbf{e}) = \langle (\varepsilon \mathbb{I} + \Psi)(\nabla \chi + \mathbf{e}) \cdot \mathbf{e} \rangle, \quad (4)$$

where  $\chi$  is the solution of the so called cell problem

$$\nabla \cdot [(\varepsilon \mathbb{I} + \Psi)(\nabla \chi + \mathbf{e})] = 0. \quad (5)$$

Note that equation (5) has to be solved in the domain of periodicity of the streamfunction  $H(x, y)$ . One class of flows for which the cell problem (5) is amenable to analysis is a special

case of the well known ABC flow, namely the case  $A = 1$ ,  $C = 0$ . The streamfunction is of the form

$$H(x, y) = \frac{1+B}{2} \cos x \cos y + \frac{1-B}{2} \sin x \sin y. \quad (6)$$

The case  $B = 1$  has been treated in [2] using boundary layer techniques where it was shown that  $D_\varepsilon^* = O(\sqrt{\varepsilon})$ . More precisely, the boundary layer analysis is performed in a boundary layer of width  $O(\sqrt{\varepsilon})$  which forms at the boundaries of the impermeable cells of the underlying velocity field  $\nabla^\perp H(x, y)$ . Heuristically, since the amount of the tracer transported along the boundary layer is proportional to its area, the effective diffusivity has to be proportional to  $\sqrt{\varepsilon}$ . An analytical solution of the cell problem in the boundary layer approximation was given in [3] using Wiener–Hopf technique. In the case  $B < 1$  the effective diffusivity is anisotropic and as has been shown in [4] the effective diffusivity across the streamlines is of order  $O(\varepsilon)$  while along the stream lines of the flow it is of order  $O(1/\varepsilon)$ .

The large-scale picture obtained by the homogenization approach as presented above does not give any information on the microscale structure of the diffusion processes happening in the flow. However, small scales do play a major role in the form of boundary layers which is typical for diffusion processes at high Péclet numbers.

In principle, stochastic differential equations (2) allow us to describe the diffusion of particles in much more detail. But how much information can we obtain on the limit  $\varepsilon \rightarrow 0$ ? A standard approximating technique in this framework is the so called Wentzell–Freidlin method. It describes the behaviour of randomly perturbed Hamiltonian systems on large time scales at high Péclet numbers by means of continuous diffusion processes on graphs, as is explained in Section 2. A priori, this technique works only for Hamiltonians  $H(x, y)$  such that  $H(x, y) \rightarrow +\infty$  when  $|(x, y)| \rightarrow \infty$  and does not allow for existence of heteroclinic orbits.

If we try to apply this technique to the case of unbounded cellular flow with  $H(x, y)$  given by (6) we arrive at a paradox. Namely, the transition from one cell to another will happen instantaneously no matter how large the spatial separation between the cells. Furthermore, the characteristic time scale of diffusion will be of order  $O(1/\varepsilon)$  which contradicts the results obtained in the homogenization framework where the characteristic time scale is of order  $O(1/\sqrt{\varepsilon})$ .

However, for bounded domains this technique works for sufficiently small  $\varepsilon$  such that  $1/\sqrt{\varepsilon}$  is much larger than the domain size (therefore it is not in contradiction to the homogenization method). This gives us an indication that the Wentzell–Freidlin method remains locally valid. In fact, it fails on unbounded domains because of its global structure which is determined by the method of “gluing” together single cells.

Actually, by changing the “gluing” prescription between the processes obtained in single cells we can make the Wentzell–Freidlin approach to be consistent with the results given by the homogenization. The main ingredient here is the conservation of probability: the probability current going out of a cell has to be matched with the probability current across the cell boundary (dominated by the boundary layer effects) into the neighbouring cells.

The structure of the present report is as follows: Section 2 is entirely devoted to the Wentzell–Freidlin technique. In Section 2.1 we explain the averaging principle for a single cell and its deterministic background. Asymptotics  $\varepsilon \rightarrow 0$  of solutions to (2) on bounded domains is described in Section 2.2. In Section 2.3 we discuss some simple models for

diffusion in unbounded cellular flows. Furthermore, using results of numerical simulations we argue that the approximating process on unbounded domain will be discontinuous. In Section 3 we outline the procedure for obtaining this process and state the result. Possible applications are discussed in Section 4.

## 2 Random perturbation of Hamiltonian systems

For small values of  $\varepsilon$  (i.e. for high Péclet numbers) equations (2) describe small random perturbation of the deterministic system

$$\dot{x} = -\partial_y H(x(t), y(t)), \quad (7a)$$

$$\dot{y} = \partial_x H(x(t), y(t)) \quad (7b)$$

which represents the limiting case  $\varepsilon = 0$ . Heuristically one would expect that the behaviour of solutions to (2) in the limit  $\varepsilon \rightarrow 0$  is to a large extent determined by the deterministic solutions, i.e. solutions of (7). The simplest ansatz of this type consists in making a perturbative expansion of solutions to (2) in powers of  $\sqrt{\varepsilon}$  around the deterministic solutions<sup>1</sup>, see [11, 12]. However, this approximation is of little use when we want to study long-time behaviour. Indeed, it works well only for a finite period of time (which also remains true when we include higher-order terms) and does not take into account the separation into fast and slow variables. The latter point is of special interest to us because the underlying structure of the deterministic case (to be described in Section 2.1.1) is at the basis of the approximating method discussed in Section 2.1.

### 2.1 Slow-scale motion inside a cell

#### 2.1.1 Case of vanishing viscosity

In terms of (1) the deterministic case corresponds to the passive scalar equation with vanishing viscosity  $\varepsilon = 0$

$$\partial_t \theta + \nabla^\perp H \cdot \nabla \theta = 0 \quad (8)$$

and an initial condition  $\theta_0$ . The characteristics of this equation are given by (7) so that the solutions of the Cauchy problem for equation (8) can be constructed in terms of the one-parametric flow (by taking the inverse Lagrangian mapping) generated by the velocity field  $\nabla^\perp H(x, y)$ , see e.g. [5].

If we choose the streamfunction (6), then equations (7) can be solved explicitly, see [6]. For the particular case  $B = 1$  the solution is given in terms of Jacobi elliptic functions (see [7])

$$x(t, h) = \arcsin \left( \sqrt{1 - h^2} \operatorname{sn}(t, \sqrt{1 - h^2}) \right), \quad (9a)$$

$$y(t, h) = \arcsin \left( \sqrt{1 - h^2} \operatorname{cd}(t, \sqrt{1 - h^2}) \right), \quad (9b)$$

---

<sup>1</sup>In the case of the Hamiltonian (6) with  $B = 1$  the explicit solution of (7) given by (9) allows us to compute analytically the first order term in the expansion. It turns out to be a stochastic integral the integrand being a complicated expression involving Jacobi elliptic, hyperbolic and logarithmic functions.

where  $x(0) = 0$  and  $H(x, y) = h$  is kept fixed along a trajectory. Obviously, a particle initially located in one particular cell will stay inside this cell. The period of motion along a level line with  $H(x, y) = h$  is given by a complete elliptic integral  $4K(\sqrt{1-h^2})$ . For the special case  $h = 0$  the equation of motion along the separatrix can be solved in terms of elementary functions

$$x(t, 0) = 2 \arctan e^t - \frac{\pi}{2}, \quad (10)$$

where the initial conditions are specified as  $x(0, 0) = 0$  and  $y(0, 0) = \pi/2$ . Note that in the deterministic case it takes an infinite time to reach the equilibrium point  $(\pi/2, \pi/2)$ .

It is crucial for the following analysis that we can interpret (7) as a Hamiltonian system with one degree of freedom by identifying  $(x, y) \rightarrow (p, q)$ . The streamfunction  $H(x, y) \rightarrow H(p, q)$  is then identified with the Hamiltonian of the system. As usually, an action variable  $I(h)$  can be introduced as

$$I(h) = \frac{2}{\pi} \int_h^1 K(\sqrt{1-h'^2}) dh', \quad (11)$$

which is equal to the area inclosed inside the orbit  $H(p, q) = h$  divided by  $2\pi$ , see [8].

### 2.1.2 Effective Fokker-Planck equation

We will first study the behaviour of solutions to (2) with  $H$  given by (6) with  $B = 1$  such that the particle is staying inside one cell. The typical technique for analyzing the evolution of slow variables of such a system subject to small random perturbations is the technique of averaging out the fast variables. Then an effective evolution equation for slow variables inside a cell is obtained in a way similar to the analysis of small perturbations in classical mechanics [8]. In the framework of stochastic differential equations this ansatz was introduced by Wentzell and Freidlin, see [12] and references therein. For analogous consideration in the framework of passive scalar equation see [17].

In our case the averaging principle can be briefly summarized as follows: Inside the cell the deterministic system (7) can be described in terms of motion on invariant tori. We parametrize these tori by the values of  $H(x, y) = h$ . In the perturbed system (at least for small perturbations) particles will still rotate rapidly along the tori, however they will slowly drift across the tori. To describe this slow drift we calculate  $dH(X_t, Y_t)$ . Using Itô's formula we obtain

$$dH(X_t, Y_t) = \sqrt{2\varepsilon} \nabla H(X_t, Y_t) \cdot d\mathbf{W}_t + \varepsilon \Delta H(X_t, Y_t) dt, \quad (12)$$

where  $d\mathbf{W}_t = (dW_t^{(x)}, dW_t^{(y)})$  is the two-dimensional Brownian motion. Of course, we cannot evaluate the terms  $\nabla H(X_t, Y_t) \cdot d\mathbf{W}_t$  and  $\Delta H(X_t, Y_t)$  explicitly without solving equations (2). However, using the integral form of (12)

$$H(X_t, Y_t) = H(X_0, Y_0) + \sqrt{2\varepsilon} \int_0^t \nabla H(X_s, Y_s) \cdot d\mathbf{W}_s + \varepsilon \int_0^t \Delta H(X_s, Y_s) ds, \quad (13)$$



we see that because of the smallness of the perturbation (i) the second integral is approximately equal<sup>2</sup> to the integral  $\int_0^t \langle \Delta H \rangle_{H=h}(X_s, Y_s) ds$ , where

$$\langle \Delta H \rangle_{H=h} = \left( \oint \frac{dl}{|\nabla H|} \right)^{-1} \oint \frac{\Delta H}{|\nabla H|} dl \quad (14)$$

and the integrals are taken over the level set  $\{(x, y) : H(x, y) = h\}$ . Moreover, (ii) the first (stochastic) integral in (13) can be represented as

$$\int_0^t \nabla H(X_s, Y_s) \cdot d\mathbf{W}_s = W \left( \int_0^t |\nabla H(X_s, Y_s)|^2 ds \right), \quad (15)$$

where  $W(\cdot)$  is a one-dimensional Wiener process. With the same argument as before  $\int_0^t |\nabla H(X_s, Y_s)|^2 ds$  can be approximated by the ergodic average of  $|\nabla H|^2$

$$\langle |\nabla H|^2 \rangle_{H=h} = \left( \oint \frac{dl}{|\nabla H|} \right)^{-1} \oint |\nabla H| dl \quad (16)$$

The obtained effective diffusion process is most conveniently formulated in terms of an effective Fokker-Planck equation with time rescaled as  $t \rightarrow \varepsilon t$

$$\partial_t p = \partial_h^2 (A(h)p) - \partial_h (B(h)p) \quad (17)$$

The coefficients  $A(h)$  and  $B(h)$  given by

$$A(h) = \langle |\nabla H|^2 \rangle_{H=h}, \quad B(h) = \langle \Delta H \rangle_{H=h}. \quad (18)$$

In the case of  $H$  given by (6) with  $B = 1$  these coefficients can be calculated explicitly using formulas (9)

$$A(h) = 2 \frac{E(\sqrt{1-h^2})}{K(\sqrt{1-h^2})} - 2h^2, \quad B(h) = -2h. \quad (19)$$

Here  $K(\cdot)$  and  $E(\cdot)$  are complete elliptic integrals of the first and second kind, see [7, 15]. Note that instead of the Hamiltonian we could have used the action variable (11). Indeed, the formulation in terms of the action turns out to be very convenient for generalization of the averaging principle to higher dimensions.

## 2.2 Construction of an approximating Feller process (Wentzell-Freidlin technique)

In this subsection we study asymptotic behaviour of solutions of (2) constrained to a bounded domain (with periodic boundary conditions) approximating them by a process with essentially one-dimensional state space. We have seen that (17) specifies completely the behaviour of the system up to the first exit time out of a cell. Once having left the cell after some transitional time (during which it will stay in some neighbourhood of the boundary of the original cell) the particle will again slowly diffuse, either in the original cell or in another neighbouring cell.

---

<sup>2</sup>This is due to the averaging principle.

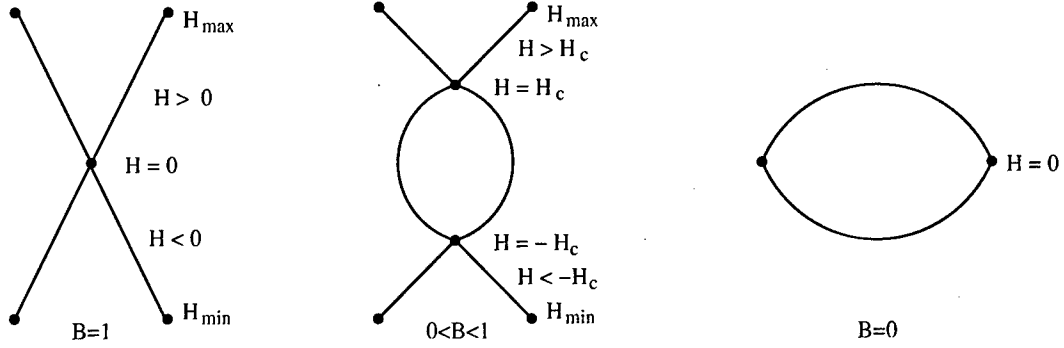


Figure 1: Reeb graphs of the flow (6) for the cases  $B = 1$ ,  $0 < B < 1$  and  $B = 0$  on the domain of width  $2\pi \times 2\pi$ .

To describe the transition phase of the particle from one cell to another we need to (i) give a geometrical description of the way in which the cells are connected to each other, (ii) analyze in detail the behaviour of the diffusion process during this transition.

The geometrical description is given using the topological notion of a Reeb graph of  $H(x, y)$  [9]. For a general Hamiltonian  $H(x, y)$  it is defined in the following way: Let  $(x_c, y_c)$  be a critical point, i.e. a point such that  $\nabla H(x_c, y_c) = 0$ . Then each connected component of the level set  $H^{-1}(H(x_c, y_c))$  is identified with a vertex. The points on the edges which connect the vertices are identified with connected components of the noncritical level sets  $H^{-1}(H(x, y))$ . Figure 1 shows the Reeb graphs of  $H(x, y)$  given by (6) on the domain  $[0, 2\pi] \times [0, 2\pi]$  for the cases  $B = 0$ ,  $0 < B < 1$ ,  $B = 1$ . Note that in the case  $B = 1$  the edges of the Reeb graph correspond to the interior of the cells.

The geometrical description above suggests that the appropriate state space of the process approximating the solutions of (2) is the Reeb graph  $\Gamma$  of the Hamiltonian  $H(x, y)$  with edges denoted by  $e_i$  and vertices denoted by  $O_k$ . In side each edge  $e_i$  the approximating process is governed by the evolution equation of the type (17)

$$\partial_t p_i = \partial_h^2 (A_i(h) p_i) - \partial_h (B_i(h) p_i) \quad (20)$$

To determine the process completely we have to specify the boundary conditions at the ends of each edge, “gluing” the edges together in a consistent way. This “gluing” procedure determines the behaviour of the process during the passage through the vertices of the graph. Physically it describes transitions of a particle from one cell to another.

Specifying boundary conditions for a stochastic process is in general a quite delicate point. One possibility to specify the boundary conditions is to require the approximating process to have “nice” mathematical properties.<sup>3</sup> In [13] all possible continuous Markov processes with Feller property<sup>4</sup> on graphs were described such that the diffusion inside an edge is governed by a second order elliptic operator (which can possibly depend on the edge). In our case the elliptic operator is given by the right hand side of (20). Furthermore, at each edge the sum of the incoming probability currents has to vanish. This leads to the

<sup>3</sup>As we shall see later, this requirement is not always consistent with the behaviour of solutions of (2).

<sup>4</sup>This means that in course of time continuous distributions of probability remain continuous.

following boundary conditions at a vertex  $O_k$

$$\sum_{i: e_i \sim O_k} J_i(O_k) = 0, \quad p_i(O_k) = p_j(O_k), \quad i, j : e_i \sim O_k, e_j \sim O_k \quad (21)$$

where  $e_i, e_j \sim O_k$  denote the edges incident to the vertex  $O_k$ .

Thus, the approximating technique (in the following referred to as Wentzell–Freidlin technique) consists in (i) approximating the solutions of (2) inside of the cell by (17), (ii) gluing together the cells by matching continuously the probability distributions at the boundaries of the cells.

In the case of the Hamiltonian specified by (6) on bounded domain we expect that the process on the graph approximates well solutions of (2). Furthermore, similarly to [12] a particle spends a zero time (on the time scale  $\varepsilon t$ ) at the vertex. From this follows that once the particle reaches the cell (edge) boundary, it can hop instantaneously to any other cell. Furthermore, the behaviour of the process after it reaches the vertex does not depend on its prehistory, i.e. on the edge it came from. Thus, the transition probability from one edge to another is not dependent on their spatial separation. Note that for  $\varepsilon \rightarrow 0$  this does not result in any contradiction, because of the very long relevant time  $O(1/\varepsilon) \rightarrow \infty$ .

Altogether the Wentzell–Freidlin technique yields the following picture for advection of passive scalar in a bounded domain: Let us chose an initial coondition which corresponds to the passive scalar being concentrated in the center of a cell at  $t = 0$ . Then, as time goes on, the passive scalar will slowly (i.e. on time scale  $O(1/\varepsilon)$ ) diffuse untill it reaches the cell boundary. As soon as it reaches the boundary it will very quickly (instantaneously on time scale  $O(1/\varepsilon)$ ) spread across the domain along the network of separatrices. After this the passive scalar will penetrate the cells on slow time scale  $O(1/\varepsilon)$  untill the stationary distribution is established.

However, the above implies immediately that the Wentzell-freidlin technique cannot be applied in the unbounded case. Indeed, it would state that a transition from one edge to another happens instantaneously, no matter how large the spatial distance. It can also be readily seen from the structure of the Reeb graph corresponding to the unbounded case. Indeed, in this case the Reeb graph consists of one vertex with infinitely many incoming vertices.

### 2.3 Diffusion in cellular flows: unbounded case

As we have seen previously, the knowledge of the behaviour of solutions to (2) in the vicinity of the cell boundaries is of crucial importance. To describe this behaviour one has to take into account events such as a particle crossing of a separatrice and going to another cell. Qualitatively, we can discribe them as follows: We artificially separate the cells by channels (which play the role of the boundary layers along the separatrices) to take into account the transport along the boundaries. Let  $\delta(\varepsilon)$  be the width of the channel. The motion of a particle consists of two types of events: (i) slow motion across streamlines inside the cells with typical time spent inside a cell  $t_{\text{cell}} = O(1/\varepsilon)$  and mean square displacement  $O(\varepsilon^0)$ ; (ii) fast transport in the channels with velocity of order  $O(\varepsilon^0)$  and time spent inside the

channel  $O(\delta^2/\varepsilon)$ . The effective diffusion is given by

$$\kappa_{\text{eff}} = O\left(\frac{\langle X^2 \rangle_{\text{channel}}}{t_{\text{cell}}}\right) = O(\delta^2) \quad (22)$$

Setting  $\delta(\varepsilon) = \varepsilon^{\frac{1}{4}}$  we obtain  $\kappa_{\text{eff}} = O(\sqrt{\varepsilon})$ . However, the width of the channel is something that we have to insert by hand into this model. Furthermore, for solution of the cell problem the width of the boundary layer is usually assumed to be  $\sqrt{\varepsilon}$ . Nevertheless, this simple model is usefull because it gives an additional intuition about the nature of diffusion in the cellular flow. Indeed, numerical simulations of (2) show long flights along the cell boundaries interrupted by trapping of the particle inside the cells, see Fig. 2.

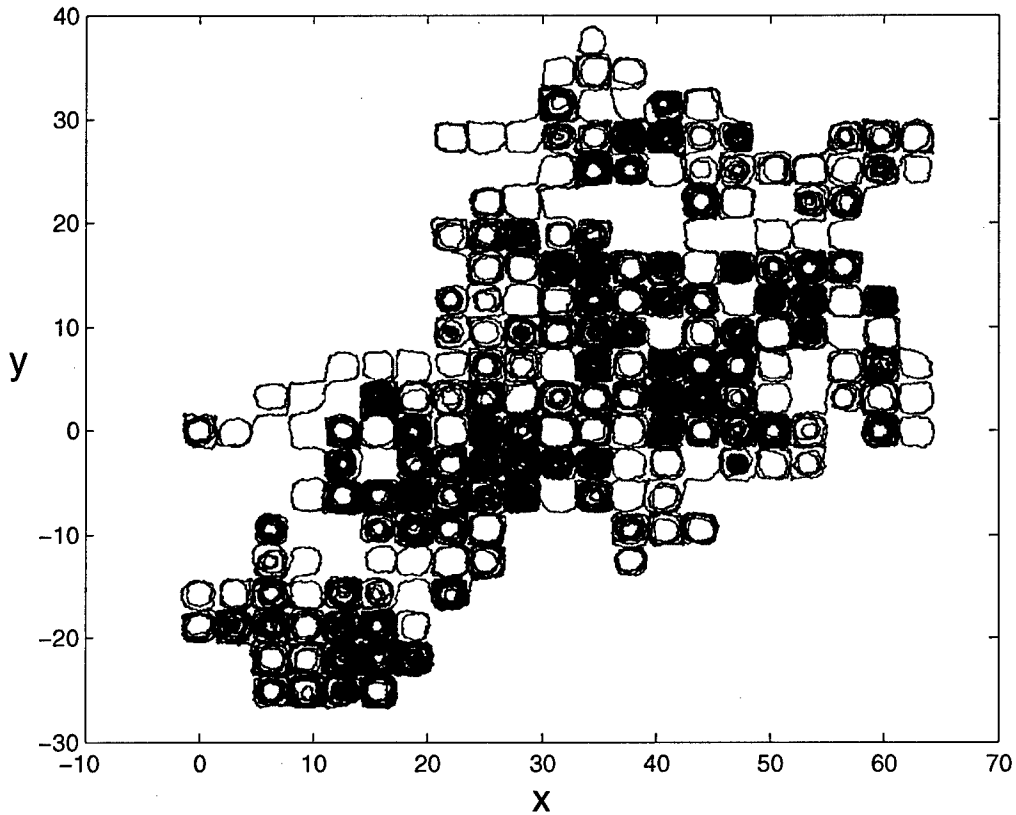


Figure 2: Random motion of a Brownian particle the cellular flow  $B = 1$ .

During the excursions the stochastique motion can be described by a very simple one-dimensional model

$$d\Theta_t = |\cos \Theta_t| + \sqrt{2\varepsilon} dW_t, \quad (23)$$

where  $\theta \in [0, 4\pi]$ . The backward Kolmogorov equation is given by

$$\partial_t p + |\cos \theta| \partial_\theta p = \varepsilon \partial_\theta^2 p. \quad (24)$$

Solutions<sup>5</sup> are most easily found by writing the drift  $|\cos \Theta|$  as the derivative of the following continuous potential

$$V(\theta) = \begin{cases} -4k - \sin \theta & \text{for } x \in [-\frac{\pi}{2} + 2k\pi, \frac{\pi}{2} + 2k\pi]; \\ -2(2k+1) + \sin \theta & \text{for } x \in [-\frac{\pi}{2} + (2k+1)\pi, \frac{\pi}{2} + (2k+1)\pi], \end{cases} \quad (25)$$

such that  $|\cos \theta| = -\partial_\theta V(\theta)$ . Note that this potential contains two parts: a periodic part  $V_0(\theta)$  with period  $\pi$  and a tilting force  $F = \frac{2}{\pi}$ . Obviously, the function  $V_0(\theta) = V(\theta) + \theta F$  satisfies  $V_0(\theta + \pi) = V_0(\theta)$ . Stationary distributions are easily found which allows to determine the mean velocity and the effective diffusion

$$\langle v \rangle = \lim_{t \rightarrow \infty} \frac{\mathbb{E}[\Theta_t]}{t} \quad D = \lim_{t \rightarrow \infty} \frac{\mathbb{E}[\Theta_t^2] - (\mathbb{E}[\Theta_t])^2}{2t} \quad (26)$$

It turns out that the mean velocity does not vanish and the effective diffusion is proportional to  $1/\epsilon$ , see [22]. The behaviour of the diffusion process in the neighbourhood of the cell boundaries has been studied in [14] using boundary layer asymptotics. It turns out that the time a particle spends in a cell is of order  $O(\epsilon)$ .

Note that events (i) and (ii) have two different time scales: (i) is on time scale  $O(1/\sqrt{\epsilon})$  while (ii) is on time scale  $O(1/\epsilon)$ . A similar situation has been discussed in [18] for effective diffusion along a pipe with semiinfinite pipes branching off the main pipe. The fast motion happens inside the main pipe while trapping occurs inside the side branches.

Since the stochastic motion of a particle inside of the unbounded cellular flow is a mixture of random walk on the lattice of cells (jump process) and slow diffusion inside the cells (continuous process) we cannot expect the Wentzell-Freidlin technique to hold on unbounded domains. Indeed, as Fig. 3 shows, in numerical simulations of diffusion of passive tracer on the cellular flow (6) we find high gradients of the passive scalar across the cell boundaries.

### 3 Approximating process with jumps

In this section we propose a generalization of Wentzell-Freidlin method to the case of unbounded domains. The main idea is to give up the mathematical condition of continuity of the process at the vertices of the Reeb graph which in the previous paragraph has been shown to inconsistent and allow for processes which can have jumps at vertices. The continuity condition has to be replaced by another condition which takes into account processes happening at the separatrices analyzing them more carefully than it has been done in Section 2.2.

We begin by outlining the procedure which can be used for obtaining the approximating process on the domain  $\mathbb{R}^2$ . We label each cell by a two-dimensional integer vector  $(n_1, n_2) \in \mathbb{Z}^2$ . The effective evolution equation inside each cell is given by

$$\partial_{\epsilon t} p_{(n_1, n_2)} = \partial_h^2 (A(h)p_{(n_1, n_2)}) - \partial_h (B(h)p_{(n_1, n_2)}) \quad (27)$$

Consider now, analogously to [20] a water-pipe network  $\Omega_N^\epsilon = \{(x, y) \in \Omega : |H(x, y)| \leq N\sqrt{\epsilon}\}$  around the separatrices. The corresponding water-pipe approximation is

$$\epsilon \Delta \theta_N^\epsilon - \nabla^\perp H \cdot \nabla \theta_N^\epsilon = 0, \quad (x, y) \in \Omega_N^\epsilon, \quad (28)$$

---

<sup>5</sup>Stochastic equations with periodic drift are intensively studied in [21].

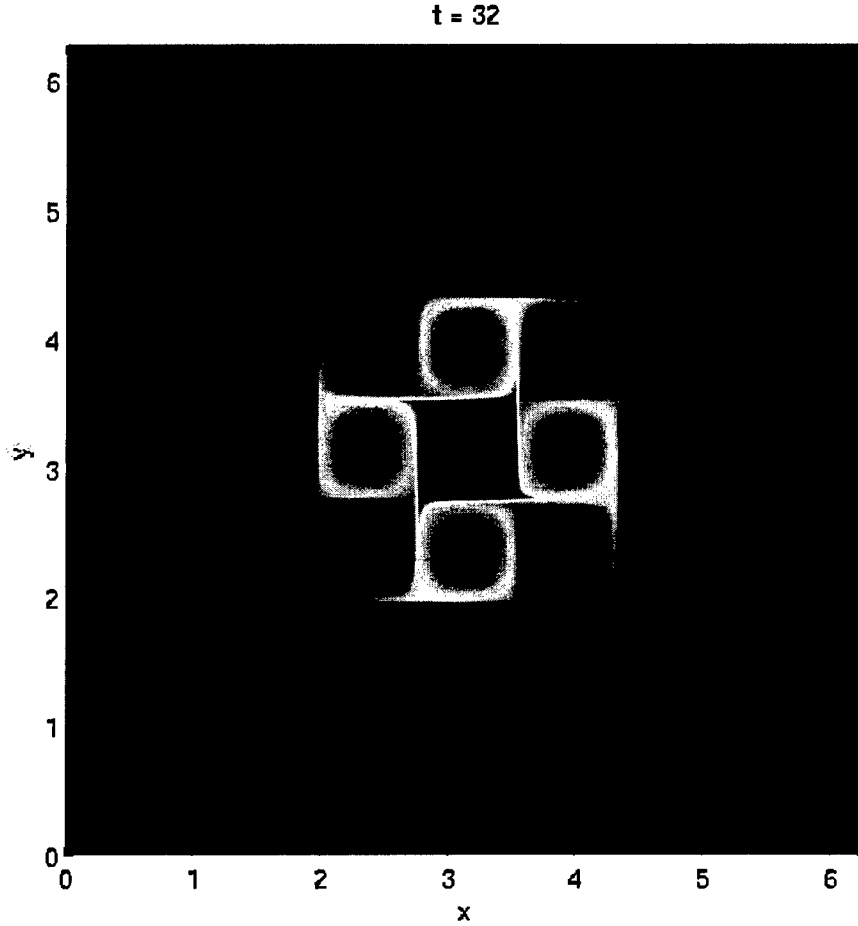


Figure 3: Diffusion in the cellular flow given by (6) with  $B = 1$  for  $\varepsilon = 0.0009765625$  at  $t = 32$ .

however, instead of zero gradient von Neumann boundary conditions at the level set

$$\mathcal{L}_{(n_1, n_2)}(N\sqrt{\varepsilon}) = \{(x, y) \in \Omega : |H(x, y)| = N\sqrt{\varepsilon}, (x, y) \text{ lies in the cell } (n_1, n_2)\} \quad (29)$$

used in [20], we introduce the following conditions

$$\frac{\partial \theta_N^\varepsilon}{\partial \mathbf{n}} = (D\theta)_{(n_1, n_2)}, \quad (x, y) \in \mathcal{L}_{(n_1, n_2)}(N\sqrt{\varepsilon}). \quad (30)$$

The two descriptions, in the interior of the cells and at the cell boundary, have to be glued together. It is here that the conservation of probability enters. We have to match probability current leaving the edge with the probability current entering the water-pipe network. This gives the equation

$$\oint_{\mathcal{L}_k(N\sqrt{\varepsilon})} (D\theta)_k dl = \varepsilon [B(h)p_{(n_1, n_2)}(h) - \partial_h (A(h)p_{(n_1, n_2)})]_{h=N\sqrt{\varepsilon}}. \quad (31)$$

The expression on the right hand side is just the probability current entering the boundary of the cell.

Now we turn to description of the approximating process. First of all, in order to describe the transport from one cell to another in the asymptotics  $\varepsilon \rightarrow 0$  we find it convenient to consider the network of lines connecting the neighbouring cells which is in fact a network dual to the water-pipe network. In our case of  $H(x, y)$  given by (6) with  $B = 1$  it is just the two-dimensional lattice  $\mathbb{Z}^2$ . At each vertex of this network we specify a function  $f_{(n_1, n_2)}(t)$ . This function serves as a boundary condition for the effective Fokker-Planck equation (27) (with the original time) in the cell  $(n_1, n_2)$ . For a particle the probability of leaving this cell through the boundary adjacent to one of the neighbouring cell, e.g. the cell  $(n_1, n_2 + 1)$  is proportional to  $f_{(n_1, n_2+1)} - f_{(n_1, n_2)}$ . Therefore the discontinuous part of the process is governed by the Laplace lattice operator on the lattice  $\mathbb{Z}^2$

$$\Delta_{\mathbb{Z}^2} f_{(n_1, n_2)}(t) = f_{(n_1+1, n_2)}(t) + f_{(n_1-1, n_2)}(t) + f_{(n_1, n_2+1)}(t) + f_{(n_1, n_2-1)}(t) - 4f_{(n_1, n_2)}(t) \quad (32)$$

The evolution equation for  $f_{(n_1, n_2)}(t)$  is then given by

$$\frac{d}{dt} f_{(n_1, n_2)} + \frac{d}{dt} \int p_{(n_1, n_2)}(h) dh = \Delta_{\mathbb{Z}^2} f_{(n_1, n_2)} \quad (33)$$

In this way we obtain a coupled system of equations which yield the complete description of the approximating process.<sup>6</sup>

## 4 Discussion

The generalization of the Wentzell-Freidlin technique proposed in the previous paragraph is easily generalized to the cases of nonperiodic cellular flows. In fact, it suffices to replace the Laplace operator on  $\mathbb{Z}^2$  by the Laplace operator on the network (graph) dual to the network of separatrices of the original flow. Of course, the spectral properties of the graph Laplacian then depend strongly on the topological structure of the dual network. Therefore the cellular structure of the flow can nontrivially influence the solutions of (33).

One application of the Wentzell-Freidlin technique is connected to the study of reaction-diffusion equations. However, as has been stated in [10], in its usual formulation it is not applicable without any restrictions. The generalized form of this technique proposed in the report seems to be suitable to a wider range of applications, including nonperiodic cellular flows.

## 5 Acknowledgements

I would like to thank E. Vanden Eijnden, G. Papanicolaou, W. Young and J.-L. Thiffeault for helping me in my work on this project. Many thanks to G. Veronis and C. Doering for softball coaching. And of course, I would like to thank all fellows for the wonderful summer we spent together.

---

<sup>6</sup>In fact, analogous constructions were discussed in [19, 18].

## References

- [1] G. Papanicolaou, GFD lecture series, 2005.
- [2] S. Childress, Alpha-effect in flux ropes and sheets, *Physics of the Earth and Planetary Interior* **20**, pp. 172–180, 1979.
- [3] A. Soward, Fast dynamo action in a steady flow, *Journal of Fluid Mechanics* **180**, pp. 267–295, 1987.
- [4] S. Childress and A. Soward, *Journal of Fluid Mechanics* **180**, pp. 267–295, 1987.
- [5] V. I. Arnold, *Geometric Methods in the Theory of Ordinary Differential Equations*, Springer-Verlag, 1983.
- [6] T. Dombre, U. Frisch, J. Green, M. Hénon, A. Mehr and A. Soward, Chaotic streamlines in the ABC flows, *Journal of Fluid Mechanics* **167**, pp. 353–391, 1986.
- [7] M. Abramowitz and I. Stegun, *Handbook of Mathematical Functions*, Dover Publications, 1965.
- [8] V. I. Arnold, *Mathematical Methods of Classical Mechanics*, Springer-Verlag, 1997.
- [9] G. Reeb, Sur les points singuliers d’une forme de Pfaff complètement intégrable ou d’une fonction numérique, *Compte Rendus de l’Académie des Sciences* **222**, pp. 847–849, 1946.
- [10] A. Fannjiang, A. Kiselev and L. Ryzhik, Quenching of reaction by cellular flows, Arxiv preprint math.AP/0505654, 2005.
- [11] C. W. Gardiner, *Handbook of Stochastic Methods*, Springer-Verlag, 1983.
- [12] M. I. Freidlin and A. D. Wentzell, *Random perturbations of dynamical systems*, second edition, Springer-Verlag, 1998.
- [13] M. I. Freidlin and A. D. Wentzell, Diffusion process on graphs and the averaging principle, *Annals of Probability* **21**, pp. 2215–2245, 1993.
- [14] L. Korolov, Random perturbations of 2-dimensional Hamiltonian flows, *Probability Theory and Related Fields* **129**, pp. 37–62, 2004.
- [15] I. S. Gradshteyn and I. M. Ryzhik, *Tables of Integrals, Series and Products*, Academic, New York, 1980.
- [16] A. Fannjiang and G. Papanicolaou, Convection enhanced diffusion for periodic flows, *SIAM Journal on Applied Mathematics* **54**, pp. 333–408, 1994.
- [17] P. B. Rhines and W. R. Young, How rapidly is a passive scalar mixed within closed streamlines, *Journal of Fluid Mechanics* **133**, pp. 133–145, 1983.
- [18] W. R. Young, Arrested shear dispersion and other models of anomalous diffusion, *Journal of Fluid Mechanics* **193**, pp. 129–149, 1988.



- [19] W. Young, A. Pumir and Y. Pomeau, Anomalous diffusion of tracer in convection rolls, *Physics of Fluids* **1**, pp. 462–469, 1989.
- [20] A. Novikov, G. Papanicolaou and L. Ryzhik, Boundary layers for cellular flows at high Péclet numbers,
- [21] H. Risken, *The Fokker-Planck Equation*, Springer-Verlag, 1989.
- [22] P. Reimann, C. Van den Broeck, H. Linke, P. Hänggi, J. M. Rubi, and A. Pérez-Madrid, Diffusion in tilted periodic potentials: enhancement, universality, and scaling, *Phys. Rev. E* **65**, 031104, 2002.

# Scattering past a cylinder with weak circulation

John Rudge

August 25, 2005

## 1 Introduction

Wave phenomena arise in a wide variety of geophysical problems. Indeed, in this year's principal lectures a main focus was the modelling of waves in the ocean. It was in this context that ray tracing and the geometrical theory of diffraction were introduced.

An important distinguishing feature of waves in the atmosphere and the ocean is that they propagate through a fluid, and that fluid is often already in motion. Familiar examples include the propagation of acoustic waves in the atmosphere in the presence of winds, or gravity waves in the ocean in the presence of currents. Ray tracing has routinely been used to solve such problems, and there is a large amount of current research devoted to understanding these wave-mean interactions.

Diffraction is the apparent bending and spreading of waves when they meet an obstruction. It is a phenomenon not described by ordinary geometric optics. However, an extension to ray tracing called the geometrical theory of diffraction (GTD) can overcome this problem. On the whole GTD has been little applied to wave-mean problems, and the focus of this project is to understand how GTD can be used in the presence of a mean flow.

We consider a new twist on the canonical problem of scattering of a plane wave past a circular cylinder. Scattering past a cylinder is a classical problem with a long history. A good introduction to the ideas behind this work can be found in [5] and in particular the application of GTD to the circular cylinder can be found in [7]. Special functions abound in scattering problems, and [1] is an invaluable source for looking up their properties.

Our problem considers the addition of a weak circulation around the cylinder, which could be motivated by the problem of modelling weak currents around an island. We emphasise here that the circulation is weak as this simplifies matters considerably [3].

The geometry is shown in Figure 1. We let the radius of the circular cylinder be  $a$  and take coordinates centred on the cylinder. We take the plane wave to be incoming from  $+\infty$  on the  $x$ -axis. The cylinder is taken to be impermeable.

## 2 The governing equations

Following [2], we set up our governing equations as those of 2-D compressible gas dynamics, which have as a special case the familiar shallow water equations. The continuity equation

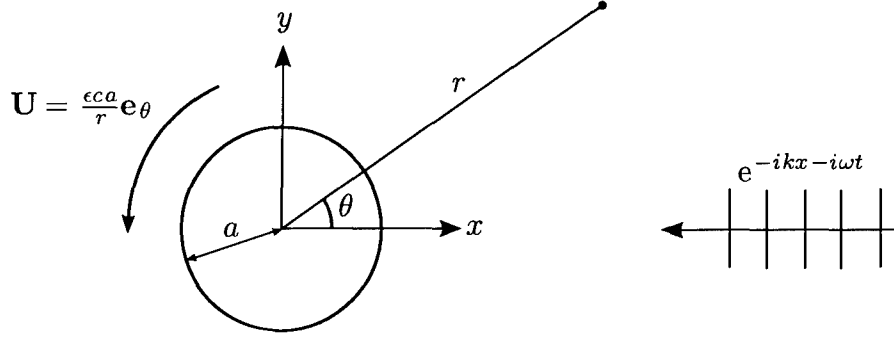


Figure 1: The geometry of the problem. An incoming plane wave is incident on a cylinder with circulation.

is

$$\frac{Dh}{Dt} + h \nabla \cdot \mathbf{u} = 0, \quad (1)$$

and the momentum equation is

$$\frac{D\mathbf{u}}{Dt} + \frac{c_0^2}{\gamma - 1} \nabla (h^{\gamma-1}) = 0. \quad (2)$$

Here  $\mathbf{u}$  is the two dimensional velocity vector of the fluid, and  $h$  is the density of the gas, or the height of the free surface in the case of shallow water. For gas dynamics  $\gamma$  is the polytropic exponent and  $c = c_0 \sqrt{H^{\gamma-1}}$  is the undisturbed sound speed for a gas of uniform density  $H$ . For shallow water  $\gamma = 2$ ,  $c_0^2 = g$  the acceleration due to gravity, and the undisturbed gravity wave speed for a layer of uniform depth  $H$  is  $c = \sqrt{gH}$ . The corresponding equation of state is

$$p \equiv \frac{c_0^2}{\gamma} h^\gamma, \quad (3)$$

where the additive constant has been neglected. The momentum equation can then be written in momentum flux form as

$$\frac{\partial (h\mathbf{u})}{\partial t} + \nabla \cdot (h\mathbf{u}\mathbf{u}) + \nabla p = 0. \quad (4)$$

We will assume that our flow is irrotational,  $\nabla \times \mathbf{u} = 0$ . This implies we can write  $\mathbf{u}$  in terms of a velocity potential,  $\mathbf{u} = \nabla \phi$ . The momentum equation can then be integrated to give Bernoulli's equation

$$\frac{\partial \phi}{\partial t} + \frac{1}{2} |\nabla \phi|^2 + \frac{c_0^2 h^{\gamma-1}}{\gamma - 1} = G(t), \quad (5)$$

where  $G(t)$  is an arbitrary function of time alone. Note that Bernoulli's equation determines  $h$  as a function of the velocity potential  $\phi$ .

### 3 Small amplitude waves

#### 3.1 Time averaged equations

When studying wave phenomena it is often useful to decompose fields into a time averaged mean part and a disturbance part, namely  $\phi = \bar{\phi} + \phi'$ , where  $\overline{(\phi')} = 0$ . Averaging (1), the averaged continuity equation is

$$\nabla \cdot (\bar{h}\bar{\mathbf{u}} + \overline{h'\mathbf{u}'}) = 0, \quad (6)$$

and averaging (5) the averaged Bernoulli equation is

$$c_0^2 \frac{\bar{h}^{\gamma-1}}{\gamma-1} = \text{constant} - \frac{1}{2} \left( |\bar{\mathbf{u}}|^2 + \overline{|\mathbf{u}'|^2} \right). \quad (7)$$

We perform a standard perturbation analysis of the governing equations in terms of a small non-dimensional wave amplitude parameter  $\eta$ . We will assume the  $O(1)$  flow has no disturbance part, and that the  $O(\eta)$  flow has no mean part. For the mean flow we write

$$\bar{\phi} = \Phi + 0 + \eta^2 \bar{\phi}_2 + \dots, \quad (8)$$

$$\bar{h} = H + 0 + \eta^2 \bar{h}_2 + \dots, \quad (9)$$

$$\bar{\mathbf{u}} = \mathbf{U} + 0 + \eta^2 \bar{\mathbf{u}}_2 + \dots. \quad (10)$$

where capital letters are used to denote the  $O(1)$  flow. For the disturbance we write

$$\phi' = 0 + \eta \phi'_1 + \eta^2 \phi'_2 + \dots, \quad (11)$$

$$h' = 0 + \eta h'_1 + \eta^2 h'_2 + \dots, \quad (12)$$

$$\mathbf{u}' = 0 + \eta \mathbf{u}'_1 + \eta^2 \mathbf{u}'_2 + \dots. \quad (13)$$

#### 3.2 Mean flow

The mean flow that we are applying is that of a line vortex:

$$\Phi = \epsilon c a \theta, \quad (14)$$

$$\mathbf{U} = \frac{\epsilon c a}{r} \mathbf{e}_\theta, \quad (15)$$

$$c_0^2 \frac{H^{\gamma-1}}{\gamma-1} = \text{constant} - \frac{\epsilon^2 c^2 a^2}{2r^2}. \quad (16)$$

Here  $\epsilon$  is a non-dimensional parameter determining the strength of the vortex. Throughout this work will neglect terms  $O(\epsilon^2)$ . Hence (16) becomes simply  $H = \text{constant}$ . We have non-dimensionalised on  $c$  the constant undisturbed wave speed, and  $a$  the radius of the cylinder. Note that the maximum mean flow occurs on the cylinder where  $|\mathbf{U}| = \epsilon c$ , so the non-dimensionalisation is such that  $\epsilon$  is a ratio of mean flow speed to wave speed (a Froude/Mach number). The circulation  $\Gamma$  associated with the line vortex is  $\Gamma = 2\pi\epsilon c a$ . Note that the chosen mean flow is incompressible,  $\nabla \cdot \mathbf{U} = 0$ .

### 3.3 Linear waves

The  $O(\eta)$  continuity equation is found from (1) to be

$$\frac{\partial h'_1}{\partial t} + \mathbf{U} \cdot \nabla h'_1 + H \nabla^2 \phi'_1 = 0, \quad (17)$$

where we have used incompressibility of the mean flow, and that  $H$  is constant. The  $O(\eta)$  Bernoulli equation is found from (5) to be

$$h'_1 = \frac{H}{c^2} \left( -\frac{\partial \phi'_1}{\partial t} - \mathbf{U} \cdot \nabla \phi'_1 \right). \quad (18)$$

Combining these equations we find

$$c^2 \nabla^2 \phi'_1 - \frac{\partial^2 \phi'_1}{\partial t^2} - 2\mathbf{U} \cdot \left( \frac{\partial \nabla \phi'_1}{\partial t} \right) - \mathbf{U} \cdot \nabla (\mathbf{U} \cdot \nabla \phi'_1) = 0. \quad (19)$$

Neglecting  $O(\epsilon^2)$  terms this becomes

$$c^2 \nabla^2 \phi'_1 - \frac{\partial^2 \phi'_1}{\partial t^2} - 2\mathbf{U} \cdot \left( \frac{\partial \nabla \phi'_1}{\partial t} \right) = 0, \quad (20)$$

or in polar coordinates

$$c^2 \nabla^2 \phi'_1 - \frac{\partial^2 \phi'_1}{\partial t^2} - 2\frac{\epsilon c a}{r^2} \frac{\partial^2 \phi'_1}{\partial \theta \partial t} = 0. \quad (21)$$

In the case of no mean flow,  $\epsilon = 0$  and this reduces to the familiar wave equation.

We can define the local energy density  $E$  by

$$E = \frac{c^2 h'^2_1}{2H} + \frac{H |\mathbf{u}'_1|^2}{2}. \quad (22)$$

Using equations (17) and (18) the energy equation can be derived:

$$\frac{\partial E}{\partial t} + \nabla \cdot (E\mathbf{U} + c^2 h'_1 \mathbf{u}'_1) = -H \mathbf{u}'_1 \cdot \left( \frac{\nabla \mathbf{U} + \nabla \mathbf{U}^T}{2} \right) \cdot \mathbf{u}'_1. \quad (23)$$

### 3.4 Terms of second order in wave amplitude

On the whole we shall not be concerned with second order terms, but they are important when calculating the force on the cylinder. The quantity of interest is the time averaged pressure

$$\bar{p} = \frac{c_0^2}{\gamma} \overline{h^\gamma} = \frac{c_0^2}{\gamma} H^\gamma + \eta^2 \left( \frac{\gamma-1}{2} c_0^2 H^{\gamma-2} \overline{h_1'^2} + c_0^2 H^{\gamma-1} \overline{h_2} \right) + O(\eta^3). \quad (24)$$

The time averaged Bernoulli equation (7) implies that to second order we have

$$\frac{\gamma-2}{2} c_0^2 H^{\gamma-3} \overline{h_1'^2} + c_0^2 H^{\gamma-2} \overline{h_2} = \text{constant} - \mathbf{U} \cdot \overline{\mathbf{u}_2} - \frac{1}{2} \overline{|\mathbf{u}'_1|^2}. \quad (25)$$

Hence we can rewrite the averaged pressure as

$$\bar{p} = \text{constant} + \eta^2 \left( \frac{c^2}{2H} \overline{h_1'^2} - \frac{H}{2} \overline{|\mathbf{u}_1'|^2} - H \mathbf{U} \cdot \overline{\mathbf{u}_2} \right) + O(\eta^3). \quad (26)$$

Note that without a mean flow (26) gives the  $O(\eta^2)$  pressure purely in terms of first order quantities. With a mean flow,  $\overline{\mathbf{u}_2}$  (a second order term) must also be specified to calculate the pressure. To  $O(\epsilon)$  we have from (18) that

$$h_1'^2 = \frac{H^2}{c^4} \left( \left( \frac{\partial \phi_1'}{\partial t} \right)^2 + 2 \frac{\partial \phi_1'}{\partial t} \mathbf{U} \cdot \nabla \phi_1' \right). \quad (27)$$

Hence the time averaged pressure can be written in terms of the velocity potentials as

$$\bar{p} = \text{constant} + \eta^2 H \left( \frac{1}{2c^2} \overline{\left( \frac{\partial \phi_1'}{\partial t} \right)^2} - \frac{1}{2} \overline{|\nabla \phi_1'|^2} + \frac{1}{c^2} \overline{\frac{\partial \phi_1'}{\partial t} \mathbf{U} \cdot \nabla \phi_1'} - \mathbf{U} \cdot \nabla \overline{\phi_2} \right) + O(\eta^3). \quad (28)$$

The second order term we are interested in is  $\overline{\phi_2}$ , and since its term in the above expression is multiplied by  $\mathbf{U}$  we may neglect  $O(\epsilon)$  terms in its solution. From the time averaged continuity equation (6) we find neglecting  $O(\epsilon)$  terms

$$H \nabla \cdot \overline{\mathbf{u}_2} = -\nabla \cdot \left( \overline{h_1' \mathbf{u}_1'} \right). \quad (29)$$

Now by time averaging the energy equation (23) we find that  $\nabla \cdot \left( \overline{h_1' \mathbf{u}_1'} \right) = O(\epsilon)$ . Hence, the leading order governing equation for  $\overline{\phi_2}$  is simply Laplace's equation  $\nabla^2 \overline{\phi_2} = 0$ .

## 4 Eigenfunction solution

We will seek time harmonic solutions to (20) of the form  $\phi_1'(\mathbf{x}, t) = \psi(\mathbf{x})e^{-i\omega t}$ , where  $\omega$  is a chosen constant angular frequency, and the real part is assumed. (20) then reduces to

$$c^2 \nabla^2 \psi + \omega^2 \psi + 2i\omega \mathbf{U} \cdot \nabla \psi = 0. \quad (30)$$

Let  $k_\infty = \omega/c$ , the constant wavenumber at infinity where the mean flow is absent. Then this can be written as

$$\nabla^2 \psi + k_\infty^2 \psi + 2ik_\infty \frac{\mathbf{U}}{c} \cdot \nabla \psi = 0, \quad (31)$$

or in polar coordinates as

$$\nabla^2 \psi + k_\infty^2 \psi + \frac{2i\epsilon k_\infty a}{r^2} \frac{\partial \psi}{\partial \theta} = 0. \quad (32)$$

which in the case of no mean flow is the familiar Helmholtz equation.

(32) can be solved by separation of variables. Let  $\psi(\mathbf{x}) = R(r)\Theta(\theta)$ . Then

$$r^2 R'' + r R' + (k_\infty^2 r^2 - \lambda^2) R = 0, \quad (33)$$

$$\Theta'' + 2i\epsilon k_\infty a \Theta' + \lambda^2 \Theta = 0. \quad (34)$$

where  $\lambda$  is a constant. These have solutions of the form

$$R(r) = H_{\lambda}^{(1,2)}(k_{\infty}r), \quad (35)$$

$$\Theta(\theta) = e^{i(\pm\lambda - \epsilon k_{\infty}a)\theta}. \quad (36)$$

where  $H_{\nu}^{(1,2)}(z)$  are Hankel functions of the first and second kinds of order  $\nu$ . Since we must have a single valued function of  $\theta$ , we have that  $\lambda = \pm(m + \epsilon k_{\infty}a)$ , where  $m \in \mathbb{Z}$ . Also, since  $H_{-\nu}^{(1,2)}(z) = e^{-\nu\pi i} H_{\nu}^{(1,2)}(z)$ , the eigenfunctions of (32) are thus just  $H_{\tilde{m}}^{(1,2)}(k_{\infty}r) e^{im\theta}$ , where  $\tilde{m} = m + \epsilon k_{\infty}a$ . As we are solving a self adjoint problem these eigenfunctions are orthogonal and we can express the general solution in terms of these eigenfunctions as

$$\psi(r, \theta) = \sum_{m \in \mathbb{Z}} \left( A_m H_{\tilde{m}}^{(1)}(k_{\infty}r) + B_m H_{\tilde{m}}^{(2)}(k_{\infty}r) \right) e^{im\theta} \quad (37)$$

for constants  $A_m, B_m$  to be determined.

#### 4.1 Green's function for a point source

Consider a point source at  $\mathbf{x}_0 = (r_0, \theta_0)$  in polar coordinates. The governing equation for the Green's function  $G(\mathbf{x}, \mathbf{x}_0)$  is

$$\nabla^2 G + k_{\infty}^2 G + \frac{2i\epsilon k_{\infty}a}{r^2} \frac{\partial G}{\partial \theta} = \delta(\mathbf{x} - \mathbf{x}_0). \quad (38)$$

Using the eigenfunction expansion (37) it can be shown that

$$G(\mathbf{x}, \mathbf{x}_0) = \frac{1}{8i} \sum_{m \in \mathbb{Z}} \frac{H_{\tilde{m}}^{(2)}(k_{\infty}r_{\min}) H_{\tilde{m}}'^{(1)}(k_{\infty}a) - H_{\tilde{m}}^{(1)}(k_{\infty}r_{\min}) H_{\tilde{m}}'^{(2)}(k_{\infty}a)}{H_{\tilde{m}}'^{(1)}(k_{\infty}a)} H_{\tilde{m}}^{(1)}(k_{\infty}r_{\max}) e^{im(\theta - \theta_0)}, \quad (39)$$

where  $r_{\max} = \max(r, r_0)$ ,  $r_{\min} = \min(r, r_0)$ . An alternative expression for  $G(\mathbf{x}, \mathbf{x}_0)$ , easier to compute numerically, is

$$G(\mathbf{x}, \mathbf{x}_0) = \frac{1}{4} \sum_{m \in \mathbb{Z}} \frac{J_{\tilde{m}}(k_{\infty}r_{\min}) Y_{\tilde{m}}'(k_{\infty}a) - Y_{\tilde{m}}(k_{\infty}r_{\min}) J_{\tilde{m}}'(k_{\infty}a)}{H_{\tilde{m}}'^{(1)}(k_{\infty}a)} H_{\tilde{m}}^{(1)}(k_{\infty}r_{\max}) e^{im(\theta - \theta_0)}, \quad (40)$$

where  $J_{\nu}(z)$  and  $Y_{\nu}(z)$  are Bessel functions of first and second order respectively.

Note that since the problem is self-adjoint, the Green's function satisfies a reciprocity relation  $G(\mathbf{x}, \mathbf{x}_0) = G^*(\mathbf{x}_0, \mathbf{x})$ , where  $*$  denotes complex conjugation. Since  $G^*(\mathbf{x}, \mathbf{x}_0)$  satisfies

$$\nabla^2 G^* + k_{\infty}^2 G^* - \frac{2i\epsilon k_{\infty}a}{r^2} \frac{\partial G^*}{\partial \theta} = \delta(\mathbf{x} - \mathbf{x}_0), \quad (41)$$

then the reciprocity relation can be simply stated as: the field at  $\mathbf{x}$  due to a point source at  $\mathbf{x}_0$  is the same as the field at  $\mathbf{x}_0$  due to a point source at  $\mathbf{x}$  with the direction of the vortex reversed.

## 4.2 Eigenfunction solution for an incoming plane wave

We want to find the field due to scattering of an incoming plane wave on the cylinder. The potential  $\psi_i$  for a plane wave incident from  $+\infty$  on the  $x$ -axis is

$$\psi_i = e^{-ik_\infty r \cos \theta - i\epsilon k_\infty a \theta}. \quad (42)$$

Note that the above expression satisfies (32) neglecting terms of  $O(\epsilon^2)$ . Note also that this expression has a branch, and so  $\theta$  has to be defined so that  $-\pi < \theta < \pi$ . Unless  $\epsilon k_\infty a$  is an integer,  $\psi_i$  will be discontinuous.  $\psi_i$  can be expanded in terms of Bessel functions as

$$\psi_i = \sum_{m \in \mathbb{Z}} J_{\tilde{m}}(kr) e^{-i\tilde{m}\pi/2} e^{im\theta} \quad (43)$$

$$= \frac{1}{2} \sum_{m \in \mathbb{Z}} \left( H_{\tilde{m}}^{(1)}(k_\infty r) + H_{\tilde{m}}^{(2)}(k_\infty r) \right) e^{-i\tilde{m}\pi/2} e^{im\theta}. \quad (44)$$

To solve the problem of scattering on the cylinder by the incident wave we propose a solution of the form  $\psi = \psi_i + \psi_s$ , where  $\psi_s$  is an outgoing scattered wave of the form

$$\psi_s = \sum_{m \in \mathbb{Z}} A_m H_{\tilde{m}}^{(1)}(k_\infty r) e^{im\theta}. \quad (45)$$

Applying the boundary condition  $\frac{\partial \psi}{\partial r} = 0$  on  $r = a$  yields

$$\psi_s = -\frac{1}{2} \sum_{m \in \mathbb{Z}} \frac{H_{\tilde{m}}^{(1)}(k_\infty a) + H_{\tilde{m}}^{(2)}(k_\infty a)}{H_{\tilde{m}}^{(1)}(k_\infty a)} H_{\tilde{m}}^{(1)}(k_\infty r) e^{-i\tilde{m}\pi/2} e^{im\theta}, \quad (46)$$

$$\psi = \frac{1}{2} \sum_{m \in \mathbb{Z}} \frac{H_{\tilde{m}}^{(2)}(k_\infty r) H_{\tilde{m}}^{(1)}(k_\infty a) - H_{\tilde{m}}^{(1)}(k_\infty r) H_{\tilde{m}}^{(2)}(k_\infty a)}{H_{\tilde{m}}^{(1)}(k_\infty a)} e^{-i\tilde{m}\pi/2} e^{im\theta}. \quad (47)$$

The expression for  $\psi$  can be rewritten as

$$\psi = i \sum_{m \in \mathbb{Z}} \frac{J_{\tilde{m}}(k_\infty r) Y_{\tilde{m}}'(k_\infty a) - Y_{\tilde{m}}(k_\infty r) J_{\tilde{m}}'(k_\infty a)}{H_{\tilde{m}}^{(1)}(k_\infty a)} e^{-i\tilde{m}\pi/2} e^{im\theta} \quad (48)$$

which is easier to compute numerically.

The eigenfunction solutions are useful for plotting for moderate  $k_\infty a$ . However for large  $k_\infty a$  a large number of modes  $m$  must be taken to provide an accurate approximation. Ray tracing overcomes this restriction by providing an asymptotic theory for large  $k_\infty a$ .

## 5 Ray Tracing

Ray tracing can be used to provide an asymptotic solution to (21) for a slowly varying wavetrain embedded in a slowly varying background environment. Let

$$\phi_1' \sim z(\mathbf{x}) e^{i\Theta(\mathbf{x}, t)}, \quad (49)$$



where we will suppose the phase  $\Theta$  is rapidly varying, and the wave amplitude  $z$  slowly varying. The local wavenumber  $\mathbf{k}$  and local frequency  $\omega$  are defined by

$$\mathbf{k} = \nabla \Theta, \quad \omega = -\frac{\partial \Theta}{\partial t}. \quad (50)$$

The standard ray tracing equations are then given in terms of the dispersion relation

$$\omega = \Omega(\mathbf{x}, \mathbf{k}) = ck + \mathbf{U} \cdot \mathbf{k}, \quad (51)$$

where  $k = |\mathbf{k}|$ , as Hamilton's equations

$$\frac{d\mathbf{x}}{dt} = +\frac{\partial \Omega}{\partial \mathbf{k}}, \quad \frac{d\mathbf{k}}{dt} = -\frac{\partial \Omega}{\partial \mathbf{x}}. \quad (52)$$

The ray tracing equations imply that  $d\omega/dt = 0$ , i.e. that absolute frequency is conserved along a ray, and we will consider  $\omega$  a global constant along all rays. The group velocity  $\mathbf{c}_g$  is given by

$$\mathbf{c}_g = \frac{d\mathbf{x}}{dt} = c\hat{\mathbf{k}} + \mathbf{U}, \quad (53)$$

where  $\hat{\mathbf{k}} = \mathbf{k}/k$ . Another important consequence of the ray tracing approximation is the conservation of wave action. Define the intrinsic frequency by  $\tilde{\omega} = ck$ , the frequency of the wave in a frame moving with the fluid. Then the wave action  $A = E/\tilde{\omega}$ , where  $E$  is energy density defined in (22), satisfies

$$\frac{\partial A}{\partial t} + \nabla \cdot (A\mathbf{c}_g) = 0. \quad (54)$$

Note also that the energy density satisfies equipartition in the ray tracing approximation, namely

$$\frac{c^2 \overline{h_1'^2}}{2H} = \frac{H \overline{|\mathbf{u}_1'|^2}}{2}. \quad (55)$$

### 5.1 Consequences of the weak mean flow

For an irrotational mean flow there is a curious result which states that to order  $\epsilon$  the ray paths are straight [3, 6]. However, there is still refraction of the wave due to the  $O(\epsilon)$  variation in  $\mathbf{k}$  given by

$$\mathbf{k} = \mathbf{k}_\infty - k_\infty \frac{\mathbf{U}}{c} = \mathbf{k}_\infty - \frac{\epsilon k_\infty a}{r} \mathbf{e}_\theta, \quad (56)$$

where  $\mathbf{k}_\infty$  is the wavenumber vector at infinity for the ray in question, and  $k_\infty = |\mathbf{k}_\infty|$  (Figure 2).

The phase progression along the ray is given by

$$\Theta = \int \mathbf{k} \cdot d\mathbf{x} = \int (\mathbf{k}_\infty - \epsilon k_\infty a \nabla \theta) \cdot d\mathbf{x} \quad (57)$$

$$= \text{constant} + (\mathbf{k}_\infty \cdot \mathbf{x} - \epsilon k_\infty a \theta) \quad (58)$$

Since  $\mathbf{k}_\infty$  is in the direction of the ray, this can be written as

$$\Theta = \Theta_0 + k_\infty (s - s_0 - \epsilon a(\theta - \theta_0)) \quad (59)$$

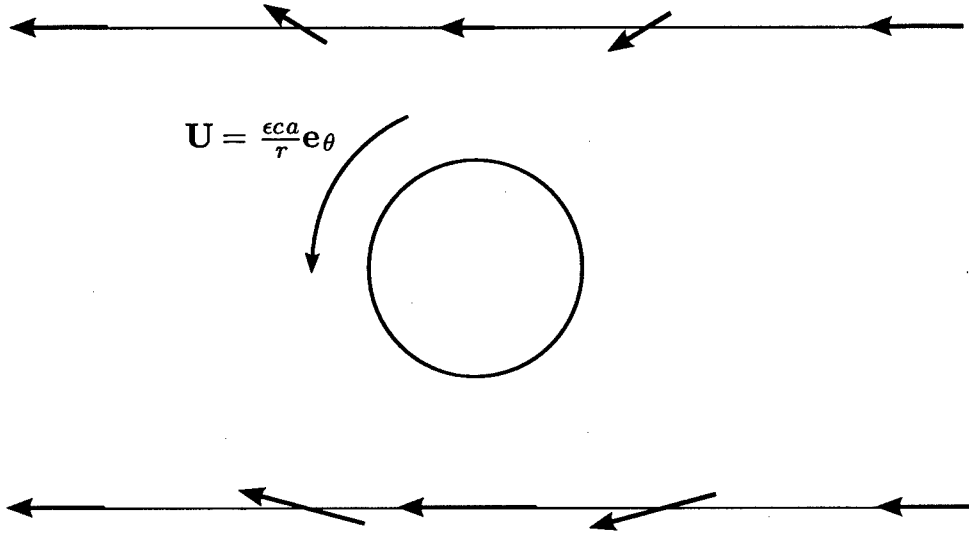


Figure 2: A cartoon of refraction of the incident wave. Two incident rays are shown, one above the cylinder and one below. The arrows along the rays indicate the direction and magnitude of the wavenumber vector at various points along the ray. The rays themselves are straight, but there is refraction from the changing wavenumber vector given by (56). Far away from the cylinder the wavenumber vector aligns with the ray direction. Note that the wavenumber becomes larger as the ray passes the cylinder for the bottom ray, but smaller for the top ray.

where  $s - s_0$  is the distance travelled along the ray, and  $\theta - \theta_0$  is the angular change along the ray.

The wave action is given by

$$A = \frac{E}{\tilde{\omega}} = \frac{Hkz^2}{c}. \quad (60)$$

(54) implies that  $\nabla \cdot (A\mathbf{c}_g) = 0$ , which to  $O(\epsilon)$  implies simply

$$\nabla \cdot (z^2 \mathbf{k}_\infty) = 0. \quad (61)$$

Consider an infinitesimal ray tube  $R$  with ends  $E_1, E_2$  orthogonal to the ray. Note that  $\mathbf{k}_\infty$  is parallel to the sides of the ray tube and orthogonal to its ends. Then by applying the divergence theorem to (61)

$$0 = \int_R \nabla \cdot (z^2 \mathbf{k}_\infty) dV = \int_{E_2} z^2 \mathbf{k}_\infty \cdot \mathbf{n} dS - \int_{E_1} z^2 \mathbf{k}_\infty \cdot \mathbf{n} dS. \quad (62)$$

Since  $\mathbf{k}_\infty \cdot \mathbf{n}$  is a constant this leads to the simple result that  $z^2 dS$  is constant along a ray tube.

For a plane wave incident from  $x = \infty$  it follows that the incident wave field is  $\phi_i = e^{-ik_\infty(x+\epsilon a\theta)}$ , where we have prescribed that the incident wave has unit amplitude.

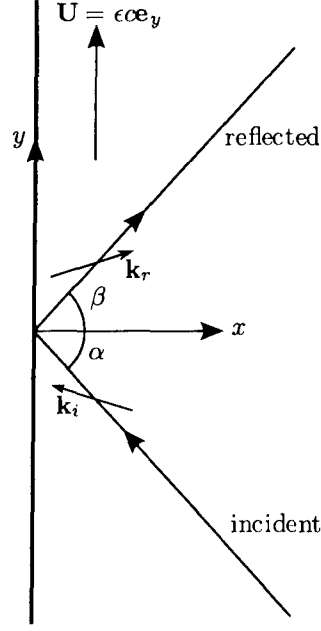


Figure 3: Close up of reflection at the cylinder, where it can be considered locally as a flat wall. Note that the wavenumber vectors (the small arrows) are not in the same direction as the rays as they hit the wall.

## 5.2 Reflected Wave

We now consider reflection of a ray on the cylinder. Locally we can consider the cylinder as a flat wall (Figure 3). Define new coordinates with  $x$  perpendicular to the wall and  $y$  parallel. Let the mean flow along the wall be  $\mathbf{U} = (0, \epsilon c)$ . Let the incident ray hit the wall at  $(0, 0)$  with angle of incidence  $\alpha$  and the reflected ray leave with angle of reflection  $\beta$ . Far from the wall the wavenumber vector of each ray is in the same direction as the ray. Moreover, since  $\omega/c$  is constant everywhere, both incident and reflected wavenumber vectors must have same magnitude far from the wall. Hence we may write

$$\mathbf{k}_\infty^i = k_\infty (-\cos \alpha, \sin \alpha), \quad (63)$$

$$\mathbf{k}_\infty^r = k_\infty (\cos \beta, \sin \beta), \quad (64)$$

for the incident and reflected wavenumbers at infinity respectively. From (56) we see that the incident and reflected wavenumbers at the wall are given by

$$\mathbf{k}_0^i = k_\infty (-\cos \alpha, \sin \alpha - \epsilon), \quad (65)$$

$$\mathbf{k}_0^r = k_\infty (\cos \beta, \sin \beta - \epsilon). \quad (66)$$

Hence locally we have that

$$\psi = \psi^i + \psi^r = z_i e^{i\mathbf{k}_0^i \cdot \mathbf{x} + \Theta_0^i} + z_r e^{i\mathbf{k}_0^r \cdot \mathbf{x} + \Theta_0^r}. \quad (67)$$

Using the boundary condition  $\frac{\partial \psi}{\partial x} = 0$  at  $x = 0$  we find

$$-z_i \cos \alpha + z_r \cos \beta = 0, \quad (68)$$

$$-\Theta_0^i + \Theta_0^r = 0. \quad (69)$$

From this it follows that  $z_i = z_r$  and  $\alpha = \beta$ . Hence the angle of incidence is equal to the angle of reflection, and the reflected wave has the same amplitude and phase as the incident wave as it leaves the wall.

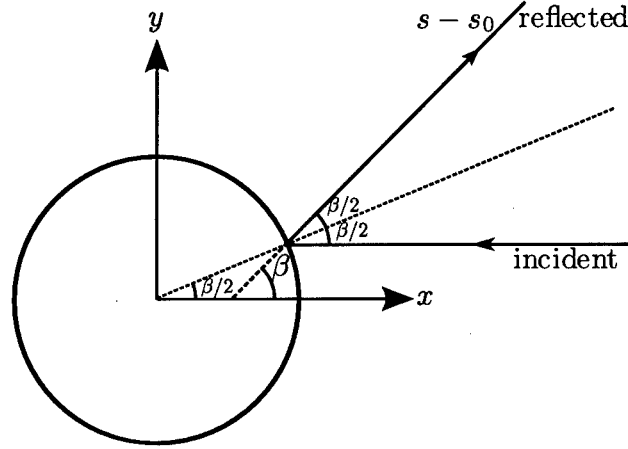


Figure 4: Reflection on the cylinder with an incident ray of angle of incidence  $\beta/2$ .

We now return to the global view (Figure 4). Consider a ray hitting the cylinder at an angle of incidence  $\beta/2$ . Then it hits the cylinder at  $(x, y) = a(\cos \beta/2, \sin \beta/2)$ . At that point the incident ray has phase

$$\Theta_0^i = -k_\infty(a \cos \beta/2 + \epsilon a \beta/2). \quad (70)$$

The phase progression along the reflected ray is given from (59) as

$$\Theta^r = \Theta_0^r + k_\infty(s - s_0 - \epsilon a(\theta - \beta/2)), \quad (71)$$

where  $s$  is the distance along the ray from the focus, and  $s_0$  is the distance from the focus to the point at which the incident ray hits. The focus is the point inside the cylinder from which rays locally spread out from. Geometrically  $s_0$  is found to be  $s_0 = a/2 \cos \beta/2$ . Hence combining (69), (70), and (71) we find the phase progression along the reflected ray as

$$\Theta^r = k_\infty \left( s - \frac{3a}{2} \cos \beta/2 - \epsilon a \theta \right). \quad (72)$$

Rays spread out radially from the focus.  $z^2 dS = \text{constant}$  along a ray tube, and the incident wave has unit amplitude. Hence we have that the amplitude of the reflected ray is given by

$$z_r = \sqrt{\frac{s_0}{s}} = \sqrt{\frac{a \cos \beta/2}{2s}}. \quad (73)$$

Hence the reflected field takes the form

$$\psi_r = \sqrt{\frac{a \cos \beta/2}{2s}} e^{ik_\infty(s - 3a/2 \cos \beta/2 - \epsilon a \theta)}. \quad (74)$$

### 5.3 Diffracted Wave

To calculate the diffracted field we first go back to the problem of a point source rather than an incoming plane wave, as we will find diffraction coefficients by comparison with the Green's function of a point source. We apply the geometrical theory of diffraction (GTD) to the problem (Figure 5).

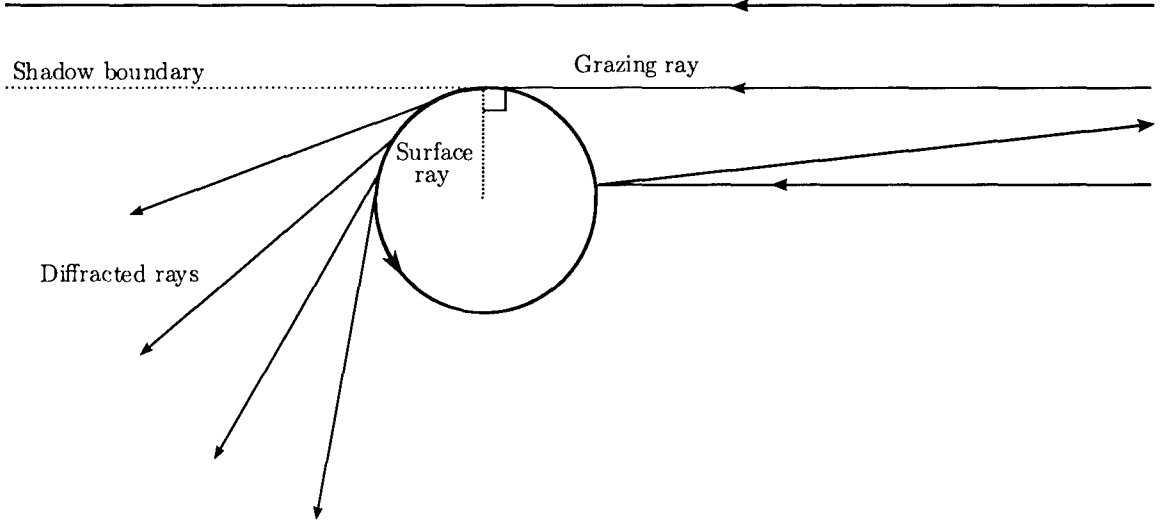


Figure 5: Cartoon of the geometrical theory of diffraction. The grazing ray hits normal to the cylinder and produces a surface ray. This surface ray travels around the cylinder constantly shedding diffracted rays normal to the cylinder.

#### 5.3.1 Incident rays

Consider a point source located at the point  $(r_0, 0)$  in Cartesian coordinates (Figure 6). Consider the two rays which leave this point and hit the cylinder at right angles. Let  $\alpha$  be the angle between the point at which the rays hit the cylinder and the horizontal. Then the wavenumber at infinity for this ray is given by  $\mathbf{k}_\infty = (-\sin \alpha, \pm \cos \alpha)$  where  $+$  is the top ray and  $-$  is the bottom ray. At the points at which the rays hit,  $\mathbf{U} = \pm \epsilon c(-\sin \alpha, \pm \cos \alpha)$ , so that the top ray hits going with the flow, and the bottom ray hits going against the flow. The wavenumber vector at the points the rays hit are then given by (56) as

$$\mathbf{k} = k_\infty(1 \mp \epsilon)(-\sin \alpha, \pm \cos \alpha), \quad (75)$$

or in terms of the unit vector  $\mathbf{e}_\theta$  as

$$\mathbf{k}^{\text{top}} = k_\infty(1 - \epsilon)\mathbf{e}_\theta, \quad \mathbf{k}^{\text{bot}} = -k_\infty(1 + \epsilon)\mathbf{e}_\theta. \quad (76)$$

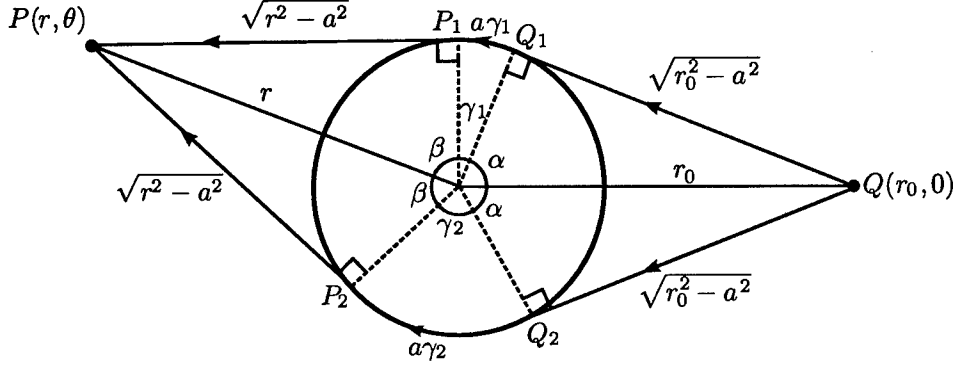


Figure 6: Geometrical theory of diffraction construction for a point source. There is a point source at  $Q$  and we are observing the field at a point  $P$  in the shadow region. Two rays paths are shown, one which involves an anticlockwise surface ray from  $Q_1$  to  $P_1$ , and another which involves a clockwise surface ray from  $Q_2$  to  $P_2$ .

Hence as these incident rays hit the cylinder their wavenumber vectors are tangent to the cylinder. The phase progression along these two rays is given by (59) as

$$\Theta(Q_1) = k_\infty \left( \sqrt{r_0^2 - a^2} - \epsilon a \alpha \right), \quad (77)$$

$$\Theta(Q_2) = k_\infty \left( \sqrt{r_0^2 - a^2} + \epsilon a \alpha \right). \quad (78)$$

The field due to a point source in free space with no mean flow has the form

$$\psi^i = \frac{i}{4} H_0^{(1)}(k_\infty r') \sim \frac{e^{i\pi/4} e^{ik_\infty r'}}{\sqrt{8\pi k_\infty r'}}, \quad (79)$$

where  $r'$  is the distance from the point source. Hence the amplitude of the rays as they hit the cylinder is given by

$$z^i(Q_1) = \frac{e^{i\pi/4}}{\sqrt{8\pi k_\infty \sqrt{r_0^2 - a^2}}}. \quad (80)$$

### 5.3.2 Surface rays

In the geometrical theory of diffraction, a ray hitting the cylinder at right angles causes the production of a surface ray. This ray is constrained to go around the cylinder, and sheds diffracted rays tangent to the cylinder as it progresses around. On the surface ray  $\mathbf{k} = \pm k \mathbf{e}_\theta$ . The surface dispersion relation is then

$$\omega = \Omega_s(\mathbf{x}, \mathbf{k}) = ck(1 \pm \epsilon) \quad (81)$$

which is a constant independent of position. Hence the magnitude of the wavenumber vector is a constant along the surface ray, and depends only on the direction of travel. For a surface

ray travelling with the flow  $\mathbf{k} = k_\infty(1 - \epsilon)\mathbf{e}_\theta$ , and against the flow  $\mathbf{k} = -k_\infty(1 + \epsilon)\mathbf{e}_\theta$ . Thus the corresponding phase progression along the with flow surface ray is

$$\Theta(P_1) = \Theta(Q_1) + k_\infty(1 - \epsilon)a\gamma_1, \quad (82)$$

where  $\gamma_1$  is the angle travelled around the cylinder. Similarly for the against flow surface ray

$$\Theta(P_2) = \Theta(Q_2) + k_\infty(1 + \epsilon)a\gamma_2, \quad (83)$$

where  $\gamma_2$  is measured in the opposite direction.

Using the GTD we assume the amplitude of the surface ray is proportional to the amplitude of the incident ray that created it. Namely, that

$$z^s(Q_1) = d_1(Q_1)z^i(Q_1), \quad (84)$$

where  $d_1(Q_1)$  is a diffraction coefficient depending only on the curvature of the surface. In the GTD it is proposed that the rate of decay of wave action  $A$  travelling along the ray is proportional to the wave action. Namely, that

$$\frac{dA}{d\sigma} = -2\alpha A, \quad (85)$$

where  $\sigma$  is arc length along the ray and  $\alpha$  is a constant depending solely on the curvature of the surface. The wave action of the surface ray is proportional to the square of the amplitude and hence the surface ray decays exponentially in amplitude as

$$z^s(P_1) = e^{-\alpha a \gamma} z^s(Q_1). \quad (86)$$

### 5.3.3 Diffracted rays

As the surface ray travels around the cylinder it sheds diffracted rays. A diffracted ray leaves tangent to the cylinder, so the phase progression along the diffracted rays is given by a similar equation to the incident rays, namely

$$\Theta(P) = \Theta(P_1) + k_\infty \left( \sqrt{r^2 - a^2} - \epsilon a \beta \right), \quad (87)$$

$$\Theta(P) = \Theta(P_1) + k_\infty \left( \sqrt{r^2 - a^2} + \epsilon a \beta \right), \quad (88)$$

where  $\beta$  is the appropriate angular progression after leaving the cylinder. We assume the amplitude of the diffracted ray is proportional to the amplitude of the surface ray which shed it. As diffracted rays leave the cylinder they spread out, and so the amplitude is inversely proportional to the square root of the distance from the cylinder. Hence

$$z^d(P) = \frac{d_2(P_1)}{(k_\infty \sqrt{r^2 - a^2})^{1/2}} z^s(P_1). \quad (89)$$

where  $d_2(P_1)$  is a further diffraction coefficient dependent only on curvature, and  $k_\infty$  is an appropriate non-dimensionalisation factor. By the reciprocity relation of the Green's function we must have that  $d_1(Q_1) = d_2(P_1) = d$ , a constant. However there is still a possibility that the diffraction coefficient  $d$  and decay coefficient  $\alpha$  may depend on the direction of travel around the cylinder, whether going with or against flow. However, when considering an asymptotic evaluation of the Green's function later it will turn out that they do not.

### 5.3.4 The diffracted field

Diffracted rays are simply ordinary geometric optics rays. Combining the phase progression equations we find that for the top travelling rays the phase at  $P$  is

$$\Theta(P) = k_{\infty} \left( \sqrt{r_0^2 - a^2} + a\gamma_1 + \sqrt{r^2 - a^2} - \epsilon a\theta \right), \quad (90)$$

and for the bottom travelling rays the phase at  $P$  is

$$\Theta(P) = k_{\infty} \left( \sqrt{r_0^2 - a^2} + a\gamma_2 + \sqrt{r^2 - a^2} + \epsilon a(2\pi - \theta) \right), \quad (91)$$

where

$$\gamma_1 = \theta - \cos^{-1} \frac{a}{r_0} - \cos^{-1} \frac{a}{r}, \quad (92)$$

$$\gamma_2 = 2\pi - \theta - \cos^{-1} \frac{a}{r_0} - \cos^{-1} \frac{a}{r}. \quad (93)$$

Combining the amplitude equations we find

$$z(P) = \frac{e^{i\pi/4} e^{-\alpha\gamma} d^2}{(8\pi k_{\infty}^2 \sqrt{r_0^2 - a^2} \sqrt{r^2 - a^2})^{1/2}} \quad (94)$$

Hence

$$\begin{aligned} \phi_d(P) = & \frac{e^{i\pi/4} d^2}{(8\pi k_{\infty}^2 \sqrt{r_0^2 - a^2} \sqrt{r^2 - a^2})^{1/2}} e^{ik_{\infty} (\sqrt{r_0^2 - a^2} + \sqrt{r^2 - a^2}) - (ik_{\infty} - \alpha_j)a \left( \cos^{-1} \frac{a}{r_0} + \cos^{-1} \frac{a}{r} \right)} \\ & \times \left( e^{(ik_{\infty}(1-\epsilon) - \alpha)a\theta} + e^{(ik_{\infty}(1+\epsilon) - \alpha)a(2\pi - \theta)} \right). \end{aligned} \quad (95)$$

However, note also that there are also further rays due to multiple orbits of the cylinder by the surface ray. These rays just give additional factors of  $2m\pi$  added to  $\theta$  and  $2\pi - \theta$  where  $m \in \mathbb{N}$ . These extra terms are easily summed as they form geometric series. Furthermore, when the ray hits it excites numerous surface rays with different  $\alpha_j$  and  $d_j$ . This leads to the final expression

$$\begin{aligned} \phi_d(P) = & \sum_j \frac{e^{i\pi/4} d_j^2}{(8\pi k_{\infty}^2 \sqrt{r_0^2 - a^2} \sqrt{r^2 - a^2})^{1/2}} e^{ik_{\infty} (\sqrt{r_0^2 - a^2} + \sqrt{r^2 - a^2}) - (ik_{\infty} - \alpha_j)a \left( \cos^{-1} \frac{a}{r_0} + \cos^{-1} \frac{a}{r} \right)} \\ & \times \left( \frac{e^{(ik_{\infty}(1-\epsilon) - \alpha_j)a\theta}}{1 - e^{2\pi a(ik_{\infty}(1-\epsilon) - \alpha_j)}} + \frac{e^{(ik_{\infty}(1+\epsilon) - \alpha_j)a(2\pi - \theta)}}{1 - e^{2\pi a(ik_{\infty}(1+\epsilon) - \alpha_j)}} \right). \end{aligned} \quad (96)$$

Unfortunately, to obtain the coefficients  $\alpha_j$  and  $d_j$  we must look back to the eigenfunction solution.



### 5.3.5 Asymptotics of the eigenfunction solution

We return to the Green's function solution for a point source (39). Write this as

$$G(\mathbf{x}, \mathbf{x}_0) = \sum_{\nu \in \mathbb{Z}} F_{\nu + \epsilon k_{\infty} a} e^{i\nu\theta} \quad (97)$$

where

$$F_{\nu} = \frac{1}{8i} \frac{H_{\nu}^{(2)}(k_{\infty} r_{\min}) H_{\nu}^{\prime(1)}(k_{\infty} a) - H_{\nu}^{(1)}(k_{\infty} r_{\min}) H_{\nu}^{\prime(2)}(k_{\infty} a)}{H_{\nu}^{\prime(1)}(k_{\infty} a)} H_{\nu}^{(1)}(k_{\infty} r_{\max}). \quad (98)$$

Let  $F(\nu)$  be the function which gives analytic continuation of  $F_{\nu}$  to all complex  $\nu$ . Then by performing a Watson transform we may write

$$G(\mathbf{x}, \mathbf{x}_0) = -\frac{i}{2} \oint_{\Gamma} \frac{e^{i\nu(\theta-\pi)}}{\sin \nu\pi} F(\nu + \epsilon k_{\infty} a) d\nu, \quad (99)$$

where  $\Gamma$  is a contour around the real axis. Exploiting the fact  $F(\nu) = F(-\nu)$  this integral can then be rewritten as

$$G(\mathbf{x}, \mathbf{x}_0) = \frac{i}{2} \int_{-\infty+i\delta}^{\infty+i\delta} \frac{e^{i\nu(\theta-\pi)}}{\sin \nu\pi} F(\nu + \epsilon k_{\infty} a) + \frac{e^{-i\nu(\theta-\pi)}}{\sin \nu\pi} F(\nu - \epsilon k_{\infty} a) d\nu. \quad (100)$$

where  $\delta > 0$ , with the contour being just above the real axis. Consider the integral  $I^{\pm}$  defined by

$$I^{\pm} = \int_{-\infty+i\delta}^{\infty+i\delta} \frac{e^{\pm i\nu(\theta-\pi)}}{\sin \nu\pi} F(\nu \pm \epsilon k_{\infty} a) d\nu. \quad (101)$$

We close the contour in the upper half plane. Note that this can only be done in the diffracted region. The only contribution to the integral comes from residues in the upper half plane. We get residue contributions wherever  $H_{\tilde{\nu}}^{\prime(1)}(k_{\infty} a)$  has zeros, where  $\tilde{\nu} = \nu \pm \epsilon k_{\infty} a$ . For large  $\tilde{\nu}$ ,  $k_{\infty} a$  the zeros of  $H_{\tilde{\nu}}(k_{\infty} a)$  are given by

$$\tilde{\nu}_j \sim k_{\infty} a - \left( \frac{k_{\infty} a}{2} \right)^{1/3} e^{i\pi/3} q'_j, \quad (102)$$

where  $q'_j$  are the roots of the derivative of the Airy function,  $\text{Ai}'(q'_j) = 0$ . Hence

$$\nu_j^{\pm} = \tilde{\nu}_j \mp \epsilon k_{\infty} a \sim k_{\infty} a (1 \mp \epsilon) - \left( \frac{k_{\infty} a}{2} \right)^{1/3} e^{i\pi/3} q'_j. \quad (103)$$

The poles are in the upper half plane, and are all simple so we find

$$I^{\pm} \sim -\frac{\pi}{4} \sum_j \frac{e^{\pm i\nu_j^{\pm}(\theta-\pi)}}{\sin \nu_j^{\pm} \pi} H_{\nu_j^{\pm}}^{(1)}(k_{\infty} r_0) H_{\nu_j^{\pm}}^{(1)}(k_{\infty} r) \frac{H_{\tilde{\nu}_j}^{\prime(2)}(k_{\infty} a)}{\frac{\partial}{\partial \tilde{\nu}_j} H_{\tilde{\nu}_j}^{\prime(1)}(k_{\infty} a)}. \quad (104)$$

The factors in front can be rewritten as

$$\frac{e^{+i\nu_j^{+}(\theta-\pi)}}{\sin \nu_j^{+} \pi} = \frac{2ie^{i\nu_j^{+}\theta}}{e^{2\pi i\nu_j^{+}} - 1}, \quad \frac{e^{-i\nu_j^{-}(\theta-\pi)}}{\sin \nu_j^{-} \pi} = \frac{2ie^{i\nu_j^{-}(2\pi-\theta)}}{e^{2\pi i\nu_j^{-}} - 1}. \quad (105)$$

Since  $\tilde{\nu} \sim k_\infty a$ , for large  $\tilde{\nu}$ ,  $k_\infty r$  the Hankel function has asymptotic form

$$H_{\tilde{\nu}_j}^{(1)}(k_\infty r) \sim \sqrt{\frac{2}{\pi k_\infty \sqrt{r^2 - a^2}}} e^{ik_\infty \sqrt{r^2 - a^2} - i\tilde{\nu}_j \cos^{-1} \frac{a}{r} - i\pi/4}, \quad (106)$$

and  $H_{\tilde{\nu}_j}^{(1)}(k_\infty r_0)$  will have a similar asymptotic expression. It can be shown that

$$\frac{H_{\tilde{\nu}_j}^{\prime(2)}(k_\infty a)}{\frac{\partial}{\partial \tilde{\nu}_j} H_{\tilde{\nu}_j}^{\prime(1)}(k_\infty a)} = \frac{e^{5i\pi/6}}{2\pi(-q'_j) \left(\text{Ai}(q'_j)\right)^2} \left(\frac{k_\infty a}{2}\right)^{1/3}. \quad (107)$$

Combining all these expressions, and comparing with GTD solution (96) eventually yields the diffraction coefficients as

$$\alpha_j = \frac{e^{5i\pi/6}}{a} \left(\frac{k_\infty a}{2}\right)^{1/3} q'_j, \quad (108)$$

$$d_j = \frac{-e^{i\pi/24}}{(2\pi)^{1/4} (-q'_j)^{1/2} |\text{Ai}(q'_j)|} \left(\frac{k_\infty a}{2}\right)^{1/6}. \quad (109)$$

Note that  $q'_j$  is real and negative, and  $\text{Ai}(q'_j)$  is real.

#### 5.4 The diffracted field of an incident plane wave

Now the diffraction coefficients have been found, the case of an incident plane wave can be solved by a similar construction. The corresponding solution is

$$\begin{aligned} \phi_d = & \sum_j \frac{d_j^2}{(k_\infty \sqrt{r^2 - a^2})^{1/2}} e^{ik_\infty \sqrt{r^2 - a^2} - (ik_\infty - \alpha_j)a(\pi/2 + \cos^{-1} \frac{a}{r})} \\ & \times \left( \frac{e^{(ik_\infty(1-\epsilon) - \alpha_j)a\theta}}{1 - e^{2\pi a(ik_\infty(1-\epsilon) - \alpha_j)}} + \frac{e^{(ik_\infty(1+\epsilon) - \alpha_j)a(2\pi - \theta)}}{1 - e^{2\pi a(ik_\infty(1+\epsilon) - \alpha_j)}} \right). \end{aligned} \quad (110)$$

### 6 Fresnel Region

We return to our governing equation

$$\nabla^2 \psi + k_\infty^2 \psi + \frac{2i\epsilon k_\infty a}{r^2} \frac{\partial \psi}{\partial \theta} = 0. \quad (111)$$

Note the substitution  $\psi = \varphi e^{-i\epsilon k_\infty a \theta}$  yields simply

$$\nabla^2 \varphi + k_\infty^2 \varphi = 0, \quad (112)$$

the Helmholtz equation for  $\varphi$  to  $O(\epsilon^2)$ . This reflects what we have been seeing in our ray calculations so far: the effect of the  $O(\epsilon)$  mean flow is simply a phase shift determined by the angular procession of rays around the cylinder.

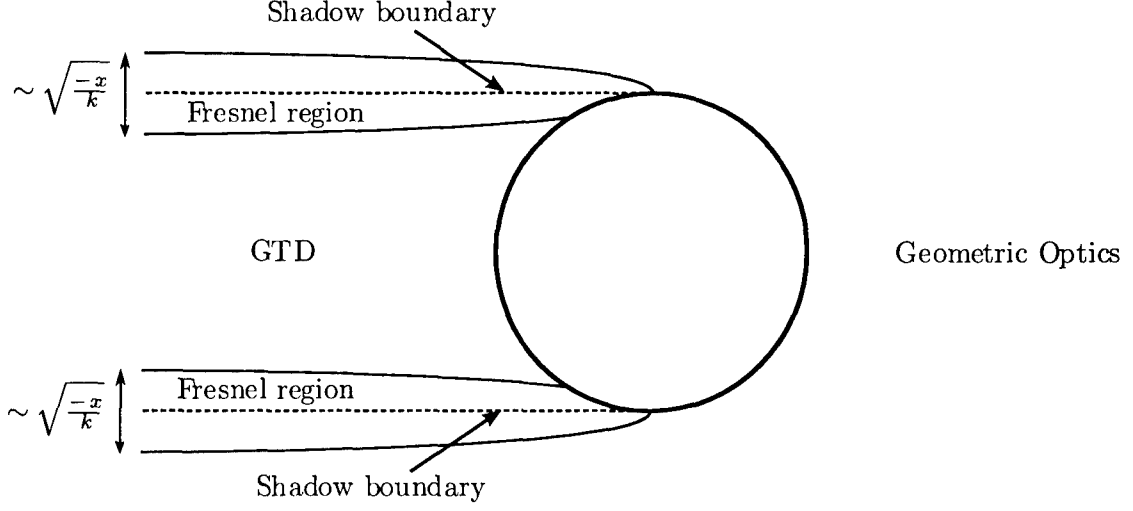


Figure 7: Cartoon of the different asymptotic regions. There is a further asymptotic region in the neighbourhood of the point at which the grazing ray hits (the Fock-Leontovich region) which we have not solved for.

At the shadow boundary the geometric optics field is discontinuous. Moreover, the GTD solution blows up at the shadow boundary. On the shadow boundary the solution takes the form of a Fresnel integral which we now derive (Figure 7). Solving for the Fresnel region is equivalent to solving for the field due to an incident wave past a flat screen. It is important to note that the Fresnel solution has no knowledge of the curvature of the surface.

Consider the ray which hits the top of the cylinder defining the shadow boundary. Far above this shadow boundary the field is dominated by the incident field, which takes the form  $\psi^i = e^{-ik_\infty x - i\epsilon k_\infty a\theta}$ . This motivates searching for solutions to (111) of the form

$$\phi = v e^{-ik_\infty x - i\epsilon k_\infty a\theta} \quad (113)$$

along the shadow boundary. We are solving in the left half plane for a wave coming from the top, so  $\theta$  must be defined so that  $\pi/2 < \theta < 3\pi/2$ . Substituting in to (111) yields

$$v_{xx} - 2ik_\infty v_x + v_{yy} = 0. \quad (114)$$

Introduce boundary layer variables  $x' = -x$ ,  $y' = k_\infty^{1/2}(y - a)$ . This boundary layer scaling implies that far away enough from the cylinder the Fresnel regions fill in the shadow region. (114) becomes

$$v_{x'x'} + 2ik_\infty v_{x'} + k_\infty v_{y'y'} = 0. \quad (115)$$

Hence expanding for large  $k_\infty$  we find the leading order term  $v_0$  is given by

$$2iv_{0x'} + v_{0y'y'} = 0. \quad (116)$$

This is the paraxial wave equation. We introduce a similarity variable  $\eta = y'/x'^{1/2}$  and let  $v_0 = f(\eta)$ . The above then reduces to

$$f'' - i\eta f' = 0. \quad (117)$$

As we go out from the boundary layer we want the solution to match on to the incident field for  $y > a$  and to go to zero for  $y < a$  in the shadow region. This allows us to give the final solution for the top Fresnel region as

$$\psi_{\text{top}}^f = e^{-ik_\infty x - i\epsilon k_\infty a \theta} \left( \frac{1}{2} + \frac{e^{-i\pi/4}}{\sqrt{2}} \text{Fr} \left( \frac{k_\infty^{1/2}(y-a)}{\sqrt{-\pi x}} \right) \right), \quad (118)$$

where  $\pi/2 < \theta < 3\pi/2$  and Fr is the Fresnel integral defined by

$$\text{Fr}(z) = \int_0^z e^{i\pi t^2/2} dt. \quad (119)$$

A similar derivation for the bottom shadow boundary leads to

$$\psi_{\text{bot}}^f = e^{-ik_\infty x - i\epsilon k_\infty a \theta} \left( \frac{1}{2} + \frac{e^{-i\pi/4}}{\sqrt{2}} \text{Fr} \left( \frac{k_\infty^{1/2}(-a-y)}{\sqrt{-\pi x}} \right) \right), \quad (120)$$

where it is important to note that  $\theta$  is defined in this expression so that  $-3\pi/2 < \theta < -\pi/2$ .

We now have three asymptotic expansions which are valid in three different regions: the geometric optics solution is valid outside the shadow region, the GTD solution is valid inside the shadow region, and the Fresnel solution is valid in a neighbourhood of the shadow boundary. From these we can construct a uniformly valid solution by forming a composite expansion, and such a solution is plotted in Figures 8 and 9.

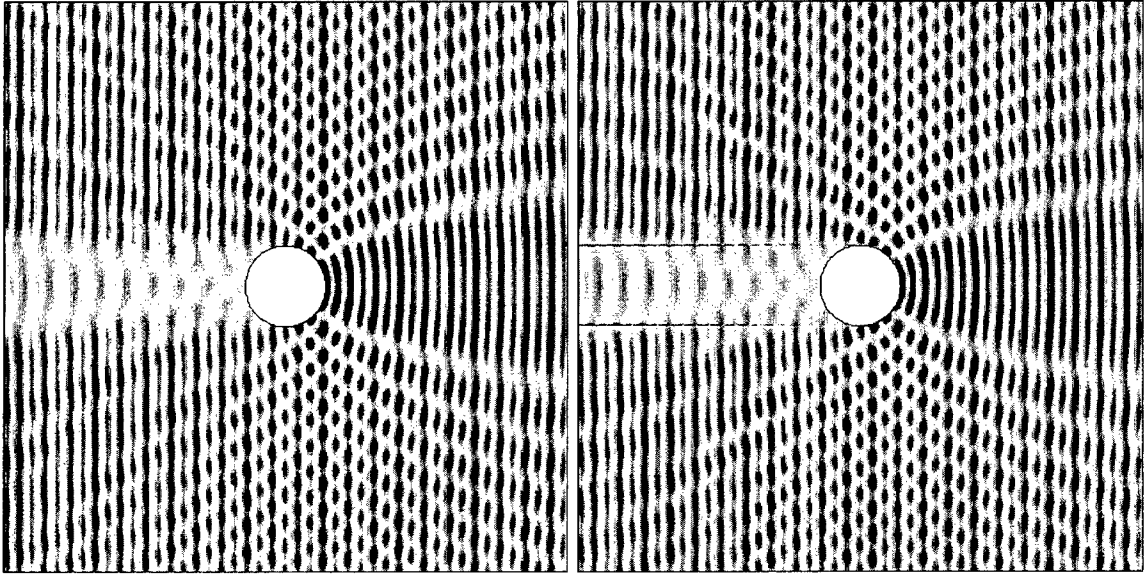


Figure 8: Plot of potential  $\phi$  with  $\epsilon = 0$ ,  $k_\infty a = 10$ . Left picture shows the eigenfunction solution, right the ray tracing solution. The two plots are remarkably similar, demonstrating the effectiveness of the ray tracing approximation. In the ray tracing solution there is a small numerical problem along the shadow boundary.

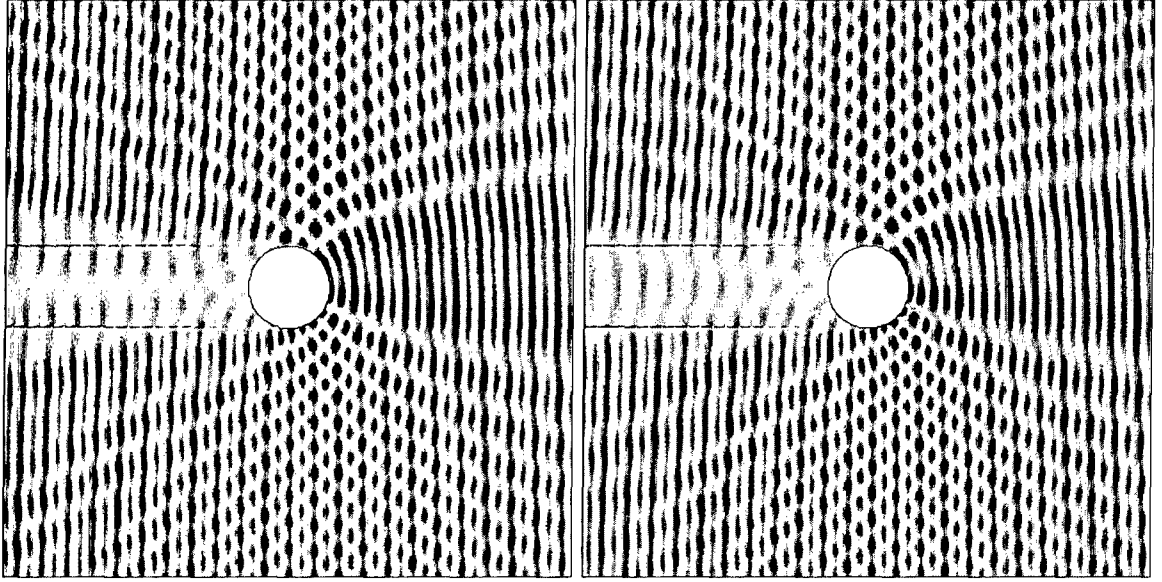


Figure 9: Plot of potential  $\phi$  with  $\epsilon = 0.25$  (left picture) and  $\epsilon = 0.3$  (right picture) and  $k_\infty a = 10$ . Notice that refraction causes wavefronts to be out of phase on the left of the cylinder on the left picture, but in phase on the right picture.

## 7 Force on the cylinder

We are interested in calculating the time averaged force  $\bar{\mathbf{F}}$  on the cylinder. This is simply given by integrating the time averaged pressure around the cylinder

$$\bar{\mathbf{F}} = - \int_{S_a} \bar{p} \mathbf{n} \, dS = - \int_{-\pi}^{\pi} \bar{p}(\cos \theta, \sin \theta) a \, d\theta. \quad (121)$$

where  $\bar{p}$  is given by (28). The previous sections were devoted to solving for  $\phi'_1$ , but to find the force at second order in wave amplitude  $\eta$  we must also specify  $\bar{\phi}_2$ . To the order we are concerned with  $\bar{\phi}_2$  is the solution to Laplace's equation. The boundary condition on  $r = a$  is simply  $\bar{\mathbf{u}}_2 \cdot \mathbf{n} = 0$ , but the question of what boundary condition to apply at  $\infty$  is harder to answer. We could apply  $\bar{\mathbf{u}}_2 = 0$  at  $\infty$ , i.e. no Eulerian mean velocity at second order. However, this would imply that there is still an  $O(\eta^2)$  mass flux past the cylinder given by  $\eta^2 \bar{h}'_1 \bar{\mathbf{u}}'_1$ ; the Lagrangian mean velocity is non-zero. This phenomenon of net mass flux is known as Stokes drift. A perfectly acceptable alternative way of setting the problem up would be to demand no mass flux past the cylinder, i.e. no Lagrangian mean velocity at second order. There is no single “right way” of choosing the boundary condition on  $\bar{\mathbf{u}}_2$  at  $\infty$ . Once we are given the constant velocity at infinity,  $\bar{\mathbf{u}}_2 \sim \bar{u}_{2\infty}(\cos \alpha, \sin \alpha)$  as  $r \rightarrow \infty$ , Laplace's equation has the classical solution

$$\bar{\phi}_2 = \bar{u}_{2\infty} \left( r + \frac{a^2}{r} \right) \cos(\theta - \alpha). \quad (122)$$

## 7.1 Force calculation by ray tracing

It is straightforward to calculate the force from the ray tracing solution. The dominant contribution to  $\psi$  comes from the side of the cylinder on which the wave is incident ("the bright side"), and there the field is given by geometric optics as the sum of the reflected field and the incident field. On the cylinder the reflected field has the same phase and amplitude as the incident field. Hence on the bright side of the cylinder

$$\psi = 2 \frac{c^2}{\omega} e^{-ik_\infty a(\cos\theta + \epsilon\theta)}, \quad (123)$$

where we have inserted  $c^2/\omega$ , an appropriate dimensional factor. We calculate each term in the time averaged pressure (28) from (122) and (123):

$$\frac{1}{2c^2} \overline{\left(\frac{\partial\phi'_1}{\partial t}\right)^2} = \frac{1}{4c^2} \text{Re} \left( \frac{\partial\phi'_1}{\partial t}^* \frac{\partial\phi'_1}{\partial t} \right) = \frac{\omega^2}{4c^2} |\psi|^2 = c^2, \quad (124)$$

$$-\frac{1}{2} \overline{|\nabla\phi'_1|^2} = -\frac{1}{4} \text{Re} (\nabla\phi'_1{}^* \cdot \nabla\phi'_1) = -\frac{1}{4} |\nabla\psi|^2 = c^2 (-\sin^2\theta + 2\epsilon\sin\theta), \quad (125)$$

$$\frac{1}{c^2} \overline{\frac{\partial\phi'_1}{\partial t} \mathbf{U} \cdot \nabla\phi'_1} = \frac{1}{2c^2} \text{Re} \left( \frac{\partial\phi'_1}{\partial t}^* \mathbf{U} \cdot \nabla\phi'_1 \right) = \frac{1}{2c^2} \text{Re} (i\omega\psi^* \mathbf{U} \cdot \nabla\psi) = -2c^2\epsilon\sin\theta, \quad (126)$$

$$-\mathbf{U} \cdot \nabla\overline{\phi_2} = 2\epsilon c \overline{u_{2\infty}} \sin(\theta - \alpha), \quad (127)$$

where we have used the identity  $\overline{AB} = \text{Re}(A^*B)/2$ . Thus the time averaged pressure on the bright side of the cylinder is

$$\overline{p} = \text{constant} + \eta^2 H c^2 \left( \cos^2\theta + 2\epsilon \frac{\overline{u_{2\infty}}}{c} \sin(\theta - \alpha) \right) + O(\eta^3), \quad -\pi/2 < \theta < \pi/2. \quad (128)$$

On the dark side of the cylinder there is no leading order contribution from the linear waves, but there is still a contribution from the  $\mathbf{U} \cdot \nabla\overline{\phi_2}$  term:

$$\overline{p} = \text{constant} + \eta^2 H c^2 \left( 0 + 2\epsilon \frac{\overline{u_{2\infty}}}{c} \sin(\theta - \alpha) \right) + O(\eta^3), \quad \begin{array}{l} -\pi < \theta < -\pi/2, \\ \pi/2 < \theta < \pi. \end{array} \quad (129)$$

Integrating the time averaged pressure around the cylinder we find the  $O(\eta^2)$  time averaged force is given by

$$\overline{\mathbf{F}} = - \int_{-\pi}^{\pi} \overline{p}(\cos\theta, \sin\theta) a \, d\theta = \eta^2 H c^2 a \left( (-4/3, 0) - 2\epsilon\pi \frac{\overline{u_{2\infty}}}{c} (-\sin\alpha, \cos\alpha) \right), \quad (130)$$

or in terms of the circulation  $\Gamma = 2\pi\epsilon ca$ ,

$$\overline{\mathbf{F}} = \eta^2 \left( H c^2 a (-4/3, 0) - H \overline{u_{2\infty}} \Gamma (-\sin\alpha, \cos\alpha) \right), \quad (131)$$

where the last term can be recognised as the usual expression for the Magnus force due to flow past a cylinder.

## 7.2 Force calculation by eigenfunction solution

We can also calculate the force using the eigenfunction solution (48). After some algebra, we find

$$\bar{\mathbf{F}} = \eta^2 (Hc^2 a(S(k_\infty a), 0) - H\overline{u_{2\infty}} \Gamma(-\sin \alpha, \cos \alpha)), \quad (132)$$

where  $S(z)$  is a real valued function defined by

$$S(z) = \frac{2i}{\pi z^4} \sum_{m \in \mathbb{Z}} \frac{z^2 - m(m-1)}{H_m^{(1)}(z) H_{m-1}^{(2)}(z)}. \quad (133)$$

Note that  $S(z)$  is independent of  $\epsilon$  so that the only  $O(\epsilon)$  contribution to the force is still the Magnus force term. Also, by comparison with the ray tracing solution we have  $S(z) \rightarrow -4/3$  as  $z \rightarrow \infty$ . The form of  $S(z)$  agrees with a similar calculation for the acoustic force on an elastic cylinder given by [4].

## 8 Conclusions

To  $O(\epsilon)$  we have found expressions for the field resulting from the scattering useful for both small  $k_\infty a$  (the eigenfunction solution) and for large  $k_\infty a$  (the ray tracing solution). The effect of the  $O(\epsilon)$  circulation is simply to add phase shifts in appropriate places in the calculation, and importantly it does not change the diffraction coefficients.

The  $O(\epsilon)$  force has been calculated. It is important to note that we now have to specify parts of the  $O(\eta^2)$  problem which we didn't have to consider in the no mean flow case. However, the only  $O(\epsilon)$  contribution to the force turns out to be a Magnus force due to the mean Eulerian flow  $\eta^2 \overline{u_{2\infty}}$  past the cylinder.

To solve the  $O(\epsilon^2)$  irrotational problem requires a lot more work. Firstly the governing partial differential equation is no longer separable. When calculating diffraction coefficients comparison with the eigenfunction solution was essential, and so this is an important stumbling block for application of the geometrical theory of diffraction. To  $O(\epsilon^2)$  the rays are no longer straight, and so also we lose a lot of the geometrical considerations which made the  $O(\epsilon)$  mean flow problem so similar to the no mean flow problem.

A probably tractable generalisation of this problem would be to look at the case of a rotational mean flow at  $O(\epsilon)$ . Here the rays are still no longer straight, but the ray curvature can be expressed simply in terms of the vorticity of the mean flow [3, 6].

## Acknowledgements

First off, many thanks to Oliver Bühler and Joe Keller for helping me through this project. Thanks also to all the fellows and staff for making it a very enjoyable summer. Special thanks must also go to Matt for the computing/cooking technical support, and Khachik for all the lifts to Falmouth hospital!

## References

- [1] M. ABRAMOWITZ AND I. A. STEGUN, eds., *Handbook of Mathematical Functions*, Dover, 9th ed., 1972.
- [2] O. BÜHLER AND M. E. MCINTYRE, *Remote recoil: a new wave-mean interaction effect*, J. Fluid Mech., 492 (2003), pp. 207–230.
- [3] K. B. DYSTHE, *Refraction of gravity waves by weak current gradients*, J. Fluid Mech., 442 (2001), pp. 157–159.
- [4] T. HASEGAWA, K. SAKA, N. INOUE, AND K. MATSUZAWA, *Acoustic radiation force experienced by a solid cylinder in a plane progressive sound field*, J. Acoust. Soc. Am., 83 (1988).
- [5] J. B. KELLER AND R. M. LEWIS, *Asymptotic methods for partial differential equations: the reduced wave equation and Maxwell's equations*, in *Surveys in Applied Mathematics*, J. B. Keller, G. Papanicolaou, and D. McLaughlin, eds., Plenum Publishing, NY, 1995.
- [6] L. D. LANDAU AND E. M. LIFSHITZ, *Fluids Mechanics*, Pergamon, 1959.
- [7] B. R. LEVY AND J. B. KELLER, *Diffraction by a smooth object*, Comm. Pure Appl. Math., 12 (1959).



# Fluctuations in chemical reactions in a large volume

Khachik Sargsyan

July 18, 2006

## 1 Introduction

Chemical reactions are very often modelled by ordinary differential equations, where the concentration of a particular particle evolves according to a deterministic law. But, in order to be able to answer several questions where the discreteness, hence the intrinsic fluctuations play a role, one needs to describe the system by a stochastic model. We assume the chemical system to be well-stirred, so that all the particles are distributed in space appropriately uniformly. Also we assume the number of reactions occurred to be Poisson-distributed, i.e. the waiting times between different reactions are distributed exponentially with given rates. This is, in a nutshell, the essence of the *Kinetic Monte Carlo (KMC)* models of chemical reactions. These models are discrete and non-deterministic, as opposed to the deterministic, continuous models governed by Ordinary Differential Equations (ODE), and the non-deterministic, continuous ones, governed by Stochastic Differential Equations (SDE). The last two models, are simpler and can be obtained from the KMC in certain limits.

The drawbacks of the deterministic description are well-known. It leads to no fluctuations, a very important characteristics in certain cases. The model governed by SDE is the so-called diffusion approximation of the original system. It is a non-deterministic model, hence it detects the intrinsic fluctuations. However, it may not be good enough, if we are concerned in the exponentially large (small) variables and/or we deal with exponentially unlikely events. We will consider the Schlögl model as the simplest model with bistability (two stable equilibriums predicted by the deterministic description) and, as an example of an exponentially large observable, we will consider the switching times between two stable states. On that example it will become clear why the diffusion approximation governed by SDE is not satisfactory.

This report is organized as follows: first, in Sec. 2 the Schlögl model is introduced as a deterministic one. Next, in Sec. 3, we will introduce the KMC model, where the number of particles evolves as a Markov jump process. In the Sec. 4 we will show how to get the simpler descriptions (ODE and SDE) as large system volume limits of the Markov jump process. Also, in order to motivate the use of the exponentially large observables, we will introduce the simplest theorem in the large deviations theory, in Sec. 5. Afterwards, in Sec. 6, we will apply the introduced ideas to the Schlögl model, emphasizing the calculations of

the mean first passage times, that are exponentially large, hence reveal the the drawbacks of the diffusion approximation. Finally, the Sec. 7 will be devoted to a short discussion and conclusions, as well as future work.

## 2 The Schlögl model and its deterministic description

Consider the following chemical reaction, introduced by Schlögl [1] as a catalysis model:



We denote the number of particles  $X$ ,  $A$  and  $B$  by the corresponding letters. Then, keeping  $A$  and  $B$  fixed and of the order of the system volume  $V$ , we are interested in the evolution of  $X$ .  $k_i$  are the rates of the corresponding reactions in (1).

The simplest description of the system is the deterministic one, where the concentration  $x = X/V$  is a deterministic, continuous variable, time evolution of which is governed by the ODE:

$$\frac{dx}{dt} = u(x) - d(x).$$
(2)

Here we denoted  $u(x) = k_1x^2 + k_4$  and  $d(x) = k_2x^3 + k_3x$ .

For appropriate choice of parameters, the function  $f(x) = u(x) - d(x)$  has three real roots: the middle one corresponds to the unstable equilibrium, while two others are the stable equilibrium values. See Fig. 1. Hence, depending on the initial value,  $x$  will exponentially approach to one of the two stable equilibriums, see Fig. 2. In a certain sense, the Schlögl model is the simplest one that leads to the bistability. Third order polynomial is normally the first choice, if we want to have a function of three real roots.

Although the deterministic model is simple to analyze, it is a good approximation to the real, discrete system only in the limit of large volume and for finite time intervals [2, 3]. It is not able to answer to questions related to the stochastic behaviour of the system, namely, the intrinsic fluctuations of the system are not detected. Consequently, it leaves open the question of relative stability: near which of the two stable equilibrium states we are more likely to find the system at a randomly chosen time? The system spends most of the time near one of the equilibrium states, but fluctuations can sporadically drive it to the neighborhood of the other equilibrium. In order to analyze the intrinsic fluctuative behaviour of the system, we will next introduce the discrete stochastic model (Kinetic Monte-Carlo scheme) according to which the chemical reaction happens.

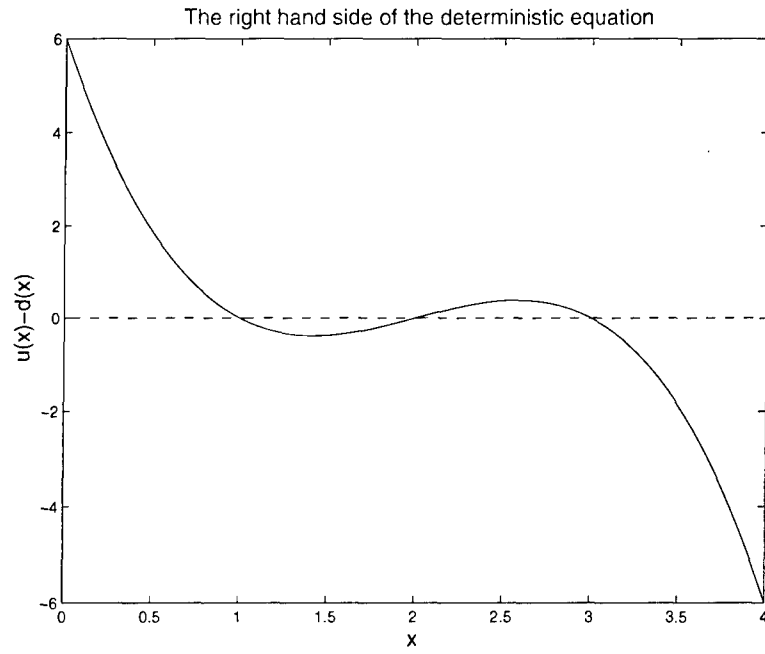


Figure 1: The deterministic rate  $u(x) - d(x)$  for  $u(x) = 6x^2 + 6$  and  $d(x) = x^3 + 11x$ , i.e.  $k_1 = k_4 = 6$ ,  $k_2 = 1$  and  $k_3 = 11$ .

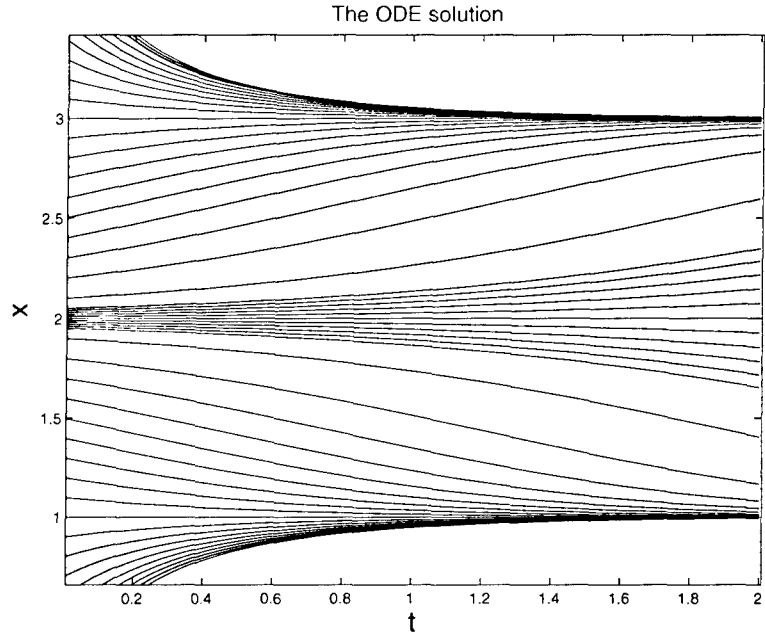


Figure 2: The time evolution of  $x(t)$ . Depending on the initial value, it approaches one or the other equilibrium state.

### 3 Discrete model as a Markov jump process (Kinetic Monte Carlo)

The reaction (1) can be rewritten as:



Here the rates of moving “up” and “down” are, correspondingly,

$$U(X) = \frac{k_1}{V} X(X-1) + k_4 V \text{ and } D(X) = \frac{k_2}{V^2} X(X-1)(X-2) + k_3 X. \quad (4)$$

Recall that, without loss of generality, we absorbed  $A$  and  $B$  into the system volume  $V$ .

Hence, our model is one-step Markov jump process (see [4]) and is governed by the following *Master Equation* (forward Kolmogorov equation) for the probabilities  $P(n, t) = \mathbb{P}\{X(t) = n\}$ :

$$\begin{aligned} \frac{\partial P(n, t)}{\partial t} &= U(n-1)P(n-1, t) + D(n+1)P(n+1, t) - (U(n) + D(n))P(n, t) = \\ &= (\mathcal{L}^* P)(n, t), \end{aligned} \quad (5)$$

where  $\mathcal{L}^*$  is the adjoint of the *generator*  $\mathcal{L}$  of the process. The generator of a Markov process  $X(t)$ , by definition, is the operator

$$(\mathcal{L}f)(n) = \lim_{t \rightarrow 0} \frac{\mathbb{E}\{f(X(t)) - f(X(0)) | X(0) = n\}}{t}, \quad (6)$$

which for one-step Markov jump processes takes the form

$$(\mathcal{L}f)(n) = U(n)[f(n+1) - f(n)] + D(n)[f(n-1) - f(n)]. \quad (7)$$

The generator defines the Markov process completely. Also, if we define

$$v(n, t) = \mathbb{E}[f(X(t)) | X(0) = n] \quad (8)$$

for any *observable*  $f(n)$ , then  $v(n, t)$  solves the partial differential equation (backward Kolmogorov equation)

$$v_t = \mathcal{L}v \quad (9)$$

with initial condition  $v(n, 0) = f(n)$ , see [5].

### 4 Large system volume limits

In order to analyze large system size limits, let us pass to *intensive variable*  $x = n/V = \epsilon n$ . In terms of  $x$ , the generator has the form

$$(\mathcal{L}_\epsilon f)(x) = \epsilon^{-1} u_\epsilon(x)[f(x + \epsilon) - f(x)] + \epsilon^{-1} d_\epsilon(x)[f(x - \epsilon) - f(x)]. \quad (10)$$

Here

$$u_\epsilon(x) = \epsilon U(x/\epsilon) = k_1 x(x - \epsilon) + k_4 = u(x) + \epsilon u_1(x)$$

and

$$d_\epsilon(x) = \epsilon D(x/\epsilon) = k_2 x(x - \epsilon)(x - 2\epsilon) + k_3 x = d(x) + \epsilon d_1(x) + \mathcal{O}(\epsilon^2).$$

Hence, the leading order rates are, correspondingly,  $u(x) = k_1 x^2 + k_4$  and  $d(x) = k_2 x^3 + k_3 x$ .

The Markov process corresponding to the generator (10) is the same as in the original model, only with the rates and jump sizes rescaled by  $\epsilon$ . Instead of working with the Master equation, we will explore the generator  $\mathcal{L}_\epsilon$  itself, i.e. the backward form

$$v_t = \mathcal{L}_\epsilon v. \quad (11)$$

Expanding the generator (10) in the small  $\epsilon$  limit leads to

$$(\mathcal{L}_\epsilon f)(x) = [u(x) - d(x)]f'(x) + \epsilon[u_1(x) - d_1(x)]f'(x) + \frac{\epsilon}{2} [u(x) + d(x)]f''(x) + o(\epsilon^2).$$

To the leading order, we get the differential operator

$$(\mathcal{L}_0 f)(x) = [u(x) - d(x)]f'(x) \quad (12)$$

corresponding to the deterministic description (2), discussed in Sec. 2.

To the next order  $\mathcal{O}(\epsilon)$  we obtain the *backward form of the Fokker-Planck equation* (see [6])

$$(\mathcal{L}_{FP} f)(x) = [u(x) - d(x)]f'(x) + \epsilon[u_1(x) - d_1(x)]f'(x) + \frac{\epsilon}{2} [u(x) + d(x)]f''(x), \quad (13)$$

which leads to a stochastic differential equation for  $x(t)$ :

$$dx = [u(x) - d(x) + \epsilon(u_1(x) - d_1(x))]dt + \sqrt{\epsilon(u(x) + d(x))}dW. \quad (14)$$

This corresponds to the *diffusion approximation* of the process, with *drift*  $u(x) - d(x) + \epsilon(u_1(x) - d_1(x))$  and *diffusion*  $\epsilon[u(x) + d(x)]/2$ .

In contrast with the deterministic description, the diffusion approximation takes the fluctuations into account, but it is not good enough if we are dealing with rare events, that arise when we calculate exponentially large (small) observables. In the next section we will introduce basic large deviations ideas, in order to qualify “rare events” in a more formal way.

## 5 Large deviations principles

### 5.1 Large deviations principle for random variables

Let us start off with the large deviations principle for the random variables. Suppose we have independent, identically distributed random variables  $x_i$  with the common mean  $\mathbb{E}x_i = m$  and moment generating function  $M(\theta) = \mathbb{E} e^{\theta x_i}$ .

The well-known law of large numbers states that the average of these variables goes to  $m$  in probability as the ensemble size goes to infinity:

$$\frac{x_1 + \dots + x_n}{n} \xrightarrow{\mathbb{P}} m \quad \text{as} \quad n \rightarrow \infty, \quad (15)$$

hence, for any  $a > m$ ,

$$\mathbb{P} \left\{ \frac{x_1 + \dots + x_n}{n} > a \right\} \longrightarrow 0 \quad \text{as} \quad n \rightarrow \infty. \quad (16)$$

The natural question arises: what is the convergence rate in (16)? Since  $e^{\theta x}$  is a monotone function, we have

$$\mathbb{P} \{x_1 + \dots + x_n > na\} = \mathbb{P} \left\{ e^{\theta(x_1 + \dots + x_n)} > e^{\theta na} \right\} \leq e^{-\theta na} \mathbb{E} e^{\theta(x_1 + \dots + x_n)}. \quad (17)$$

The last step is just an application of the Chebyshev's inequality. By independence, we get

$$\mathbb{P} \{x_1 + \dots + x_n > na\} \leq e^{-\theta na} M(\theta)^n = e^{-n(\theta a - \log M(\theta))} \quad \text{for all } \theta. \quad (18)$$

Since (18) works for all  $\theta$  we can define the *action (rate) function*  $l(a) = \sup_{\theta} \{\theta a - \log M(\theta)\}$  to obtain a stronger inequality:

$$\mathbb{P} \{x_1 + \dots + x_n > na\} \leq e^{-nl(a)}. \quad (19)$$

The basic theorem in the large deviations theory states that the bound in (19) is sharp, namely,

$$\frac{1}{n} \log \mathbb{P} \left\{ \frac{x_1 + \dots + x_n}{n} > a \right\} \sim -l(a) \quad (20)$$

as  $n \rightarrow \infty$ . See, say, [7, 8]. We say that the exponentially unlikely event  $\{x_1 + \dots + x_n > na\}$  satisfies the large deviations principle with the action function  $l(a)$ .

## 5.2 Large deviations expansion

We will look at an observable  $v(x, t) = \mathbb{E}[f(X(t)) | X(0) = x]$  with  $f(x) = e^{g(x)/\epsilon}$  for some function  $g(x)$ . This motivates the ansatz  $v(x, t) = e^{\phi(x, t)/\epsilon}$ . We plug it into (11) and expand the nearby values of the exponent  $\phi(x, t)$  to obtain, in the highest order  $\epsilon^{-1}$ , the partial differential equation

$$\phi_t = u(x)(e^{\phi_x} - 1) + d(x)(e^{-\phi_x} - 1) \quad (21)$$

with initial condition  $\phi(x, 0) = g(x)$ .

From the other hand, if we used the diffusion approximation with its generator  $\mathcal{L}_{FP}$  before applying the WKB ansatz above, then we would get, again in the leading order  $\epsilon^{-1}$ , a *wrong* PDE for the exponent function  $\phi(x, t)$ , namely,

$$\phi_t = [u(x) - d(x)]\phi_x + \frac{u(x) + d(x)}{2}\phi_x^2. \quad (22)$$

Therefore, if we are interested in exponentially large observables with the exponent of  $\mathcal{O}(\epsilon^{-1}) = \mathcal{O}(V)$ , then the diffusion approximation, hence the corresponding SDE (14) lead to a systematic error in the exponent function  $\phi(x, t)$ .

We may go to the next order by taking  $\phi(x, t) = \phi_0(x, t) + \epsilon\phi_1(x, t)$ . Then  $\phi_0(x, t)$  satisfies (21), whereas  $\phi_1(x, t)$  can be expressed as  $\phi_1(x, t) = \ln z(x, t)$  with  $z(x, t)$  satisfying

$$z_t = z_x(u(x)e^{(\phi_0)_x} + d(x)e^{-(\phi_0)_x}) + \frac{z(\phi_0)_{xx}}{2}(u(x)e^{(\phi_0)_x} - d(x)e^{-(\phi_0)_x}), \quad (23)$$

which can be solved, as soon as  $\phi_0(x, t)$  is found explicitly.

### 5.3 Moderate deviations expansion

Let us now look at an observable of the form  $f(x) = e^{g(x)/\delta}$  with  $1 \gg \delta \gg \epsilon$ , so we are dealing with *moderate deviations*, as opposed to the large deviations, where we had  $\delta = \epsilon$ . One can think of  $\delta = \epsilon^\alpha$  with  $0 < \alpha < 1$ . This will motivate the moderate deviation ansatz  $v(x, t) = e^{\phi(x, t)/\delta}$  which, with both the correct generator  $\mathcal{L}_\epsilon$  and the Fokker-Planck generator  $\mathcal{L}_{FP}$  in the backward equation, leads, in the first two orders, to the *same* equation for the exponent function  $\phi(x, t)$

$$\phi_t + (u(x) - d(x))\phi_x + \frac{\epsilon}{\delta} \frac{u(x) + d(x)}{2} \phi_x^2 = 0 \quad (24)$$

with initial condition  $\phi(x, 0) = g(x)$ , as before.

Therefore, we can claim that the diffusion approximation is good enough in describing up to moderate deviation events. At least, it gives the correct exponent (action) function.

## 6 Solving for the action function

### 6.1 Classical mechanics interpretation

We will focus on the large deviations case  $v(x, t) = e^{\phi(x, t)/\epsilon}$  leading to the equation for the action function  $\phi(x, t)$

$$\phi_t = u(x)(e^{\phi_x} - 1) + d(x)(e^{-\phi_x} - 1) \quad (25)$$

with initial condition  $\phi(x, 0) = g(x)$ .

Notice that this equation is of the Hamilton-Jacobi form  $\phi_t + H(x, \phi_x) = 0$ , hence can be solved by the method of characteristics. The  $(x, t)$ -plane is being covered by the characteristics (rays), and the evolution of  $\phi(x, t)$ , as well as  $x$ , is tracked along these characteristics according to a system of ODE, see [9, 10].

First, we read off the formal Hamiltonian  $H(x, p) = u(x)(e^p - 1) + d(x)(e^{-p} - 1)$ , and the momentum is introduced by  $p = \phi_x$ . The corresponding Lagrangian can also be calculated:

$$L\left(x, \frac{dx}{dt}\right) = \frac{dx}{dt} \log \frac{\frac{dx}{dt} + \sqrt{\left(\frac{dx}{dt}\right)^2 + 4u(x)d(x)}}{2u(x)} + u(x) + d(x) - \sqrt{\left(\frac{dx}{dt}\right)^2 + 4u(x)d(x)}. \quad (26)$$

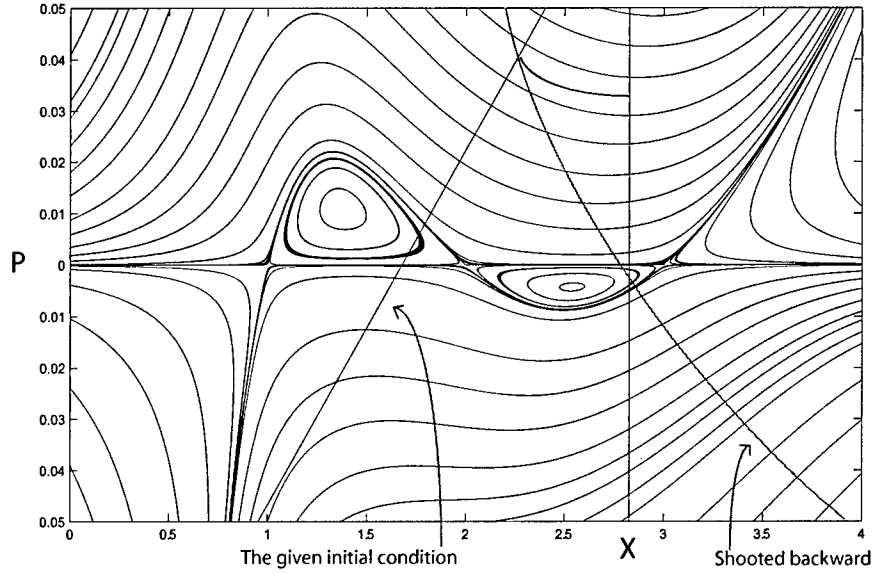


Figure 3: The phase portrait of the Hamiltonian system corresponding to the Hamilton-Jacobi equations for the action function  $\phi(x, t)$ .

The system evolves along the characteristics  $H = \text{const}$  according to the Hamiltonian system of ODE

$$\begin{cases} \frac{dx}{dt} = u(x)e^p - d(x)e^{-p} \\ \frac{dp}{dt} = -u'(x)(e^p - 1) - d'(x)(e^{-p} - 1) \end{cases} \quad (27)$$

while  $\phi(x, t)$  evolves by

$$\begin{aligned} \frac{d\phi}{dt} &= \phi_t + \phi_x \frac{dx}{dt} = -H(x, p) + p \frac{dx}{dt} = \\ &= L\left(x, \frac{dx}{dt}(x, p)\right) = u(x)(pe^p - e^p + 1) - d(x)(pe^{-p} + e^{-p} - 1). \end{aligned} \quad (28)$$

Also, by Hamilton's principle,  $\phi(x, t)$  solves the variational problem

$$\phi(x, t) = \inf \left\{ \int_0^t L(x, dx/ds) ds + g(x(0)) \right\}, \quad (29)$$

where the infimum is taken over all  $C^1[0, t]$  functions  $x(\cdot)$  with  $x(t) = x$ .

## 6.2 Switching times in the Schlögl model

For the Schlögl model,  $H = \text{const}$  paths are shown in Fig. 3. Using the phase portrait of the corresponding Hamiltonian system, the solution  $\phi(X, T)$  of Hamilton-Jacobi equation with an initial condition  $\phi(x, 0) = g(x)$  is obtained in the following way. We take the vertical line  $x = X$  and trace all the points backward for time  $T$ . That will give an "initial" profile  $f(x, p) = 0$  of the points that lead to  $X$  at time  $T$ . The intersection of this profile with the



real initial curve  $p = g'(x)$  will give the initial value (in fact, there could be more than one intersection points), therefore, the correct characteristics, leading to the point  $X$  in time  $T$ . This is the essence of the “shooting” method [9].

As mentioned in Sec. 2, one of the most important questions for bistable systems is: which of the stable states is more stable? To answer it, we should compare the mean first passage times (called switching times) from one stable state to the other.

Mean first passage time  $T(x)$  from a state  $x$  to a fixed state  $x_f$  solves the backward equation  $-1 = \mathcal{L}T(x)$  with the appropriate boundary conditions [4, 5]. For the one-step jump Markov processes the mean first passage times can be calculated exactly from the backward master equation and it leads to the large deviations asymptotics of the form  $e^{\phi(x)/\epsilon}$  for some action function  $\phi(x)$ . In general, deterministically forbidden switches between two states (in the deterministic case, see Fig. 2, switches that have to pass through  $x = 2$  are not allowed) are large deviation events. The large deviation analysis applied to the  $-1 = \mathcal{L}T(x)$  (as opposed to (9), discussed above) now will lead to the time-independent Hamilton-Jacobi equation

$$0 = u(x)(e^{\phi_x} - 1) + d(x)(e^{-\phi_x} - 1) = H(x, \phi_x). \quad (30)$$

Therefore, large deviation paths on the phase portrait are the ones corresponding to  $H(x, p) = 0$ . These are the heteroclinic connections, and they correspond to  $p = 0$  and  $p = \log \frac{d(x)}{u(x)}$ , as can be seen in Fig. 4. From (27) one can see that  $p = 0$  leads to the deterministic description  $\dot{x} = u(x) - d(x)$ , where the switches between the first and third equilibria  $x_1$  and  $x_3$  are not allowed (in order to go from one to the other, the path necessarily leaves the axis  $p = 0$ ). To switch from  $x_1$  to  $x_3$ , while staying on the  $H = 0$  curves, the system has to “climb” the non-deterministic path  $x_1$ -to- $x_2$  and then follow the deterministic one,  $x_2$ -to- $x_3$  on the  $x$ -axis. Similarly, the switch from  $x_3$  to  $x_1$  has to go through the “valley”  $x_3$ -to- $x_2$  and then follow the deterministically allowed path on the  $x$ -axis,  $x_2$ -to- $x_1$ .

By (28), the exponent (action)  $\phi_{13} = \epsilon \log T_{13}$  for the switching time  $T_{13}$  from  $x_1$  to  $x_3$  can be found by

$$\phi_{13} = \int \left( -H + p \frac{dx}{dt} \right) dt = \int_{x_1}^{x_2} p dx = \int_{x_1}^{x_2} \log \frac{d(x)}{u(x)} dx = \text{the area } S_1, \quad (31)$$

since  $p = 0$  on the second part of the path and  $H = 0$  throughout the whole path. Similarly,

$$\phi_{31} = \int_{x_3}^{x_2} p dx = \int_{x_2}^{x_3} \log \frac{u(x)}{d(x)} dx = \text{the area } S_2. \quad (32)$$

For instance, from the Fig. 4 we can see that in this particular parameter regime  $S_1 > S_2$ , hence  $T_{13} > T_{31}$ . Since it takes longer to switch from  $x_1$  to  $x_3$  than vice-versa, we can conclude that the first equilibrium is the more stable one.

The important point here is that if we used SDE to model the chemical reaction (or, equivalently, if we used the diffusion approximation *before* the large deviation ansatz), it would not give the correct Hamiltonian, hence the switching times would be miscalculated.

Also, the parameters  $k_i$  can be tuned so that the two stable equilibria are equally stable, and there are certain parameter regimes where the diffusion approximation gives the opposite, wrong answer to the relative stability question.

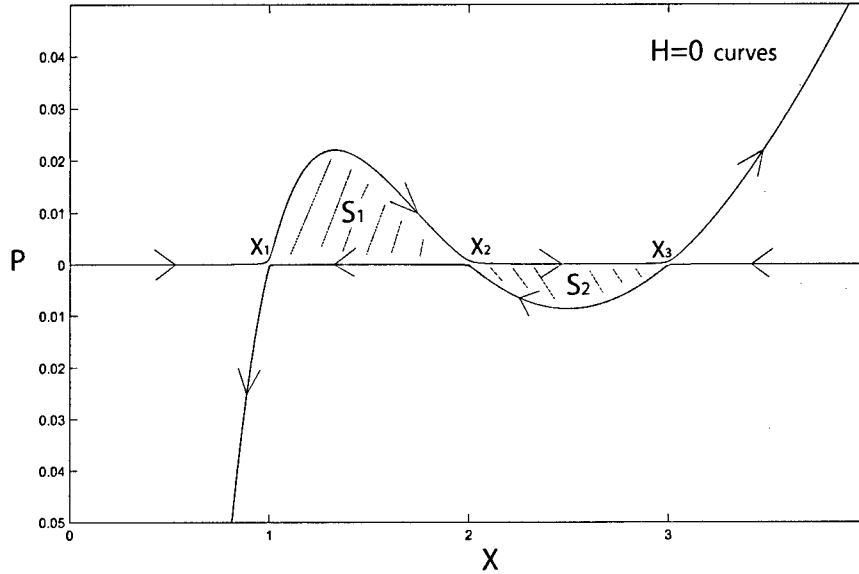


Figure 4: The  $H = 0$  curves are heteroclinic connections. They correspond to  $p = 0$  and  $p = \log \frac{d(x)}{u(x)}$ . Parameters are picked so that  $x_i = i$  for  $i=1,2,3$  are the equilibrium states.

## 7 Conclusion and future work

In this report we have introduced the Kinetic Monte Carlo modeling of chemical reactions, paying particular attention to the benchmark bistable system - the Schlögl model. The main reason of using KMC is that the simplest, deterministic model of a chemical reaction is not satisfactory at all as we are interested in fluctuations in concentrations. We have also discussed the SDE approach to the problem and have shown that it is not able to correctly answer questions concerning large deviation events/observables. If we are interested in exponentially large observables (e.g., switching times between two states that are not reachable from each other in the deterministic case) with the exponent proportional to the volume of the system, then SDE approach gives a systematic error in the exponent function. The reason is hidden in (10): we need to plug the exponential ansatz into it *first* and then expand the exponent function, as opposed to the SDE approach, where we expanded (10) to arrive to (13), and then plugged in the exponential ansatz.

In fact, the work can be carried out for general Markov jump processes with generator

$$(\mathcal{L}f)(n) = \sum_{i=1}^k \lambda_i(n) [f(n + e_i) - f(n)] \quad (33)$$

and its rescaled version

$$(\mathcal{L}_\epsilon f)(x) = \sum_{i=1}^k \epsilon^{-1} \lambda_i(x) [f(x + \epsilon e_i) - f(x)], \quad (34)$$

where  $e_i$  are the jump sizes (there are  $k$  possible ones) and  $\lambda_i(n)$  are the  $\epsilon$ -independent *propensity functions* (rates) corresponding to these jumps. Then the deterministic generator is  $(\mathcal{L}_0 f)(x) = \left[ \sum_{i=1}^k \lambda_i(x) e_i \right] f'(x)$  and the Fokker-Planck one is  $(\mathcal{L}_{FP} f)(x) = \left[ \sum_{i=1}^k \lambda_i(x) e_i \right] f'(x) + \frac{\epsilon}{2} \left[ \sum_{i=1}^k \lambda_i(x) e_i^2 \right] f''(x)$ . Finally, the Hamilton-Jacobi equation (25) will be generalized as

$$\phi_t = \sum_{i=1}^k \lambda_i(x) (e^{e_i \phi_x} - 1). \quad (35)$$

For the particular model, the Schlögl's bistable system, we answered the question of relative stability, pointing out again, that SDE approach does not answer it correctly, while the deterministic description can not address that question at all. We have found the exact formulae for the switching times from one stable state to the other and vice versa.

Similar questions may be posed for 2D models. The further work may include exploring the competition models from population dynamics in a manner of KMC. Here, the SDE approach is even more widely used, hence it is important to understand that it may not be good enough explaining the rare events, such as, in some cases, the competitive exclusion of one species.

## 8 Acknowledgements

I am very thankful to Eric Vanden-Eijnden for supervising this project throughout the summer. Many thanks to Charlie Doering for all the help concerning this project as well as for introducing me to softball. I am also grateful to George Veronis for all the great times in the softball field. Of course, I can not forget all the Fellows and the pseudo-Fellow Matt Finn, they made this summer a memorable one. Finally, thanks to the remaining staff members and the visitors of the Walsh Cottage.

## References

- [1] F. SCHLÖGL, *Chemical reaction models for non-equilibrium phase transitions*, Z. Phys., 253 (1972), p.147.
- [2] T. G. KURTZ, *Solutions of ordinary differential equations as limits of pure jump markov processes*, J. Appl. Prob., 7(1) (1970), p. 49.
- [3] T. G. KURTZ, *Limit theorems for sequences of jump markov processes approximating ordinary differential processes*, J. Appl. Prob., 8(2) (1971), p. 344.
- [4] N. G. VAN KAMPEN, *Stochastic processes in physics and chemistry*, North-Holland, Amsterdam, 1992.
- [5] C. W. GARDINER, *Handbook of stochastic methods*, Springer-Verlag, Berlin, New York, 1983.

- [6] H. RISKEN, *The Fokker-Planck equation*, Springer-Verlag, New York, 1984.
- [7] A. SHWARTZ AND A. WEISS, *Large deviations for performance analysis*, Chapman-Hall, London, 1995.
- [8] M. I. FREIDLIN AND A. D. WENTZELL, *Random perturbations of dynamical systems*, Springer-Verlag, New York, 1998.
- [9] E. ZAUDERER, *Partial differential equations*, Wiley-Interscience, New York, 1989.
- [10] D. LUDWIG, *Persistence of dynamical systems under random perturbations*, SIAM Review, 17(4) (1975), p. 605-640.

# Simple Models with Cascade of Energy and Anomalous Dissipation

Ravi Srinivasan

July 18, 2006

## 1 Introduction

The phenomenon of turbulence remains one of modern physics greatest unresolved challenges. Turbulent fluid flow exhibits an extraordinarily complex structure which manifests itself in a wide range of length and time scales, posing a significant problem in its analytical study as well as in numerical simulation. While many aspects of turbulence are quite controversial, it is generally accepted that turbulence is characterized by a nonlinear transfer of energy from large length scales to smaller and smaller ones, wherein energy is dissipated at the length scale of the molecular viscosity  $\nu$  [5, 6, 8]. What can then be said about energy dissipation in the regime of fully-developed turbulence—that is, as  $Re \rightarrow \infty$ , or equivalently, as  $\nu \rightarrow 0$ ?

In his 1949 paper, Onsager [7] made the surprising conjecture that turbulent flow can remain dissipative *even in the inviscid limit*. By transferring energy to ever smaller scales and gradually dividing it amongst infinitely many degrees of freedom, the driving mechanism behind such “anomalous dissipation” is the energy cascade itself! Onsager thus suggested that the role of viscosity in energy dissipation is secondary to that of the cascade process. The purpose of this paper is to present simple exactly solvable models which exhibit these very features of a cascade of energy and anomalous dissipation, and to demonstrate that Onsager’s conjecture is indeed realizable within this elementary framework.

### 1.1 Energy Balance and Onsager’s Conjecture

We begin our discussion in the context of the 3D incompressible Navier-Stokes equations with viscosity  $\nu > 0$ , forcing  $\mathbf{f}$ , and periodic boundary conditions

$$\begin{cases} \mathbf{u}_t + (\mathbf{u} \cdot \nabla) \mathbf{u} = -\nabla p + \nu \Delta \mathbf{u} + \mathbf{f}, & \mathbf{x} \in \Omega = [0, L_f]^3 \\ \nabla \cdot \mathbf{u} = 0 \end{cases} \quad (1)$$

where  $\mathbf{f}(\mathbf{x}, t)$  is a stationary, homogeneous forcing acting on large scales:

$$\mathbb{E} \mathbf{f}(\mathbf{x}, t) = 0, \quad \mathbb{E} \mathbf{f}(\mathbf{x}, t) \mathbf{f}(\mathbf{x}', t') = F \left( \frac{\mathbf{x} - \mathbf{x}'}{L_f} \right) \delta(t - t'). \quad (2)$$

For our present discussion, let

$$\mathbf{f}(\mathbf{x}, t) = \sigma \sum_{i=1}^3 \left( \dot{W}_{x_i}(t) \sin \frac{2\pi x_i}{L} + \dot{W}'_{x_i}(t) \cos \frac{2\pi x_i}{L} \right) \hat{\mathbf{e}}_i \quad (3)$$

which satisfies (2) with  $F(\mathbf{x}) = \frac{1}{2}\sigma^2 \sum_{i=1}^3 \cos(2\pi|\mathbf{x} \cdot \mathbf{e}_i|)$ . Consider now the energy density of the system

$$E(t) \doteq \frac{1}{|\Omega|} \int_{\Omega} \frac{1}{2} \mathbb{E} \mathbf{u}^2(\mathbf{x}, t) d\mathbf{x} = \frac{1}{|\Omega|} \int_{\Omega} \frac{1}{2} \left( \lim_{T \rightarrow \infty} \frac{1}{t+T} \int_{-T}^t \mathbf{u}^2(\mathbf{x}, t') dt' \right). \quad (4)$$

where the last equality holds by ergodicity. Multiplying (1) by  $\mathbf{u}$  and integrating by parts gives

$$\dot{E}(t) = \frac{d}{dt} \frac{1}{|\Omega|} \int_{\Omega} \frac{1}{2} \mathbb{E} |\mathbf{u}|^2 d\mathbf{x} = -\nu \frac{1}{|\Omega|} \int_{\Omega} \mathbb{E} |\nabla \mathbf{u}|^2 d\mathbf{x} + \varepsilon \quad (5)$$

where  $\varepsilon = \frac{3}{2}\sigma^2$ , the density of the energy flux into the system through forcing, appears by Itô's formula. Assuming the system is in a statistical steady state ( $\dot{E}(t) = 0$ ) then there exists a global energy balance between forcing and dissipation through viscosity:

$$\nu \frac{1}{|\Omega|} \int_{\Omega} \mathbb{E} |\nabla \mathbf{u}|^2 d\mathbf{x} = \varepsilon \quad (6)$$

To arrive at a local energy balance, consider a dimensional argument with  $L = \text{length}$  and  $T = \text{time}$ . Since

$$[L_f] = L \quad [\varepsilon] = \frac{L^2}{T^3} \quad [\nu] = \frac{L^2}{T}, \quad (7)$$

the only length scale which can be derived from  $\nu$  and  $\varepsilon$  is the viscous length scale

$$l_{\nu} = C \varepsilon^{-\frac{1}{4}} \nu^{\frac{3}{4}} \quad (8)$$

which vanishes in the inviscid limit. From a local perspective, energy that is pumped into the system at the forcing length scale  $L_f$  cascades to smaller and smaller scales and is subsequently removed from the system at the length scale of the viscosity  $l_{\nu}$  (see Figure 1).

The cascade picture is more readily observed in the Fourier space setting. The Fourier representation of (1) is

$$\frac{d}{dt} \hat{\mathbf{u}}_{\mathbf{k}} = -i \mathbf{P}_{\mathbf{k}^{\perp}} \sum_{\mathbf{q}} (\mathbf{q} \cdot \hat{\mathbf{u}}_{\mathbf{k}-\mathbf{q}}) \hat{\mathbf{u}}_{\mathbf{q}} - \nu |\mathbf{k}|^2 \hat{\mathbf{u}}_{\mathbf{k}} + \hat{\mathbf{f}}_{\mathbf{k}} \quad (9)$$

where  $\mathbf{P}_{\mathbf{k}^{\perp}} = \mathbf{I} - \frac{\mathbf{k} \otimes \mathbf{k}}{|\mathbf{k}|^2}$  is the projection on the space of divergence-free velocity fields and

$$\begin{aligned} \hat{\mathbf{u}}_{\mathbf{k}}(t) &= \frac{1}{L^{\frac{3}{2}}} \int_{[0,L]^3} \mathbf{u}(\mathbf{x}, t) e^{i\mathbf{k} \cdot \mathbf{x}} d\mathbf{x} \\ \hat{\mathbf{f}}_{\mathbf{k}}(t) &= \frac{1}{L^{\frac{3}{2}}} \int_{[0,L]^3} \mathbf{f}(\mathbf{x}, t) e^{i\mathbf{k} \cdot \mathbf{x}} d\mathbf{x}. \end{aligned}$$

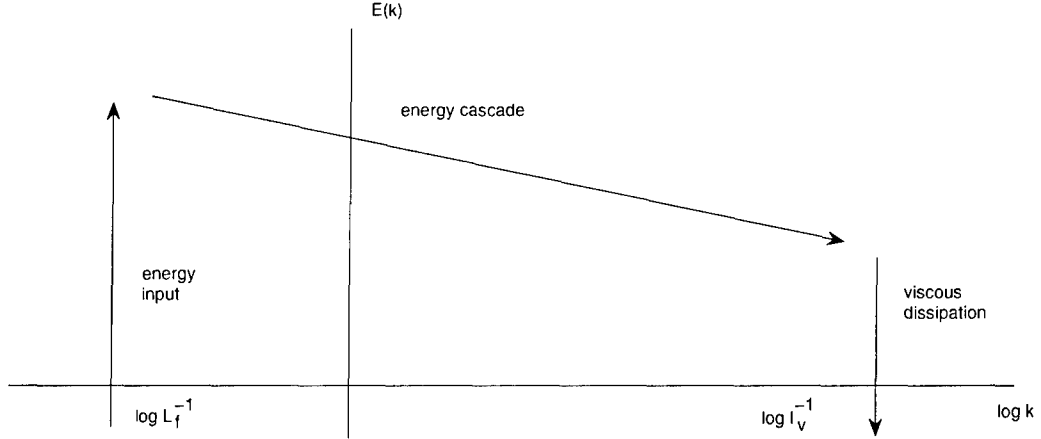


Figure 1: Cascade of energy from forcing length scale  $L_f$  to viscous length scale  $l_v$ .

The first, second, and third terms on the right-hand side of (9) correspond to the mechanism of energy transfer between modes, dissipation at  $l_v^{-1}$ , and energy input at  $L_f^{-1}$ , respectively. By Parseval's identity, the energy equation is then

$$\begin{aligned}\dot{E}(t) &= \frac{d}{dt} \sum_{\mathbf{k}} \frac{1}{2} \mathbb{E} |\hat{u}_{\mathbf{k}}|^2 \\ &= i \sum_{\mathbf{k}} \mathbf{P}_{\mathbf{k}^\perp} \mathbb{E} \sum_{\mathbf{q}} (\mathbf{q} \cdot \hat{u}_{\mathbf{k}-\mathbf{q}}) (\hat{u}_{\mathbf{k}}^* \cdot \hat{u}_{\mathbf{q}}) + c.c. - \nu \sum_{\mathbf{k}} |\mathbf{k}|^2 \mathbb{E} |\hat{u}_{\mathbf{k}}|^2 + \varepsilon\end{aligned}\quad (10)$$

with  $c.c.$  denoting the complex conjugate of the first term. The summands within the energy transfer terms are commonly known as “triad interactions” due to the appearance of coupling between the modes  $\mathbf{k}$ ,  $\mathbf{q}$ , and  $\mathbf{k} - \mathbf{q}$ , consequently resulting in a nonlinear transfer of energy. A formal rearrangement of the sum gives that

$$i \sum_{\mathbf{k}} \mathbf{P}_{\mathbf{k}^\perp} \mathbb{E} \sum_{\mathbf{q}} (\mathbf{q} \cdot \hat{u}_{\mathbf{k}-\mathbf{q}}) (\hat{u}_{\mathbf{k}}^* \cdot \hat{u}_{\mathbf{q}}) + c.c. = 0, \quad (11)$$

implying a global energy balance between forcing and viscous dissipation analogous to (6) for statistical steady state solutions to 3D Navier-Stokes:

$$\nu \sum_{\mathbf{k}} |\mathbf{k}|^2 \mathbb{E} |\hat{u}_{\mathbf{k}}|^2 = \varepsilon. \quad (12)$$

Is this formal rearrangement actually valid? If we presume the existence of a steady state solution to (1) in the inviscid limit (Euler equation with forcing) then (11) is strikingly false! For steady state solutions to Euler, the energy transfer and forcing terms balance:

$$i \sum_{\mathbf{k}} \mathbf{P}_{\mathbf{k}^\perp} \mathbb{E} \sum_{\mathbf{q}} (\mathbf{q} \cdot \hat{u}_{\mathbf{k}-\mathbf{q}}) (\hat{u}_{\mathbf{k}}^* \cdot \hat{u}_{\mathbf{q}}) + c.c. = \varepsilon. \quad (13)$$

The fact that the sum in (13) does not vanish provides some insight into the lack of regularity of solutions to the forced Euler equation [3, 4]. In particular, since the Fourier coefficients of  $\mathbf{u}$  do not decay rapidly enough to allow absolute convergence of the sum we have that such solutions maintain shocks, which allow for the anomalous dissipation of energy. This is the heart of Onsager's conjecture: In the regime of fully-developed turbulence, steady state solutions correspond to the *most regular* weak solutions of the 3D Euler equation that allow for anomalous dissipation. In addition, Onsager proposed that weak solutions of Euler conserve energy if they are Hölder continuous with exponent  $n$  greater than  $1/3$  [5]. In Fourier space, the Hölder condition is

$$\sum_{\mathbf{k}} |\mathbf{k}|^n |\hat{u}_{\mathbf{k}}| < \infty \quad (14)$$

so if the previous sum is absolutely convergent with  $n > 1/3$  then the conjecture gives that the formal rearrangement in (11) is valid and energy is conserved. The sufficiency of this condition was proved in 1994 by Constantin *et al.* [2] but necessity still remains an open question.

The loss of regularity of steady solutions to forced 3D Euler can be observed through a dimensional analysis argument. Define the second-order structure function

$$E(\mathbf{x} - \mathbf{x}', t) \doteq \mathbb{E} |\mathbf{u}(\mathbf{x}, t) - \mathbf{u}(\mathbf{x}', t)|^2, \quad (15)$$

where the homogeneity of solutions  $\mathbf{u}$  to (1) has been used. Then

$$[E(\mathbf{x}, t)] = \frac{L^2}{T^2} \quad [\mathbf{x}] = L. \quad (16)$$

and there exists a function  $\mathcal{F}$  such that

$$\mathcal{F} \left( E^{-\frac{3}{2}} \varepsilon \mathbf{x}, \frac{\mathbf{x}}{L_f}, \frac{\mathbf{x}}{l_\nu} \right) = 0. \quad (17)$$

Assuming isotropy,

$$E = C' \varepsilon^{\frac{2}{3}} |\mathbf{x}|^{\frac{2}{3}} g \left( \frac{|\mathbf{x}|}{L_f}, \frac{|\mathbf{x}|}{l_\nu} \right) \quad (18)$$

for some  $g$ . Since we are interested in the inertial range  $l_\nu \ll |\mathbf{x}| \ll L_f$  with  $L_f$  fixed, we first let  $l_\nu \rightarrow 0$  (that is, let  $\nu \rightarrow 0$ ) and then take  $|\mathbf{x}| \rightarrow 0$  to arrive at the celebrated Kolmogorov two-thirds law

$$E = C \varepsilon^{\frac{2}{3}} |\mathbf{x}|^{\frac{2}{3}}, \quad (19)$$

where we have made the assumption that  $\lim_{\varepsilon \rightarrow 0} \lim_{\eta \rightarrow \infty} g(\xi, \eta)$  exists and is finite. In Fourier space, the previous display is equivalent to the five-thirds law

$$E_{\mathbf{k}} \sim \varepsilon^{\frac{2}{3}} |\mathbf{k}|^{-\frac{5}{3}} \quad (20)$$

with  $E_{\mathbf{k}} = \mathbb{E} |\hat{u}_{\mathbf{k}}|^2$ . Using (19) and Hölder's inequality, one finds that the velocity field is Hölder continuous with exponent  $1/3$ :



$$\mathbb{E}|\mathbf{u}(\mathbf{x}, t) - \mathbf{u}(\mathbf{x}', t)| \leq \sqrt{E(\mathbf{x} - \mathbf{x}', t)} = O(|\mathbf{x} - \mathbf{x}'|^{\frac{1}{3}}). \quad (21)$$

Formally,

$$\mathbb{E}|\nabla \mathbf{u}(\mathbf{x})|^2 = \lim_{|\mathbf{y}| \rightarrow 0} \frac{1}{|\mathbf{y}|^2} \mathbb{E}|\mathbf{u}(\mathbf{x} + \mathbf{y}) - \mathbf{u}(\mathbf{x})|^2 \simeq |\mathbf{y}|^{-\frac{4}{3}} \simeq |l_\nu|^{-\frac{4}{3}} \sim \nu^{-1} \quad (22)$$

where we have used the two-thirds law and concerned ourselves with the regularity of  $\mathbf{u}$  at the level of the viscous length scale. It can then be seen that

$$\nu \frac{1}{|\Omega|} \int_{\Omega} \mathbb{E}|\nabla \mathbf{u}|^2 d\mathbf{x} \sim O(1).$$

Alternatively, since (6) is valid for all  $\nu > 0$ , we have that  $\lim_{\nu \rightarrow 0} \nu \frac{1}{|\Omega|} \int_{\Omega} \mathbb{E}|\nabla \mathbf{u}|^2 d\mathbf{x} = \varepsilon$ . Even in the inviscid limit energy is *still* removed by loss of regularity of solutions to Euler's equation!

## 1.2 Anomalous Dissipation in Burgers' Equation

In our discussion to present we have made several significant assumptions, such as that of the existence of a unique steady state solution to 3D Navier-Stokes with random forcing (which is in fact a reasonable assumption, see [1]). While Onsager's conjecture is somewhat speculative for the 3D or 2D Navier-Stokes and Euler equations, it is realizable and easily illustrated within the framework of Burgers' equation with forcing and periodic boundary conditions:

$$u_t + \frac{1}{2}(u^2)_x = \nu u_{xx} - \frac{\pi}{2} \sin(2\pi x), \quad x \in [0, 1]. \quad (23)$$

For  $\nu > 0$ , (23) admits smooth solutions with “shock layers” of size  $O(\nu)$ ; however, if  $\nu \rightarrow 0$ , solutions develop discontinuities which allow for anomalous dissipation of energy. In Fourier space, the solution of (23) with  $\nu = 0$  is

$$u(x, t) = \frac{1}{2} \sum_{n \in \mathbb{Z}} b_n(t) \sin(2n\pi x) \quad (24)$$

where  $b_n(t) = \text{Im } \hat{u}_n(t) = 2 \int_0^1 u(x, t) \sin(2n\pi x) dx$  and satisfies

$$\begin{aligned} \dot{b}_n &= 2 \int_0^1 u_t \sin(2n\pi x) dx \\ &= 2 \int_0^1 [-uu_x + f(x)] \sin(2n\pi x) dx \\ &= -2n\pi \sum_{m \in \mathbb{Z}} b_m b_{m-n} - \frac{\pi}{2} (\mathbb{1}_{n=1} - \mathbb{1}_{n=-1}). \end{aligned} \quad (25)$$

By Parseval's identity and the previous display, the unique steady state solution must satisfy

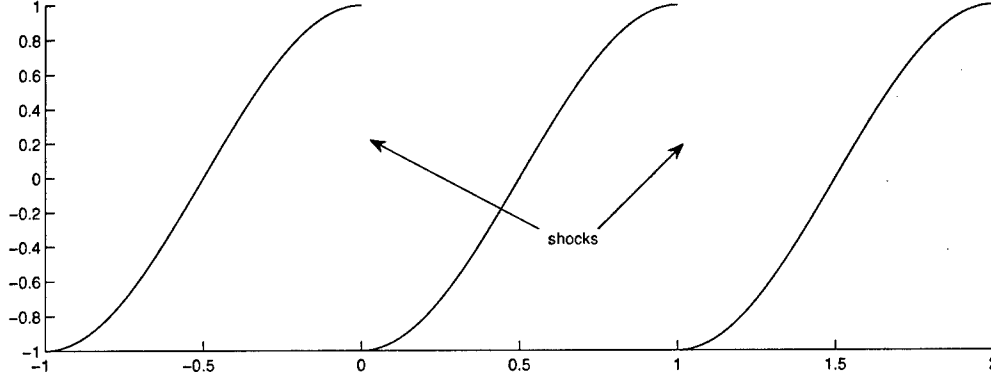


Figure 2: Dissipative solution to forced inviscid Burgers' equation.

$$\dot{E}(t) = \frac{d}{dt} \sum_{n \in \mathbb{Z}} \frac{1}{2} b_n^2 = - \sum_{n, m \in \mathbb{Z}} 2n\pi b_n b_m b_{n-m} + \pi b_1 = 0. \quad (26)$$

If the sum in the previous display is formally reorganized,

$$\begin{aligned} \sum_{n, m \in \mathbb{Z}} 2n\pi b_n b_m b_{n-m} &= \sum_{n, m \in \mathbb{Z}} 2n\pi b_{-n} b_m b_{-n-m} \\ &= - \sum_{n+m+p=0} 2n\pi b_n b_m b_p \\ &= -\frac{1}{3} \sum_{n+m+p=0} 2(n+m+p)\pi b_n b_m b_p \\ &= 0. \end{aligned} \quad (27)$$

We are then led to believe that the system has no steady state solution (with  $b_1 \neq 0$ ). Yet, it is simple to show that

$$w(x) = -\cos \pi x \quad (28)$$

is a solution of (23) in the inviscid limit! How can this be?

The answer lies in the fact that  $w$  is a *weak* solution and rearrangement of the sum is invalid because the coefficients  $b_n$  do not decay fast enough. In order to compensate for the lack of a viscous dissipation mechanism,  $w$  has lost regularity and developed shocks (see Figure 2). One has that

$$b_n = -\frac{8n}{\pi(4n^2 - 1)} \sim -\frac{2}{\pi n} \text{ as } |n| \rightarrow \infty \quad (29)$$

so  $b_n^2 \sim O(|n|^{-2})$ . In this case, the energy of the steady state  $E = \sum_{n \in \mathbb{Z}} \frac{1}{2} b_n^2 < \infty$  and dissipation is nonzero:

$$\sum_{n,m \in \mathbb{Z}} 2n\pi b_n b_m b_{n-m} = \pi b_1 = -\frac{8}{3} < 0. \quad (30)$$

The above example illustrates that there exist steady state solutions with finite energy that dissipate through shocks. In the next section, we develop yet simpler models that exhibit an energy cascade and anomalous dissipation.

## 2 Simple Models

Consider the following infinite dimensional dynamical system:

$$\begin{cases} \dot{a}_n = \alpha \{(n-1)^p a_{n-1} - n^p a_{n+1}\} + f(t) \mathbb{1}_{n=1}, & n \in \mathbb{N} \\ a_0 = 0 \end{cases} \quad (31)$$

where  $\alpha \in \mathbb{R}$ ,  $p = 0, 1, 2$  and  $f(t) \mathbb{1}_{n=1}$  is a time-dependent forcing term on the first mode. The system (31) describes a linear shell model with nearest-neighbor coupling and (as we shall see) the feature that it allows for anomalous dissipation. We will focus here on the case  $p = 1$  with forcing  $f(t) = \sqrt{2\varepsilon} \dot{W}(t)$  and will speculate on cases with  $p \neq 1$ . In the case of white noise forcing—which has the advantage of being uncorrelated with the modes  $a_n$ —an energy balance relation analogous to (5) can be derived:

$$\dot{E}(t) = \frac{d}{dt} \sum_{n \in \mathbb{N}} \frac{1}{2} \mathbb{E} a_n^2 = \alpha \sum_{n \in \mathbb{N}} \mathbb{E} \{(n-1)^p a_n a_{n-1} - n^p a_n a_{n+1}\} + \varepsilon \quad (32)$$

and we have that anomalous dissipation is possible if

$$-\alpha \sum_{n < N} \mathbb{E} \{(n-1)^p a_n a_{n-1} - n^p a_n a_{n+1}\} = \alpha N^p \mathbb{E} a_N a_{N+1} \xrightarrow{N \rightarrow \infty} \varepsilon. \quad (33)$$

This requires that for steady state solutions

$$a_n \sim n^{-p/2} \text{ as } n \rightarrow \infty \quad (34)$$

since if  $a_n$  scales with any other exponent, solutions will have either zero or infinite dissipation. This is consistent with Onsager's conjecture since steady states of the model correspond to the most rapidly decaying  $\{a_n\}$  which allow for anomalous dissipation! By a simple scaling argument, one has that steady state solutions must lie on the boundary of the weighted  $l_2$  spaces

$$l_{2,p} \doteq \left\{ \{a_n\}_{n \in \mathbb{N}} : \sum_{n \in \mathbb{N}} n^{p-1} a_n^2 < \infty \right\}, \quad (35)$$

with no dissipation in the interior of  $l_{2,p}$  and infinite dissipation in the exterior of  $l_{2,p}$  (see Figure 3). The representation formula for the unique steady state with  $p = 1$ , to be derived in a subsequent section, agrees with this picture.

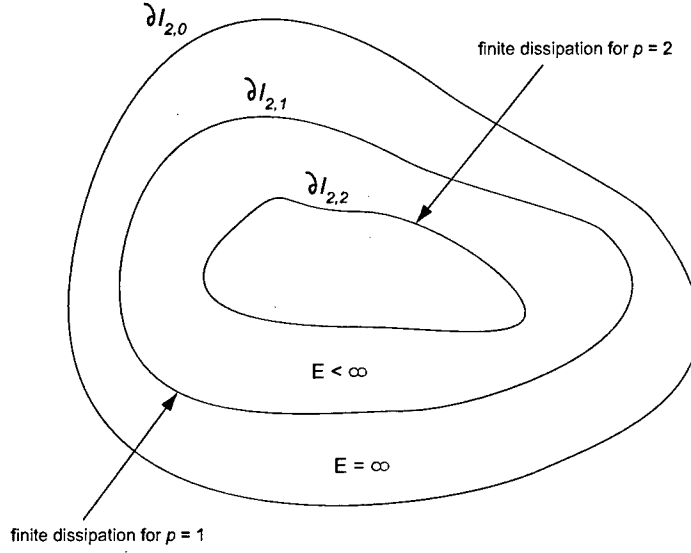


Figure 3: Spaces  $l_{2,p}$  and corresponding rates of dissipation.

## 2.1 The case $p = 1$

We now show how to solve the simple model in the case  $p = 1$  with forcing  $f(t) = \sqrt{2\varepsilon}\dot{W}(t)$ . Some remarks on the case  $p = 2$  will be made in Section 3.

Consider the set of Laguerre polynomials  $L_n(x)$  which satisfy

$$\begin{aligned}
 & \text{(i)} \quad L_0(x) = 1 \\
 & \text{(ii)} \quad (n+1)L_{n+1}(x) = (2n+1-x)L_n(x) - nL_{n-1}(x), \quad n \in \mathbb{N} \\
 & \text{(iii)} \quad xL'_n(x) = nL_n(x) - nL_{n-1}(x) \\
 & \text{(iv)} \quad \int_0^\infty L_m(x)L_n(x)e^{-x}dx = \delta_{nm}
 \end{aligned} \tag{36}$$

Let  $f_0 = 0$ ,  $f_n(z) = L_{n-1}(z)$  for  $n \in \mathbb{N}$ , and define

$$g(z, t) = \sum_{n \in \mathbb{N}} a_n(t) f_n(z). \tag{37}$$

Then one has that

$$\begin{aligned}
 \dot{g}(z, t) &= \sum_{n \in \mathbb{N}} \dot{a}_n(t) f_n(z) \\
 &= \sum_{n \in \mathbb{N}} \alpha \{ (n-1)a_{n-1} - na_{n+1} \} f_n(z) + \sqrt{2\varepsilon}\dot{W}(t) \\
 &= \sum_{n \in \mathbb{N}} \alpha a_n \{ 2zf'_n(z) + (1-z)f_n(z) \} + \sqrt{2\varepsilon}\dot{W}(t) \\
 &= 2\alpha z \frac{\partial g}{\partial z}(z, t) + \alpha(1-z)g(z, t) + \sqrt{2\varepsilon}\dot{W}(t)
 \end{aligned} \tag{38}$$

by shifting indices and by properties (36) of the Laguerre polynomials. Solving the stochastic partial differential equation in the previous display, one can use the orthonormality of  $\{f_n(z)\}_{n \in \mathbb{N}}$  to find  $a_n$ :

$$a_n(t) = \int_0^\infty g(z, t) f_n(z) e^{-z} dz. \quad (39)$$

Furthermore,

$$\begin{aligned} E(t) &= \sum_{n \in \mathbb{N}} \frac{1}{2} \mathbb{E} a_n^2 = \int_0^\infty \frac{1}{2} \mathbb{E} g^2(z, t) e^{-z} dz \\ \dot{E}(t) &= \sum_{n \in \mathbb{N}} \mathbb{E} a_n \dot{a}_n = \int_0^\infty \mathbb{E} g(z, t) \dot{g}(z, t) e^{-z} dz \end{aligned} \quad (40)$$

where equality follows from Parseval's identity. Note that from (38) one can also derive the conservation form

$$\begin{aligned} \frac{1}{2} (g^2 e^{-z})' &= g \dot{g} e^{-z} \\ &= g \left[ 2\alpha z \frac{\partial g}{\partial z} + \alpha(1-z)g + \sqrt{2\varepsilon} \dot{W} \right] e^{-z} \\ &= \frac{\partial}{\partial z} (\alpha z g^2 e^{-z}) + \sqrt{2\varepsilon} \dot{W} g e^{-z}. \end{aligned} \quad (41)$$

We are now equipped with the tools necessary to determine properties of explicitly determined solutions.

## 2.2 Representation Formulas for the Steady State and IVP

We now derive the steady state solution of (31) for  $p = 1$  with white-noise forcing and examine the initial value problem (IVP) without forcing. To simplify discussion, take  $\alpha = 1$ . Solving (38) with initial conditions  $g_0(z) \doteq g(z, 0) = \sum_{n \in \mathbb{N}} a_n(0) f_n(z)$ , one has that

$$g(z, t) = e^{(\frac{z}{2} + t)} \left[ e^{(-\frac{z}{2} e^{2t})} g_0(z e^{2t}) + \sqrt{2\varepsilon} \int_0^t e^{(-\frac{z}{2} e^{2(t-s)})} dW(s) \right]. \quad (42)$$

The explicit representation for the unique statistical steady state solution is then

$$a_n(t) = \sqrt{2\varepsilon} \int_{-\infty}^t dW(s) \int_0^\infty dz L_{n-1}(z) e^{[t-s-\frac{z}{2}(e^{2(t-s)}+1)]} \quad (43)$$

so  $a_n(t)$  is a Gaussian field with mean 0 and covariance

$$\begin{aligned} \mathbb{E}(a_n(t) a_m(t)) &= 2\varepsilon \int_0^\infty ds \int_0^\infty dz_1 \int_0^\infty dz_2 L_{n-1}(z_1) L_{m-1}(z_2) e^{[2s - \frac{z_1 + z_2}{2}(e^{2s} + 1)]} \\ &= \frac{2\varepsilon}{n + m - 1}. \end{aligned} \quad (44)$$

In particular,

$$-\lim_{N \rightarrow \infty} \sum_{n \leq N} \{(n-1)\mathbb{E}(a_n a_{n-1}) - n\mathbb{E}(a_n a_{n+1})\} = \lim_{N \rightarrow \infty} N\mathbb{E}a_N a_{N+1} \equiv \varepsilon$$

and we have anomalous dissipation.

A simple consequence of the conservation form (41) is that energy is conserved if one begins with finite energy:

$$\sum_{n \in \mathbb{N}} \mathbb{E}a_n^2(0) < \infty \text{ implies } \sum_{n \in \mathbb{N}} \mathbb{E}a_n^2(t) = \sum_{n \in \mathbb{N}} \mathbb{E}a_n^2(0) \text{ for } t > 0. \quad (45)$$

There also exist dissipative solutions with  $\sum_{n \in \mathbb{N}} \mathbb{E}a_n^2(0) = \infty$ ; that is, solutions such that

$$\mathbb{E}|a_n| \geq Cn^{-1/2} \text{ as } n \rightarrow \infty. \quad (46)$$

Finally, as we have shown above, with forcing there exists a unique statistical steady state with equilibrium distribution supported on the the most regular dissipative solutions, i.e., such that

$$\mathbb{E}a_n^2 = O(n^{-1}) \quad \text{as } n \rightarrow \infty.$$

### 3 PDE Approximation to Simple Models

When scaled properly, the system (31) very closely resembles a finite difference scheme for the wave equation  $u_t = cu_x$ . Keeping this in mind, for  $\alpha > 0$  one can find PDEs whose solutions mimic those of the simple model for the IVP.

We begin by setting  $\alpha = 1$  and by recalling that with no forcing,

$$\dot{a}_n = (n-1)^p a_{n-1} - n^p a_{n+1}.$$

Let  $a_n(t) = A(nh, th^{-p+1})$  and send  $h \rightarrow 0$  with  $nh \rightarrow x$  and  $th^{-p+1} \rightarrow \tau$  to obtain

$$\frac{\partial A}{\partial \tau} = -px^{p-1}A - 2x^p \frac{\partial A}{\partial x}. \quad (47)$$

The previous equation can also be written in the conservation form

$$\frac{1}{2} \frac{\partial A^2}{\partial \tau} = -\frac{\partial}{\partial x}(x^p A^2). \quad (48)$$

Thus, one has

$$\frac{1}{2} \frac{d}{d\tau} \int_0^L A^2(x, \tau) dx = -L^p A^2(L, \tau) \underset{L \rightarrow \infty}{\not\rightarrow} 0 \quad \text{if } A^2(L, \tau) > CL^{-p} \quad (49)$$

which is exactly the phenomenon of anomalous dissipation!

Now consider the characteristic equation and solution of (47):

$$\frac{dX}{d\tau} = -2X^p, \quad X(0) = x \quad (50)$$

$$A(x, \tau) = A_0(X(\tau)) \exp \left( -p \int_0^\tau X^{p-1}(\tau') d\tau' \right). \quad (51)$$

### 3.1 The case $p = 1$

If  $p = 1$ , then  $X(\tau) = xe^{-2\tau}$  and there is no anomalous dissipation if  $\int_0^\infty A_0^2(x) dx < \infty$  since energy is conserved:

$$\int_0^\infty A^2(x, \tau) dx = \int_0^\infty A_0^2(xe^{-2\tau}) e^{-2\tau} dx = \int_0^\infty A_0^2(\eta) d\eta. \quad (52)$$

Anomalous dissipation only occurs in this case if  $A_0^2(x) > Cx^{-1}$  as  $x \rightarrow \infty$ , and in particular,  $A^2(x, \tau) = Cx^{-1}$  if  $A_0^2(x) = Cx^{-1}$ .

### 3.2 The case $p = 2$

If  $p = 2$ , then  $X(\tau) = \frac{x}{1+2\tau x}$  and anomalous dissipation occurs even if  $\int_0^\infty A_0^2(x) dx < \infty$  since

$$\begin{aligned} \int_0^\infty A^2(x, \tau) dx &= \int_0^\infty A_0^2 \left( \frac{x}{1+2\tau x} \right) \frac{dx}{(1+2\tau x)^2} \\ &= \int_0^{1/2\tau} A_0^2(\eta) d\eta \\ &\leq \int_0^\infty A_0^2(\eta) d\eta. \end{aligned} \quad (53)$$

Notice also that

$$A^2(x, \tau) = A_0^2 \left( \frac{x}{1+2\tau x} \right) \frac{1}{(1+2\tau x)^2} \sim A_0^2(1/2\tau) (2x\tau)^{-2} \quad \text{as } x \rightarrow \infty \quad (54)$$

so that one has anomalous dissipation for  $\tau \geq \tau_*$ , where

$$\tau_* = \min\{\tau : A_0^2(1/2\tau) \neq 0\}. \quad (55)$$

### 3.3 Properties of the Solutions

It can easily be seen that the approximating PDE is consistent with the simple model for  $p = 1$  since the aforementioned properties exactly mirror those given in the previous section. We can speculate that this is true for all other values of  $p$  as well. Moreover, since the behavior of the characteristics completely determine the properties of the IVP solution, by (50) one has that solutions with  $p < 1$  behave like the  $p = 1$  solution, and solutions with  $p > 2$  behave like the  $p = 2$  solution with regards to anomalous dissipation.

There is an interesting analog between solutions of the approximating PDE for  $p = 2$  and  $p = 1$  and those of the 3D and 2D Euler equations, respectively. As discussed in [3], solutions of 3D Euler with finite energy are expected to dissipate, as in the case  $p = 2$ . In contrast, it has been proved [4] that solutions to 2D Euler (in which the *enstrophy*

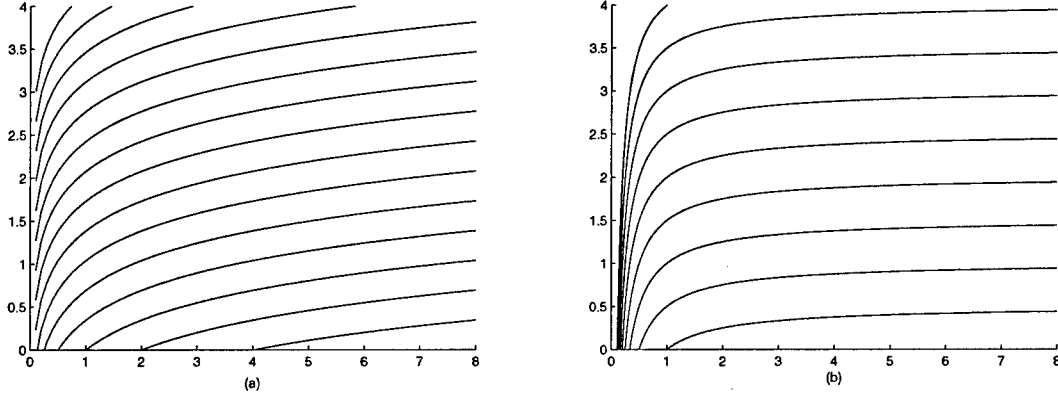


Figure 4: Characteristics of the approximating PDE for (a)  $p = 1$  and (b)  $p = 2$ .

$\mathcal{E} = \frac{1}{2}|\omega|^2 = \frac{1}{2}|\nabla \times \mathbf{u}|^2$ , rather than the energy, cascades to small scales) conserve enstrophy whenever the enstrophy itself is finite, just as in the case  $p = 1$ ! Furthermore, if we define the “turnover time”  $\tau(k)$  in the context of 3D Euler as the only time scale which can be derived from the wavenumber magnitude  $k = |\mathbf{k}|$  and energy flux  $\varepsilon$  (equivalently, the enstrophy flux  $\hat{\varepsilon}$  in 2D Euler), dimensional analysis gives that

$$\tau(k) = C\varepsilon^{-1/3}k^{-2/3} \text{ (3D Euler)}, \quad \hat{\tau}(k) = C\hat{\varepsilon}^{-2/3} \text{ (2D Euler)}. \quad (56)$$

Since the turnover time describes the time required for energy (enstrophy) to pass through wavenumbers of magnitude  $k$  and  $\mu(k) = \ln(k)$  is the natural scale-invariant measure associated with  $k$ , the total time for energy (enstrophy) to move from  $k = 1/L_f$  to  $k = \infty$  is

$$\int_{1/L_f}^{\infty} \tau(k) d\mu(k) < \infty \text{ (3D Euler)}, \quad \int_{1/L_f}^{\infty} \hat{\tau}(k) d\mu(k) = \infty \text{ (2D Euler)}. \quad (57)$$

Analogously, characteristic lines in the case  $p = 2$  go to infinity in finite time, while those for  $p = 1$  go to infinity in infinite time (see Figure 4)!

It is worth noting that in the derivation of the PDE (47) we have made some smoothness assumptions on solutions of the IVP in the simple model. These assumptions can be justified if  $\alpha > 0$  but are quite wrong if  $\alpha < 0$ . To see this, let  $\alpha = -1$  and consider the IVP  $a_n(0) = \mathbb{1}_{n=1}$  for  $p = 0$ . Then for  $0 < t \ll 1$  one has that  $a_n \gg a_m$  for  $n < m$ , and so

$$\dot{a}_n(t) \simeq -a_{n-1}(t) \text{ for } n \in \mathbb{N}, \text{ with } a_0 = 0.$$

This implies that for small values of  $t$ ,

$$a_n(t) \simeq (-1)^{n-1} t^n.$$

The solution of the IVP is thus initially highly oscillatory and cannot be approximated by a smooth function in any strong sense.



## Acknowledgements

I would like to thank my advisor Eric Vanden-Eijnden for providing me the opportunity to explore this very interesting problem, and for his guidance and support throughout the summer. The calculation in Section 2.2 is based on results in an unpublished paper by Jonathan Mattingly, Toufic Suidan, and Eric. Many thanks to Charlie and Oliver for organizing an amazing program, to George for an enjoyable and successful summer on the softball field, and to all the faculty, staff, and students who made Woods Hole a wonderful place to both work and play. I would also like to give special thanks to Rick Salmon, who introduced me to the GFD program and a community in which I will remain in close touch with for years to come. To my fellow GFD fellows and Barn residents with whom I will share many happy memories: I had a great time spending the summer with you!

## References

- [1] Y. Bakhtin. Existence And Uniqueness of Stationary Solutions for 3D Navier-Stokes System with Small Random Forcing via Stochastic Cascades. Preprint, 2004.
- [2] P. Constantin, W. E, and E. S. Titi. Onsager’s conjecture on the energy conservation for solutions of Euler’s equation. *Commun. Math. Phys.*, 165:207–209, 1994.
- [3] J. Duchon and R. Robert. Inertial energy dissipation for weak solutions of incompressible Euler and Navier-Stokes equations. *Nonlinearity*, 13:249–255, 2000.
- [4] G. L. Eyink. Dissipation in turbulent solutions of 2D Euler equations. *Nonlinearity*, 14:787–802, 2001.
- [5] G. L. Eyink and K. R. Sreenivasan. Onsager and the Theory of Hydrodynamic Turbulence. Preprint, 2005.
- [6] Uriel Frisch. *Turbulence: The Legacy of A.N. Kolmogorov*. Cambridge University Press, Cambridge, UK, 1995.
- [7] L. Onsager. Statistical Hydrodynamics. *Nuovo Cimento (Supplemento)*, 6:279, 1949.
- [8] Rick Salmon. *Lectures on Geophysical Fluid Dynamics*. Oxford University Press, New York, 1998.

# Vibrating pendulum and stratified fluids

Inga Koszalka

## 1 Abstract

The problem posed is the stabilization of the inverted state of a simple pendulum induced by high-frequency vertical oscillations of the pivot point. The stability conditions are derived by means of the multiscale perturbation leading to the averaged dynamics as well as by linearization. Then the concept and methods are applied to the study of an incompressible, inviscid, stratified fluid under the Boussinesq approximation. The mechanism of the stabilization of the fluid system was found to be analogous to that of pendulum provided that the density disturbance has the form of a wave or the sum of waves. However, the analogy in case of a general density disturbance is not obvious.

## 2 Introduction

A simple pendulum has only one stable state, the straight-down position. However, if its support vibrates in the vertical or, equivalently, when the gravity is modulated at a frequency much greater than the natural frequency of the pendulum, then it is also possible for the inverted (upside-down) position to be a stable state. The problem dates back to 1908 when Stephenson showed that it is indeed possible to stabilize an inverted pendulum by subjecting the pivot to small vertical oscillations of suitably high frequency ([17], [18], [19]). However, it was the work of Piotr Kapitza ([10]) that drew broader attention and commenced a series of studies concerned with this interesting phenomenon, called sometimes for that reason "Kapitza pendulum". Similar behavior of parametrically forced systems in this parameter regime was found in other problems, like particle trapping and even evolution of market prices (e.g see [6], [7]).

The purpose of this work is to investigate the stabilization of the inverted pendulum and to apply the concept and the methods developed to fluid dynamics. The pendulum system is treated by means of the multiscale perturbation which leads to the averaged dynamics, as well as by linearization, which reduces the problem to Mathieu equation. As a simple fluid analog we choose incompressible, stratified fluid under the Boussinesq approximation in periodic domain, subjected to a rapidly varying gravitational field. We focus on the multiscale technique and averaged dynamics to find the stabilization mechanism equivalent to that obtained for the Kapitza pendulum.

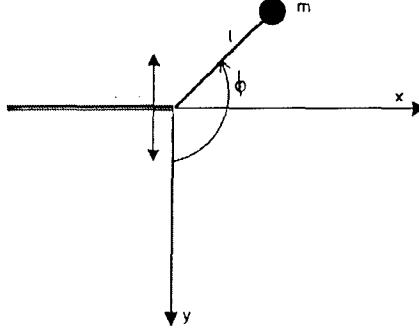


Figure 1: Kapitza pendulum.

### 3 Vibrating inverted pendulum

#### 3.1 Problem formulation. Equation of motion

We consider a simple, nonlinear pendulum of mass  $m$  and length  $l$ , moving on a vertical plane in the uniform gravitational field and subjected to a vertical, rapid vibration of the pivot point. By rapid vibration we mean oscillation of high frequency and small amplitude of the pivot motion, given a form:

$$\zeta(t) = a \cos(\gamma t). \quad (1)$$

The parameters of the external forcing, the amplitude of the vertical motion and the frequency, obey

$$a \sim \mathcal{O}(\epsilon), \quad \gamma \sim \mathcal{O}\left(\frac{1}{\epsilon}\right),$$

where  $\epsilon$  is a small number. Following the classical work of [11], we choose the coordinate system depicted in figure 1 and the following transformation:

$$\begin{aligned} x &= l \sin \phi \\ y &= l \cos \phi + a \cos(\gamma t), \end{aligned} \quad (2)$$

where  $\phi \in \mathbb{R}/2\pi\mathbb{Z}$  is the angle that the pendulum forms with the downward vertical. From the Lagrangian of the system (for the derivation, see Appendix A), we obtain the equation of motion of the vibrationally forced pendulum:

$$ml^2\ddot{\phi} + mg_0l \sin \phi + mal\gamma^2 \cos(\gamma t) \sin \phi = 0, \quad (3)$$

where  $g_0$  is the gravitational constant. It is worth noting that by a simple rearrangement leading to:

$$l\ddot{\phi} + (g_0 - a\gamma^2 \cos(\gamma t)) \sin \phi = 0,$$

we can regard the system of the pendulum with the vertically oscillating support as a immotile pendulum in the field of a modulated, rapidly varying modified gravity of the form:

$$g = g_0 + \frac{1}{\epsilon} g_{-1}\left(\frac{t}{\epsilon}\right).$$

Defining the natural frequency  $\omega_o$  of the pendulum by  $\omega_o^2 = \frac{g}{l}$ , we get a more concise form of the equation of motion:

$$\ddot{\phi} + (\omega_o^2 + \frac{a}{l}\gamma^2 \cos(\gamma t)) \sin \phi = 0. \quad (4)$$

It is more convenient to operate with non-dimensional parameters. Without the loss of generality, we let  $\omega_o^2 = 1$  and divide (4) by it. The nondimensional time is set to be  $t^* = \omega_o t$ . We define the ratio of forcing and natural frequencies  $\Omega$ , and the relative amplitude of the forcing  $\beta$  as, respectively:

$$\Omega = \frac{\gamma}{\omega_o} = \gamma, \quad \beta = \frac{a}{l},$$

where  $\Omega \sim \mathcal{O}(\frac{1}{\epsilon})$  and  $\beta \sim \mathcal{O}(\epsilon)$ . Dropping asterics, the equation of motion of the so-called "normalized pendulum" becomes:

$$\ddot{\phi} + (1 + \beta\Omega^2 \cos(\Omega t)) \sin \phi = 0. \quad (5)$$

This is a nonlinear equation with periodic coefficients, and is nonintegrable. Note that it describes a forced motion in a uniform field of gravitational potential  $U_o$ :

$$\frac{\partial^2 \phi}{\partial t^2} = -\frac{\partial U_o}{\partial \phi} - \beta\Omega^2 \cos(\Omega t) \sin \phi, \quad \text{where } U_o = -\cos \phi \quad (6)$$

The stability properties of this system have been studied either by means of averaging (e.g. [10], [11]), i.e. effective potential method, or by linearization around fixed points which leads to Mathieu equation (e. g. [18], [8]). The information obtained by neither of the two approaches is complete, however it is in some sense complementary; therefore we found worthwhile to apply both of them. We obtain the averaged dynamics by an alternative technique, the multiscale perturbation, and then zoom into the neighborhood of the equilibria by means of linearization.

### 3.2 $\frac{1}{\epsilon}$ problem and multiscale perturbation

We note that there are two well separated time scales in our problem, corresponding to the **slow** motion of the pendulum and **fast** oscillation of the pivot point. We can therefore attempt to find an asymptotic solution valid on long time scales of the pendulum motion. We will define a perturbation parameter and its relation with the forcing parameters by:

$$\epsilon = \frac{1}{\Omega}, \quad |\epsilon| \ll 1, \quad \beta = \frac{a}{l} = \epsilon \tilde{\beta}. \quad (7)$$

The independent time scales in our problem are:

$$\begin{aligned} \text{slow time: } t, \quad t &\sim \mathcal{O}(1) \\ \text{fast time: } \tau = \frac{t}{\epsilon}, \quad \tau &\sim \mathcal{O}(\frac{1}{\epsilon}), \end{aligned}$$

and so the equation of motion (4) can be expressed as:

$$\ddot{\phi} + (1 + \frac{\tilde{\beta}}{\epsilon} \cos \tau) \sin \phi = 0. \quad (8)$$

The first and the second time derivatives become, respectively:

$$\frac{d}{dt} = \frac{\partial}{\partial t} + \frac{1}{\epsilon} \frac{\partial}{\partial \tau}, \quad \frac{d^2}{dt^2} = \frac{\partial^2}{\partial t^2} + \frac{2}{\epsilon} \frac{\partial^2}{\partial \tau \partial t} + \frac{1}{\epsilon^2} \frac{\partial^2}{\partial \tau^2}.$$

Expanding the variable  $\phi$  in power series of  $\epsilon$  yields:

$$\phi(t, \tau) = \phi_o(t, \tau) + \epsilon \phi_1(t, \tau) + \epsilon^2 \phi_2(t, \tau) + \dots \quad (9)$$

Inserting the perturbation series (9) into (8) and assembling powers of  $\epsilon$  yields a set of equations for the subsequent orders in  $\epsilon$ . Manipulation of these equations results in a group of terms that give unbounded, linear growth of the solution in fast time  $\tau$  which obviously destroys the solution on long time scales. Such terms are called secular terms and a standard procedure in multiscale perturbation technique is to remove them by making them equal to zero and vanish ([9]). For the justification and more detailed treatment of the problem, see Appendix B. The condition for the solution to be valid uniformly on  $t$  gives the equation of motion of the leading order quantity:

$$\frac{\partial^2 \phi_o}{\partial t^2} = -(1 + \frac{(\beta\Omega)^2}{2} \cos \phi_o) \sin \phi_o. \quad (10)$$

It is worth to note that the same result would be obtained if the **average** of the  $\mathcal{O}(1)$  equation over the fast time has been taken, defined as following:

$$\epsilon \ll T \ll 1, \quad \bar{\psi}(t) \equiv \frac{1}{T} \int_{\tau}^{\tau+T} \psi(t, \tau') d\tau', \quad (11)$$

(see Appendix B). Using the fact that  $\overline{\cos^2 \tau} = \frac{1}{2}$ , we get:

$$\frac{\partial^2 \bar{\phi}}{\partial t^2} = -(1 + \frac{(\beta\Omega)^2}{2} \cos \bar{\phi}) \sin \bar{\phi}. \quad (12)$$

Therefore, we can consider (10), governing the dynamics of the  $\mathcal{O}(1)$  quantity, to be equivalent to the dynamics of a variable averaged over the fast oscillations (12).

### 3.3 Averaged dynamics. Effective potential.

We can note the averaged dynamics of the vibrationally forced pendulum governed by (12), can be perceived as a motion in the field of effective potential  $\mathcal{U}$ :

$$\frac{\partial^2 \bar{\phi}}{\partial t^2} = -\frac{\partial \mathcal{U}}{\partial \bar{\phi}}, \quad \text{where} \quad \mathcal{U} = -\cos \bar{\phi} + \frac{\beta^2 \Omega^2}{4} \sin^2 \bar{\phi}. \quad (13)$$

Interestingly, there is no explicit time dependence in the governing equation, as the effective potential is dependent only on the mean state of the system and parameters of the forcing (compare with (6)). This observation allows for the following physical explanation of the process, given by [10]. Vibrational gravitational field (induced by the oscillatory motion of the pivot) leads to the production the vibrational torque which on average manifests as an ordinary force. This force tends to set the rod of the pendulum in the direction of the axis of the oscillations. Provided the vibrational force is balanced by the gravity, the inverted state exhibits the dynamical equilibrium and becomes stable. We can now express the stability condition for the upper equilibrium in terms of the parameters of the forced system. Let's take a closer look into the stability of the system.

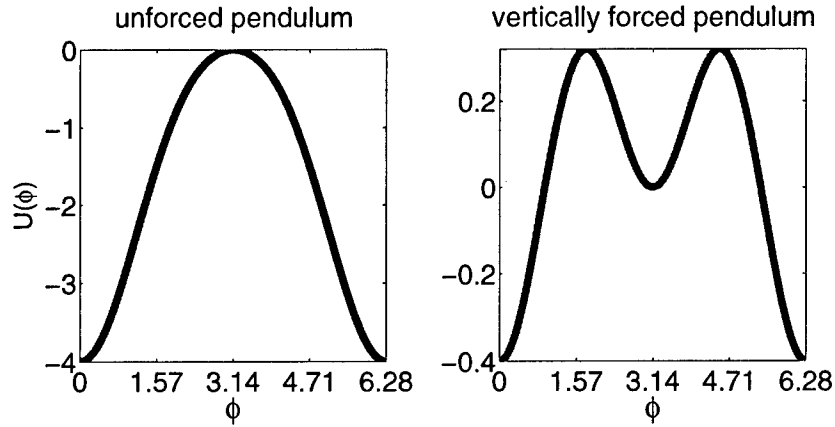


Figure 2: Left: Potential as a function of  $\phi$  for the unforced, nonlinear pendulum. Right: effective potential for vibrationally forced pendulum. Note that scales of the two figures are set different show the shape of the functions.

### 3.4 Stability of equilibria of averaged dynamics

The stability of equilibria can be most easily determined from (13). By setting the right hand side to zero, we find positions of equilibria, i.e the extrema of  $\mathcal{U}$ . There are four such points, in contrary to the case of the unforced nonlinear pendulum, when there are only two (fig. 2). The nature of the extremum is determined by the sign of the second derivative of  $\mathcal{U}$ ,  $\frac{\partial^2 \mathcal{U}}{\partial \phi^2} < 0$  indicates maximum (i.e. an unstable equilibrium),  $\frac{\partial^2 \mathcal{U}}{\partial \phi^2} > 0$ , minimum (a stable equilibrium called a potential well):

Equilibrium	Stability
$\phi_1^* = 0$ (noninverted)	stable
$\phi_2^* = \arccos(-\frac{(\beta\Omega)^2}{2})$	unstable
$\phi_3^* = \arccos(-\frac{(\beta\Omega)^2}{2})$	unstable
$\phi_4^* = \pi$ (inverted)	conditionally stable

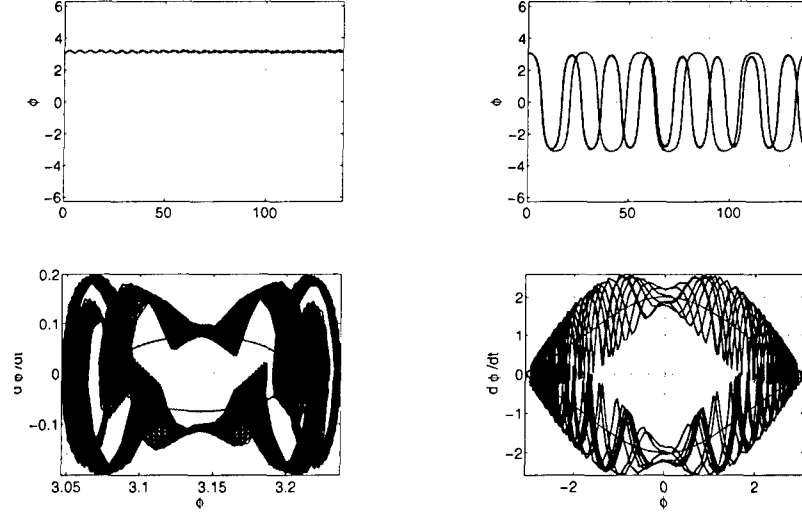


Figure 3: Time series and phase plots of the stabilized inverted pendulum. Blue color indicates the nonaveraged and red – averaged dynamics. Left: stable configuration  $\Omega = 11$ ,  $\beta = 0.2$ . Right: unstable configuration (rotational mode)  $\Omega = 11$ ,  $\beta = 0.1$ . Note that the scales of the phase space plots are set different to show the shape of trajectories.

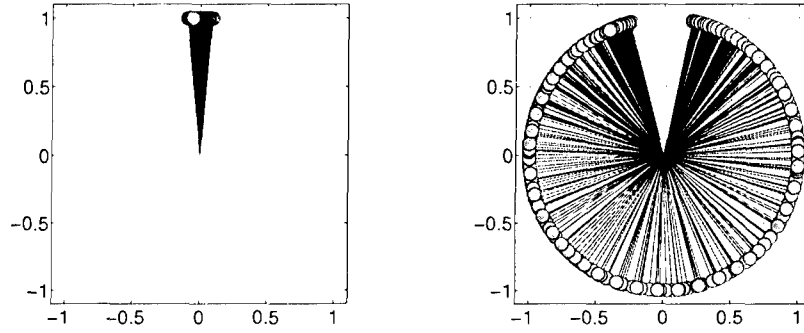


Figure 4: Time trace of the vibrationally forced pendulum in physical space. Left: stable configuration  $\Omega = 11$ ,  $\beta = 0.2$ . Right: unstable configuration  $\Omega = 11$ ,  $\beta = 0.1$ .

From (13), the condition for the stable upper equilibrium  $\phi_4^*$  is:

$$\frac{\beta^2 \Omega^2}{2} > 1. \quad (14)$$

The stability of the inverted position depends solely on the parameters of the system and requires a forcing of suitably high frequency. Note also that an angle  $\phi_{2,3}^* = \arccos(-\frac{(\beta\Omega)^2}{2})$  can be interpreted as a width of the potential well, namely maximum initial displacement that allows for the stabilization of the upper equilibrium for given properties of the forcing. Exemplary time series and phaseplots of the pendulum in a stable and unstable regime is presented on figure 3, for both nonaveraged and averaged dynamics. Corresponding behavior of the pendulum in the physical space is shown in figure 4.

There is another point of view of the averaged dynamics. The problem of the invertible pendulum may be considered in the  $1\frac{1}{2}$ -degree-of-freedom Hamiltonian setting. The nonlinear dynamics is then described by the Poicaré map or equivalently by its integrable approximation, a planar Hamiltonian, obtained from the normal form theory: successive transformations leading to the removal of the explicit time dependence. As the effective potential corresponds to the potential energy, the planar Hamiltonian is equal to the total energy of the averaged system. In this framework, by defining a parameter  $\lambda = \frac{2}{\beta^2 \Omega^2}$ , the transition of the inverted equilibrium from a minimum for  $\lambda < 1$  to a saddle point for  $\lambda > 1$  may be considered a subcritical Hamiltonian pitchfork bifurcation ([5]), see figure 5.

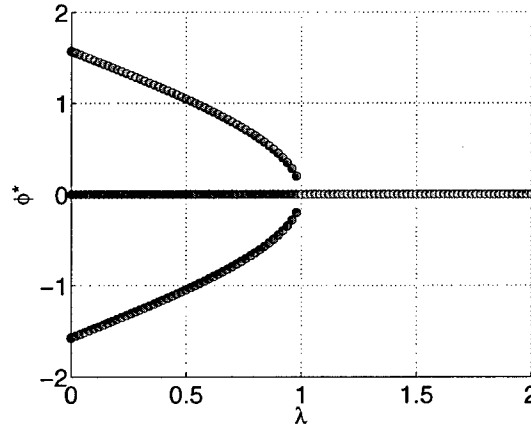


Figure 5: Bifurcation diagram in the  $(\lambda, \phi^*)$  - plane for the inverted pendulum, where  $\lambda = \frac{2}{\beta^2 \Omega^2}$  and  $\phi^*$  is a fixed point. Green dots indicate instability, magenta dots – stability.

### 3.5 Mathieu equation

Another approach to the study of the inverted pendulum is the linearization of the dynamics near an equilibrium. We define  $\alpha = \frac{1}{\Omega^2}$  and look again into the dynamics of (5), but now as



evolving in the fast time  $\tau = \gamma t$ :

$$\phi_{\tau\tau} + (\alpha + \beta \cos \tau) \sin \phi = 0. \quad (15)$$

Now we zoom into the dynamics near  $\pi$ , so it is convenient to define the complementary angular displacement  $\varphi$  with respect to  $\phi$ ,  $\varphi = \pi - \phi$ . This is the angular displacement from the upper equilibrium position. Then  $\sin \varphi = \sin(\pi - \phi) = +\sin \phi$  and  $\varphi_{\tau\tau} = -\phi_{\tau\tau}$ . The governing equation becomes:

$$\varphi_{\tau\tau} - (\alpha + \beta \cos \tau) \sin \varphi = 0. \quad (16)$$

The sign of  $\beta$  is not important as it corresponds to the instantaneous amplitude of the pivot motion around the center of the coordinate system, which can be positive or negative. The sign of  $\alpha$ , however, matters. We define the variable  $\psi$  as

$$\psi = \begin{cases} \phi : & \text{angular displacement near the lower equilibrium} \\ \varphi : & \text{angular displacement near the upper equilibrium} \end{cases}$$

and linearize  $\sin \psi \sim \psi$ , obtaining the canonical form of **Mathieu equation**:

$$\frac{\partial^2 \psi}{\partial \tau^2} + (\alpha + \beta \cos \tau) \psi = 0. \quad (17)$$

Thus equation (17) describes linearized dynamics around the either fixed point, depending on the sign of  $\alpha$ :

$$\alpha > 0 : \quad \text{lower equilibrium} \quad \alpha < 0 : \quad \text{upper equilibrium} \quad (18)$$

This specific formulation allows the investigation of the linear stability near the either equilibrium based on the general results for the Mathieu equation. It is also a manifestation of the fact that we can tackle the stability of the inverted state by changing the sign of the gravity  $g$ . The stability of the periodic solutions of the Mathieu equation, given by the Floquet theory, can be determined from the diagram in  $(\beta, \alpha)$  – parameter space ([9]). The so-called transition curves separate regions of values  $\alpha$  and  $\beta$  corresponding to unstable and stable solutions. Kapitza pendulum regime, with high forcing frequency (small  $\alpha$ ) and small amplitude of the pivot motion (small  $\beta$ ) lies in the region marked by the red circle in fig (6). The most surprising is the fact that, contrary to the averaged dynamics, linearized approach gives the possibility for destabilization of the lower equilibrium! We can obtain quite exact values for the parameter regions corresponding to stable inverted and noninverted equilibria:

Equilibrium	Stability condition
inverted	$\frac{\sqrt{2}}{\Omega} < \beta < 0.45 + \frac{1.799}{\Omega^2}$
noninverted	$0 < \beta < 0.45 - \frac{1.799}{\Omega^2}$

It is worth noting, that the linear stability condition for inverted pendulum based on linearization was generalized to an inverted  $N$ -pendulum and proven by [1]. In that case the system can be reduced to  $N$  uncoupled Mathieu equations and the stability condition yields

$$\frac{\sqrt{2}g}{\gamma\omega_{min}} < \beta < \frac{0.450g}{\omega_{max}^2}, \quad (19)$$

where  $\omega_{min}$  and  $\omega_{max}$  are the lowest and the highest of the natural frequencies of any single pendulum member of the full configuration.

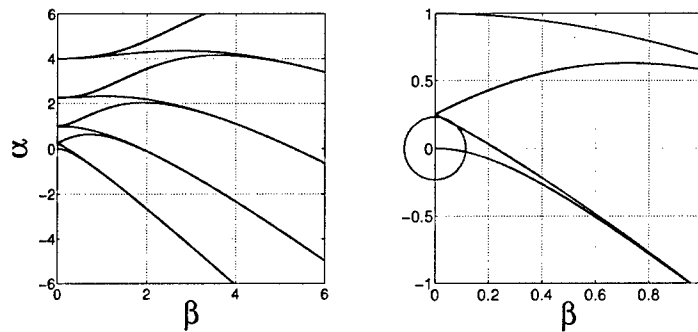


Figure 6: Left: Stability diagram for Mathieu equation. Right: the Kapitza pendulum regime.

### 3.6 Averaged dynamics vs Mathieu equation

Both approaches to the study of the dynamics of the pendulum system under the influence of a rapidly oscillating forcing are not completely adequate, i.e the relevance of either of them is limited. Here we summarize the key points concerning the applicability of the two methods.

#### Averaged dynamics:

- approximates long time asymptotic behavior,
- concerns global dynamics, i.e arbitrary displacements from the equilibrium position. Hence, apart from the very proximity of the inverted state, allows the study of the rotating state of the pendulum,
- gives only lower stability bound in the parameter space for the inverted equilibrium,
- gives the maximum angular displacement that permit stabilization of the inverted state for a given set of parameter values,

- predicts the stability of the lower equilibrium for all the values of the parameters,
- gives physical explanation for the dynamical stabilization phenomenon in terms of the effective potential.

Certainly some subtle details in the pendulum dynamics are lost in the approximate average analysis, which refers only to the slow component of the motion. In this method one introduces an approximation with no control on the relevance of the discarded dynamics, except of the estimate of their magnitude in terms of  $\epsilon$ . There is always a region in parameter space where the averaging fails predicting unstable configuration – the region over the upper bound in case of the inverted state and the whole unstable region for the lower equilibrium, which can be found from the Mathieu equation.

#### **Linearized theory:**

- reduces the problem to the well-known Mathieu equation,
- applies only to the vicinity of the fixed points, i.e is valid only for small angular displacements from the equilibrium position,
- gives more precisely defined stability regions: lower and upper bounds on the parameter values,
- admits the possibility for destabilization of the lower equilibrium and gives the range of parameter values for which it should be observed,
- does not provide with any physical explanation of the phenomenon.

In general, the applicability of the Mathieu equation is limited as in general the linear stability cannot be extended immediately to the full system. However, it gives correct results for the zoomed view into the dynamics near the equilibria.

## **4 Kapitza pendulum in fluid systems**

### **4.1 Kapitza pendulum vs fluid systems**

As already mentioned, we can regard a pendulum with a vertically oscillating support as equivalent to a pendulum with a stationary support in a periodically varying gravity field. This observation allows to attempt at finding an analogy between the Kapitza pendulum and fluid systems acted upon by vibrating gravitational forces, and thus study the dynamics of the latter by methods developed in the preceding sections. A similar analogy was already mentioned by Lord Rayleigh ([15]), who considered a phenomenon observed in the famous Faraday experiment: a surface wave instability in a vertically vibrated container filled with fluid, with the frequency close to resonance with the natural frequency of the system. From that time on the problem has been studied widely both analytically (e.g. [2], [12], [13]) and experimentally (e.g. [4]). The "Kapitza regime" discussed here is different as the forcing frequency is much higher than the natural one and it would not be trivial to

think of an experiment similar to that of Faraday. One can rather search for an idealized physical situation. We have chosen a simple fluid system described by Boussinesq equations, characterized by density stratification and related buoyancy force, which action, combined with that of gravity, provides the mechanism for inertial oscillations with bounded natural frequency.

## 4.2 Boussinesq equations. Problem formulation

We will study the dynamics of a incompressible, inviscid, stratified, hydrostatic, non-rotating fluid, governed by nonlinear Boussinesq equations (the momentum equations, continuity and conservation of density), see e.g. [16]):

$$\frac{Du}{Dt} + \frac{1}{\bar{\rho}} \frac{\partial p}{\partial x} = 0 \quad (20)$$

$$\frac{Dw}{Dt} + \frac{1}{\bar{\rho}} \frac{\partial p}{\partial z} = -\frac{g\rho}{\bar{\rho}} = b \quad (21)$$

$$\frac{\partial u}{\partial x} + \frac{\partial w}{\partial z} = 0 \quad (22)$$

$$\frac{D\rho}{Dt} = 0 \quad (23)$$

Here  $t$  is time and  $u$  and  $w$  are the components of the nondivergent velocity field in horizontal ( $x$ ) and vertical ( $z$ ) directions in a Cartesian frame of reference. The positive  $z$ -direction is antiparallel to gravity. We will work in the  $(x, z)$  - plane, which implies that all characteristics of the system are uniform in  $y$ .

We consider a hydrostatically balanced reference state upon which perturbations are to be imposed and make use of the Boussinesq approximation, which means that the density field, represented by  $\rho(x, z, t) = \bar{\rho} + \rho_o(z) + \Delta\rho(x, z, t) = \bar{\rho}(1 - S(\frac{z}{H})) + \Delta\rho(x, z, t)$ , satisfies  $\bar{\rho} \gg \rho_o(z) \gg \Delta\rho$ . The mean fluid density  $\bar{\rho}$  is a uniform constant. The density stratification is assumed to be linear and  $S$  is a stability parameter defined as:

$$S = \begin{cases} +1 & \text{stable stratification} \\ -1 & \text{unstable stratification} \end{cases}$$

The vertical extent of the domain is small compared to a density depth scale  $H = |\frac{1}{\bar{\rho}} \frac{d\rho_o}{dz}|^{-1}$ . Pressure field  $p$  is assumed to be hydrostatically related. The joint effect of gravity and density stratification leads to a buoyancy force  $b$  in the vertical. The natural frequency of the system, so-called the Brunt-Väisälä frequency, is defined through  $N^2(z) = -(\frac{g}{\bar{\rho}} \frac{d\rho_o}{dz})$ , which is constant in case of linear stratification, and with notation used here  $N = \frac{gS}{H}$ . We will constraint us to the flows with periodic boundary conditions.

Nondivergence of the velocity field allows to introduce a stream function  $\psi$ , such that  $u = \psi_z$  and  $w = -\psi_x$ . In an infinite medium the Boussinesq equations are satisfied by planar internal waves of the form  $\psi = \Psi \cos(kx + mz) e^{-i\omega t}$  (with horizontal and vertical wave numbers  $k$  and  $m$  and  $\kappa = \sqrt{k^2 + m^2}$ ), which obey the dispersion relation  $\omega = \pm N \frac{k}{\kappa}$ . In polar coordinates chosen so that  $k = \kappa \cos \alpha$  and  $m = \kappa \sin \alpha$  we have  $\omega = \pm N \cos \alpha$ . The

frequency is therefore a function of the angle that the wave vector makes with the vertical. The condition for progressive waves is therefore  $0 \leq \omega \leq N$  so  $N$  acts as the upper bound of internal wave frequencies, corresponding to entirely vertical flow (buoyancy oscillation) ([3]).

Now we will embed the system in a modified gravity field, varying in vertical as  $g(t) = g_o + a\gamma^2 \cos(\gamma t)$ , where  $g_o$  is a gravitational constant, the amplitude of oscillatory motion satisfies  $a \ll g_o$ , and the frequency of the oscillations  $\gamma$  is much higher than the Brunt-Väisälä frequency, that is  $\gamma \gg N$ .

We will nondimensionalize the system as follows:

$$(x^*, z^*) = \left( \frac{x}{H}, \frac{z}{H} \right), \quad t^* = \frac{t}{\sqrt{\frac{H}{g_o}}},$$

which results in the nondimensional components of the velocity:

$$(u^*, w^*) = \left( \frac{u}{\sqrt{g_o H}}, \frac{w}{\sqrt{g_o H}} \right).$$

The nondimensional density and pressure fields are:

$$\rho^*(x, z, t) = \left( 1 - \mathcal{S} \left( \frac{z}{H} \right) \right) + \Delta \rho^*(x, z, t), \quad \text{where} \quad \Delta \rho^* = \frac{\Delta \rho}{\bar{\rho}}, \quad \text{and} \quad p^* = \frac{p}{\bar{\rho} g_o H},$$

which gives the nondimensional Brunt-Väisälä frequency  $N^{*2} = \mathcal{S}$ . By introducing the nondimensional parameters:

$$\Omega = \frac{\gamma}{\frac{H}{g_o}}, \quad \beta = \frac{a}{H},$$

the ratio of the forcing and natural frequencies and the relative magnitude of the forcing, respectively, we get

$$g^*(t) = \frac{g(t)}{g_o} = 1 + \beta \Omega^2 \cos(\Omega t^*). \quad (24)$$

By dropping asterics, the nondimensional Boussinesq equations are:

$$\frac{Du}{Dt} + \frac{\partial p}{\partial x} = 0 \quad (25)$$

$$\frac{Dw}{Dt} + \frac{\partial p}{\partial z} = -\Delta \rho (1 + \beta \Omega^2 \cos(\Omega t)) \quad (26)$$

$$\frac{\partial u}{\partial x} + \frac{\partial w}{\partial z} = 0 \quad (27)$$

$$\frac{\partial \Delta \rho}{\partial t} + u \frac{\partial \Delta \rho}{\partial x} + w \frac{\partial \Delta \rho}{\partial z} - w \mathcal{S} = 0 \quad (28)$$

We can eliminate the pressure by focusing on the vorticity equation, which is:

$$\frac{Dq}{Dt} = \frac{D}{Dt} \left( \frac{\partial u}{\partial z} - \frac{\partial w}{\partial x} \right) = \frac{\partial \Delta \rho}{\partial x} (1 + \beta \Omega^2 \cos(\Omega t)). \quad (29)$$

It is evident that the vibrating gravity field modifies the basic mechanism of the baroclinic generation of vorticity. We will now investigate this phenomenon in detail, using the methods derived for the stabilized inverted pendulum.

### 4.3 Multiscale expansion

We can observe that, similarly to the case of the Kapitza pendulum discussed above, in our Boussinesq problem we have two well separated time scales: the slow gravity oscillations and the fast oscillation of the gravity field. Thus, an attempt to find an asymptotic solution valid on long time scales is justified. Analogously as for the pendulum, we can define a perturbation parameter by  $\epsilon = \frac{1}{\Omega}$ , and we have  $\beta \sim \mathcal{O}(\epsilon)$ . The slow time is then  $t \sim \mathcal{O}(1)$ , and the fast time  $\tau = \Omega t$ ,  $\tau \sim \mathcal{O}(\frac{1}{\epsilon})$ , compare with (7). The oscillating gravity field (24) can be expressed as  $g(t) = 1 + \frac{1}{\epsilon} \tilde{g}_{-1}(\tau)$ . Unlike in the pendulum case, system variables depend now not only on time, but also on space, therefore we have for the first, the second and material time derivatives, respectively:

$$\frac{\partial}{\partial t} \rightarrow \frac{\partial}{\partial t} + \frac{1}{\epsilon} \frac{\partial}{\partial \tau}, \quad \frac{\partial^2}{\partial t^2} \rightarrow \frac{\partial^2}{\partial t^2} + \frac{2}{\epsilon} \frac{\partial^2}{\partial \tau \partial t} + \frac{1}{\epsilon^2} \frac{\partial^2}{\partial \tau^2}, \quad \frac{D}{Dt} = \frac{\partial}{\partial t} + u \frac{\partial}{\partial x} + w \frac{\partial}{\partial z}.$$

With the averaging operator defined as (11), the components of the velocity perturbation are expanded in perturbation series as:

$$\begin{aligned} u(x, z, t, \tau) &= \overline{u_o}(x, z, t) + u'_o(x, z, t, \tau) + \dots \\ w(x, z, t, \tau) &= \overline{w_o}(x, z, t) + w'_o(x, z, t, \tau) + \dots, \end{aligned} \quad (30)$$

where  $(\overline{u_o}, \overline{w_o})$  refer to the mean perturbation velocity, while  $(u'_o, w'_o)$  correspond to the disturbance due to modified acceleration of the order  $\mathcal{O}(\frac{1}{\epsilon})$ ; after time integration, we can expect them to be of the order  $\mathcal{O}(1)$ , but as they came from the oscillatory motion, they will vanish when averaged over the fast time. We will define the mean substantial derivative:

$$\overline{D} = \frac{\partial}{\partial t} + \overline{u_o} \frac{\partial}{\partial x} + \overline{w_o} \frac{\partial}{\partial z}.$$

The density perturbation is expanded in  $\epsilon$  as:

$$\Delta \rho(x, z, t, \tau) = \Delta \rho_o(x, z, t, \tau) + \epsilon \Delta \rho_1(x, z, t, \tau) + \dots \quad (31)$$

Inserting the series (31) and (30) into the density equation (28), we get:

$$\begin{aligned} \frac{\partial \Delta \rho_o}{\partial t} + \frac{1}{\epsilon} \frac{\partial \Delta \rho_o}{\partial \tau} + \epsilon \frac{\partial \Delta \rho_1}{\partial t} + \frac{\partial \Delta \rho_1}{\partial \tau} + \overline{u_o} \frac{\partial \Delta \rho_o}{\partial x} + u'_o \frac{\partial \Delta \rho_o}{\partial x} + \overline{u_o} \frac{\partial \Delta \rho_1}{\partial x} + u'_o \frac{\partial \Delta \rho_1}{\partial x} + \\ + \overline{w_o} \frac{\partial \Delta \rho_o}{\partial z} + w'_o \frac{\partial \Delta \rho_o}{\partial z} + \overline{w_o} \frac{\partial \Delta \rho_1}{\partial z} + w'_o \frac{\partial \Delta \rho_1}{\partial z} - \overline{w_o} S - w'_o S = 0, \end{aligned} \quad (32)$$

Gathering terms of the order  $\mathcal{O}(\frac{1}{\epsilon})$  we conclude that  $\Delta \rho_o = \overline{\Delta \rho_o}(x, z, t)$ . In the order of  $\mathcal{O}(1)$ , we will first average out the terms containing perturbation quantities  $\Delta \rho_1$  and  $(u'_o, w'_o)$ , so that the remaining terms give an evolution equation for the mean density perturbation:

$$\frac{\overline{D} \overline{\Delta \rho}}{Dt} - \overline{w_o} S = 0. \quad (33)$$

Subtraction of (33) from (32) results in an evolution equation for  $\Delta \rho_1$ :

$$\frac{\partial \Delta \rho_1}{\partial \tau} + u'_o \frac{\partial \overline{\Delta \rho_o}}{\partial x} + w'_o \frac{\partial \overline{\Delta \rho_o}}{\partial z} - w'_o S = 0. \quad (34)$$

Inserting the perturbation series (30) into (29), we get:

$$\begin{aligned} & \frac{\partial}{\partial t} \left( \frac{\partial \bar{u}_o}{\partial z} - \frac{\partial \bar{w}_o}{\partial x} \right) + \frac{1}{\epsilon} \frac{\partial}{\partial \tau} \left( \frac{\partial u'_o}{\partial z} - \frac{\partial w'_o}{\partial x} \right) + \bar{u}_o \frac{\partial}{\partial x} \left( \frac{\partial \bar{u}_o}{\partial z} - \frac{\partial \bar{w}_o}{\partial x} \right) + \bar{w}_o \frac{\partial}{\partial z} \left( \frac{\partial \bar{u}_o}{\partial z} - \frac{\partial \bar{w}_o}{\partial x} \right) + \\ & + \bar{u}_o \frac{\partial}{\partial x} \left( \frac{\partial u'_o}{\partial z} - \frac{\partial w'_o}{\partial x} \right) + \bar{w}_o \frac{\partial}{\partial z} \left( \frac{\partial u'_o}{\partial z} - \frac{\partial w'_o}{\partial x} \right) + u'_o \frac{\partial}{\partial x} \left( \frac{\partial \bar{u}_o}{\partial z} - \frac{\partial \bar{w}_o}{\partial x} \right) + w'_o \frac{\partial}{\partial z} \left( \frac{\partial \bar{u}_o}{\partial z} - \frac{\partial \bar{w}_o}{\partial x} \right) + \\ & + u'_o \frac{\partial}{\partial x} \left( \frac{\partial u'_o}{\partial z} - \frac{\partial w'_o}{\partial x} \right) + w'_o \frac{\partial}{\partial z} \left( \frac{\partial u'_o}{\partial z} - \frac{\partial w'_o}{\partial x} \right) = \frac{\partial \bar{\Delta} \rho_o}{\partial x} + \frac{1}{\epsilon} \tilde{g}_{-1}(\tau) \frac{\partial \bar{\Delta} \rho_o}{\partial x} + \tilde{g}_{-1}(\tau) \frac{\partial \Delta \rho_1}{\partial x} + \epsilon \frac{\partial \Delta \rho_1}{\partial x}. \end{aligned}$$

Terms of the order  $\mathcal{O}(\frac{1}{\epsilon})$  gather in the evolution equation for  $q'_o$ :

$$\frac{\partial q'_o}{\partial \tau} = \frac{\partial}{\partial \tau} \left( \frac{\partial u'_o}{\partial z} - \frac{\partial w'_o}{\partial x} \right) = \tilde{g}_{-1}(\tau) \frac{\partial \bar{\Delta} \rho_o}{\partial x}. \quad (35)$$

By applying the averaging operation to the  $\mathcal{O}(1)$  ensemble, terms containing products of the leading order and prime quantities are eliminated and the evolution equation for the mean perturbation vorticity follows:

$$\frac{D\bar{q}}{Dt} = \frac{\partial \bar{\Delta} \rho_o}{\partial x} + \left( \frac{\partial \Delta \rho_1}{\partial x} \tilde{g}_{-1}(\tau) \right) - \left( u'_o \frac{\partial q'_o}{\partial x} + w'_o \frac{\partial q'_o}{\partial z} \right). \quad (36)$$

We will use the fact that averaging is a linear operator so that from the continuity equation (28) to obtain:

$$\frac{\partial \bar{u}_o}{\partial x} + \frac{\partial \bar{w}_o}{\partial z} = 0, \quad \text{and} \quad \frac{\partial u'_o}{\partial x} + \frac{\partial w'_o}{\partial z} = 0. \quad (37)$$

To summarize, we have arrive at two separated sets of equations with no explicit time dependence: for averaged perturbation variables and those generated by the forcing of our system. By analogy to the Kapitza pendulum, a stable stratification corresponds to the stable equilibrium of the pendulum, while the unstable stratification – to the inverted state. Now we will analyze the response of the system to the instantenous density disturbance to determine how the vertical oscillations of the gravity field influence stability properties of the system as a whole.

## 4.4 Stability of the vibrating Boussinesq system

### 4.4.1 Monochromatic wave disturbance in $x$ direction

We will start with a perturbation of the mean state of the form:

$$\bar{\Delta} \rho = \rho_o \cos(kx). \quad (38)$$

Assuming a perturbation streamfunction of the form  $\psi'_o = \Psi'_o \cos(kx)$ , from (35) we have  $u'_o = 0$  and  $w'_o = w'_o(x) = \frac{(\Delta \rho_o)_{xx}}{k^2} \int \tilde{g}_{-1}(\tau') d\tau'$ . Therefore in the (35), the advection terms cancel out yielding  $\frac{d\Delta \rho_1}{d\tau} = \mathcal{S} w'_o$  and they vanish in the equations for the evolution of the mean density perturbation (33) the mean vorticity perturbation (36) to give:

$$\frac{D\bar{q}}{Dt} = \frac{\partial \bar{\Delta} \rho_o}{\partial x} \left( 1 + \frac{\mathcal{S}(\beta\Omega)^2}{2} \right), \quad \frac{D\Delta \rho_o}{Dt} = \mathcal{S} \bar{w}_o. \quad (39)$$

Manipulation of these expressions yields the evolution equation for the mean density perturbation:

$$\frac{\overline{D}^2 \overline{\Delta \rho}}{Dt^2} + S_*^2 \overline{\Delta \rho} = 0, \quad \text{where} \quad S_*^2 = S + \frac{\beta^2 \Omega^2}{2}, \quad (40)$$

is the new modified nondimensional frequency, expressed by means of the stability parameter (note that  $S^2 = 1$  irrespective of the initial stability). Thus we conclude that in case of a stable initial stratification ( $S = 1$ ), the stability is augmented, while in case of unstable initial stratification there is a stabilizing effect of the vertically oscillating gravity field. The stability condition in the initially unstable case is:

$$\frac{\beta^2 \Omega^2}{2} > 1, \quad (41)$$

which is identical to the analogous condition for the inverted Kapitza pendulum (14). In fact, the equation (40) itself may be perceived as a linear analog of (12) – unintentionally linearized by the dynamics itself. We can thus expect all the results obtained from the Mathieu equation for the inverted pendulum to be valid in the problem discussed here.

Assuming the plane wave solution of the form  $\overline{\psi} = \overline{\psi}_o \cos(kx - \omega t)$ , we obtain the dispersion relation for the internal waves supported by our system:

$$\omega^2 = S_*^2,$$

which is equivalent to the dispersion relation of the buoyancy oscillation typical to the unforced Boussinesq system, with  $N$  replaced by  $S_*$ , i.e. the system is stabilized and the frequency of the vertical oscillation is higher than the maximum frequency in the unforced case.

#### 4.4.2 Monochromatic plane wave disturbance

In case the initial density perturbation has a form of the planar wave:

$$\overline{\Delta \rho} = \rho_o \cos(kx + mz), \quad (42)$$

the procedure is conducted analogously as in the previous case. Although  $u'_o \neq 0$ , from the continuity equation (37) we have  $\overline{u}_o \frac{\partial}{\partial x} = \overline{w}_o \frac{\partial}{\partial z} = u'_o \frac{\partial}{\partial x} = w'_o \frac{\partial}{\partial x} = 0$  leading to the cancellation of the advection terms. Consequently, the multiscale technique and averaging leads to the following stability condition for the averaged system:

$$\frac{\overline{D}^2}{Dt^2} \left( \frac{\partial^2}{\partial x^2} + \frac{\partial^2}{\partial z^2} \right) \overline{\Delta \rho} + S_*^2 \left( \frac{\partial^2}{\partial x^2} \right) \overline{\Delta \rho} = 0, \quad \text{where} \quad S_*^2 = S + \left( \frac{k^2}{k^2 + m^2} \right) \frac{\beta^2 \Omega^2}{2}.$$

As before, we conclude that in case of a stable initial stratification the stability is amplified, while in case of the unstable initial stratification, the vibrating gravity results in the stabilizing effect whenever:

$$\left( \frac{k^2}{k^2 + m^2} \right) \frac{\beta^2 \Omega^2}{2} > 1, \quad (43)$$



which is equivalent to (41), except that now the orientation of the perturbation in space (i.e.  $(\frac{k^2}{k^2+m^2})$ ), matters. The dispersion relation in this case is:

$$\omega^2 = S_*^2 \frac{k^2}{k^2 + m^2}. \quad (44)$$

Again, the form of the dispersion relation is equivalent to the dispersion relation of the internal gravity wave solutions to the unforced case, with  $N$  replaced by  $S^*$ . The effect of the vibrational gravity forcing depends not only on the values of the parameters of the forcing, but also on the angle of the wavevector  $\mathbf{k}$ : for a given forcing properties, vertical disturbances are more difficult to suppress.

#### 4.4.3 Perturbation of an arbitrary form

If we allow the instantaneous density disturbance to have an arbitrary form  $\overline{\Delta\rho}(x, z)$ , the advective terms in (33, 34) and (36) do not cancel out and the mean vorticity equation takes a form of an integro-differential equation:

$$\frac{D\bar{q}}{Dt} = \frac{\partial \overline{\Delta\rho}}{\partial x} + \left( \frac{\partial \overline{\Delta\rho_1}}{\partial x} \tilde{g}_{-1} \right) - \mathcal{J}(\psi', \nabla^2 \psi'). \quad (45)$$

Without further assumptions, it is difficult to construct any meaningful stability condition. However, if we could represent  $\overline{\Delta\rho}$  in Fourier series and linearize in  $u'_o, w'_o$  and  $\Delta\rho$ , we can get rid of the advective terms and obtain the following form of the mean vorticity equation:

$$\frac{D\bar{q}}{Dt} = \sum_{n=1}^{\infty} \left( \frac{\partial \overline{\Delta\rho_o}}{\partial x} \right)_n \left( 1 + \left( \frac{k_n^2}{k_n^2 + m_n^2} \right) \frac{\beta^2 \Omega^2}{2} \right), \quad (46)$$

which shows the additive effect of any single perturbation wave component of the series to the baroclinic generation of the mean vorticity, modified by the vibrating gravity in similar way as in the previous simpler cases. The corresponding stability condition for an unstable initial stratification is:

$$\frac{\beta^2 \Omega^2}{2} \sum_{n=1}^{\infty} \left( \frac{k_n^2}{k_n^2 + m_n^2} \right) > 1, \quad (47)$$

so again we can see that provided the instantaneous density perturbation can be given a form of the sum of waves, there is an analogy between the effect of the vibrational forcing on the stability of the system in case of the Kapitza pendulum and dynamics of a fluid described by ideal Boussinesq equations, with a modification due to nonlocality of the problem: for a given values of forcing parameters the stability is strongly affected by the direction of the propagation of the density disturbance.

## 5 Summary and conclusions

In this work we considered the inverted pendulum with the vibrating support. The application of multiscale perturbation, leading to the averaged dynamics, as well as linearization, allowed us to study the stabilization phenomenon. Then we used the multiscale technique

and averaging to an incompressible, inviscid, linearly stratified, nonlinear Boussinesq system in a periodic domain, subjected to rapidly oscillating gravity field. We have shown that, provided the instantaneous density perturbation can be given a form of a wave or sum of waves, the stabilization mechanism induced by the vibrational forcing is analogous to that exhibited by the Kapitza pendulum. However, the dynamics of the Boussinesq system is more complicated, as it evolves not only in time, but also in space. The resulting stability condition for the initially unstable configuration is modified: it requires not only suitably high frequency and small amplitude of the vibrating motion – the direction of propagation of the density perturbation in the space also plays a role. In case of a disturbance of a general form it is difficult to draw the conclusions about the system stability without further assumptions.

The work presented here is not just an idealized, educative example that contributes to the understanding of the instability phenomena. There are indeed real physical situations that permits the use of Boussinesq approximation with the forcing regime as prescribed here, though certainly requiring adequate boundary conditions and generally more complex analysis. As an example, we give convective phenomena in radially pulsating stars, treated in ([14]) by means of linearization. The appeal of the multiscale perturbation and averaging methods discussed here is that they provide the description of the global behavior of the averaged variable, expected to be the one related to any observed quantity. This observation strongly encourages the application of these methods in any future investigation of the stability mechanisms in more realistic and complex fluid systems forced parametrically.

## 6 Acknowledgements

I would like to thank to my summer supervisor Oliver Buhler for his patience and indispensable help with the project and to all the GFD faculty and fellows for a great summer.

## References

- [1] D. J. ACHESON, *A pendulum theorem.*, Proc. Roy. Soc. London, 443 (1993), pp. 239–245.
- [2] T. N. BENJAMIN AND F. URSELL, *The stability of the plane free surface of a liquid in vertical periodic motion.*, Proc. Roy. Soc. London, 225 (1954), pp. 505–515.
- [3] O. BUHLER, *Wave–mean interaction theory. Lecture notes.*, Courant Institute of Mathematical Sciences, New York University, New York, 2004.
- [4] W. S. EDWARDS AND S. FAUVE, *Patterns and quasi-patterns in the faraday experiment.*, J. Fluid Mech., 278 (1994), pp. 123–148.
- [5] I. H. H. W. BROER AND M. VAN NOORT, *A reversible bifurcation analysis of the inverted pendulum.*, Physica D, 112 (1998), pp. 50–63.

- [6] J. A. HOLYST AND W. WOJCIECHOWSKI, *The effect of kapitza pendulum and price pendulum*, Physica A, 324 (2003), pp. 388–395.
- [7] S. R. I. GILARY, N. MOISEYEV AND S. FISHMAN, *Trapping of particles by lasers: the quantum kapitza pendulum*, J. Phys. A., 36 (2003), pp. 409–415.
- [8] H. J. T. S. J. A. BLACKBURN AND N. GRONBECH-JENSEN, *Stability and hopf bifurcations in an inverted pendulum.*, Am. J. Phys., 60 (10) (1992), pp. 903–908.
- [9] D. W. JORDAN AND P. SMITH, *Nonlinear ordinary differential equations*, Oxford University Press Inc., New York, 1987.
- [10] P. KAPITZA, *Dynamical stability of a pendulum when its point of suspension vibrates and Pendulum with a vibrating suspension. In Collected Papers of Kapitza, edited by D. Haar.*, Pergamon Press, 1965.
- [11] L.D.LANDAU AND E. LIFSHITZ, *Course in Theoretical Physics. Mechanics. Vol(1). Third Edition.*, Pergamon Press, Oxford, 1976.
- [12] J. MILES, *Nonlinear faraday resonance*, 146 (1984), pp. 451–460.
- [13] J. R. OCKENDON AND H. OCKENDON, *Resonant surface waves*, J. Fluid Mech., 59 (1973), pp. 397–413.
- [14] A. P. POYET AND E. A. SPIEGEL, *The onset of convection in a radially pulsating star*, Astron. J, 84 (12) (1979), pp. 1918–1931.
- [15] L. RAYLEIGH, *On maintained oscillations*, Phil. Mag., 15 (1883), pp. 229–235.
- [16] R. SALMON, *Lectures On Geophysical Fluid Dynamics*, Oxford University Press, New York, 1998.
- [17] A. STEPHENSON, *On a new type of dynamical stability*, Mem. Proc.Manch. Lit. Phil. Soc., 52 (8) (1908), pp. 1–10.
- [18] —, *On induced stability*, Phil. Mag., 15 (1908), pp. 233–236.
- [19] —, *On induced stability*, Phil. Mag., 17 (1909), pp. 765–766.

## 7 Appendix A

In the coordinate system (2), the kinetic energy of the system is expressed as:

$$\begin{aligned}
 T &= \frac{1}{2}m(\dot{x}^2 + \dot{y}^2) = \frac{1}{2}m(l^2\dot{\phi}^2 + a^2\gamma^2 \sin^2(\gamma t) + 2al\gamma \sin(\gamma t) \sin \phi \dot{\phi}) = \\
 &= \frac{1}{2}ml^2\dot{\phi}^2 + mal\gamma^2 \cos(\gamma t) \cos \phi + \frac{1}{2}ma^2\gamma^2 \sin^2(\gamma t) - \frac{d}{dt}[mal\gamma \sin(\gamma t) \cos(\phi)],
 \end{aligned}$$

and the potential is  $U = -mg_o y = -mg_o l \cos \phi$ . The Lagrangian of the system is therefore:

$$L = T - U = \frac{1}{2}ml^2\dot{\phi}^2 + mal\gamma^2 \cos(\gamma t) \cos \phi + mg_o l \cos \phi + \frac{d}{dt}[mal\gamma \sin(\gamma t) \cos(\phi) + \frac{1}{2}ma\gamma \sin^2(\gamma t)].$$

The complete time derivative on RHS does not enter the action, so from the Lagrange equation:

$$\frac{d}{dt} \left( \frac{\partial L}{\partial \dot{\phi}} \right) - \frac{\partial L}{\partial \phi} = 0,$$

we obtain the equation of motion of the vibrationally forced pendulum (3):

$$ml^2 \ddot{\phi} + mg_o l \sin \phi + mal\gamma^2 \cos(\gamma t) \sin \phi = 0.$$

## 8 Appendix B

Inserting the perturbation series (9) into (8) gives:

$$\frac{d^2 \phi_o}{dt^2} = -\sin \phi_o - \epsilon \phi_1 \cos \phi_o \epsilon^2 \phi_2 \cos \phi_o - \frac{\tilde{\beta}}{\epsilon} \cos \tau \sin \phi_o - \tilde{\beta} \phi_1 \cos \tau \cos \phi_o - \tilde{\beta} \epsilon \phi_2 \cos \tau \cos \phi_o$$

A typical initial condition we can think about is the initial displacement from the inverted position with zero angular velocity:

$$\phi_o|_{t=0} = A_o, \quad \frac{d\phi_o}{dt}|_{t=0} + \frac{1}{\epsilon} \frac{d\phi_o}{d\tau}|_{t=0} = 0. \quad (48)$$

And the absence of the perturbed quantities (no fast initialization):

$$\phi_n|_{t=0} = 1, \quad \frac{d\phi_n}{dt}|_{t=0} + \frac{1}{\epsilon} \frac{d\phi_n}{d\tau}|_{t=0} = 0, \quad n > 0. \quad (49)$$

By assembling powers of  $\epsilon$  one obtains equations for the subsequent orders:

$$\begin{aligned} \mathcal{O}(\frac{1}{\epsilon^2}): \quad & \frac{\partial^2 \phi_o}{\partial \tau^2} = 0, \\ \mathcal{O}(\frac{1}{\epsilon}): \quad & \frac{\partial^2 \phi_1}{\partial \tau^2} = -\tilde{\beta} \cos \tau \sin \phi_o(t), \\ \mathcal{O}(1): \quad & \frac{\partial^2 \phi_2}{\partial \tau^2} = -\frac{\partial^2 \phi_o}{\partial t^2} - 2 \frac{\partial^2 \phi_1}{\partial \tau \partial t} - \sin \phi_o - \tilde{\beta} \phi_1 \cos \tau \cos \phi_o(t). \end{aligned}$$

Let's look at them in detail. The integral of the first of them is:

$$\mathcal{O}(\frac{1}{\epsilon^2}): \quad \frac{\partial^2 \phi_o}{\partial \tau^2} = 0, \quad \phi_o = F_o(t)\tau + G_o(t).$$

This gives unbounded, linear growth of the solution in fast time  $\tau$  which obviously destroys the solution on long time scales. Such terms are called secular terms and a standard procedure in multiscale perturbation technique is to remove them by making them equal to zero and vanish ([9]). This argument can be justified by using the initial conditions (48), from which we get  $F_o(t) = 0$  and  $G_o(t) = A_o$ . Therefore, the leading order solution is equal to  $A_o(t)$ , a function of long time  $t$  but a constant with respect to  $\tau$ ,  $\phi_o = \phi_o(t)$ . Using analogous argument with the initial conditions (49) incorporated, we get for the next order term:

$$\mathcal{O}(\frac{1}{\epsilon}): \quad \phi_1 = \tilde{\beta}(\cos \tau - 1) \sin \phi_o(t). \quad (50)$$

The equation for the order  $\mathcal{O}(1)$  becomes:

$$\begin{aligned} \mathcal{O}(1): \quad & \frac{\partial^2 \phi_2}{\partial \tau^2} = 2\tilde{\beta} \sin \tau \cos \phi_o \dot{\phi}_o(t) + \tilde{\beta}^2 \cos \tau \sin \phi_o \cos \phi_o - \frac{\tilde{\beta}^2}{2} \cos 2\tau \sin \phi_o \cos \phi_o - \\ & - \frac{\partial^2 \phi_o}{\partial t^2} - \sin \phi_o - \frac{1}{2} \tilde{\beta}^2 \sin \phi_o(t) \cos \phi_o(t). \end{aligned}$$

Terms that are constants with respect to the fast time  $\tau$  are a potential source for a secular growth in our solution. The condition for the solution to be valid uniformly on  $t$  gives the equation of motion of the leading order quantity (10). Note also that by taking the average defined by (11) of the equation (50), one gets (12).

# A Search for Baroclinic Structures

Alexander E. Hasha

August 26th, 2005

## 1 Introduction

The calculation reported in this paper is a standard one for those who study pattern formation in nonlinear systems. Pattern formation is prevalent when instability breaks symmetries present in a basic state. In the canonical example, stationary fluid heated from below gives way to patterns through Rayleigh-Bénard instability. For a wide class of problems, one may derive amplitude equations that govern the weakly nonlinear development of an instability. Amplitude equations describe the slow modulation in space and time of disturbances excited near the threshold of an instability. The form of the amplitude equations is determined generically by symmetries of the governing equations and the structure of the linear instability ([5], [3]).

When a large, dissipative, system undergoes a Hopf bifurcation, with a trivial steady state losing stability to a growing, unsteady wave pattern, an amplitude equation that generically arises is the complex Ginzburg-Landau equation (CGL)

$$\frac{\partial A}{\partial t} = \mu A + \nu \frac{\partial^2 A}{\partial x^2} - \zeta A |A|^2. \quad (1)$$

The function  $A = A(x, t)$  is a complex valued function of two real variables. It represents the slowly varying amplitude envelope of packets of waves generated by the instability. The variable  $x$  is spatial displacement in a frame moving at the group velocity of the unstable wavepackets. The coefficients  $\mu, \nu$ , and  $\zeta$  are complex, with  $\text{Re}\{\mu\} > 0$ ,  $\text{Re}\{\nu\} > 0$ . When  $\text{Re}\{\zeta\} > 0$ , the cubic nonlinearity will balance the linear growth term and halt the growth of the disturbance when  $|A|$  becomes large enough. This case is a supercritical bifurcation. If  $\text{Re}\{\zeta\} < 0$ , the cubic term will never balance the linear growth term and the equation predicts growth without bound. In such cases, the bifurcation is subcritical and equation (1) is not a good asymptotic description of the nonlinear dynamics. Higher order terms must be calculated that balance the exponential growth. Whereas  $\mu$  and  $\nu$  can be predicted from a knowledge of the linear theory alone,  $\zeta$  and the all important sign of  $\text{Re}\{\zeta\}$  cannot be predicted without a nonlinear theory, and must be determined case by case by direct calculation.

To understand the origin of equation (1), consider the situations depicted in figure 6. When a system is weakly unstable, the unstable modes grow exponentially, but very slowly.

Most of the stable modes, on the other hand are relatively strongly damped. Because the stable modes decay rapidly, they are present in the system only to the extent that they are forced by nonlinear interactions with the unstable modes. Their evolution is slaved to that of the unstable modes. In many cases, Ginzburg-Landau type amplitude equations emerge from asymptotic methods that exploit the timescale separation between the stable and unstable modes.

Equation (1) governs only systems that are sufficiently large in the following sense. The spatial variations of the unstable wave packets must be produced by the interaction of a large number of closely spaced unstable modes. In a system of finite size, the spectrum of available wavenumbers must be discrete to satisfy boundary conditions. The smaller the system becomes, the larger the separation between neighboring modes in wavenumber space. If the modes are widely spaced, then a weakly unstable state may consist of only one or a small number of weakly unstable modes with all others relatively strongly damped, as shown in figure 6b. The amplitude equations governing such a situation would be a finite system of real, ordinary differential equations in time for the amplitudes of the unstable modes [2]. However, if the system is infinitely large, then the wavenumber spectrum is continuous. In that case, when the system is weakly unstable, a narrow band containing an infinite number of modes becomes unstable as shown in figure 6a. The nonlinear interaction of an infinite number of slowly evolving unstable modes leads to amplitude PDEs such as equation (1), rather than amplitude ODEs. Even when a system is finite, if it is sufficiently large that weak instability leads to the nonlinear interaction of a large number of closely spaced unstable modes, then equation (1) is still the appropriate asymptotic description of the evolution of the instability.

Though the form of equation (1) can be guessed *a priori* from considerations of symmetry [5], one must calculate the equation in detail in order to discover an expression for  $\zeta$ . Knowing the coefficients is useful, and not only because the sign of  $\text{Re}\{\zeta\}$  determines whether the Hopf bifurcation is supercritical or subcritical. Solutions of the complex Ginzburg-Landau equation exhibit a rich variety of different qualitative behaviors as the coefficients are varied. In large regions of parameter space, spatiotemporal chaos, intermittency, or the spontaneous formation of coherent structures may be observed. In others regions, stable, monochromatic plane wave solutions dominate. By computing the coefficients in terms of physical variables, it is possible to determine which of these behaviors are characteristic of the real physical system.

In this paper, we derive a complex Ginzburg-Landau equation for baroclinic instability. Baroclinic instability is important in the study of the atmosphere and oceans. It is the mechanism that generates weather systems in the midlatitude atmosphere, and it generates eddies in the oceans that are responsible for a great deal of heat transport from the equator to the poles. Baroclinic instability occurs when vertical shear flows driven by horizontal temperature gradients in a rotating domain become unstable, and large, wavelike disturbances develop that redistribute temperature fields in a kind of horizontally slanted convection.

A number of models have been used to study this phenomenon, the most well known of which are the Charney model and the Eady model. A basic introduction to these models and others can be found in the textbooks by Pedlosky [9], and Gill [4]. In this analysis, we use perhaps the simplest model exhibiting baroclinic instability. Introduced by Phillips in

1954 [10], it consists of a two-layer quasi-geostrophic flow in a rotating channel as shown in figure 1. Phillips analyzed the linear stability of a shear flow in which the fluid in each layer moves with a uniform zonal velocity. The basic state differs from that of the standard Kelvin-Helmholtz instability because rotation forces a slanting of the free surface between the two layers in order to balance the Coriolis force on the zonal flow. Phillips found that instability occurs when the difference between the velocities of the two layers exceeds a critical threshold. The model can easily be modified to include important physical effects, such as dissipation or a planetary vorticity gradient  $\beta$ .

The present work is motivated by a series of papers by Pedlosky ([6], [7], and a paper by Romea [11] that analyzed the nonlinear development of baroclinic instability in the Phillips model in a number of physically interesting situations. Pedlosky's papers, in particular, were the first to use multiscale asymptotic methods to compute amplitude equations for baroclinic instability. In contrast to the present effort, Pedlosky and Romea used periodic zonal boundary conditions and were therefore investigating the nonlinear interaction of a discrete spectrum of unstable modes. Consequently, their calculation led to amplitude ODEs as described above. Periodic boundary conditions are physically motivated for a model of atmospheric dynamics, because the midlatitude  $\beta$ -plane is typically conceived as a periodic strip wrapping around the earth. A typical wavelength for a baroclinic disturbance in the atmosphere is about 2000 km, which leaves space for only ten to fifteen wave periods in a complete traversal of the globe at midlatitudes. Nonetheless, there are physical examples of baroclinic instability to which the large aspect ratio approximation is applicable. For example, baroclinic instability produces eddies in ocean currents on the scale of 200 km. In an ocean measuring several thousand kilometers across, there is plenty of room for large scale structures to emerge. Our analysis of the large aspect ratio Phillips model should provide some insight into the kinds of structures one might expect in these situations.

To relate the CGL derived here to preexisting analysis of the qualitative behaviors of solutions of the CGL, we make use of two studies by Shraiman et al [12] and Chaté [1]. These papers present a fairly exhaustive numerical study of the parameter space of the one dimensional CGL. By mapping the coefficients calculated here onto the coefficients used in those studies, we determine what region of parameter space is inhabited by baroclinic instability. We find that most of the physical parameter space maps onto a region of CGL parameter space where non-chaotic, stable, monochromatic waves are the dominant solution at long times. Intermittent behavior may be possible when the  $\beta$  effect is strong compared to dissipation, but this has not been confirmed either analytically or by numerical simulation.

In §2, we give a detailed description of the Phillips Model, the physical variables involved, and the scaling limits underpinning its derivation. The physical situations examined by Pedlosky in [6], [7], and [8] are then described and contrasted with the situation considered here. In §3, the linear theory of baroclinic instability is outlined, and the CGL for baroclinic instability is derived in detail. In §4, we use the calculated coefficients to map realistic physical values of the variables onto Shraiman et al and Chaté's parameter regime, thus giving a preliminary prediction of the structures that may be observable in baroclinic instability



## 2 Description of the Phillips Model

The physical picture underlying the Phillips Model is given in figure 1. Two layers of fluid with different constant densities  $\rho_1 < \rho_2$  lie in an infinitely long channel of finite width  $L$  and height  $D$ . The thickness of the lower layer is given by  $h(x, y)$ . When undisturbed, each layer has thickness  $D/2$ . The fluid is bounded above and below by rigid horizontal planes. The  $x$ -axis is oriented along the channel, the  $y$ -axis is oriented across the channel, and the  $z$ -axis points upward. The velocities  $u_1, v_1$ , and  $w_1$  are the upper layer fluid velocities in the  $x, y$ , and  $z$  directions respectively. The lower layer velocities are likewise called  $u_2, v_2$ , and  $w_2$ . The pressures are given by  $p_1$  and  $p_2$ . Each layer has viscosity  $\nu$ . The gravitational acceleration is  $g$ , and the entire channel rotates with angular velocity  $\Omega$ . To include the effect of the earth's sphericity, the rotation rate is assumed to vary linearly with  $y$ ,

$$\Omega = \frac{1}{2} (f_0 + \tilde{\beta}y).$$

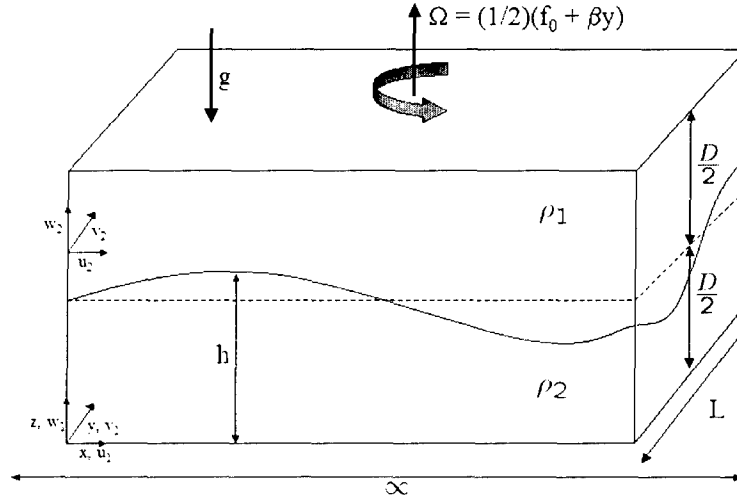


Figure 1: Physical picture of two layer channel model.

The Phillips model is derived as a scaling limit of the Navier-Stokes equations for flow in the channel. The derivation is given in greater detail in §2 of [6], but we will cover the salient points of the derivation here. Dimensionless equations of motion are obtained by

scaling the dimensional variables as follows

$$\begin{aligned}(x', y') &= \frac{(x, y)}{L}, & z' &= \frac{z}{D}, & t' &= \frac{U}{L}t, \\ (u'_n, v'_n) &= \frac{(u_n, v_n)}{U}, & w'_n &= \frac{L}{D} \frac{w_n}{U}, & h' &= (h - D/2) \frac{\rho_1 U L f_0}{g(\rho_2 - \rho_1)}, \\ p'_1 &= \frac{p_1 + \rho_1 g(z - D)}{\rho_1 U f_0 L}, \\ p'_2 &= \frac{p_2 + \rho_2 g(z - D/2) - \rho_1 g D/2}{\rho_2 U f_0 L}.\end{aligned}$$

where  $U$  is a characteristic scale for the horizontal velocities. On dropping primes we find

Dimensionless Parameter	Name	Size
$\epsilon = U/(f_0 L)$ ,	Rossby number	$\ll 1$
$E = 2\nu/f_0 D^2$ ,	Ekman number	$\sim \epsilon^2$
$F = \frac{2f_0^2 L^2}{g'D}$	rotational Froude number	$O(1)$
$\delta = D/L$ ,	cross section aspect ratio	$\ll 1$
$\beta = \tilde{\beta} L^2/U$	planetary vorticity factor	$O(1)$

Table 1: Dimensionless parameters appearing in derivation of Phillips Model.

that the dimensionless equations are

$$\epsilon \left[ \frac{\partial u_n}{\partial t} + u_n \frac{\partial u_n}{\partial x} + v_n \frac{\partial u_n}{\partial y} + w_n \frac{\partial u_n}{\partial z} \right] - (1 + \epsilon \beta y) v_n = -\frac{\partial p_n}{\partial x} + \frac{E}{2} \nabla_\delta^2 u_n, \quad (2)$$

$$\epsilon \left[ \frac{\partial v_n}{\partial t} + u_n \frac{\partial v_n}{\partial x} + v_n \frac{\partial v_n}{\partial y} + w_n \frac{\partial v_n}{\partial z} \right] + (1 + \epsilon \beta y) u_n = -\frac{\partial p_n}{\partial y} + \frac{E}{2} \nabla_\delta^2 v_n, \quad (3)$$

$$\delta^2 \epsilon \left[ \frac{\partial w_n}{\partial t} + u_n \frac{\partial w_n}{\partial x} + v_n \frac{\partial w_n}{\partial y} + w_n \frac{\partial w_n}{\partial z} \right] = -\frac{\partial p_n}{\partial z} + \frac{\delta^2 E}{2} \nabla_\delta^2 w_n, \quad (4)$$

$$\frac{\partial u_n}{\partial x} + \frac{\partial v_n}{\partial y} + \frac{\partial w_n}{\partial z} = 0. \quad (5)$$

where

$$\nabla_\delta^2 = \frac{\partial^2}{\partial z^2} + \delta^2 \left( \frac{\partial^2}{\partial x^2} + \frac{\partial^2}{\partial y^2} \right).$$

It is assumed that  $\delta \ll 1$ , so that horizontal straining contributes negligibly to viscous dissipation. The kinematic condition at the interface between the two layers is

$$\frac{\epsilon F}{2} \left[ \frac{\partial h}{\partial t} + u_n \frac{\partial h}{\partial x} + v_n \frac{\partial h}{\partial y} \right] = w_n, \text{ at } z = \frac{1}{2} (1 + \epsilon F h). \quad (6)$$

And no normal flow at the channel walls requires

$$v_n = 0, \text{ at } y = 0, 1. \quad (7)$$

Several dimensionless parameters have appeared, all of which are defined in table 1.

The parameter  $F$  is a dimensionless measure of the width of the channel. Specifically, it compares the channel width to the distance a linear gravity wave on the interface can travel during a rotation period. The maximum speed of these waves is  $c_0 = \sqrt{g'D/2}$ , where  $g' = g(\rho_2 - \rho_1)/\rho_2$  is the reduced gravity. The rotational period is  $T = 2\pi/f_0$ . Therefore,

$$F = \frac{2f_0^2 L^2}{g'D} = 4\pi^2 \left( \frac{L}{c_0 T} \right)^2.$$

The Rossby number  $\epsilon$  measures the relative importance of inertial forces and Coriolis forces. We will assume  $\epsilon \ll 1$ , so that the influence of rotation will be very strong. The Ekman number  $E$  measures the ratio of viscous forces to Coriolis forces, and determines the thickness of boundary layers in which viscosity plays an important role. We set  $E \ll 1$  with  $E^{1/2}/\epsilon = O(1)$ . These limits are exploited by introducing asymptotic expansions of all the dimensionless variables in powers of  $\epsilon$ , such as

$$u_n \sim u_n^{(0)} + \epsilon u_n^{(1)} + \epsilon^2 u_n^{(2)} + \dots$$

Then, to leading order, the flow in both layers is in geostrophic and hydrostatic balance. That is,

$$u_n^{(0)} = -\frac{\partial p_n^{(0)}}{\partial y}, \quad v_n^{(0)} = \frac{\partial p_n^{(0)}}{\partial x}, \quad \frac{\partial p_n^{(0)}}{\partial z} = 0.$$

The leading order flow is also horizontally nondivergent,

$$\frac{\partial u_n^{(0)}}{\partial x} + \frac{\partial v_n^{(0)}}{\partial y} = 0,$$

which motivates the introduction of layer stream functions  $\psi_n$  such that

$$\left( u_n^{(0)}, v_n^{(0)} \right) = \hat{z} \times \nabla \psi_n.$$

By hydrostatic and geostrophic balance, the stream function is proportional to both the pressure fluctuation and the height of the interface disturbance.

Additionally, viscous forces are significant only in thin boundary layers near the top and bottom of the channel. Nevertheless, viscosity plays an important role in the dynamics of the bulk. Carefully considering the dynamics of the boundary layers, one finds that vorticity in the bulk forces fluid to emerge from those layers with weak vertical velocities. This phenomenon is known as Ekman pumping. These vertical velocities act to damp vorticity in the bulk through vortex stretching. From here, one may derive the evolution equations for  $\psi_n$  by manipulating the vertical vorticity equation to obtain

$$\left( \frac{\partial}{\partial t} + \frac{\partial \psi_1}{\partial x} \frac{\partial}{\partial y} - \frac{\partial \psi_1}{\partial y} \frac{\partial}{\partial x} \right) (\nabla^2 \psi_1 + F(\psi_2 - \psi_1) + \beta y) = -r \nabla^2 \psi_1 \quad (8)$$

$$\left( \frac{\partial}{\partial t} + \frac{\partial \psi_2}{\partial x} \frac{\partial}{\partial y} - \frac{\partial \psi_2}{\partial y} \frac{\partial}{\partial x} \right) (\nabla^2 \psi_2 + F(\psi_1 - \psi_2) + \beta y) = -r \nabla^2 \psi_2 \quad (9)$$

where  $r = E^{1/2}\epsilon = O(1)$ . In these equations, fast gravity waves have been filtered out and only the slow, vortical dynamics remain.

To investigate baroclinic instability, we write down evolution equations for perturbations from a shear solution where the velocity of the upper layer is  $U$  and the velocity of the lower layer is  $-U$ . Let

$$\psi_1 = -Uy + \psi'_1, \quad \psi_2 = Uy + \psi'_2.$$

and substitute into equations (8) and (9). Dropping primes, we find

$$\left(\frac{\partial}{\partial t} + U\frac{\partial}{\partial x}\right)q_1 + \frac{\partial\psi_1}{\partial x}(\beta + 2FU) + r\nabla^2\psi_1 = -J(\psi_1, q_1), \quad (10)$$

$$\left(\frac{\partial}{\partial t} - U\frac{\partial}{\partial x}\right)q_2 + \frac{\partial\psi_2}{\partial x}(\beta - 2FU) + r\nabla^2\psi_2 = -J(\psi_2, q_2), \quad (11)$$

$$q_1 = \nabla^2\psi_1 + F(\psi_2 - \psi_1), \quad (12)$$

$$q_2 = \nabla^2\psi_2 + F(\psi_1 - \psi_2). \quad (13)$$

with boundary conditions

$$\frac{\partial\psi_n}{\partial x} = 0, \quad y = 0, 1.$$

These equations are the Phillips model of baroclinic instability.

Pedlosky and Romea's papers worked with these equations for a the channel periodic in  $x$ . In [6], Pedlosky derived amplitude ODEs for the purely viscous case  $\beta = 0$  and  $r = O(1)$ , and the inviscid cases with  $r = 0$  and  $\beta = O(1)$  or  $\beta = 0$ . Pedlosky obtained a Ginzburg-Landau ODE with real coefficients for  $\beta = 0$ ,  $r = O(1)$ . However, the small viscosity cases do not lead to Ginzburg-Landau type amplitude equations, because there is no scale separation between the decay rate of the stable modes and the growth rate of the unstable modes. Also, the case of  $0 < r \ll 1$  is a singular limit of the linear theory. The introduction of an infinitesimal viscosity actually *destabilizes* the flow, reducing the critical value of  $U$  by an  $O(1)$  amount. Pedlosky derived amplitude equations for this subtle case with  $\beta = 0$  in [7]. In [11], Romea tackled the small  $r$  case with  $\beta = O(1)$ .

It seems, however, that the case with both  $\beta = O(1)$  and  $r = O(1)$  has never been addressed. It is interesting to know how these two effects compete when they are of comparable strength. The infinite-size limit, which introduces the possibility of spatio-temporal disorder and localized structures, has also never been investigated.

### 3 Derivation of CGL

The Phillips model equations (10)-(13) may be written in the form

$$\frac{\partial}{\partial t}M\Psi = L\Psi - J(\Psi, M\Psi), \quad (14)$$

$$\frac{\partial\Psi}{\partial x} = 0, \quad \text{for } y = 0, 1. \quad (15)$$

where

$$\begin{aligned}\Psi &= \begin{pmatrix} \psi_1 \\ \psi_2 \end{pmatrix} \\ M &= \begin{bmatrix} \nabla^2 - F & F \\ F & \nabla^2 - F \end{bmatrix} \\ L &= \begin{bmatrix} -U \frac{\partial}{\partial x} (\nabla^2 - F) - (\beta + 2FU) \frac{\partial}{\partial x} - r \nabla^2 & -UF \frac{\partial}{\partial x} \\ UF \frac{\partial}{\partial x} & U \frac{\partial}{\partial x} (\nabla^2 - F) - (\beta - 2FU) \frac{\partial}{\partial x} - r \nabla^2 \end{bmatrix}\end{aligned}$$

and

$$J(A, B) = \frac{\partial A}{\partial x} \star \frac{\partial B}{\partial y} - \frac{\partial A}{\partial y} \star \frac{\partial B}{\partial x}.$$

The  $\star$  operator is termwise multiplication of vectors without summing. That is

$$\begin{pmatrix} a_1 \\ a_2 \end{pmatrix} \star \begin{pmatrix} b_1 \\ b_2 \end{pmatrix} = \begin{pmatrix} a_1 b_1 \\ a_2 b_2 \end{pmatrix}.$$

### 3.1 Linear Theory

Much of the structure of the finite amplitude evolution equations is determined by the linear instability properties of the system. The linearized equations are

$$\begin{aligned}\frac{\partial}{\partial t} M \Psi &= L \Psi, \\ \frac{\partial \Psi}{\partial x} &= 0, \text{ for } y = 0, 1.\end{aligned}\tag{16}$$

One may seek normal mode solutions of the form

$$\Psi(x, y, t) = \text{Re} \left\{ \hat{\Psi}(k, m, U) e^{i(kx + my - \omega t)} \right\}.$$

Substitution of this form into equation (16) yields a system of algebraic equations

$$(\hat{L} + i\omega \hat{M}) \hat{\Psi} = 0\tag{17}$$

where

$$\begin{aligned}\hat{M}(k, m) &= \begin{bmatrix} -(k^2 + m^2 + F) & F \\ F & -(k^2 + m^2 + F) \end{bmatrix} \\ \hat{L}(k, m, U) &= \begin{bmatrix} Uik(k^2 + m^2 + F) + \dots & -ikUF \\ +r(k^2 + m^2) - ik(\beta + 2FU) & -ikU(k^2 + m^2 + F) - \dots \\ ikUF & -ik(\beta - 2FU) + r(k^2 + m^2) \end{bmatrix}\end{aligned}$$

For a null vector  $\hat{\Psi}$  to exist,

$$\det(\hat{L} + i\omega \hat{M}) = 0\tag{18}$$

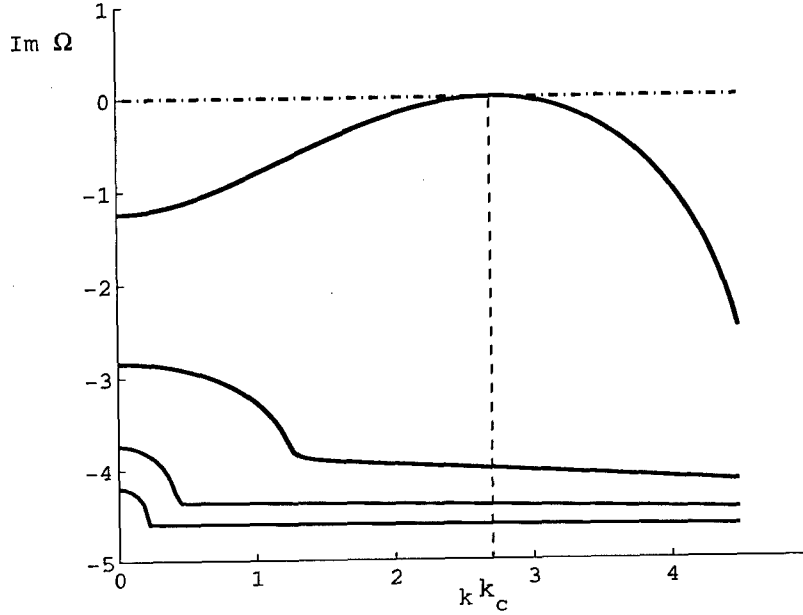


Figure 2: Growth rate curves for  $m = \pi, 2\pi, 3\pi, 4\pi$ , calculated for the critical shear  $U = U_c$  at which a single mode  $k = k_c$  is marginally stable.

must hold. Equation (18) implies that  $\omega$  must be a root of a second order polynomial with coefficients that are functions of  $k$ ,  $m$ , and the physical parameters of the system. Thus, for fixed values of these arguments there are at most two distinct values of  $\omega$  satisfying equation (18). This condition defines the dispersion relationships

$$\begin{aligned} \omega &= \Omega(k, m, U, d) \\ &= -\left(\frac{\beta k}{K^2} + ir\right) \frac{(K^2 + F)}{(K^2 + 2F)} + (-1)^d \frac{\sqrt{k^2 K^4 (K^4 - 4F^2) U^2 + F^2 (\beta k + ir K^2)^2}}{K^2 (K^2 + 2F)} \end{aligned} \quad (19)$$

where  $d = 1, 2$ , and  $K^2 = k^2 + m^2$ . A mode is stable if  $\text{Im}\{\Omega\} < 0$  and unstable if  $\text{Im}\{\Omega\} > 0$ .

Because of the boundary condition (15), normal mode solutions exist only for  $m = \pi, 2\pi, 3\pi, \dots$  when  $k \neq 0$ . However, because the channel is infinite in the  $x$  direction there is a continuous spectrum of solutions in  $k$ . Plotting  $\text{Im}\{\Omega\}$  for admissible  $k$  and  $m$  produces a discrete set of growth rate curves, as shown in figure (2).

When all the growth rate curves lie in  $\text{Im}\{\Omega\} < 0$ , the system is stable to infinitesimal perturbations. For fixed  $(k, m)$ , one may compute the critical value of the shear  $U = U_{\text{marg}}(k, m)$  at which that particular mode becomes marginally stable by setting  $\text{Im}\{\Omega(k, m, U, d)\} = 0$  and solving for  $U$ . One may use the identity

$$\text{Re}\{\sqrt{a + bi}\} = \text{sgn}(a) \sqrt{\frac{1}{2} \sqrt{a^2 + b^2} + \frac{1}{2} a}$$

and perform some lengthy algebra, the result of which is

$$U_{\text{marg}}(k, m) = \sqrt{\frac{\left(\frac{r}{k}\right)^2 K^4 (K^2 + F)^2 + F^2 \beta^2}{K^2 (K^2 + F)^2 (2F - K^2)}} \quad (20)$$

The mode is stable for  $U < U_{\text{marg}}(k, m)$ . Therefore, the entire system is stable for

$$U < U_c = \inf_{\substack{0 \leq K^2 \leq 2F \\ m = n\pi}} U_{\text{marg}}(k, m) \quad (21)$$

It is worth noting that equation (20) implies that instability is impossible for  $F < \pi^2/2$ . Furthermore, one can show that  $U_{\text{marg}}$  increases monotonically with  $m$ , so that the first modes to become marginally stable as  $U$  is increased will lie on the  $m = \pi$  curve.

### 3.2 Nonlinear modulation

At  $U = U_c$ , a single mode  $(k_c, \pi)$  has  $\text{Im}\{\Omega(k_c, \pi)\} = 0$ , and all other modes are stable. The purpose of this work is to learn what happens when the shear is increased slightly above  $U_c$  and the system becomes weakly unstable. As the modes grow, their nonlinear interactions play a pivotal role in the subsequent evolution of the instability.

Figure (6) visually summarizes the insight into this situation that linear theory provides. If  $U = U_c + \Delta$ , with  $|\Delta| \ll 1$ , then the maximum growth rate is positive and  $O(|\Delta|)$ . The growth rate curve is well described by a parabolic function in the neighborhood of its maximum, so there is a band of unstable wavenumbers of width  $O(|\Delta|^{1/2})$  around  $k = k_c$ .

Any exact solution to (14), (15) can be written in the form

$$\Psi(x, y, t) = \sum_{n=1}^{\infty} \int_{-\infty}^{\infty} A_{k, n\pi}(t) \hat{\Psi}(k, n\pi, U) e^{i[kx + n\pi y - \Omega(k, n\pi, U)t]} dk \quad (22)$$

Here,  $\hat{\Psi}(k, m, U)$  is the mode eigenvector defined by equation (17), and  $A_{k, m}(t)$  tracks the time evolution of the amplitude of mode  $(k, m)$ . The amplitudes of the unstable modes will dominate because, as mentioned above, strongly stable modes decay rapidly and are present due only to nonlinear forcing by the slowly evolving stable modes. That is,  $A_{k, m}$  should be strongly peaked near  $k = k_c$  on the  $m = \pi$  branch.

Using this assumption to write an approximate form for the Fourier series-transform solution (22) will motivate scalings for an asymptotic solution of this problem. First, neglecting the summands for  $n \neq 1$  and changing the integration variable to center on  $k = k_c$  gives

$$\Psi(x, y, t) \approx \int_{-\infty}^{\infty} A_{k_c + k', \pi}(t) \hat{\Psi}(k_c + k', \pi) e^{i((k_c + k')x + \pi y - \Omega(k_c + k', \pi, U_c + \Delta)t)} dk'$$

Now, we make use of the fact that the dominant contribution to the integral comes from  $k' = O(|\Delta|^{1/2})$ . Let  $\tilde{k} = |\Delta|^{-1/2} k'$  and Taylor expand the integrand about  $k_c$ . One finds:

$$\Psi(x, y, t) \approx \hat{\Psi}(k_c, \pi) e^{i(k_c x + \pi y - \Omega(k_c, \pi, U_c)t)} \int_{-\infty}^{\infty} \tilde{A}_{\tilde{k}}(t) e^{i|\Delta|^{1/2} \tilde{k} \left( x - \frac{\partial \Omega}{\partial k} \Big|_{k=k_c} t \right) - i\Delta \frac{\partial \Omega}{\partial U} \Big|_{U=U_c} t} d\tilde{k}$$

where  $\tilde{A}_{\tilde{k}} = |\Delta|^{1/2} A_{k_c + |\Delta|^{1/2} \tilde{k}}(t)$ . This expression is the product of the marginally stable mode at criticality with an amplitude envelope slowly varying in space and time:

$$\Psi(x, y, t) \approx A \left( |\Delta|^{1/2} (x - c_g t), |\Delta| t \right) \hat{\Psi}(k_c, \pi, U_c) e^{i(k_c x + \pi y - \Omega_c t)}. \quad (23)$$

Here,

$$c_g = \left. \frac{\partial \Omega}{\partial k} \right|_{k=k_c} \quad (24)$$

is the group velocity of the marginally unstable mode. We also write  $\Omega_c = \Omega(k_c, \pi, U_c)$  and  $\hat{\Psi}_c = \hat{\Psi}(k_c, \pi, U_c)$ .

Note that there is only one marginal wave at criticality, and not a pair of waves traveling in opposite directions. This fact can be established by noting that, though the critical branch satisfies  $\text{Im}\{\Omega\} = 0$  for both  $k_c$  and  $-k_c$ , we have  $\text{Re}\{\Omega(-k_c, \pi, 1)\} = -\text{Re}\{\Omega(k_c, \pi, 1)\}$ . This implies that the critical modes  $(k_c, \pi)$  and  $(-k_c, \pi)$  differ by only a phase shift. The second branch associated with  $(k_c, \pi)$  is strongly damped. This loss of symmetry is due to the  $\beta$ -effect, which imposes a directionality to the propagation of waves supported by the planetary vorticity gradient.

### 3.3 Method of Multiple Scales

The considerations leading to equation (23) reveal the proper scalings to use in a multiple-scales approach to this problem. Let

$$U = U_c + \Delta, \quad T = |\Delta|^{1/2} t, \quad \tau = |\Delta| t, \quad X = |\Delta|^{1/2} x.$$

Then, seek a solution for  $\Psi$  of the form

$$\Psi = |\Delta|^{1/2} \Psi^{(1)}(t, x, y, T, \tau, X) + |\Delta| \Psi^{(2)}(t, x, y, T, \tau, X) + |\Delta|^{3/2} \Psi^{(3)}(t, x, y, T, \tau, X) + \dots$$

The introduction of new space and time scales requires, by the chain rule,

$$\begin{aligned} \frac{\partial}{\partial t} &\rightarrow \frac{\partial}{\partial t} + |\Delta|^{1/2} \frac{\partial}{\partial T} + |\Delta| \frac{\partial}{\partial \tau}, \\ \frac{\partial}{\partial x} &\rightarrow \frac{\partial}{\partial x} + |\Delta|^{1/2} \frac{\partial}{\partial X}, \\ \nabla^2 &\rightarrow \nabla^2 + 2|\Delta|^{1/2} \frac{\partial^2}{\partial x \partial X} + |\Delta| \frac{\partial^2}{\partial X^2}. \end{aligned}$$

Substituting these transformations into the system (14), (15) and collecting terms of like order in  $|\Delta|$ , one may obtain a hierarchy of inhomogeneous linear problems. The most straightforward way of doing this requires the explicit manipulation of the terms of  $M$  and  $L$ . Unfortunately, proceeding in this manner produces extremely messy algebra and complicated expressions that are difficult to interpret in terms of physical properties of the system. However, it is possible to develop the expansion in general terms without considering the detailed structure of the operators  $M$  and  $L$ . By keeping track of only the formal structure of the expansion, we will be able to make useful simplifications throughout the computation.



When the linear operators  $M$  and  $L$  are applied to slowly varying wave packets, they can be expanded in the following way. First, note that

$$M\left(\partial_x + |\Delta|^{1/2} \partial_X, \partial_y\right) A(X, T, \tau) \hat{\Psi}(k, m) e^{i(kx+my)} = \hat{M}\left(k - i|\Delta|^{1/2} \frac{\partial}{\partial X}, m\right) A \hat{\Psi} e^{i(kx+my)}.$$

Formally, we may treat  $\partial_X$  as a variable and Taylor expand  $\hat{M}$  to find

$$\begin{aligned} M\left(\partial_x + |\Delta|^{1/2} \partial_X, \partial_y\right) A \hat{\Psi} e^{i(kx+my)} &= \left[ \hat{M}(k, m) - i|\Delta|^{1/2} \frac{\partial \hat{M}}{\partial k}(k, m) \frac{\partial}{\partial X} \right. \\ &\quad \left. - \frac{|\Delta|}{2} \frac{\partial^2 \hat{M}}{\partial k^2}(k, m) \frac{\partial^2}{\partial X^2} + \dots \right] A \hat{\Psi} e^{i(kx+my)}. \end{aligned}$$

Thus, the formal expansion of  $M$  takes the form

$$\begin{aligned} MA(X, T, \tau) \hat{\Psi}(k, m, U) e^{i(kx+my-\Omega t)} &\rightarrow \left[ A \hat{M} \hat{\Psi} - |\Delta|^{1/2} \frac{\partial A}{\partial X} \left( i \frac{\partial \hat{M}}{\partial k} \hat{\Psi} \right) \right. \\ &\quad \left. - \frac{|\Delta|}{2} \frac{\partial^2 A}{\partial X^2} \left( \frac{\partial^2 \hat{M}}{\partial k^2} \hat{\Psi} \right) + \dots \right] e^{i(kx+my-\Omega t)}. \end{aligned}$$

Likewise, the formal expansion of  $L$  takes the form

$$\begin{aligned} LA(X, T, \tau) \hat{\Psi}(k, m, U) e^{i(kx+my-\Omega t)} &\rightarrow e^{i(kx+my-\Omega t)} \left[ A \hat{L} \hat{\Psi} - |\Delta|^{1/2} \frac{\partial A}{\partial X} \left( i \frac{\partial \hat{L}}{\partial k} \hat{\Psi} \right) \right. \\ &\quad \left. + |\Delta| \left( \text{sgn}(\Delta) A \frac{\partial \hat{L}}{\partial U} \hat{\Psi} - \frac{1}{2} \frac{\partial^2 A}{\partial X^2} \left( \frac{\partial^2 \hat{L}}{\partial k^2} \hat{\Psi} \right) \right) \right]. \end{aligned}$$

To simplify notation, let  $\hat{L}_o = \hat{L}(k_c, \pi, U_c)$  and  $\hat{M}_o = \hat{M}(k_c, \pi)$ .

Utilizing these expansions and collecting terms of  $O(|\Delta|^{1/2})$  yields the leading order problem

$$\left( \frac{\partial}{\partial t} M_o - L_o \right) \Psi^{(1)} = 0, \quad (25)$$

$$\frac{\partial \Psi^{(1)}}{\partial x} = 0, \quad \text{for } y = 0, 1. \quad (26)$$

This is the linear problem (16) at the marginal shear  $U_c$ . There are infinitely many normal mode solutions, but all will decay at long times  $T = O(1)$  except for the marginally stable mode. As we are concerned with the long time evolution of the instability, we take the leading order solution to be

$$\Psi^{(1)} = \text{Re} \left\{ A(X, T, \tau) \hat{\Psi}_c e^{i(k_c x - \Omega_c t)} \sin \pi y \right\}. \quad (27)$$

Collecting terms of  $O(|\Delta|)$  yields

$$\begin{aligned} \left( \frac{\partial}{\partial t} \hat{M}_o - \hat{L}_o \right) \Psi^{(2)} &= -\frac{\partial}{\partial T} \hat{M}_o \Psi^{(1)} + i \frac{\partial}{\partial t} \frac{\partial \hat{M}}{\partial k} \frac{\partial \Psi^{(1)}}{\partial X} - i \frac{\partial \hat{L}}{\partial k} \frac{\partial \Psi^{(1)}}{\partial X} - J \left( \Psi^{(1)}, \hat{M}_o \Psi^{(1)} \right), \\ \frac{\partial \Psi^{(2)}}{\partial x} &= 0, \text{ for } y = 0, 1. \end{aligned} \quad (28)$$

The operator on the left hand side of this equation is the same as in equation (26). Thus, inhomogeneous terms proportional to the marginally stable mode will produce a secular response in  $\Psi^{(2)}$ . The elimination of these secular terms introduces a first constraint on the evolution of  $A(X, T, \tau)$ .

Substituting the solution (27) into equation (28), one finds

$$\begin{aligned} \left( \frac{\partial}{\partial t} \hat{M}_o - \hat{L}_o \right) \Psi^{(2)} &= \text{Re} \left\{ \left( -\hat{M}_o \hat{\Psi}_c \frac{\partial A}{\partial T} - i \left[ \frac{\partial \hat{L}}{\partial k} + i \Omega_c \frac{\partial \hat{M}}{\partial k} \right] \hat{\Psi}_c \frac{\partial A}{\partial X} \right) e^{i(k_c x - \Omega_c t)} \right\} \sin \pi y \\ &\quad + \text{Im} \left\{ \hat{\Psi}_c \star \overline{\hat{M}_o \hat{\Psi}_c} \right\} \frac{\pi k_c}{2} |A|^2 \sin 2\pi y. \end{aligned} \quad (29)$$

The overbar represents complex conjugation. Since equation (29) is linear,  $\Psi^{(2)}$  takes the form

$$\Psi^{(2)} = \text{Re} \left\{ A^{(2)}(X, T, \tau) e^{i(k_c x - \Omega_c t)} \right\} \sin \pi y + B^{(2)}(X, T, \tau) \sin 2\pi y + U^{(2)}(X, T, \tau) \left( y - \frac{1}{2} \right).$$

The first term represents a correction proportional to the marginally stable mode. The second two terms are independent of  $x$ , and represent an  $O(|\Delta|)$  correction to the zonal mean flow. Substituting this form into equation (29) and collecting terms proportional to  $\sin 2\pi y$  yields a problem for  $B^{(2)}$ :

$$-\hat{L}(0, 2\pi, U_c) B^{(2)} = \frac{k_c \pi}{2} \text{Im} \left\{ \hat{\Psi}_c \star \overline{\hat{M}_o \hat{\Psi}_c} \right\} |A|^2$$

Using

$$\hat{L}(0, 2\pi, U_c) = 4\pi^2 r l$$

gives

$$B^{(2)} = -\frac{k_c}{8\pi r} \text{Im} \left\{ \hat{\Psi}_c \star \overline{\hat{M}_o \hat{\Psi}_c} \right\} |A|^2. \quad (30)$$

Collecting terms proportional to  $\sin \pi y$  yields a problem for  $A^{(2)}$ :

$$\left( \hat{L}_o + i \Omega_c \hat{M}_o \right) A^{(2)} = \hat{M}_o \hat{\Psi}_c \frac{\partial A}{\partial T} + i \left( \frac{\partial \hat{L}}{\partial k} + i \Omega_c \frac{\partial \hat{M}}{\partial k} \right) \hat{\Psi}_c \frac{\partial A}{\partial X}$$

Now, as demonstrated by equation (17), the operator on the left hand side is singular. For the equation to be solvable, the right hand side must be orthogonal to the operator's left null vector. That is, for  $\hat{\Psi}_c^\dagger$  such that

$$\hat{\Psi}_c^\dagger \left( \hat{L}_o + i \Omega_c \hat{M}_o \right) = 0,$$

we must have

$$\hat{\Psi}_c^\dagger \left[ \hat{M}_o \hat{\Psi}_c \frac{\partial A}{\partial T} + i \left( \frac{\partial \hat{L}}{\partial k} + i \Omega_c \frac{\partial \hat{M}}{\partial k} \right) \hat{\Psi}_c \frac{\partial A}{\partial X} \right] = 0. \quad (31)$$

This equation implies something about the evolution of  $A$ . Unfortunately, it is a mess and difficult to interpret physically, especially if the matrix products are written out in full. It is at this point that our attention to the formal structure of the expansion becomes useful. Note that

$$\frac{\partial}{\partial k} \left[ \left( \hat{L}_o + i \Omega_c(k, \pi, U_c) \right) \hat{\Psi}(k, \pi, U_c) \right] = 0.$$

If we expand this expression with the product rule and evaluate at  $k = k_c$ , we find

$$\left( \frac{\partial \hat{L}}{\partial k} + i \Omega_c \frac{\partial \hat{M}}{\partial k} \right) \hat{\Psi}_c = -i \frac{\partial \Omega}{\partial k} \Big|_{k=k_c} \hat{M}_o \hat{\Psi}_c - \left( \hat{L}_o + i \Omega_c \hat{M}_o \right) \frac{\partial \hat{\Psi}}{\partial k}.$$

That is, the operator splits into a term proportional to the group velocity of the marginal wave (see equation (24)) and a term that is orthogonal to the left null vector  $\hat{\Psi}_c^\dagger$  by definition! Substituting this new relation into equation (31) yields a more familiar evolution equation for  $A$ :

$$\frac{\partial A}{\partial T} + c_g \frac{\partial A}{\partial X} = 0.$$

The amplitude envelope propagates at the group velocity of the marginally stable wave. We now write  $A(X, T, \tau) = A(\eta, \tau)$  where  $\eta = X - c_g T$ . We also have

$$\frac{\partial}{\partial X} = \frac{\partial}{\partial \eta}, \quad \frac{\partial}{\partial T} = -c_g \frac{\partial}{\partial \eta}.$$

It is still necessary to solve for  $A^{(2)}$ . One solution is

$$A^{(2)} = -i \frac{\partial \hat{\Psi}}{\partial k} \frac{\partial A}{\partial \eta}. \quad (32)$$

One might add a homogeneous term proportional to  $\hat{\Psi}_c$  to this solution, but the inclusion of such a term has no impact on the results of the computation. The term is proportional to  $\Psi^{(1)}$ , so we may simply require that it be absorbed into the leading order solution.

Finally,  $U^{(2)}$  is determined by enforcing the boundary condition (15). It can be shown [10] that the normal flow condition implies a constraint on the zonally averaged flow at the boundaries,

$$\frac{\partial}{\partial t} u_n = \lim_{M \rightarrow \infty} \frac{1}{2M} \int_{-M}^M \frac{\partial^2 \psi_n}{\partial y \partial t} dx = 0, \quad \text{for } y = 0, 1.$$

This equation implies that, as higher order corrections develop, they cannot alter the mean zonal flow at the boundaries. We deduce that,

$$U^{(2)} = -2\pi B^{(2)}$$

To summarize, we have found

$$\Psi^{(2)} = \Re \left\{ -i \frac{\partial \hat{\Psi}}{\partial k} \frac{\partial A}{\partial \eta} e^{i(k_c x - \Omega_c t)} \right\} \sin \pi y - \frac{k_c}{8\pi r} \Im \left\{ \hat{\Psi}_c \star \overline{\hat{M}_o \hat{\Psi}_c} \right\} |A|^2 \left( \sin 2\pi y - 2\pi \left( y - \frac{1}{2} \right) \right).$$

Collecting terms of  $O(|\Delta|^{3/2})$  yields

$$\begin{aligned} \left( \frac{\partial}{\partial t} \hat{M}_o - \hat{L}_o \right) \Psi^{(3)} = & - \left( \frac{\partial}{\partial T} \hat{M}_o + i \left( \frac{\partial \hat{L}}{\partial k} - \frac{\partial}{\partial t} \frac{\partial \hat{M}}{\partial k} \right) \frac{\partial}{\partial X} \right) \Psi^{(2)} \\ & - \left( \frac{\partial}{\partial \tau} \hat{M}_o - i \frac{\partial^2}{\partial X \partial T} \frac{\partial \hat{M}}{\partial k} + \frac{1}{2} \frac{\partial^2}{\partial X^2} \left( \frac{\partial^2 \hat{L}}{\partial k^2} - \frac{\partial}{\partial t} \frac{\partial^2 \hat{M}}{\partial k^2} \right) + \Delta \frac{\partial \hat{L}}{\partial U} \right) \Psi^{(1)} \\ & - J \left( \Psi^{(2)}, \hat{M}_o \Psi^{(1)} \right) - J \left( \Psi^{(1)}, \hat{M}_o \Psi^{(2)} \right) + \tilde{J} \left( \Psi^{(1)}, \hat{M} \Psi^{(1)} \right). \end{aligned} \quad (33)$$

where

$$\tilde{J} \left( \Psi^{(1)}, \hat{M} \Psi^{(1)} \right) = \frac{\partial \Psi^{(1)}}{\partial X} \frac{\partial}{\partial y} \left( \hat{M}_o \Psi^{(1)} \right) - \frac{\partial \Psi^{(1)}}{\partial y} \frac{\partial}{\partial X} \left( \hat{M}_o \Psi^{(1)} \right).$$

Since our only purpose in proceeding to this order is to find another evolution equation for  $A$ , it is not necessary to solve for  $\Psi^{(3)}$  in full. We simply note that the right hand side of equation (33) contains terms proportional to  $e^{i(k_c x - \Omega_c t)} \sin \pi y$ ,  $\sin 2\pi y$ , and  $e^{i(k_c x - \Omega_c t)} \sin 3\pi y$ . Therefore, since the problem is linear we may assume

$$\Psi^{(3)} = \text{Re} \left\{ e^{i(k_c x - \Omega_c t)} \left( A^{(3)} \sin \pi y + B^{(3)} \sin 3\pi y \right) \right\} + C^{(3)} \sin 2\pi y - U^{(3)} y.$$

The evolution equation we seek will emerge as we attempt to solve for  $A^{(3)}$ . Substituting in the solutions for  $\Psi^{(1)}$  and  $\Psi^{(2)}$  and equating terms proportional to  $\sin \pi y$  yields

$$\left( \hat{L}_o + i\Omega_c \hat{M} \right) A^{(3)} = \left( \hat{M}_o \hat{\Psi}_c \right) \frac{\partial A}{\partial \tau} - \left( \frac{\Delta}{|\Delta|} \frac{\partial \hat{L}}{\partial U} \hat{\Psi}_c \right) A + \Pi_1 \frac{\partial^2 A}{\partial \eta^2} + \Pi_2 A |A|^2. \quad (34)$$

where

$$\Pi_1 = \frac{1}{2} \left[ \left( \frac{\partial^2 \hat{L}}{\partial k^2} + i\Omega_c \frac{\partial^2 \hat{M}}{\partial k^2} \right) \hat{\Psi}_c + 2 \left( \frac{\partial \hat{L}}{\partial k} + i\Omega_c \frac{\partial \hat{M}}{\partial k} \right) \frac{\partial \hat{\Psi}}{\partial k} + 2i \frac{\partial \Omega}{\partial k} \frac{\partial}{\partial k} \left( \hat{M}_o \hat{\Psi}_c \right) \right],$$

and

$$\Pi_2 = -\frac{ik_c^2}{8r} \left[ 3 \text{Im} \left\{ \hat{\Psi}_c \star \hat{M}_o \hat{\Psi}_c \right\} \star \left( \hat{M}_o \hat{\Psi}_c \right) - \mathcal{M} \text{Im} \left\{ \hat{\Psi}_c \star \hat{M}_o \hat{\Psi}_c \right\} \star \hat{\Psi}_c \right],$$

where

$$\mathcal{M} = \hat{M}(0, 2\pi) + \begin{pmatrix} -2F & 2F \\ 2F & -2F \end{pmatrix} = \begin{pmatrix} -4\pi^2 - 3F & 3F \\ 3F & -4\pi^2 - 3F \end{pmatrix}.$$

Using the relationship

$$\frac{\partial^2}{\partial k^2} \left[ \left( \hat{L}_o + i\Omega(k, \pi, U_c) \right) \hat{\Psi}(k, \pi, U_c) \right] = 0,$$

one can show that

$$\Pi_1 = -\frac{1}{2} i \frac{\partial^2 \Omega}{\partial k^2} \hat{M}_o \hat{\Psi}_c - \left( \hat{L}_o + i\Omega_c \hat{M}_o \right) \frac{\partial^2 \hat{\Psi}}{\partial k^2}.$$

Likewise, using

$$\frac{\partial}{\partial U} \left[ \left( \hat{L}_o + i\Omega(k, \pi, U_c) \right) \hat{\Psi}(k_c, \pi, U) \right] = 0,$$

one may show that

$$\frac{\partial \hat{\mathcal{L}}}{\partial U} \hat{\Psi}_c = -i \frac{\partial \Omega}{\partial U} \hat{\mathcal{M}}_o \hat{\Psi}_c - \left( \hat{\mathcal{L}}_o + i \Omega_c \hat{\mathcal{M}}_o \right) \frac{\partial \hat{\Psi}}{\partial U}.$$

Finally, forming the solvability condition as in equation (31) gives

$$\frac{\partial A}{\partial \tau} = \mu A + \nu \frac{\partial^2 A}{\partial \eta^2} - \zeta A |A|^2. \quad (35)$$

where the coefficients are given by

$$\mu = \text{sgn}(\Delta) \frac{\hat{\Psi}_c^\dagger \frac{\partial \hat{\mathcal{L}}}{\partial U} \hat{\Psi}_c}{\hat{\Psi}_c^\dagger \hat{\mathcal{M}}_o \hat{\Psi}_c} = -i \text{sgn}(\Delta) \left. \frac{\partial \Omega}{\partial U} \right|_{k=k_c}, \quad (36)$$

$$\nu = \left. \frac{1}{2} i \frac{\partial^2 \Omega}{\partial k^2} \right|_{k=k_c} \quad (37)$$

$$\zeta = \frac{ik_c^2 \hat{\Psi}_c^\dagger \left( 3 \mathbb{I} \mathbb{m} \left\{ \hat{\Psi}_c \star \overline{\hat{\mathcal{M}}_o \hat{\Psi}_c} \right\} \star \left( \hat{\mathcal{M}}_o \hat{\Psi}_c \right) - \mathcal{M} \mathbb{I} \mathbb{m} \left\{ \hat{\Psi}_c \star \overline{\hat{\mathcal{M}}_o \hat{\Psi}_c} \right\} \star \hat{\Psi}_c \right)}{8r \hat{\Psi}_c^\dagger \hat{\mathcal{M}}_o \hat{\Psi}_c}. \quad (38)$$

We have derived a complex Ginzburg-Landau equation governing the onset of baroclinic instability in a two layer model. The expressions for the coefficients are expressed in terms of quantities computable from the linear theory of baroclinic modes. Specifically, we have

$$\hat{\Psi}_c = (1, \gamma)^T,$$

where

$$\gamma = \frac{K_c^2 + F}{F} - \frac{\beta + 2FU_c}{F(U_c - c)} - i \frac{r}{k_c} \frac{K_c^2}{F(U_c - c)}.$$

where  $c = \Omega_c/k_c$ . A useful fact about  $\gamma$  is that

$$\gamma^{-1} = \frac{K_c^2 + F}{F} + \frac{\beta - 2FU_c}{F(U_c + c)} + i \frac{r}{k_c} \frac{K_c^2}{F(U_c + c)}.$$

The left null vector  $\hat{\Psi}_c^\dagger$  is simply

$$\hat{\Psi}_c^\dagger = \left( 1, -\frac{U_c - c}{U_c + c} \gamma \right).$$

After some algebra, one finds the following explicit expressions for the coefficients:

$$\mu = \frac{ik_c F \text{sgn}(\Delta) \left[ \frac{1+\gamma}{U_c - c} + \frac{\gamma+\gamma^2}{U_c + c} - \frac{K_c^2}{F(U_c - c)} - \frac{\gamma^2 K_c^2}{F(U_c + c)} \right]}{Z + \gamma^2 Z'}, \quad (39)$$

$$\nu = \frac{1}{Z + \gamma^2 Z'} \left[ ik_c \left( 1 + \gamma^2 + 2 \frac{U_c - c_g}{U_c - c} + 2\gamma^2 \frac{U_c + c_g}{U_c + c} \right) + r \left( \frac{1}{U_c - c} - \frac{\gamma^2}{U_c + c} \right) + \frac{(U_c - c_g) Z + Y}{ik_c F} \left( F \frac{U_c - c_g}{U_c - c} - (K_c^2 + F) \gamma \frac{U_c + c_g}{U_c + c} + \gamma Y' \right) \right] \quad (40)$$

$$\zeta = \frac{ik_c K_c^2}{8(Z + \gamma^2 Z')} \left[ \frac{4\pi^2 + 3F}{(U_c - c)^2} + \frac{\gamma^2 |\gamma|^2 (4\pi^2 + 3F)}{(U_c + c)^2} + \frac{3F (|\gamma|^2 + \gamma^2)}{U_c^2 - c^2} + \frac{3\gamma^2 |\gamma|^2 Z'}{U_c + c} - \frac{3Z}{U_c - c} \right]. \quad (41)$$

where

$$\begin{aligned} Z &= \frac{\beta + 2FU_c}{(U_c - c)^2} + i \frac{r}{k_c} \frac{K_c^2}{(U_c - c)^2}, \\ Z' &= \frac{\beta - 2FU_c}{(U_c + c)^2} + i \frac{r}{k_c} \frac{K_c^2}{(U_c + c)^2}, \\ Y &= 2k_c^2 - \frac{\beta + 2FU_c + 2ik_cr}{U_c - c}, \\ Y' &= 2k_c^2 + \frac{\beta - 2FU_c + 2ik_cr}{U_c + c}. \end{aligned}$$

## 4 Parameter Regime Analysis

Having computed the coefficients of equation (35) in terms of physical variables, we are now prepared to determine which of the qualitative dynamics of the CGL observed numerically in [1] and [12] may be observable in baroclinic instability.

In [1], Chaté analyzes the CGL in the form

$$\frac{\partial B}{\partial t} = B + (1 + ib_1) \frac{\partial^2 B}{\partial x^2} - (b_3 - i) |B|^2 B. \quad (42)$$

where  $b_1, b_3$  are real and  $b_3 > 0$ . This simple form is obtained from equation (35) by making the transformations

$$t = \text{Re}\{\mu\} \tau, \quad x = \sqrt{\frac{\text{Re}\{\mu\}}{\text{Re}\{\nu\}}} \eta, \quad B(x, t) = \sqrt{-\frac{\text{Im}\{\zeta\}}{\text{Im}\{\mu\}}} e^{-i \frac{\text{Im}\{\mu\}}{\text{Re}\{\mu\}} t} A\left(\sqrt{\frac{\text{Re}\{\nu\}}{\text{Re}\{\mu\}}} x, t/\text{Re}\{\mu\}\right),$$

from which we find

$$b_1 = -\text{sgn}(\text{Im}\{\zeta\}) \frac{\text{Im}\{\nu\}}{\text{Re}\{\nu\}}, \quad (43)$$

$$b_3 = \left| \frac{\text{Re}\{\zeta\}}{\text{Im}\{\zeta\}} \right|. \quad (44)$$

Thus, the parameter space of the CGL has two real dimensions.<sup>1</sup>

The qualitatively different regimes of parameter space are mapped with respect to  $b_1$  and  $b_3$  in figure 3a. This figure is reproduced from [1]. To discover which regimes are relevant to baroclinic instability,  $b_1$  and  $b_3$  were computed numerically for a range of  $\beta$ ,  $r$ , and  $F$ .

It was found that  $b_1, b_3$  are functions of  $F$  and  $\beta/r$  only, though this fact is not immediately obvious from the formulas for  $\zeta$  and  $\nu$ . For all tested values of  $F$ ,  $\beta/r$ , we found  $b_1 \leq 0$ . At fixed  $F$ , decreasing  $\beta/r$  increases  $b_3$  and decreases  $|b_1|$ . As  $\beta/r$  is varied, the coefficients roughly satisfy  $b_1 b_3 = C(F)$ . Decreasing  $F$  at fixed  $\beta/r$  also increases  $b_3$  and decreases  $|b_1|$ . In the limit that  $\beta/r \rightarrow 0$  or  $F \rightarrow \pi^2/2$ , we find that  $b_3 \rightarrow \infty$  and  $b_1 \rightarrow 0$ .<sup>2</sup> In this limit,

<sup>1</sup>Technically, this form can be obtained from equation (35) only if  $\text{Im}\{\zeta\} < 0$ , as is apparent from an inspection of the transformations. However, if  $\text{Im}\{\zeta\} > 0$ , taking the complex conjugate of equation (1) and then applying the transformations yields equation (42) for  $\bar{B}$ .

<sup>2</sup>Recall from §3 that for  $F \leq \pi^2/2$ , baroclinic instability is impossible.

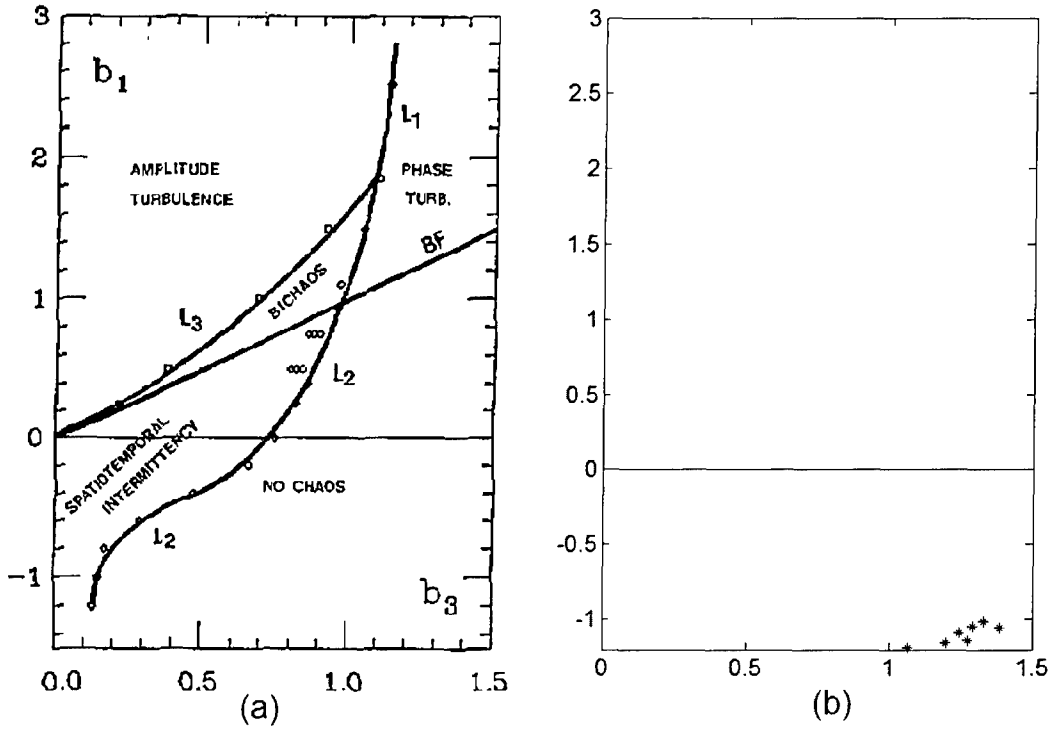


Figure 3: (a) The parameter regime diagram of the CGL produced by Chat  , Shraiman, et al. Reproduced from [1]. (b) These points represent the only points for  $5 < F < 50$  and  $0.1 < \beta/r < 50$  that fall in the sector of parameter space studied in [1], [12]. The points correspond to  $\beta/r \approx 10 - 40$  and fall well within the “no chaos” regime.

the coefficients of the CGL are purely real. The real Ginzburg-Landau equation, unlike its complex cousin, is derivable from a variational principle, and its solutions always relax to a stationary equilibrium state.

The values of  $b_1$  and  $b_3$  for  $5 < F < 50$  and  $0.1 < \beta/r < 50$  are plotted in figure 4. The lower limits of these ranges were chosen to exclude divergent values of  $b_3$  as  $F \rightarrow \pi^2/2 \approx 4.93$  and  $\beta/r \rightarrow 0$ . An upper limit of 50 was chosen for both  $F$  and  $\beta/r$  to prevent these parameters from being much more than an order of magnitude larger than one. It is implicit in the derivation of equation (35) that  $F, \beta, r \ll |\Delta|^{-1/2}$ . The larger these parameters become, the smaller  $|\Delta|$  must be for equation (35) to be asymptotically consistent.

As baroclinic instability resides exclusively in the region  $b_1 \leq 0$ , we focus on the dynamical regimes present there. For  $b_1 < b_3$ , a band of stable plane wave solutions<sup>3</sup> of the form

$$B = \tilde{B}(k)e^{i(kx - \omega(k)t)}$$

exists with  $\tilde{B}^2 = (1 - k^2)/b_3$  and  $\omega = 1/b_3 - (b_1 + 1/b_3)k^2$ . These solutions are linearly

<sup>3</sup>When  $b_1 = b_3$ , this band of wavenumbers vanishes, and stable monochromatic plane wave solutions cease to exist. This bifurcation is known as the Benjamin-Feir instability of the  $k = 0$  state. The turbulent regimes in the Benjamin-Feir unstable region  $b_1 > b_3$  are the subject of [12], but because these regimes appear to be inaccessible to baroclinic instability in the Phillips model, we omit discussion of them here.

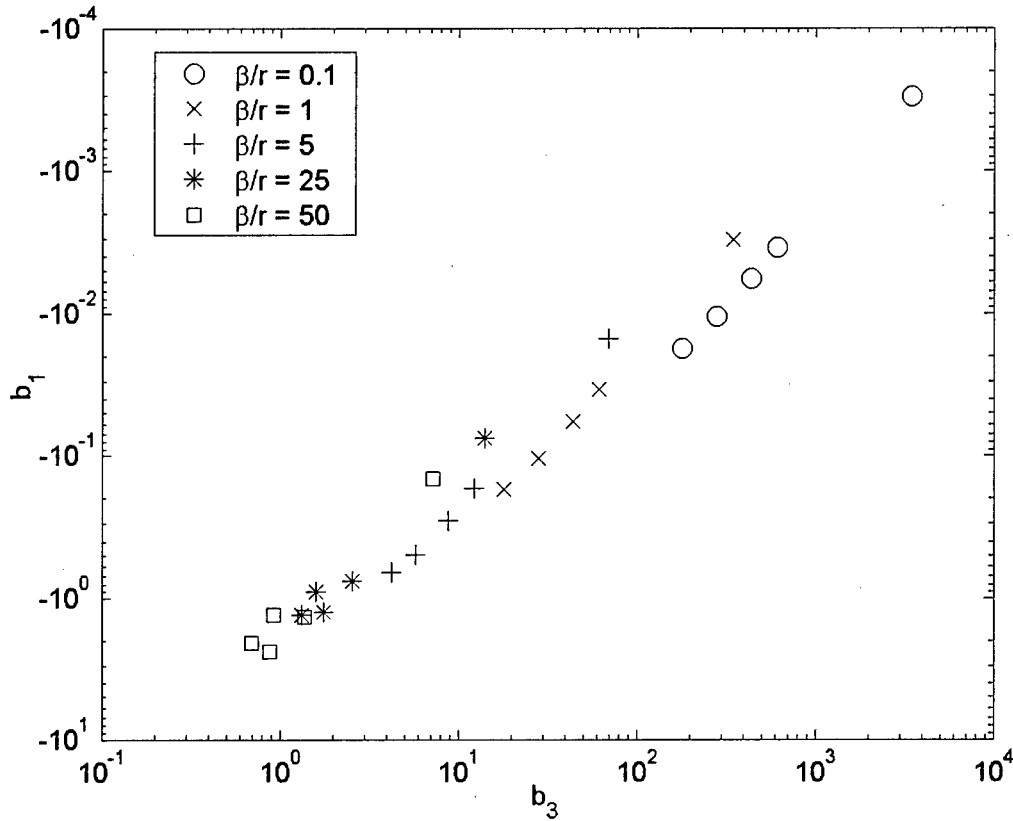


Figure 4: Values of  $b_1$  and  $b_3$  computed for a range of values of  $\beta/r$  and  $F$ . Each streak of like-shaped markers corresponds to a fixed value of  $\beta/r$  with  $F = 5, 7, 9, 16, 50$ . Increasing  $F$  with fixed  $\beta/r$  decreases  $b_3$  and increases  $|b_1|$ . Increasing  $\beta/r$  with fixed  $F$  yields the same trend, but the dependence of  $\beta/r$  is stronger than on  $F$ .

stable for

$$k^2 < \frac{(b_3 - b_1)}{3b_3 + \frac{2}{b_3} - b_1}.$$

However, the existence of stable plane wave solutions does not preclude the existence of chaotic solutions or localized structures in the same parameter regime. Chat   found that for sufficiently small  $b_3$  solutions could be found numerically in which localized, propagating structures separate large regions of stable plane waves. The structures are characterized by a sharp reduction in  $|A|$ , and discontinuities or rapid variations in the phase of  $A$ . The structures act as nucleation sites for disorder; the stable plane wave regions do not break down until they are contaminated by one of these structures. The nature of these structures is discussed in the context of known exact solutions of the CGL at some length in [1] and [13].

However, it is not yet clear whether these structures can be expected to appear in baroclinic instability. For the range of  $\beta$ ,  $r$ , and  $F$ , tested here, the coefficients  $b_1$ , and  $b_3$



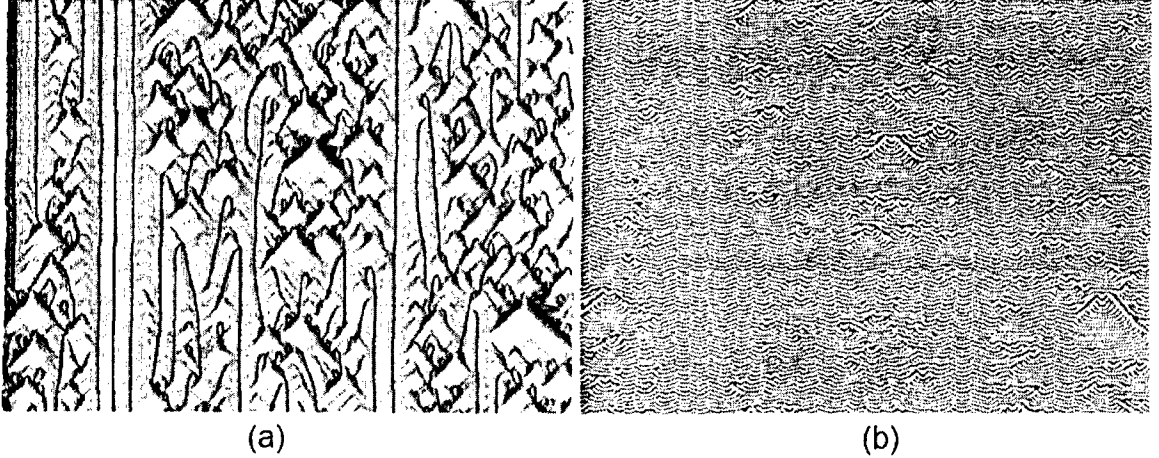


Figure 5: (a) Space-time plot of  $|A|$ .  $x$  increases left to right and  $t$  increases upwards. White represents the amplitude maximum  $|A| = 2.37$ , and black represents  $|A| = 0$ . (b) Space-time plot of the phase  $\phi$  of  $A$ . Reproduced from [1]. In this run,  $b_1 = -0.75$ ,  $b_3 = 0.18$ .

generally lie far outside the region of parameter space explored directly by Chaté. Figure 3b shows those parameter values that did lie in that region, and all of those are well within the “no chaos” zone in which intermittency was not observed. For small  $\beta/r$  and  $F$ , we have seen that the coefficients asymptote to  $b_1 = 0$  and  $b_3 = 0$ , where the dynamics collapse to those of the real Ginzburg-Landau equation. It is unlikely that disordered states will be discovered in this limit, since solutions of the real Ginzburg-Landau always relax to equilibrium. But as  $\beta/r$  increases,  $b_3$  becomes small. This raises the possibility of intermittency for sufficiently large  $\beta/r$ . However,  $|b_1|$  simultaneously becomes large as  $\beta/r$  increases, pushing the coefficients out of the sector of parameter space observed by Chaté. Chaté found that as  $|b_1|$  increases,  $b_3$  must be ever smaller for intermittency to be observed. The question, then, is whether  $b_3$  decreases quickly enough to counteract the stabilizing effect of increased  $|b_1|$ . Furthermore,  $\beta/r$  cannot be increased without bound. We must have  $|\Delta|^{1/2} \ll r \ll \text{absdel}-1/2$  and  $\beta \ll |\Delta|^{-1/2}$  for equation (35) to be accurate, and thus  $\beta/r \ll |\Delta|$ . Numerical simulations of CGL at parameter values appropriate to baroclinic instability are necessary to determine if “baroclinic structures” will emerge or not.

## 5 Conclusions

We have computed a complex Ginzburg-Landau equation for baroclinic instability in the Phillips model. We have compared the coefficient of this equation to a parameter regime study by Chaté [1] and Shraiman et al [12]. The comparison suggests that, for most physical situations, baroclinic instability should saturate to a monochromatic wave train without intermittency or spatial disorder.

However, the search for baroclinic structures should not be called off yet. The possibility remains that localized structures and spatiotemporal disorder could emerge for large  $\beta/r$ .

Further numerical simulation of the CGL is necessary to determine whether this will happen, as this region of parameter space was not explored in Chaté's paper. In future work, we intend to search for baroclinic structures in numerical solutions of both the CGL and more realistic models of baroclinic instability, such as the Phillips model or a continuously stratified QG model.

## 6 Acknowledgements

I heartily thank Ed Spiegel, who both introduced me to Pattern theory and pushed me to follow it toward whatever interested me. I also thank Joe Pedlosky for several valuable discussions. I had a wonderful time in Woods Hole this summer, and I want to thank Oliver Bühler and Charles Doering for directing the program.

## References

- [1] H. CHATÉ, *Spatiotemporal intermittency regimes of the one-dimensional complex Ginzburg-Landau equation*, Nonlinearity, 7 (1994), pp. 185–204.
- [2] P. H. COULLET AND E. A. SPIEGEL, *Amplitude Equations for Systems with Competing Instabilities.*, SIAM Journal on Applied Mathematics, 43 (1983), pp. 776–821.
- [3] M. C. CROSS AND P. C. HOHENBERG, *Pattern formation outside of equilibrium*, Reviews of Modern Physics, 65 (1993), pp. 851–1112.
- [4] A. E. GILL, *Atmosphere-Ocean Dynamics*, Academic Press, San Diego, California, 1982.
- [5] A. C. NEWELL, T. PASSOT, AND J. LEGA, *Order parameter equations for patterns*, Annual Review of Fluid Mechanics, 25 (1993), pp. 399–453.
- [6] J. PEDLOSKY, *Finite-Amplitude Baroclinic Waves.*, J. Atmos. Sci., 27 (1970), pp. 15–30.
- [7] ———, *Finite-Amplitude Baroclinic Waves with Small Dissipation.*, J. Atmos. Sci., 28 (1971), pp. 587–597.
- [8] ———, *Limit Cycles and Unstable Baroclinic Waves.*, J. Atmos. Sci., 29 (1972), pp. 53–63.
- [9] J. PEDLOSKY, *Geophysical Fluid Dynamics*, Springer Verlag, New York, second ed., 1987.
- [10] N. A. PHILLIPS, *Energy transformations and meridional circulations associated with simple baroclinic waves.*, Tellus, 6 (1954), pp. 273–286.
- [11] R. D. ROMEA, *The Effects of Friction and  $\beta$  on Finite-Amplitude Baroclinic Waves.*, J. Atmos. Sci., 34 (1977), pp. 1689–1695.

- [12] SHRAIMAN, B. I., PUMIR, A. VAN SAARLOOS, W. HOHENBERG, P. C. CHATÉ, AND M. H. HOLEN, *Spatiotemporal chaos in the one-dimensional complex Ginzburg-Landau equation*, Physica D Nonlinear Phenomena, 57 (1992), pp. 241–248.
- [13] A. TORCINI, H. FRAUENKRON, AND P. GRASSBERGER, *Studies of phase turbulence in the one dimensional complex ginzburg-landau equation*, pre, 55 (1997), p. 5073.

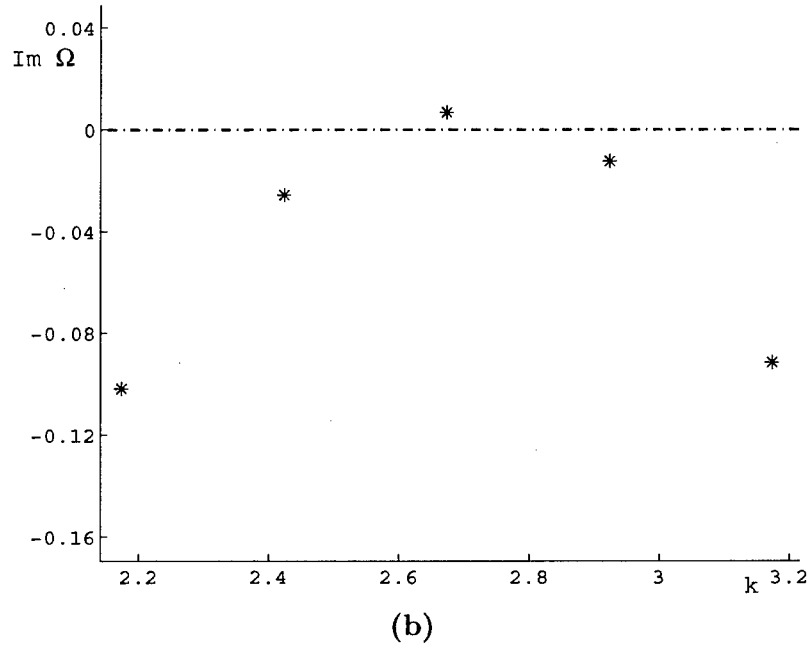
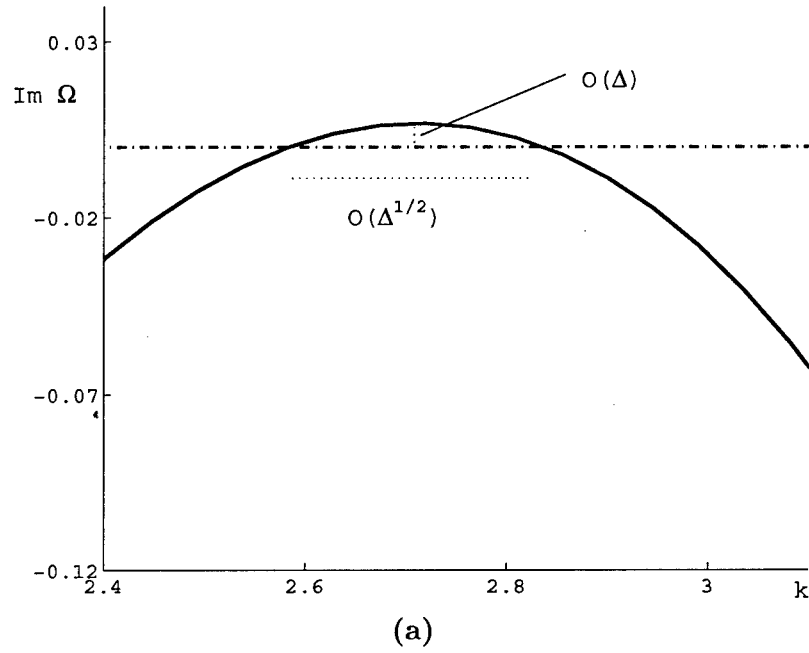


Figure 6: In both these figures, waves modes' growth rates  $\text{Im}\{\Omega\}$  are plotted against zonal wavenumber  $k$ . (a) When  $U = U_c + \Delta$ , zooming in around  $k = k_c$  reveals a band of unstable wavenumbers  $k$  with growth rates of  $O(\Delta)$ . The unstable band has width  $O(|\Delta|^{1/2})$ . (b) When the channel has finite length, only a discrete spectrum of wavenumbers  $k$  are allowed. In this case, one mode may become unstable alone, while all others remain stable.

# Intermittency in Some Simple Models for Turbulent Transport

Arghir Dani Zarnescu

## 1 Introduction

Consider the passive scalar equation

$$T_t + (u \cdot \nabla)T = \varepsilon \Delta T + F, \quad T|_{t=0} = \phi \quad (1)$$

where  $T$  is a quantity which is passively advected by a fluid with velocity  $u$  and  $F$  is an external forcing. The quantity  $T$  can be for instance heat, or dye used in visualizing turbulent effects, or a pollutant. The passive term refers to the fact that the effect of  $T$  on the fluid is negligible so that one can regard  $u$ , the velocity of the fluid, as being an externally given quantity, which does not depend on the evolution of  $T$ .

Although (1) is a linear equation for  $T$ , the relation between the passive scalar field  $T$  and the velocity field  $u$  is nonlinear. The influence of the velocity field on the statistics of  $T$  is very subtle and difficult to analyze in general. For instance, the interplay between  $u$  on the one hand and  $F$  and  $\phi$  on the other hand may lead to rare but large amplitude fluctuations of  $T$  (in space, time or both) which differ considerably from the average and contribute significantly to the statistics.

The matter of interest is then how rare these large fluctuations are. In many situations, based on the Central Limit Theorem as a heuristical principle, one would expect things to organize themselves so that in the average the distribution of the variable of interest is Gaussian. But large fluctuations can be more frequent than what is required for the Central Limit theorem to apply, and then fluctuations can dominate the statistics in a non-Gaussian way. This phenomenon is referred to as intermittency.

One signature of intermittency is the presence of non-Gaussian tails for the probability distribution function (PDF from now on) of  $T$ . It should be mentioned that there are physical experiments where such a behavior has been observed ([1],[2]).

We will be interested in identifying flows as simple as possible in which the large scale intermittency appears. Our goal is thus to identify some of the simplest mechanisms capable of producing intermittency.

While the flows we choose are simplistic, these models can provide intuition about the phenomena that occur in real turbulence, and with these specific choices the calculations are completely rigorous and unambiguous. This is the path followed also in [5] and there

one can find some more discussions on the relevance of this kind of approach. Results in a similar framework can be found in [3], [4],[6].

Our choice of flows will fall in the general class of flows proposed by M. Avellaneda and A. Majda, namely flows of the type

$$u(x, y, t) = \begin{pmatrix} w(t) \\ v(x, t) \end{pmatrix}$$

which can be regarded as nonlinear two dimensional shear velocity fields.

## 2 Heuristics

We will start by offering a heuristical interpretation of the mechanism of intermittency in a general setting and then rigorously prove it for a particular choice of flow. The explanation for the decaying case (no forcing) has already been given in [3] and it is included here for the sake of completeness.

In the decaying case we have the following representation formula for the solution of (1)

$$T(x, t) = \int_{\mathbb{R}^d} \phi(y) g(t, x, y) dy \quad (2)$$

where  $g(t, x, y)$  is the random function (for fixed  $x$  and  $t$ ) giving the probability density function of  $X(t)$  in each realization of  $u$ , where  $X(t)$  is the solution of the characteristic SDE associated to (1))

$$dX(t) = u(X(t), t)dt + \sqrt{2\epsilon}d\beta(t), X(0) = x \quad (3)$$

where  $\beta(t)$  is a Brownian motion accounting for molecular diffusion. In terms of  $X(t)$ , (2) can be written as

$$T(x, t) = \mathbb{E}_x^\beta \phi(X(t))$$

where  $\mathbb{E}_x^\beta$  denotes expectation over  $\beta(t)$  conditional on  $X(0) = x$ .

As time evolves  $g(t, x, y)$  broadens and assuming that  $\phi$  has mean zero, it is clear from the representation formula (2) that the dynamics will smooth out any spatial fluctuations in the initial data, with an average rate depending on the average growth rate of the width of  $g(t, x, y)$ .

On the other hand in any realization where  $g(t, x, y)$  broadens abnormally slowly, one will observe a large fluctuation in the scalar field amplitude at point  $x$ , even if the initial data sampled by  $X(t)$  is very typical (see Figure 1).

The situation is different in the forced case. Then, the representation formula for the solution becomes

$$T(x, t) = \int_{\mathbb{R}^d} \phi(y) g(t, x, y) dy + \int_0^t \int_{\mathbb{R}^d} F(y) g(t-s, x, y) dy ds \quad (4)$$

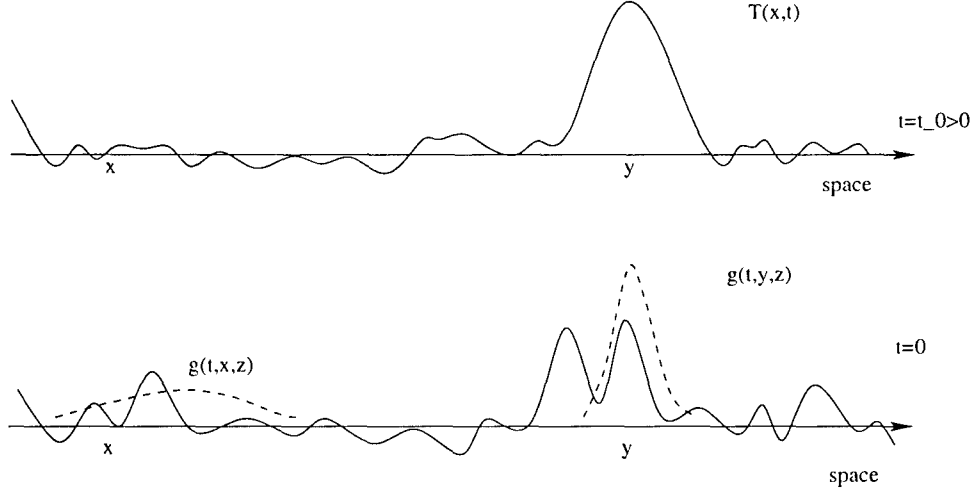


Figure 1: The heuristics in the decaying case

Equivalently, the above formula can be written in terms of averages over  $X(t)$ , giving us a Lagrangian picture of the evolution of  $T$

$$T(x,t) = \mathbb{E}_x^\beta \phi(X(t)) + \int_0^t \mathbb{E}_x^\beta F(X(t-s)) ds \quad (5)$$

In general, as  $t \rightarrow \infty$  one has  $\mathbb{E}_x^\beta \phi(X(t)) = \int_{\mathbb{R}^d} \phi(y) g(t,x,y) dy \rightarrow 0$  and thus one is left with analyzing the effect of the forcing term

$$\int_0^t \mathbb{E}_x^\beta F(X(t-s)) ds \quad (6)$$

Generically the trajectories of the  $X(t-s)$  will tend not to be on the level curves of  $F$ , and given the mixing effect of the flow they will be relatively uniformly spread within a short time, so  $F(X(t-s))$  will average to a zero value. On the other hand there will be (rare!) realizations of  $u$  where the effect of mixing will not be so strong, the diffusion will be the main (slow) mechanism for the spreading of  $X(t)$ , which will happen in a slow time. Thus, those  $X(t-s)$  which start on a level curve of  $F$  will have the possibility of remaining on the level curves for a time long enough so that the average of  $F(X(t-s))$  will be equal to a nonzero constant (close to the value of  $F$  on that level set).

In both cases rare realizations may have very strong effects on large scales. This will prevent the type of averaging which leads, by the Central Limit Theorem to a Gaussian distribution for the PDF of  $T$ , and indeed one will observe "fat" (non-Gaussian) tails for the PDF, consistent with large scale intermittency.

In our approach we will use a Lagrangian picture as this offers a simple understanding of the phenomena which occur. Indeed, we will consider the associated stochastic differential equations associated to the passive scalar equation and we will use them to obtain

representations formula for  $T$  from which we will compute the PDF of  $T$ . Thus, one can see the appearance of intermittency as the result of clustering of close trajectories in the realizations where the effect of turbulent mixing is abnormally weak.

### 3 The Decaying Case

We will take the flow to be

$$u = \begin{pmatrix} 0 \\ g \sin(x) \end{pmatrix} \quad (7)$$

where  $g$  is a Gaussian random variable, with mean zero and variance one. This is a time independent, "periodic shear" analogue of the random shear model of A.Majda (see [5]), model in which the  $\sin(x)$  from our equation is just  $x$  and  $g$  is time dependent.

In this case (1) reduces to

$$\frac{\partial T}{\partial t} + g \sin(x) \frac{\partial T}{\partial y} = \epsilon \Delta T, \quad T|_{t=0} = \phi(y) \quad (8)$$

We also assume that the initial data depends only on  $y$  and it is a mean zero Gaussian random process, statistically independent of the random velocity field, and

$$\phi(y) = \int_{\mathbb{R}} e^{ipy} \sqrt{E(p)} dW(p) \quad (9)$$

with energy spectrum

$$E(p) = C_E |k|^\alpha \psi(k) \quad (10)$$

where  $\psi(k)$  is a cutoff function, rapidly decaying for  $|k| > 1$ ,  $\psi(0) = 1$  and satisfying  $\psi(k) = \psi(-k)$ . The quantity  $C_E$  is a normalizing constant and  $dW$  is a complex white noise process (independent of  $g$ ), with

$$\langle dW(p), d\bar{W}(q) \rangle = \delta(p - q) dp dq$$

The exponent  $\alpha > -1$  in formula (10) measures the decay of the spatial correlation of the initial condition  $\phi(y)$ ; the smaller  $\alpha$ , the longer the spatial correlation.

In the case where there is no forcing, it is well known that  $T$  will decay to zero. Therefore, in order to observe the intermittency we will look at  $T$  rescaled by the energy  $E = \mathbb{E}T^2$  which we shall denote by  $\theta = \frac{T}{\sqrt{E}}$ . We will compute in the following the PDF of  $\theta$  in the long time limit and we will obtain that

$$\mathbb{P}(\bar{X} > \lambda) \approx C_1 \lambda^{-\frac{2}{\alpha+1}} \text{ as } \lambda \rightarrow \infty \quad (11)$$

where  $C_1$  is a constant, independent of time, whose value can be computed explicitly (in general in the following  $C_1, C_2, \dots$  will be used to denote constants which can be explicitly computed, and are independent of time).

Consider the stochastic differential equations associated with (8)



$$\begin{cases} X(t) = \sqrt{2\epsilon}d\beta_x(t) \\ Y(t) = g \sin(X(t))dt + \sqrt{2\epsilon}d\beta_y(t) \end{cases} \quad (12)$$

The equations (12) have the solution

$$\begin{cases} X(t) = x + \sqrt{2\epsilon}\beta_x(t) \\ Y(t) = y + g \int_0^t \sin(x + \sqrt{2\epsilon}\beta_x(s))ds + \sqrt{2\epsilon}\beta_y(t) \end{cases} \quad (13)$$

Since  $g$  and  $\beta$  are independent, we have then that

$$\begin{aligned} \mathbb{E}_\beta Y(t) &= y + g \int_0^t \sin(x) e^{-\epsilon s} ds = y + \frac{g}{\epsilon} \sin(x)(1 - e^{-\epsilon t}) \\ &\sim y + \frac{g}{\epsilon} \sin(x), \text{ as } t \rightarrow \infty \end{aligned} \quad (14)$$

and

$$\begin{aligned} &\mathbb{E}_\beta(Y(t) - \mathbb{E}_\beta(Y(t)))^2 = \\ &= \mathbb{E}_\beta g^2 \int_0^t \int_0^t \sin(x + \sqrt{2\epsilon}\beta_x(s)) \sin(x + \sqrt{2\epsilon}\beta_x(s')) ds ds' + \epsilon t + g^2 \left( \int_0^t \sin(x) e^{-\epsilon s} ds \right)^2 \\ &= \frac{g^2}{2} \int_0^t \int_0^t (e^{-\epsilon|s-s'|} - \cos(2x) e^{-\epsilon(s+s'+2\min(s,s'))}) ds ds' + \epsilon t + \frac{g^2}{\epsilon^2} \sin^2(x)(1 - e^{-\epsilon t})^2 \\ &= \epsilon t + g^2 \left( \frac{t}{\epsilon} + \frac{1-e^{-\epsilon t}}{\epsilon^2} \right) - \frac{g^2 \cos(2x)}{2\epsilon^2} \left( \frac{e^{-4\epsilon t}-1}{3} - \frac{7(e^{-\epsilon t}-1)}{12} \right) + g^2 \sin^2(x) \frac{(e^{-\epsilon t}-1)^2}{\epsilon^2} \end{aligned} \quad (15)$$

Thus, for  $t \gg 1$  we have

$$\mathbb{E}_\beta(Y(t) - \mathbb{E}_\beta(Y(t)))^2 \sim \epsilon t + g^2 \frac{t}{\epsilon} \quad (16)$$

Next observe that, using (9), we have an explicit representation of  $T$  as

$$T = \mathbb{E}_\beta \phi(Y_t) = \int_{R^2} e^{ipm(t) - \frac{1}{2}p^2v(t)} \sqrt{E(p)} dW(p) \quad (17)$$

where we used the fact that  $\phi$  is a function of only one variable;  $m(t)$  and  $v(t)$  are respectively the mean and variance of  $Y(t)$  with respect to the Brownian motion  $\beta$  which, taking into account (14) and (16), for large  $t$  become

$$\begin{aligned} m(t) &\sim y + \frac{g}{\epsilon} \sin(x) \\ v(t) &\sim \epsilon t + g^2 \frac{t}{\epsilon} \end{aligned} \quad (18)$$

Introduce the rescaled variable

$$z = p\sqrt{v(t)} \quad (19)$$

and the rescaled white noise

$$d\hat{W}_t(z) \stackrel{d}{=} v(t)^{\frac{1}{4}} dW\left(\frac{z}{\sqrt{v(t)}}\right) \quad (20)$$

where  $\stackrel{d}{=}$  stands for the equality in the sense of distributions. In terms of these quantities we can rewrite the representation formula of  $T$  as

$$T \stackrel{d}{=} \int_{\mathbb{R}} e^{i\frac{z}{\sqrt{v}}m - \frac{z^2}{2}} v(t)^{-\frac{1+\alpha}{4}} \sqrt{C_E} |z|^{\frac{\alpha}{2}} \psi^{1/2} \left( \frac{z}{\sqrt{v(t)}} \right) d\hat{W}_t(z) \quad (21)$$

Therefore (using (18))

$$\bar{\phi} - \sqrt{C_E} \int_{\mathbb{R}} e^{i\frac{z}{\sqrt{v(t)}}m(t) - \frac{z^2}{2}} |z|^{\frac{\alpha}{2}} \psi^{1/2} \left( \frac{z}{\sqrt{v(t)}} \right) d\hat{W}_t(z) \rightarrow 0 \text{ as } t \rightarrow \infty$$

where the limit here and below is understood in the sense of distributions and

$$\bar{\phi} = \sqrt{C_E} \int_{\mathbb{R}} e^{-\frac{z^2}{2}} |z|^{\frac{\alpha}{2}} d\hat{W}_t(z) \quad (22)$$

This implies that for large times we have

$$T(t, \cdot) \stackrel{d}{\sim} v(t)^{-\frac{(1+\alpha)}{4}} \bar{\phi} \quad (23)$$

Using the explicit formula for  $T$  we can compute  $E(t) = \mathbb{E}_{g,\beta} T^2$  which is

$$\mathbb{E}_{g,\beta} T^2 = C_E \mathbb{E}_g [v(t)^{-\frac{1+\alpha}{2}} \int_{\mathbb{R}} e^{-z^2} |z|^{\alpha} \psi \left( \frac{z}{\sqrt{v(t)}} \right) dz] \quad (24)$$

From (18), this is

$$E(t) \stackrel{d}{=} C_2 t^{-\frac{(1+\alpha)}{2}} + o(t^{-\frac{(1+\alpha)}{2}}) \quad (25)$$

By rescaling  $T$  we will obtain a finite limit, namely let us consider the quantity:

$$\theta = \frac{T}{\sqrt{E}} \quad (26)$$

Then the above allow us to conclude that

$$\theta(t, \cdot) \stackrel{d}{\sim} \bar{\theta}(t) \text{ as } t \rightarrow \infty \quad (27)$$

where

$$\bar{\theta} = C_3 \left( \epsilon + \frac{g^2}{\epsilon} \right)^{-\frac{1+\alpha}{4}} \bar{\phi} \quad (28)$$

We can now compute the tails of the probability distribution of  $\bar{\theta}$ . As  $\bar{\phi}$  is normally distributed with mean zero and variance  $\bar{\sigma}$  (which can be explicitly computed, see (22)), we have (assuming without loss of generality that  $C_3 = 1, \bar{\sigma} = 1$  for the sake of simplifying the computation):

$$\mathbb{P}(\bar{\theta} > \lambda) = P\left(\left(\epsilon + \frac{2g^2}{\epsilon}\right)^{-\frac{1+\alpha}{4}} \bar{\phi} > \lambda\right) = \int_0^\infty \int_{|a|\delta^{-\frac{1+\alpha}{4}} \geq \lambda} \frac{e^{-\frac{a^2}{2}}}{\sqrt{2\pi}} da dP_\delta \quad (29)$$

where

$$P_\delta = \mathbb{P}\left(\epsilon + \frac{2g^2}{\epsilon} \leq \delta\right) = \int_{-\sqrt{\frac{|\epsilon\delta-\epsilon^2|}{2}}}^{\sqrt{\frac{|\epsilon\delta-\epsilon^2|}{2}}} e^{-\frac{z^2}{2}} dz \quad (30)$$

Integrating by parts in (29) we obtain:

$$\mathbb{P}(\bar{\theta} > \lambda) = \frac{(1+\alpha)\lambda}{2\sqrt{2\pi}} \int_0^\infty \delta^{\frac{\alpha-3}{4}} e^{-\frac{1}{2}\lambda^2\delta^{\frac{1+\alpha}{2}}} P_\delta d\delta \quad (31)$$

In order to compute the integral, for  $\lambda \gg 1$  thanks to the exponential factor and to the Laplace method, we only need to know  $P_\delta$  for small  $\delta$ . Using the change of variables  $\delta = s\lambda^{-\frac{4}{1+\alpha}}$  by standard, though tedious, computations we get (11) to the leading order in  $\lambda$  (as  $\lambda \rightarrow \infty$ ).

## 4 The Forced Case

### 4.1 The one mode, time independent, stirring

We will consider the flow to be given by:

$$u = \begin{pmatrix} g \\ \sin(x + \varphi) \end{pmatrix} \quad (32)$$

where  $g$  is a Gaussian random variable which has mean zero and variance one and  $\varphi$  is a random variable uniformly distributed on  $[0, 2\pi]$ . The two random variables are independent.

The passive scalar equation becomes

$$T_t + gT_x + \sin(x + \varphi)T_y = \epsilon\Delta T \quad (33)$$

Assume also that the mean gradient of  $T$  is imposed

$$T = \frac{y}{L} + \tilde{T} \quad (34)$$

Then  $\tilde{T}$  will satisfy the equation

$$\tilde{T}_t + g\tilde{T}_x + \sin(x + \varphi)\tilde{T}_y + \frac{\sin(x + \varphi)}{L} = \epsilon\Delta\tilde{T} \quad (35)$$

In this specific case, the general heuristics from the second section can be made more precise and we have a simpler mechanism which is responsible for intermittency and can be understood as follows.

Let us assume that  $T$  represents the temperature and we have a region made of two parts, one hot ( $(x, y) \in \mathbb{R}^2$  with  $x > 0$ ) and one cold ( $(x, y) \in \mathbb{R}^2$  with  $x \leq 0$ ). In the generic case, when  $g \neq 0$  we will have transport in both  $x$  and  $y$  directions, and thus mixing of the cold and hot which will lead to a decrease in the average temperature. In the realizations

when  $g \approx 0$ , however, the flow  $u$  points only in the  $y$  direction, so (neglecting the effect of diffusion) there is transport only in the  $y$  direction. The hot region remains hot, and the cold one cold. The extreme values of temperature will not be significantly changed. Therefore one expects that the rare realizations where  $g \approx 0$  will strongly influence the average over all the realizations leading to a non-Gaussian distribution of  $T$ . Indeed, we will obtain that the tails of the PDF of  $T$  decay like  $\lambda^{-2}$ .

In order to make the above reasoning rigorous let us consider the stochastic differential equations associated to (33)

$$\begin{cases} dX(t) = gdt + \sqrt{2\epsilon}d\beta_x(t), & X_0 = x \\ dY(t) = \sin(X(t) + \phi)dt + \sqrt{2\epsilon}d\beta_y(t), & Y_0 = y \end{cases}$$

which have the solution

$$\begin{cases} X(t) = x + gt + \sqrt{2\epsilon}\beta_x(t) \\ Y(t) = y + \int_0^t \sin(x + \phi + gs + \sqrt{2\epsilon}\beta_x(s))ds + \sqrt{2\epsilon}\beta_y(t) \end{cases}$$

Assuming that the initial data is zero (if not it can be shown it decays) by Feynman-Kac formula we get the following representation of the solution

$$\tilde{T} = -\mathbb{E}_\beta \int_0^t \frac{1}{L} \sin(x + \phi + gs + \sqrt{2\epsilon}\beta_x(s))ds \quad (36)$$

Thus in each realization we have that

$$\lim_{t \rightarrow \infty} \tilde{T}(x, y, t) - \bar{T}(x, t) = 0 \quad (37)$$

where  $\bar{T}$  is

$$\bar{T}(x) = \frac{1}{L} \frac{[g \cos(x + \phi) - \epsilon \sin(x + \phi)]}{\epsilon^2 + g^2} \quad (38)$$

We are interested now in computing

$$f(\lambda) = \mathbb{P}(\bar{T}(x) \geq \lambda) \quad (39)$$

To this extent, taking into account the independence of  $\phi$  and  $g$ , we will compute first the moments only with respect to the uniformly distributed random variable  $\phi$ . Indeed, we have

$$\mathbb{E}_\phi T^{2n} = [L(\epsilon^2 + g^2)]^{-2n} \frac{1}{2\pi} \int_0^{2\pi} (g \cos(\phi) - \epsilon \sin(\phi))^{2n} d\phi \quad (40)$$

One can compute the last integral, namely

$$\begin{aligned}
\int_0^{2\pi} (g \cos(\phi) - \epsilon \sin(\phi))^{2n} d\phi &= \frac{1}{2^{2n}} \int_0^{2\pi} [(g + \epsilon i)e^{ix} + (g - \epsilon i)e^{-ix}]^{2n} dx \\
&= \frac{1}{2^{2n}} \int_0^{2\pi} \sum_{m=0}^{2n} \binom{2n}{m} (g + \epsilon i)^{2n-m} (g - \epsilon i)^m e^{ix(2n-m-m)} dx \\
&= \frac{1}{2^{2n}} \binom{2n}{n} (g^2 + \epsilon^2)^n
\end{aligned} \tag{41}$$

So

$$\begin{aligned}
\mathbb{E}_\phi e^{ikT} &= \sum_{n=0}^{\infty} \frac{(-1)^n k^{2n}}{(2n)!} \mathbb{E}_\phi T^{2n} \\
&= \sum_{n=0}^{\infty} (-1)^n \left(\frac{k}{2L}\right)^{2n} \frac{1}{(n!)^2} (\epsilon^2 + g^2)^{-n} \\
&= J_0 \left( \sqrt{\frac{-k^2}{L^2(\epsilon^2 + g^2)}} \right)
\end{aligned} \tag{42}$$

(where  $J_0$  is the Bessel function of the first kind) and thus

$$\hat{f}(k) = \int_{\mathbb{R}} \frac{e^{-\frac{g^2}{2}}}{\sqrt{2\pi}} J_0 \left( \sqrt{\frac{-k^2}{L^2(\epsilon^2 + g^2)}} \right) dg \tag{43}$$

Expressing  $f(\lambda)$  in terms of its inverse Fourier transform and using the fact that  $f(\lambda)$  is real valued we have

$$\begin{aligned}
f(\lambda) &= \Re \frac{1}{2\pi} \int_{\mathbb{R}} \hat{f}(k) e^{ik\lambda} dk = \Re \frac{1}{\pi} \int_0^{\infty} \hat{f}(k) \cos(k\lambda) dk \\
&= \Re \frac{1}{\sqrt{2\pi}^{3/2}} \int_0^{\infty} \left( \int_{\mathbb{R}} e^{-g^2/2} J_0 \left( \sqrt{\frac{-k^2}{L^2(\epsilon^2 + g^2)}} \right) dg \right) \cos(k\lambda) dk \\
&= \Re \frac{1}{\sqrt{2\pi}^{3/2}} \int_{-\sqrt{\frac{1}{L^2\lambda^2} - \epsilon^2}}^{\sqrt{\frac{1}{L^2\lambda^2} - \epsilon^2}} e^{-g^2/2} \int_0^{\infty} J_0 \left( \sqrt{\frac{-k^2}{L^2(\epsilon^2 + g^2)}} \right) \cos(k\lambda) dk dg \\
&+ s \Re \frac{1}{\sqrt{2\pi}^{3/2}} \int_{\mathbb{R}/[-\sqrt{\frac{1}{L^2\lambda^2} - \epsilon^2}, \sqrt{\frac{1}{L^2\lambda^2} - \epsilon^2}]} e^{-g^2/2} \int_0^{\infty} J_0 \left( \sqrt{\frac{-k^2}{L^2(\epsilon^2 + g^2)}} \right) \cos(k\lambda) dk dg
\end{aligned}$$

where for the second we used the fact that the Bessel function of the first kind is an even function; also for the fourth equality we used Fubini to interchange the order of integration.

Recall that

$$\int_0^{\infty} J_0 \left( \sqrt{\frac{-k^2}{L^2(\epsilon^2 + g^2)}} \right) \cos(k\lambda) dk = \sqrt{\frac{\epsilon^2 + g^2}{1 - L^2\epsilon^2\lambda^2 - L^2\lambda^2g^2}} \tag{44}$$

which is a real number if

$$g \in [-\sqrt{\frac{1}{L^2\lambda^2} - \epsilon^2}, \sqrt{\frac{1}{L^2\lambda^2} - \epsilon^2}] \quad (45)$$

and purely imaginary (i.e. with zero real part) otherwise. Using this observation and combining the last two relations with get:

$$f(\lambda) = \frac{1}{\sqrt{2}\pi^{3/2}} \int_{-\sqrt{\frac{1}{L^2\lambda^2} - \epsilon^2}}^{\sqrt{\frac{1}{L^2\lambda^2} - \epsilon^2}} e^{-g^2/2} \sqrt{\frac{\epsilon^2 + g^2}{1 - L^2\epsilon^2\lambda^2 - L^2\lambda^2g^2}} dg \quad (46)$$

which clearly holds if and only if  $\lambda < \frac{1}{\epsilon L}$ . On the other hand, taking into account the definition of  $\bar{T}(x)$  and of  $f(\lambda)$  it is easy to see that for  $\lambda > \frac{1}{\epsilon L}$  we will have  $f(\lambda) = 0$  and thus  $f(\lambda)$  is a function with bounded support.

It follows that

$$\begin{aligned} \lim_{\epsilon \rightarrow 0} f(\lambda) &= \frac{\sqrt{2}}{\pi^{3/2}} \int_0^\infty \frac{e^{-\frac{g^2}{2}} g}{\sqrt{1 - L^2\lambda^2g^2}} \\ &= \frac{e^{-\frac{1}{2L^2\lambda^2}} \operatorname{erf}(\frac{1}{\sqrt{L|\lambda|}})}{\pi L|\lambda|} \end{aligned} \quad (47)$$

which asymptotically, in the limit  $\lambda \rightarrow \infty$  behaves like

$$\lim_{\epsilon \rightarrow 0} f(\lambda) \approx \frac{\sqrt{2}}{\pi^{3/2}} \lambda^{-2} \quad (48)$$

## 4.2 The Gaussian multimode forcing

In this section we consider the flow

$$u = \begin{pmatrix} g \\ v(x) \end{pmatrix} \quad (49)$$

where  $g$  is a Gaussian random variable which has mean 0 and variance 1, and  $v(x)$  is a Gaussian process specified by

$$v(x) = \int_{\mathbb{R}} dW(k) \sqrt{E(k)} e^{ikx} \quad (50)$$

(we will need to assume that the function  $E(k)$  is compactly supported away from 0 and also that  $\int_{\mathbb{R}} \frac{E(k)dk}{k^2} < \infty$ ).

In this case we obtain a similar behavior as before, though the ingredients are quite different. Namely we will obtain that the tails of the PDF of  $T$  will decay like  $\lambda^{-2}$ .

Indeed, arguing analogously as before we will obtain the solution will evolve as  $t \rightarrow \infty$  to the solution of stationary equation

$$0 = -gT_x + \epsilon T_{xx} - \frac{v(x)}{L} \quad (51)$$

which will give us the representation formula for the solution:

$$\begin{aligned}
T(x) &= -\frac{1}{L} \int_0^\infty dt \int_{\mathbb{R}} dW(k) \sqrt{E(k)} e^{ik(x-gt)-\epsilon k^2 t} \\
&= -\frac{1}{L} \int_{\mathbb{R}} dW(k) \sqrt{E(k)} e^{ikx} \frac{1}{\epsilon k^2 + ikg}
\end{aligned} \tag{52}$$

This is a Gaussian random variable (as a superposition of Gaussians ) whose moments with respect to  $W$  are:

$$\mathbb{E}_W(T(x))^{2n} = \frac{(2n)!}{2^n n!} (\mathbb{E}_W T^2(x))^n = \frac{2n}{2^n n!} \underbrace{\left( \int_{\mathbb{R}} \frac{E(k) dk}{k^2(\epsilon k^2 + g^2)} \right)^n}_{F(\epsilon, g)} \tag{53}$$

Hence

$$\mathbb{E}_W e^{ikT} = \sum_{n=0}^\infty \frac{-1^n k^{2n}}{(2n)!} \cdot \frac{(2n)!}{2^n n!} F(\epsilon, g)^n = e^{-\frac{1}{2} k^2 F(\epsilon, g)} \tag{54}$$

which implies

$$f_\epsilon(\lambda) = \frac{1}{2\pi} \int_{\mathbb{R}} \int_{\mathbb{R}} e^{-g^2/2} e^{-\frac{1}{2} F(\epsilon, g)} e^{ik\lambda} dk dg \tag{55}$$

Since  $F(\epsilon, g) \rightarrow \frac{M}{g^2}$  (when  $\epsilon \rightarrow 0$ , with  $M = \int_{\mathbb{R}} \frac{E(k) dk}{k^2} < \infty$ ) and by Lebesgue's dominated convergence theorem it follows that  $f_\epsilon(\lambda) \rightarrow f(\lambda)$  where (assuming without loss of generality for the sake of computational simplicity that  $M = 1$ )

$$\begin{aligned}
f_\epsilon(\lambda) &= \int_{\mathbb{R}} \int_{\mathbb{R}} e^{-\frac{g^2}{2}} e^{-\frac{k^2}{2g^2} + ik\lambda} dk dg = \sqrt{2\pi} \int_{\mathbb{R}} e^{-\frac{g^2(1+\lambda^2)}{2}} g dg \\
&= \frac{1}{1+\lambda^2} \int_{\mathbb{R}} e^{-\frac{\delta^2}{2}} \delta d\delta = \frac{1}{\pi(1+\lambda^2)}
\end{aligned} \tag{56}$$

## 5 Acknowledgments

I want to thank Eric Vanden-Eijnden for suggesting these problems to me and for his help all over the summer. I would also like to thank Charles Doering for many useful suggestions and for his patience in practicing softball with me. Finally I want to thank Joe Keller for useful discussions, as well as all the fellows for a great summer.

## References

- [1] F. Heslot, B. Castaing, A. Libchaber *Transition to turbulence in helium gas*, Phys. Rev. A. 36(1987) 5870-5873
- [2] B. Castaing, G. Gunaratne, F. Heslot, L. Kadanoff, A. Libchaber, S. Thomae, X.Z. Wu, S. Zaleski, G. Zanetti *Scaling of hard thermal turbulence in Rayleigh-Benard convection* J. Fluid Mech. 204(1989) 1-30

- [3] E.Vanden Eijnden *Non-Gaussian invariant measures for the Majda model of decaying turbulent transport* Comm. Pure Appl. Math. 54 (2001), no. 9, 1146–1167
- [4] A.Bourlioux and A.J. Majda *Elementary models with probability distribution function intermittency for passive scalars with a mean gradient* Phys. Fluids 14 (2002), no. 2, 881–897
- [5] A.J. Majda and P.R. Kramer *Simplified models for turbulent diffusion: theory, numerical modelling, and physical phenomena* Phys. Rep. 314 (1999), no. 4-5, 237–574
- [6] R. McLaughlin and A.J. Majda *An explicit example with non-Gaussian probability distribution for nontrivial scalar mean and fluctuation* Phys, Fluids 8 (1996) no.2, 536–547



# Internal wave breaking and mixing in the deep ocean

Marcus L. Roper

July 18, 2006

## 1 Introduction

We begin by outlining the two pieces of observational evidence that motivate this study.

### 1.1 Anomalous diffusion

The density of the abyssal ocean decreases by almost 3% from the ocean bed to the seat of the thermocline. Even when compressibility effects, such as would exist in any hydrostatically balanced fluid body, are accounted for there remains a significant potential density variation with depth, representing unequal distributions of temperature and salinity. The maintenance of this density stratification must be understood as a dynamic process. In narrow regions of the ocean at high latitudes, fluid near the ocean surface is cooled sufficiently that it becomes denser than the fluid that supports it, and sinks to great depths, mixing with entrained fluid. Accordingly, latitudinal sections of the potential density in the ocean often depict cold dense intrusions of fluid from the Antarctic or Arctic Oceans, see the Figure 1. It is estimated that in the Pacific Ocean such cold intrusions supply fluid to the lowest kilometre of ocean at a rate of  $25\text{--}30 \times 10^9 \text{kg s}^{-1}$  [16]. There must be a corresponding upwelling of fluid in the mid-ocean or else the centre of mass of the fluid system would be lowered with time. Such an upwelling would annihilate any variation in density, unless thwarted by downward diffusion. Specifically, if we write  $w$  for the mid-ocean upwelling velocity, we can construct an approximate balance for the two rates of density transport in the vertical direction  $z$ <sup>1</sup>:

$$w \frac{\partial \rho}{\partial z} \approx \kappa \frac{\partial^2 \rho}{\partial z^2} . \quad (1)$$

Balance in this equation leads to equilibrium distributions with a vertical scale height  $H = \kappa/w$ , and with  $w \approx 10^{-7} \text{m s}^{-1}$  and  $H \approx 1 \text{km}$  known for the abyssal ocean, we may use this formula to estimate the effective diffusion of density:  $\kappa \approx 10^{-4} \text{m}^2 \text{s}^{-1}$  [16]. This greatly exceeds the molecular diffusivities of salt and heat (on the order of  $10^{-9} \text{m}^2 \text{s}^{-1}$  and

---

<sup>1</sup>A great deal of coarse-graining of horizontal effects, and averaging out of vertical variations must take place before this one dimensional equation may be arrived at, but the inferences drawn from it are supported by more nuanced calculations. In particular, the balance may immediately be put on a more firm footing by interpreting  $z$  as a local diapycnal coordinate – that is relating the isopycnal surface-normal components of the velocity field and diffusive flux [15].

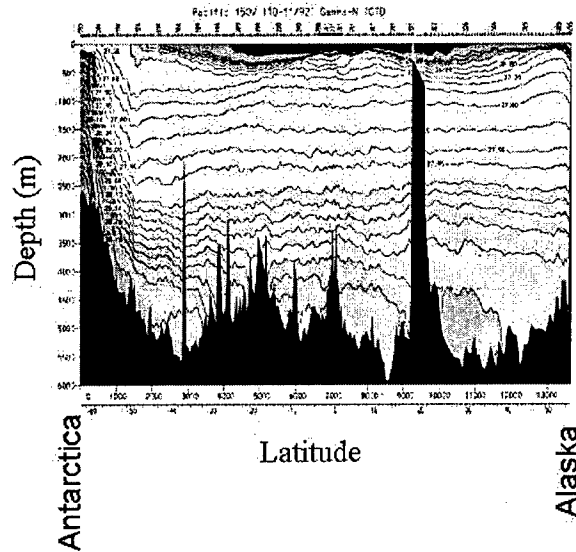


Figure 1: Potential density ( $\sigma$ ) distribution in a section of the Pacific Ocean stretching from Antarctica (south) to the Aleutians (north). Isosurfaces are labelled by the  $(\sigma - 1000) \times 10^3/\text{kgm}^{-3}$ , in increments ranging from 0.20 in the thermocline to 0.02 in the ocean abyss. The black corrugations are the ocean bed. (Figure taken from [16]).

$10^{-7}\text{m}^2\text{s}^{-1}$  respectively. This disparity gives strong evidence for the dominance of other dynamical mixing processes over molecular diffusion. In the past decade strong observational evidence has emerged for enhanced eddy diffusion localised within layers of ocean hundreds of metres thick above rough or steepening regions of the ocean floor [7, 11, 13]. These mixing zones extend far beyond the turbulent boundary layer of ocean in immediate contact with the bed, signalling that the anomalous diffusion is a non-local effect: that fluid driven over the ocean floor in tidal flow, mesoscale eddies or else wave-driven currents generates internal waves which break at some distance from the ocean floor and in so doing mix up the local density field.

## 1.2 A universal spectrum of internal waves

The oceans are never silent, but resound with internal inertio-gravity waves at all length-scales. Compared to the energies and velocities associated with the ever-present wave field, the currents that are conventionally thought to control the global transport of temperature and salinity are in many places rather feeble. Studies by Garrett and Munk in the 1970s, culminating in [4], showed that data collected from moored, towed and dropped sensor studies of the spectrum of waves within the ocean can be united into a single common spectrum. There are various equivalent ways for casting the spectrum (see Section 2), but one common form is in terms of the horizontal and vertical wavenumbers  $m$  and  $k_H$ :

$$E(k_H, m) = \frac{3fNE_*m/m_*}{\pi(1 + m/m_*)^{5/2}(N^2k_H^2 + f^2m^2)} \quad (2)$$

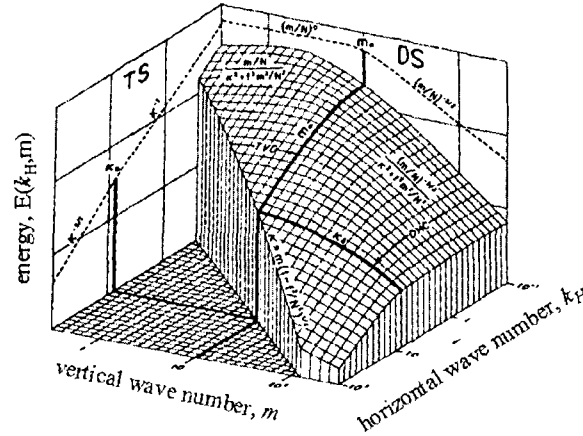


Figure 2: Energy spectrum in  $(k_H, m)$  space. Transects represent permitted observational probes of the spectrum by towed horizontal correlation (THC) and dropped vertical correlation (DVC) detecting instruments. The cleavage plane  $k_H = m(1 - f^2/N^2)^{1/2}$  does not represent a physical cut-off, but is intended to clarify the plot.

where  $N$  is the buoyancy frequency, and  $f$  the frequency of purely inertial waves, and the significance of these two parameters will be discussed in Section 2. The wave-field is isotropic in any horizontal plane, so only a single horizontal wavenumber enters the relation. The spectrum is graphically shown, including various distinguished limits of small or large wavenumber, in Figure 2 drawn from [4]. The variation of the dimensional spectral density  $E_*$  and the bandwidth  $m_*$  with  $f$  (viz latitude) and  $N$  have been obtained theoretically and validated by observation [6].

The existence of a universal spectrum has become a dogma of oceanography, allowing the rate of mixing on centimetre scales to be backed out from the amount of energy in wavelengths of tens or hundreds of metres, scales which are much easier to probe experimentally. A raft of interlocking assumptions takes us from the measurements of long wavelength modes that can be relatively easily performed (using for instance acoustic Doppler profiling) to the small scale dynamics of interest. The rate of turbulent dissipation equals the rate at which energy is supplied from to the mixing scales, and this can be computed using a semi-empirical formula (see footnote 13 in [11]) comparing the mean-square shear rate, latitude and buoyancy frequency to the open ocean Garrett-Munk spectrum at a reference latitude of  $30^\circ$ . The rate of turbulent dissipation stands as a proxy for the dissipation of available potential energy. Total turbulent dissipation ( $\epsilon$ ) is assumed to exceed dissipation of available potential energy by some factor between three and five. Thus the effective diffusivity  $\kappa = \Gamma \epsilon N^{-2}$ , with  $\Gamma$  taken to be between 0.2 and 0.3. Various links in this chain of inferences have already been scrutinised theoretically (see e.g. the discussion of the use of a constant value of  $\Gamma$  in [10]).

### 1.3 Outline: A new weakly nonlinear model

In reviewing the observation evidence for a universal spectrum of internal waves, and the detailed use of this spectrum to estimate mixing rates, three questions should immediately be apparent to the reader. How can an equilibrium spectrum arise as an equilibrium state of interacting waves? How do the waves interact? How is the rate of mixing related to the energy present in the wave-field? There have been several attempts to reproduce limits of the Garrett-Munk spectrum from theoretical arguments, in particular a recent result by Lvov et al. [9] showing that the high frequency and short wavelength part of the spectrum is consistent with a model of resonant triad interactions between waves of different wavenumbers. In this report we propose a weakly nonlinear theory in which interactions between waves are viewed as spatially and temporally isolated but highly non-linear events, producing well-mixed zones of fluid. Between interactions waves evolve according to the linearised equations of motion. The use of linearised equations of motion to describe the collapse of well-mixed zones in stratified fluids is known to result in not too severe errors [1] in predictions of the density and velocity fields.

## 2 Evolving the linear modes

We restrict to two dimensional disturbances with uniform background stratification and no associated mean flow. We apply the Boussinesq approximation that variation in the fluid density occurs on a much longer length-scale than variation in any of the perturbation velocity fields, in which case it may be shown (see §6.4 of [5]) that the density may be taken to be constant in any evaluation of the rate of change of fluid momentum, and density variation admitted only when buoyancy forces are computed. The density field is then decomposed into three separate components:  $\rho = \rho_0 + \bar{\rho}(z) + \delta\rho(x, z, t)$ , and a hydrostatic component is subtracted off the pressure field to balance the background stratification  $\rho_0 + \bar{\rho}$ .

Following §8.4 of [5], we may write down a triple of equations representing linearised momentum balance:

$$u_t - fv = -\frac{p_x}{\rho_0} + F \quad (3a)$$

$$v_t + fu = 0 \quad (3b)$$

$$w_t = b - \frac{p_z}{\rho_0} + H, \quad (3c)$$

where  $(F, 0, H)$  are the components of a specific body force that sets the fluid into motion,  $(u, v, w)$  is the disturbance velocity field, and  $b = -\frac{g\delta\rho}{\rho_0}$  the buoyancy field. The dynamical effect of the rotating frame has been trammelled up into the pair of Coriolis force terms on the right-hand side of (3), in which we have followed convention by defining a parameter  $f = 2\Omega$ : centrifugal terms are assumed to have been assimilated into a redefined gravitational acceleration  $g$ .

Mass continuity then takes linearised form:

$$b_t + N^2 w = 0, \quad (4)$$

while, consistent with the Boussinesq approximation, we may assume that fluid parcels neither gain nor lose mass as they are advected by the fluid, giving rise to the standard

incompressibility relation:

$$u_x + w_z = 0 . \quad (5)$$

We make immediate use of the incompressibility equation by defining a streamfunction  $\psi$  such that  $u = \psi_z$ ,  $w = -\psi_x$ , allowing us to reduce the number of time-evolution equations by one. Specifically, subtracting the  $x$ -derivative of (3c) from the  $z$ -derivative of (3a) gives the vorticity equation:

$$\nabla^2 \psi_t - f v_z = -b_x + \tau , \quad (6)$$

where  $\tau \equiv F_z - G_x$  is the specific torque associated with the body force posited above. We define a *potential temperature* for the fluid:

$$\theta \equiv -\frac{g(\rho - \rho_0)}{\rho_0} = N^2 z + b \quad (7)$$

so that the disturbed fluid is stably or unstably stratified according to whether  $\theta_z \gtrless 0$ .

We scale lengths by the horizontal and vertical dimensions of our experimental box  $(L_x, L_z)$ , defining dimensionless hatted variables  $z = L_z \hat{z}$ ,  $x = L_x \hat{x}$ . We also define an aspect ratio  $\epsilon \equiv L_z/L_x$ , which we anticipate being small. It is natural to scale the buoyancy field using the background potential temperature:  $b = N^2 L_z \hat{b}$ , and the time by the buoyancy period  $t = \hat{t}/N$ , which will turn out to be the minimum period of any of the linear inertia-gravity wave modes of the fluid body. Scalings for the other dynamical variables follow from selecting dominant balances between pairs of terms in the vorticity and mass conservation equations. Balancing the rate of increase of vorticity  $\psi_{zzt}$  with the rate of baroclinic generation  $b_x$ , suggests a scaling for the velocity fields:  $\psi = \epsilon N L_z^2 \hat{\psi}$ , and we scale  $v$  to balance the  $y$ -component of the fluid acceleration  $v_t$  with the Coriolis force  $f u$ :  $v = \epsilon^2 N L_z$ . To ensure that the specific torque term participates in the dominant balance of terms in the vorticity equation set  $\tau = \epsilon N^2 \hat{\tau}$ . We drop the hat decorations straightaway, and present in dimensionless form our remaining governing equations:

$$\left( \epsilon^2 \frac{\partial^2}{\partial x^2} + \frac{\partial^2}{\partial z^2} \right) \psi_t - \epsilon \text{Pr } v_z + b_x = \tau \quad (8a)$$

$$\epsilon v_t + \text{Pr } \psi_z = 0 \quad (8b)$$

$$b_t - \epsilon^2 \psi_x = 0 . \quad (8c)$$

Here  $\text{Pr} \equiv f/N$  is sometimes called the *Prandtl ratio*, and encodes the relative strengths of buoyancy to inertial forces. It is natural to take  $\epsilon = \text{Pr}$ , i.e. to consider a box with aspect ratio dictated by the balance between rotational stiffness in the horizontal direction (the tendency of fluid to move in Taylor columns), and stratification stiffness in the vertical (resisting any lifting of isopycnal surfaces). A typical deep ocean value of the Prandtl ratio is  $\text{Pr} = 0.1$ .

## 2.1 Unforced modes

With  $F$  and  $H$  set to zero, the fluid body supports free inertigravity waves. It suffices to consider the evolution of plane-wave disturbances, with well defined wavenumber  $\mathbf{k} =$

$(k, 0, m)$ . The time evolution of the  $(\psi, v, b)$  fields must satisfy the triplet of equations:

$$-(\epsilon^2 k^2 + m^2)\psi_t - i\epsilon \text{Pr} m v + i k b = 0 \quad (9a)$$

$$\epsilon v_t + i m \text{Pr} \psi = 0 \quad (9b)$$

$$b_t = i\epsilon^2 k \psi. \quad (9c)$$

Since there is no explicit time dependence in these equations, we are allowed to seek solutions with monochromatic time dependence:  $(\psi, v, b) \propto e^{-i\omega(\mathbf{k})t}$  for some eigenfrequency  $\omega$ . Determination of the eigenvalues and eigenvectors of the associated linear operator reveals the existence of three unforced modes of the body:

- (i) A *geostrophically balanced* steady mode, with  $\omega = 0$ . The pressure field is hydrostatic  $p_z/\rho_0 = b$ , and the  $y$ -component of the velocity field fixed by the Coriolis-buoyancy balance in (3a):

$$\psi_b = 0 \quad \text{and} \quad k b_b = \epsilon \text{Pr} m v_b. \quad (10)$$

- (ii),(iii) Two propagating modes with frequencies

$$\omega_{\pm}(\mathbf{k}) = \pm \sqrt{\frac{\text{Pr}^2 m^2 + \epsilon^2 k^2}{m^2 + \epsilon^2 k^2}}, \quad (11)$$

with wave-components

$$\text{Pr} m \psi_{\pm} = \pm \epsilon \omega_{\pm} v_{\pm} \quad \text{and} \quad \text{Pr} m b_{\pm} = -\epsilon^3 k v_{\pm}. \quad (12)$$

With a little algebra, we see that an arbitrary initial disturbance may be decomposed into balanced and propagating wave fields as:

$$\psi_b = 0 \quad b_b = \frac{\text{Pr}^2 m^2 b + \epsilon^3 k \text{Pr} m v}{\text{Pr}^2 m^2 + \epsilon^2 k^2} \quad v_b = \frac{k \text{Pr} m b + \epsilon^3 k^2 v}{\epsilon (\text{Pr}^2 m^2 + \epsilon^2 k^2)}, \quad (13)$$

with

$$\psi_{\pm} = \frac{1}{2} \left( \psi \mp \frac{\omega k b - \epsilon \omega \text{Pr} m v}{\text{Pr}^2 m^2 + \epsilon^2 k^2} \right) \quad b_{\pm} = \frac{1}{2} k \epsilon^2 \left( \mp \frac{\psi}{\omega} + \frac{k b - \epsilon \text{Pr} m v}{\text{Pr}^2 m^2 + \epsilon^2 k^2} \right), \quad (14)$$

and

$$v_{\pm} = \frac{1}{2\epsilon} \left( \pm \frac{\text{Pr} m \psi}{\omega} - \frac{k \text{Pr} m b - \epsilon \text{Pr}^2 m^2 v}{\text{Pr}^2 m^2 + \epsilon^2 k^2} \right); \quad (15)$$

where we have identified  $\omega \equiv \omega_{\pm}$ , and note that such modes can then be evolved with time analytically. Note that the above expressions are singular if both  $k$  and  $m$  vanish: this corresponds to static raising or lowering of the entire body of fluid.

## 2.2 Forced modes

Grave modes of the system are forced by some external agency. To avoid imparting unwanted spatial or temporal structure to the disturbance thereby set up, we assume white noise forcing. Each mode may therefore include a forced component:

$$\frac{\partial}{\partial t} \begin{pmatrix} \psi \\ b \\ v \end{pmatrix} = \begin{pmatrix} -\frac{i\epsilon \text{Pr} m}{m^2 + \epsilon^2 k^2} & 0 & \frac{ik}{m^2 + \epsilon^2 k^2} \\ 0 & i\epsilon^2 k & 0 \\ 0 & -\frac{i\text{Pr} m}{\epsilon} & 0 \end{pmatrix} \begin{pmatrix} \psi \\ b \\ v \end{pmatrix} - \frac{\tau}{m^2 + \epsilon^2 k^2} \begin{pmatrix} 1 \\ 0 \\ 0 \end{pmatrix}. \quad (16)$$

where, by appropriate choice of the unforced component, it suffices to consider the initial conditions  $\psi = b = v = 0$  at  $t = 0$ . Now, it can easily be seen that the form of the forcing is such as to never excite the geostrophically balanced mode, so that any forced mode can be instantaneously decomposed into contributions from the two propagating eigenmodes. Supposing that we have not chosen to force a mode with vanishing vertical wavenumber (although the extension to such purely buoyancy driven waves is trivial) it is convenient to chart the evolution of these two modes via the  $v$ -amplitudes:

$$v_{\pm}(t) = \mp \frac{\text{Pr } m}{2\epsilon\omega(\epsilon^2 k^2 + m^2)} \int_0^t e^{\pm i\omega(s-t)} \tau(s) ds, \quad (17)$$

where for white noise forcing the integration measure may be written as  $\tau(s) ds = \tau_0(dW_{1s} + idW_{2s})$ , where  $\tau_0$  is some constant representing the strength of the forcing, and  $W_{1s}, W_{2s}$  are independent Wiener-processes. We therefore see that  $v_{\pm}(t)$  are both (complex-valued) Gaussian random variables, with easily computable mean and expectations. A little algebra then gives the evolution of the forced modes:

$$v(\mathbf{k}, t) = X(\mathbf{k}, t), \quad b(\mathbf{k}, t) = -\frac{\epsilon^3 k}{\text{Pr } m} X(\mathbf{k}, t) \quad \text{and} \quad \psi(\mathbf{k}, t) = \frac{\epsilon\omega}{\text{Pr } m} Y(\mathbf{k}, t), \quad (18)$$

where  $X$  and  $Y$  are complex Gaussian random variables with covariance matrix:

$$\mathbb{E} \begin{pmatrix} \Re X \\ \Im X \\ \Re Y \\ \Im Y \end{pmatrix} \begin{pmatrix} \Re X \\ \Im X \\ \Re Y \\ \Im Y \end{pmatrix}^T = \frac{\text{Pr}^2 m^2 \tau_0^2}{\epsilon^2 \omega^2 (m^2 + \epsilon^2 k^2)^2} \times \begin{pmatrix} \frac{1}{2} \left(t - \frac{1}{2\omega} \sin 2\omega t\right) & 0 & 0 & \frac{1}{4\omega} (1 - \cos 2\omega t) \\ 0 & \frac{1}{2} \left(t - \frac{1}{2\omega} \sin 2\omega t\right) & \frac{1}{4\omega} (1 - \cos 2\omega t) & 0 \\ 0 & \frac{1}{4\omega} (1 - \cos 2\omega t) & \frac{1}{2} \left(t + \frac{1}{2\omega} \sin 2\omega t\right) & 0 \\ \frac{1}{4\omega} (1 - \cos 2\omega t) & 0 & 0 & \frac{1}{2} \left(t + \frac{1}{2\omega} \sin 2\omega t\right) \end{pmatrix} \quad (19)$$

The stochastic evolution of the forced linear modes can therefore also be performed analytically. It will be necessary in diagnosing the proximity of the system to an equilibrium state to relate the rate at which energy is supplied to the system by white-noise forcing, to the rate of dissipation in breaking events. As an intermediate step to doing this, it is useful to write down an energy balance the distribution of energy between system modes:

$$\frac{1}{2} \frac{d}{dt} \sum_{\mathbf{k}} (|b(\mathbf{k})|^2 + \epsilon^4 |v(\mathbf{k})|^2 + \epsilon^2 (\epsilon^2 k^2 + m^2) |\psi(\mathbf{k})|^2) = \epsilon^2 \sum_{\mathbf{k}} \tau(\mathbf{k}) \psi(-\mathbf{k}) \quad (20)$$

the first term on the left hand side gives the available potential energy of the system (the amount of energy that would be liberated if the preexisting stratification were restored), and the remaining two terms the kinetic energy for out-of-plane and in-plane motion respectively. For freely propagating disturbances it may be shown that energy is equipartitioned between the first pair of terms and the third.

### 3 Wave-breaking

Large amplitude wave-disturbances are vulnerable to both shear and Rayleigh-Taylor instabilities. In general these two mechanisms act together. Many experimental, numerical and

theoretical studies have addressed the cascade of instabilities in a linearly stratified shear layer. It is known that for simple shear flows, shear instabilities set in only if the Richardson number ( $Ri = N^2/u_z^2$ ) does not exceed  $1/4$  [8], and direct numerical simulations have tracked the instabilities then produced, starting with the formation of Kelvin-Helmholtz billows that overturn the stratification gradient, and followed by production of streamwise eddies [12]. However, this Richardson number criterion is known not to be an accurate predictor of instability in other flow configurations [3], and the Reynolds numbers for which accurate simulations of the instability-induced mixing are feasible remain an order of magnitude below those seen in the ocean. Regardless of the obscurity of the conditions needed for instability and of the kinematics of mixing, experiments [8] and observations of atmospheric clear-air turbulence [3, figure 5] give a clear and consistent picture of the effect of mixing upon the stratification in a fluid: compact patches of well-mixed fluid are produced (with stratification obliterated) and gravity waves shed into the surrounding medium. The mixed patches are typically surrounded by layers of steeply stratified fluid, giving rise to an easily identified “rabbit-ear” signature in radiosonde studies of the thermal profile, which would correspond to sharp spikes in  $N^2$  in our system.

We introduce a simple diffusive model for the mixing of fluid by a breaking gravity wave. Mixing is taken to occur whenever the fluid becomes gravitationally unstable (so that at some site  $\theta_z < 0$ ), with no accounting for shear enhancement. The mixing time-scale is assumed to be much smaller than the period of the wave that triggered mixing, so that the continuing evolution of the wave-field can be halted while mixing occurs. For simplicity, mixing is assumed only to redistribute fluid mass so that the Eulerian distribution of velocity is *frozen in* during mixing. This is unphysical, but allows the question of parametrising the turbulent dissipation of kinetic energy to be side-stepped. To select a diffusive model we impose the following constraints:

- (i) Mixing must be energy-dissipative. Since the velocity field is unaffected by mixing, this means that the available potential energy must decrease monotonically with time.
- (ii) Mixing zones must have compact support, and must include all regions of fluid in which  $\theta_z < 0$ .
- (iii) Density must be exactly conserved at all times.
- (iv) Mixing must terminate upon reaching a stably stratified state. The mixing scheme should produce well-mixed zones, rather than set up a stable stratification.
- (v) The “rabbit ear” structure should be reproduced in the layers of fluid surrounding mixed-zones.

Constraints (ii)-(iv) point towards a diffusive scheme in which the diffusive flux is proportional to the gradient in the potential temperature rather than buoyancy (that is  $\mathbf{J} \propto -\nabla\theta$ , rather than  $\propto -\nabla b$ ). A simple candidate scheme has:

$$\frac{\partial b}{\partial T} = \nabla \cdot (D[\theta_z] \nabla \theta) \quad \text{with} \quad D[\theta_z] = -H(-\theta_z) \theta_z. \quad (21)$$

Here the  $H(x)$  is the Heaviside function, and we have introduced a mixing-time variable  $T$ . In our scaled geometry  $\nabla = (\epsilon \frac{\partial}{\partial x}, \frac{\partial}{\partial z})$ . Check that property (i) is satisfied: Multiplying



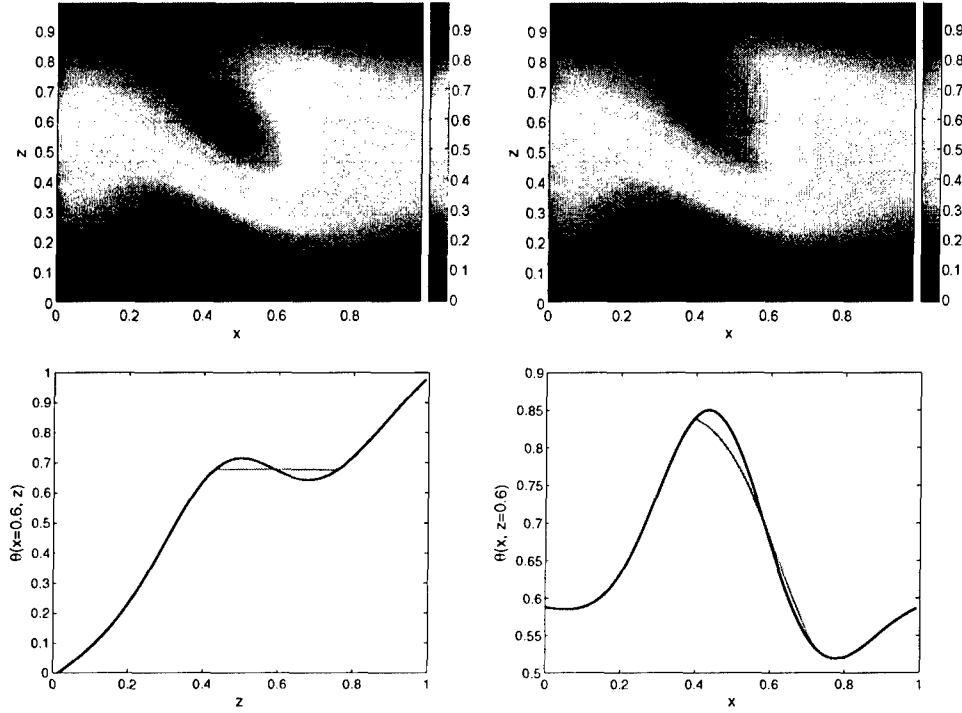


Figure 3: Diffusive scheme applied to the unstable buoyancy profile:  $b(x, z) = 0.3 \exp[-((x - 0.5)^2 + (z - 0.5)^2)/0.09] \cos[2\pi(x + z)]$ . (a) (b) are surface plots of the potential temperature distribution before and after mixing. (c) and (d) give potential temperature profiles on the transects  $x = 0.6$  and  $z = 0.6$  respectively. The blue curve is the profile before mixing, and the green curve is the profile after mixing.

both sides of (21) by  $b$  and integrating over the entire of the fluid domain, we have

$$\frac{d}{dt} \frac{1}{2} \int b^2 dx dz = - \int D[\theta_z] \left( \frac{\partial b}{\partial z} + |\nabla b|^2 \right) dx dz < 0 \quad (22)$$

since by construction  $D \equiv 0$  except where  $\partial b / \partial z < -1$ . In integrating by parts and discarding boundary contributions, we have made tacit use of the fact that periodic boundary conditions will be imposed upon  $b$ . Physically we expect strong diffusion initially in zones where  $\theta_z < 0$ , but that diffusivity will bleed away with time, leaving patches of uniform  $\theta$  (in  $z$  if not in  $x$ ). An example of the application of this diffusive mixing scheme to an initially unstable density profile is shown in Figure 3. Note that for typical aspect ratios ( $\epsilon \approx 0.1$ ) density is almost conserved at each  $x$ -station. At  $x$ -stations with a single density inversion (i.e. interval in which  $\theta_z < 0$ ) this means that the mixing produces a Maxwell-type construction, with the density made uniform in the smallest  $z$ -interval that contains the unstable zone, while conserving total fluid mass and giving a continuous final density distribution (see Figure 3c). The weakness of density diffusion between  $x$ -stations means that density distribution is markedly less smooth on horizontal sections than on vertical sections (see Figure 3d). This is intuitively appealing: although the breaking inertigravity

waves respect the  $x$  and  $z$  scalings introduced here, Coriolis forces act only weakly upon the turbulent eddies generated during wave breaking, so that we expect mixing to be isotropic in the *unscaled*  $x$  and  $z$  coordinates.

Note that condition (v) is not satisfied by the diffusive scheme (21) which always produces continuous  $\theta$  profiles, and does not in general enhance the stable  $\theta$  gradients surrounding a mixing zone. One remedy for this would be to extend the support of the diffusivity function  $D$  to include some region of stably stratified fluid. Ensuring that this is compatible with the dissipative condition (i) is difficult. In the direct numerical simulation literature the *Thorpe displacement* is sometimes invoked for this purpose [12]. The Thorpe displacement  $d(z; x)$  is defined for the column of fluid occupying each of the  $x$ -stations, as the minimum distance that the fluid particle at  $z$  must be moved in a vertical reordering of the fluid particles in the column to create a stable stratification. It has been suggested that at any instant the region in which turbulent overturning must occur can be identified with the part of the fluid having non-zero Thorpe displacement [2]. However, one may easily construct examples in which diffusion over the entire zone of non-zero Thorpe displacement would lead to a gain in available potential energy, in violation of condition (i). A more promising approach attempts a more careful budgeting of the energy available for mixing from both the kinetic energy and available potential energy of the flow. The diffusivity  $D$  is identified with the amount of turbulent energy present, and is allowed to self-diffuse. Zones of fluid in which  $\theta_z \leq 0$  are treated as diffusivity sources and sinks respectively. While these models allow diffusion over significantly larger fluid regions than (21) and may therefore satisfy (v), and can be constructed so as to conserve [14] or dissipate energy, they also require the addition of multiple ill-constrained parameters for the separate diffusivities of density, momentum and turbulent energy.

## 4 Numerical implementation

A cartoon of the numerical scheme for combining linear evolution (§2) with diffusive mixing (§3) is given in Figure 4.

We describe briefly some of the numerical desiderata. We impose periodic boundary conditions upon the  $b$ ,  $\psi$  and  $v$  fields, and discretise the numerical domain with a grid of  $M$  points in the  $x$  direction and  $N$  points in the  $z$ -direction. Typically we let  $M$  and  $N$  range from 32 up to 256. Fast Fourier Transforms are used to pass between physical and wavenumber representations of the wave fields. The time interval  $\Delta t$  over which the fields are allowed to evolve between mixing events is held fixed throughout the simulation, so that the evolution of the unforced components can be determined in advance by the computation of time evolution operators  $\exp(\mp i\omega(\mathbf{k})\Delta t)$  for each of the modes. Stochastic evolution of the forced modes requires us to generate the Gaussian random variables  $X$  and  $Y$  that feature in the equation (18). We do this by calculating the covariance matrix (denoted by  $C(\Delta t; \mathbf{k})$ ) for  $(\Re X, \Im X, \Re Y, \Im Y)$ , and finding its Cholesky decomposition  $C \equiv LL^T$ . The requisite  $X, Y$  at each time step may then be generated as  $(\Re X, \Im X, \Re Y, \Im Y) = L\xi$ , where  $\xi$  is a quadruple of  $N(0, 1)$  random variables.

For the implementation of the diffusive mixing step, spatial derivatives are approximated by second order centred differences, and the time stepping is performed with a fully implicit second order scheme (the Matlab routine `ode23s`, based on the Rosenbrock formula, which

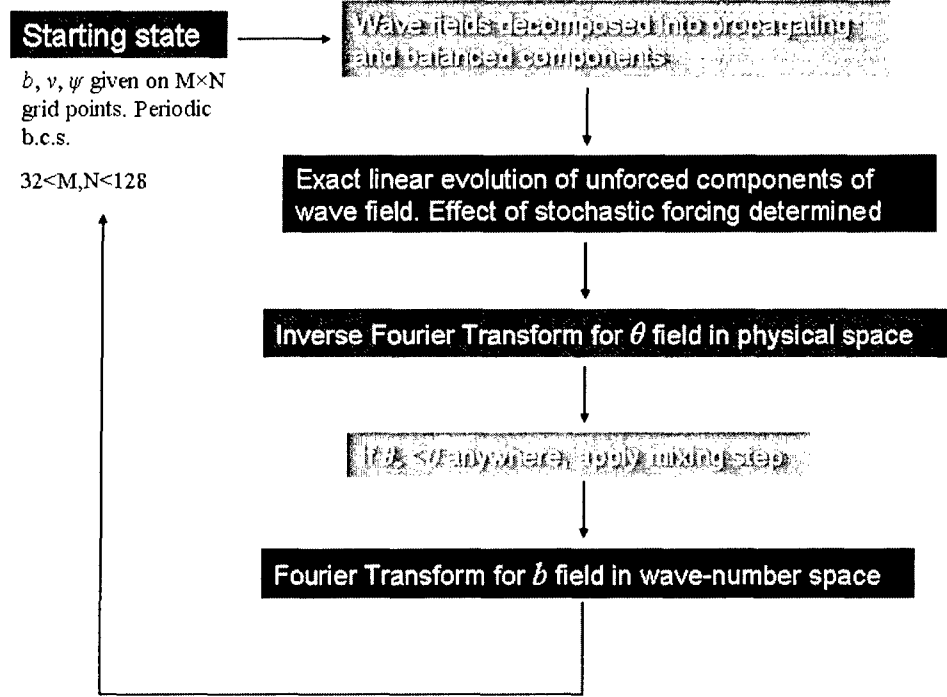


Figure 4: A numerical scheme for combining linear evolution with diffusive mixing.

we have altered to make use of UMFPACK to perform an LU-factorisation of the large but sparse Jacobian matrix). To ensure that the associated system of time equations have a well-defined Jacobian it is necessary to smooth the Heaviside function term appearing in the diffusivity. In practice we use:

$$H(x) \approx \frac{1}{2} \left( x + \sqrt{x^2 + 4\epsilon} \right), \quad (23)$$

where the smoothing length  $\epsilon$  is set at machine precision  $\epsilon \approx 10^{-12}$  without any evident irregularity in the running of the code. Diffusion was terminated when  $\theta_z$  exceeded some critical value (typically -0.005) throughout the fluid domain. Numerical results for the mixing step were tested using a finite element package (COMSOL Multiphysics 3.2).

There are two fundamentally different experiments that can be performed using the numerical scheme described here. In the first, *relaxation*, all wavenumbers are initially given identical energies, randomly allocated between leftward and rightward propagating modes, and with uniformly randomly distributed phases for each component. The system is then allowed to evolve without forcing until it reaches equilibrium with, in the end stages, exponential decay in the total energy, and increase in the waiting time between mixing events. In the second experiment, *build-up*, one or two of the gravest modes of the system are supplied with white noise forcing, and the transmission of energy from these modes to other modes is charted.

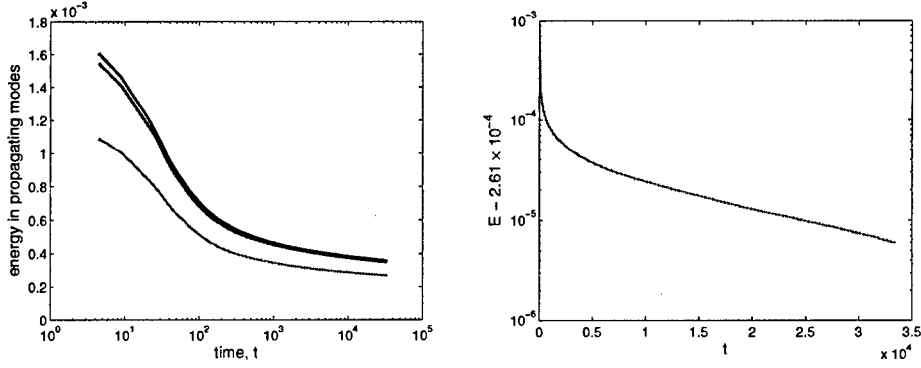


Figure 5: (a) Effect of varying initial state. The three curves give relaxation dynamics of system starting with different random initial states. (b) Green data set replotted on log-log scale. All simulations are run with  $M = N = 64$ .

## 5 Results

### 5.1 Relaxation experiments

The *effect of the initial state* upon the evolution of the system is shown in Figure 5a. Only the energy in propagating modes is plotted - the contribution from geostrophically balanced modes is an order of magnitude smaller. In part b of the figure, one of the data sets is replotted on a linear-log scale to show the exponential convergence of the total wave energy. It can be seen that the initial state is not forgotten, but helps to determine the total energy that the system relaxes to. Two systems with initially closely separated energies ultimately equilibrate with similar energies, as the red and blue curves show.

*Phase structure in evolved states.* It must be asked whether the equilibrium states of the system have definite phase as well as energy spectra - i.e. that the different wave components must have specific phase lags to avoid constructive interference that may lead to breaking. We test for this by taking one of the late time system states from Figure 5a, randomising all of the phases and allowing it to evolve with time, to see if the equilibrium is altered. Results are shown in Figure 6. It is seen that the apparent equilibrium energy of the propagating modes (which is found by fitting the energy-time curve to a decaying exponential and extrapolating to infinity) varies by less than 2%. This suggests that the equilibrium phase spectrum of the system is white.

The *effect of varying the time-interval between mixing events* is shown in Figure 7, in which an identical initial state is let evolve three times, with different time intervals  $\Delta t$  between mixing events for each of the iterations. The energy of the system is sensitive at early times to the value of  $\Delta t$ , but not the value of energy that the system ultimately converges to. Smaller values of  $\Delta t$  give faster convergence to the equilibrium energy.

*Evolved spectra.* In Figure 8 we compute the detailed distribution of energy among wave-modes for the green data set from Figure 5. The spectra corresponding to other data sets are qualitatively similar, and we are developing methods for direct comparison. The redness of the spectrum is similar to that of the Garrett-Munk spectrum, although lack of resolution

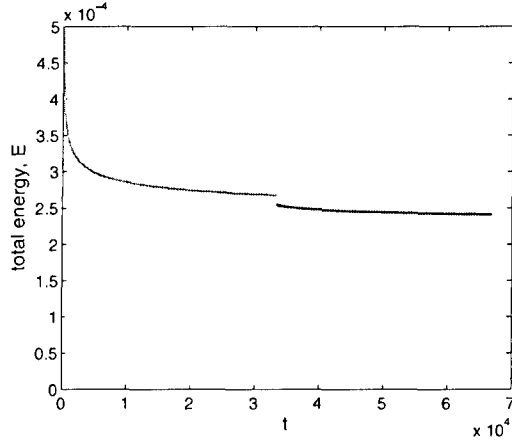


Figure 6: Effect of randomisation of phase of wave modes upon the relaxation of a system to equilibrium. Green curve shows initial evolution (identical to the green data set in Figure 5), and purple curve the continuing evolution after phases are randomised at a time  $t = 3.3 \times 10^4$ .

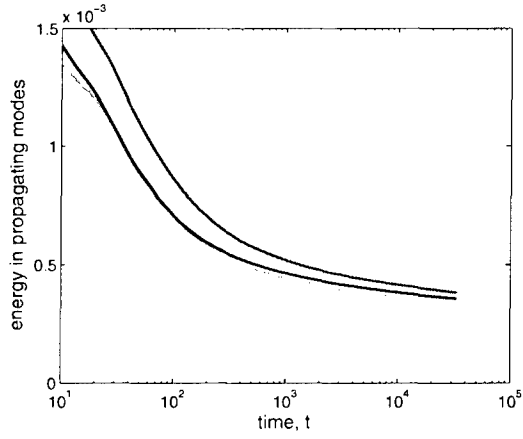


Figure 7: Effect of varying time interval between mixing events upon relaxation dynamics. Red curve corresponds to  $\Delta t = 13.40$ , blue curve to  $\Delta t = 4.46$ , and cyan curve to  $\Delta t = 1.12$  (all times are measured in units of  $1/N$ ).

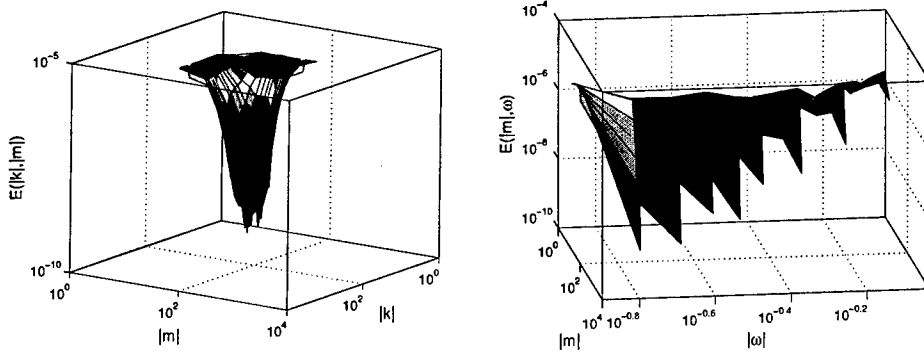


Figure 8: Relaxation spectra in (a)  $(|k|, |m|)$  and (b)  $(|m|, |\omega|)$  space.

prevents direct comparison of the scalings for the inertial peaks. The spectrum is also peaked at small  $m$  (corresponding to purely buoyancy driven waves) in visible disagreement with the GM spectrum. These modes correspond to lifting of vertical columns of fluid, and do not therefore participate in breaking: either in determining whether breaking will occur, or in mixing, because, as was discussed in §3, this mainly leads to vertical transport of mass. The persistence of these modes, once excited, is a knotty problem for the model.

## 5.2 Build-up experiments

It is not feasible to force a single mode of the system, since any spatial periodicity of the forced mode will be inherited by the modes created during wave breaking, leading to a sparse energy spectrum. To break this symmetry we force a *pair* of grave modes  $(k, m) = (2\pi, \pm 2\pi)$  with the same forcing constant  $\tau_0$ , and the first mode initially just below its breaking amplitude and the second mode started from zero amplitude. It is also necessary to impose an adiabaticity constraint upon the forcing, that the time taken for the forcing to bring the forced mode to breaking must greatly exceed the period of the mode, i.e. that:

$$\tau_0 \ll \left( \frac{\omega^3}{2\pi} \right)^{1/2} \frac{m^2 + \epsilon^2 k^2}{\epsilon^2 k m}. \quad (24)$$

For  $\tau_0$  significantly greater than this threshold value, the energy in the forced modes is observed to grow without bound. Wave-breaking only removes energy from the buoyancy field, and we can only be assured that energy is equipartitioned between the available potential energy (plus the out-of-plane kinetic energy) and the in-plane kinetic energy if the adiabaticity condition is met.

It can be seen that the energy spectrum is dominated by the handprint of the forced modes. These modes remain saturated (at the brink of breaking) and transmission of energy to other modes is inefficient. In Figure 9a we show the total energy budget for one realisation of this system, showing that it attains a flux-dissipative equilibrium (with the rate of dissipation by mixing equal to the energy input from the white noise). Experimentally the mean energy value in this equilibrium depends upon the particular modes being forced, but not upon the strength of the forcing  $\tau_0$  or upon the time between mixing events  $\Delta t$ .

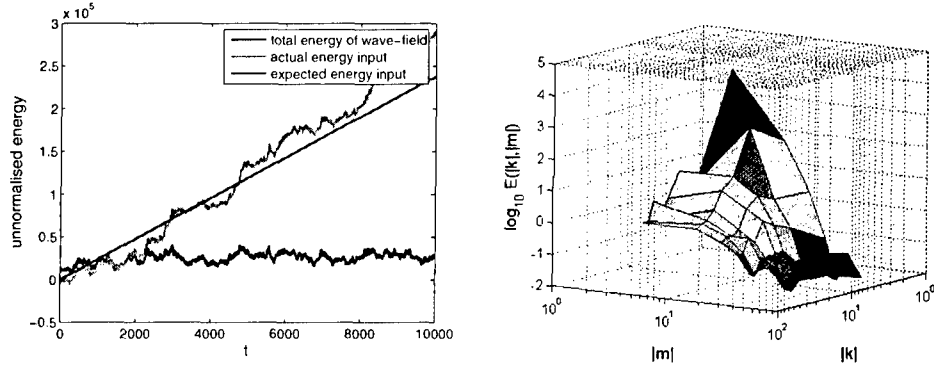


Figure 9: (a) Energy budget for forced mode, showing rate of energy input from white noise, against total energy of all wave modes. (b) Time-averaged energy spectrum when system has attained flux-dissipative equilibrium. Simulations were run on an older version of the code, on an  $M = N = 2^5$  grid, with unnormalised energies (which must be divided by  $M^2 N^2 = 2^{20}$  for comparison with Figure 5) and anisotropic diffusion (setting  $\nabla = (\partial/\partial x, \partial/\partial z)$  in (21)), but are in qualitative accord with experiments using the modified code described in this report.

The rate of energy increase in unforced modes is slow, and it is unclear whether a forced-dissipative equilibrium has actually been reached by the end of the simulation. In truth Figure 9a probably represents no more than the achievement of a flux-dissipative equilibrium for the single forced mode of the system. In Figure 9b we show the (coarsely-binned) energy spectrum of the system as a function of wave-number, showing clear peaking at the forced wavelengths. It may be possible to clarify whether equilibrium has been attained by running a hybrid of the relaxation and build-up experiments, in which the other modes are given some initial energy and allowed to *relax to* rather than *build up to* a steady state.

## 6 Discussion

Basic questions about the capabilities and limitations of the model remain unasked. The preliminary simulations described here show that a large number of energy equilibria can be accessed when an unforced wave-field is allowed to relax from some higher-energy initial state. These states appear to all have structure-free phase spectra and relatively homologous energy spectra, suggesting that the family of equilibrium states could be parametrised by their total energy, and we are in the process of running simulations to simulate relaxation for a large assay of initial states at a higher resolution, in order to confirm this. The problem of the persistence of  $m = 0$  states remains unresolved. Results of the *build-up* simulations are less promising - a method must be found to subtract out the forced mode from the final spectra (Figure 9), or for hastening the equilibration of these modes. Incorporation of forcing is vital to our efforts to use the model to tackle the problem of anomalous diffusion (§1.1), since the rate of mixing will be ultimately controlled by the rate of energy input into the wave-field.

The author thanks Oliver Bühler for guidance over the duration of the GFD summer school, and gratefully acknowledges discussions with Neil Balmforth, Paul Milewski, Esteban Tabak and Bill Young.

## References

- [1] O. BÜHLER, M. E. MCINTYRE, AND J. F. SCINOCICA, *On shear-generated gravity waves that reach the mesosphere. Part I: Wave generation*, J. Atmos. Sci., 56 (1999), pp. 3749–3763.
- [2] P. J. DIAMESSIS AND K. K. NOMURA, *The structure and dynamics of overturns in stably stratified homogeneous turbulence*, J. Fluid Mech., 499 (2004), pp. 197–229.
- [3] D. C. FRITTS, C. BIZON, J. A. WERNE, AND C. K. MEYER, *Layering accompanying turbulence generation due to shear instability and gravity-wave breaking*, J. Geophys. Res. D, 108 (2003), pp. PMR 20–1.
- [4] C. GARRETT AND W. MUNK, *Internal waves in the ocean*, Ann. Rev. Fluid Mech., 11 (1979), pp. 339–369.
- [5] A. E. GILL, *Atmosphere-Ocean Dynamics*, Academic Press, San Diego, 1982.
- [6] M. C. GREGG, T. B. SANFORD, AND D. P. WINKEL, *Reduced mixing from the breaking of internal waves in equatorial waters*, Nature, 422 (2003), pp. 513–515.
- [7] J. R. LEDWELL, E. T. MONTGOMERY, K. L. POLZIN, L. C. S. LAURENT, R. W. SCHMITT, AND J. M. TOOLE, *Evidence for enhanced mixing over rough topography in the abyssal ocean*, Nature, 403 (2000), pp. 179–182.
- [8] P. F. LINDEN, *Mixing in stratified fluids*, Geophys. Astro. Fluid Dyn., 13 (1979), pp. 3–23.
- [9] Y. V. LVOV, K. L. POLZIN, AND E. G. TABAK, *Energy spectra of the ocean's internal wave field: Theory and observations*, Phys. Rev. Lett., 92 (2004).
- [10] M. E. MCINTYRE, *On dynamics and transport near the Polar Mesopause in summer*, J. Geophys. Res. D, 94 (1989), pp. 14617–14628.
- [11] A. C. NAVEIRA GARABATO, K. L. POLZIN, B. A. KING, K. J. HEYWOOD, AND M. VISBECK, *Widespread intense turbulent mixing in the southern ocean*, Science, 303 (2004), pp. 210–213.
- [12] W. R. PELTIER AND C. P. CAULFIED, *Mixing efficiency in stratified shear flows*, Ann. Rev. Fluid Mech., 35 (2003), pp. 135–167.
- [13] K. L. POLZIN, J. M. TOOLE, J. R. LEDWELL, AND R. W. SCHMITT, *Spatial variability of turbulent mixing in the abyssal ocean*, Science, 276 (1997), pp. 93–96.



- [14] E. G. TABAK AND F. A. TAL, *Mixing in simple models for turbulent diffusion*, Comm. Pure Appl. Math., 57 (2004), pp. 563–589.
- [15] K. B. WINTERS AND E. A. D’ASARO, *Diascalar flux and the rate of fluid mixing*, J. Fluid Mech., 317 (1996), pp. 179–193.
- [16] C. WUNSCH AND R. FERRARI, *Vertical mixing, energy, and the general circulation of the oceans*, Ann. Rev. Fluid Mech., 36 (2004), pp. 281–314.

# Laboratory experiments on mesoscale vortices colliding with multiple islands

Aya Tanabe  
Imperial College London

July 18, 2006

## 1 Introduction

### 1.1 Oceanic background

Mesoscale vortices have recently been recognized to play an important role in redistribution and transport of water properties (e.g. temperature, salinity) around the oceans. The interaction of vortices with seamounts, submerged ridges, or islands might result in enhanced and localized transfer of anomalous fluid from the vortices to the surrounding environment. In addition, the interaction could end in the formation of new vortices downstream otherwise complete destruction of the incident vortices. This topic has been investigated for the past several decades for e.g. Meddies in the eastern North Atlantic, Agulhas rings in the eastern South Atlantic, and North Brazil Current (NBC) rings in the western tropical Atlantic. In the current study, we will focus on, in particular, the behaviour of the last kind of vortices, NBC rings which interact with the Lesser Antilles.

It is believed that NBC rings are one of the leading mechanisms for transporting the upper ocean equatorial and South Atlantic water into the North Atlantic as part of the Meridional Overturning Cell (MOC). The MOC transports cold deep water southward across the equator and, to be balanced, transports upper ocean South Atlantic waters northward. In the upper layers, the NBC is a northward flowing western boundary current that carries warm water across the equator along the coast of Brazil (Figure 1). Near  $5^{\circ} - 10^{\circ} N$ , the NBC separates sharply from the coastline and retroflects to feed the eastward North Equatorial Counter Current (NECC) [7]. During its retroflexion, the NBC occasionally pinches off isolated anticyclonic warm-core vortices exceeding  $450 km$  in overall diameter,

2 km in vertical extent, and swirling at speed approaching  $100 \text{ cm s}^{-1}$ . These NBC rings move north-westward toward the Caribbean at  $8 - 17 \text{ cm s}^{-1}$  on a path parallel to the coast-line of Brazil. As part of the MOC, in most cases, they then interact with a complex island chain, the Antilles islands [6] and enter the Caribbean Sea. (Episodically, they enter the North Atlantic subtropical gyre.) The inflow into the Caribbean Sea ultimately feeds the Florida Current which is now recognized to be a fundamental passage for northward transport of upper ocean waters in the global thermohaline circulation. Therefore, the Atlantic MOC (hence NBC rings) is an important element of the global thermohaline circulation and a fundamental component of the global climate system. Recent observations reveal that relatively large (average diameter 200 km) energetic anticyclonic vortices were found downstream of the Antilles islands in the Eastern Caribbean Sea and translated westward in the central part of it whereas cyclonic vortices were observed primarily near boundaries in the Eastern Caribbean Sea [11] (Figure 2). Unfortunately, it is difficult, by observations, to know whether or not such large anticyclonic and cyclonic vortices observed in the Eastern Caribbean Sea have been produced as a consequence of the interaction between NBC rings and the Antilles islands, and if so, how they have been formed. In the present work, we shall try to answer part of this question through laboratory experiments.

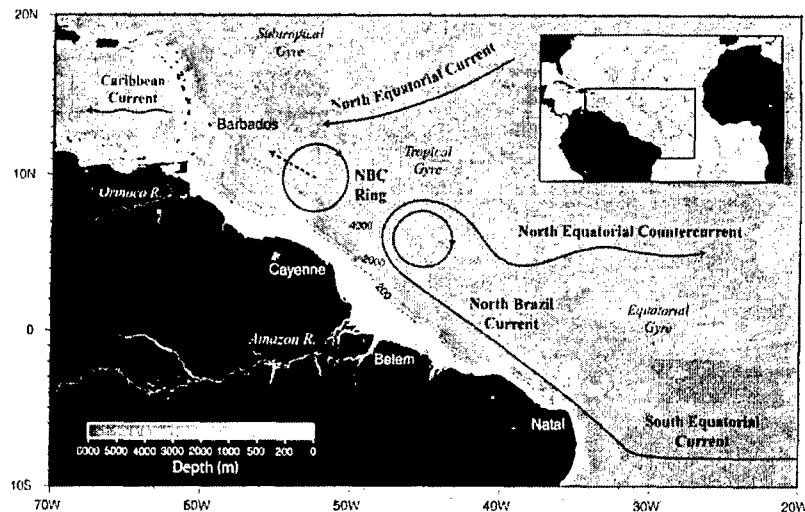


Figure 1: Sketch of the upper-ocean circulation in the western tropical Atlantic from [5].

## 1.2 The previous works

Before mentioning a possible mechanism for the large anticyclonic and cyclonic vortices formation in the Eastern Caribbean Sea, let us introduce briefly two previous works on

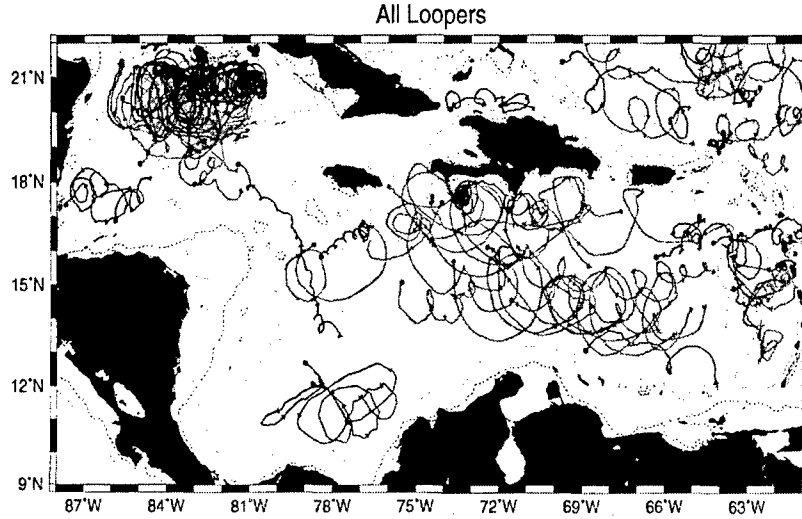


Figure 2: Drift trajectories of 28 cyclones (blue) and 29 anticyclones (red). Anticyclones seem to be dominant in the Eastern Caribbean Sea between  $65^{\circ}W$  and  $75^{\circ}W$ , from [11].

interaction of vortices with multiple islands.

The interaction of a monopolar, self-propagating cyclonic vortex with two circular cylinders was investigated in the laboratory [2] (Figure 3 (a)). Typically after the vortex came in contact with the two cylinders, the outer edge of the vortex was peeled off and a so-called “streamer” (or two “streamers”) went around one of the cylinders (or each of the cylinders) (Figure 3 (b)). When the streamer velocity  $v_s$  was large enough (i.e.  $400 < Re < 1100$  where  $Re = v_s d / \nu$ , and  $d$  is the diameter of the incident vortex), the “streamer(s)” turned into a new cyclonic vortex (or two new vortices). During the experiments in [2], three parameters were varied:  $G$ , the separation between the cylinders;  $d$ ; and  $Y$ , the perpendicular distance of the center of the vortex from an axis passing through the center of the gap between the cylinders (see Figure 3 (a)). One of the remarkable observations in [2] is that the flow within the vortex was “funneled” between the two cylinders and formed a dipole vortex, much like water ejected from a circular nozzle generates a dipole ring. This behaviour occurred provided that  $-2 < Y/g < 0$ ,  $0.25 \leq G/d \leq 0.4$ , and  $Re_G > 200$ , where  $g = G/2$ ,  $Re_G = U_G G / \nu$  is the Reynolds number based on a length scale  $\sim O(G)$ , and  $U_G$  is the maximum velocity of the vortex fluid in the gap. The size of the created cyclonic and anticyclonic vortices (i.e. a dipole) was smaller than that of the original vortex.

A second relevant work is a numerical investigation of the interaction of both a self-propagating and an advected vortex with multiple islands [13]. The islands were represented by thin vertical walls aligned in the North-South direction with gaps having a width of 20% of the vortex diameter. This study showed that if the individual islands were small

compared with the vortex radius (e.g.  $L/R_i = 0.3$  where  $L$  is the island length,  $R_i$  is the initial vortex diameter<sup>1</sup>), the vortex reorganized in the basin downstream of the islands, whereas it always split into multiple offsprings if the islands were large (e.g.  $L/R_i = 1.5$ ) (Figure 4). Moreover, intense vortices experienced relatively greater amplitude loss than weak vortices. The results of [13] may give an account of the observations of anticyclones in the Eastern Caribbean Sea, but the generation of cyclones in the Sea can not be explained by their results as no cyclones were seen in [13].

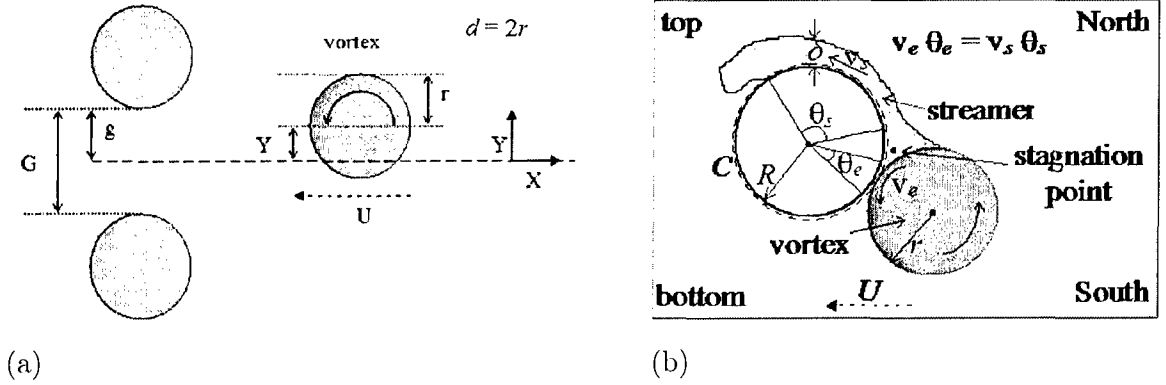


Figure 3: (a): sketch illustrating the geometry of the encounter between the vortex and two cylinders, from [2]. The diameter of the cylinders,  $D$ , is  $5\text{ cm}$ . (b): sketch of a streamer, from [3].

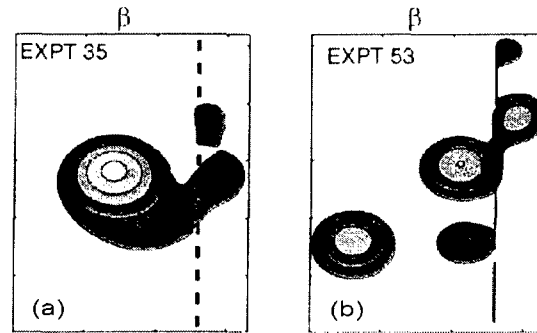


Figure 4: Multiple-islands numerical experiments from [13]. (a):  $L/R_i = 0.3$ . (b):  $L/R_i = 1.5$ .

### 1.3 Hypothesis

Since the Lesser Antilles have passage width between  $30 - 60\text{ km}$  and the approaching NBC vortices' size varies between  $200 - 400\text{ km}$ ,  $G/d$  lies in the range  $0.07 - 0.3$ . Although this

<sup>1</sup>The definition of the vortex initial radius is not stated in [13], hence  $R_i$  and  $d$  (defined in [2]) are not necessarily equal.

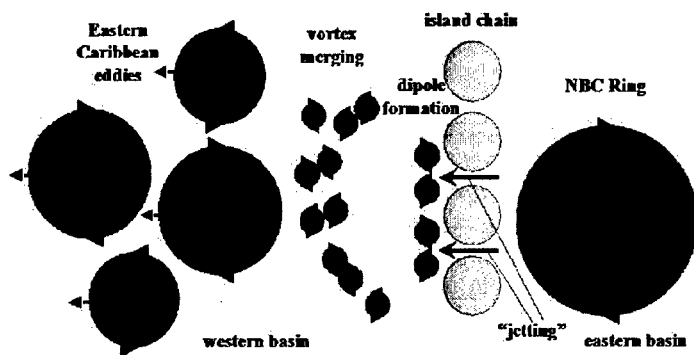


Figure 5: Sketch illustrating a possible formation mechanism for the large Eastern Caribbean vortices [11].

range does not exactly fit in  $0.25 \leq G/d \leq 0.4$  obtained in [2], it is natural to anticipate that dipole formation is likely to occur downstream of the Lesser Antilles' passages. Assuming that several pairs of dipoles are formed at western side of the islands, we expect that transition from small scale vortices to large scale structures will occur by the merging of vortices of like sign (Figure 5). When rotation is present, the scale to which the vortices grow is determined by instability processes that inhibit vortices to grow to scales larger than the Rossby radius of deformation [9]. The coalescence of same sign vortices is similar to the well-known feature of inverse energy cascade in two-dimensional flow [10]. Finally, vortices having a diameter of the order of the Rossby radius of deformation will form and drift westward due to the planetary  $\beta$ -plane (Figure 5).

## 2 The experiments

### 2.1 Experimental apparatus

The experiments were performed in a square tank of depth 45 cm, length and width of 115 cm. Both 'top-view' and 'side-view' illustrations of the apparatus are shown in Figures 6 & 7. Some experiments were carried out in a much smaller tank (depth 36 cm, length and width 60 cm). However, as we are interested in knowing not only whether or not *several* dipoles are formed when vortices interact with a chain of obstacles, but also the fate of the dipoles (if they are really formed), it was appropriate to focus on experiments performed in the larger tank. The apparatus in Figures 6 & 7 was mounted concentrically on a 2 m-diameter rotating turntable with a vertical axis of rotation. The sense of rotation of the turntable was anticlockwise. A square tank was used to avoid optical distortion from side views associated with a circular tank. The tank had a sloping bottom which makes an angle  $\alpha$  to the bottom of the tank in order for a vortex to self-propagate leftward when looking

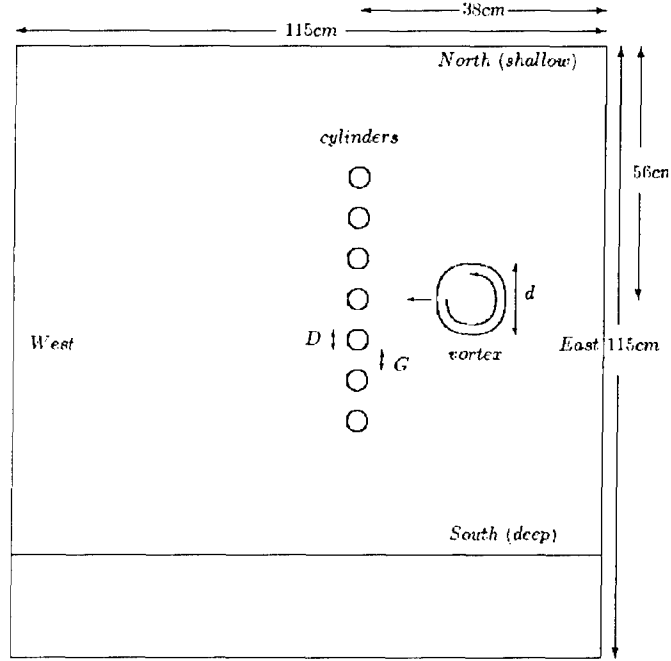


Figure 6: Sketch of the experimental apparatus: top view.

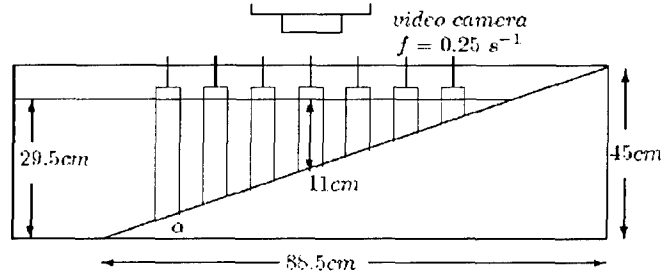


Figure 7: Sketch of the experimental apparatus: side view.

upslope [4]. We note that there is an analogy between the  $\beta$ -plane effect and the sloping topography effect provided that the angle of the slope  $\alpha$  and the Rossby number  $Ro$  (the ratio of the advection term to the Coriolis term in the horizontal momentum equations) are sufficiently small [4]. The shallowest part of the tank corresponds to North. Hence, East is to the right when looking upslope, West is to the left, and South is the deepest part of the tank. The tank was filled with fresh water, which was initially in solid body rotation. Seven circular cylinders whose diameter is  $D$  were aligned in the North-South direction, and each of them was separated by a gap  $G$  as shown in Figures 6. The position of the central cylinder (the fourth one from North (or South)) was always fixed. However, the position of the other cylinders could be changed to vary the value  $G$ . The depth of the water at the

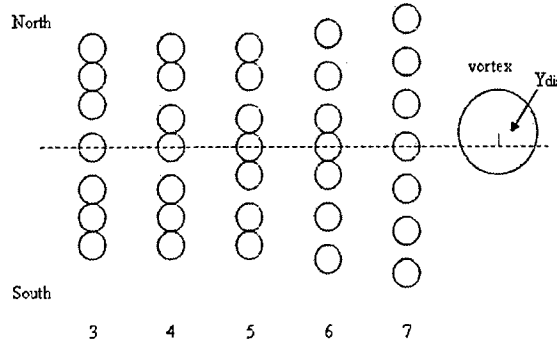


Figure 8: The five configurations of the obstacles used in the experiments. The position of the fourth cylinder from North (or South) was kept fixed.

central cylinder,  $h_0$ , was chosen to be 11 cm which was much larger than the Ekman layer depth  $\delta_{Ek} = \sqrt{2\nu/f} \approx 3 \text{ mm}$ , where  $\nu$  is the kinematic viscosity of the water and  $f$  is the Coriolis parameter. The bottom of each cylinder was sliced at an angle so it rested flush with the sloping bottom.

A barotropic cyclonic vortex was generated by placing an ice cube in the water [14], a method dynamically similar to withdrawing fluid from a sink positioned on the sloping bottom. The water surrounding the ice cube, due to conduction, becomes colder than the surrounding water and sinks as a cold plume, forming a cold dense lens within the thin bottom Ekman layer. The dense plume induces inward velocities along the entire column depth above the bottom lens, and then, influenced by the Coriolis force, the water column (above the dense lens) starts to spin cyclonically. In order to conserve mass, the dense fluid in the bottom Ekman layer flows radially outwards with a rapid velocity in comparison to the rotation period of the tank and thus a dense anticyclonic vortex does not form on the bottom. The fluid within the dense lens moves downslope together with the established barotropic vortex above it. Influenced by the Coriolis force, both the cyclonic water column and the cold lens change their direction and start drifting westward with a very small meridional displacement. Although NBC rings are anticyclonic vortices, in the laboratory it was not possible to reproduce stable barotropic anticyclones as they tend to be centrifugally unstable [8] and become non-axisymmetric in a few rotation periods. Furthermore, NBC rings have a baroclinic structure and move within a stratified fluid. As shown by [3], the use of cyclonic vortices does not limit the generality of the results, which can be easily extended to anticyclones. In particular, the circulation equation around the obstacle and the equation relating the streamer velocity to the vortex velocity (the equation in Figure 3 (b)) still hold for anticyclones. We neglected the effect of a stratified environment and



the influence of the advection mechanism on the interaction in our present study. Lack of stratification is possibly the weakest point of our model but the good agreement between the results obtained in [1, 2, 3] and the oceanic observations suggests that stratification does not invalidate the relevance of the results discussed here.

For all the experiments, the Coriolis parameter  $f$  was fixed at  $0.25 \text{ s}^{-1}$ , and  $\nu = 0.01 \text{ cm}^2 \text{ s}^{-1}$ . The bottom slope was set at  $s = \tan \alpha = 0.5$ , where  $\alpha$  is the angle between the sloping bottom and the horizontal so that the self-propagating vortex could move westward with a speed  $U \approx 0.2 \text{ cm s}^{-1}$ . The vortex was produced approximately  $20 \text{ cm}$  westward of the eastern wall of the tank. Hence, the vortex moved  $20 \text{ cm}$  westward and interacted with the chain of cylinders before the spindown time  $\tau = h_0/\sqrt{\nu f} \approx 200 \text{ s}$ . The diameter of the cylinders,  $D$ , is  $3.3 \text{ cm}$ . Three values for the size of the gaps,  $G = 3, 1.5, 0.7 \text{ cm}$  and five types of configurations of the obstacles (Figure 8) were studied. The azimuthal velocity profile of the vortex in the experiments,  $v_\theta$ , is similar to that of a Rankine vortex with an approximately constant vorticity (solid body rotation) for  $0 \leq r' \leq r'_{max}$  and a velocity which decays roughly like  $1/r'$  for  $r' > r'_{max}$ , where  $r'$  is the radial coordinate originating in the vortex center. We define the vortex radius  $r$  to be not  $r'_{max}$  where the azimuthal velocity of the vortex is maximum, but the radial distance (from the center of the vortex) where the velocity has decayed by approximately 30% (i.e.  $r = r'_{max}/0.7$ ). This definition for the vortex radius is same as the one in [1, 2]. The *incident* vortex diameter  $d$  ranged between  $7.6 - 19 \text{ cm}$  due to non-uniformity of the size of the ice cubes used.

## 2.2 Measurements

A video camera was mounted above the tank and was fixed to the turntable so that we were able to observe the flow in the rotating frame. For half of the experiments, the vortex was made visible by using a white sloping bottom, dripping dye (food coloring) on the ice cube and adding buoyant paper pellets on the free surface. The motion of the dyed vortex was also observed from the side of the tank. For the rest of the experiments, the paper pellets on the free surface and a black sloping bottom were used in order to measure the velocity field and to calculate, for instance, the circulation of the vortex. Images were grabbed from the recorded video tape by using XCAP. The time interval between each image was  $0.15 \text{ s}$ . An image processing software, DigiFlow was used to do particle tracking, and then calculate the velocity field by mapping the individual velocity vectors onto a rectangular grid using a spatial average over  $2 \text{ cm}$  and the time average over  $10 \text{ s}$ . Once the gridded velocity was obtained, quantities such as the position (center), the radial distance  $r'$  where the velocity is maximum (i.e.  $r'_{max}$ ), and the circulation of the vortex (before and after the interaction with the obstacles) were computed by using Matlab. Let  $x, y$  be the zonal and meridional

coordinates in Figure 9, respectively. Further, let us define  $U$ ,  $V$  to be the  $x$ -,  $y$ -component of the vortex velocity, respectively. The position of the vortex center was determined as the intersection of two lines; one is a line where  $|U|$  is maximum and parallel to the  $y$ -axis while the other is a line where  $|V|$  is maximum and parallel to the  $x$ -axis (red lines in Figure 9). Two different  $r'_{max}$  were computed by defining two radial distances from the vortex center, namely

$$r_{max} = \max(r_1, r_2, r_3, r_4), \quad r_{av} = \text{average}(r_1, r_2, r_3, r_4),$$

where  $r_1$  is the radial distance from the vortex center to the eastward location where  $|V|$  is maximum,  $r_2$  is the distance from the vortex center to the northward location where  $|U|$  is maximum, etc. Defining  $r_{max}$ ,  $r_{av}$  was important particularly when the vortex was distorted. Since  $r_{av}$  turned out to be better in general (that is,  $|U|$  and  $|V|$  are almost maximum at  $r' = r_{av}$ ), we focused only on the case  $r'_{max} = r_{av}$ . Once  $r'_{max}$  was obtained, the circulations of the vortex  $\Gamma_B$ ,  $\Gamma_A$  (before and after the interaction, respectively) were computed:

$$\Gamma_B = A \sum_i \omega_i,$$

where  $A$  is the area of the single grid square, and  $\omega_i$  is the relative vorticity at each grid point within  $r' = r'_{max} = r_{av,B}$  ( $r_{av,B} = r_{av}$  before the interaction). A similar expression can be written for  $\Gamma_A$ . By looking at the video tape, it is possible to know the number of the offsprings  $N$ , whether or not a dipole was formed (or several dipoles were formed), and whether there was a backward flow (fluid flowing between the cylinders from west to east) or not.

### 3 Experimental results

#### 3.1 $G = 3\text{ cm}$

Let us firstly discuss the results for  $G = 3\text{ cm}$  with  $d = 7.6 \sim 19\text{ cm}$  ( $0.16 \leq G/d \leq 0.4$ ) because it corresponds to the kind of geometry found when the NBC rings interact with the Lesser Antilles. As soon as a vortex encountered the obstacles, a dipole almost always formed for all the configurations showed in Figure 8. However, the formation of two or more dipoles *never* occurred although the vortex extended for several cylinder and gap lengths. After a dipole formed, the cyclonic part of the dipole became dominant. Depending on the configurations of the obstacles and the initial vortex position, a relatively large cyclonic offspring was produced either directly from the cyclonic part of the dipole, or from the "remnant" of the original vortex at the gap positioned just "South" of the gap where the dipole was formed. (The vortex moved south due to its image vortex. The degree of

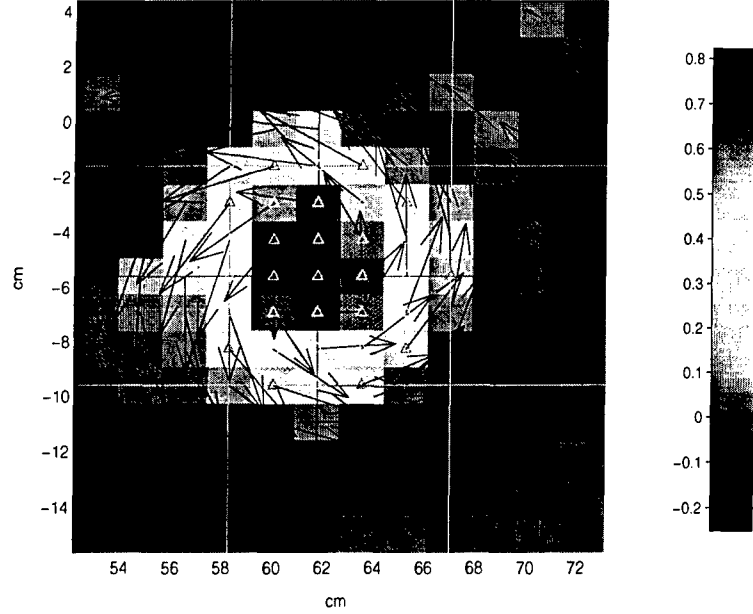
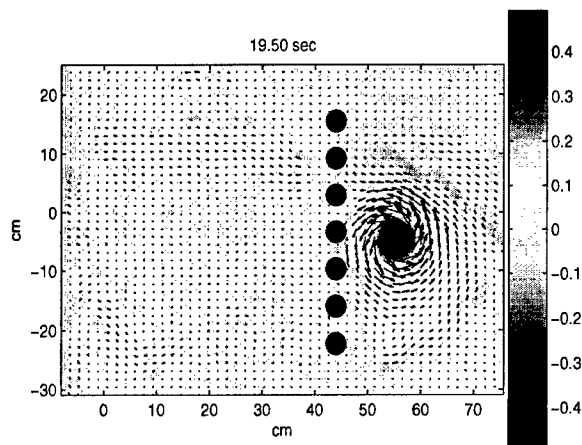
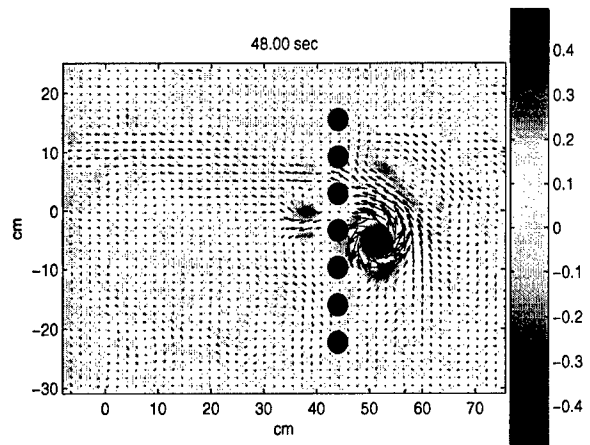


Figure 9: Velocity (arrows) and vorticity (colors) fields of a typical vortex in the experiments. The intersection of the red lines is the center of the vortex.  $r_i$  ( $i = 1 \dots 4$ ) are perpendicular distances from the center to the green lines. The circulation based on  $r_{av}$  is the sum of the vorticity at each of the yellow triangles.

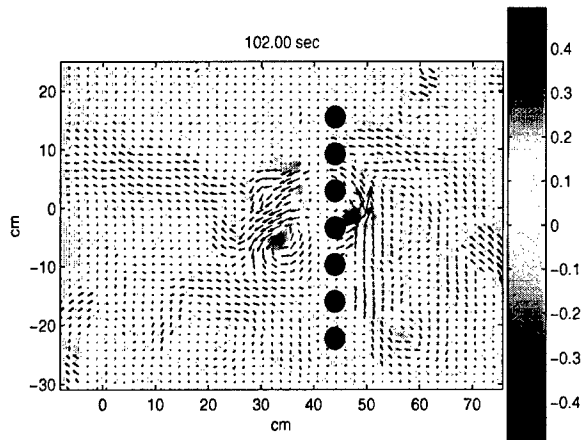
the southward movement of the vortex depends on the configurations.) The number of offsprings,  $N$ , was 1 in most cases, rarely 2, and never 0. The formation of large vortices downstream of the obstacles is surprising as the gap width was only  $16 \sim 40\%$  of the initial vortex diameter. Figures 10 & 11 show two laboratory experiments with  $G = 3$  cm. Figure 10 shows the velocity and vorticity fields for a configuration 7, while Figure 11 shows an experiment with configuration 3 in which a white sloping bottom and dye were used to visualize the flow. By Figures 12 & 13, our experimental results and the numerical observations [13] discussed in §1.2 can be compared. According to Figure 12, the relative reduction of vortex intensity tends to be large (small  $\Gamma_A/\Gamma_B$ ) for intense vortices (large  $\Gamma_B$ ), as observed in [13]. Figure 13(a) (Figure 13 (b)) is a plot of ' $D_{isl}/r_{av,B}$  vs  $N$ ' (' $D_{isl}/r_{av,B}$  vs Backward flow'), where  $D_{isl}$  is the total length of the 'middle' island (e.g.  $D_{isl} = D = 3.3$  cm for configuration 3,  $D_{isl} = 2D = 6.6$  cm for configuration 4 etc). So  $D_{isl}/r_{av,B}$  is equivalent to  $L/R_i$  used in [13]. Figure 13 (a) shows that, in most cases,  $N = 1$ , independently of the value of  $D_{isl}/r_{av,B}$  (or  $L/R_i$ ). This result is in disagreement with the main result of [13]. On the contrary, Figure 13 (b) agrees with a result of [13] because there is a backward flow when  $D_{isl}/r_{av,B}$  (or  $L/R_i$ ) is small. ([13] says a vortex did not 'notice' the existence of the islands if  $L/R_i$  is small.)



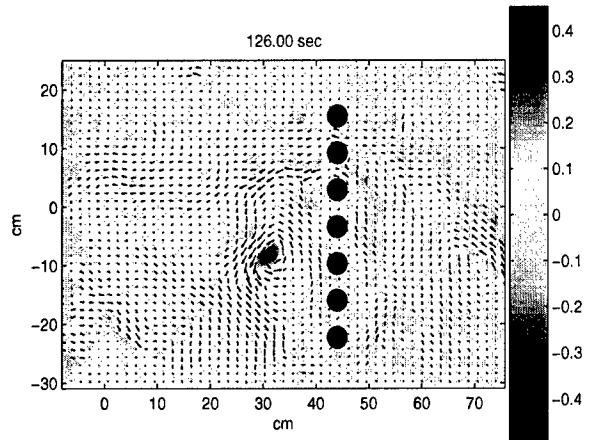
(a)



(b)



(c)

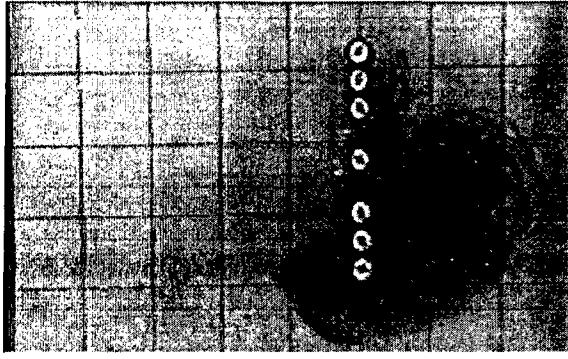


(d)

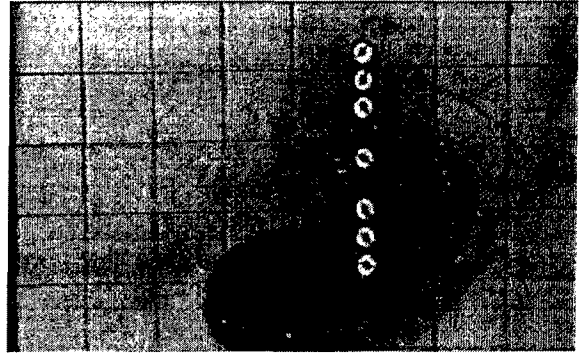
Figure 10: Velocity and vorticity fields for a configuration 7 experiment: (a) just before the interaction,  $t = 19.5\text{ s}$ ; (b) dipole formation,  $t = 48\text{ s}$ ; (c) the cyclonic part became dominant,  $t = 102\text{ s}$ ; (d) offspring formation,  $t = 126\text{ s}$ .

### 3.2 $G = 1.5\text{ cm}$ , $0.7\text{ cm}$

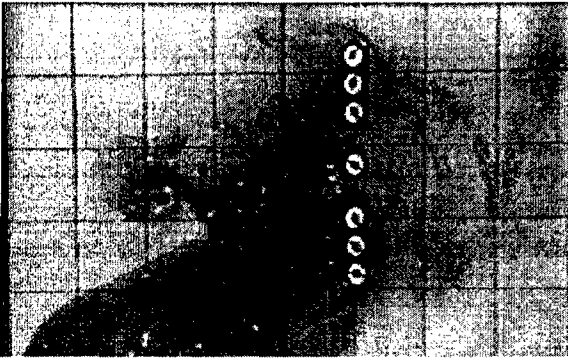
When  $G$  was decreased, a different behaviour was observed: when  $G = 1.5\text{ cm}$ , a small dipole still formed and the cyclonic part was dominant, and  $N = 0$  or  $1$ . When  $G = 0.7\text{ cm}$ , a small portion of the vortex leaked through the gaps but no coherent structure was formed (i.e. always  $N = 0$ ). The reason why the vortex generation was suppressed for  $G = 0.7\text{ cm}$



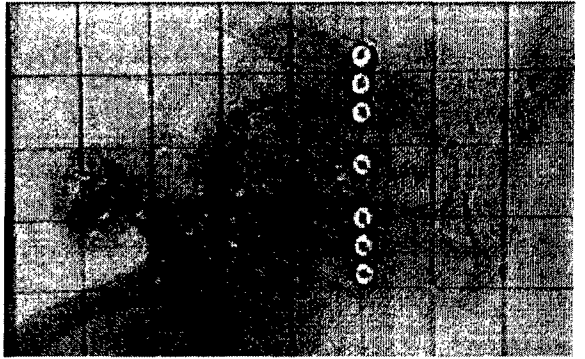
(a):  $t = 7\text{ s}$



(b):  $t = 48\text{ s}$



(c):  $t = 144\text{ s}$



(d):  $t = 182\text{ s}$

Figure 11: A dye experiment for a configuration 3: (a) just before the interaction,  $t = 7\text{ s}$ ; (b) dipole formation,  $t = 48\text{ s}$ ; (c) the cyclonic part became dominant,  $t = 144\text{ s}$ ; (d) offspring formation,  $t = 182\text{ s}$ .

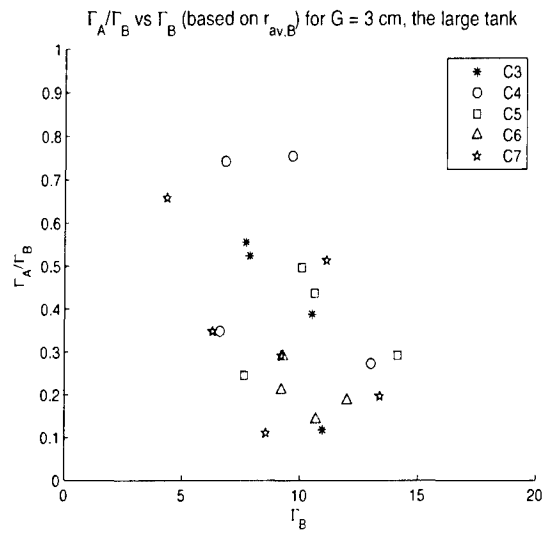


Figure 12:  $\Gamma_A/\Gamma_B$  vs  $\Gamma_B$ . The legend represents the configurations of the obstacles illustrated in Figure 8.

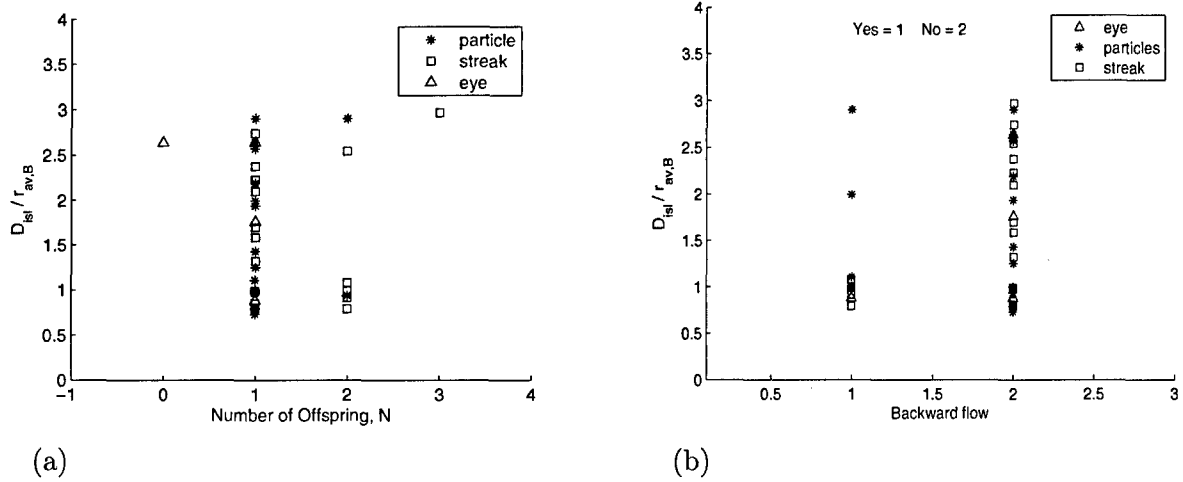


Figure 13: (a):  $D_{isl}/r_{av,B}$  vs  $N$  where  $D_{isl}$  is the total length of the ‘middle’ island (see the text for details), and  $r_{av,B}$  is  $r_{av}$  before interaction with the cylinders. (b):  $D_{isl}/r_{av,B}$  vs ‘Backward flow’. \* are experiments with a black bottom slope, analysed by particle tracking.  $\square$  and  $\triangle$  are experiments with a white bottom slope and dye, analysed by streak and eyes, respectively.

and was reduced for  $G = 1.5 \text{ cm}$  might be explained by considering the thickness of the boundary layers (b.l.s) over the vertical walls of the obstacles. (We are interested in only the zonal b.l.s since the flow through the gaps is zonal.) On the  $f$ -plane, the b.l thickness  $\delta$  is expressed as

$$\delta = LE_H^{1/2}/E_L^{1/4} = \nu^{1/4} H^{1/2} / \Omega^{1/4},$$

where  $E_L = \nu/(\Omega L^2)$  is the Ekman number based on the horizontal length scale  $L$ ,  $E_H = \nu/(\Omega H^2)$  is the Ekman number based on the vertical length scale  $H$ , and  $\Omega$  is the rotation rate of the system. In the laboratory,  $\nu = 0.01 \text{ cm}^2 \text{ s}^{-1}$ ,  $\Omega = f/2 = 0.125 \text{ s}^{-1}$ ,  $L = D = 3.3 \text{ cm}$ , and  $H = h_0 \approx 10 \text{ cm}$ .

$$\Rightarrow \boxed{\delta = 1.68 \text{ cm}}.$$

On the  $\beta$ -plane, two kinds of zonal Ekman b.l.s exist, namely

$$\delta_{zonal,m} = (\delta_m^3 L)^{1/4}, \quad \delta_{zonal,s} = (\delta_s L)^{1/2},$$

where  $\delta_m = (\nu/\beta_0)^{1/3}$  is the Munk b.l.,  $\delta_s = r/\beta_0$  is the Stommel b.l.,  $r = \delta_{Ek} f/(2H)$  is the linear friction coefficient,  $\beta_0$  is the beta parameter, and  $\delta_{Ek} = \sqrt{2\nu/f}$  is the bottom Ekman layer depth.  $\beta_0 = sf/H = 0.0125 \text{ s}^{-1} \text{ cm}^{-1}$  in the laboratory.

$$\Rightarrow \boxed{\delta_{zonal,m} = 1.26 \text{ cm}, \quad \delta_{zonal,s} = 0.97 \text{ cm}}.$$

Therefore, the largest thickness of these zonal b.l.s is  $1.68 \text{ cm}$ . If the gap width  $G$  between the cylinders is much smaller than  $3 \text{ cm}$ , then the viscous b.l.s occupy the entire region

within each gaps, and consequently, the presence of the b.l.s make the fluid within the gaps slow. This is the reason why the number of offsprings,  $N$ , decreased as  $G$  was reduced.

## 4 Conclusions and further studies

For  $G = 3\text{ cm}$ , a dipole was observed to form in most experiments for all the configurations of the islands, however the formation of two or more dipoles never occurred. This result invalidates our hypothesis. After a dipole formed, the cyclonic part of the dipole became dominant. Depending on the configurations of the obstacles and the initial vortex position, a relatively large offspring was produced either directly from the cyclonic part of the dipole, or from the “remnant” of the original vortex at the gap positioned just “South” of the gap where the dipole was formed. We also found that intense vortices experienced relatively greater amplitude loss than weak vortices, and the number of offspring,  $N$ , was 1 in general, independently of the size of the ‘middle’ islands. Observations of drifters in the Caribbean Sea [11] mentioned in §1.1 might be explained from our experimental results. According to [11], large energetic anticyclonic vortices were found downstream of the Lesser Antilles and translated westward while cyclonic vortices were observed primarily near boundaries in the Eastern Caribbean Sea. The weak cyclonic vortices may have been produced from the cyclonic part of a dipole formed when a NBC ring collided with the islands. It seems likely that the dominant anticyclonic offspring was formed either directly from the anticyclonic part of the dipole, or from the “remnant” of the original vortex (after the dipole formation). When  $G$  is smaller than a critical value ( $G \leq 0.7\text{ cm}$ ), no vortices were formed. This may suggest that for small enough island passages, no vortices are formed in the ocean due to the presence of b.l.s that can slow the fluid within the gaps. This hypotheses is hard to prove because the oceanic kinematic viscosity  $\nu$  is not known for this particular process.

In the present study, the vortices were cyclonic and barotropic. Moreover, they approached perpendicularly to the chain of obstacles. On the contrary, in the ocean, NBC rings are anticyclonic and baroclinic, and they move along an oblique direction to the line of the islands. It would be interesting to see how the results described above would be modified by the inclusions of these details (i.e. anticyclonic vortices, baroclinicity, direction of propagation) in the laboratory experiments.

*Acknowledgements:* I would like to thank C. Cenedese for a number of useful discussions and supports, and K. Bradley for preparation the experimental apparatus. This work was completed during the Geophysical Fluid Dynamics Summer School 2005 Program at the Woods Hole Oceanographic Institution.

## References

- [1] Adduce, C. & Cenedese, C. (2004) An experimental study of a monopolar vortex colliding with topography of varying geometry in a rotating fluid. *J. Marine Res.* **62**, 611-638.
- [2] Cenedese, C. & Fratantoni, D. M. & Adduce, C. (2005) Laboratory experiments on mesoscale vortices interacting with two islands. *J. Geophys. Res.* Vol **110**. In press.
- [3] Cenedese, C. (2002) Laboratory experiments on mesoscale vortices colliding with a seamount. *J. Geophys. Res.* **107**, (C6).
- [4] Cushman-Roisin, B. (1994) *Introduction to geophysical fluid dynamics*. Prentice Hall, Englewood Cliffs, New Jersey 07632.
- [5] Fratantoni, D. M. & Glickson, D. A. (2002) North Brazil Current rings generation and evolution observed with SeaWiFS. *J. Phys. Oceanogr.* **32**, 1058-1074.
- [6] Fratantoni, D. M. & Richardson, P. L. (2005) The evolution and demise of North Brazil Current rings. *J. Phys. Oceanogr.* Submitted.
- [7] Jones, W. E. & Lee, T. N. & Schott, F. A. & Zantopp, R. J. & Evans, R. H. (1990) The North Brazil Current retroflection: Seasonal structure and eddy variability. *J. Geophys. Res.* **95**, 22103-22120.
- [8] Kloosterzil, R. C. & van Heijst, G. J. F. (1991) An experimental study of unstable barotropic vortices in a rotating fluid. *J. Fluid Mech.* **223**, 1-24.
- [9] Linden, P. F. & Boubnov, B. M. & Dalziel, S. B. (1995) Source-sink turbulence in a rotating stratified fluid. *J. Fluid Mech.* **298**, 81-112.
- [10] McWilliams, J. C. (1984) The emergence of isolated coherent vortices in turbulent flow. *J. Fluid Mech.* **146**, 21-43.
- [11] Richardson, P. L. (2004) Caribbean Current and eddies as observed by surface drifters. *Deep-Sea Res II.* **52**, 429-463.
- [12] Schmitz, W. J. (1996) On the world ocean circulation. 1, Some global features North Atlantic Circulation. WHOI technical report, WHOI-96-03, June.
- [13] Simmons, H. L. & Nof, D. (2002) The squeezing of eddies through gaps. *J. Phys. Oceanogr.* **32**, 314-335.
- [14] Whitehead, J. A. & Stern, M. E. & Flierl, G. R. & Klinger, B. A. (1990) Experimental observations of baroclinic eddies on a sloping bottom. *J. Geophys. Res.* **95**, 9585-9610.





<b>REPORT DOCUMENTATION PAGE</b>	<b>1. REPORT NO.</b> WHOI-2006-12	<b>2.</b>	<b>3. Recipient's Accession No.</b>
<b>4. Title and Subtitle</b> 2005 Program of Studies: Fast Times and Fine Scales			<b>5. Report Date</b> July 2006
			<b>6.</b>
<b>7. Author(s)</b> Oliver Buhler and Charles Doering, Co-Directors; Joseph Keller, George C. Papanicolaou and Eric Vanden Eijnden, Principal			<b>8. Performing Organization Rept. No.</b>
<b>9. Performing Organization Name and Address</b> Woods Hole Oceanographic Institution Woods Hole, Massachusetts 02543			<b>10. Project/Task/Work Unit No.</b>
			<b>11. Contract(C) or Grant(G) No.</b> (C) OCE 03-25296 (G)
<b>12. Sponsoring Organization Name and Address</b> National Science Foundation			<b>13. Type of Report &amp; Period Covered</b> Technical Report
			<b>14.</b>
<b>15. Supplementary Notes</b> This report should be cited as: Woods Hole Oceanog. Inst. Tech. Rept., WHOI-2006-12.			
<b>16. Abstract (Limit: 200 words)</b> <p>The 2005 GFD program was entitled "Fast Times and Fine Scales" with a focus on asymptotic and stochastic modeling methods that exploit a physical scale separation of some kind. An extremely strong application pool resulted in the appointment of the unusually large class of eleven GFD Fellows for the summer. The first week consisted of principal lectures from Joe Keller on waves in fluids, ray methods and a variety of applications. The second week was divided between Eric Vanden-Eijnden's lectures on Brownian motion and stochastic differential equations, and George Papanicolaou's lectures on variational principles and asymptotic methods in homogenization theory. The principal lectures were particularly well-attended but the lecture room at Walsh Cottage proved up to the task of accommodating the full audience.</p> <p>Research lectures by staff and visitors were delivered daily throughout the program addressing topics ranging from applications of multiscale modeling methods in ocean and atmosphere dynamics, to applications of stochastic methods in populations dynamics and chemical kinetics, to applications of homogenization theory in materials science and engineering. The program also included a popular public lecture on the timely subject of tsunamis. And as usual this summer ended with the Fellows' reports including two experimental projects and theoretical work on a variety of problems inspired by the summer's research theme.</p> <p>Oliver Bühler and Charlie Doering acted as co-Directors for the summer. Janet Fields, Jeanne Fleming and Penny Foster provided the administrative backbone for the program. Keith Bradley supplied technical support, and Matt Finn ran the computer network and graciously helped with the production of the summer's proceedings volume. As always we are grateful to Woods Hole Oceanographic Institution for the use of Walsh Cottage, the perfect setting for the GFD program.</p>			
<b>17. Document Analysis a. Descriptors</b> asymptotic and stochastic modeling ocean and atmosphere dynamics multiscale modeling methods  <b>b. Identifiers/Open-Ended Terms</b>    <b>c. COSATI Field/Group</b>			
<b>18. Availability Statement</b> Approved for public release; distribution unlimited.		<b>19. Security Class (This Report)</b> UNCLASSIFIED	<b>21. No. of Pages</b> 309
		<b>20. Security Class (This Page)</b>	<b>22. Price</b>